Physics of the Solid State, Vol. 45, No. 4, 2003, pp. 605–609. Translated from Fizika Tverdogo Tela, Vol. 45, No. 4, 2003, pp. 577–581.

METALS AND SUPERCONDUCTORS

Vibrational and Electronic Properties of the Amorphous Systems $Ni_{44}Nb_{56}$, $Ni_{62}Nb_{38}$, and $Cu_{33}Zr_{67}$ as Derived from Specific Heat Measurements

G. Kh. Panova, G. F. Syrykh, M. N. Khlopkin†, and A. A. Shikov

Russian Research Centre Kurchatov Institute, pl. Kurchatova 1, Moscow, 123182 Russia

e-mail: shikov@isssph.kiae.ru

Received July 16, 2002

Abstract—The specific heats of the amorphous systems $Ni_{44}Nb_{56}$, $Ni_{62}Nb_{38}$, and $Cu_{33}Zr_{67}$ were studied in the temperature range 3–273 K. The data obtained allow one to isolate the contribution due to atomic vibrations from the experimentally measured specific heat, to determine the density of electronic states at the Fermi level and the temperature dependence of the characteristic Debye parameter Θ over a broad temperature range, and to calculate a few frequency moments that characterize the vibrational spectrum. The information derived on the average characteristics of vibrational spectra is in good agreement with earlier data on inelastic neutron scattering. In transferring from $Ni_{44}Nb_{56}$ to $Ni_{62}Nb_{38}$, the density of electronic states at the Fermi level decreases and the characteristic vibrational frequencies increase. The density of electronic states at the Fermi level for $Cu_{33}Zr_{67}$ is close to that for $Ni_{62}Nb_{38}$. The characteristic frequencies of the vibrational spectrum of the $Cu_{33}Zr_{67}$ system are substantially lower (by 30%) than those of the $Ni_{44}Nb_{56}$ and $Ni_{62}Nb_{38}$ systems. © *2003 MAIK "Nauka/Interperiodica".*

1. INTRODUCTION

Investigation of the dynamics of atomic vibrations and of the electronic properties of amorphous systems of the metal–metal type may broaden our understanding of many other physical properties of metallic glasses consisting of two or more components [1, 2]. The most complete and reliable information on the dynamics of such systems can be extracted from inelastic neutron scattering experiments made using the isotopic contrast method and, to a certain extent, from heat capacity measurements.

Information on the heat capacity measured within a broad temperature range allows one to judge the characteristics of the vibrational and electronic excitation spectra. It should be stressed that experimental data on low-temperature heat capacity offer the possibility of analyzing the low-frequency part of the vibrational spectrum ($\hbar\omega < 2$ meV), which is difficult to access using the inelastic cold-neutron scattering technique. Valuable information on the electronic properties can also be gained from data on the temperature dependence of heat capacity.

In this paper, we report on a thermodynamic investigation of integrated characteristics of vibrational and electronic excitation spectra in amorphous systems of the metal–metal type, namely, in $Cu_{33}Zr_{67}$ and the amorphous compounds $Ni_{44}Nb_{56}$ and $Ni_{62}Nb_{38}$, which differ in component concentration, and make a comparison of spectrum-averaged vibrational-frequency moments $\langle\omega^n\rangle$ derived from the temperature dependence of heat capacity and directly from neutron measurements.

2. EXPERIMENTAL TECHNIQUE

The heat capacity was measured on samples that were employed in inelastic neutron scattering experiments [3, 4]. Samples in the amorphous state were prepared by rapid quenching of the melt on the surface of a rotating copper disc in an inert atmosphere. The sample composition was verified using chemical analysis. The structure of the systems under study was determined from x-ray and neutron diffraction studies. The x-ray diffraction curves had an overall pattern typical of amorphous systems that exhibited a lack of long-range order.

The heat capacity of the samples was measured using the adiabatic pulsed-heating method on two setups, namely, a microcalorimeter intended for the interval 2–30 K (experimental error 1–2%) and an instrument covering the range from 4 to 300 K (error of 2% in the 3- to 5-K interval, 1% for 5–10 K, and 0.2–0.5% in the region 10–273 K).

3. EXPERIMENTAL RESULTS

The results of the heat capacity measurements conducted on amorphous metallic alloys at constant pressure are displayed in Figs. 1–4 and Tables 1 and 2. As seen from Fig. 1 and Table 1, throughout the tempera-

† Deceased.

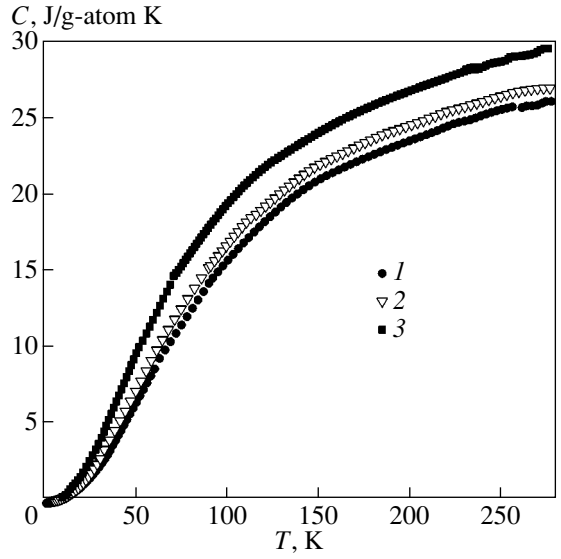

Fig. 1. Specific heat plotted vs. temperature in the range 3–270 K for (*1*) $Ni_{62}Nb_{38}$, (*2*) $Ni_{44}Nb_{56}$, and (*3*) $Cu_{33}Zr_{67}$ amorphous alloys.

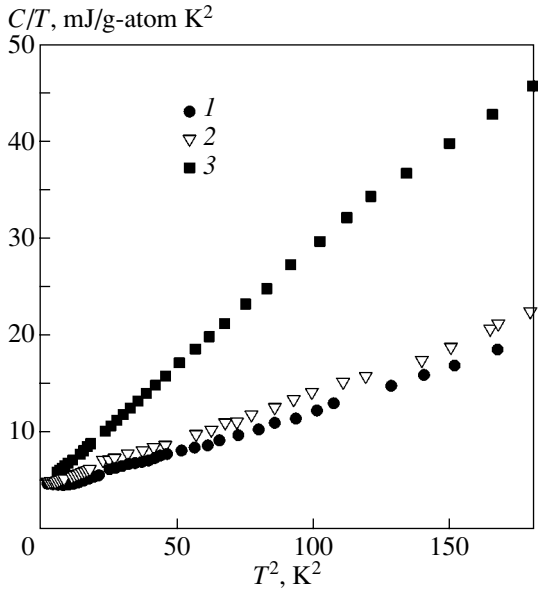

Fig. 2. Temperature dependence of the specific heat at low temperatures plotted in the C/T vs. T^2 coordinates for (*1*) $Ni_{62}Nb_{38}$, (*2*) $Ni_{44}Nb_{56}$, and (*3*) $Cu_{33}Zr_{67}$ amorphous alloys.

ture range covered, the specific heat of the $Ni_{44}Nb_{56}$ amorphous system is larger than that of $Ni_{62}Nb_{38}$ and the specific heat of $Cu_{33}Zr_{67}$ substantially exceeds that of the Ni–Nb alloys.

The temperature dependences of the specific heats measured at low temperatures (3–10 K) are plotted in Fig. 2 in the $C/T - T^2$ coordinates. One readily sees that, in the low-temperature domain, the specific-heat data are fitted well by the relation $C = \gamma T + \beta T^3$, which is a straight line when presented in the C/T vs. T^2 form. Note that the above relation holds for these amorphous systems within a broader temperature range than is the case with the Ni–B alloys [5]. In the region 3–10 K the rms deviation of experimental data from the $C = \gamma T + \beta T^3$ relation is about 1.5%.

Estimates of the coefficients γ and β obtained by least squares fitting of experimental data and the limiting low-temperature value of the characteristic Debye temperature Θ_L, which is related to β through $\beta = 12\pi^4 R/5\Theta_L^3$, are listed in Table 2. Here and in what follows, R is the gas constant.

As follows from Fig. 2 and Table 2, replacement of light nickel atoms by heavy niobium atoms brings about an increase in the coefficients for both terms that are linear or cubic in temperature, with the coefficient γ increasing by 25% and β increasing by 9%. The coefficients of the terms that are linear in temperature for $Cu_{33}Zr_{67}$ and $Ni_{62}Nb_{38}$ are similar in magnitude.

4. ANALYSIS AND DISCUSSION OF RESULTS

The vibrational specific heat C_{vib} was isolated from the experimentally measured quantity C_p by subtracting the correction C_A, which includes the contributions to the specific heat due to the anharmonic effects and thermal expansion of matter, as well as to conduction electrons:

$$C_{vib} = C_p - C_A = C_p - [\gamma + (A - \gamma)(C_{vib}/3R)^2]T, \quad (1)$$

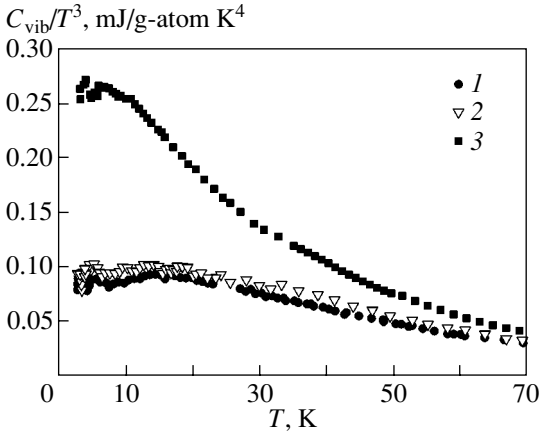

Fig. 3. Temperature dependence of the vibrational specific heat plotted in the C_{vib}/T^3 vs. T coordinates for (*1*) $Ni_{62}Nb_{38}$, (*2*) $Ni_{44}Nb_{56}$, and (*3*) $Cu_{33}Zr_{67}$ amorphous alloys.

where C_p is the molar heat capacity at constant pressure, C_{vib} is the vibrational component of the specific heat in harmonic approximation, γ is the coefficient in the low-temperature electronic specific heat, and A is the coefficient of the term that is linear in temperature for the isobaric specific heat at high temperatures.

The interpolation expression for C_A yields the corresponding linear-in-temperature asymptotic behavior for both low and high temperatures and provides a smooth transition between the low- and high-temperature asymptotic curves following a law similar to the Nernst–Lindemann expression.

The value of γ was determined following the standard technique from the low-temperature approximation of the temperature dependence of the specific heat $C = \gamma T + \beta T^3$. The quantity A, together with the parameters Ω_2, Ω_4, and Ω_* characterizing the vibrational spectrum, was derived from the high-temperature asymptotic approximation of the temperature dependence of the specific heat:

$$C_p = 3R\left[1 - \frac{1}{12}\left(\frac{\Omega_2}{T}\right)^2 + \frac{1}{240}\left(\frac{\Omega_4}{T}\right)^4 + \varphi\left(\frac{\Omega_*}{T}\right)\right] + AT, \quad (2)$$

where

$$\varphi(z) = \frac{z^2 \exp z}{1 - (\exp z)^2} - \left(1 - \frac{z^2}{12} + \frac{z^4}{240}\right).$$

This approximation for the asymptotic expansion of vibrational specific heat at high temperatures was proposed in [6] and used in [7, 8]. The quantities Ω_2 and Ω_4 are expressed in temperature units and are related to the frequency moments of the vibrational spectrum through the expression

$$(\Omega_n)^n = \langle \omega^n \rangle = \left(\int_0^\infty g(\omega)\omega^n d\omega\right)\left(\int_0^\infty g(\omega) d\omega\right)^{-1}. \quad (3)$$

Here, $g(\omega)$ is the vibrational density-of-states function. The quantity Ω_* in Eq. (2) is close in magnitude to Ω_n in Eq. (3) at $n = 6$.

By properly varying the four fitting parameters (A, Ω_2, Ω_4, Ω_*), we succeeded in fitting Eqs. (1)–(3) to the experimental results within the temperature region 60–260 K with an rms deviation of about 0.15%. The values of the parameters A, Ω_2, Ω_4, and Ω_* derived using Eqs. (1)–(3) from the high-temperature asymptotic behavior of the specific heat are presented in Table 2. Also given is the limiting high-temperature Debye temperature Θ_H, which is related to the rms frequency of the vibrational spectrum through

$$\Omega_2 = \Theta_H/\sqrt{3/5}.$$

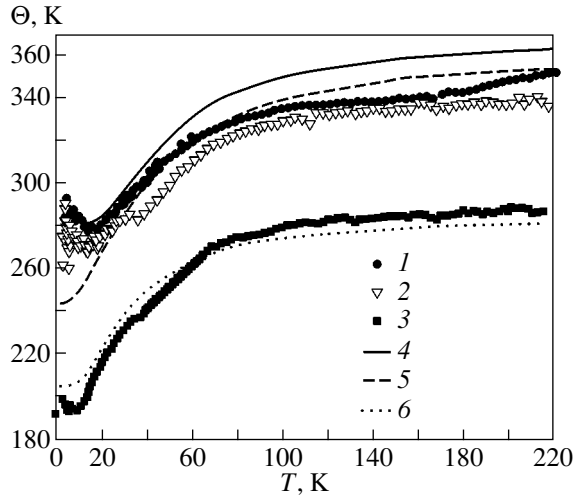

Fig. 4. Debye parameter Θ plotted vs. temperature T (*1–3*) as derived from heat capacity and (*4–6*) as calculated from the vibrational spectrum derived from inelastic neutron scattering measurements [3, 4] for (*1*, *4*) $Ni_{62}Nb_{38}$, (*2*, *5*) $Ni_{44}Nb_{56}$, and (*3*, *6*) $Cu_{33}Zr_{67}$.

The frequency moments of the vibrational spectrum that primarily characterize its low-energy part (average inverse, average logarithmic, and average frequencies) are expressed through integrals of the vibrational specific heat [8]. Those expressions were used to calculate the moments by performing integration over experimental points in the temperature region 10–270 K, while beyond this region, the specific heat was extrapolated with the use of either the low-temperature asymptotic function of the type of $C = \beta T^3$ or the high-temperature behavior in the Debye model spectrum, as was done in [9]. The results of the calculations are given in Table 2, which presents, to facilitate comparison, not the spectral moments $\langle \omega^n \rangle$ but rather the corresponding average frequencies Ω_n, determined in accordance with Eq. (3) and expressed in temperature units, and the average logarithm of frequency Ω_{ln}found from

$$\log(\Omega_{ln}) = \frac{\langle \omega^{-1} \ln \omega \rangle}{\langle \omega^{-1} \rangle} = \left(\int_0^\infty \frac{g(\omega)\ln\omega}{\omega} d\omega\right)\left(\int_0^\infty \frac{g(\omega)}{\omega} d\omega\right)^{-1}. \quad (4)$$

Because only phonons of energies $E < 5\,kT$ provide a substantial contribution to the vibrational heat capacity at temperature T, the low-temperature heat capacity contains information on the low-frequency part of the vibrational spectrum. The quantity C_{vib}/T^3 was shown in [10] to closely approximate the function $g(\omega)/\omega^2$ at $\omega = 4.93\,T$ at low temperatures and energies (the frequency is expressed here in temperature units). Therefore, the vibrational component of the heat capacity at low temperatures can be conveniently analyzed by plot-

Table 1. Specific heat at constant pressure C_p of the amorphous systems $Ni_{44}Nb_{56}$, $Ni_{62}Nb_{38}$, and $Cu_{33}Zr_{67}$ presented as a function of temperature T

T, K	C_p, J/g-atom K		
	$Ni_{44}Nb_{56}$ (1 g-atom = 77.85 g)	$Ni_{62}Nb_{38}$ (1 g-atom = 71.7 g)	$Cu_{33}Zr_{67}$ (1 g-atom = 82.09 g)
3	0.0150	0.0128	0.0185
4	0.0232	0.0191	0.0240
5	0.0335	0.0280	0.0510
6	0.0465	0.0395	0.0790
7	0.0628	0.0536	0.1157
8	0.0832	0.0708	0.1642
9	0.1080	0.0923	0.2234
10	0.1390	0.1203	0.2934
12	0.1760	0.1940	0.467
14	0.329	0.2937	0.688
16	0.469	0.422	0.956
18	0.642	0.580	1.265
20	0.846	0.769	1.610
22	1.079	0.988	1.987
25	1.486	1.371	2.622
30	2.355	2.144	3.873
35	3.056	3.117	5.309
40	4.732	4.150	6.82
45	5.91	5.23	8.30
50	7.10	6.33	9.69
55	8.27	7.44	11.00
60	9.42	8.52	12.16
70	11.60	10.66	14.50
80	13.52	12.55	16.42
90	15.22	14.24	18.05
100	16.73	15.75	19.45
120	19.18	18.24	21.70
140	21.05	20.14	23.14
160	22.49	21.62	24.77
180	23.64	22.79	25.87
200	24.58	23.73	26.82
220	25.37	24.51	27.64
240	26.05	25.18	28.37
260	26.65	25.76	29.05
273.15	27.01	26.11	29.46

ting the temperature dependence of specific heat as a C_{vib}/T^3 vs. T function. Figure 3 displays such graphs for the systems under study. This functional relation is traditionally used to analyze the deviation of the temperature dependence of heat capacity from the Debye law, according to which the vibrational heat capacity at low temperatures scales as the temperature cubed.

As is evident from Fig. 3, at temperatures below 10 K, the quantity $C_{vib}(T)/T^3$ remains practically constant. As the temperature increases, the quantity $C_{vib}(T)/T^3$ in the $Cu_{33}Zr_{67}$ system falls off monotonically, while in $Ni_{44}Nb_{56}$ and $Ni_{62}Nb_{38}$, it passes through a small maximum at 15 K and then decays smoothly with increasing temperature. The existence of the maximum is connected with the vibrational heat capacity deviating from the T^3 law, which indicates that there is rearrangement of the density of vibrational states in the low-frequency domain.

Note that the information contained in this relation loses its value with increasing temperature because of the fast decay of C_{vib}/T^3. Therefore, it is preferable to discuss the behavior of the temperature dependence of heat capacity within a broad temperature range in terms of the temperature dependence of the characteristic Debye parameter Θ which is a finer characteristic and determines, in particular, the rate with which $C_{vib}(T)$ reaches its high-temperature asymptotic course. Figure 4 presents temperature dependences of the characteristic parameter Θ for the systems under study, derived both from the heat capacity data obtained in this work and from the partial vibration energy spectra, obtained in inelastic neutron scattering experiments made using the isotopic contrast method in [3, 4]. In those experiments, the density of vibrational states at low energies (below 4 meV) was replaced by a quadratic relation of the type $g(\omega) = \text{const}\,\omega^2$, which joins smoothly with the experimental $g(\omega)$ data at $\hbar\omega = 4$ meV.

At temperatures above 10 K, both the absolute values of the Debye parameter and its variation with Ni concentration in the Ni–Nb alloys, as derived from heat capacity, agree well with those determined from neutron scattering measurements. The maximum difference between the neutron and calorimetric data in the temperature region 10–220 K does not exceed 6%.

At temperatures above 10 K for the $Cu_{33}Zr_{67}$ system and above 15 K for the systems $Ni_{44}Nb_{56}$ and $Ni_{62}Nb_{38}$, the Debye parameter Θ is observed to grow with increasing temperature, reaching a constant level above 70 K for $Cu_{33}Zr_{67}$ and above 100 K for the Ni–Nb systems. The range of variation of the Θ parameter with increasing temperature is 50% for $Cu_{33}Zr_{67}$ and 25% for the Ni–Nb systems.

Figure 4 and Table 2 also show that the average frequencies characterizing the vibrational spectrum moments increase by 4–5.5% as one goes from $Ni_{44}Nb_{56}$ to $Ni_{62}Nb_{38}$. This scale of frequency variation is in rough agreement with the $\Theta(T)$ relation expected to occur when the change in the average atomic mass M is taken into account.

As for the Cu–Zr system, the corresponding frequencies are substantially (by 30%) lower than those for the Ni–Nb systems, which implies a noticeable

Table 2. Parameters characterizing the amorphous systems $Ni_{44}Nb_{56}$, $Ni_{62}Nb_{38}$, and $Cu_{33}Zr_{67}$

Parameter	$Ni_{44}Nb_{56}$		$Ni_{62}Nb_{38}$		$Cu_{33}Zr_{67}$	
	from $C_p(T)$	from $g(\omega)$	from $C_p(T)$	from $g(\omega)$	from $C_p(T)$	from $g(\omega)$
γ, mJ/g-atom K^2	4.33		3.45		3.68	
β, mJ/g-atom K^4	0.0960		0.0883		0.267	
$N_F(0)$, state/eV atom	0.92		0.73		0.78	
Θ_L, K	272		280		194	
Θ_H, K	337	359	356	367	292	284
Ω_{ln}, K	171	171	179	182	132	139
Ω_{-2}, K	163	160	170	173	125	131
Ω_{-1}, K	196	203	207	213	157	164
Ω_1, K	241	258	255	265	199	205
Ω_2, K	261	278	276	284	226	220
Ω_4, K	278	310	293	313	248	243
Ω_*, K	282		298		255	
A, mJ/mol K^2	14.1		11.5		21	

Note: The coefficients γ and β approximate the specific heat at low temperatures in a relation of the type $C = \gamma T + \beta T^3$. $N_F(0)$ is the density of electronic states at the Fermi surface. Θ_L and Θ_H are the low- and high-temperature values of the characteristic Debye parameter, respectively. The quantities Ω_{-2}, Ω_{-1}, Ω_1, Ω_2, Ω_4, and Ω_{ln} characterize the average frequencies (moments) of the vibrational spectrum in accordance with Eqs. (3) and (4). This table presents data derived from the specific heat $C_p(T)$ and data calculated from the vibrational spectra $g(\omega)$ obtained in inelastic neutron scattering measurements made using the isotopic contrast method.

decrease in the force constants in this system as compared with the Ni–Nb system.

5. CONCLUSIONS

Thus, our studies permit the following conclusions. A change in the relative content of the Ni and Nb atoms brings about a change in both the phonon and electron subsystems. Significantly, the change in the phonon subsystem follows strictly that which occurs in the average atomic mass of the compound. For the $Cu_{33}Zr_{67}$ system, the quantity characterizing the vibrational frequency spectrum is smaller (by 30%) than that for the $Ni_{44}Nb_{56}$ and $Ni_{62}Nb_{38}$ alloys.

The general characteristic of the vibrational spectrum of the three systems ($Ni_{44}Nb_{56}$, $Ni_{62}Nb_{38}$, $Cu_{33}Zr_{67}$), as derived from the temperature dependence of heat capacity, is in agreement (within 6%) with the data obtained from inelastic neutron scattering measurements made using the isotopic contrast method.

An analysis of the low-frequency part of the vibrational spectrum ($\hbar\omega < 2$ meV), which is difficult to access using the inelastic neutron scattering technique, revealed that the density of electronic states at the Fermi level decreases as one goes over from $Ni_{44}Nb_{56}$ to $Ni_{62}Nb_{38}$, while for $Cu_{33}Zr_{67}$, the density of states is close in magnitude to that obtained for $Ni_{62}Nb_{38}$.

ACKNOWLEDGMENTS

The authors are indebted to M.G. Zemlyanov for helpful discussions and valuable criticism.

This study was supported by the Russian Foundation for Basic Research, project no. 00-02-16181.

REFERENCES

1. *Glassy Metals II. Atomic Structure and Dynamics, Electron Structure, Magnetic Properties*, Ed. by H. Beck and H.-J. Guntherodt (Springer, Berlin, 1983; Mir, Moscow, 1986); Top. Appl. Phys. **53** (1983).
2. G. Kh. Panova, in *Proceedings of V School on Neutron Physics, Alushta, 1986* (Ob. Inst. Yad. Issled., Dubna, 1987).
3. G. F. Syrykh, M. N. Khlopkin, S. N. Ishmaev, and P. I. Soldatov, J. Non-Cryst. Solids **192–193**, 282 (1995).
4. G. F. Syrykh, S. N. Ishmaev, M. G. Zemlyanov, and I. L. Sashin, J. Non-Cryst. Solids **250–252**, 642 (1999).
5. G. Kh. Panova, M. N. Khlopkin, N. A. Chernoplekov, and A. A. Shikov, Fiz. Tverd. Tela (St. Petersburg) **44** (7), 1168 (2002) [Phys. Solid State **44**, 1218 (2002)].
6. V. N. Naumov, Phys. Rev. B **49** (18), 13247 (1994).
7. M. I. Katsnelson, I. I. Naumov, A. V. Trefilov, *et al.*, Philos. Mag. B **75** (3), 389 (1997).
8. A. Junod, Solid State Commun. **33** (1), 55 (1980).
9. A. V. Mirmel'shteĭn, A. E. Kar'kin, V. E. Arkhipov, and V. I. Voronin, Fiz. Met. Metalloved. **58** (5), 1008 (1984).
10. A. Junod, T. Jarlborg, and J. Muller, Phys. Rev. B **27** (3), 1568 (1983).

Translated by G. Skrebtsov

Physics of the Solid State, Vol. 45, No. 4, 2003, pp. 610–614. Translated from Fizika Tverdogo Tela, Vol. 45, No. 4, 2003, pp. 582–596.

METALS AND SUPERCONDUCTORS

Calculation of the Vibrational Spectra of Copper Crystals with Vacancies

A. N. Kislov, V. G. Mazurenko, and K. N. Korzov

Ural State Technical University, ul. Mira 19, Yekaterinburg, 620002 Russia

e-mail: ank@dpt.ustu.ru

Received September 4, 2002

Abstract—The local vibrational spectra of copper crystals containing vacancies are calculated using the pair atomic potential derived in the framework of the resonance pseudopotential theory. The calculations are performed by a recursive method with due regard for the symmetry of the defect region. The frequencies of the vacancy-induced resonance vibrations of different symmetries are determined. © *2003 MAIK "Nauka/Interperiodica".*

1. INTRODUCTION

Investigation into the physicochemical and mechanical properties of copper crystals with different structural defects has attracted the particular attention of researchers, because these materials are widely used in many fields of engineering. The study of the phenomena associated with atomic vibrations in the vicinity of defects is of considerable practical interest. There are a number of works dealing with the effect of vacancies (i.e., the simplest structural point defects) on the phonon subsystem of copper crystals [1, 2]. The data obtained in these works and numerous investigations concerned with the effect of intrinsic defects on the properties of copper [3–7] have revealed that the results of calculations are very sensitive to the type of interatomic interaction potential used. In this respect, correct description of the real interatomic interaction is important for the simulation of processes with the participation of defects.

In the majority of earlier works, the physical characteristics of copper crystals were calculated in the approximation of the pair central interaction. In this case, the interatomic forces, as a rule, can be described using the Morse [1, 3, 5–7], Born–Mayer [4], and other [2, 8] empirical pair potentials. The parameters of these potentials are fitted to the available experimental data. In addition to the aforementioned potentials, a number of more physically justified pair potentials, which were derived within different approaches applied in terms of the pseudopotential theory, have also been used in calculations [9–15]. In particular, Lam *et al.* [12] obtained the potential for copper crystals in the framework of the resonance potential theory developed by Dagens [13]. Vaks *et al.* [14] and Antonov *et al.* [15] used the potentials determined on the basis of the local pseudopotential theory. More recent calculations have been performed within the models allowing for different additional contributions to the pair atomic potential [16–21].

Analysis of the data available in the literature has demonstrated that the potential obtained by Lam *et al.* [12] for copper crystals is one of the most reliable pair atomic potentials. The adequacy of this potential for the correct determination of the physical characteristics of copper crystals is confirmed by the fact that the results of calculations of the dispersion curves [22, 23] and energy characteristics of intrinsic point defects [12] are in good agreement with experimental data.

In [1, 2], the phonon spectra of copper crystals with vacancies were calculated using interatomic potentials that poorly reproduced the vibrational spectrum of the copper crystal with a perfect structure. In our opinion, the authors of these works obtained incorrect quantitative data on defect-induced vibrations.

In the present work, the atomic structure and vibrational spectra of copper crystals containing vacancies were calculated in the harmonic approximation with the use of the pair atomic potential proposed in [12] but with allowance made for the symmetry of the defect region.

2. COMPUTATIONAL TECHNIQUE, RESULTS, AND DISCUSSION

The interatomic potential $\varphi(r)$ [12] used for simulating the lattice dynamics is a long-range oscillating potential. By virtue of its long-range character, the application of the $\varphi(r)$ potential to the calculation of the vibrational spectrum of a copper crystal with vacancies involves considerable difficulties. The problem concerning the constraint of the effective range of a potential of this type was treated by Vaks *et al.* [14], who calculated the energy of formation of a vacancy. The results of calculations showed that relaxation of the lattice to a new equilibrium configuration is governed pri-

marily by the short-range part of the interatomic potential. The truncation of the potential after approximately six oscillations does not lead to appreciable errors. With this potential, the energies of formation of point defects can be calculated to sufficient accuracy.

As is known, the elastic constants and phonon frequencies are determined by the first and second derivatives of the potential energy of interatomic interaction with respect to the interatomic distance r. For the interatomic potential $\varphi(r)$ described in [12], the first and second derivatives obtained for closely spaced atoms are substantially larger than those for atoms separated by distances r larger than 5.5 Å. Therefore, we can make the inference that the dynamic and elastic properties can be described with some error if the interaction of each atom with its surrounding atoms located inside a sphere of radius 5.5 Å is taken into account. The inclusion of the long-range Friedel oscillations in the potential leads to a decrease in the error when calculating the elastic constants and phonon frequencies.

With the aim of determining the optimum effective range of the interatomic potential $\varphi(r)$ and elucidating the influence of this range on the dynamic and elastic characteristics, we calculated the dispersion curves $\nu(\mathbf{q})$ for three high-symmetry directions of the Brillouin zone and the elastic constants for a perfect copper crystal.

The dispersion curves calculated using the potential $\varphi(r)$ with effective ranges of 15.0 and 5.5 Å are similar to each other and agree reasonably with data on the phonon frequencies obtained from inelastic neutron scattering experiments [24, 25]. In both cases, the frequencies of the transverse phonon branch at the boundary of the Brillouin zone in the vicinity of the X point differ only slightly from the experimental frequencies.

The calculated elastic constants are as follows: C_{11} = 181 GPa, C_{12} = 143 GPa, and C_{44} = 99 GPa for a potential range of 5.5 Å and C_{11} = 183 GPa, C_{12} = 121 GPa, and C_{44} = 75 GPa for a potential range of 15.0 Å. As is seen, the numerical values of the elastic constants C_{12} and C_{44} differ insignificantly. In [26, 27], the elastic constants C_{11} = 177 GPa, C_{12} = 125 GPa, and C_{44} = 81 GPa (extrapolated to the corresponding values at T = 0 K) were experimentally obtained from the longitudinal and transverse ultrasonic wave velocities. It is evident that the elastic constants calculated with the interatomic potential truncated at 15.0 Å are in better agreement with the experimental data. Note that the largest deviation (8%) from the experimental value is observed for the elastic constant C_{44}. At the same time, the elastic constants determined using the potential with an effective range of 5.5 Å are also in reasonable agreement with the experimental data. In this case, the largest difference (approximately 22%) between the calculated and experimental values is observed for the elastic constant C_{44}.

Reasoning from the above results and the fact that the calculations of the dynamics of the copper lattice with vacancies are significantly complicated in the case when the long-range part of the interatomic potential is taken into account, we chose the potential with an effective range of 5.5 Å for our calculations of the vibrational spectra of copper crystals with vacancies.

The formation of a vacancy in the metal lattice is accompanied by changes in the states of the ionic and electronic subsystems of the metal. These states correspond to new equilibrium conditions; as a result, the atoms arranged about the vacancy are displaced to new equilibrium positions. The distortion of the crystal lattice in the vicinity of the vacancy in the bulk of the crystal was determined by minimizing the potential energy of the vacancy-containing metal in the framework of the lattice statics method [28]. For an equilibrium configuration, the energy of formation of a vacancy was calculated in the constant volume approximation [12, 14, 29]. This energy is found to be equal to 1.36 eV, which agrees well with the energies obtained in similar calculations with the same interaction potential: 1.42 [12] and 1.45 eV [29]. The difference between the numerical values is associated with the fact that the above calculations were performed using the interatomic potentials with different effective ranges. Moreover, in [12, 29], the interatomic potential before the truncation was replaced by the effective potential. Note that the experimentally found energy of formation of a vacancy in the copper lattice is 1.31 eV [12].

According to our calculations, the largest displacements toward the vacancy are observed for the nearest neighbor atoms located along the [110] direction. It should be noted the atoms of the second and third coordination spheres also relax toward the vacancy. The displacements of the atoms located in the first, second, and third coordination spheres are equal to 0.031, 0.003, and 0.016 Å, respectively. The atoms of the other coordination shells also change their equilibrium positions. However, since these atomic displacements are relatively small, they are disregarded in calculations of the lattice dynamics.

The distortion of the metal lattice leads to changes in the conditions of atomic vibrations. As a consequence, there can arise resonance local vibrations. In real physical processes with the participation of phonons, these vibrations often play an important role. The atomic vibrations are most strongly disturbed by the vacancy in its nearest environment. For atoms of the next coordination shells, the effect of the vacancy weakens as the distance from it increases. On this basis, we calculated the local densities of phonon states in the region consisting of the first two coordination spheres and containing the vacancy.

It is known that, in a physical process involving phonons, vibrations can be active when they are allowed by the symmetry selection rules for this process. Therefore, in order to simplify analysis of the

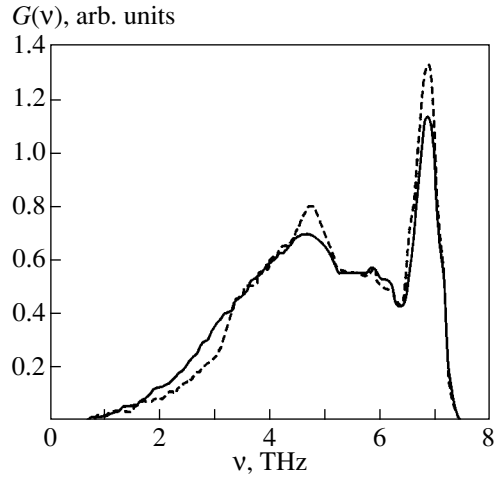

Fig. 1. Total densities of phonon states for copper with a perfect structure (dashed line) and copper with vacancies (solid line). The calculations are performed using the recursive method.

experimental data, the calculations should be carried out with due regard for the symmetry of the vibrations. For this reason, as in our earlier work [30], we calculated the symmetrized local densities of phonon states. These densities characterize the dependence of the square of the amplitude of the symmetrized atomic displacements on the frequency of normal vibrations. The symmetrized local density of phonon states is related to the imaginary part of the diagonal element of the Fourier transform of the one-particle Green's function for displacements. In turn, the diagonal element is determined by the dynamic matrix constructed in real space for a particular atomic cluster. The use of the recursive method [31] makes it possible to transform the dynamic matrix into a three-diagonal form. As a result, the diagonal element of the Green's function takes the form of a readily calculable continued fraction. The computational algorithm used was described in more detail in [30]. Note that the summation of the symmetrized local densities of phonon states over all possible vibrational modes for the metal with a perfect or defect structure gives the corresponding total density of phonon states $G(\nu)$. In order to separate the vibrations associated with the vacancy, the symmetrized local densities of phonon states for the metal with a perfect structure were compared with those for the vacancy-containing metal. The frequency of the localized vibrations induced by the vacancy was determined from the maxima in the symmetrized local density of phonon states for the metal with the vacancy provided these maxima did not coincide with the maxima in the symmetrized local density of phonon states for the perfect metal.

When calculating the symmetrized local densities of phonon states in the framework of the recursive method, the initial vectors were chosen in the form of symmetrized displacements, which, in turn, were taken as the normal coordinates of the region composed of two coordination spheres about a copper atom subsequently replaced by a vacancy. The center of this region occupies a position characterized by the symmetry group O_h. According to the group-theoretic analysis, the vibration representation $\Gamma(57 \times 57)$ for 19 atoms of this region can be divided into irreducible representations of the point group O_h as follows:

$$\Gamma(57 \times 57) = 2A_{1g} + A_{2g} + 3E_g + 3F_{1g} + 3F_{2g} + A_{2u} + E_u + 6F_{1u} + 3F_{2u}.$$

For a specific symmetry Γ, the symmetrized local densities of phonon states $G_\Gamma^0(\nu)$ for a perfect copper crystal and $G_\Gamma(\nu)$ for a copper crystal with a vacancy were calculated using the basis vector of the irreducible representation as the initial vector. The basis vector was determined by standard methods of the group theory.

Exact calculation of the density of phonon states in the bulk of the crystal requires the construction of the dynamic matrix for an atomic cluster of sufficiently large size. In our calculations performed for a spherically symmetric cluster ~77 Å in size (containing approximately 20000 atoms), we obtained 18 pairs of exact recursive coefficients, which were then used for calculating the density of phonon states. The validity of the interatomic interaction model with the aforementioned cluster was verified by calculating the total density of phonon states $G(\nu)$ for a perfect copper crystal (Fig. 1) with the use of the recursive method. A comparison shows that the results obtained in these calculations are in good agreement with data on the total density $G(\nu)$ determined by integrating over the Brillouin zone [24, 25].

The symmetrized local densities of phonon states for all symmetries in the copper crystal with a vacancy were calculated using the above procedure. For the copper crystal with a perfect structure and the copper crystal with a vacancy, Fig. 2 shows the symmetrized local densities of phonon states projected onto the A_{2g} displacements of the atoms in the first coordination sphere with respect to an atom subsequently replaced by a vacancy. It can be seen that the local density of states is redistributed in the low- and high-frequency ranges of the vibrational spectrum. Resonance vibrations are induced at frequencies $\nu(A_{2g}) = 3.0$, 5.9, and 6.8 THz. The calculated frequencies of vacancy-induced resonance vibrations of different symmetries are listed in the table.

Note that, in [1], the localized vibrations with due regard for the symmetry in vacancy-containing copper crystals were also calculated using interatomic potentials of three types. However, as was noted above, the quantitative results obtained in [1] are incorrect. The reason for this is that, unlike our results, the elastic constants and phonon spectra calculated in [1] with the use of these potentials for copper crystals with a perfect

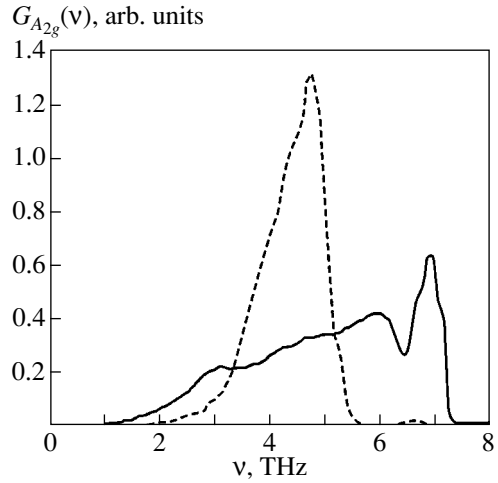

Fig. 2. Symmetrized local densities of phonon states projected onto the A_{2g} displacements of the atoms of the first coordination sphere for the copper crystal with a perfect structure (dashed line) and the copper crystal with a vacancy (solid line). The calculations are performed using the recursive method.

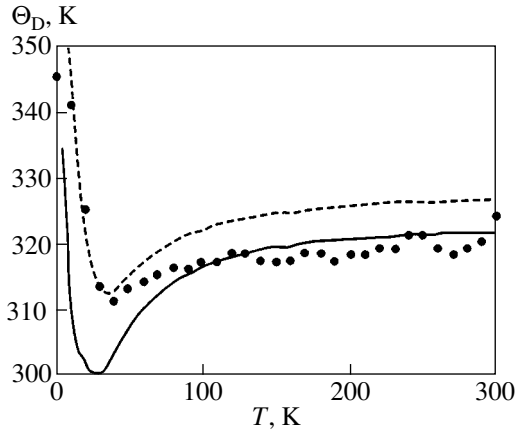

Fig. 3. Temperature dependences of the Debye temperature for the copper crystal with a perfect structure (dashed line) and the copper crystal with vacancies (solid line). Points are the experimental data taken from [32, 33] for the copper crystal with a perfect structure.

structure differ significantly from the experimental data.

We calculated the total density of phonon states for copper crystals with vacancies in the approximation of noninteracting vacancies with a concentration approximately equal to 2%. Figure 1 presents the results of these calculations and the total density of phonon states for a perfect copper crystal. As follows from the comparison of the results obtained, the formation of vacancies leads to an increase in the total density of phonon states in the low-frequency range below 3.0 THz and at frequencies close to 5.9 THz. Hence, it can be assumed that the transformation from a perfect copper structure into a defect structure should be accompanied by variations in the thermodynamic properties of the copper crystal.

The problem regarding the influence of the vacancy formation on the temperature dependence of the Debye temperature $\Theta_D(T)$ is of special interest. It is common knowledge that the calculation of the Debye temperature $\Theta_D(T)$ involves, first, the calculation of the lattice heat capacity $C_V(T)$ at a constant volume (recall that the lattice heat capacity $C_V(T)$, which, like any thermodynamic function in the harmonic approximation, is an additive function of natural frequencies, i.e., it depends on the total density of phonon states $G(\nu)$ [24]) and, second, the standard calculation of $C_V(T)$ in the Debye approximation [24].

Figure 3 shows the temperature dependence of the Debye temperature $\Theta_D(T)$ calculated for the copper crystal with a perfect structure within the approach proposed in [24]. For comparison, the Debye temperatures determined from the experimental lattice heat capacities $C_V(T)$ [32, 33] are also given in Fig. 3. It should be noted that the Debye temperatures $\Theta_D(T)$ at $T = 0$ K were obtained using the method described by Jules de Launay [34], who used the elastic constants in the calculation. In our case, the calculated Debye temperatures $\Theta_D(T)$ are somewhat higher than the experimental Debye temperatures over the entire range of temperatures from 0 to 300 K. This can be explained by the inaccuracy in calculating the frequency distribution function $G(\nu)$ due to the approximations used in our model.

The temperature dependence of the Debye temperature $\Theta_D(T)$ for the copper crystal with vacancies (Fig. 3) was also determined using the calculated frequency distribution function $G(\nu)$ (Fig. 1). It can be seen from Fig. 3 that, over the entire temperature range covered,

Frequencies (in THz) of vacancy-induced resonance atomic vibrations of different symmetries in copper

Coordination sphere	A_{1g}	A_{2g}	A_{2u}	E_g	E_u	F_{1g}	F_{2u}	F_{2g}	F_{2u}
First	4.4	3.0	3.0	3.0	5.9	3.0	3.0	4.6	3.0
		5.9	4.8		6.8		4.3		6.8
		6.8							
Second	6.8			5.9		5.9			4.6

the Debye temperatures $\Theta_D(T)$calculated for the copper crystal with vacancies are less than those calculated for the copper crystal with a perfect structure. Since the Debye temperature $\Theta_D(T)$ accounts for the nature of the interatomic forces, the obtained result agrees well with the fact that the vacancy formation leads to a weakening of the interatomic interaction in the vicinity of the vacancy.

3. CONCLUSIONS

Thus, the effect of bulk vacancies on the vibrational spectra of copper crystals was investigated using the interatomic potential proposed by Lam *et al.* [12]. The frequencies of vacancy-induced resonance vibrations of different symmetries in a copper crystal were calculated with allowance made for the atomic displacements in the vicinity of the vacancy. As far as we know, experimental data on the resonance vibrations induced by vacancies in copper crystals are not available in the literature. In this respect, we believe that our results can predict the effect of a vacancy on the vibrational spectrum of copper and serve as a basis for the experimental verification of this effect. Moreover, we calculated the temperature dependences of the Debye temperature $\Theta_D(T)$ for copper crystals containing vacancies and free of them. The data obtained can be used to interpret the physical processes associated with the presence of vacancies in copper crystals.

REFERENCES

1. P. L. Land and B. Goodman, J. Phys. Chem. Solids **28** (2), 113 (1967).
2. R. Yamamoto, K. Haga, and M. Doyama, J. Phys. Soc. Jpn. **48** (1), 341 (1980).
3. L. A. Girifalco and V. G. Weizer, J. Phys. Chem. Solids **12** (3/4), 260 (1960).
4. R. A. Jonson, Phys. Chem. Solids **26** (1), 75 (1965).
5. R. M. J. Cotterill and M. Doyama, Phys. Rev. **145** (2), 465 (1966).
6. A. Sholz and C. Lehmann, Phys. Rev. B **6** (3), 813 (1972).
7. H. R. Schober, J. Phys. F **7** (7), 1127 (1977).
8. D. M. Esterling and A. Swaroop, Phys. Status Solidi B **96** (1), 401 (1979).
9. J. A. Moriarty, Phys. Rev. B **6** (4), 1239 (1972).
10. A. O. E. Animalu, Phys. Rev. B **8** (8), 3542 (1973).
11. A. O. E. Animalu, Phys. Rev. B **8** (8), 3555 (1973).
12. N. Q. Lam, L. Dagens, and N. V. Doan, J. Phys. F **13** (12), 2503 (1983).
13. L. Dagens, J. Phys. F **7** (7), 1167 (1977).
14. V. G. Vaks, V. G. Kapinos, Yu. N. Osetskiĭ, *et al.*, Fiz. Tverd. Tela (Leningrad) **31** (3), 139 (1989) [Sov. Phys. Solid State **31**, 427 (1989)].
15. V. N. Antonov, V. Yu. Milman, V. V. Nemoshkalenko, and A. V. Zhalko-Titarenko, Z. Phys. B **79** (2), 223 (1990).
16. M. I. Baskes and C. F. Melius, Phys. Rev. B **20** (8), 3197 (1979).
17. K. Maeda, V. Vittek, and A. P. Sutton, Acta Metall. **30** (11), 2001 (1982).
18. R. H. Rautioaho, Phys. Status Solidi B **115** (1), 95 (1983).
19. S. M. Foiles, M. I. Baskes, and M. S. Daw, Phys. Rev. B **33** (12), 7983 (1986).
20. S. Erkoc, Phys. Status Solidi B **171** (2), 317 (1992).
21. Jian-Yun Fang, R. L. Johnston, and J. N. Murrell, J. Chem. Soc., Faraday Trans. **89** (11), 1659 (1993).
22. J. C. Upadhyaya and L. Dagens, J. Phys. F **8** (2), L21 (1978).
23. J. C. Upadhyaya and L. Dagens, J. Phys. F **9** (11), 2177 (1979).
24. E. C. Svensson, B. N. Brockhouse, and J. M. Rowe, Phys. Rev. **155** (3), 619 (1967).
25. R. M. Nicklow, G. Gilat, H. G. Smith, *et al.*, Phys. Rev. **164** (3), 922 (1967).
26. W. C. Overton, Jr. and J. Gaffney, Phys. Rev. **98** (4), 969 (1955).
27. A. G. Denisov, I. I. Novikov, and V. B. Proskurin, Fiz. Met. Metalloved. **39** (2), 375 (1975).
28. D. D. Richardson, Comput. Phys. Commun. **28** (1), 75 (1982).
29. V. G. Kapinos, Yu. N. Osetskiĭ, and P. A. Platonov, Fiz. Tverd. Tela (Leningrad) **28** (12), 3603 (1986) [Sov. Phys. Solid State **28**, 2031 (1986)].
30. V. G. Mazurenko and A. N. Kislov, Fiz. Tverd. Tela (St. Petersburg) **34** (11), 3403 (1992) [Sov. Phys. Solid State **34**, 1822 (1992)].
31. R. Haydock, V. Heine, and M. J. Kelly, J. Phys. C **5** (20), 2845 (1972).
32. D. L. Martin, Can. J. Phys. **38** (1/3), 17 (1960).
33. G. Ahlers, J. Chem. Phys. **41** (1), 86 (1964).
34. Jules de Launay, J. Chem. Phys. **30** (1), 91 (1959).

Translated by O. Borovik-Romanova

Physics of the Solid State, Vol. 45, No. 4, 2003, pp. 615–618. Translated from Fizika Tverdogo Tela, Vol. 45, No. 4, 2003, pp. 587–589.

SEMICONDUCTORS AND DIELECTRICS

Thermopower in the Region of Hopping Conduction in $TlNiS_2$

S. N. Mustafaeva, É. M. Kerimova, and A. I. Dzhabbarly

Institute of Physics, National Academy of Sciences of Azerbaijan, pr. Dzhavida 33, Baku, 370143 Azerbaijan

Received June 13, 2002

Abstract—Samples of the composition $TlNiS_2$ in the hexagonal system with the unit cell parameters a = 12.28 Å, c = 19.32 Å, and ρ = 6.90 g/cm^3 are synthesized. The results of the investigation into the electrical and thermoelectrical properties of $TlNiS_2$ samples in the temperature range 80–300 K indicate that $TlNiS_2$ is a p-type semiconductor. It is found that, at temperatures ranging from 110 to 240 K, $TlNiS_2$ samples in a dc electric field possess variable-range-hopping conduction at the states localized in the vicinity of the Fermi level. The density of localized states near the Fermi level is determined to be $N_F = 9 \times 10^{20}$ eV^{-1} cm^{-3}, and the scatter of the states is estimated as $J \approx 2 \times 10^{-2}$ eV. In the temperature range 80–110 K, $TlNiS_2$ exhibits activationless hopping conduction. At low temperatures (80–240 K), the thermopower of $TlNiS_2$ is adequately described by the relationship $\alpha(T) = A + BT$, which is characteristic of the hopping mechanism of charge transfer. In the case when the temperature increases to the temperature of the onset of intrinsic conduction with the activation energy ΔE = 1.0 eV, there arise majority intrinsic charge carriers of both signs. This leads to an increase in the electrical conductivity σ and, at the same time, to a drastic decrease in the thermopower α; in this case, the thermopower is virtually independent of the temperature. © *2003 MAIK "Nauka/Interperiodica".*

1. INTRODUCTION

Chalcogenides of the general formula $Tl\mathit{MeX}_2$ (*Me* = Cr, Fe, or Co; and *X* = S, Se, or Te) are representatives of a new class of magnetic semiconductors. The electrical, magnetic, and thermal properties of these compounds were studied earlier in [1–7]. In the present work, we propose a method of synthesizing $TlNiS_2$ samples and present the results of investigations into the electrical and thermodynamic properties of the prepared compound.

2. SAMPLE PREPARATION AND EXPERIMENTAL TECHNIQUE

The synthesis of $TlNiS_2$ was carried out in an ampule evacuated to a pressure of 10^{-3} Pa. The ampule was fabricated from a fused silica tube. In this case, $TlNiS_2$ samples were prepared through the interaction of initial elements (Tl, Ni, S) of high-purity grade. In order to prevent explosion of the ampule filled with reactants, the furnace temperature was raised to the melting temperature of sulfur (391 K) and the ampule was held at this temperature for 3 h. Then, the furnace temperature was raised to 1400 K at a rate of 100 K/h and the ampule was held at this temperature for 1.5–2.0 h, after which it was cooled to 300 K. Thereafter, the ampule was broken; the alloy contained in it was crushed to powder; the powder thus prepared was placed in a new ampule, which was then evacuated to a pressure of 10^{-3} Pa; and the above process was repeated with subsequent cooling to 600 K. At this temperature, the $TlNiS_2$ sample was annealed for 240 h.

The $TlNiS_2$ samples thus synthesized were subjected to x-ray powder diffraction analysis on a DRON-3M diffractometer (CuK_α radiation, Ni filter, λ_α = 1.5418 Å). The x-ray diffraction patterns were recorded continuously. The diffraction angles were determined by measuring the intensity peaks. The error in determining the angles of reflection did not exceed 0.02°. For the $TlNiS_2$ sample, 24 diffraction reflections measured were unambiguously indexed in the hexagonal system with the lattice parameters a = 12.28 Å, c = 19.32 Å, and ρ = 6.90 g/cm^3.

The $TlNiS_2$ samples used in electrical measurements had the form of parallelepipeds 12.2 × 5.2 × 1.6 mm in size. The ohmic contacts were produced through the electrolytic deposition of copper. The electrical conductivity σ and the thermopower α of the $TlNiS_2$ samples prepared were measured by the four-point probe method with an accuracy up to 1% in the temperature range 80–300 K.

3. RESULTS AND DISCUSSION

The results of the investigations into the electrical and thermodynamic properties of $TlNiS_2$ samples are presented below. Figure 1 depicts the temperature dependence of the thermopower for $TlNiS_2$ in the temperature range 80–300 K. As the temperature increases from 80 K, the thermopower increases first moderately and then more rapidly and, at $T \approx 235$ K, reaches a max-

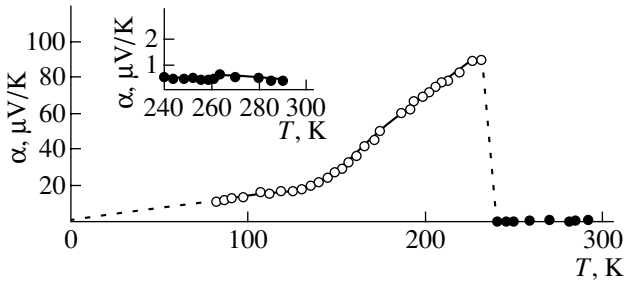

Fig. 1. Temperature dependence of the thermopower in $TlNiS_2$. The inset shows the high-temperature branch $\alpha(T)$ on an enlarged scale.

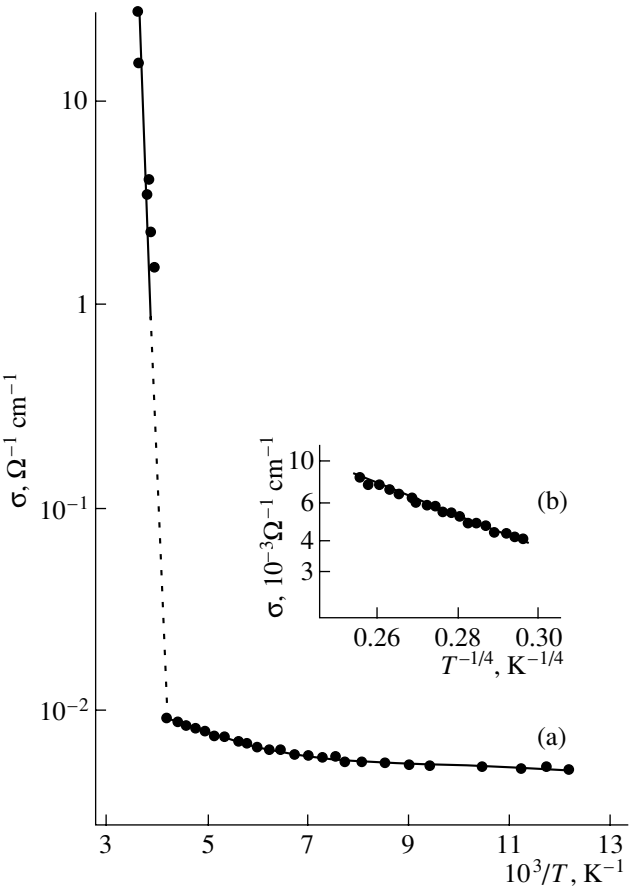

Fig. 2. Dependence of the conductivity of $TlNiS_2$ on (a) $10^3/T$ and (b) $T^{-1/4}$.

imum (91 μV/K). With a further increase in the temperature, the thermopower sharply decreases from 91 to ~0.5 μV/K and then remains nearly constant to room temperature. In Fig. 1, the inset shows the high-temperature branch of the thermopower on a tenfold enlarged scale of the ordinate axis. The positive sign of the thermopower indicates that holes are the majority charge carriers in $TlNiS_2$.

According to [8], the thermopower of chalcogenide semiconductors in the case of *p*-type conduction can be represented in the form

$$\alpha(T) = -\frac{k}{e}\left[\frac{\Delta E}{kT} + \gamma\right], \quad (1)$$

where γkT is the mean energy transferred by holes, $\gamma \approx 1$, ΔE is the activation energy of conduction, k is the Boltzmann constant, and e is the elementary charge.

It should be noted that, when the thermopower is not very high (of the order of k/e = 86 μV/K or less), the analysis of the temperature dependence $\alpha(T)$ is more complicated. If the material remains a *p*-type semiconductor (as in the case under consideration), small values of the thermopower can be due to the fact that the activation energy ΔE is of the order of kT. In order to check the fulfillment of this criterion, we estimated the activation energy ΔE from the slope of the temperature dependence of the conductivity for $TlNiS_2$ at $T < 240$ K (Fig. 2a). It is evident from Fig. 2a that the temperature dependence of the conductivity has a variable slope. For this reason, we estimated the activation energy ΔE in the temperature range 160–240 K; as a result, the activation energy was found to be equal to 1.54×10^{-2} eV. For these temperatures, the values of kT were determined to be $(1.38–2.00) \times 10^{-2}$ eV. In other words, the values of ΔE and kT for $TlNiS_2$ at low temperatures are actually of the same order of magnitude, as is the case with metals. In metals, the current is transferred by charge carriers in the energy band whose thickness is of the order of kT in the vicinity of the Fermi energy (E_F). According to [8], the thermopower of a metal has the form

$$\alpha(T) = \frac{\pi^3 k^2 T}{3e}\left(\frac{\partial \ln\sigma}{\partial E}\right)_{E = E_F}. \quad (2)$$

Formula (2) is valid only when $kT \ll E_F$.

As was noted above and shown in Fig. 2a, the dependence of $\log\sigma$ on $1/T$ at temperatures $T < 240$ K is characterized by a monotonic decrease in the activation energy with a decrease in the temperature. This behavior of the conductivity in $TlNiS_2$ at low temperatures suggests that charge transfer occurs through the variable-range-hopping mechanism [8], provided the current is transferred by charge carriers at the states localized in the vicinity of the Fermi level. This is also confirmed by the temperature dependence $\log\sigma \sim T^{-1/4}$ (Fig. 2b). The slope of this curve (T_0) allowed us to estimate the density of localized states near the Fermi level from the formula [8]

$$N_F = \frac{16}{T_0 k a^3}, \quad (3)$$

where a is the localization length.

The density of states N_F was found to be equal to 9×10^{20} eV^{-1} cm^{-3}. The localization length was taken as a = 20 Å (by analogy with binary sulfides of Group III elements [9]). Such a high value of N_F is characteristic of amorphous semiconductors. Therefore, it can be concluded that the energy-band structure of $TlNiS_2$ is similar to that of amorphous semiconductors. We calculated the hopping distance in $TlNiS_2$ according to the formula

$$R(T) = \frac{3}{8}a(T_0/T)^{1/4}. \quad (4)$$

As a result, we found that, at T = 110 K, $R \approx 30$ Å.

From the expression given in [8],

$$J = \frac{3}{2\pi R^3 N_F}, \quad (5)$$

we estimated the scatter of the trapping states about the Fermi level: $J = 1.97 \times 10^{-2}$ eV. As was shown above, the approximate activation energy of conduction ΔE, which was determined from the dependence of $\log\sigma$ on $10^3/T$ at low temperatures, is of the same order of magnitude.

In the temperature range 80–110 K, the activation energy of conduction becomes zero. The activationless conduction also exhibits hopping nature, which manifests itself in the hopping of charge carriers over spatially more distant but energetically more closely located centers without phonon absorption [10].

In contrast to formula (2) for the thermopower of metals, the temperature dependence of α in the region of hopping conduction can be represented by the relationship [8]

$$\alpha(T) = A + BT, \quad (6)$$

where B is the temperature coefficient for the thermopower. In our case, the dependence $\alpha(T)$ for $TlNiS_2$ (Fig. 1) is characterized by two slopes.

In the temperature range 80–110 K, where $TlNiS_2$ samples possess activationless hopping conduction (ΔE = 0), the slope of the curve $\alpha(T)$ is equal to 0.13 μV/K^2. At temperatures T > 110 K, when the activation energy of conduction varies monotonically with temperature, the temperature coefficient for the thermopower is approximately six times larger: $B = \partial\alpha/\partial T$ = 0.8 μV/K^2.

The extrapolated low-temperature branch $\alpha(T)$ passes through zero; i.e., A = 0 in formula (6). This indicates that, in the temperature range 80–110 K, where the electrical conductivity σ does not depend on T, the experimental values of α satisfy formula (2) for the thermopower of metals. In the temperature range 110–240 K, the thermopower obeys relationship (6). The thermopower is determined primarily by the density of states and, hence, has positive sign in the region of hopping conduction.

Earlier [1], we showed that similar behavior of $\alpha(T)$ is also observed in $TlFeSe_2$; i.e., under conditions of hopping conduction, the sign of the thermopower is positive and the temperature dependence $\alpha(T)$ is linear ($\alpha \sim T$).

It is evident from Figs. 1 and 2 that, at temperatures close to 240 K, the dependences $\alpha(T)$ and $\sigma(T)$ exhibit a jump; i.e., the thermopower sharply decreases, whereas the conductivity increases by more than three orders of magnitude. In this range of temperatures, the slope of the curve $\log\sigma(1/T)$ is estimated at ~1.0 eV. Such a sharp increase in the conductivity σ at the activation energy ΔE = 1.0 eV can be associated with the onset of intrinsic conduction. In the case when the current is transferred by carriers over states distributed throughout the whole sample, the parameter γ in formula (1) should be of the order of unity. At $T \approx 240$ K, the thermopower in $TlNiS_2$ sample, which was estimated from formula (1) at ΔE = 1.0 eV and γ = 1, is more than one order of magnitude higher than the experimentally observed thermopower. In other words, the experimental values of α are not as large as those calculated with the activation energy ΔE obtained from the slope of the curve $\log\sigma(1/T)$. Possibly, this difference is caused by the fact that, at high temperatures, both holes and electrons are involved in conduction. Of course, in this case, the thermopower α is less than that calculated from formula (1), which holds for semiconductors with single-type charge carriers.

4. CONCLUSIONS

Thus, it was demonstrated that, at low temperatures, when hopping conduction dominates, the thermopower of $TlNiS_2$ is proportional to the temperature. As the temperature increases, the charge carriers excited in the allowed band begin to dominate in conduction and the thermopower decreases drastically (by a factor of ~200) and becomes virtually independent of the temperature. At high temperatures, small values of the thermopower are associated with the ambipolarity of conduction, when the concentrations of holes and electrons involved in conduction are of almost the same order of magnitude. The absence of the sign inversion of the thermopower indicates that the concentration of holes in $TlNiS_2$ always exceeds the concentration of electrons involved in conduction.

REFERENCES

1. S. N. Mustafaeva, É. M. Kerimova, and A. I. Dzhabbarly, Fiz. Tverd. Tela (St. Petersburg) **42** (12), 2132 (2000) [Phys. Solid State **42**, 2197 (2000)].
2. É. M. Kerimova, F. M. Seidov, S. N. Mustafaeva, and S. S. Abdinbekov, Neorg. Mater. **35** (2), 157 (1999).

3. F. M. Seidov, É. M. Kerimova, S. N. Mustafaeva, *et al.*, Fizika **6** (1), 47 (2000).
4. E. M. Kerimova, S. N. Mustafaeva, and F. M. Seidov, in *Abstracts of the 6th International School–Conference on Phase Diagrams in Material Science* (Kiev, 2001).
5. M. A. Aldzhanov and M. D. Nadzhafzade, Fiz. Tverd. Tela (Leningrad) **32** (8), 2494 (1990) [Sov. Phys. Solid State **32**, 1449 (1990)].
6. M. A. Aljanov, E. M. Kerimova, and M. D. Nadjafzade, in *Abstracts of XIV IUPAC Conference on Chemical Thermodynamics* (Osaka, Japan, 1996), p. 25.
7. É. M. Kerimova, R. Z. Sadykhov, and R. K. Veliev, Neorg. Mater. **37** (2), 180 (2001).
8. N. F. Mott and E. A. Davis, *Electronic Processes in Non-Crystalline Materials* (Clarendon Press, Oxford, 1971; Mir, Moscow, 1974).
9. V. Augelli, C. Manfredotti, R. Murri, *et al.*, Nuovo Cimento **38** (2), 327 (1977).
10. B. I. Shklovskiĭ and A. A. Éfros, *Electronic Properties of Doped Semiconductors* (Nauka, Moscow, 1979; Springer, New York, 1984).

Translated by O. Moskalev

Physics of the Solid State, Vol. 45, No. 4, 2003, pp. 619–622. Translated from Fizika Tverdogo Tela, Vol. 45, No. 4, 2003, pp. 590–593.

SEMICONDUCTORS AND DIELECTRICS

High-Pressure Thermopower of Sulfur

V. V. Shchennikov and S. V. Ovsyannikov

Institute of Metal Physics, Ural Division, Russian Academy of Sciences, ul. S. Kovalevskoĭ 19, Yekaterinburg, 620219 Russia

Received March 25, 2002; in final form, September 12, 2002

Abstract—First measurements of the thermopower and transverse magnetoresistance of sulfur at ultrahigh pressures of up to ~40 GPa are reported. The conductivity of sulfur, as that of other elemental Group VI semiconductors (Te, Se), is shown to be due to valence band holes. The variation of band gap width is derived from the pressure dependence of thermopower. The observed negative magnetoresistance of sulfur at $P \sim 30$ GPa indicates a low hole mobility and suggests the existence of an indirect minimum gap in the electronic spectrum. The pressure-induced variation of the electronic structure of sulfur is discussed in terms of the Peierls lattice instability model. *© 2003 MAIK "Nauka/Interperiodica".*

1. INTRODUCTION

At atmospheric pressure, sulfur is a molecular crystal and crystallizes in an orthorhombic structure. In its electrical properties, sulfur is an insulator with a band gap $E_g \approx 2.9$ eV [1]. In recent years, this substance has been enjoying considerable interest spurred by the discovery that it transfers, at a high pressure, to the superconducting state with a high critical temperature, $T_c > 10$ K [2, 3]. Subsequent studies have established a series of structural transformations, from the orthorhombic phase to a monoclinic phase (5.3 GPa), an amorphous phase (25 GPa), a phase with a tentative chain structure (34 GPa), a body-centered orthorhombic phase (100 GPa), and a β-Po-type phase (162 GPa) [4–6]. At an ultrahigh pressure P, sulfur was observed to transfer to a metallic state [1–7].

Thus, structural transformations in sulfur have thus far been studied in the range up to 212 GPa [4]. These data suggest that Te, Se, and S should exhibit substantially similar electronic structures at high pressures. In these substances, pressure induces transitions to a metallic state and similar structural transformations in the metallic phases [4]. Tellurium and selenium do indeed demonstrate similar pressure-induced variation of their electronic properties [8–10]. Because of the very high electrical resistivity of sulfur, however, its properties have been investigated to a considerably lesser extent than those of its neighbors in Group VI. The transition of sulfur to a metallic state at pressures above 90 GPa was established in [1–6] from a jump in the resistivity ρ and the onset of superconductivity, as well as from a strong rise in optical reflectance. At the same time, the temperature behavior of the resistivity and the sharp decrease in the pressure coefficient of $\rho(P)$ suggested [7] that various modifications of sulfur become conducting at substantially lower pressures, 45–54 GPa. This transition was also observed to occur in later studies [3]. Because the temperature course of the resistivity revealed features of both semiconducting (hopping) and semimetallic conductivity [7], conjectures were put forward that, in these experimental conditions, a sample contains a mixture of a semiconducting phase and of a newly forming semimetallic phase [7], as well as that the electrical properties may be strongly affected by defects [4]. Our knowledge of the properties of sulfur in the semiconducting state for $P <$ 40 GPa is actually poorer than that for the metallic phases.

In some cases, data available on the resistivity are insufficient to draw a conclusion as to the conduction type [10, 11]. For instance, the high-pressure phases of the cadmium and zinc chalcogenides with rocksalt structure exhibit a metallic behavior of the temperature dependences while retaining a considerable optical gap $E_g > 1$ eV in the electronic spectrum [11] and featuring values of thermopower too high for metals, $|S| \approx$ 0.1 mV/K [10]. Studies of thermopower and magnetoresistance provide an efficient way to learn the character of conduction and the electronic-structure parameters of high-pressure phases [12–14].

The purpose of this work was to investigate the thermoelectric and galvanomagnetic properties of sulfur in the semiconducting phase at high pressures.

2. EXPERIMENTAL TECHNIQUE

Measurements of the electrical resistivity and thermopower of sulfur were conducted in high-pressure chambers with synthetic-diamond anvils [12, 14, 15]. Three chambers, with the diameter of the operating anvil area varying from 0.6 to 1 mm, were used [16]. A temperature gradient was produced by heating one anvil with a heater element, the temperature at fixed points on the anvils being measured with thermocouples [17, 18]. Thermoelectric measurements were carried out on a stand [18] after the sample resistance had

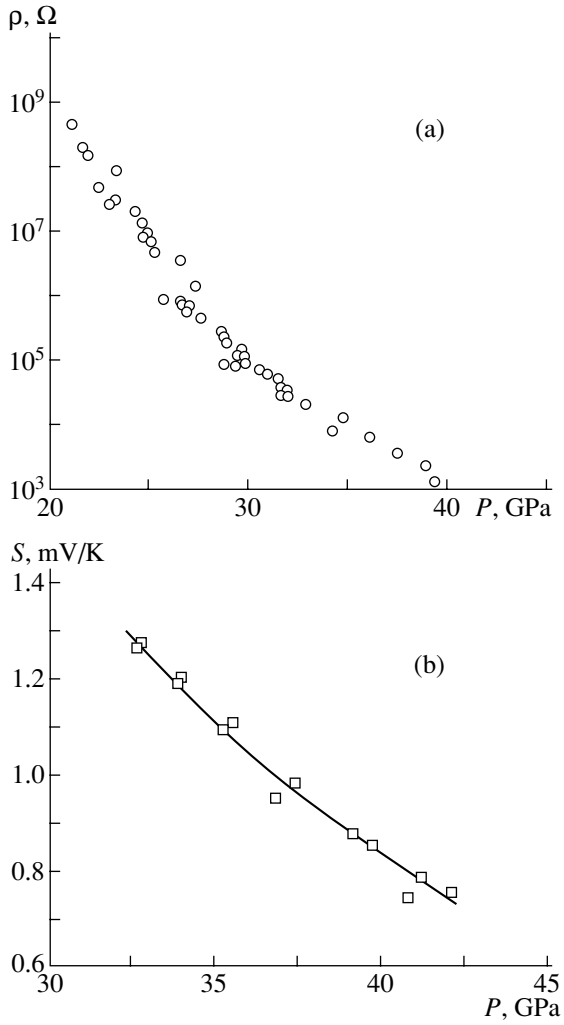

Fig. 1. Pressure dependences of (a) the electrical resistivity of sulfur measured at $T = 295$ K (sample *1*) and (b) the thermopower of sulfur (sample *2*) obtained at 305 K.

dropped under pressure to ~10^7 Ω. Crystals of OSCh-grade orthorhombic sulfur were chosen for the study. Samples ~0.1 mm thick and with transverse dimensions from ~0.2×0.2 to 0.4×0.4 mm were placed in a central hole 0.3–0.5 mm in diameter drilled in a catlinite cylinder. Platinum–silver spring ribbon contacts 5 μm in thickness or conducting diamond anvils were used to supply voltage and receive signals from a sample [12, 14]. The applied pressure was determined to within ±10% from calibration graphs based on resistance jumps in reference materials with known phase transition pressures: GaP (22 GPa), ZnS (15 GPa), NaCl (29 GPa), etc. [12, 15].

The transverse magnetoresistance of sulfur samples was measured at a fixed pressure of ~30 GPa in a self-contained diamond-chamber version [14] in the dc magnetic field of a shell-cased electromagnet, with the magnetic induction decreased and increased (up to 2 T) in two magnetic field directions. Several measurements were made at each point, and the final result was obtained by averaging. Ten series of measurements were run at 295 and 310 K and produced identical results. The parameters of the experiment and signals from the sample were measured simultaneously and stored in a nonvolatile memory, with subsequent transfer of the data to a computer [18].

3. RESULTS OF THE MEASUREMENTS AND DISCUSSION

In accordance with earlier measurements [2, 5, 7], the electrical resistivity of sulfur samples decreased with increasing pressure (Fig. 1a). In the pressure region $P > 25$ GPa, where structural transformations to the amorphous and subsequent chain-structure phase were shown to exist [4, 5], the pressure coefficient of $\rho(P)$ decreased in absolute value (Fig. 1a).

The thermopower of sulfur was measured in the pressure range from ~30 to ~40 GPa and corresponded to the hole character of conduction (Fig. 1b). Both thermopower S and ρ decreased with increasing pressure. The experimental relations were analyzed using the well-known expressions for electrical conductivity and the Seebeck coefficient [19, 20]:

$$\sigma = -\int \sigma(E)\frac{\partial f}{\partial E}dE,$$
$$S = -\frac{k}{|e|}\int \frac{\sigma(E)}{\sigma}\left[\frac{E - E_F}{kT}\right]\frac{\partial f}{\partial E}dE. \quad (1)$$

Here, $\sigma = 1/\rho$ is the electrical conductivity, E is the electron energy, E_F is the Fermi energy, f is the distribution function, k is the Boltzmann constant, and e is the electronic charge. For a nondegenerate n-type semiconductor, S is given by [19, 20]

$$S_n = -\frac{k}{|e|}\left(r + \frac{5}{2} - \frac{E_F}{kT}\right), \quad (2)$$

where r is the parameter determining the dependence of relaxation time τ on electron energy, $\tau(E) \sim E^r$ [19, 20].

In the case of two-band conduction, S is the sum of the electronic S_n and hole S_p contributions, $S = S_n\sigma_n/\sigma + S_p\sigma_p/\sigma$. For an intrinsic semiconductor, this expression can be recast to

$$S = -k/|e|\left[\frac{b-1}{b+1}(\ln\rho - \ln\rho_0)\right.$$
$$+ (r_n + 5/2)b/(b+1) - (r_p + 5/2)/(b+1) \quad (3)$$
$$\left. - 3/4\ln(m_p/m_n)\right],$$

where $\rho = \rho_0\exp(E_g/2kT)$ is the electrical resistivity of the semiconductor; m_n and m_p are the effective density-of-states masses in the electron and hole bands, respec-

tively; and b is a parameter equal to the ratio of the electronic to hole conductivity ($b = \sigma_n/\sigma_p$) [12, 19, 20].

The first term in the right-hand side of Eq. (3) has the strongest dependence on pressure in the pressure range covered and, for sulfur, is by far larger than the other terms. The parameters r_n and r_p assume values from –1/2 to 3/2, and the effective masses m_n and m_p and the parameter ρ_0 can vary considerably only near $E_g \longrightarrow 0$. Therefore, in analyzing the relation between S and ρ under pressure, one can restrict oneself to the first term. Note that a similar relation holds in the case of activated mobility (hopping conduction), but, in that case, the factor $(b - 1)/(b + 1)$ of the first term has to be replaced by the ratio of the semiconductor band gap E_g to the total activation energy for conduction, because the activation energy for mobility with inclusion of only activation terms that are proportional to $\sim 1/T$ does not contribute to the thermopower [20].

The parametric relation between the thermopower and electrical resistivity (Fig. 2), which were measured simultaneously (the values of P are excluded in this case), was used to estimate the factor $(b - 1)/(b + 1) \approx -1$, which corresponds, within experimental accuracy, to hole conduction and a negligible electronic contribution. Thus, the behavior of the resistivity and thermopower under pressure is determined by the magnitude of E_g and by its variation with increasing pressure. The above-mentioned bend in the $\rho(P)$ relation (Fig. 1) is associated with the decrease in the pressure coefficient of E_g above 25 GPa, which is in agreement with the data on absorption spectra from [1]. The width of the semiconducting gap, as estimated from the thermopower, varies in the interval ~30–40 GPa from ~0.8 to 0.4 eV. In its thermoelectric properties, sulfur resembles Te and Se, whose thermopower is likewise positive and decreases strongly with increasing pressure [8–10, 12].

The magnetoresistance measured at 295 and 310 K and $P = 30$ GPa was found to be negative; that is, ρ decreases when a magnetic field is applied (Fig. 3). The semiconducting gap E_g, as determined in this state from the $\rho(T)$ dependence, was ~1 eV. The absence of a positive effect in magnetic fields of up to 2 T indicates a low hole mobility μ_p. As follows from optical data [1, 5], the band gap in sulfur is indirect at pressures of up to 30 GPa; therefore, the pressure-induced decrease in E_g does not entail a rise in hole mobility. This distinguishes the semiconducting sulfur from the trigonal Te and Se, whose conduction- and valence-band extrema lie at the same point in the Brillouin zone, as a result of which the effective mass of holes m_p exponentially decreases and, hence, their mobility $\mu \sim 1/m$ increases with pressure [9, 10]. In the pressure interval studied, sulfur is an analog of amorphous selenium and molecular iodine, which also exhibit negative magnetoresistance [9, 21]. The scattering mechanisms which can account for the negative magnetoresistance in these substances were considered in [8, 9, 21].

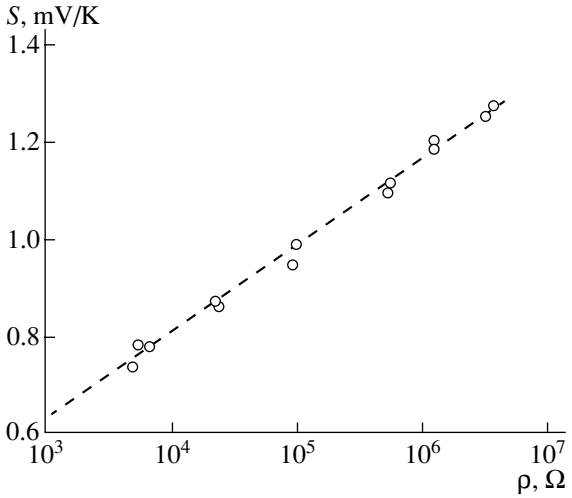

Fig. 2. Parametric dependence of thermopower on electrical resistivity at 305 K in the pressure interval ~30–40 GPa measured simultaneously on sample *2*. Symbols are experiment, and dashed line is calculation from Eq. (3).

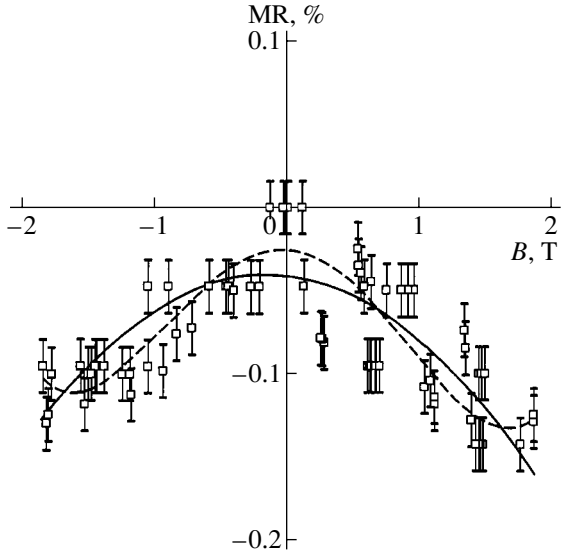

Fig. 3. Magnetoresistance of sulfur measured at 295 K and a pressure of 30 GPa. Symbols are experiment, and dashed line is approximation of the experimental data by the expression $MR = -a(B)^2/[1 + b(B)^2]$, where a and b are fitting parameters.

The experimental data obtained permit one to use the Peierls lattice instability model to describe the pressure-induced transformation of the sulfur electronic structure [22]. This approach is based on the observation that it is the p electrons that play a major role in lattice bond formation in Group V–VII materials and some compounds with an unfilled p band [23]. Calcula-

tions conducted for Group V–VII materials showed that this consideration is valid not only for ordered but also for liquid and amorphous states [23]. The model also yields accurate results when real interactions are consistently taken into account [23, 24].

Like other chalcogens, sulfur in the simple cubic structure should be a metal, because the *p* band is only partially (to two thirds) filled by electrons [22–24]. The Peierls lattice instability results in a threefold increase in the period (and the corresponding threefold splitting of the *p* band) and decreases the energy of the system through the formation of a semiconducting gap that separates the two filled lower bands from the empty one [22, 23]. Two of the six equivalent *p* bonds (in a simple cubic lattice) become strong (covalent bonding), and the other four, weak (van der Waals bonding); i.e., chain structures form in which each atom has only two nearest neighbors [22, 23]. Indeed, all Group VI elements have a structure made up of helical chains or ring-shaped modifications of them [1, 4, 5, 25, 26]. The lattice parameter *c* of Te and Se having chain structures does indeed increase threefold as compared to the cubic praphase [22], and in the orthorhombic structure of sulfur, the increase in the lattice parameter is still larger by a few times (the structure consists of S_8 rings) [25, 26]. Therefore, the electronic bands of sulfur, both in the orthorhombic and in other low-dimensional semiconducting phases [4], should be very narrow [19], which may account for the low hole mobility. Distorted Peierls structures have a lower density as compared with the starting structure, and, as shown by calculations made for these materials, the Peierls distortion becomes energetically unfavorable at a certain critical pressure; i.e., the substance undergoes metallization [23]. As sulfur transfers to the high-pressure metallic phase with the body-centered orthorhombic (layered) structure, the coordination number for this element changes from two to four, and in the next phase with the structure of β-Po, to six [4], which may be treated as lifting of the Peierls distortion.

ACKNOWLEDGMENTS

This study was supported by the Russian Foundation for Basic Research, project no. 01-02-17203.

REFERENCES

1. H. Luo, S. Desgreniers, Y. K. Vohra, and A. L. Ruoff, Phys. Rev. Lett. **67**, 2998 (1991).
2. E. N. Yakovlev, G. N. Stepanov, Yu. A. Timofeev, and B. V. Vinogradov, Pis'ma Zh. Éksp. Teor. Fiz. **28**, 369 (1978) [JETP Lett. **28**, 340 (1978)].
3. V. V. Struzhkin, R. J. Hemley, H.-K. Mao, and Yu. A. Timofeev, Nature **390**, 2662 (1997).
4. H. Luo, R. G. Greence, and A. L. Ruoff, Phys. Rev. Lett. **71**, 2943 (1993).
5. M. I. Eremets, K. Amaya, K. Shimizu, and T. C. Kobayashi, Rev. High Pressure Sci. Technol. **7**, 469 (1998).
6. R. J. Hemley and H. K. Mao, Encycl. Appl. Phys. **18**, 555 (1997).
7. F. P. Bundy and K. J. Dunn, Phys. Rev. B **22**, 3157 (1980).
8. V. V. Shchennikov and V. I. Osotov, Fiz. Tverd. Tela (St. Petersburg) **37**, 448 (1995) [Phys. Solid State **37**, 243 (1995)].
9. V. V. Shchennikov, Fiz. Tverd. Tela (St. Petersburg) **42**, 626 (2000) [Phys. Solid State **42**, 641 (2000)].
10. V. V. Shchennikov, Phys. Status Solidi B **223**, 561 (2001).
11. A. R. Goni and K. Syassen, Semicond. Semimet. **54**, 247 (1998).
12. I. M. Tsidil'kovskiĭ, V. V. Shchennikov, and N. G. Gluzman, Fiz. Tekh. Poluprovodn. (Leningrad) **17**, 958 (1983) [Sov. Phys. Semicond. **17**, 604 (1983)].
13. V. V. Shchennikov, Fiz. Met. Metalloved. **67**, 93 (1989).
14. V. V. Shchennikov and S. V. Ovsyannikov, Pis'ma Zh. Éksp. Teor. Fiz. **74**, 546 (2001) [JETP Lett. **74**, 486 (2001)].
15. F. P. Bundy, Rev. Sci. Instrum. **46**, 1318 (1975).
16. V. V. Shchennikov and V. A. Smirnov, Patent No. 2050180.
17. V. V. Shchennikov and A. V. Bazhenov, Rev. High Pressure Sci. Technol. **6**, 657 (1997).
18. V. V. Shchennikov, A. Yu. Derevskov, and V. A. Smironov, in *High Pressure Chemical Engineering*, Ed. by Ph. Rudolf von Rohr and Ch. Trepp (Elsevier, Amsterdam, 1996), p. 667.
19. N. F. Mott, *Metal–Insulator Transitions* (Taylor and Francis, London, 1974; Nauka, Moscow, 1979).
20. M. Cutler, *Liquid Semiconductors* (Academic, New York, 1977; Mir, Moscow, 1980).
21. V. V. Shchennikov, Fiz. Tverd. Tela (St. Petersburg) **38**, 2680 (1996) [Phys. Solid State **38**, 1470 (1996)].
22. B. A. Volkov, O. Pankratov, and S. V. Pakhomov, Zh. Éksp. Teor. Fiz. **86**, 2293 (1984) [Sov. Phys. JETP **59**, 1336 (1984)].
23. J. P. Gaspard, F. Marinelli, and A. Pellegatii, Europhys. Lett. **3**, 1095 (1987).
24. B. A. Volkov, O. Pankratov, and A. V. Sazonov, Zh. Éksp. Teor. Fiz. **85**, 1395 (1983) [Sov. Phys. JETP **58**, 809 (1983)].
25. E. Yu. Tonkov, *Phase Diagrams of Elements at High Pressure* (Nauka, Moscow, 1979).
26. V. V. Sobolev and A. M. Shirokov, *Electronic Structure of Chalcogens* (Nauka, Moscow, 1988).

Translated by G. Skrebtsov

Physics of the Solid State, Vol. 45, No. 4, 2003, pp. 623–629. Translated from Fizika Tverdogo Tela, Vol. 45, No. 4, 2003, pp. 594–599.

SEMICONDUCTORS AND DIELECTRICS

Dispersive Nonlinearity and Bistability of Polar Media

Ch. S. Kim, A. M. Satanin, and V. B. Shtenberg

Lobachevsky State University, pr. Gagarina 23, Nizhni Novgorod, 630600 Russia

e-mail: satanin@phys.unn.runnet.ru

Received July 15, 2002

Abstract—The nonlinear optical response of polar materials (ionic crystals and polar semiconductors) is studied. Within the generalized Born–Huang theory, the nonlinear response of a system is found to exhibit a characteristic peak near the polariton resonance. As an example, the transparency of a plate (Fabry–Perot cavity) of a weakly nonlinear polar material is studied. It is shown that the dependence of the output signal intensity on the incident radiation intensity exhibits a bistable behavior for the systems under study. © *2003 MAIK "Nauka/Interperiodica".*

1. INTRODUCTION

The interaction between electromagnetic radiation and optical phonons in polar materials (ionic crystals and polar semiconductors) can be described to good approximation in terms of the phenomenological Born–Huang theory [1] because the light wavelength is much longer than the lattice constants and the continual approximation can be justified. In order to describe the interaction between optical radiation and optical phonons, it is sufficient to introduce a few phenomenological parameters that will completely characterize the interaction. As is known, the phonon–photon coupling becomes particularly strong near the phonon–photon resonance, where polaritons form [2–4]. The interaction between lattice ions and an electromagnetic field is described by coupled equations for the fields. These equations can be derived by constructing the Lagrangian involving independent quadratic invariants in the relative ion displacements and the electromagnetic field [4, 5]. Within this approach, the energy loss can be taken into account using the Rayleigh dissipative function [6]. The linear version of the Born–Huang theory and its modifications have recently been used to describe optical phonons in three- and low-dimensional structures [7–9].

In the case of strong excitation of polar materials by laser beams, one should take into account the nonlinear polarization of materials, which can cause a number of interesting nonlinear effects, such as harmonic generation, optical bistability, nonlinear phase modulation, and self-focusing [10, 11]. The nonlinear photon–phonon interaction in crystals with a center of inversion controls the $\chi^{(3)}$ susceptibility and can cause optical bistability, which is particularly pronounced near the polariton resonance. In recent years, the optical bistability [11, 12] has been actively studied in various nonlinear media: atomic systems (gases), semiconductors, polymers, colloids, etc. [13–16]. Such studies are of major importance, since they make it possible to develop optical switches with a switching rate limited only by the characteristic response time of a nonlinear material and the time of signal passage through a sample [11]. It appears of urgency to study the influence of various nonlinearity mechanisms on the character of switching and bistability of polar materials in various frequency ranges. Nonlinear polariton-exciton mechanisms have previously been studied in semiconductors [17]. Those studies revealed the important role of the electronic mechanism of dispersion and nonlinearity. The nonlinear polarization of atomic systems was also previously studied within the two-level approximation [10, 18, 19]. To date, no studies dedicated to the polariton mechanisms of bistability have been reported in the literature.

The aim of this study is to develop a simple theory of the dispersive nonlinearity which represents a reasonable generalization of the Born–Huang linear theory. To this end, we complement the linear Lagrangian with invariants constructed from the electromagnetic field and ion displacements describing the effective nonlinear interaction between modes. Solution of the field equations will allow us to determine the nonlinear response ($\chi^{(3)}$ susceptibility). The nonlinear response functions exhibit a resonance behavior near the polariton resonance. An expression derived for the susceptibility makes it possible to study the field-amplitude-dependent transparency of the nonlinear polariton Fabry–Perot cavity. An interesting resonant structure is detected and described in terms of the polariton Fabry–Perot cavity modes. It is shown that the dependence of the output signal intensity on the input signal intensity exhibits a bistable behavior. The parameters defining the nonlinear effects in polar media are estimated.

1063-7834/03/4504-0623$24.00 © 2003 MAIK "Nauka/Interperiodica"

2. NONLINEAR RESPONSE OF A POLAR MEDIUM

Let us consider a polar material (an ionic crystal or a polar semiconductor) with two atoms per unit cell. The relative-displacement field $\mathbf{u}(\mathbf{r}, t)$ of charged ions induces an ac electric field $\mathbf{E}(\mathbf{r}, t)$, which, in turn, causes ion displacements $\mathbf{u}(\mathbf{r}, t)$. Hence, the dynamics of coupled mechanical vibrations and electromagnetic oscillations should be described self-consistently. The interaction between electromagnetic radiation and a separate optical vibrational mode can be characterized by a few parameters. The Born–Huang linear theory can be developed using the variational principle

$$\delta\int dtdV\mathcal{L}_{\text{lin}} = 0. \tag{1}$$

The field Lagrangian density $\mathcal{L}_{\text{lin}}$ is given by

$$\mathcal{L}_{\text{lin}} = \frac{1}{2}(\rho\dot{\mathbf{u}}^2 - \gamma\mathbf{u}^2) + \frac{\beta\mathbf{E}^2 - \mathbf{H}^2}{8\pi} + \alpha\mathbf{u}\cdot\mathbf{E}, \tag{2}$$

where the notation $\dot{\mathbf{u}} \equiv \dfrac{\partial\mathbf{u}}{\partial t}$ is used. The first and second terms in Eq. (2) represented the mechanical and electromagnetic fields, respectively, and the last term describes the interaction between them. The mechanical properties of the medium are characterized by the reduced mass ρ and the elastic constant $\gamma = \omega_T^2\rho$, where ω_T is the eigenfrequency of transverse ion vibrations. The electromagnetic properties are defined by the high-frequency permittivity $\beta = \varepsilon(\infty)$ (we consider a nonmagnetic medium). The field interaction is described by the constant α:

$$\alpha^2 = \frac{[\varepsilon(0) - \varepsilon(\infty)]\gamma}{4\pi},$$

where $\varepsilon(0)$ is the low-frequency permittivity. The above equations are written, in accordance with [1], using only the quadratic invariants and describing the field interaction by the lowest order term. The Born–Huang theory as applied to homogeneous media neglects the spatial dispersion of optical phonons; i.e., the terms like $\sim(\nabla\mathbf{u})^2$ are omitted in Eq. (2). The Rayleigh dissipative function is written as

$$R = \frac{\rho\nu_u}{2}\dot{\mathbf{u}}^2 + \frac{\rho\nu_E}{2c}\mathbf{E}^2, \tag{3}$$

where ν_u and ν_E are the field damping parameters.

Using the conventional approach [10], we extend the self-consistent Born–Huang theory to the case of weakly nonlinear media and calculate the response $\chi^{(3)}$ of a polar medium with an inversion center. We restrict ourselves to the case where the characteristic frequencies of the radiation field are close to the frequencies of longitudinal and transverse optical phonons. We assume that the characteristic frequencies of electron transitions are far from the external-field frequency. In practice, this means that the susceptibilities $\chi^{(3)}$ and the radiation effects described by $\chi^{(3)}$ in the infrared region can be calculated within the theory under consideration.

In the case of an isotropic centrosymmetrical polar medium, the quadratic Lagrangian should be complemented with quartic invariants:

$$\mathcal{L}_{\text{nl}} = \frac{\rho}{2}\left(\frac{g_1}{2}\mathbf{u}^4 + g_2\mathbf{u}\cdot\mathbf{E}\mathbf{u}^2 + g_3\mathbf{u}^2\mathbf{E}^2 + g_4(\mathbf{u}\cdot\mathbf{E})^2 + g_5\mathbf{u}\cdot\mathbf{E}\mathbf{E}^2 + \frac{g_6}{2}\mathbf{E}^4\right), \tag{4}$$

where $g_1, \ldots, g_6$ are parameters characterizing the degree of nonlinearity. It is obvious that the first term represents the lattice anharmonic contribution. The second term allows for the nonlinear polarization. This means that the displacement of neighboring atoms causes their shells to deform and induces an additional charge in the unit cell. The additional charge, in turn, can cause additional coupling between the atomic displacements and the electric field. The corresponding Lagrangian terms should contain the displacement vector cubed. The next terms describe the Raman scattering and higher order electronic processes. Since we are interested in resonant processes with characteristic frequencies comparable to those of optical phonons, it would be expected that highest order terms in displacements mainly contribute to the susceptibilities $\chi^{(3)}$.

The parameters $g_1, \ldots, g_6$ define the nonlinear response; to determine their values, the microscopic theory should be invoked. Numerical values of some of these parameters are given in [20]. Simple estimates of these parameters in terms of the parameters of the linear medium are

$$g_1 \sim \omega_T^2/a^2, \quad g_2 \sim \omega_T^2 a/e, \quad g_3 \sim g_4 \sim \omega_T^2 a^4/e^2,$$
$$g_5 \sim \omega_T^2 a^7/e^3, \quad g_6 \sim \omega_T^2 a^{10}/e^4,$$

where a is the lattice constant and e is the magnitude of the electronic charge. The values of these parameters will be used to estimate the nonlinear response functions in Section 3.

Using the variational principle, the complete set of the field equations can be found to be

$$\rho\frac{\partial^2\mathbf{u}}{\partial t^2} + \rho\nu_u\frac{\partial\mathbf{u}}{\partial t} + \gamma\mathbf{u} = \alpha\mathbf{E} + \frac{\partial\mathcal{L}_{\text{nl}}}{\partial\mathbf{u}}, \tag{6}$$

$$\nabla\times\mathbf{H} = \frac{1}{c}\frac{\partial}{\partial t}\left(\beta\mathbf{E} + 4\pi\alpha\mathbf{u} + 4\pi\frac{\partial\mathcal{L}_{\text{nl}}}{\partial\mathbf{E}}\right) + \frac{4\pi}{c}\rho\nu_E\mathbf{E}, \tag{7}$$

$$\nabla\cdot\left(\beta\mathbf{E} + 4\pi\alpha\mathbf{u} + 4\pi\frac{\partial\mathcal{L}_{\text{nl}}}{\partial\mathbf{E}}\right) = 0, \tag{8}$$

$$\nabla \times \mathbf{E} = -\frac{1}{c}\frac{\partial \mathbf{H}}{\partial t}, \quad \nabla \cdot \mathbf{H} = 0. \tag{9}$$

It is convenient to split the fields into longitudinal and transverse components. It is not difficult to understand that the longitudinal and transverse field components can be excited independently. Let us study the dynamics of transverse field components in more detail. Supposing the nonlinear terms to be small, we write the displacements as

$$\mathbf{u} = \mathbf{u}^{(0)} + \mathbf{u}^{(1)} + \ldots, \tag{10}$$

where $\mathbf{u}^{(0)}$ is the solution to the linear equation and $\mathbf{u}^{(1)}$ is a nonlinear correction. We retain only the first-order corrections $\mathbf{u}^{(1)}$ proportional to the constants $g_1, \ldots, g_6$ (for now, all the nonlinear terms are assumed to be of the same order of magnitude). The displacements can be written as

$$\mathbf{u}^{(0)} = \sum_n \mathbf{u}^{(0)}(\omega_n)e^{-i\omega_n t}, \quad \mathbf{u}^{(1)} = \sum_n \mathbf{u}^{(1)}(\omega_n)e^{-i\omega_n t}. \tag{11}$$

The polarization is split into linear and nonlinear parts:

$$\mathbf{P} = \mathbf{P}_{\text{lin}} + \mathbf{P}_{\text{nl}}. \tag{12}$$

The linear polarization is given by

$$\mathbf{P}_{\text{lin}} = \left(\frac{\beta - 1}{4\pi}\right)\mathbf{E} + \alpha \mathbf{u}^{(0)} \tag{13}$$

and the nonlinear third-order polarization is written as

$$\begin{aligned}\mathbf{P}_{\text{nl}}^{(3)} &= \alpha \mathbf{u}^{(1)} + \frac{1}{2}g_2(\mathbf{u}^{(0)})^2\mathbf{u}^{(0)} + g_3\mathbf{u}^{(0)} \cdot \mathbf{E}\mathbf{u}^{(0)} \\ &+ g_4\mathbf{E}(\mathbf{u}^{(0)})^2 + g_5\left(\mathbf{u}^{(0)} \cdot \mathbf{E}\mathbf{E} + \frac{1}{2}\mathbf{E}^2\mathbf{u}^{(0)}\right) + g_6\mathbf{E}^2\mathbf{E}.\end{aligned} \tag{14}$$

Substituting Eq. (10) into Eq. (6) and equating the terms of the same order on the left- and right-hand sides of Eq. (6), we derive equations for the linear displacement,

$$\frac{\partial^2 \mathbf{u}^{(0)}}{\partial t^2} + \nu_u \frac{\partial \mathbf{u}^{(0)}}{\partial t} + \omega_T^2 \mathbf{u}^{(0)} = \frac{\alpha}{\rho}\mathbf{E} \tag{15}$$

and for the correction $\mathbf{u}^{(1)}$,

$$\begin{aligned}&\frac{\partial^2 \mathbf{u}^{(1)}}{\partial t^2} + \nu_u \frac{\partial \mathbf{u}^{(1)}}{\partial t} + \omega_T^2 \mathbf{u}^{(1)} \\ &= g_1(\mathbf{u}^{(0)})^2\mathbf{u}^{(0)} + g_2\left(\mathbf{u}^{(0)} \cdot \mathbf{E}\mathbf{u}^{(0)} + \frac{1}{2}(\mathbf{u}^{(0)})^2\mathbf{E}\right) \\ &+ g_3\mathbf{u}^{(0)} \cdot \mathbf{E}\mathbf{E} + g_4\mathbf{u}^{(0)}\mathbf{E}^2 + \frac{1}{2}g_5\mathbf{E}\mathbf{E}^2.\end{aligned} \tag{16}$$

Taking the Fourier transform of Eq. (15), we obtain

$$\begin{aligned}\mathbf{u}^{(0)}(\omega_n) &= \frac{\alpha \mathbf{E}(\omega_n)}{D(\omega_n)}, \\ D(\omega_n) &= \frac{1}{\rho(\omega_T^2 - \omega_n^2 - i\nu_u\omega_n)}.\end{aligned} \tag{17}$$

The linear susceptibility $\chi^{(1)}(\omega_n)$ at the frequency $\omega_n = \omega$ is given by

$$\begin{aligned}\mathbf{P}_{\text{lin}}(\omega) &= \chi^{(1)}(\omega)\mathbf{E}(\omega), \\ \chi^{(1)}(\omega) &= \frac{\beta - 1}{4\pi} + \frac{\alpha^2}{D(\omega)}.\end{aligned} \tag{18}$$

The dielectric function can be written as

$$\varepsilon(\omega) = 1 + 4\pi\chi^{(1)}(\omega) + \frac{4\pi\rho\nu_E}{\omega}. \tag{19}$$

For a nondisspative medium ($\nu_u = \nu_E = 0$), the dielectric function is given by

$$\varepsilon(\omega) = \varepsilon(\infty)\left(\frac{\omega_L^2 - \omega}{\omega_T^2 - \omega}\right). \tag{20}$$

One can see from Eq. (20) that the dielectric function $\varepsilon(\omega)$ is negative in the frequency range $\omega_T < \omega < \omega_L$; hence, the medium will reflect radiation totally.

By splitting the fields into longitudinal and transverse components, it is not difficult to study wave propagation in a nondissipative medium on the basis of Eqs. (6)–(9). In particular, exist when the dispersion relation for transverse waves has the form

$$\begin{aligned}\omega_{\pm}(k) &= \frac{1}{2}\left(\omega_L^2 + \frac{c^2k^2}{\varepsilon(\infty)}\right. \\ &\left. \pm \sqrt{\left(\omega_L^2 + \frac{c^2k^2}{\varepsilon(\infty)}\right)^2 - 4\frac{c^2k^2}{\varepsilon(\infty)}\omega_T^2}\right),\end{aligned} \tag{21}$$

where $\omega_L = \sqrt{\varepsilon(0)/\varepsilon(\infty)}\,\omega_T$. The $\omega_+(k)$ and $\omega_-(k)$ dispersion curves are the upper and lower polariton excitation branches, respectively. For longitudinal waves, we have

$$\omega_L^2 = \omega_T^2 + \frac{\alpha^2}{4\pi\beta}.$$

The third-order nonlinear susceptibility depends on the combination of frequencies $\omega_q = \omega_n + \omega_m + \omega_s$. We look for a solution to Eq. (16) in the form

$$\mathbf{u}^{(1)} = \sum_q \mathbf{u}^{(1)}(\omega_q)e^{-i\omega_q t}. \tag{22}$$

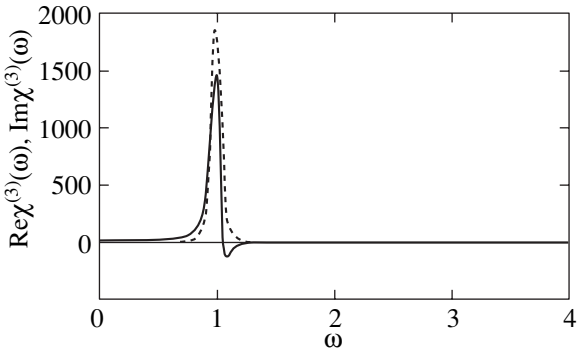

Fig. 1. Real (solid line) and imaginary (dashed line) parts of the nonlinear susceptibility $\chi^{(3)}(\omega)$ calculated using the typical parameters of a polar (NaCl-type) material: ρ = 2.2 g/cm^3, a = 0.5 nm, $\varepsilon(0)$ = 5.02, $\varepsilon(\infty)$ = 2.25, and ν_u = ν_E = $0.15\omega_T$; the nonlinear parameters were calculated using Eq. (5). The frequency is measured in units of ω_T, and $\chi^{(3)}(\omega)$, in units of $\chi_0^{(3)} = 3g_1\left(\frac{\varepsilon(0)-\varepsilon(\infty)}{4\pi}\right)^2\frac{1}{\rho a^2\omega_T^2} \simeq 2\times 10^{-13}$ esu.

Substituting Eq. (22) into Eq. (16), one finds

$$P_i^{(3)}(\omega_q) = \sum_{jkl}\chi_{ijkl}^{(3)}(\omega_q;\ \omega_n, \omega_m, \omega_s) \times \Delta(\omega_q - \omega_n - \omega_m\omega_s)E_j(\omega_n)E_k(\omega_k)E_l(\omega_s), \quad (23)$$

where $\Delta(\omega_q - \omega_n - \omega_m - \omega_s)$ is unity for $\omega_q = \omega_n + \omega_m + \omega_s$; otherwise, it is zero.

The third-order nonlinear susceptibility $\chi_{ijkl}^{(3)}(\omega_q; \omega_n, \omega_m, \omega_s)$ is responsible for various optical processes. The general properties of the tensor $\chi_{ijkl}^{(3)}$ are well known [10]. For an isotropic medium, this tensor has only three independent components. We restrict our consideration to two cases: (i) the third-order nonlinear polarization $\mathbf{P}^{(3)}(\omega)$ given by Eq. (23) with frequency $\omega_q \equiv \omega$ corresponding to the frequency combinations $\omega_q = \omega + \omega - \omega$, $\omega_q = \omega - \omega + \omega$, and $\omega_q = -\omega + \omega + \omega$ and (ii) the third harmonic generation described by the polarization $\mathbf{P}^{(3)}(3\omega)$ corresponding to $\omega_q \equiv 3\omega = \omega + \omega + \omega$.

The third-order polarization of an isotropic medium at the frequency ω can be written as

$$\mathbf{P}^{(3)}(\omega) = A(\omega)\mathbf{E}(\omega)\cdot\mathbf{E}^*(\omega)\mathbf{E}(\omega) + \frac{1}{2}B(\omega)\mathbf{E}(\omega)\cdot\mathbf{E}(\omega)\mathbf{E}^*(\omega), \quad (24)$$

where

$$A(\omega) = \rho\Big[g_1\alpha^4\frac{2}{D^2(\omega)D^2(-\omega)} + g_2\alpha^3\left(\frac{1}{D^3(\omega)} + \frac{3}{D^2(\omega)D(-\omega)}\right) + g_3\alpha^2\left(\frac{1}{D^2(\omega)} + \frac{3}{D(\omega)D(-\omega)}\right) + g_4\alpha^2\left(\frac{2}{D^2(\omega)} + \frac{2}{D(\omega)D(-\omega)}\right) + g_5\alpha\left(\frac{3}{D(\omega)} + \frac{1}{D(-\omega)}\right) + 2g_6\Big], \quad (25)$$

$$\frac{B(\omega)}{2} = \rho\Big[g_1\alpha^4\frac{2}{D^2(\omega)D^2(-\omega)} + g_2\alpha^3\left(\frac{1}{2D^3(\omega)} + \frac{3}{D^2(\omega)D(-\omega)}\right) + g_3\alpha^2\frac{2}{D^2(\omega)} + g_4\alpha^2\left(\frac{1}{D^2(\omega)} + \frac{3}{D(\omega)D(-\omega)}\right) + g_5\alpha\left(\frac{3}{2D(\omega)} + \frac{1}{2D(-\omega)}\right) + g_6\Big]. \quad (26)$$

As is evident from Eq. (24), the nonlinear polarization is expressed in terms of two functions: $A(\omega)$ and $B(\omega)$. It is notable that in the absence of damping, the quantities $A(\omega)$ and $B(\omega)$ incorporate terms which are even and odd functions of ω^2. In a dissipative medium, the real part of the odd terms can reverse sign when ω passes through the resonance frequency ω_T. These terms make a negative contribution to $\chi^{(3)}(\omega)$.

Let the system be exposed to radiation. In this case,

$$P^{(3)}(\omega) = \chi^{(3)}(\omega)|E(\omega)|^2E(\omega), \quad (27)$$

$$\chi^{(3)}(\omega) = A(\omega) + \frac{1}{2}B(\omega). \quad (28)$$

In other words, a polar material can be considered in this case as an ordinary Kerr medium with the susceptibility depending on the local-field intensity. A Kerr-type medium is characterized by the effective scalar parameter $\chi^{(3)}(\omega)$. We note that, in the high-frequency limit, we have $\chi^{(3)}(\infty) = 3g_6$. The real and imaginary parts of $\chi^{(3)}(\omega)$ are shown in Fig. 1. One can see that the real part of the susceptibility $\chi^{(3)}(\omega)$ reverses sign near the frequency ω_T.

Now, we consider the third harmonic generation in a nonlinear polar medium. The response function is written as

$$P^{(3)}(2\omega) = \chi^{(3)}(3\omega)E(\omega)E(\omega)E(\omega), \quad (29)$$

where

$$\chi^{(3)}(3\omega) = \rho\Big[g_1\alpha^4\frac{1}{D(3\omega)D^2(\omega)} + \frac{g_2}{2}\alpha^3\Big(\frac{3}{D(3\omega)D^3(\omega)} + \frac{1}{D^3(\omega)}\Big) + (g_3+g_4)\alpha^2\Big(\frac{1}{D(3\omega)D(\omega)} + \frac{1}{D^2(\omega)}\Big) + \frac{g_5}{2}\alpha\Big(\frac{1}{D(3\omega)} + \frac{3}{D(\omega)}\Big) + g_6\Big]. \quad (30)$$

The function $\chi^{(3)}(3\omega)$ is shown in Fig. 2. One can see that the real part of $\chi^{(3)}(3\omega)$ changes shape. The real and imaginary parts reverse sign when the frequency passes through ω_T.

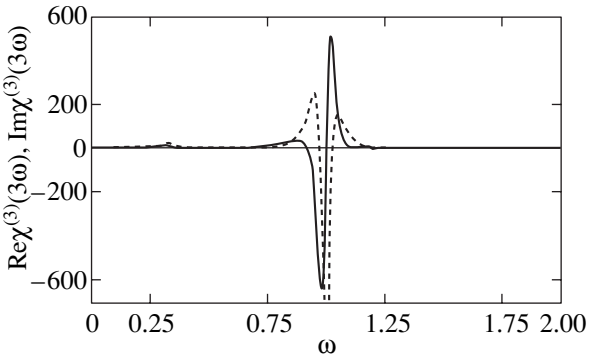

Fig. 2. Real (solid line) and imaginary (dashed line) parts of the nonlinear susceptibility $\chi^{(3)}(3\omega)$. The real and imaginary parts reverse sign when the frequency passes through the polariton resonance. The parameters are the same as in Fig. 1.

3. PASSAGE OF WAVES THROUGH A PLATE OF A NONLINEAR POLAR MATERIAL: THE FABRY–PEROT NONLINEAR CAVITY

We employ the susceptibility $\chi^{(3)}$ found in Section 2 to study the nonlinear wave propagation and the bistable behavior of the transparency of a solid-state cavity filled with a polar material. As is known, a nonlinear system with a positive feedback can exhibit a bistable behavior under certain conditions [12]. In the case under consideration, the polar medium plays the role of a nonlinear element having a transparency gap (stop band). Intriguing effects can take place in finite systems. These effects depend on the wavelength-to-thickness ratio and are much different for the upper and lower polariton branches.

We consider a plate of a polar material. As usual, it is supposed that the plate surface ("mirrors") is characterized by the transmittance t (real quantity) and the reflectances r and r' (complex quantities). To make things simpler, we consider the case where the incident field with wave vector $k = \omega/c$ has transverse polarization parallel to the plate plane. The field components outside the plate are written as

$$E(z) = A_{\text{in}}e^{ikz} + B_{\text{ref}}e^{-ikz}, \quad z < 0, \quad (31)$$

$$E(z) = C_{\text{tr}}e^{ikz}, \quad z > d, \quad (32)$$

where d is the plate thickness. In Eq. (31), the first term represents the incident field with amplitude A_{in} and the second term describes the reflected wave with amplitude B_{ref}. The electric field in Eq. (32) describes the wave transmitted through the plate.

Inside the plate, the field $E(z)$ can be determined from the nonlinear equation

$$\frac{\partial^2 E}{\partial z^2} + q^2E = -\frac{4\pi\omega^2}{c^2}\chi^{(3)}(\omega)|E|^2E, \quad (33)$$

where $q^2 = \varepsilon(\omega)\omega^2/c^2$. To solve Eq. (33), we follow the method of slowly varying amplitudes. We seek the field $E(z)$ in the form

$$E(z) = a(z)e^{iqz} + b(z)e^{-iqz}, \quad (34)$$

where $a(z)$ and $b(z)$ are slowly varying functions. From Eq. (33), it follows that functions $a(z)$ and $b(z)$ satisfy the equations

$$\frac{\partial a}{\partial z} = -\mu(|a|^2 + 2|b|^2)a, \quad (35)$$

$$\frac{\partial b}{\partial z} = \mu(2|a|^2 + |b|^2)b, \quad (36)$$

where $\mu = \dfrac{2\pi\omega^2\chi^{(3)}(\omega)}{c^2q}$. Solutions to Eqs. (35) and (36) can be written as

$$a(z) = \eta e^{i\mu(\eta^2+2\zeta^2)z}, \quad (37)$$

$$b(z) = \zeta e^{i\mu(2\eta^2+\zeta^2)z}, \quad (38)$$

where η and ζ are constants. The boundary conditions have the form

$$a(0) = rb(0) + tA_{\text{in}}, \quad B_{\text{ref}} = tb(0) + r'A_{\text{in}}, \quad (39)$$

$$C_{\text{tr}} = a(d)te^{i(q-k)d}, \quad b(d) = r'a(d)e^{2iqd}. \quad (40)$$

Using Eqs. (37) and (38) and boundary conditions (39) and (40), we find

$$T = \frac{\left|te^{i(q-k)d}\right|^2}{\left|1-|r|^2e^{2i\phi}\right|^2}, \quad (41)$$

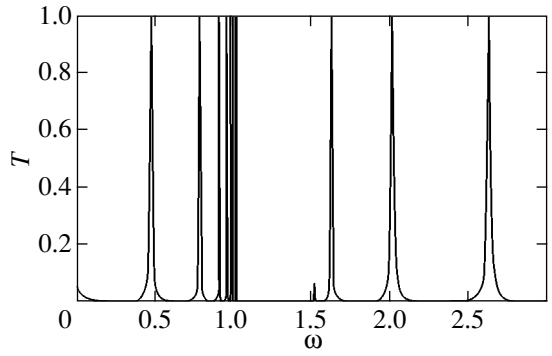

Fig. 3. Frequency dependence of the transparency of a polar plate calculated in the linear approximation for $d = 0.8\lambda_L$ ($\lambda_L = 2\pi c/\omega_L$). The resonant structure of the transparency is related to the upper and lower branches of polariton excitations (quasi-coupled Fabry–Perot modes). The reflectance of the plate surface is $R = 0.9$. The other parameters are the same as in Figs. 1 and 2.

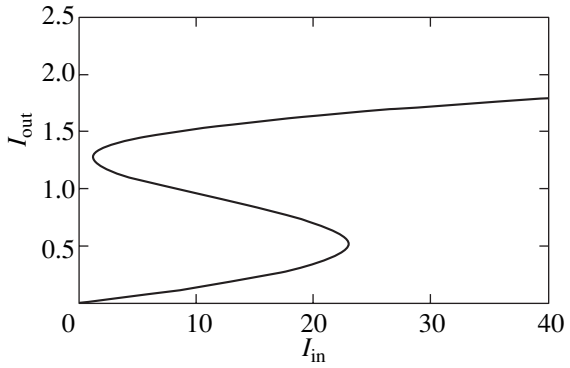

Fig. 4. Dependence of the output signal intensity on the incident radiation intensity. The operating Fabry–Perot mode belongs to the lower polariton branch $\omega = 0.565\omega_L$. The radiation intensity is normalized to $I_0 = 1$ MW/cm^2. The other parameters are the same as in Figs. 1–3.

where the phase ϕ is given by

$$\phi = \frac{3\omega^2 d\chi^{(3)}(\omega)}{4c^2 q}\left(\frac{1+|r|^2}{|t|^2}\right)T|A_{in}|^2 + qd + \varphi, \quad (42)$$

with φ being the additional phase caused by the mirrors ($rr' = |r|^2 e^{i2\varphi}$). Equations (41) and (42) allow one to consider radiation passage through the plate in a wide frequency range, including the frequencies within the stop band where $q^2 < 0$.

As a preliminary, we consider a linear medium. In this case, the positions of the transparency peaks (Fabry–Perot cavity eigenfrequencies) are given by

$$qd + \varphi = \pi n, \quad n = 1, 2, \ldots. \quad (43)$$

Employing Eq. (20), one finds

$$\omega_\pm^2 = \frac{\omega_L^2}{2}\left(\frac{\omega_L^2}{\omega_T^2} + F[n] \pm \sqrt{\left(\frac{\omega_L^2}{\omega_T^2} + F[n]\right)^2 - 4f[n]}\right), \quad (44)$$

where

$$F[n] = \left(\frac{\lambda_T}{2\pi d}\right)^2 (\pi n - \varphi)^2, \quad \lambda_T = \frac{2\pi c}{\omega_T}. \quad (45)$$

It can easily be shown that the set of frequencies $\omega_-(n)$ ($n = 1, 2, \ldots$) lies in the range $0 < \omega_-(n) < \omega_T$ and is related to the lower branch of polariton excitations; these frequencies correspond to transparency peaks and condense at the point ω_T. The frequencies $\omega_+(n)$ ($n = 1, 2, \ldots$) vary in the range $\omega_L < \omega_+(n) < \infty$; they correspond to the upper branch of polariton excitations. If the plate is exposed to radiation with the frequency lying within the stop band, the field amplitude can either exponentially damp or exponentially increase inside the plate. Figure 3 shows the plate transparency as a function of frequency for the thickness $d = 0.8\lambda_L$ ($\lambda_L = 2\pi c/\omega_L$); one can see transparency peaks corresponding to lower and upper polariton excitation branches. Using Eqs. (41) and (42) and taking into account Eq. (28), one can readily find the dependences of the output signal intensity on the input signal intensity. Figure 4 shows the plate transparency versus the input signal intensity for an eigenmode of the Fabry–Perot polariton cavity belonging to the lower branch of excitations, $\omega = 0.565\omega_L$. As indicated above, the bistable behavior is caused by the feedback, i.e., by the nonlinear modulation of the wave phase, depending on the wave intensity inside the cavity.

4. CONCLUSIONS

Thus, the macroscopic approach yields both a qualitatively and quantitatively adequate description of the phenomena under study and makes it possible to predict new effects. In this study, the Born–Huang phenomenological theory was generalized for describing the nonlinear effects in a disperse polar medium. The susceptibilities $\chi^{(3)}$ (the third-order nonlinear polarization and the third-harmonic polarization) have been calculated. It was shown that these susceptibilities contain terms that are even and odd in frequency. The odd terms reverse sign when the frequency passes through the polariton resonance, which can have a qualitative effect on the phase modulation. As an application of the theory developed, the transmittance of a plate of a polar material was calculated as a function of the frequency and intensity of the external field. An interesting resonant structure, controlled by the polariton modes of the Fabry–Perot cavity, was detected. In this case, the nonlinear transparency exhibits a bistable behavior.

ACKNOWLEDGMENTS

This study was supported by the Russian Foundation for Basic Research (project nos. 01-02-16569, 02-02-17495) and the federal program "Russian Universities" (project no. UR.01.01.057).

REFERENCES

1. M. Born and K. Huang, *Dynamical Theory of Crystal Lattices* (Inostrannaya Literatura, Moscow, 1958; Clarendon Press, Oxford, 1988).
2. U. Fano, Phys. Rev. **103** (2), 1202 (1956).
3. S. I. Pekar, Zh. Éksp. Teor. Fiz. **33** (4), 1022 (1957) [Sov. Phys. JETP **6**, 785 (1957)].
4. J. J. Hopfield, Phys. Rev. **112** (5), 1555 (1958).
5. C. Kittel, *Quantum Theory of Solids* (Wiley, New York, 1963; Nauka, Moscow, 1967).
6. W. H. Louisell, *Radiation and Noise in Quantum Electronics* (McGraw-Hill, New York, 1964; Nauka, Moscow, 1972).
7. H. Akera and T. Ando, Phys. Rev. B **40** (5), 2914 (1989).
8. B. K. Ridley and M. Babiker, Phys. Rev. B **43** (11), 9096 (1991).
9. F. Comas, C. Trallego-Giner, and M. Cardona, Phys. Rev. B **56** (7), 4115 (1997).
10. N. Bloembergen, *Nonlinear Optics* (Benjamin, New York, 1965; Mir, Moscow, 1966).
11. H. M. Gibbs, *Optical Bistability: Controlling Light with Light* (Academic, Orlando, 1985; Mir, Moscow, 1988).
12. R. Reinish and G. Vitrant, Prog. Quantum Electron. **18** (1), 1 (1994).
13. T. Ackemann, A. Heuer, Yu. A. Logvin, and W. Lang, Phys. Rev. A **56** (3), 2321 (1997).
14. E. Lidorikis, Q. Li, and C. M. Soukoulis, Phys. Rev. E **55** (3), 3613 (1997).
15. S. Coen, M. Tlidi, P. Emplit, and M. Haelterman, Phys. Rev. Lett. **83** (12), 2328 (1999).
16. E. Centeno and D. Felbacq, Phys. Rev. B **62** (12), R7683 (2000).
17. H. Haug and S. W. Koch, *Quantum Theory of the Optical and Electronic Properties of Semiconductors* (World Sci., Singapore, 1990).
18. M. Hilley and L. D. Mlodinow, Phys. Rev. A **31** (2), 797 (1985).
19. V. M. Faĭn, *Photons and Nonlinear Media* (Sovetskoe Radio, Moscow, 1972).
20. W. A. Harrison, *Electronic Structure and the Properties of Solids: The Physics of the Chemical Bond* (Freeman, San Francisco, 1980; Mir, Moscow, 1983), Vol. 1.

Translated by A. Kazantsev

Physics of the Solid State, Vol. 45, No. 4, 2003, pp. 630–633. Translated from Fizika Tverdogo Tela, Vol. 45, No. 4, 2003, pp. 600–603.

SEMICONDUCTORS AND DIELECTRICS

Anomalous Nonlinearity of IR Photoconductivity of Diamond Polycrystalline Films

V. V. Tokiĭ, V. I. Timchenko, and V. A. Soroka

Donbass State Academy of Building and Architecture, Makeevka, Donetsk oblast, 86123 Ukraine

e-mail: vlitim@mail.ru

Received September 6, 2002

Abstract—Nonlinearity of the lux–ampere characteristics of undoped polycrystalline diamond films is revealed. The spectral dependences of this nonlinearity and photoconductivity are analyzed in the framework of the available models with a single impurity level or a single type of traps. It is shown that, for undoped polycrystalline diamond films in the range of impurity photoconductivity, the lux–ampere characteristics exhibit an anomalous nonlinearity when their slopes change from 1/2 to approximately unity with a decrease in the wavelength and an increase in the excitation level and the carrier lifetime. The results obtained are explained within the model of the coexistence of two different channels of conduction in diamond films. Two ranges of carrier photogeneration are established. For photon energies below 1.4 eV, the carrier generation with quadratic recombination is observed in a single channel. At higher photon energies, the carrier generation occurs in two channels simultaneously (in addition, the carriers are excited with linear recombination in the second channel). It is demonstrated that the equilibrium concentration of carriers in the second channel with linear recombination substantially exceeds the equilibrium concentration of carriers in the first channel with quadratic recombination, which hampers the detection of the first channel without photoexcitation. *© 2003 MAIK "Nauka/Interperiodica".*

1. INTRODUCTION

In recent years, photoconductivity of carbon materials has been studied in the range of fundamental absorption with the aim of determining the basic parameters of the band structure of fullerenes [1, 2] and diamond [3]. In particular, Korovkin and Nikolaev [4] examined the impurity photoconductivity induced in fullerenes by intrinsic defects of the crystal and impurities.

The impurity photoconductivity of diamond films was investigated by Collins [5]. It was noted that, in the near-infrared (IR) range, the photoconductivity of diamond prepared through chemical vapor deposition is characterized by a complex spectrum [5], which makes it impossible to identify the defects without additional studies.

The purpose of this study was to analyze the lux–ampere characteristics and the spectral distribution of photoconductivity of polycrystalline diamond films in the IR range (in the range of impurity photoconductivity) in order to determine particular channels of conduction.

2. SAMPLE PREPARATION AND EXPERIMENTAL TECHNIQUE

An undoped polycrystalline diamond film was grown on a silicon substrate with the (111) orientation through chemical vapor deposition [6]. The volume content of the components in the gaseous mixture was 0.5% CH_4 and 99.5% H_2. The total pressure of the gaseous mixture was equal to 112 Torr, and the substrate temperature was 1170 K. The thickness of the studied film was 13.5 μm. In order to examine the photoresponse in the diamond film, the samples used were separated from the growth substrate and clamped to an insulating holder.

The suitable ohmic contacts were produced by applying an Aquadag lubricant on the surface of the polycrystalline diamond film. We also tested other methods of producing the electrodes on the surface of diamond samples, for example, pressed tungsten probes; however, they turned out to be less convenient. The contacts were prepared in the form of strips at the edges of the film with a width of 3 mm, a length of 3 mm, and a thickness of 0.5 mm. The distance between the electrodes was equal to 1.5 mm. Therefore, the area of the illuminated surface was 4.5 mm^2.

The source of monochromatic radiation was an SF-4 monochromator with a quartz prism. The film was illuminated on the side of the free surface. The light was modulated by a disk with sectoral slots and was then focused into a beam with the use of a quartz lens. This ensured uniform illumination of the interelectrode surface of the diamond film, thus exciting nonequilibrium charge carriers. Earlier [7], we examined the current–voltage characteristics of undoped polycrystalline diamond films upon exposure to modulated light and found that the contacts remain ohmic up to fields of 6×10^3 V/cm.

1063-7834/03/4504-0630$24.00

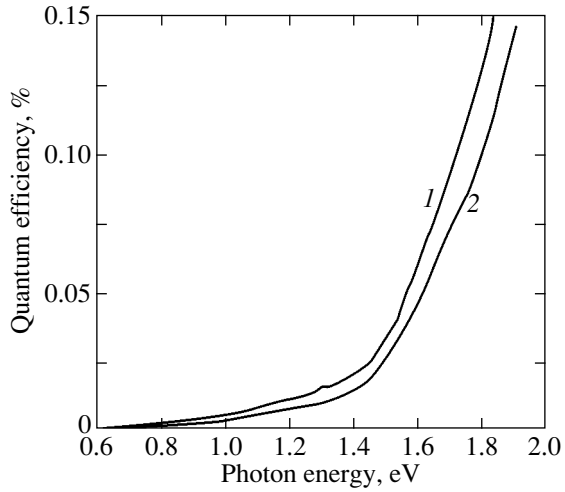

Fig. 1. Spectral dependences of the quantum efficiency of the undoped polycrystalline diamond film for different light sources. For curves *1* and *2*, the ratio of photon fluxes at a wavelength of 875 nm is 2 : 1.

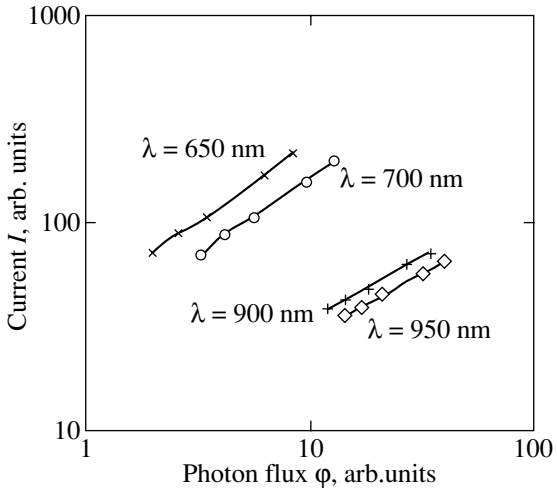

Fig. 2. The effect of the photon energy on the lux–ampere characteristics of the undoped polycrystalline diamond film.

In this work, such a dc voltage was applied to the sample and the load resistor that the field at the samples was 5×10^3 V/cm. A signal generated at the load resistor under illumination of the sample was perceived by a U2-8 amplifier connected in the mode of broad-band amplification and was then transmitted to a synchronous detector. The voltages supplied to the radiation source and to the modulator drive were stabilized.

The radiation intensity at a constant wavelength was controlled by varying the temperature of the filament of the source and was measured on an Yu-116 standard luxmeter. The filament temperature was determined using an optical pyrometer in the range from 2000 to 3000 K.

3. RESULTS AND DISCUSSION

We studied the quantum efficiency of the photodetector based on a diamond film as a function of the wavelength of incident radiation at different voltages across the contacts [6]. In the present work, the quantum efficiency was found to be equal to 0.08–0.12% in the case when the voltage across the contacts was 750 V at the wavelength $\lambda = 700$ nm (Fig. 1). Here, the photoconductivity spectra of the diamond film were normalized to one incident photon for different light sources.

Figure 2 illustrates how the wavelength of modulated monochromatic light affects the lux–ampere characteristics of undoped polycrystalline diamond films. The power of radiation incident on the sample at a wavelength of 700 nm varied in the range from 0.7×10^{-6} to 2.8×10^{-6} W/cm^2. It can be seen that, at a constant radiation wavelength, the photocurrent I_p increases with a rise in the level of the photon flux φ. For a steady radiation flux, the photoconductivity and, correspondingly, the concentration of nonequilibrium carriers $\Delta q(\lambda)$ increase as the wavelength decreases. Therefore, the following inequality is satisfied over the entire range studied:

$$\Delta q(\lambda_1) > \Delta q(\lambda_2), \quad (1)$$

where $\lambda_1 < \lambda_2$.

As can be seen from Fig. 3, the slope of the lux–ampere characteristic $\tan(\lambda) = d(\ln I_p)/d(\ln \varphi)$ depends on the wavelength λ of monochromatic radiation. At a wavelength of 875 nm ($h\nu = 1.4$ eV), the range of excitation of nonequilibrium carriers can be separated into two ranges, namely, the short-wavelength and long-wavelength ranges. It is clearly seen from Figs. 2 and 3 that the lux–ampere characteristic of the photocurrent deviates significantly from linear behavior. It is also

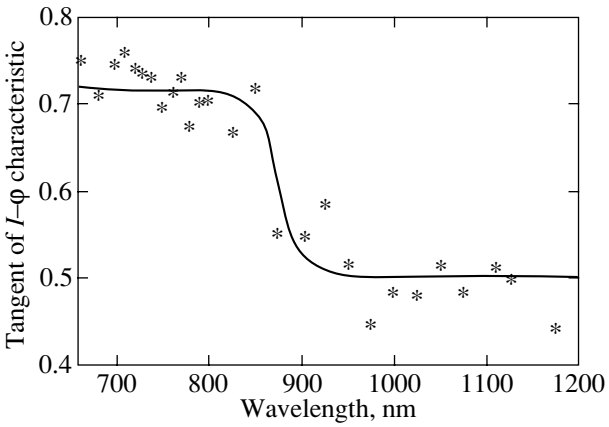

Fig. 3. Spectral dependence of the slope of the lux–ampere characteristic.

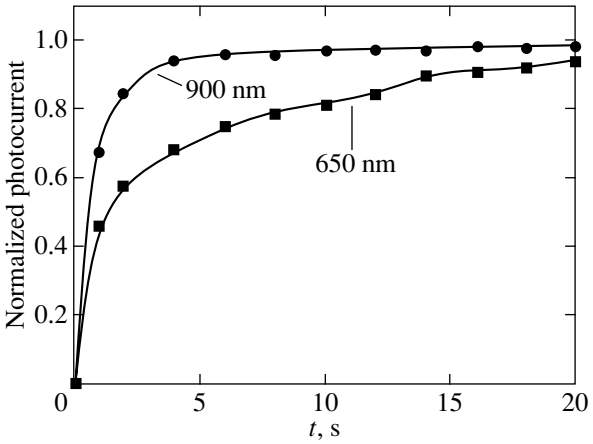

Fig. 4. Photocurrent normalized to the maximum value as a function of time for photons with energies of 1.90 (650 nm) and 1.37 eV (900 nm) at different fluxes.

evident that a decrease in the nonequilibrium carrier concentration (a decrease in the photocurrent, see Fig. 2) leads to a decrease in the slope of the lux–ampere characteristic.

Let us assume that the photoconductivity in the studied range exhibits impurity nature (the band gap of diamond is approximately equal to 5.5 eV). We should note that, under this assumption, the slope tanλ can decrease with a rise in the level of the photon flux φ. A similar situation exists in the case when the centers responsible for the generation of photocarriers are exhausted but was not observed in our experiments. The results obtained indicate the opposite trend, namely, an increase in the photocurrent with an increase in the photon flux.

The increase in the slope with increasing intensity of light for materials with a single type of traps was justified theoretically and verified experimentally for germanium in [8]. This dependence takes place under the condition that the relaxation time increases with a rise in the level of the photon flux. Analysis of the time dependences of the photocurrent at different wavelengths of modulated monochromatic light (Fig. 4) demonstrates that the relaxation time decreases with an increase in the photon flux [φ(900 nm) > φ(650 nm)]. Thus, it is established that, in the range of impurity photoconductivity of diamond, the lux–ampere characteristics of undoped polycrystalline diamond films exhibit an anomalous nonlinearity when their slopes change from 1/2 to approximately unity with a decrease in the wavelength and an increase in the carrier lifetime.

In the long-wavelength range (λ_L range), the slope is close to 1/2, which corresponds to a quadratic recombination of nonequilibrium carriers when the concentration of nonequilibrium carriers considerably exceeds the total concentration of equilibrium carriers, i.e., when the following condition is satisfied:

$$\Delta q(\lambda_L) \gg n_0 + p_0. \quad (2)$$

In the short-wavelength range (λ_S range), the slope tanλ approaches unity, which corresponds to a linear recombination of nonequilibrium carriers when the concentration of nonequilibrium carriers is substantially less than the total concentration of equilibrium carriers, i.e., when the following condition holds:

$$\Delta q(\lambda_S) \ll n_0 + p_0. \quad (3)$$

It follows from relationships (2) and (3) that $\Delta q(\lambda_L) > \Delta q(\lambda_S)$; therefore, the photoconductivity in the long-wavelength range should be higher than that in the short-wavelength range. This contradicts relationship (1) obtained in the experiment.

The observed anomalous nonlinearity of photoconductivity can be explained in terms of the spatially inhomogeneous model with two ranges of carrier photogeneration. The first range is characterized by the quadratic recombination of carriers. For photon energies above 1.4 eV, nonequilibrium carriers with $\Delta q_S(\lambda_S)$ are additionally excited in the second range; i.e., the short-wavelength excitation occurs in two concurrent channels of nonequilibrium conduction. Photocurrent in this range of excitation can be represented as the sum of currents: $I_p = I_1 + I_2$. Here, the first and second terms satisfy the relationships of quadratic ($d\ln I_1/d\ln\varphi = 1/2$) and linear ($d\ln I_2/d\ln\varphi = 1$) recombinations, respectively. Hence, the slope tan(λ) takes on values in the range from 1/2 to 1. By using these relationships and the result presented in Fig. 3, we obtain the following expression in the short-wavelength range:

$$\frac{I_2}{I_1} = \frac{\tan(\lambda_S) - 0.5}{1 - \tan(\lambda_S)}. \quad (4)$$

In our case, when $\tan(\lambda_S) = 0.7$, we have $I_2/I_1 = 2/3$.

Consequently, condition (3) should be replaced by a new condition, that is,

$$\Delta q_S(\lambda_S) \ll n_0^S + p_0^S, \quad (5)$$

where $n_0^S + p_0^S$ is the equilibrium concentration of carriers in the second range.

If the carrier mobilities in the first and second short-wavelength ranges are comparable, it follows from expression (4) that the concentrations of nonequilibrium carriers $\Delta q(\lambda_S)$ and $\Delta q_S(\lambda_S)$ in the first and second ranges are also comparable. From conditions (2) and (5), we derive the relationship

$$n_0 + p_0 \ll n_0^S + p_0^S. \quad (6)$$

The observed anomalous nonlinear photoconductivity of polycrystalline diamond films in the near-IR range can be interpreted within the model of the coexistence of two channels of nonequilibrium conduction.

For example, these can be holes in the valence band of islands on the (111) relaxed surface and holes in the valence band of islands on the (111) 2×1 reconstructed surface of diamond, for which, as is known [6, 9, 10], the distances from the valence band tops to the Fermi level are determined to be 0.6 and 1.4 eV, respectively. These can also be nonequilibrium carriers generated by electrically active bulk centers and any one of the aforementioned surface centers. By virtue of inequality (6), the first channel revealed does not manifest itself under conditions of equilibrium conduction. Only photogeneration made it possible to detect this channel. In order to elucidate the nature of the active centers unambiguously, it is necessary to examine the spectra of the photoresponse in a wider range of wavelengths and to resolve the complex spectra into sufficiently simple components (using, for example, relationship (4)). However, this is beyond the scope of the present work.

REFERENCES

1. C. H. Lee, G. Yu, D. Moses, *et al.*, Phys. Rev. B **48** (11), 8506 (1993).
2. S. Matsuura, T. Ishiguro, K. Kikuchi, and Y. Achiba, Phys. Rev. B **51** (15), 10216 (1995).
3. A. G. Zakharov, N. A. Poklonskiĭ, V. S. Varichenko, and A. G. Gontar', Fiz. Tverd. Tela (St. Petersburg) **42** (4), 647 (2000) [Phys. Solid State **42**, 664 (2000)].
4. E. V. Korovkin and R. K. Nikolaev, Fiz. Tverd. Tela (St. Petersburg) **41** (6), 1113 (1999) [Phys. Solid State **41**, 1015 (1999)].
5. A. T. Collins, in *Proceedings of the Conference "Eurodiamond-96"* (SIF, Bologna, 1996), Vol. 52, p. 43.
6. V. V. Tokiy, V. I. Timchenko, V. A. Soroka, *et al.*, in *Proceedings of the Third International Conference on the Applications of Diamond Films and Related Materials*, Ed. by A. Feldman *et al.* (National Inst. of Standards and Technology, Gaithersburg, MD, 1995), p. 145.
7. V. V. Tokiĭ, V. I. Timchenko, and V. A. Soroka, Tr. Ukr. Vakuum. Obshch. **3**, 120 (1997).
8. S. M. Ryvkin and N. B. Strokan, Dokl. Akad. Nauk SSSR **124** (5), 1034 (1959) [Sov. Phys. Dokl. **4**, 164 (1959)].
9. B. B. Pate, Surf. Sci. **165**, 83 (1986).
10. F. Bechstedt and R. Enderlein, *Semiconductor Surfaces and Interfaces: Their Atomic and Electronic Structures* (Akademie, Berlin, 1988; Mir, Moscow, 1990).

Translated by O. Moskalev

Physics of the Solid State, Vol. 45, No. 4, 2003, pp. 634–638. Translated from Fizika Tverdogo Tela, Vol. 45, No. 4, 2003, pp. 604–608.

SEMICONDUCTORS AND DIELECTRICS

Ion Transfer in Solid Solutions of Cu_2Se and Ag_2Se Superionic Conductors

M. Kh. Balapanov, R. A. Yakshibaev, and U. Kh. Mukhamed'yanov

Bashkortostan State University, ul. Frunze 32, Ufa, 450074 Bashkortostan, Russia

Received September 8, 2002

Abstract—The cationic conductivities of Cu_2Se and Ag_2Se superionic conductor solid solutions in the composition region from Cu_2Se to $Cu_{0.7}Ag_{1.3}Se$ are measured. It is demonstrated that the activation energy of ionic conduction depends only slightly on the chemical composition, varies from 0.14 to 0.17 eV, and exhibits a weakly pronounced maximum for the $Ag_{0.44}Cu_{1.56}Se$ solid solution. The ionic Seebeck coefficients are measured for the $Ag_{0.23}Cu_{1.757}Se$ solid solution. The heat of cation transfer in this solution is found to be equal to 0.144 ± 0.014 eV from the Seebeck coefficients. © *2003 MAIK "Nauka/Interperiodica".*

1. INTRODUCTION

It is known that Cu_2Se and Ag_2Se superionic conductors form quasi-binary alloys with high mixed cationic conductivity [1–3]. At temperatures above 473 K, there exist extended regions of solid solutions based on the α-Cu_2Se face-centered cubic phase (from Cu_2Se to $Cu_{0.7}Ag_{1.3}Se$) and the α-Ag_2Se body-centered cubic phase (from Ag_2Se to $Ag_{1.5}Cu_{0.5}Se$) [4]. In our earlier works [5–8], we examined the ion transfer in solid solutions based on the α-Ag_2Se body-centered cubic phase. The present paper reports on the results of investigations into the ionic conduction in solid solutions based on the α-Cu_2Se phase.

As was shown by Gorbunov [9], grain boundary diffusion in high-temperature superionic phases of polycrystalline copper chalcogenides with large-sized grains is of little importance. In this respect, our results on the ionic conductivity in solid solutions based on the α-Cu_2Se phase should be interpreted in terms of diffusion in the bulk of grains. Since the *Fm*3*m* structural type of the initial crystal lattice of α-Cu_2Se is retained in the solid solutions under consideration, we believe that mobile cations of copper and silver in these solutions migrate over interstices, as is the case in α-Cu_2Se. The crystal lattice of α-Cu_2Se is strongly disordered. Sakuma [10] proved that, in a unit cell of α-Cu_2Se, four selenium anions with the coordinates $\left(0\ 0\ 0;\ 0\ \frac{1}{2}\ \frac{1}{2};\ \frac{1}{2}\ 0\ \frac{1}{2};\ \frac{1}{2}\ \frac{1}{2}\ 0\right)$ form a rigid framework of the lattice and eight Cu^+ cations are distributed over sixteen interstitial positions. Seven copper ions statistically occupy $32(f)_{\mathrm{I}}$ (tetrahedral) positions with the coordinates *xxx*, $x\bar{x}\bar{x}$, $\bar{x}x\bar{x}$, $\bar{x}\bar{x}x$, $\bar{x}\bar{x}\bar{x}$, $\bar{x}xx$, $x\bar{x}x$, and $xx\bar{x}$ (where $x = 0.297$). One Cu^+ ion is statistically distributed over $32(f)_{\mathrm{II}}$ (octahedral) positions with the coordinates *xxx*, $x\bar{x}\bar{x}$, $\bar{x}x\bar{x}$, $\bar{x}\bar{x}x$, $\bar{x}\bar{x}\bar{x}$, $\bar{x}xx$, $x\bar{x}x$, $xx\bar{x}$ (where $x = 0.471$). The easy-diffusion paths of Cu^+ ions pass through the adjacent positions $32(f)_{\mathrm{I}}$ and $32(f)_{\mathrm{II}}$.

The thermoelectric properties of copper chalcogenides and their alloys are of considerable interest because these materials can be used in thermoelectric energy converters. The main difficulties encountered in studying the thermoelectric properties of mixed superionic conductors are associated with the measurement and interpretation of the heat of ion transfer. In this work, the heats of cation transfer Q_i in the $Ag_{0.23}Cu_{1.757}Se$ superionic conductor were measured using the Honders method [11].

2. SAMPLE PREPARATION AND EXPERIMENTAL TECHNIQUE

The experiments were performed using carefully annealed polycrystalline samples with grain sizes of 50–100 μm. The samples were prepared through solid-phase synthesis from binary selenides of copper and silver in ampules. The alloys thus obtained were ground, pressed into pellets, and homogenized at a temperature of 723 K for a period of a week. The samples were prepared in the form of parallelepipeds $2 \times 5 \times 20$ mm in size for ionic conductivity measurements and $2 \times 5 \times 30$ mm in size for thermoelectric measurements. The homogeneity of the chemical composition throughout the sample length was checked by an electron microprobe analysis of the surface. The scatter of the results was within the limits of experimental error (~1%).

The ionic conductivity of $Ag_xCu_{2-x}Se$ solid solutions was measured by suppressing the electron current [12] with the use of ion current filters of two composi-

tions (AgI/Ag or CuBr/Cu) in an electrochemical cell of type **I**:

$$\mathrm{Pt_1/Cu/CuBr/Ag_xCu_{2-x}Se/CuBr/Cu/Pt_2}$$
$$\mathrm{Pt_3/Cu/CuBr}\text{—}\uparrow \qquad \uparrow\text{—}\mathrm{CuBr/Cu/Pt_4}.$$

For a low density of the direct current passing through a sample (through the contacts Pt_1 and Pt_2), the stationary ion potential difference was measured (between the contacts Pt_3 and Pt_4) using probes of the same composition. The validity of the Iokota method [12] (developed earlier for mixed electronic–ionic conductors of the α-Cu_2Se type), as applied to $Ag_xCu_{2-x}Se$ solid solutions with mobile cations of two sorts (silver and copper), was justified by Miyatani [1].

At low densities j of the ion current (in our experiments, the current density j did not exceed 10 mA/cm^2), when the applied potential difference is considerably less than the decomposition potential of the phase, only the Ag^+ cations migrate through the sample–AgI interface. The Cu^+ cations and electrons (holes) are blocked at the interfaces. This is responsible for the appearance of the ion concentration gradient across the sample and, hence, the diffusion flux. The polarization process involves two stages. At the first stage, the current of electrons is compensated for by their diffusion counterflux (the rate of this process is determined by the coefficient of coupled chemical diffusion of cations and electrons). At the second (slower) stage, the electron concentration gradient across the sample (and the related gradient of the total cation concentration) remains constant and the current of Cu^+ ions disappears gradually (the rate of the process depends on the self-diffusion coefficient of the cations). At equilibrium, the Cu^+ cation flux induced by the electric field is compensated for by the diffusion counterflux and only the resulting current of Ag^+ ions passes through the sample. The chemical composition of the sample remains unchanged.

For the current density used in our measurements, the difference between the chemical compositions of the sample in different cross sections due to concentration polarization and the possible effect of this polarization on the ionic conductivity can be disregarded. Special investigations demonstrated that a change in the chemical composition of the AgI probes upon contact with $Ag_xCu_{2-x}Se$ alloys does not exceed 10% in the composition range $x \geq 0.1$ and decreases drastically with an increase in x. Therefore, this factor affects the results of measurements only slightly. The maximum contribution (approximately 3%) to the experimental error was associated with the finite sizes of the ion probes.

The heat of ion transfer Q was determined directly from the ionic thermoelectric coefficients (the ionic Seebeck coefficients) according to the technique described in [11]. This technique involves the replacement of ion probes of the Ag/AgI type in a conventional cell for measuring the ionic thermopower by probes of the studied sample/AgI type (for more details, see, for example, [5, 10, 13]). The ionic thermoelectric coefficient thus measured can be represented by the expression

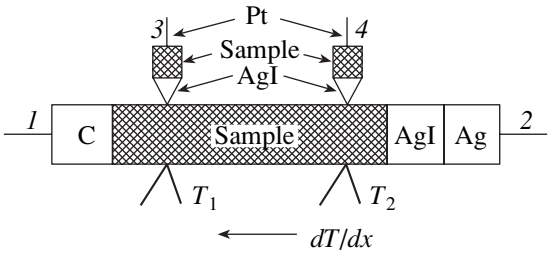

Fig. 1. Schematic drawing of the electrochemical cell for measuring the ionic thermoelectric coefficient α_i^H.

$$\alpha_i^H = -\frac{Q_i}{eT} - \alpha_{\mathrm{Pt}}, \qquad (1)$$

where α_{Pt} is the contribution of the platinum contacts to the thermopower. In the majority of cases, this contribution can be ignored.

The ionic thermopower U_i^H was measured using two composite ion probes of the $Ag_{0.23}Cu_{1.757}Se$/AgI type (contacts *3* and *4* in Fig. 1) in the absence of electric current through the sample. The thermoelectric coefficient was determined from the relationship $\alpha_i^H = U_i^H/\Delta T$, where $\Delta T = T_2 - T_1$ is the difference between the temperatures in the isothermal cross sections of the sample at points of contact with the ion probes. The thermopower was measured after the attainment of an equilibrium state of the sample.

The ionic thermoelectric coefficients α_i^H and ionic conductivities σ_i were measured in the range of temperatures at which the $Ag_xCu_{2-x}Se$ alloys are solid solutions based on the Cu_2Se face-centered cubic phase. The measuring cell was placed in a dried purified argon atmosphere. In the course of measurements, the constancy of the chemical composition and the attainment of the equilibrium state of the samples were checked against the electromotive force E of an electrochemical cell of type **II**:

Pt/Sample/AgI/Ag.

The error in determining the heats of ion transfer Q_i and the ionic conductivity σ_i did not exceed 5%.

3. RESULTS AND DISCUSSION

Figures 2–4 show the temperature dependences of the ionic conductivity for $Ag_{0.1}Cu_{1.9}Se$, $Ag_{0.23}Cu_{1.757}Se$, and $Ag_{0.44}Cu_{1.56}Se$ solid solutions measured by three

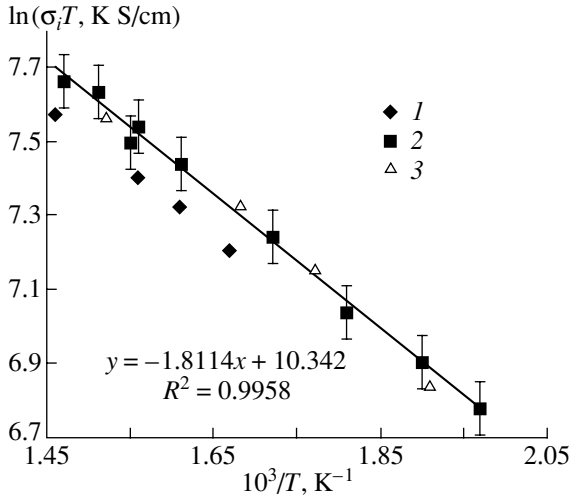

Fig. 2. Temperature dependence of the ionic conductivity measured for the $Ag_{0.1}Cu_{1.9}Se$ solid solution with the use of different potential probes and current-carrying electrodes: (*1*) ion probes and electrodes of the CuBr/Cu type, (*2*) ion probes and electrodes of the AgI/Ag type, and (*3*) platinum electron probes and electrodes.

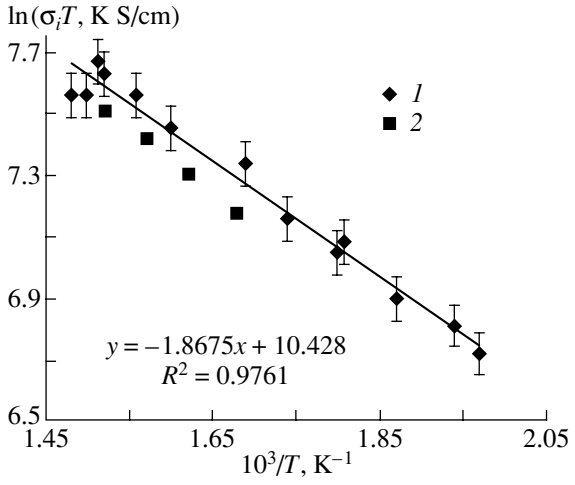

Fig. 3. Temperature dependence of the ionic conductivity measured for the $Ag_{0.23}Cu_{1.757}Se$ solid solution with the use of different potential probes and current-carrying electrodes: (*1*) ion probes and electrodes of the AgI/Ag type and (*2*) platinum electron probes and electrodes.

methods: (i) suppression of the electron current with the use of AgI/Ag ion filters, (ii) suppression of the electron current with the use of CuBr/Cu ion filters, and (iii) suppression of the ion current by electron filters (current-carrying platinum electrodes and probes). It can be seen from Figs. 2–4 that, for each solid solution, the results obtained by different methods coincide within the limits of experimental error. The use of the electron filters to suppress the cation current makes it possible to obtain the concentration polarization curve. From the parameters of this curve, we can determine the total conductivity (from the potential difference between the Pt probes at the instant of switching on the electric current), the electronic conductivity (from the steady-state potential difference between the Pt probes, which corresponds to the absence of the cation current), and the total cationic conductivity of the sample (from the difference between the aforementioned conductivities).

In our opinion, the excellent agreement between the results obtained with electron and ion filters confirms the inference drawn by Miyatani [1], according to which the use of ion filters in $(Ag_xCu_{1-x})_2Se$ systems with mobile cations of two sorts makes it impossible to determine the partial ionic conductivity. The Iokota method gives the total cationic conductivity irrespective of the conductivity of the ion (Cu^+ or Ag^+) filter.

The ionic conductivities presented in Fig. 5 for three solid solutions ($Ag_{0.6}Cu_{1.4}Se$, AgCuSe, $Ag_{1.2}Cu_{0.8}Se$) were measured using probes and electrodes of the AgI/Ag type.

The temperature dependences depicted in Figs. 2–5 exhibit an Arrhenius behavior and can be described by the relationship

$$\sigma_i T = \sigma_{i0}\exp(-E_a/kT), \quad (2)$$

where σ_{i0} is a constant and E_a is the activation energy. These dependences in the $1/T$–$\ln(\sigma_i T)$ coordinates are represented by straight lines. The equations of the straight lines and the approximation errors R^2 calculated with the inclusion of all the experimental points obtained for each solid solution are given in the figures. Table 1 lists the activation energies of ionic conduction

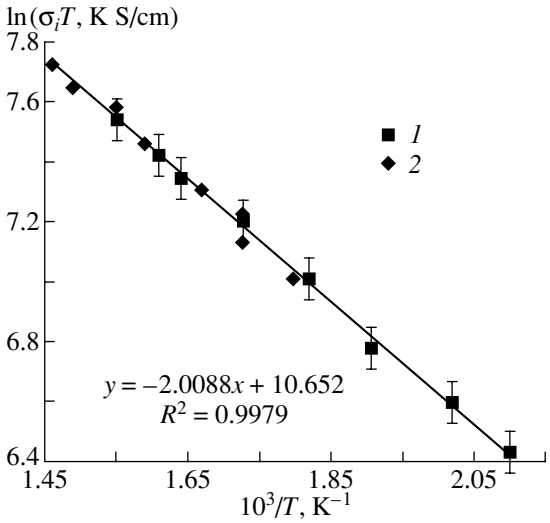

Fig. 4. Temperature dependence of the ionic conductivity measured for the $Ag_{0.44}Cu_{1.56}Se$ solid solution with the use of different potential probes and current-carrying electrodes: (*1*) ion probes and electrodes of the AgI/Ag type and (*2*) platinum electron probes and electrodes.

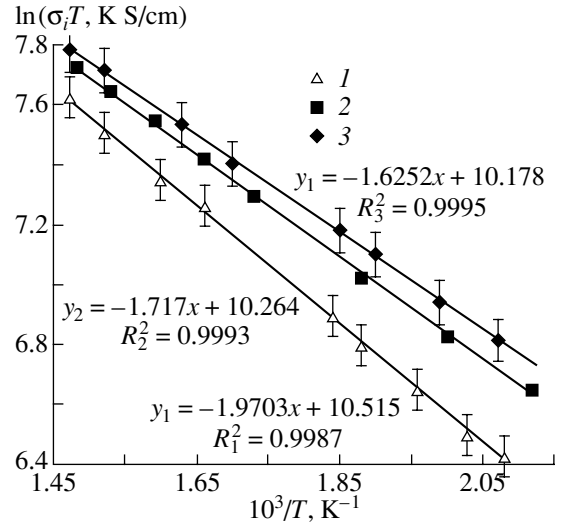

Fig. 5. Temperature dependences of the ionic conductivity measured for (*1*) $Ag_{0.6}Cu_{1.4}Se$, (*2*) AgCuSe, and (*3*) $Ag_{1.2}Cu_{0.8}Se$ solid solutions with the use of potential probes and current-carrying electrodes of the AgI/Ag type.

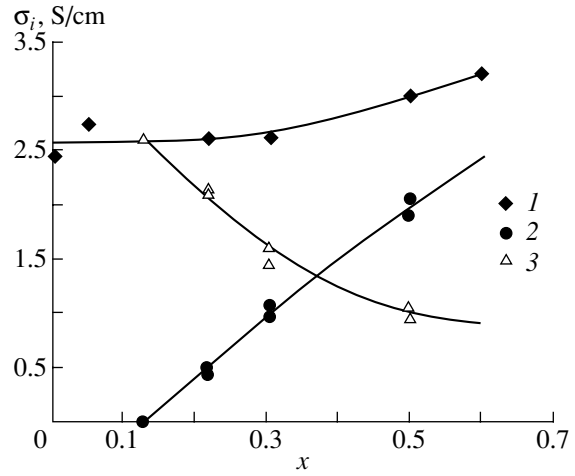

Fig. 6. Dependences of the (*1*) total, (*2*) silver, and (*3*) copper ionic conductivities on the silver content x in the $(Ag_xCu_{1-x})_2Se$ solid solutions at a temperature of 623 K according to the data taken from [8].

and the preexponential factors σ_{i0} determined from these equations according to formula (2).

Analysis of the data presented in Figs. 2–5 and Table 1 demonstrates that the substitution of silver for copper in copper selenide leads to an insignificant increase in the total cationic conductivity of the high-temperature phase. The activation energy of ionic conduction first slightly increases from 0.14 to 0.17 eV (in the composition range $0.1 \le x \le 1.0$), then decreases, and regains its initial value for the $Ag_{1.2}Cu_{0.8}Se$ solid solution. The preexponential factor σ_i has a maximum value of 42.3×10^3 K S/cm for the $Ag_{0.44}Cu_{1.56}Se$ solid solution; this solution is also characterized by the highest activation energy, $E_a = 0.173$ eV.

As is known, the activation energy of ionic conduction in the Ag_2Se binary compound is equal to 0.10 eV. It is reasonable to assume that transfer of Cu^+ and Ag^+ ions in the Cu_2Se–Ag_2Se solid solution occurs with different activation energies. Consequently, a change in the concentration ratio of these ions in the solid solution results in a change in the effective (averaged over two sorts of cations) activation energy, which is calculated from the total cationic conductivity $\sigma_i = \sigma_{Cu^+} + \sigma_{Ag^+}$. In our earlier work [8], the ratios of partial conductivities $\sigma_{Cu^+}/\sigma_{Ag^+}$ for $(Ag_xCu_{1-x})_2Se$ solid solutions were determined using a combined electrogravimetric method. The curves $\sigma_{Cu^+}(x)$ and $\sigma_{Ag^+}(x)$ obtained in [8] are plotted in Fig. 6. It can be seen from Fig. 6 that, beginning with the $Ag_{0.23}Cu_{1.757}Se$ composition, an increase in the silver content is accompanied by a decrease in the copper ionic conductivity. The ionic conductivities σ_{Cu^+} and σ_{Ag^+} become equal to each other for approximately the $Ag_{0.7}Cu_{1.3}Se$ composition. For a dominant copper component in the solid solution, this situation can be observed in the case when the activation energy of migration of silver ions is less than that of copper ions. A further increase in the silver content should lead to a decrease in the effective activation energy and an increase in the total cationic conductivity, which is observed in the experiments (Table 1, Figs. 2–6).

The obtained data on the ionic thermopower are given in Table 2.

After averaging over the entire temperature range covered, we obtained the heat of cation transfer for the $Ag_{0.23}Cu_{1.757}Se$ solid solution: $Q_i = 0.144 \pm 0.014$ eV. This heat of cation transfer is close to the activation energy of ionic conduction $E_a = 0.161 \pm 0.011$ eV. Close values of these quantities have also been observed for $Ag_{2-\delta}Te$ [14]. The heat of ion transfer and the activation energy of ionic conduction in superionic conductors are related in a complex fashion. This prob-

Table 1. Activation energies of ionic conduction and preexponential factors for Cu_2Se–Ag_2Se solid solutions

Composition	E_a, eV	σ_{i0}, 10^3 K S/cm
Cu_2Se	0.14	–
$Ag_{0.1}Cu_{1.9}Se$	0.156	31.0
$Ag_{0.23}Cu_{1.757}Se$	0.161	33.8
$Ag_{0.44}Cu_{1.56}Se$	0.173	42.3
$Ag_{0.6}Cu_{1.4}Se$	0.170	36.9
AgCuSe	0.148	28.7
$Ag_{1.2}Cu_{0.8}Se$	0.140	26.3

Table 2. Ionic thermoelectric coefficients α_i^H, heats of cation transfer Q_i, and electromotive forces E of electrochemical cell **I** for the $Ag_{0.23}Cu_{1.757}Se$ alloy at different temperatures

T, °C	α_i^H, mV/K	Q_i, eV	E, mV
205	0.307	0.147	165.5
235	0.307	0.157	180.2
245	0.270	0.140	180.3
270	0.243	0.133	203.8
310	0.236	0.138	213.2
345	0.232	0.144	228.6

lem remains unclear even though it has long been a subject of investigation [13, 15, 16]. In particular, Tsidil'kovskiĭ and Mezrin [17, 18] theoretically treated this problem for superionic conductors of the channel type, including the high-temperature phase of copper selenide [10, 19, 20]. Reasoning from the results obtained in [17, 18], the close values of Q_i and E_a for the $Ag_{0.23}Cu_{1.757}Se$ solid solution can be due to a weak interaction of mobile ions with lattice vibrations and the absence of a correlation between ion hoppings. According to Wada *et al.* [16], the interaction of mobile ions with free electrons can be responsible for the discrepancy between the values of Q_i and E_a. Therefore, we can state that electrons have no noticeable effect on the motion of ions in the $Ag_{0.23}Cu_{1.757}Se$ solid solution.

REFERENCES

1. S. Miyatani, J. Phys. Soc. Jpn. **34** (2), 423 (1973).
2. S. Miyatani, Yu. Miura, and H. Ando, J. Phys. Soc. Jpn. **46** (6), 1825 (1979).
3. V. N. Chebotin, V. N. Konev, and V. M. Berezin, Izv. Akad. Nauk SSSR, Neorg. Mater. **20** (9), 1462 (1984).
4. R. A. Yakshibaev, V. N. Konev, N. N. Mukhamadeeva, and M. Kh. Balapanov, Izv. Akad. Nauk SSSR, Neorg. Mater. **24** (3), 501 (1988).
5. R. A. Yakshibaev, M. Kh. Balapanov, and V. N. Konev, Fiz. Tverd. Tela (Leningrad) **29** (3), 937 (1987) [Sov. Phys. Solid State **29**, 537 (1987)].
6. R. A. Yakshibaev and M. Kh. Balapanov, Fiz. Tverd. Tela (Leningrad) **29** (9), 2819 (1987) [Sov. Phys. Solid State **29**, 1620 (1987)].
7. R. A. Yakshibayev, R. F. Almukhametov, and M. Kh. Balapanov, Solid State Ionics **31**, 247 (1989).
8. R. A. Yakshibaev, N. N. Mukhamadeeva, M. Kh. Balapanov, and G. R. Akmanova, Phys. Status Solidi A **112**, K97 (1989).
9. V. A. Gorbunov, Candidate's Dissertation (Sverdlovsk, 1986).
10. T. Sakuma, Bull. Electrochem. **11** (1–2), 57 (1995).
11. A. Honders, J. M. Kinderen, A. H. van Heeren, *et al.*, Solid State Ionics **14**, 205 (1984).
12. I. Iokota, J. Phys. Soc. Jpn. **16** (11), 2213 (1961).
13. C. Wagner, Prog. Solid State Chem. **7**, 1 (1972).
14. R. A. Yakshibaev and M. Kh. Balapanov, Fiz. Tverd. Tela (Leningrad) **27** (11), 3484 (1985) [Sov. Phys. Solid State **27**, 2102 (1985)].
15. J. F. Smith, D. I. Peterson, and M. F. Smith, J. Less-Common Met. **106** (1), 19 (1985).
16. C. Wada, A. Suzuki, H. Sato, and R. Kikuchi, Phys. Chem. Solids **46** (10), 1195 (1985).
17. V. I. Tsidil'kovskiĭ and V. A. Mezrin, Fiz. Tverd. Tela (Leningrad) **28** (7), 2155 (1986) [Sov. Phys. Solid State **28**, 1202 (1986)].
18. V. I. Tsidil'kovskiĭ and V. A. Mezrin, Dokl. Akad. Nauk SSSR **292** (6), 1436 (1987).
19. T. Kanashiro, Y. Kishimoto, T. Ohno, and Y. Mishihiro, Solid State Ionics **40/41**, 308 (1990).
20. K. Yamamoto and S. Kashida, Solid State Ionics **48**, 241 (1991).

Translated by O. Borovik-Romanova

Physics of the Solid State, Vol. 45, No. 4, 2003, pp. 639–642. Translated from Fizika Tverdogo Tela, Vol. 45, No. 4, 2003, pp. 609–612.

DEFECTS, DISLOCATIONS, AND PHYSICS OF STRENGTH

Effect of a Pulsed Magnetic Field on the Real Solid-Solution Structure in the Sb–As System

M. N. Levin, G. V. Semenova, T. P. Sushkova, V. V. Postnikov, and B. L. Agapov

Voronezh State University, Universitetskaya pl. 1, Voronezh, 394693 Russia

e-mail: levin@lev.vsu.ru

Received June 26, 2002; in final form, August 20, 2002

Abstract—A first study of the effect of weak pulsed magnetic fields (PMFs) on $Sb_{1-x}As_x$ solid solution crystals is reported. An effect of long-time (months) redistribution of the solid solution components at room temperature after a short (seconds) exposure to a PMF was revealed. The effect includes stages of enrichment of the crystal surface in antimony with the formation of clusters, antimony cluster breakup, and a decrease in surface antimony content, which is accompanied by a substantial improvement in solid-solution homogeneity. The PMF-induced component redistribution entails a decrease in the crystal melting temperature. Rupture of stressed chemical bonds in arsenic vacancy complexes, which is induced by a change in their multiplicity under PMF exposure, is considered as a possible trigger mechanism. *© 2003 MAIK "Nauka/Interperiodica".*

1. INTRODUCTION

The binary Sb–As system is known to form a continuous series of solid solutions with a minimum in their phase diagram [1]. A thermodynamic analysis based on tensometric measurements showed a trend to decomposition of a solid solution at low temperatures [2]. However, no experimental evidence for the existence of a heterophase region in this system has thus far been produced. The possibility of solid solution decomposition in the Sb–As system initiated by an external factor has not been established either.

On the other hand, there have been reports on the unique capability of weak (<1 T) pulsed magnetic fields (PMFs) to affect the real structure of solids and the character of the processes occurring in them [3–5]. In particular, short exposures to PMFs were found to initiate long-term low-temperature decomposition of a solid solution of oxygen in Czochralski-grown silicon crystals (Cz-Si), which entails a radical change in the whole microstructure of the crystal [6].

The above observations account for the interest in the possibility of initiating structural changes in $Sb_{1-x}As_x$ solid solutions using PMFs.

This study deals with the effect of PMFs on the stability and real structure of solid solutions in the Sb–As system.

2. EXPERIMENTAL TECHNIQUE

The studies were conducted on crystals of an $Sb_{0.8}As_{0.2}$ solid solution whose composition corresponded to the minimum in the antimony–arsenic phase diagram. The starting components used to prepare the solid solution crystals were Su-000-grade antimony and OSCh-9-5 arsenic, which was additionally vacuum-sublimated to remove oxides. The synthesis was performed using the one-temperature method in thick-walled glass ampules evacuated to a base pressure of 5×10^{-4} Pa. To homogenize the solid solutions and remove intracrystallite segregation, the ingot was subjected to directed crystallization followed by annealing for 100 h at 823 K. The alloys thus obtained had a large-block structure. The studies were carried out on samples measuring $5 \times 4 \times 4$ mm cut from the central part of the same crystal.

The PMF exposure was made at $T = 300$ K in a low-inductance solenoid through which a capacitor bank was discharged periodically. The experiment consisted in applying a train of 3000 symmetric triangular-shaped pulses of amplitude $B = 0.3$ T, length $\tau = 3 \times 10^{-5}$ s, and repetition frequency $f = 50$ Hz. The samples thus treated were stored at $T = 300$ K between reference measurements together with the samples that were not subjected to PMF action.

The effect of PMFs on the $Sb_{1-x}As_x$ crystals was studied using x-ray microprobe analysis, scanning electron microscopy, and differential thermal analysis.

The x-ray microprobe analysis was used to investigate the distribution of chemical elements on the sample surface. Measurements were conducted on a CamScan S4 scanning electron microscope equipped with a Link AN10/55S x-ray energy-dispersive-analysis system. The planar element distribution was determined in a surface layer ~1 μm thick using the characteristic x-ray radiation excited by an electron beam scanning the sample surface. The same CamScan scanning electron microscope was used to obtain surface micrographs of the samples before and after PMF exposure.

1063-7834/03/4504-0639$24.00

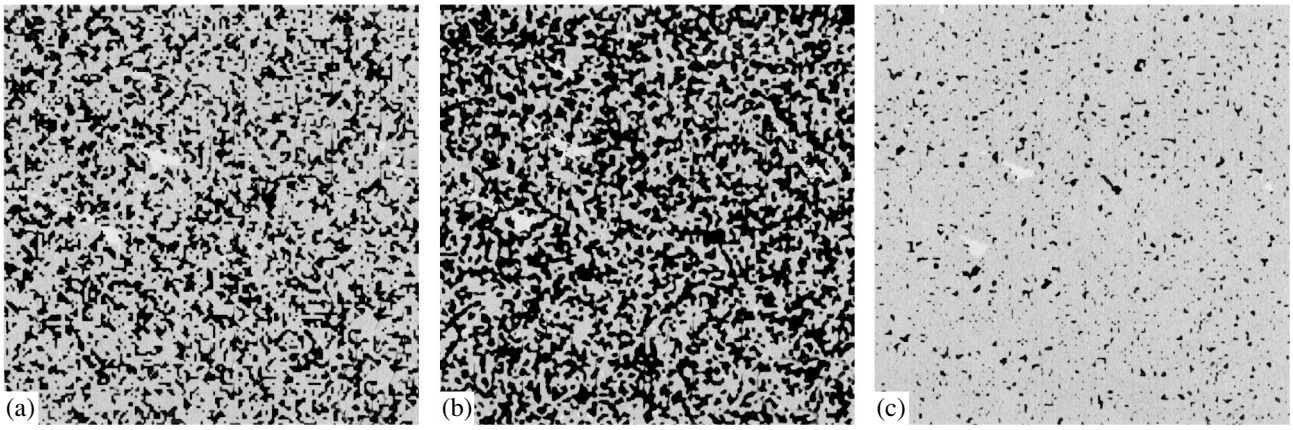

Fig. 1. Planar distribution of the elemental composition in a surface layer of an $Sb_{0.8}As_{0.2}$ sample: (a) before, (b) five days later, and (c) 100 days after PMF exposure. Sb is shown in black; As, in white; and the Sb–As solid solution (elements present in comparable concentrations), in gray. Image size, 500×500 μm.

The differential thermal analysis was performed following the standard technique on FRU-64 and NTR-75-type instruments.

3. EXPERIMENTAL RESULTS

The results of the x-ray microprobe analysis of the $Sb_{0.8}As_{0.2}$ samples are shown in Fig. 1.

The initial elemental distribution is given in Fig. 1a. Note that arsenic is a volatile component of the binary system and builds up, in the course of crystal preparation, in defect regions, which are clearly seen in the electron micrographs of the same region of the sample in Fig. 2a.

A short (seconds) exposure of the $Sb_{0.8}As_{0.2}$ crystals to a PMF initiates long-term (thousands of hours at T = 300 K) spatial redistribution of the solid solution components. In the first stage, the crystal surface becomes enriched in antimony, which segregates in clusters (Figs. 1b, 2b). In the second stage, the reverse process sets in, i.e., the antimony clusters formed dissolve (Fig. 2c), and the Sb content in the surface layer decreases (Figs. 1c, 2c).

The percentage contents of the Sb and As aggregates and of the $Sb_{0.8}As_{0.2}$ solid solution in the surface layer (~1 μm) at various times after the PMF action are given in the table.

Relative contents of arsenic, antimony, and the solid solution (%) in a surface layer of an $Sb_{0.8}As_{0.2}$ sample

Component	Before PMF exposure	Time elapsed after PMF exposure (days)			
		5	10	50	100
As	2.1	2.6	1.2	1.6	0.4
Sb	31.5	42.6	34.6	12.1	4.4
Sb + As	66.4	54.8	64.2	86.3	95.2

As seen from the table, the concentration of free antimony aggregated in clusters was the highest five days after the PMF exposure, after which the antimony concentration decreased monotonically by nearly an order of magnitude to a level considerably below the initial value.

The x-ray microprobe studies were accompanied by measurements of the melting temperature of reference samples prepared from the same ingots.

It was found that exposure to a PMF brings about a considerable decrease in the sample melting point in the course of the PMF-induced element redistribution. It should be pointed out that an alloy having a composition corresponding to the minimum in the phase diagram (azeotrope) melts not within a temperature interval (a feature characteristic of a solid solution) but rather at a fixed temperature (878 ± 3 K). After the exposure to a PMF, the phase transition temperature decreased by 25–30 K; however, 300–350 h thereafter, the melting points of the treated and reference samples became practically the same.

4. DISCUSSION

The totality of the experimental results obtained can be summed up as follows. A short-term (seconds) action of a weak PMF on crystals of $Sb_{1-x}As_x$ solid solutions brings about a long-term (thousands of hours at T = 300 K) redistribution of the components in consecutive stages of enrichment in antimony of surface layer with the formation of clusters, segregation of these clusters, and a decrease in antimony content on the crystal surface accompanied by a substantial increase in the homogeneity of the $Sb_{1-x}As_x$ solid solution. The observed structural changes are followed by a temporary decrease in the crystal melting point.

Thus, the enrichment of the $Sb_{1-x}As_x$ crystal surface in antimony and the subsequent homogenization of the solid solution accompanied by a temporary decrease in its melting temperature require explanation.

Because the above results are completely new and the dependence of the effect on the PMF parameters has not yet been established, we can attempt, in this stage of investigation, only to qualitatively interpret the revealed phenomenon.

We note immediately that the PMFs employed satisfy the condition $\mu_n B \ll kT$ (μ_n is the Bohr magneton, and B is the magnetic field induction); i.e., the change in electron energy in the magnetic field caused by the Zeeman effect is negligible compared to the kinetic energy of thermal motion per degree of freedom of the electron. In other words, the energy involved in the PMF effect is small and cannot account for the observations.

The electric field induced by magnetic pulses, as follows from earlier estimates [5], does not exceed 5×10^3 V/m, which is likewise not large enough to produce radical changes in the crystal structure.

According to the currently accepted model concepts, the effect of weak magnetic fields on the formation and rupture of chemical bonds is of a spin nature. Developed originally to account for the effect of magnetic fields on the kinetics of radical reactions in liquid phase [6, 7], these concepts were later successfully used to explain the magnetoplastic phenomenon (dislocation depinning from paramagnetic stoppers) in diamagnetic crystals [8].

The concepts involving spin-dependent PMF-induced breakup of impurity–defect complexes with the release of rapidly diffusing point defects were considered earlier as an approach to accounting for the long-term changes in the parameters of $Si–SiO_2$ heterostructures subjected to a PMF [9].

We interpret the effects exerted by PMFs on crystals of an Sb–As solid solution by taking into account the unavoidable presence of intrinsic defects.

While the vacancy concentration in a crystal depends on the actual conditions of its growth, it is always in excess of the thermodynamically equilibrium level. In view of the smaller size of a arsenic atom as compared to that of an antimony atom and the high volatility of this component, one may expect the presence of an excess of arsenic vacancies in the structure of an $Sb_{1-x}As_x$ alloy. It is known that aggregation in complexes is energetically more favorable for vacancies than remaining free [10].

By acting on the spins of the electrons involved in the formation of stressed bonds in the original vacancy complexes, a PMF favors weakening of these bonds, which, in turn, may give rise to breakdown of a fraction of the original vacancy complexes, accompanied by a release of mobile single vacancies. The vacancies thus formed migrate to drains, the most important of them being the crystal surface. Diffusion of arsenic vacancies to the surface is equivalent to their being healed in the bulk of the crystal by arsenic atoms that diffuse toward their vacancies from the surface. The arsenic transport into the bulk of the crystal results in the surface layer becoming enriched in the second component of the solid solution, antimony. In this way, the equilibrium vacancy concentration corresponding to the temperature of observation sets in the sample. After this, antimony atoms start to diffuse from the regions where they are present in a high concentration into the bulk of the

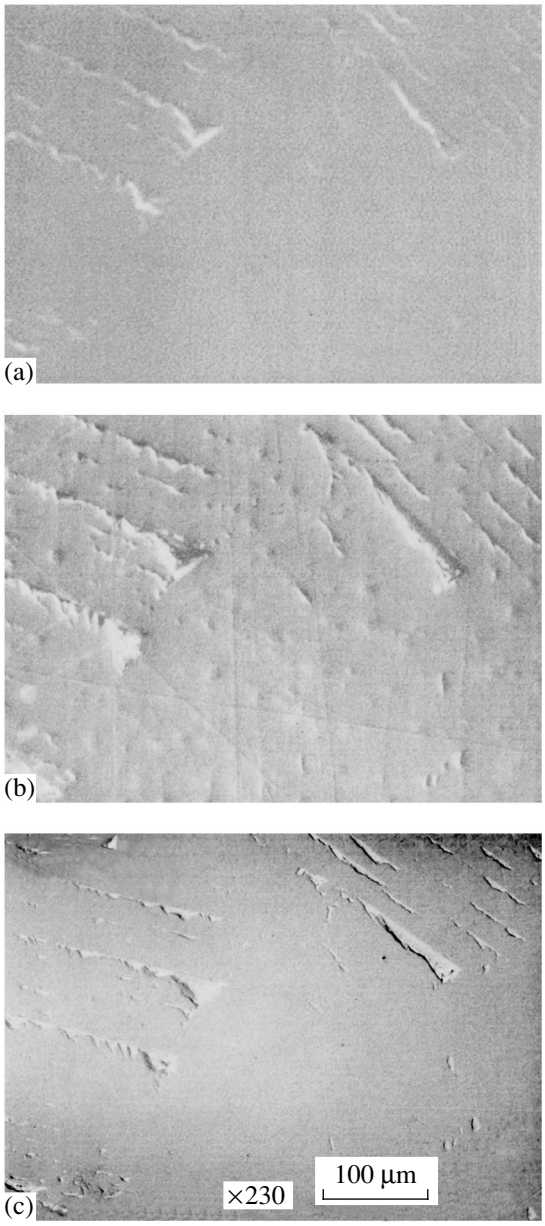

Fig. 2. Electron micrograph of an $Sb_{0.8}As_{0.2}$ crystal surface (a) before, (b) five days later, and (c) 100 days after PMF exposure. The sample region chosen is the same as in Fig. 1.

crystal and the component distribution becomes more uniform than in the original state.

The weakening and rupture of bonds in vacancy complexes induced by a PMF and followed by a loss of diffusion stability in the crystal provide a reasonable explanation for the temporal lowering of the crystal melting temperature observed to occur during the subsequent diffusion of the components making up the solid solution.

REFERENCES

1. M. Hansen and K. Anderko, *Constitution of Binary Alloys*, 2nd ed. (McGraw-Hill, New York, 1958; Metallurgizdat, Moscow, 1962).
2. Ya. A. Ugaĭ, E. G. Goncharov, G. V. Semenova, and V. B. Lazarev, *Phase Equilibria between Phosphorus, Arsenic, Antimony, and Bismuth* (Nauka, Moscow, 1989).
3. G. I. Distler, V. M. Kanevskiĭ, V. V. Moskvin, *et al.*, Dokl. Akad. Nauk SSSR **268** (3), 591 (1983) [Sov. Phys. Dokl. **28**, 43 (1983)].
4. Yu. I. Golovin and R. B. Morgunov, Chem. Rev. **23**, 23 (1998).
5. M. N. Levin and B. A. Zon, Zh. Éksp. Teor. Fiz. **111** (4), 1373 (1997) [JETP **84**, 760 (1997)].
6. Ya. B. Zel'dovich, A. L. Buchachenko, and E. L. Frankevich, Usp. Fiz. Nauk **155** (1), 3 (1988) [Sov. Phys. Usp. **31**, 385 (1988)].
7. U. E. Steiner and T. Ulrich, Chem. Rev. **89**, 51 (1989).
8. M. I. Molotskiĭ, Fiz. Tverd. Tela (Leningrad) **33** (10), 3112 (1991) [Sov. Phys. Solid State **33**, 1760 (1991)].
9. M. N. Levin and V. M. Maslovsky, Solid State Commun. **90** (12), 813 (1994).
10. S. V. Bulyarskiĭ and V. I. Fistul', *Thermodynamics and Kinetics of Interacting Defects in Semiconductors* (Nauka, Moscow, 1997).

Translated by G. Skrebtsov

Physics of the Solid State, Vol. 45, No. 4, 2003, pp. 643–648. Translated from Fizika Tverdogo Tela, Vol. 45, No. 4, 2003, pp. 613–617.

DEFECTS, DISLOCATIONS, AND PHYSICS OF STRENGTH

Dynamics of Surface Dislocation Ensembles in Silicon under Conditions of Mechanical and Magnetic Perturbations

A. M. Orlov, A. A. Skvortsov, and A. A. Solov'ev

Ul'yanovsk State University, Ul'yanovsk, 432970 Russia

e-mail: amo@orlov.ulsu.su, scvor@sv.uven.ru

Received May 14, 2002; in final form, August 15, 2002

Abstract—This paper reports on the results of investigations into the dynamics of surface dislocation ensembles in silicon under conditions of mechanical and magnetic perturbations. The motion of defects is described with due regard for barriers of three types, including magnetically sensitive point defects and dislocations. Within the concept of spin-dependent reactions between structural defects, a kinetic model is proposed for the magnetic-field-stimulated changes observed in the dislocation mobility due to the formation of long-lived complexes involving paramagnetic impurities. It is experimentally proved that the preliminary treatment of dislocation-containing crystals in a magnetic field (B = 1 T) for 5–45 min leads to an increase in the velocity of dislocations in *n*-Si and *p*-Si samples by factors of two and three, respectively. The magnetic memory effect is observed in dislocation-containing silicon crystals. Consideration is given to the decay kinetics of the magnetic memory during storage of the silicon samples under natural conditions after magnetic treatment. The basic quantitative characteristics of the motion of linear defects in a magnetic field (for example, the partial velocities of dislocations, the dynamics of dislocation segments at stoppers of different types, and the expectation times for the appearance of the appropriate stoppers) are determined by fitting the experimental data to the theoretical results. © *2003 MAIK "Nauka/Interperiodica".*

1. INTRODUCTION

It is well known that a magnetic field with an induction $B \sim 1$ T can affect the mobility of linear defects in ionic crystals, metals, and semiconductors [1–8]. The physical mechanism of the influence of weak magnetic fields on the dynamics of the dislocation structure, as a rule, is interpreted within the model of spin-dependent reactions [1–12]. This model describes the magnetically stimulated evolution of impurity electron spin centers that are capable of removing the spin forbiddenness from particular electron transitions. As a result, the defect structure undergoes a transformation. Specifically, the rate of motion of linear defects changes in both the field of internal stresses of the crystal and the field of external forces.

Although available experimental data relevant to this subject matter are rather reliable, many problems regarding the magnetically stimulated dynamics of dislocations remain unclear. In particular, the mobility of dislocation segments in elemental semiconductors subjected to magnetic field treatment for different times is poorly understood. There are no data on the kinetic and field dependences of the mean free path of dislocations in elemental semiconductors exposed to a magnetic field. Nothing definite is known about the role played by different-type stoppers that interact with a dislocation moving in a doped semiconductor. Information on the kinetics of variation in the mean free path of dislocations in crystals with an inhomogeneous spatial distribution of linear defects is lacking. The present study is aimed at analyzing these important problems.

2. THEORETICAL BACKGROUND

Let us consider a dislocation moving in a field of external forces. Under these conditions, the dislocation motion is governed by stoppers of three types: (1) stoppers associated with the proper potential relief of the crystal lattice (hereafter, stoppers of this type will be denoted by the subscript i = 1), (2) magnetically sensitive (i = 2) point defects (majority doping impurities), and (3) crossing linear defects, including dislocations trees (i = 3).

In the field of elastic stresses, the resultant velocity of dislocations v and their mechanical mobility $\mu_m = v/F$ are determined by the partial contributions of the aforementioned stoppers and can be represented by the relationship

$$\mu_m = \frac{1}{F(\tau_1 C_1 + \tau_2 C_2 + \tau_3 C_3)}. \quad (1)$$

Here, F is the force acting on the defect [N]; C_i is the concentration of stoppers per unit length of the dislocation path [m^{-1}]; $C = 1/a$ (a is the period of the Peierls relief [m]); $\tau_i = \tau_0 \exp(E_i/k_B T)$ is the expectation time for the appearance of stoppers of type i [s]; E_1 is the Peierls barrier; E_2 and E_3 are the energies of pinning of dislocations at stoppers of types i = 2 and 3, respec-

tively [J]; k_B is the Boltzmann constant [J/K]; and T is the temperature [K].

Actually, a dislocation executing a motion meets with stoppers of different types and is halted by them for a characteristic expectation time. Depending on the number of encountered barriers $n_i = xC_i$, the dislocation traverses a distance x for the time

$$\tau = \sum_{i=3} \tau_i n_i = x \sum_{i=3} \tau_i C_i. \quad (2)$$

The resultant velocity of dislocations in the field of elastic stresses can be written as

$$v = \frac{x}{\tau} = \frac{1}{\sum_{i=3} \tau_i C_i}, \quad (3)$$

which is consistent with Eq. (1). From expression (3), it follows that the resultant velocity of dislocations is governed by the largest value of $C_i\tau_i$ (or by the smallest value of v_i).

Now, we analyze the components $C_i\tau_i$. The first type of stoppers is associated with the proper potential relief of the crystal lattice (the Peierls relief), which is responsible for the dislocation motion in a defect-free crystal. Hence, the first term $C_1\tau_1$ in the above expression can be represented as a constant independent of the coordinates and the travel time of the dislocation. Consequently, the partial velocity of the moving dislocation,

$$v_1 = \frac{1}{C_1\tau_1} = \text{const}, \quad (4)$$

should also be constant.

A somewhat more intricate situation occurs with stoppers of the second type (magnetically sensitive stoppers with a concentration C_2). In our case, stoppers of this type are attributed to boron or phosphorus impurities in silicon. Either of these paramagnetic impurities [1–3, 10] is redistributed between the impurity centers with concentrations C_{2a} and C_{2b}, which are characterized by different orientations of the electron spins and the expectation times τ_{2a} and τ_{2b}.

From relationships (1)–(4) and the equation of material balance

$$C_2 = C_{2a} + C_{2b}, \quad (5)$$

it can easily be shown that, in Eq. (1), the second term $\tau_2 C_2$ satisfies the expression

$$\tau_2 C_2 = \tau_{2a} C_{2a} + \tau_{2b} C_{2b} = C_2\tau_{2b} - C_{2a}(\tau_{2b} - \tau_{2a}). \quad (6)$$

Hence, the partial velocity of dislocations v_2, which is related to the concentration of magnetically sensitive stoppers, should be governed by the equation

$$v_2 = \frac{1}{\tau_{2a}C_{2a} + \tau_{2b}C_{2b}}$$

or

$$v_2 = \frac{1}{C_2\tau_{2b} - C_{2a}(\tau_{2b} - \tau_{2a})}. \quad (7)$$

However, the C_2 components, unlike the C_1 components, vary with time t, because the magnetic field initiates an active formation of stoppers with shorter expectation times and, at $t > t_B$ (i.e., after the completion of treatment in the magnetic field), the magnetic-field-induced system of structural defects relaxes toward its initial unperturbed state. Therefore, proper allowance must be made for the changes in the C_2 components at different stages of the redistribution of magnetically sensitive stoppers.

In the case when the relaxation processes after magnetic treatment occur, e.g., for the C_2 components, at a rate given by the formula

$$\frac{dC_{2a}}{dt} = -kC_{2a}, \quad (8)$$

the concentration of stoppers accelerating the dislocation motion owing to shorter times τ_{2a} will satisfy the relationship

$$C_{2a} = C_{2a}^0 \exp(-kt^*), \quad (9)$$

where k is the rate constant of the recovery of the electronic subsystem [s^{-1}], $t^* = (t > t_B)$ is the relaxation time of magnetic-field-stimulated changes [s], and C_{2a}^0 is the initial concentration of stoppers with the corresponding orientation of electron spins.

The initial concentration C_{2a}^0 is determined by the degree of magnetic perturbation. It is evident that, at fixed **B**, the rate of redistribution of magnetically sensitive stoppers for C_{2a} can be represented by the equation

$$\frac{dC_{2a}^0}{dt_B} = k_{2b}C_{2b}^0 - k_{2a}C_{2a}^0$$

or

$$\frac{dC_{2a}^0}{dt_B} = k_{2b}(C_2 - C_{2a}^0) - k_{2a}C_{2a}^0, \quad (10)$$

where k_{2a} and k_{2b} are the formation constants for stoppers with the corresponding orientations of electron spins.

Table 1. Parameters of the silicon samples under investigation

No.	Crystallographic orientation	Conductivity type, impurity, resistivity	Size (mm) and scribing direction	Density of introduced dislocations N_d, cm^{-2}	Deformation about the crystallographic axis	Mechanical stress, MPa
1	[111]	*n*-type, phosphorus, 2Ω cm	$30 \times 10 \times 0.4$ [$\bar{1}$10], [11$\bar{2}$], [111]	10^4–10^6	[$\bar{1}$10]	30
2	[100]	*p*-type, boron, 0.5Ω cm	$25 \times 10 \times 0.6$ [100], [010], [001]	10^4–10^6	[001]	50

The solution to Eq. (10) has the following form:

$$C_{2a}^0 = \frac{k_{2b}}{k_{2a}+k_{2b}}C_2 - \left[\frac{k_{2b}}{k_{2a}+k_{2b}}C_2 - C_{2a}^{00}\right]\exp(-(k_{2a}+k_{2b})t_B), \quad (11)$$

where C_{2a}^{00} is the equilibrium concentration at $t_B = 0$.

Therefore, the velocity of dislocations controlled by magnetically sensitive stoppers should satisfy relationship (7) with due regard for Eqs. (9) and (11); that is,

$$v_2 = \left[C_2\tau_{2b} - \left(\frac{k_{2b}}{k_{2a}+k_{2b}}C_2 - \left(\frac{k_{2b}}{k_{2a}+k_{2b}}C_2 - C_{2a}^{00}\right)\right.\right. \times \exp(-(k_{2a}+k_{2b})t_B)\Big)(\tau_{2b}-\tau_{2a})\exp(-k(t-t_B))\Big]^{-1}. \quad (12)$$

As regards stoppers of the third type, which, according to [13, 14], are associated with the nodes of crossing of linear defects, they affect the velocity of dislocations v and the dislocation mobility μ_m through the dislocation density N_d [m^{-2}]. The concentration of stoppers of the third type can be defined as

$$C_3 = \gamma\sqrt{N_d}\cos\alpha\cos\beta, \quad (13)$$

where γ is the number of slip planes and α and β are the angles between the slip planes and the Burgers vectors of the interacting dislocations, respectively.

In this case, the partial velocity of dislocations at sufficiently high dislocation densities N_d should be governed by the expression

$$v_3 = \frac{1}{C_3\tau_3} = \frac{1}{\tau_3\gamma\sqrt{N_d}\cos\alpha\cos\beta}. \quad (14)$$

At small quantities $C_3\tau_3$, the partial velocity v^3 will increase indefinitely and, hence, the dislocation motion will be controlled by stoppers of other types.

3. EXPERIMENTAL TECHNIQUE

Experimental verification of the basic relationships derived above was performed using single-crystal silicon wafers doped with boron or phosphorus. The main parameters of the studied samples are listed in Table 1. Dislocations were introduced into dislocation-free silicon wafers according to the procedure described in [15–17]. For this purpose, two parallel scratches were cut in a specified crystallographic direction on the surface of each sample (Fig. 1). The separation between the scratches considerably exceeded the maximum path length of dislocation half-loops. The samples with scratches were exposed to a magnetic field ($B \le 1$ T). At every instant, the magnetic induction vector was perpendicular to the scratches. The time t_B of treatment in the magnetic field was varied in the range 30–2800 s at a fixed time interval ($t^* = 180$ s) between the completion of the magnetic treatment and the onset of the high-temperature plastic deformation. The choice of the constant time t^* was governed by the rate of relaxation processes in magnetically sensitive stoppers after the magnetic treatment of the silicon samples.

The motion of surface dislocation loops in silicon wafers was initiated under 40-min tensile stresses (up to 50 MPa) with the use of the four-support bending method. The maximum path length of individual dislocations was measured after selective etching of the sample in a CP-4 standard solution with simultaneous

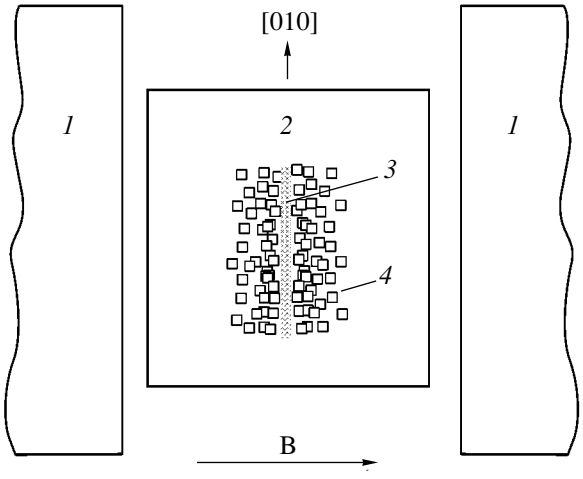

Fig. 1. Schematic arrangement of the silicon wafers between the magnet poles: (*1*) electromagnet poles, (*2*) silicon wafer, (*3*) stress concentrator (scratch), and (*4*) etch pits of surface dislocations (dislocation segments).

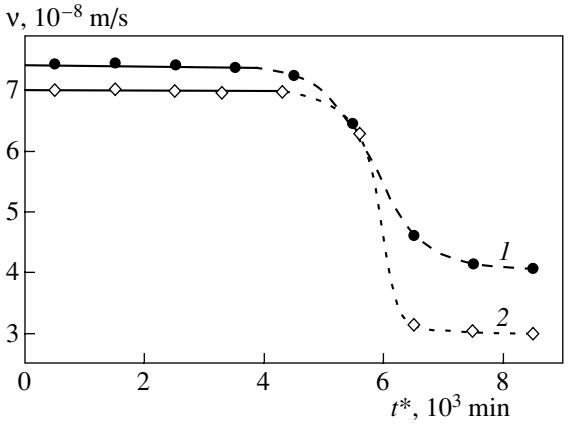

Fig. 2. Variation in the velocity of dislocations during storage of (*1*) *p*-Si and (*2*) *n*-Si samples under natural conditions after a 20-min treatment in a magnetic field at $B = 1$ T. Points are experimental data. Solid portions of the curves correspond to the results of calculations according to relationship (12) ($v = 3.7$ and 2.4 m/s at $t_B = 0$ for *p*-Si and *n*-Si samples, respectively).

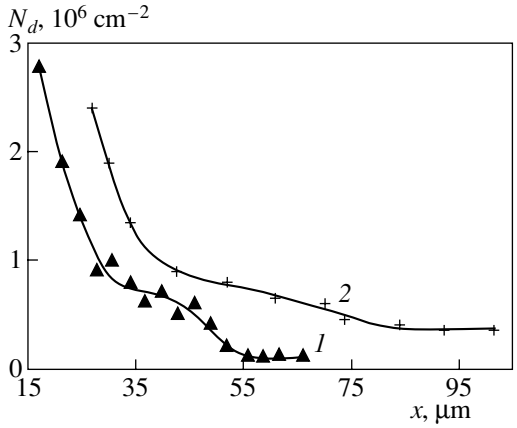

Fig. 3. Spatial distribution of the dislocation density with distance from the scratch in the course of plastic deformation of (*1*) *n*-Si and (*2*) *p*-Si samples for 40 min at a temperature of 675°C. $t_B = 0$.

recording of the concentration profile of the dislocation ensemble for 15 different portions of each scratch. The basic experimental results are presented in Figs. 2–6.

4. RESULTS AND DISCUSSION

After the preliminary treatment of the samples in a magnetic field, dislocations become more active and undergo rapid mixing in the crystal. This effect, which we identified as the magnetic memory effect,[1] persists for at least three days, after which the mobility of dislocations (and, correspondingly, their velocity) decreases drastically and approaches values characteristic of the initial samples not treated in the magnetic field (Fig. 2). The changes observed in the dislocation velocity $v = f(t^*)$ during the 73-h monotonic decay of the magnetic memory are in good agreement with the results obtained in calculations using relationship (12) at fixed times t_B. This made it possible to determine the rate constants k of the recovery of the electronic subsystem (Table 2).

As can be seen from Fig. 3, the velocity of linear defects in the field of elastic stresses strongly depends on the dislocation density N_d. In particular, the velocity of dislocations in *n*-Si samples increases by a factor of three with a decrease in the dislocation density from 3×10^6 to 0.3×10^6 cm^{-2}. It is worth noting that the maximum changes in the dislocation velocity v are observed in spatial regions with high dislocation densities N_d, whereas the velocities of fast dislocations in the vicinity of low densities N_d either remain nearly constant or change insignificantly. In the temperature range under investigation, the depth of penetration of individual dislocations in a sample depends linearly n the duration of isothermal annealing of the crystal (0.5–16 h). These findings indicate that dislocation stoppers with the concentration C_3 play a dominant role only in the defect regions adjacent to scratches, in which their effect on the resultant velocity v is most pronounced. Therefore, in the case of distant dislocations, we can exclude stoppers with the concentration C_3 from our consideration and examine only the effects associated with magnetic perturbations.

Figure 4 shows the dependences of the highest velocity of dislocations in *n*-Si and *p*-Si samples on the time of treatment in a magnetic field ($B = 1$ T). Despite the quantitative difference observed in the velocities of

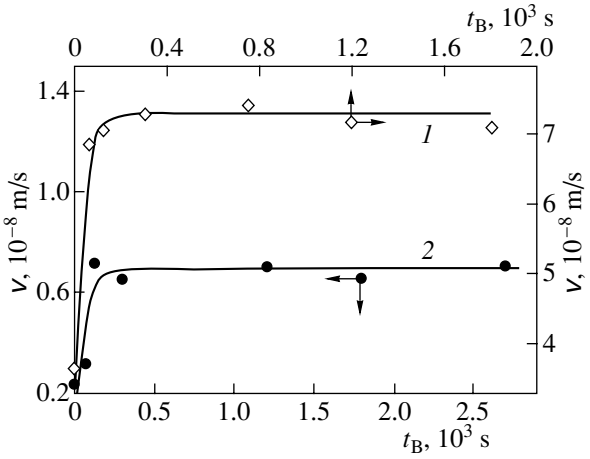

Fig. 4. Dependences of the highest velocity of dislocations in (*1*) *p*-Si and (*2*) *n*-Si samples on the time of treatment in a magnetic field at $B = 1$ T. Points are experimental data. Solid lines represent the results of calculations according to relationship (12).

[1] The magnetic memory effect in magnetic-disordered crystals was first revealed by Golovin and Morgunov [18] in 1993.

dislocations in *n*-Si and *p*-Si samples, there exists a clear tendency toward an increase in the velocity and, hence, in the concentration of magnetically sensitive stoppers C_{2a} with increasing time of treatment of silicon wafers in the magnetic field. This suggests that the C_2 concentration (and its components) is the decisive factor in the motion of dislocation segments in regions with low densities N_d.

The excellent agreement between the experimental results and relationship (12) allowed us to estimate the basic parameters of the dislocation motion (Table 2) at a fixed relaxation time t^*. The curves depicted in Fig. 5 characterize the redistribution of stopper concentrations C_{2i} and partial velocities of dislocations $v_{2i} = 1/C_{2i}\tau_{2i}$ at different expectation times after the controlled stages of magnetic treatment. It should be noted that the expectation times for the appearance of dislocations at magnetically sensitive stoppers are relatively large (Table 2); in particular, they exceed the characteristic times of spin conversion (10^{-11}–10^{-10} s [1, 2, 10]) by a factor of ~10^{10}. Therefore, the delayed response of the partial velocity of dislocations v_2 to magnetic perturbations (Fig. 4) can be primarily associated not with the spin dynamics but with the delayed formation of complexes involving impurity centers with different orientations of electron spins:

$$C_{2a} \xrightarrow{k_{2a}} C_{2a}^{+} + \xi_{2a},$$
$$C_{2b} \xrightarrow{k_{2b}} C_{2b}^{-} + \xi_{2b}. \qquad (15)$$

Here, the superscripts "+" and "–" specify the configurations of electron spins of the impurity centers and ξ_{2i} stands for the structural components of the complexes with concentrations C_{2i}.

The quantitative results obtained in this work are only appropriate for isolated dislocations that are at a significant distance from the defect regions of the crystal. At the same time, an examination of the single-crystal silicon regions with high dislocation densities N_d, in which dislocation stoppers with concentration C_3 play a dominant role, can also provide important information. This information can be obtained by fitting the experimental data (Fig. 6) to the velocities v_3 calculated from relationship (14).

In actual fact, the velocities of dislocations in spatial regions controlled by stoppers with concentration C_3 (Fig. 6) agree well with the results obtained in calculations using relationship (14) for all the temperature regimes under investigation. This made it possible to determine both the mean time of pinning of dislocations at relevant stoppers τ_3 = 50 s and the energy E = 0.9 eV required by the dislocations to overcome the barrier for depinning from these stoppers. Specifically, the activation barriers to depinning of dislocations from the magnetically sensitive stoppers, according to our data for isolated dislocations, correspond to 2.1 eV.

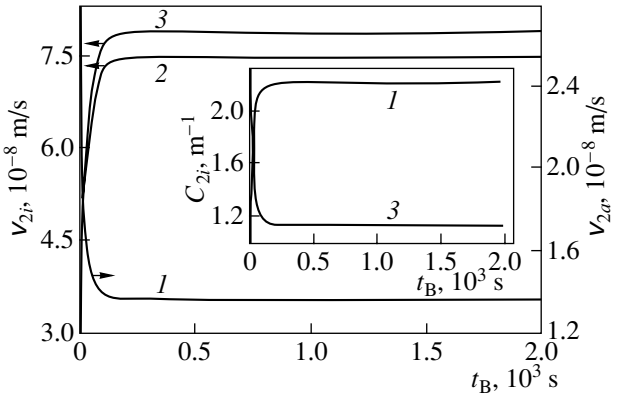

Fig. 5. Influence of the magnetic treatment duration on the concentration redistribution of magnetically sensitive stoppers and partial velocities of dislocations in the *n*-Si sample: (*1*) C_{2a}, v_{2a}; (*2*) the resultant velocity; and (*3*) C_{2b}, v_{2b}.

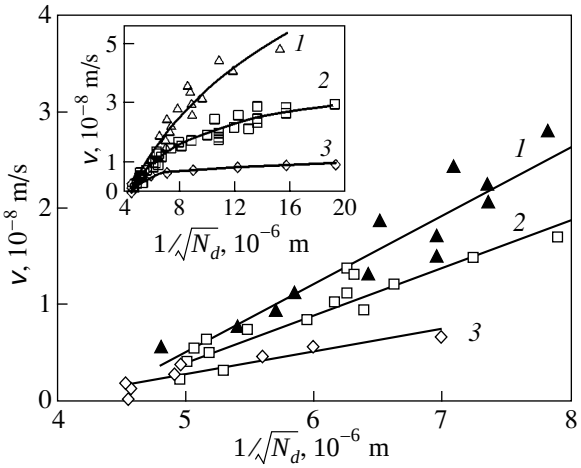

Fig. 6. Dependences of the velocity of dislocations in spatial regions controlled by stoppers with concentration C_3 (solid lines) on the quantity $1/\sqrt{N_d}$, which determines the spacing of dislocations. T, °C: (*1*) 630, (*2*) 600, and (*3*) 550. The inset shows the total dependence $v(N_d)$.

Table 2. Parameters of the magnetic-field-stimulated motion of dislocations after a 40-min isothermal annealing (B = 1 T, t^* = 180 s)

No.	Crystal type, resistivity	Impurity concentration, m^{-3}	C_2, m^{-1}	C_{2a}^{00}, m^{-1}	τ_{2b}, s	τ_{2a}, s	k_{2b}, s^{-1}	k_{2a}, s^{-1}	k, s^{-1}
1	*p*-type, 0.5Ω cm	4×10^{22}	3.4×10^7	3.3×10^7	0.64	0.02	1.3×10^{-2}	2.0×10^{-2}	1×10^{-6}
2	*n*-type, 2Ω cm	5×10^{21}	1.8×10^7	1.4×10^7	1.17	0.06	3.4×10^{-3}	7.6×10^{-3}	5×10^{-6}

These values are in agreement with the data available in the literature [13, 14].

Finally, we note that stoppers of the first type, which were not examined thoroughly in our study, are unrelated to majority impurity centers and rank below them in quantity. These stoppers play a dominant role only in high-purity silicon samples, in which the velocity of dislocations is 10–150 times higher [13] than that in the samples studied in the present work.

5. CONCLUSIONS

Thus, in this work, we analyzed the mechanism of dislocation motion involving stoppers of three types. It was found that the preliminary treatment of silicon wafers in a weak magnetic field leads to an increase in the velocity of dislocation segments by a factor of two or three. The dependence of the maximum path of dislocations on the time of exposure of the studied sample to a magnetic field was revealed. The kinetics of variations induced by a magnetic field was described within the model of spin-dependent reactions of structural defects. The quantitative characteristics of the dislocation motion under conditions of magnetic perturbations were determined, and the energy parameters of the depinning of linear defects from magnetically sensitive and dislocation stoppers were estimated.

REFERENCES

1. V. I. Al'shits, E. V. Darinskaya, and T. M. Perekalina, Fiz. Tverd. Tela (Leningrad) **29** (2), 467 (1987) [Sov. Phys. Solid State **29**, 265 (1987)].
2. Yu. I. Golovin, R. B. Morgunov, and S. E. Zhulikov, Fiz. Tverd. Tela (St. Petersburg) **39** (3), 495 (1997) [Phys. Solid State **39**, 430 (1997)].
3. V. I. Al'shits, E. V. Darinskaya, and O. L. Kazakova, Zh. Éksp. Teor. Fiz. **111** (2), 615 (1997) [JETP **84**, 338 (1997)].
4. O. I. Datsko and V. I. Alekseenko, Fiz. Tverd. Tela (St. Petersburg) **39** (7), 1234 (1997) [Phys. Solid State **39**, 1094 (1997)].
5. Yu. S. Boyarskaya, D. Z. Grabko, M. I. Medinskaya, and K. A. Palistrant, Fiz. Tekh. Poluprovodn. (St. Petersburg) **31** (2), 243 (1997) [Semiconductors **31**, 139 (1997)].
6. V. A. Makara, L. P. Steblenko, and N. Ya. Gorid'ko, Fiz. Tverd. Tela (St. Petersburg) **43** (3), 462 (2001) [Phys. Solid State **43**, 480 (2001)].
7. E. V. Darinskaya, E. A. Petrzhik, S. V. Erofeeva, and V. P. Kisel', Pis'ma Zh. Éksp. Teor. Fiz. **70** (4), 298 (1999) [JETP Lett. **70**, 309 (1999)].
8. V. I. Al'shits, E. V. Darinskaya, and E. A. Petrzhik, Fiz. Tverd. Tela (St. Petersburg) **34** (1), 155 (1992) [Sov. Phys. Solid State **34**, 81 (1992)].
9. M. I. Molotskiĭ, Fiz. Tverd. Tela (Leningrad) **33** (10), 3112 (1991) [Sov. Phys. Solid State **33**, 1760 (1991)].
10. V. I. Al'shits, E. V. Darinskaya, and E. A. Petrzhik, Fiz. Tverd. Tela (Leningrad) **33** (10), 3001 (1991) [Sov. Phys. Solid State **33**, 1694 (1991)].
11. A. L. Buchachenko, R. Z. Sagdeev, and E. M. Salikhov, *Magnetic and Spin Effects in Chemical Reactions* (Nauka, Novosibirsk, 1978).
12. M. I. Molotskii, R. E. Kris, and V. Fleurov, Phys. Rev. B **51** (18), 12531 (1995).
13. T. Suzuki, H. Yosinaga, and S. Takeucti, *Dislocation Dynamics and Plasticity* (Syokabo, Tokyo, 1986; Mir, Moscow, 1989).
14. N. N. Novikov, *Structure and Structure-Sensitive Properties of Real Crystals* (Vysshaya Shkola, Kiev, 1983).
15. I. V. Ostrovskiĭ, L. P. Steblenko, and A. B. Nadtochiĭ, Fiz. Tverd. Tela (St. Petersburg) **42** (3), 478 (2000) [Phys. Solid State **42**, 488 (2000)].
16. A. A. Skvortsov, A. M. Orlov, V. A. Frolov, *et al.*, Fiz. Tverd. Tela (St. Petersburg) **42** (10), 1814 (2000) [Phys. Solid State **42**, 1861 (2000)].
17. A. A. Skvortsov, A. M. Orlov, and L. I. Gonchar, Zh. Éksp. Teor. Fiz. **120** (1), 134 (2001) [JETP **93** (1), 117 (2001)].
18. Yu. I. Golovin and R. B. Morgunov, Pis'ma Zh. Éksp. Teor. Fiz. **58** (3), 189 (1993) [JETP Lett. **58**, 191 (1993)].

Translated by O. Borovik-Romanova

Physics of the Solid State, Vol. 45, No. 4, 2003, pp. 649–655. Translated from Fizika Tverdogo Tela, Vol. 45, No. 4, 2003, pp. 618–624.

DEFECTS, DISLOCATIONS, AND PHYSICS OF STRENGTH

Theoretical and Experimental Investigation of the Effect of an Applied Load on Pores in Solids

V. I. Betekhtin*, S. Yu. Veselkov, Yu. M. Dal'**, A. G. Kadomtsev*, and O. V. Amosova***

** Ioffe Physicotechnical Institute, Russian Academy of Sciences, Politekhnicheskaya ul. 26, St. Petersburg, 194021 Russia*
e-mail: Vladimir.Betekhtin@pop.ioffe.rssi.ru
*** St. Petersburg State University, Universitetskaya nab. 7/9, St. Petersburg, 199034 Russia*
Received July 24, 2002

Abstract—The stressed state of nonlinearly elastic bodies in the vicinity of spherical and elliptical pores is considered. The development of plastic regions near such pores is analyzed. Calculations are compared with the experimental data on pore healing under hydrostatic pressure. © *2003 MAIK "Nauka/Interperiodica".*

1. INTRODUCTION

Microscopic pores and cracks form during plastic deformation of solids or the processes of their fabrication [1]. An increase in the deformation-induced porosity or self-porosity, as a rule, deteriorates the physical-mechanical properties of solids, whereas the regeneration of their continuity (owing to complete or partial healing of pores) improves them [2].

The vast majority of investigations into the strength of porous materials are based on the linear theory of elasticity. This approach, however, has a number of substantial disadvantages. First, it cannot take into account the appearance and development of plastic zones near individual or grouped stress concentrators, including pores. Second, boundary conditions in problems of the classical theory of elasticity are satisfied at an original (undeformed) contour in a solid; therefore, solutions turn out to be valid for only weak changes in the configuration of internal defects (pores, vacancies, inclusions, microcracks, etc.).

Based on the consideration given above, the aim of this work is as follows:

(1) To obtain an analytical solution for the problem of severe deformation of a spherical void in an elastic body under hydrostatic pressure with allowance for the physical nonlinearity of this problem (within the framework of a two-dimensional model).

(2) To reveal specific features of the development of plastic deformation near an individual pore and an ensemble of individual pores and to estimate the effect of the surface of a body on the configuration of plastic regions in the vicinity of near-surface pores.

(3) To experimentally study the effect of hydrostatic pressure on elliptic pores with various degrees of oblongness.

(4) To compare calculated and experimental data on the effect of pressure on the healing of pores near the surface and in the bulk of solids.

2. SPHERICAL PORE IN ELASTIC SPACE UNDER HYDROSTATIC PRESSURE

Consider an infinite isotropic elastic space S with a spherical void of radius R_0. Let the space be under a uniform hydrostatic pressure p = const at infinity. We determine the stressed state of S. We introduce spherical coordinates r, θ, and φ with the origin at the center of the pore. From the symmetry of the problem, it follows that stresses σ_{rr}, $\sigma_{\theta\theta}$, and $\sigma_{r\theta}$ are principal stresses; the tangential displacements are $u_\varphi = u_\theta = 0$; and the radial displacement is $u_r = u(r)$.

The radius of the deformed void is

$$R_* = R_0 + u(R_0). \tag{1}$$

2.1. Linear Solution

Within the classical theory of elasticity [3], we have

$$u(r) = ar + b/r^2,$$
$$\sigma_{rr} = \frac{Ea}{1-2\nu} - \frac{2Eb}{(1+\nu)r^3}, \tag{2}$$
$$\sigma_{\theta\theta} = \sigma_{\varphi\varphi} = \frac{Ea}{1-2\nu} + \frac{Eb}{(1+\nu)r^3}.$$

Here, E is Young's modulus, ν is the Poisson ratio of the material in the space, and r is the distance (prior to deformation) from the origin of coordinates to a given point. Unknown constants a and b in Eq. (2) are determined from the boundary conditions

$$\sigma_{rr}(R_0) = 0, \quad \sigma_{rr}(\infty) = -p.$$

Whence it follows that

$$a = -\frac{(1-2\nu)p}{E}, \quad b = -\frac{(1+\nu)R_0^3 p}{2E}.$$

Substituting these relations into Eq. (2), we find

$$u(r) = -\frac{p(1-2\nu)}{E}r - \frac{p(1+\nu)R_0}{2E}\left(\frac{R_0}{r}\right)^2,$$
$$\sigma_{rr} = -p\left(1-\frac{R_0^3}{r^3}\right), \quad \sigma_{\theta\theta} = \sigma_{\varphi\varphi} = -p\left(1+\frac{R_0^3}{2r^3}\right). \tag{3}$$

The radial displacement of the spherical void is calculated from the formula

$$u(R_0) = -\frac{3p(1-\nu)}{2E}R_0.$$

Substituting this formula into Eq. (1), we obtain the deformed void radius

$$R = R_0\left(1-\frac{3(1-\nu)}{2E}p\right). \tag{4}$$

Hence it follows that the spherical void in the elastic half-space disappears when the hydrostatic pressure at infinity becomes

$$p = p_* = \frac{2E}{3(1-\nu)}.$$

Of course, this conclusion is taken to be qualitative. As mentioned above, quantitative estimations based on the linear theory of elasticity are valid for small deformations of the spherical void, where $|R - R_0| \ll R_0$.

2.2. Nonlinear Solution

Taking into account the results obtained, we note the basic points related to the geometrical nonlinearity of the problem. The further analysis is based on the natural assumption that an infinitesimal change in the pressure at infinity causes increments in the displacements and stresses near the spherical void; these increments depend on the current (deformed) void configuration. In other words, Eqs. (3) and (4) are thought to be true if the parameter p in them is substituted by dp($|dp| \ll |p|$). We denote the radius of the deformed spherical void in the nth loading stage as R_n. Then, we have from Eq. (4)

$$R_n = R_0\left[1-\frac{3(1-\nu)p}{En}\right]^n.$$

In the limit $n \longrightarrow \infty$, we obtain

$$R_* = \lim_{n\to\infty} R_n = R_0\exp\left(1-\frac{3(1-\nu)p}{2E}\right). \tag{5}$$

It follows from Eq. (5) that the deformed spherical void in the elastic isotropic space will always be present at arbitrarily high hydrostatic pressures at infinity.

3. NONLINEAR TWO-DIMENSIONAL MODEL OF AN ELLIPTIC PORE IN AN INFINITE PLANE

3.1. Uniaxial Tension (Compression)

Consider an elliptic hole in a nonlinear-elastic plane. We place the origin of the Cartesian coordinate system at the center of the hole and direct the x and y axes along the semimajor (a) and semiminor (b) axes of the hole, respectively. Let stresses

$$\sigma_{yy}^{\infty} = p = \text{const}, \quad \sigma_{xx}^{\infty} = \sigma_{xy}^{\infty} = 0,$$

operate in the plane at infinity. Following the assumption formulated above, we write the current values of the semimajor and semiminor axes of the deformed hole [4] as

$$a_{i+1} = a_i\left(1-\frac{c}{E_i}dp_i\right),$$
$$b_{i+1} = b_i\left(1-\frac{c}{E_i}dp_i\right) + \frac{2ca_i}{E_i}dp_i. \tag{6}$$

Here, dp_i is the increment of the applied stresses at infinity ($|dp_i| \ll |p|$) and E_i is the secant modulus of elasticity of the stress–strain curve in the segment $p_i < p < p_{i+1}$. For plane deformation, $c = (1 - \nu^2)$; for the generalized plane state of stress, we have $c = 1$. Note that the contour of the deformed hole retains its elliptic shape [3].

Let a_n be the length of the semimajor axis of the hole after n steps of loading the plane with stresses dp_0, dp_1, …, dp_{n-1}. Based on the previous formula, we have

$$a_n = a_0\left(1-\frac{cdp_0}{E}\right)\left(1-\frac{cdp_1}{E_1}\right)\ldots\left(1-\frac{cdp_{n-1}}{E_{n-1}}\right),$$
$$p = dp_0 + dp_1 + \ldots + dp_{n-1},$$

where a_0 is the length of the semimajor hole axis prior to deformation. We rewrite this expression as

$$a_n = a_0\left(1-\frac{cdp_0}{E}\right)\left[\left(1-\frac{cdp_0}{E}\right)-\left(\frac{cdp_1}{E_1}-\frac{cdp_0}{E}\right)\right]$$
$$\times\ldots\left[\left(1-\frac{cdp_0}{E}\right)-\left(\frac{cdp_{n-1}}{E_{n-1}}-\frac{cdp_0}{E}\right)\right].$$

Whence it follows that

$$a_n = a_0\left(1-\frac{cdp_0}{E}\right)^n[(1-\alpha_0)(1-\alpha_1)\ldots(1-\alpha_{n-1})],$$

where

$$\alpha_k = \frac{\frac{cdp_k}{E_k}-\frac{cdp_0}{E}}{1-\frac{cdp_0}{E}}, \quad k = 1, 2, \ldots, n-1.$$

Since $dp_k/E_k \ll 1$ and $dp_0/E \ll 1$, we may believe that $\alpha_k \ll 1$. Therefore, with accuracy to higher order infinitesimal terms, we get

$$a_n = a_0\left(1 - \frac{c\,dp_0}{E}\right)^n [1 - (\alpha_1 + \alpha_2 + \ldots + \alpha_{n-1})].$$

Let us assume that $dp_0 = p/n$. Then, at the limit $n \longrightarrow \infty$, the previous equation becomes

$$a_* = a_0 \exp\left(-\frac{cp}{E}\right)[1 - c(\varepsilon_* - \varepsilon_0)], \quad (7)$$

where ε_* and ε_0 are the total and elastic strains of the material, respectively. Performing similar manipulations for the sum

$$a_{i+1} + b_{i+1} = (a_i + b_i)\left(1 + \frac{c\,dp_i}{E_i}\right),$$

we find

$$a_* + b_* = (a_0 + b_0)[1 + c(\varepsilon_* - \varepsilon_0)]\exp\left(\frac{cp}{E}\right). \quad (8)$$

From Eqs. (7) and (8), we derive

$$b_* = a_0\left\{\exp\left(\frac{cp}{E}\right)[1 + c(\varepsilon_* - \varepsilon_0)] - \exp\left(-\frac{cp}{E}\right)[1 - c(\varepsilon_* - \varepsilon_0)]\right\} + b_0 \exp\left(\frac{cp}{E}\right)[1 + c(\varepsilon_* - \varepsilon_0)]. \quad (9)$$

If $cp/E \ll 1$ and $\varepsilon_* = \varepsilon_0$, Eqs. (7) and (8) reduce to the known dependences given by the linear theory of elasticity:

$$a_* = a_0\left(1 - \frac{cp}{E}\right), \quad b_* = b_0 + (b_0 + 2a_0)\frac{cp}{E}. \quad (10)$$

Comparing Eqs. (7), (9), and (10), we arrive at the following conclusions:

(1) The geometrical nonlinearity of the problem causes an exponential dependence of the dimensions of the deformed elliptic hole on the applied stresses at infinity.

(2) Taking the physical nonlinearity into account generates additional terms $1 \pm c(\varepsilon_* - \varepsilon_0)$ in the formulas for the displacements, with $(\varepsilon_* - \varepsilon_0)$ specifying the plastic strain of the material.

Now, we analyze stresses at the end of the major axis of the deformed elliptic hole. Without dwelling on the details of the relatively simple calculations, we give the final relation:

$$\sigma_{yy}(a_*, 0) = p\left(1 + \frac{2a_*}{b_*}\right). \quad (11)$$

Since most solids fail at $p/E \ll 1$, we may suppose that

$$\exp\left(\frac{cp}{E}\right) = 1 + \frac{cp}{E}, \quad \exp\left(-\frac{cp}{E}\right) = 1 - \frac{cp}{E}.$$

By introducing this simplification into Eqs. (7) and (9) and substituting them into Eq. (11), we obtain

$$\sigma_{yy}(a_*, 0) = p\left[1 + \frac{2[1 - (\varepsilon_* - \varepsilon_0)]}{b_0/a_0 + 2cp/E + c(\varepsilon_* - \varepsilon_0)(2 + b_0/a_0)}\right]. \quad (12)$$

The relationships derived above indicate that tension ($p > 0$) decreases the pore ellipticity (ratio b/a), while compression ($p < 0$), on the contrary, increases the ellipticity.

3.2. Biaxial Tension (Compression)

Let stresses

$$\sigma_{yy}^{\infty} = \sigma_{xx}^{\infty} = q = \text{const}, \quad \sigma_{xy}^{\infty} = 0$$

operate in the plane at infinity. Using the results obtained in [4, 5] and the above assumption, we write the current values for the major and minor axes of the deformed elliptic pore as

$$a_{i+1} = a_i + \frac{2cb_i}{E_i}dq_i, \quad b_i = b_i + \frac{2ca_i}{E_i}dq_i.$$

Performing manipulations similar to those described above, we find the dimensions of the deformed elliptic pore,

$$a_* = \frac{a_0}{2}\left\{\exp\left(\frac{2cq}{E}\right)[1 + 2c(\varepsilon_* - \varepsilon_0)]\left(1 + \frac{b_0}{a_0}\right) + \exp\left(-\frac{2sq}{E}\right)[1 - 2(\varepsilon_* - \varepsilon_0)]\left(1 - \frac{b_0}{a}\right)\right\}, \quad (13)$$

$$b_* = \frac{a_0}{2}\left\{\exp\left(\frac{2cq}{E}\right)[1 + 2c(\varepsilon_* - \varepsilon_0)]\left(1 + \frac{b_0}{a_0}\right) - \exp\left(-\frac{2cq}{E}\right)[1 - 2(\varepsilon_* - \varepsilon_0)]\left(1 - \frac{b_0}{a_0}\right)\right\} \quad (14)$$

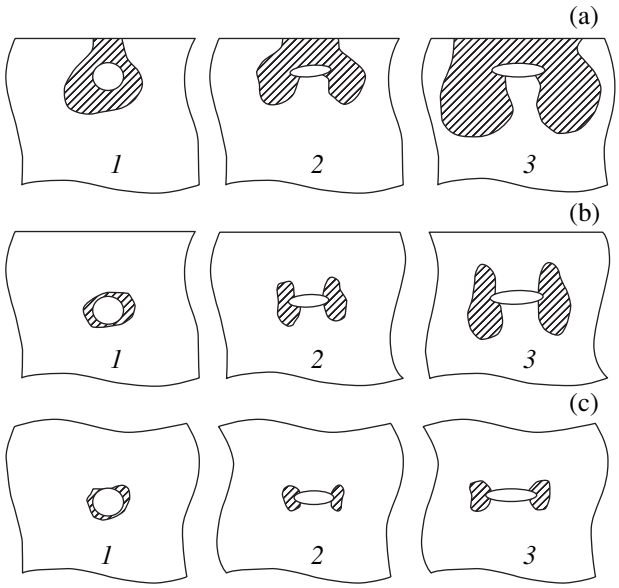

Fig. 1. Regions of elastoplastic strain that appear (*1–3*) near pores of various shapes placed (*a–c*) at various distances from the surface.

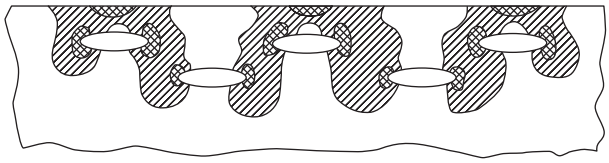

Fig. 2. Regions of elastoplastic strain that appear near closely spaced pores of the same size located near the surface.

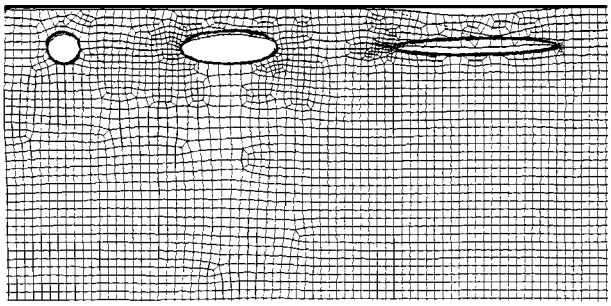

Fig. 3. Changes in the contours of pores and of the surface over them induced by a biaxial pressure. The initial contours of pores and of the surface are shown by heavy lines.

and the stresses at the end of the major axis of the deformed hole,

$$\sigma_{yy}(a_*, 0) = \frac{2qa_*}{b_*}. \quad (15)$$

As follows from Eqs. (13) and (14), biaxial tension ($q > 0$) decreases the pore ellipticity, while compression ($q < 0$), increases it.

4. THE DEVELOPMENT OF ELASTOPLASTIC-STRAIN REGIONS NEAR ELLIPTIC PORES

For numerical calculation of plastic regions near pores, we used the MS Nastran 4.0 software package. We solve the problem on the plane deformation of a body with elliptic voids subjected to biaxial compression. The applied pressure $p < 0$ was taken to be approximately 3 times greater than the yield strength of the body material. Pores placed near the surface and far from it were studied.

Figure 1 shows the configuration of elastoplastic-strain regions for pores placed at different distances from the surface: (a) in the immediate vicinity of the surface, (b) at a greater distance from it, and (c) far from it. For calculation, we chose pores with principal-axis ratios of 1, 1/3, and 1/5 (regions *1*, *2*, *3*, respectively). As can be seen in Fig. 1, the closer a pore is to the surface, the larger the elastoplastic-strain region near the ends of its major axis. Moreover, regions of elastoplastic strains appear and develop over near-surface pores; this process is more intense for pores with a larger ellipticity.

Figure 2 shows the shapes of plastic zones near three closely spaced pores of the same size located near the surface. The middle pore is seen to interact with the two pores adjacent to it, which induces an increase in the plastic regions near its ends. This effect becomes more pronounced as the system of pores approaches the surface.

Finally, in the two-dimensional case, near-surface pores substantially unload adjacent pores located at a larger distance from the surface. Chains of three pores located closer to the surface shield the lower system of two pores (Fig. 2). The sizes of elastoplastic regions in the latter system decrease. Moreover, no surface plastic zones appear over this system.

Apart from the sizes of the elastoplastic-strain regions, we determined changes in the contours of the pores and of the surface over the pores induced by biaxial compression (the initial contours of the pores and the surface are shown by heavy lines in Fig. 3). Figure 3 shows that biaxial compression causes significant deformation of the contours of pores and the surface above them; this process is most pronounced for pores with a large ellipticity.

The data obtained provided semiquantitative dependences of the degree of pore healing on various parameters.

The calculations also indicate that, in the case of elongated pores located at a small angle with the surface, the shapes of plastic zones change only slightly and the general features of their appearance and development remain the same.

5. EFFECT OF PLASTIC REGIONS ON THE DEFORMATION CONFIGURATION OF PORES

The formulas derived above describe the displacement of the contour of an elliptic pore for uniaxial or biaxial compression (tension) of a solid. Unfortunately, they cannot be used to estimate the effect of the zones of localized plastic deformation on the displacement of the pore contour. Rigorous theoretical analysis of this problem is extremely difficult and labor-intensive. Therefore, it is natural to introduce corresponding corrections into the calculation formulas based on the following simple model. We will consider the part of the body located over an elongated elliptic pore ($a/b > 3$) as a beam under a uniform load q, with the beam ends kept fixed. In the absence of plastic zones, the flexures and angles of rotation at the beam ends are zero, while the beam maximum flexure ω^* is given by

$$\omega^* = \frac{q(2a)^3}{384EI}. \quad (16)$$

where I is the moment of inertia of the beam.

If plastic zones appear at the beam ends at a given q, its end sections should be treated as pin-ended. In this case, the maximum flexure is

$$\omega^* = \frac{5q(2a)^3}{384EI}. \quad (17)$$

Thus, the existence of localized plastic zones increases the beam flexure by a factor of five. Hence it follows that the factor $\alpha = 5$ should be introduced into Eqs. (9) and (14) as a correction for plasticity. New plastic zones will appear predominantly over near-surface pores (Fig. 1). In our model, this circumstance can be taken into account by placing a "plastic hinge" at the center of the beam. Due to the hinge, the beam flexure will increase; therefore, we should introduce another additional factor β into Eqs. (9) and (14). The value of β for elongated near-surface pores is estimated to be equal to α.

6. EXPERIMENTAL RESULTS AND COMPARISON WITH THEORY AND CALCULATIONS

We compare the results of analytical calculations and simulations with experimental values. This can be done primarily for two aspects of the problem: the effects of the pore shape and the distance of pores to the surface during pore healing under pressure. We will preliminarily analyze the role of interaction between pores in this process.

The process of pore healing was experimentally studied mainly on Cu samples and partly on an amorphous alloy. Copper samples were subjected to high-temperature creep tests at $T = 500$°C and $\sigma = 12.5$ MPa to failure (creep life $\tau \approx 40$ h). Such a test mode provides the formation of a rather high concentration of grain boundary pores ($\Delta V/V \approx 0.1$–1%) [6]. The shape of the pores is close to an oblate spheroid, with its major axis oriented along a grain boundary. The spheroid major axis a varied from 3 to 80 μm in different samples, and the ratio b/a was 0.1–1. Figure 4 (curve *1*) shows the dependence of the minor axis b on the major axis a found by measuring all pores in a sample followed by averaging the data. Relatively small pores are seen to be almost spherical, whereas pores with large values of a become more elongated. The pore parameters were determined both in the bulk of a sample and in its near-surface layer 50–100 μm thick. For all samples studied, the size and concentration of pores in the near-surface layer was found to be slightly smaller than in the bulk.

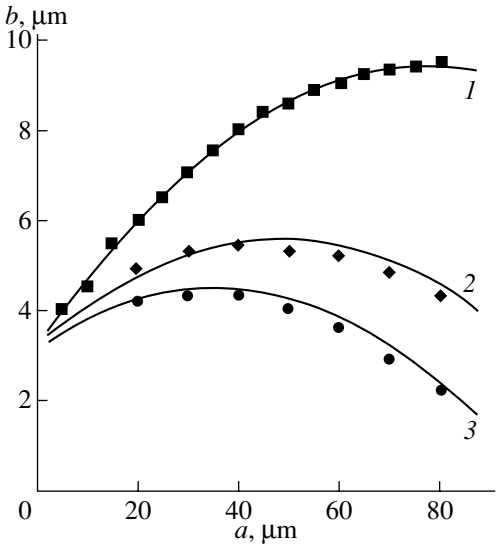

Fig. 4. Minor axis b of a pore as a function of its major axis a (*1*) before and after the application of a pressure of (*2*) 0.6 and (*3*) 1.0 GPa. Points represent experiment; solid lines, theory.

Pores in copper were studied metallographically. Random sections of pores by the plane of polish, rather than the actual pore sizes, were measured experimentally under these conditions. Hence, we had to estimate how much the true axes a and b differed from their measured values. As will be shown below, the ratio of b to a, i.e., the oblateness of a pore, rather than their absolute values are important for comparison with theory; therefore, we first estimated the error of determining this parameter. Two factors were taken into account: the distribution of spheroid sections along an axis perpendicular to a and the orientation dependence of the spheroid with respect to the plane of polish (metallographic specimen). Calculations showed that the former factor did not affect a/b and that the orientation factor contributes ~10% in the averaged curve for pores with large a/b ratios.

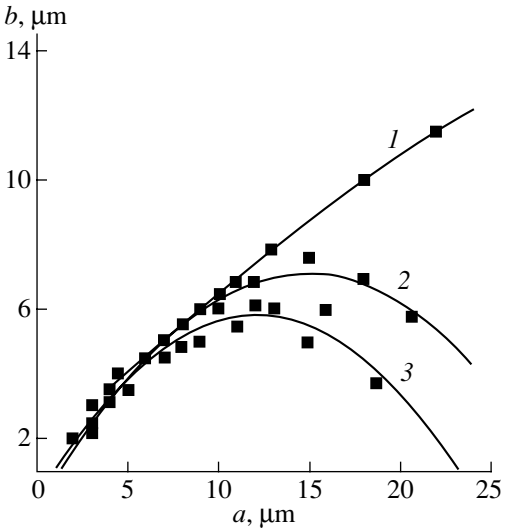

Fig. 5. Minor axis *b* of a pore as a function of its major axis *a* (*1*) for the initial sample and after the application of pressure to this sample for pores (*2*) in the bulk of the sample and (*3*) in its near-surface layer.

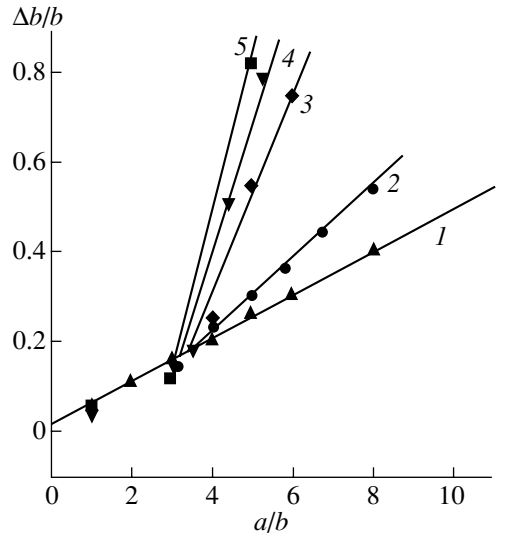

Fig. 6. Relative change $\Delta b/b$ of the minor axis of a pore as a function of its major axis *a*. Pores in the bulk of a sample: (*1*) analytical calculation and (*2*) experiment; near-surface pores: (*3*) analytical calculation, (*4*) experiment, and (*5*) numerical calculations by using Nastran.

Treatment with hydrostatic pressure (up to 1.4 GPa) was carried out in an oil medium on samples protected against it.

Before presenting our experimental results on pore healing under pressure, we will recall the most important theoretical data. First, the degree of healing depends on the ratio *b*/*a* of the spheroid axes rather than on the size of the pore and varies in direct proportion to this ratio in the linear approximation, with the value of *a* remaining virtually unchanged. Second, the degree of healing is significantly higher at distances of the order of several pore diameters from the surface than in the bulk of a sample.

Taking the aforesaid into account, we plotted the data obtained as a graph of *b* versus *a*. Figure 4 shows such curves for the initial sample (curve *1*) and samples subjected to pressures of 0.6 and 1.0 GPa (curves *2*, *3*, respectively). The applied pressures are seen to substantially reduce *b*, whereas the maximum value of *a* remains virtually the same. Moreover, pores with lower values of *b*/*a* (which corresponds to larger values of *a*) are seen to be healed more rapidly, whereas almost spherical small pores change only insignificantly. To quantitatively compare theory and experiment, we used Eqs. (9), (14), and (17). The calculations are shown in Fig. 4 as solid lines. The calculated and experimental curves are seen to coincide. Pressures used in this calculation were taken to be αP. The best agreement between the experimental and calculated data was observed at $\alpha \approx 5.8$, which is very close to the value ($\alpha = 5$) predicted by the theory.

Now, we consider the healing of near-surface pores.

Figure 5 shows the *b* vs *a* curves for one of the initial samples (curve *1*) and after applying a pressure of 1 GPa to this sample for pores in the bulk (curve *2*) and in the near-surface layer (curve *3*) of the sample. (We chose the initial sample such that the dependences of *b* on *a* in the bulk and the surface layer were close to each other.) The healing of pores in the near-surface layer is seen to obey the same law but to proceed more rapidly. The elongation of long pores becomes so great that it is difficult to interpret it.

Consider the results of analytical examination, numerical calculation, and experiment from the viewpoint of the effect of the pore shape on the pore healing in more detail. To this end, we analyze the variation in the axis *b* with the initial value of *b*/*a* upon pressure-induced healing. These curves are given in Fig. 6 for bulk and near-surface pores. For curve *1*, we took into account the coefficient α, and for curve *3*, α and β; in other words, plasticity was partly taken into account.

It can be seen from Fig. 6 that the calculated and experimental data almost coincide for near-surface pores. An important and new point is that the degree of healing for such pores increases jumpwise with *a*/*b*.

The degree of healing for bulk pores increases linearly with *a*/*b*. The experimental data exhibit a higher slope for this dependence than does the analytical calculation, which is likely due to the allowance made for local plastic strain near pores being incomplete.

Based on the data obtained, we may conclude that the degree of pore healing in a sample directly depends on the initial pore *b*/*a* ratio distribution. If this distribution is linear and its slope is close to unity, healing is insignificant; the healing degree increases as the slope decreases. If the dependence falls off (which is of most

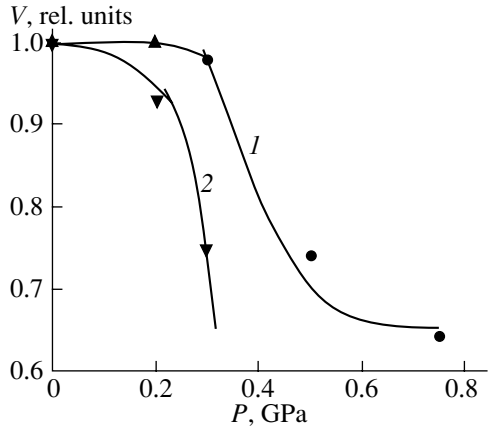

Fig. 7. Dependence of the mean pore volume V on the applied pressure for (*1*) individual pores and (*2*) their chains.

frequent occurrence in experiment), pressure mainly influences pores with large values of a. Interestingly, the total volume of pores and their mean dimensions affect the healing degree only slightly.

After describing the experimental results, we will briefly dwell on the effect of the interaction between closely spaced pores on the process of their healing. This process is rather difficult to study in real porous materials, since it is almost impossible to select a sufficient number of similar objects (chains of closely spaced pores with a fixed spacing between them) for investigation. Nevertheless, we tried to perform such an investigation on copper samples.

The objects for study were chains of grain boundary pores that occupied no less than half the length of a boundary from a triple junction to an adjacent junction. Most of such chains were found to be in a layer as thick as 150 μm measured from the surface. Figure 7 shows the variation of the mean pore volume with applied pressure P. Curve *1* corresponds to the healing of individual pores with the ratio $a/b = 1–3$, and curve *2*, to the healing of chains of pores. As is seen, the healing of chains of pores is most efficient. The results obtained are preliminary, although the general tendency is beyond question.

To evaluate the degree of generality for the effects found, we consider data on the effect of a hydrostatic pressure of 1 GPa on the porosity in an $Fe_{77}Ni_1Si_9B_{13}$ amorphous alloy fabricated through ultrarapid melt-quenching. This alloy contains ellipsoidal pores as large as 100 nm in diameter, which are localized in a thin surface layer of an amorphous ribbon [7, 8]. (Here, we do not analyze pores that are in the bulk of the ribbon; they are smaller by an order of magnitude.) Small-angle x-ray scattering studies showed that pores become thinner in the direction normal to the surface (this direction coincides with the minor axis of the ellipsoid). In the direction parallel to the surface, the pore dimensions remain virtually unchanged. The small-angle x-ray scattering data and the relevant published data [9, 10] indicate that the flattening of pores under pressure should lead to a decrease in the ribbon thickness by ≈2%. This value agrees well with the results of measuring the thickness of ribbons subjected to pressure treatment. Measurements showed that the decrease in the ribbon thickness was 2.3 ± 0.4.

7. CONCLUSIONS

Thus, we have made a quantitative (or semiqualitative in some cases) comparison of the experimental data with the results of analytical and numerical calculations and found that the agreement of rather good. Experiment and theory unambiguously showed that the degree of pore healing at a fixed pressure depends mainly on the ratio a/b of the lengths of the pore axes. Hydrostatic pressure or biaxial compression (two-dimensional case) applied to either copper or an amorphous alloy causes a decrease in the minor axis b, whereas the major axis a remains virtually unchanged.

We have established that the process of pore healing in the near-surface layers is more efficient than in the bulk of a sample. Both experiment and numerical calculations demonstrated that the dependence of the degree of healing on the ratio a/b becomes more pronounced in this case. Closely spaced pores were shown to be healed more efficiently due to the interaction between their stress fields.

REFERENCES

1. P. G. Cheremskoĭ, V. V. Slezov, and V. I. Betekhtin, *Pores in Solids* (Énergoatomizdat, Moscow, 1990).
2. V. I. Betekhtin, in *Proceedings of Anniversary Scientific and Technical Conference* (St.-Peterb. Gos. Tekh. Univ., St. Petersburg, 2001), p. 7.
3. L. D. Landau and E. M. Lifshitz, *Course of Theoretical Physics*, Vol. 7: *Theory of Elasticity*, 4th ed. (Pergamon, New York, 1986; Nauka, Moscow, 1987).
4. N. I. Muskhelishvili, *Some Main Problems of the Mathematical Theory of Elasticity* (Nauka, Moscow, 1966).
5. Yu. M. Dal', Izv. Akad. Nauk SSSR, Mekh. Tverd. Tela **2**, 130 (1980).
6. I. V. Sklenička, V. I. Betekhtin, A. I. Petrov, *et al.*, Scr. Metall. Mater. **25**, 2159 (1991).
7. V. I. Betekhtin, A. M. Glezer, A. G. Kadomtsev, and A. Yu. Kipyatkova, Fiz. Tverd. Tela (St. Petersburg) **40** (1), 85 (1998) [Phys. Solid State **40**, 74 (1998)].
8. V. I. Betekhtin, E. L. Gyulikhandanov, A. G. Kadomtsev, and O. V. Tolochko, Fiz. Tverd. Tela (St. Petersburg) **42** (8), 1420 (2000) [Phys. Solid State **42**, 1460 (2000)].
9. I. V. Zolotukhin, *Physical Properties of Amorphous Metallic Materials* (Metallurgiya, Moscow, 1986).
10. K. Suzuki, H. Fujimori, and K. Hashimoto, *Amorphous Metals*, Ed. by T. Masumoto (Metallurgiya, Moscow, 1987).

Translated by K. Shakhlevich

Physics of the Solid State, Vol. 45, No. 4, 2003, pp. 656–661. Translated from Fizika Tverdogo Tela, Vol. 45, No. 4, 2003, pp. 625–629.

DEFECTS, DISLOCATIONS, AND PHYSICS OF STRENGTH

Thermal "Softening" and "Hardening" of Titanium and Its Alloy at High Strain Rates of Shock-Wave Deforming

G. I. Kanel, S. V. Razorenov, E. B. Zaretsky, B. Herrman, and L. Meyer

Institute for High Energy Densities, Associated Institute for High Temperatures, Russian Academy of Sciences, ul. Izhorskaya 13/19, Moscow, 127412 Russia

e-mail: kanel@ficp.ac.ru

Received August 6, 2002

Abstract—The effect of temperature on the dynamic yield strength and ultimate tensile strength of high-purity and commercial-purity titanium and an $\alpha + \beta$ alloy Ti–6Al–2Sn–2Zr–2Cr–2Mo–Si upon submicrosecond-scale shock-wave loading was studied. An anomalous increase in the dynamic yield strength with temperature was detected in high-purity titanium, whereas the behavior of commercial-purity titanium and the titanium alloy was similar to that under regular conditions. It was found that the dynamic ultimate tensile strength is less sensitive to the composition and structure of the alloy and to the test temperature than is the yield strength. Our experiments corroborate the occurrence of polymorphic transformation during shock compression of high-purity titanium, but the transformation pressure and its temperature dependence are inconsistent with the data available in the literature. © *2003 MAIK "Nauka/Interperiodica".*

1. INTRODUCTION

The crystalline-solid resistance to deformation is known to increase with the loading rate. This dependence becomes more pronounced for many metals as the strain rate exceeds ~10^3–10^4 s^{-1}. This is interpreted as the consequence of a change in the mechanism of dislocation motion [1]: at high strain rates, working stresses are large enough to overcome obstacles without an additional contribution from thermal fluctuations. Here, phonon drag becomes the dominant mechanism of retardation of dislocations.

The mechanical properties of materials in the submicrosecond loading-duration range at strain rates higher than 10^4 s^{-1} are studied by analyzing compression and rarefaction waves. Measurements are based on the fact that the wave structure and the dynamics of wave interactions are determined not only by the thermodynamic equation of state but also by the processes of elastoplastic strain and fracture in the material [2]. Recent measurements of the single-crystalline aluminum resistance to strain and fracture under shock-wave loading [3, 4] have revealed that the yield strength anomalously increases with temperature at a strain rate of 10^6 s^{-1} and higher. This anomaly was interpreted as a change in the main mechanism of retardation of dislocations. However, it is still unclear whether the anomalous increase in the dynamic yield strength with temperature is inherent in pure aluminum alone or if this phenomenon is rather general.

Therefore, it is of interest to compare the behavior of high-strength alloys, including titanium alloys, and that of pure metals with low yield strength. Titanium alloys are also interesting because of their tendency to localized deformation with the formation of so-called adiabatic shear bands upon high-rate loading. In the existing theories, the adiabatic shear is assumed to be due to the competing contributions from strain hardening and thermal softening to the resistance to plastic deformation under adiabatic conditions [5]. A change in the sign of the temperature dependence of the yield strength at extremely high strain rates should restrict the validity range of this mechanism.

In this work, we compare the results of investigating the effect of temperature on the dynamic yield and ultimate tensile strengths of high-purity and commercial-purity titanium and the data published earlier in [6] for an $\alpha + \beta$ alloy, Ti–6Al–2Sn–2Zr–2Cr–2Mo–Si (Ti–6–22–22S), subjected to submicrosecond shock-wave loading.

2. EXPERIMENTAL TECHNIQUE

Experiments were carried out on 2- to 2.3-mm-thick samples in which plane compression waves were generated by an impact of a flyer plate. Flyer plates of aluminum, titanium, or copper 0.4- to 1.0-mm thick were thrown at speeds of 0.4–0.66 km/s with explosive [2] and gaseous gun barrel [7] facilities. The shock compression pressure was 4.5–6.5 GPa. We recorded lack-free-surface velocity profiles using VISAR laser interference Doppler velocimeters [8]. The transmission band of the measuring path was broader than 0–350 MHz. The velocimeter output signals were

recorded using digital oscilloscopes; the time intervals between measured points were 0.4 or 2.0 ns.

Measurements were performed at room and elevated (up to 405–465°C) temperatures. Samples were heated with resistive nichrome heaters; their power provided a desired temperature within 10 min. The temperature was monitored with an accuracy of ±5°C using a chromel–alumel thermocouple placed on the back surface of a sample near the point at which the shock-wave process was recorded.

Titanium samples of 99.99% purity were cut from a rod 23 mm in diameter fabricated by electron-beam crucibleless zone melting [9]. The mean grain size in polycrystalline samples was about 1 mm.

Commercial-purity titanium contained (in wt %) 0.15 O_2, 0.10 Fe, 0.018 Cr, 0.015 Ni, and 0.016 C; the Al content was less than 0.02, and the Cu, Zr, V, and Mn contents were less than 0.01 each. Its density was 4.53 g/cm^3, the measured velocity of longitudinal acoustic waves was c_l = 6.195 ± 0.005 km/s, and the velocity of shear acoustic waves propagating in the plane of a sample (at right angles to the loading direction) was c_s = 3.26 ± 0.01 km/s. Samples were cut out of a rolled sheet of the corresponding thickness and were not subjected to any additional heat treatment. X-ray diffraction analysis showed that the material is highly textured, with its basal plane being predominantly parallel to the surface of samples. The crystal structure of both the commercial-purity and high-purity titanium corresponded to that of the α phase. A mean grain size of commercial titanium was 22 μm.

The Ti–6Al–2Sn–2Zr–2Cr–2Mo–Si (Ti–6–22–22S) alloy contained (in wt %) 5.75 Al, 1.96 Sn, 1.99 Zr, 2.15 Mo, 2.10 Cr, 0.13 Si, 0.04 Fe, 0.082 O, 0.006 N, and 0.009 C. After heat treatment, this alloy consisted of a globular α phase surrounded by α- and β-phase lamellas. The alloy density was measured to be 4.53 g/cm^3, the longitudinal sound velocity was c_l = 6.01 ± 0.04 km/s, and the Poisson ratio was ν = 0.327. The bulk sound velocity was c_b = 4.87 km/s.

3. EXPERIMENTAL RESULTS

Figure 1 shows free-surface velocity profiles for samples of the Ti–6–22–22S alloy measured at room temperature and at 405°C [6]. From the wave profiles, it is clearly seen that the shock wave is split into an elastic precursor (with the material parameters continuously increasing behind its front) and a plastic compression wave. The jump in velocity at the precursor front is proportional to the dynamic yield strength of the material [2]. An increase in the material parameters behind the front of the elastic precursor of the compression wave in the alloy is likely due to strain hardening. After waves have been circulated in the flyer, a rarefaction wave is formed in the sample; this wave decelerates the sample surface. As a result of the compression pulse being reflected from the sample surface, tensile

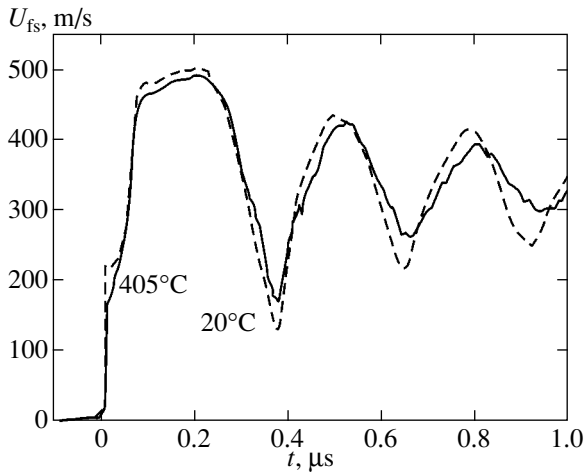

Fig. 1. Free-surface velocity profiles $U_{fs}(t)$ for samples of the Ti–6–22–22S alloy 2.24-mm thick after impact by a flyer aluminum plate 0.85-mm thick at a speed of 670 ± 20 m/s at room temperature and at 405°C.

stresses are generated inside the sample and initiate its fracture, so-called spalling. As the fracture develops, the tensile stresses are relaxed. Therefore, a compression wave forms in the tensed material; as this wave reaches the sample surface, its velocity increases again and the so-called spalling pulse forms. The velocity decrement before the spalling pulse front is proportional to the breaking stress, which is called the spalling strength of the material. The following surface-velocity oscillations are caused by multiple wave reflections inside a spalling plate. Hence, the oscillation period is determined by the thickness of the spalling plate and the sound velocity. A more detailed discussion of the wave-profile structure and the dynamics of wave interactions in solids is presented in monograph [2].

The wave profiles are similar in shape but differ quantitatively. As the temperature increases, the amplitude of the elastic precursor decreases and the material parameters behind its front increase more sharply, whereas the steepness of the plastic compression wave remains virtually unchanged. The time interval between the elastic and plastic waves slightly decreases with increasing temperature because of the decreased shear modulus and, hence, the decreased difference between the elastic and plastic wave velocities. Heating induces no qualitative changes in the material behavior during sample spalling.

Figure 2 shows the experimental results for the commercial-purity titanium. The behavior of this material differs quantitatively and qualitatively from that of the Ti–6–22–22S alloy. The elastic precursor has a characteristic peak at the front; its amplitude is small at room temperature but sharply increases with heating. Note that a similar shape of elastic precursors has also been detected in high-temperature experiments on aluminum single crystals [3, 4]. Although the surface velocity at

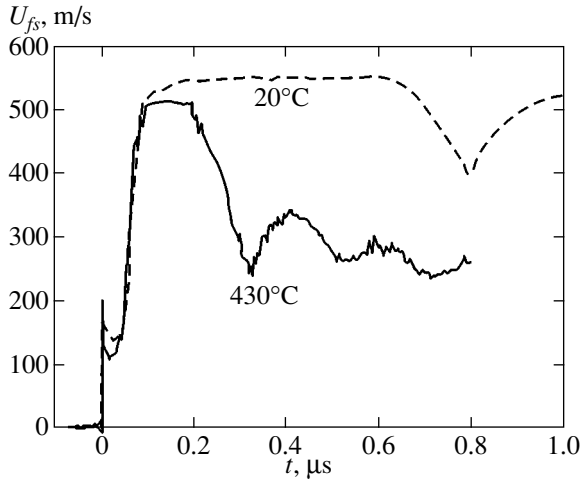

Fig. 2. Free-surface velocity profiles for samples of the commercial-purity titanium at room temperature and at 430°C. At room temperature, a symmetrical impact was used: the flyer plate was made of a material identical to that of the sample. The plate thickness was 1.97 mm, and the sample thickness was 2.03 mm. In the high-temperature experiment, the 1.97-mm-thick sample was loaded with a flyer copper plate 0.5-mm thick.

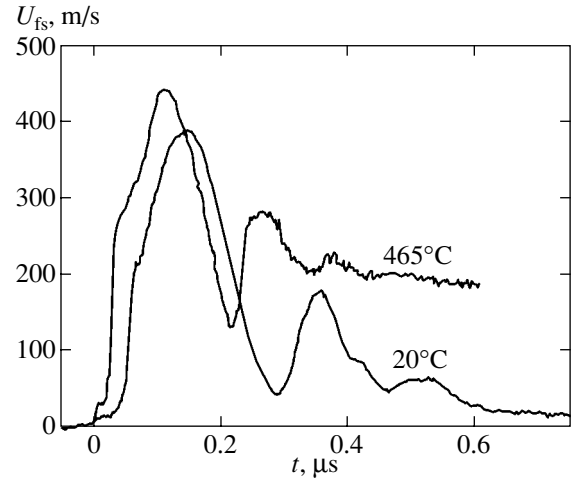

Fig. 3. Free-surface velocity profiles for samples of high-purity titanium at room temperature and at 465°C. Samples were loaded with a 0.4-mm-thick flyer aluminum plate moving at a speed of 640 ± 20 m/s. The sample thickness was 2.07 and 2.30 mm in the experiments at 20 and 465°C, respectively.

the peak of the elastic precursor is high and even increases upon heating, the wave velocity profiles suggest that, on the whole, the dynamic yield strength decreases with increasing temperature. Sample spalling at an elevated temperature becomes similar to ductile long-term fracture: the long retardation of a spalling plate indicates a rather long bond between it and the rest of the sample. The elastic-precursor amplitude and the velocity decrement before the front of the spalling pulse in this material are smaller than in the Ti–6–22–22S alloy. Metallographic and x-ray diffraction analyses of samples after shock-wave treatment at room temperature revealed intense twinning and a decrease in the degree of texture.

The experimental results for the high-purity titanium shown in Fig. 3 are of great importance. In these experiments, the elastic-precursor amplitude anomalously increases rather than decreases with temperature and the precursor amplitude values at both room and elevated temperatures are significantly lower than those for the titanium alloy and commercial-purity titanium. The plastic compression wave has a unique feature; namely, the rate of increase of the surface velocity drops abruptly after the velocity reaches about 200 m/s at 20°C or ~270 m/s at 465°C. A similar loss of stability of the shock wave is ordinarily related to an anomalous increase in the compressibility and is characteristic of materials that undergo polymorphic transformations with decreasing volume upon compression. Obviously, we detected the known $\alpha \longrightarrow \omega$ transformation [10] during compression in our experiments. The $\alpha \longrightarrow \omega$ transformation that proceeds during a shock compression of titanium and the relevant reported data are discussed in [2, 11]. The rarefaction wave does not exhibit any specific features that can be associated with the reverse $\omega \longrightarrow \alpha$ transformation. Note that no clear signs of polymorphic transformations were observed either in compression waves or upon unloading in our experiments on the commercial-purity titanium and its alloy.

4. ANALYSIS AND INTERPRETATION OF THE RESULTS

In Fig. 4, we compare the temperature dependences of the dynamic yield strengths that correspond to the mean strain rate in elastoplastic compression waves of about 5×10^5 s^{-1} in titanium and its two alloys. The yield strengths Y were calculated from the stresses $\sigma_e = \rho_0 c_1 u_{fse}/2$ measured behind the elastic-precursor front using the relationship [2]

$$Y = (3/2)\sigma_e(1 - c_b^2/c_l^2),$$

where the initial density ρ_0, the longitudinal sound velocity c_l, and the bulk sound velocity $c_b = \sqrt{K/\rho}$ were taken with allowance for their temperature dependences; the free-surface velocities behind the elastic-precursor front u_{fse} were measured. The effect of temperature on c_l was estimated using the data on the temperature-dependent shear modulus presented in [12] (the experimental temperature derivative of the shear modulus was $\partial G/\partial T = -27$ MPa/K, and the generalized

estimate of this quantity was –23 MPa/K). The temperature derivative of the bulk modulus K was estimated as

$$\partial K/\partial T \approx -K\alpha(\partial K/\partial p - \Gamma),$$

where $\partial K/\partial p = 4.37$, the Grüneisen parameter is $\Gamma = 1.23$, and the volumetric thermal expansion coefficient is $\alpha = (2.9 \pm 0.4) \times 10^{-5}$ 1/K. To estimate the contribution from the nonlinear compressibility of the material, we plotted shock adiabats for titanium and its alloys as a linear relation between the shock-wave velocity U_s and the particle velocity of the shock-compressed material u_p:

$$U_s = c_b + bu_p,$$

where the coefficient b was assumed to be 1.05 irrespective of the test temperature.

Figure 5 summarizes the spalling-strength data for titanium and the alloys as a function of the test temperature. The spalling-strength values were obtained by processing the measured free-surface velocity profiles according to [13] with allowance for the nonlinear compressibility of the materials and the difference in the velocities of the spalling pulse front and the rarefaction wave before it. In the experiment on commercial-purity titanium at room temperature, a compression pulse was excited during an impact by a flyer plate made of the same material and having practically the same thickness as the sample; therefore, stresses in this sample did not reach the spalling strength. Figure 5 presents the value of the spalling strength at 20°C obtained when testing a thicker sample (6 mm).

The data in Fig. 5 demonstrate that, although the yield strengths of the high-purity titanium, commercial-purity titanium, and titanium alloy differ manyfold, their dynamic breaking strengths are similar. The spalling strength of the alloy decreases much slower with increasing temperature than does its dynamic yield strength; as for the pure titanium, the variations of the yield strength and of the spalling strength with temperature are different even in sign in this material.

Using the simple-wave approximation [2], we estimated the compression stress at the point of a sharp decrease in the compression wave steepness in the high-purity titanium. This stress likely characterizes the onset of the $\alpha \longrightarrow \omega$ transformation in titanium and is equal to 2.37 GPa at 20°C and 3.05 GPa at 465°C. According to the titanium phase diagram, which is based on the results of both shock-wave and quasi-static experiments [10], the equilibrium pressure of the $\alpha \longrightarrow \omega$ transformation at room temperature is 2.0 GPa and increases with temperature at a rate of dp/dT = 0.011 GPa/K. According to this phase diagram, the transformation at 465°C would take place at a pressure of 6.7–7.0 GPa.

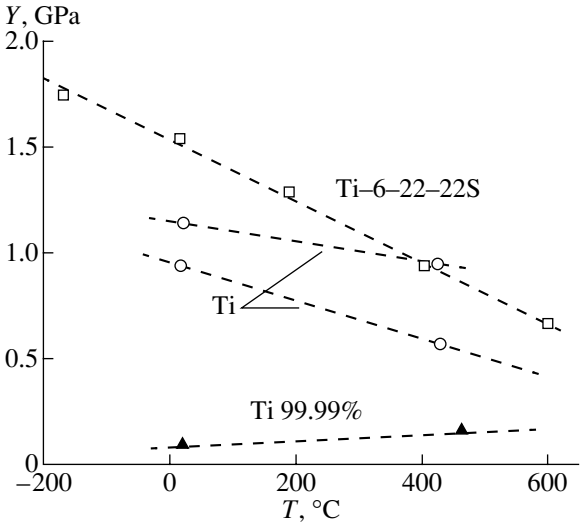

Fig. 4. Dynamic yield strength Y of titanium and the Ti–6–22–22S alloy at the front of elastic precursors as a function of the test temperature T. For the commercial-purity titanium, the values at the peak of a precursor and behind it are shown.

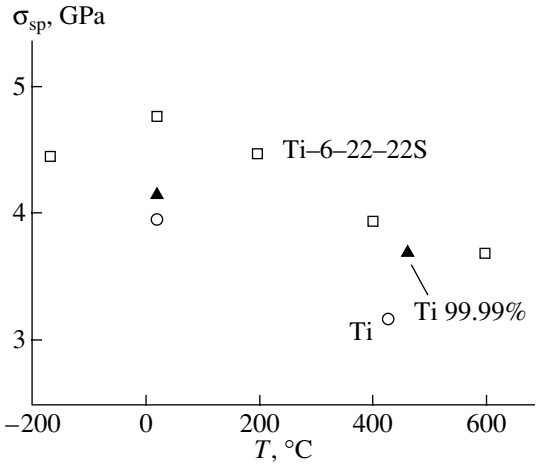

Fig. 5. Variation of the spalling strength σ_{sp} of the high-purity and commercial-purity titanium and the alloy with the test temperature T.

5. DISCUSSION OF THE RESULTS

It is known [14] that, under normal conditions, the yield strength and ultimate tensile strength of titanium increase and its plasticity decreases with increasing oxygen content. The strength of titanium with about 2 at. % oxygen is more than three times that of oxygen-free titanium. Our experiments on high-purity and commercial-purity titanium corroborate this effect of oxygen on the yield strength at high rates, but this is not the case with the effect of oxygen on the dynamic ultimate tensile strength.

Our experimental results demonstrate an anomalous increase in the dynamic yield strength upon heating during shock compression of the soft high-purity titanium, whereas the behavior of the high-strength commercial-purity titanium and the titanium alloy is similar to their behavior under regular conditions. On the whole, this situation agrees with the assumption that the main mechanism of retardation of dislocations changes at high strain rates. In the high-purity titanium, the flow stress is low and comparable to the phonon drag forces; therefore, the increase in the latter forces with temperature significantly contributes to the retardation of plastic-strain carriers (dislocations). To increase the flow stresses in alloys, numerous obstacles in the form of inclusions and interphase boundaries are intentionally created. The stresses required to overcome such large obstacles exceed the phonon drag forces significantly. A comparison of the results for the shock-wave tests of the Ti–6–22–22S alloy and for the yield strengths at lower strain rates [6] shows that all the data follow the same logarithmic dependence of the yield strength on the strain rate in the range 10^{-4}–10^{5} s^{-1}. Hence, the thermal activation mechanisms of overcoming obstacles by dislocations in high-strength alloys remain efficient at strain rates up to at least 10^{6} s^{-1}.

The different temperature dependences of the flow stresses at high strain rates explain why the tendency toward strain localization in adiabatic shear bands in high-strength alloys is higher than in pure metals. Interestingly, the extrapolation of the dependences of the dynamic yield strengths to higher temperatures shows that these dependences intersect at 800–900°C, i.e., in the range of the high-temperature $\alpha \longrightarrow \beta$ transformation.

Spalling of solids during shock wave-loading is known to proceed through the nucleation, growth, and coalescence of numerous voids. The resistance to void growth is determined by the yield strength and viscosity of the surrounding material [15]. Therefore, it is surprising that there is no correlation between the temperature dependences of the dynamic yield strength and of the spalling strength of titanium and its alloys. It is likely that the breaking strength at its initial stage is mainly determined by the nucleation of voids rather than by their growth.

Our measurements supported the fact that polymorphic transformation proceeds during the shock compression of pure titanium, although the transformation pressure and its temperature dependence found by us do not agree with the available data [10]. It should be noted that an increase in the shock compression pressure [11] leads to an increase in the pressure (to be more exact, the compressive stress) at the "breakpoint" of the compression wave. Since the volume decrease due to the $\alpha \longrightarrow \omega$ transformation is only 1.2%, we may assume that this phase transformation does not bring about the formation of a "closed region" in the shock adiabat of titanium in which the shock wave loses its stability and splits into two sequential compression waves; instead, it only reduces the adiabat slope. This assumption allows us to explain the change in the compression wave steepness in terms of the changing material viscosity at the beginning of the transformation.

As for comparison of the experimental results for the high-purity and commercial-purity titanium, we would like to note that the available experimental data exhibit a significant scatter in the pressures of the $\alpha \longrightarrow \omega$ transformation in titanium, namely, from 2 to 7.5 GPa under quasi-static conditions and up to 12 GPa under shock-wave loading conditions. One of the possible causes of this scatter was assumed to be the effect of impurities. In particular, oxygen in commercial-purity titanium is an α-phase stabilizer [14, 16] and can hinder the polymorphic transformation.

Meshcheryakov *et al.* [17] claim that a reversible $\alpha \longrightarrow \omega$ transformation also occurs during shock-wave loading of titanium alloys. Our experiments, as well as the results of [18], did not reveal any signs of transformations occurring in the high-strength titanium alloys during their shock compression and unloading; moreover, no solid evidence of such a transformation was obtained in [16] either.

ACKNOWLEDGMENTS

This work was supported by the Russian Foundation for Basic Research (project no. 00-02-17604) and the complex program of the Russian Academy of Sciences "Physics and Chemistry of Extremal Substance States."

REFERENCES

1. A. Kumar and R. G. Kumble, J. Appl. Phys. **40** (9), 3475 (1969).
2. G. I. Kanel, S. V. Razorenov, A. V. Utkin, and V. E. Fortov, *Shock–Wave Phenomena in Condensed Media* (Yanus-K, Moscow, 1996).
3. G. I. Kanel and S. V. Razorenov, Fiz. Tverd. Tela (St. Petersburg) **43** (5), 839 (2001) [Phys. Solid State **43**, 871 (2001)].
4. G. I. Kanel, S. V. Razorenov, K. Baumung, and J. Singer, J. Appl. Phys. **90** (1), 136 (2001).
5. R. F. Recht, J. Appl. Mech. **31**, 189 (1964).
6. L. Krüger, G. I. Kanel, S. V. Razorenov, *et al.*, AIP Conf. Proc. **620**, 1327 (2002).
7. S. Jacobi, E. Zaretsky, and D. Shvarts, J. Phys. IV **10**, 805 (2000).
8. L. M. Barker and R. E. Hollenbach, J. Appl. Phys. **45** (11), 4872 (1974).
9. V. G. Glebovsky, V. N. Semenov, and V. V. Lomeyko, J. Less-Common Met. **117**, 385 (1986).

10. E. Yu. Tonkov, *Phase Transformations of Compounds at High Pressure* (Metallurgiya, Moscow, 1988).
11. S. V. Razorenov, A. V. Utkin, G. I. Kanel, *et al.*, High Press. Res. **13**, 367 (1995).
12. M. W. Guinan and D. J. Steinberg, J. Phys. Chem. Solids **35**, 1501 (1974).
13. G. I. Kanel, Prikl. Mekh. Tekh. Fiz. **42** (2), 194 (2001) [J. Appl. Mech. Tech. Phys. **42** (2), 358 (2001)].
14. U. Zwicker, *Titan und Titanlegierungen* (Springer, Berlin, 1974; Metallurgiya, Moscow, 1979).
15. J. N. Johnson, J. Appl. Phys. **52** (4), 2812 (1981).
16. B. A. Kolachev, V. I. Elagin, and V. A. Livanov, *Physical Metallurgy and Heat Treatment of Non-Ferrous Metals and Alloys* (MISIS, Moscow, 1999).
17. Yu. I. Mescheryakov, A. K. Divakov, N. I. Zhigacheva, and Yu. A. Petrov, AIP Conf. Proc. **505**, 439 (2000).
18. G. T. Gray III, in *Shock Compression of Condensed Matter-1989: Proceedings of the American Physical Society Topical Conference, Albuquerque, New Mexico, 1989*, Ed. by S. C. Schmidt, J. N. Johnson, and L. W. Davison (Elsevier, Amsterdam, 1990).

Translated by K. Shakhlevich

Physics of the Solid State, Vol. 45, No. 4, 2003, pp. 662–669. Translated from Fizika Tverdogo Tela, Vol. 45, No. 4, 2003, pp. 630–637.

MAGNETISM AND FERROELECTRICITY

Optical Harmonic Generation in Magnetic Garnet Epitaxial Films near the Fundamental Absorption Edge

V. V. Pavlov*, R. V. Pisarev*, M. Fiebig, and D. Fröhlich****

**Ioffe Physicotechnical Institute, Russian Academy of Sciences, Politekhnicheskaya ul. 26, St. Petersburg, 194021 Russia*

***Institut für Physik, Universität Dortmund, 44221 Dortmund, Germany*

Received June 20, 2002

Abstract—Spectra of the second and third optical harmonics generated in epitaxial films of magnetic garnets were studied in the ranges 1.7–3.2 and 2.4–4.2 eV, respectively. A large magnetic contrast was revealed in second-optical-harmonic spectra, which reaches 100% at certain photon energies. By contrast, the symmetry-allowed magnetic contribution to spectra of the third optical harmonic was not found. While linear absorption in ferrite-garnet films grows by two orders of magnitude above the fundamental absorption edge at ~3.2 eV, the intensity of nonlinear spectra did not reveal any noticeable increase over this spectral range. © *2003 MAIK "Nauka/Interperiodica".*

1. INTRODUCTION

We are presently witnessing considerable progress in various areas of nonlinear optics, which may be attributed primarily to the development of novel sources of coherent radiation and the synthesis of new nonlinear-optical crystals. The interest shown in nonlinear solid-state optics is spurred by both fundamental problems of light interaction with matter and the application potential inherent in nonlinear optical phenomena for information processing and transfer and various diagnostics methods. New directions of research have been appearing over the past decade in this area. For instance, the observation of optical second harmonic generation (SHG) depending on the sample magnetization state [1, 2] stimulated fast development of nonlinear magnetooptics. A large number of publications dealing with nonlinear-optical studies of magnetic materials are currently available. Many related findings have been discussed in reviews of nonlinear magnetooptics research [3–6]. As follows from an analysis of those publications, the vast majority of those studies deal with the magnetic aspect of the problem. In many studies, optical SHG was used in the diagnostics of the magnetic state of a material. It goes without saying that, in order to reveal the microscopic mechanisms of the nonlinear interaction of light with magnetic materials, investigations of nonlinear optical phenomena need to be conducted over a broad spectral range. The present communication reports on a study of the spectra of second and third optical harmonic generation in classical model magnetooptical materials, such as epitaxial films of ferrite garnets. No reports on the nonlinear spectroscopy of transition-metal oxides have been available in the literature until recently, with the exception of a lone study of optical third harmonic generation (THG) in La_2CuO_4 [7].

Bulk magnetic garnets and epitaxial garnet films are two well-known groups of materials characterized by a rich variety of magnetic, acoustic, optical, and magnetooptical properties [8–11]. For more than four decades, these materials have been among the most actively studied magnetic dielectrics, which attract attention both from a fundamental standpoint as many-sublattice ferrimagnets and as having application potential. The prototype of bulk crystals and thin ferrite garnet films is the yttrium–iron garnet $\{Y\}_3[Fe]_2(Fe)_3O_{12}$ (YIG). The YIG unit cell contains eight formula units. Ions of yttrium, Y^{3+}, or of another rare-earth element, R^{3+}, occupy 24*c* dodecahedral positions $8\{\ldots\}_3$, and the Fe^{3+} ions sit at the 16*a* octahedral $(8[\ldots]_2)$ and 24*d* tetrahedral $(8(\ldots)_3)$ positions. Superexchange interaction between the Fe^{3+} magnetic ions brings about antiparallel ferrimagnetic ordering of the magnetic moments of the octahedral and tetrahedral sublattices. This fairly strong interaction accounts for the high Curie point, which lies in the range 500–600 K. Superexchange interaction among the rare-earth magnetic ions and the iron sublattice results in the rare-earth magnetic moments being oriented antiparallel to the magnetization of the tetrahedral sublattice. A remarkable feature of the magnetic garnets is the possibility of ions on any of the three magnetic sublattices being substituted for by other magnetic and nonmagnetic ions of the periodic table. This degree of freedom permits one to vary, within a broad range, practically all physical properties of bulk crystals and epitaxial films.

Crystals of magnetic garnets are highly transparent in the IR spectral range 0.2–1.0 eV [12]. At energies below 0.2 eV, absorption grows rapidly because of lattice vibrations. At photon energies above ~1 eV, absorption increases noticeably due to electronic transitions between the $(3d)^5$ levels of the Fe^{3+} iron ions.

The substantial rise in absorption at energies higher than 3.2 eV is associated with intense interband and charge transfer transitions. The absorption coefficient α reaches values as high as $\sim 5 \times 10^5$ cm^{-1} at energies above 5 eV [13]. The magnetooptical properties of garnets, particularly, of bismuth-substituted garnets, have attracted considerable interest because of a high specific Faraday rotation $\sim 10^5$ deg/cm being observed at room temperature. As far as we know, these values are presently the largest ever observed at room temperature in magnetically ordered materials.

Crystals of magnetic garnets are centrosymmetric and belong to cubic point group $m3m$ (space group $Ia3d$). Observations of the linear magnetoelectric effect [14] and SHG [15–17] showed, however, that the crystal structure of thin epitaxial films of garnets is off-centrosymmetric. The reason for this lies in the fact that the lattice parameter of films grown by liquid-phase epitaxy on substrates of cubic crystals of gadolinium–gallium garnet $Gd_3Ga_5O_{12}$ (GGG) or a substituted GGG (SGGG) differs from that of the substrate, which brings about noncubic lattice distortions with a loss of space inversion symmetry and the appearance of a polar direction along the film normal. Previous studies of SHG in magnetic garnet films were carried out in a limited spectral range determined by the lasers employed. Some authors reported on the use of solid-state lasers based on Nd : $Y_3Al_5O_{12}$ (1.17 eV) [15–17] and Ti : Al_2O_3 (1.44–1.72 eV) [18–20] for this purpose. Although breakdown of inversion symmetry in a crystal structure does not play any role when analyzing magnetic properties, this point is of fundamental significance in studies of the electrooptical and nonlinear-optical properties. The off-centrosymmetric character of a structure allows the existence of a crystallographic and a magnetically induced contribution to SHG in the electric-dipole approximation. Obviously, the observation of a nonlinear response at certain photon energies cannot reveal a connection between the observed SHG signals and specific features of the electronic structure of absorption and magnetooptical spectra. In this communication, we report on a spectral study of optical SHG and TGH in epitaxial films of magnetic garnets in the vicinity of the fundamental absorption edge at ~3.2 eV.

2. ELECTRONIC TRANSITIONS IN FERRITE GARNETS

Optical absorption and reflectance spectra of ferrite garnets with different compositions have been studied in a large number of publications, the most important of the findings being presented in [11]. Despite extensive research carried out in this area, the spectral features remain unresolved in most cases because of the complexity of the spectra and ambiguous assignment of electron transitions in magnetic ions occupying different crystallographic positions. Figure 1 presents an electron transition diagram for the yttrium iron garnet derived from experimental data and electronic-level calculations made in the crystal-field approximation. The central part of Fig. 1 shows the experimentally observed electron transitions in YIG reported by vari-

Nonzero components of nonlinear-optical tensors $\hat{\chi}_{cr}^{(3)}$ and $\hat{\chi}_{m}^{(4)}$, which determine the crystallographic and magnetic contributions to THG for point group $3m$ ($m \perp x$) in the $\mathbf{k} \parallel \mathbf{z}$ geometry [(111)-type films]

Crystallographic third harmonic, $\chi_{ijkl}^{(3)}$
$1/3yyyy = 1/3xxxx = xxyy = yxxy$
Magnetic third harmonic, $\chi_{ijklm}^{(4)}$
$yyyyx, yxyyy, yxxyx$
$xxxxx = -1/2yyyyx - yxyyy - 1/2yxxyx$
$xxxyy = 1/2yyyyx - 1/2yxxyx$
$xxyyx = -1/2yyyyx + yxyyy - 1/2yxxyx$
$xyyyy = 1/2yyyyx + yxxyx$
$yxxxy = yyyyx - yxyyy + yxxyx$
$yxyyz = -xxxyz = -1/3xyyyz = 1/3yxxxz$

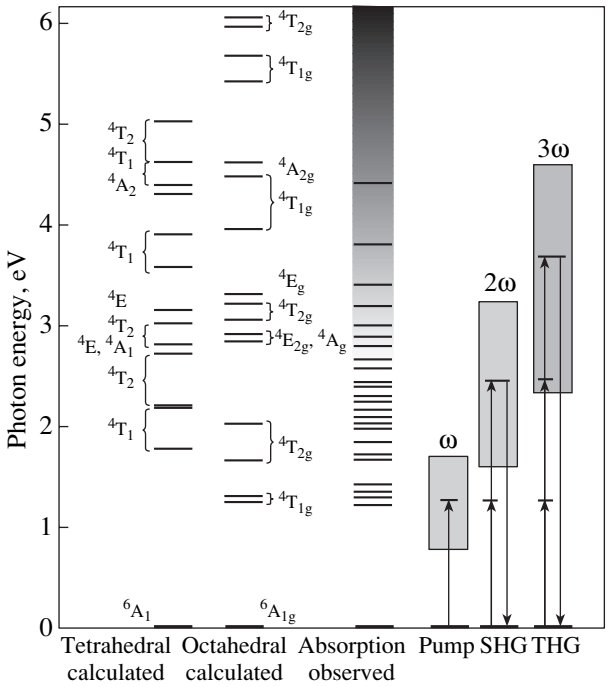

Fig. 1. Energy levels of Fe^{3+} ions in tetrahedral and octahedral crystal fields calculated with inclusion of noncubic distortions (left). Shown in the middle are experimentally observable localized electron transitions and the continuous spectrum above the fundamental absorption edge in YIG [12, 13, 21–27]. The right-hand part of the figure shows the energy range of optical pumping and harmonic generation.

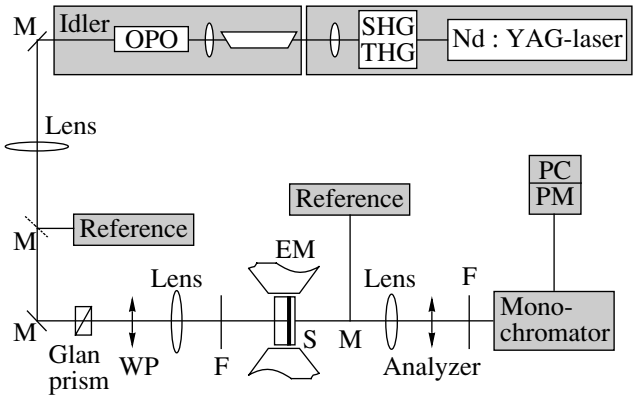

Fig. 2. Schematic of experimental setup.

ous authors [12, 13, 21–27]. The electronic structure of the ferrite garnets has been a subject of theoretical studies based on crystal-field and molecular-orbital theories [12, 21, 26, 28–30]. Shown on the left of Fig. 1 are the electronic states of the Fe^{3+} iron ion on the tetrahedral and octahedral sublattices. These states were calculated in terms of crystal-field theory with allowance for tetragonal distortions in the tetrahedral sublattice and for trigonal distortions in the octahedral sublattice [30]. Calculations reveal that the corresponding splittings and changes in the electronic states may be of the order of 0.5 eV and, therefore, are comparable to the electronic-state splitting in cubic-crystal fields of $T_d(\bar{4}32)$ and $O_h(m3m)$ symmetry. Below the fundamental-absorption edge, electronic transitions can be studied using methods based on measuring the optical and magnetooptical transmission spectra, whereas above the absorption edge at ~3.2 eV, methods involving reflection appear more effective [21, 23, 24]. Nevertheless, absorption spectra of very thin YIG films (t = 0.26 μm) have been obtained up to 5.0 eV [13]. It should be pointed out that all optical transitions between the localized electronic states of the Fe^{3+} ion are spin forbidden. Furthermore, transitions in this ion on the octahedral sublattice are parity forbidden in the electric-dipole approximation and become allowed when electron–phonon coupling is included. Optical absorption in YIG in the IR spectral region starts in the region ~1.2 eV and originates from the $^6A_{1g} \longrightarrow {}^4T_{1g}$ localized electronic transition between the $(3d)^5$ levels of the Fe^{3+} ion on the octahedral sublattice. This transition is of the magnetic-dipole type and gives rise to the appearance of two very weak lines in the absorption spectrum [22]. As seen from Fig. 1, at higher energies, the electron transitions occurring on the tetrahedral and octahedral sublattices become superimposed, thus making unambiguous assignment difficult. Actually, the experimentally observed YIG spectrum exhibits a more complex structure than expected from the theory that takes into account tetragonal and trigonal distortions. The fact is that the position of electronic levels depends not only on the parameters of the cubic and noncubic crystal fields but also on other intraatomic parameters, such as the spin–orbit coupling and the exchange interaction constant. In strongly correlated systems, such as ferrite garnet compounds, pair transitions may give rise to additional absorption bands in the optical spectra. For instance, the absorption bands in the spectral region near 2.5 eV are associated, at least partially, with pair transitions. Being comparable in magnitude and not completely established, these factors complicate unambiguous assignment of optical absorption bands. Optical and magnetooptical studies performed at low temperatures are capable of only partially resolving the problems associated with the assignment of optical transitions and electronic-level splitting in the complex structures of energy spectra.

The exact position of the fundamental absorption edge is not very well established and is usually assumed to lie near 3.2–3.4 eV, where the optical absorption coefficient of YIG starts to grow noticeably, to approach ~5×10^5 cm^{-1} at energies above 5 eV [13]. This value of absorption is typical of intraband transitions in the oxides of transition metals. Substitution of Bi^{3+} ions in ferrite garnets for Y^{3+} results in a shift of the absorption edge toward lower energies and a substantial enhancement of magnetooptical effects in the visible and UV spectral regions. The proposed microscopic mechanisms of enhancement of the magnetooptical Faraday and Kerr effects involve an increase in the spin–orbit coupling as a result of the formation of a molecular orbit between the 3*d* orbitals of the Fe^{3+} ions and the 2*p* orbitals of the O^{2-} ions. This entails mixing with the 6*p* orbital of the Bi^{3+} ions, which have a high spin–orbit coupling coefficient. An analysis shows that the most important electron transitions responsible for Faraday rotation in bismuth-substituted garnets lie at energies of 2.6, 3.15, and 3.9 eV [31].

3. SAMPLES AND EXPERIMENTAL SETUP

The present study was made on thin films of magnetic garnets grown by liquid-phase epitaxy on transparent nonmagnetic substrates of bulk GGG or SGGG crystals. Films grown on substrates with four different orientations, (001), (110), (111), and (210), differed in thickness, chemical composition, and substrate parameters [20].

The experimental setup used in SHG and THG measurements is shown in Fig. 2. The setup included a pulsed solid-state Nd : YAG laser with a photon energy of 1.17 eV and a pulse repetition frequency of 10 Hz. The light emitted by this laser was transformed into the second, and, subsequently, third, optical harmonic by means of a KDP nonlinear crystal and was then used to pump a β-BaB_2O_4-based optical parametric oscillator (OPO). The OPO served as a light source. The intensity and wavelength of light were monitored by a power meter and monochromator, respectively. The observed

SHG and THG signals were normalized by measuring the pulse energy of the light passed through the sample at the fundamental frequency. This was dictated by the ferrite garnet films having different compositions and thicknesses, which affected the light intensity at the fundamental frequency and, hence, the measured SHG and THG signals. A half-wave plate and a polarizer were employed to set the required light polarization at the fundamental frequency. An optical filter mounted before the sample was used to suppress possible parasitic SHG and THG signals. An optical filter placed behind the sample served to suppress light at the fundamental frequency. An analyzer isolated the desired polarization at the SHG and THG frequencies. To exclude possible signals due to two-photon luminescence, a monochromator was used in some experiments. A long-focal-length objective lens was used to focus the light of the double or triple frequency onto a cooled CCD array or a PM tube. The spectral response of the filter and of light-measuring systems was taken into account in the processing of the data.

4. NONLINEAR OPTICAL SUSCEPTIBILITIES IN MAGNETICALLY ORDERED CRYSTALS

The relation between the light-wave electric field E at the fundamental frequency and the induced nonlinear polarization P at the doubled and tripled frequencies in magnetic crystals in the electric-dipole approximation has the form

$$\begin{aligned}\mathbf{P}(2\omega) &= \varepsilon_0\hat{\chi}_{cr}^{(2)}(-2\omega;\omega,\omega)\mathbf{E}(\omega)\mathbf{E}(\omega)\\ &+\hat{\chi}_{m}^{(3)}(-2\omega;\omega,\omega,0)\mathbf{E}(\omega)\mathbf{E}(\omega)\mathbf{M}(0),\\ \mathbf{P}(3\omega) &= \varepsilon_0\hat{\chi}_{cr}^{(3)}(-3\omega;\omega,\omega,\omega)\mathbf{E}(\omega)\mathbf{E}(\omega)\mathbf{E}(\omega)\\ &+\hat{\chi}_{m}^{(4)}(-3\omega;\omega,\omega,\omega,0)\mathbf{E}(\omega)\mathbf{E}(\omega)\mathbf{E}(\omega)\mathbf{M}(0),\end{aligned} \quad (1)$$

where M is the spontaneous magnetization. The polar $\hat{\chi}_{cr}^{(2)}$ and axial $\hat{\chi}_{m}^{(3)}$ nonlinear-optical tensors are allowed in media with no inversion symmetry and describe the crystallographic and magnetic contributions to SHG, respectively. These two contributions can, in principle, be separated by measuring the SHG rotational anisotropy [18]. The polar $\hat{\chi}_{cr}^{(3)}$ and axial $\hat{\chi}_{m}^{(4)}$ tensors are allowed in any medium and describe the crystallographic and magnetic contributions to THG, respectively. In the region of transparency of magnetic crystals, the components of the $\hat{\chi}_{cr}^{(2)}$ and $\hat{\chi}_{m}^{(3)}$ tensors are real quantities and those of $\hat{\chi}_{m}^{(3)}$ and $\hat{\chi}_{m}^{(4)}$ are purely imaginary. The SHG and THG signal intensity can be calculated from the relations

$$\begin{aligned}I(2\omega) &\propto E_0^4\left|\chi_{cr}^{(2)} \pm \chi_{m}^{(3)}M\right|^2\\ &= E_0^4\left(\left|\chi_{cr}^{(2)}\right|^2 + \left|\chi_{m}^{(3)}\right|^2M^2 \pm 2\left|\chi_{cr}^{(2)}\right|\left|\chi_{m}^{(3)}\right|M\cos(\varphi_1)\right),\\ I(3\omega) &\propto E_0^6\left|\chi_{cr}^{(3)} \pm \chi_{m}^{(4)}M\right|^2\\ &= E_0^6\left(\left|\chi_{cr}^{(3)}\right|^2 + \left|\chi_{m}^{(4)}\right|^2M^2 \pm 2\left|\chi_{cr}^{(3)}\right|\left|\chi_{m}^{(4)}\right|M\cos(\varphi_3)\right),\end{aligned} \quad (2)$$

where φ_1 and φ_2 are phase differences between the optical waves induced by the crystallographic and magnetic contributions to SHG and THG, respectively. The terms proportional to magnetization M in the relations for the SHG and THG intensities originate from the interference of these waves in the spectral region where optical absorption is nonzero but the optical phases φ_1 and φ_2 may not equal 90°. The plus an minus signs refer to opposite projections of the magnetization **M**. The symmetry properties of the tensors $\hat{\chi}_{cr}^{(2)}$, $\hat{\chi}_{cr}^{(3)}$, $\hat{\chi}_{m}^{(3)}$, and $\hat{\chi}_{m}^{(4)}$ are strictly determined by the crystallographic point group. The nonzero components of the tensors $\hat{\chi}_{cr}^{(2)}$ and $\hat{\chi}_{m}^{(3)}$ are given in [20], and the table lists the nonzero components of the $\hat{\chi}_{cr}^{(3)}$ and $\hat{\chi}_{m}^{(4)}$ tensors for the point group 3*m*. The magnetic contrast of SHG and THG is defined as the normalized difference between the harmonic-signal intensities for opposite orientations of the saturation magnetization:

$$\begin{aligned}\rho^{SHG} &= \frac{I(2\omega,+M)-I(2\omega,-M)}{I(2\omega,+M)+I(2\omega,-M)},\\ \rho^{THG} &= \frac{I(3\omega,+M)-I(3\omega,-M)}{I(3\omega,+M)+I(3\omega,-M)}.\end{aligned} \quad (3)$$

5. EXPERIMENTAL RESULTS AND DISCUSSION

The optical absorption spectra of ferrite garnet films were measured with a Cary-2300 spectrophotometer and were found to agree with the published data. The absorption spectra of three different films at $T = 15$ K are displayed in Figs. 3c, 4c, and 5c. Optical densities above $D = 4.5$ were outside the operating range of the spectrophotometer and could not be measured.

Figures 3a and 3b present SHG spectra of a YIG/GGG(111) film for two opposite orientations of the magnetization **M** in transverse geometry, i.e., with light waves propagating at the fundamental and double frequencies in a direction perpendicular to the magnetization vector **M**. The spectra relate to two cases, namely, (a) to an SHG signal obtained directly from the free film surface (film-to-photodetector case) and (b) to an SHG signal obtained from the film–substrate interface (substrate-to-photodetector). The SHG spectra taken in these two experimental configurations are dif-

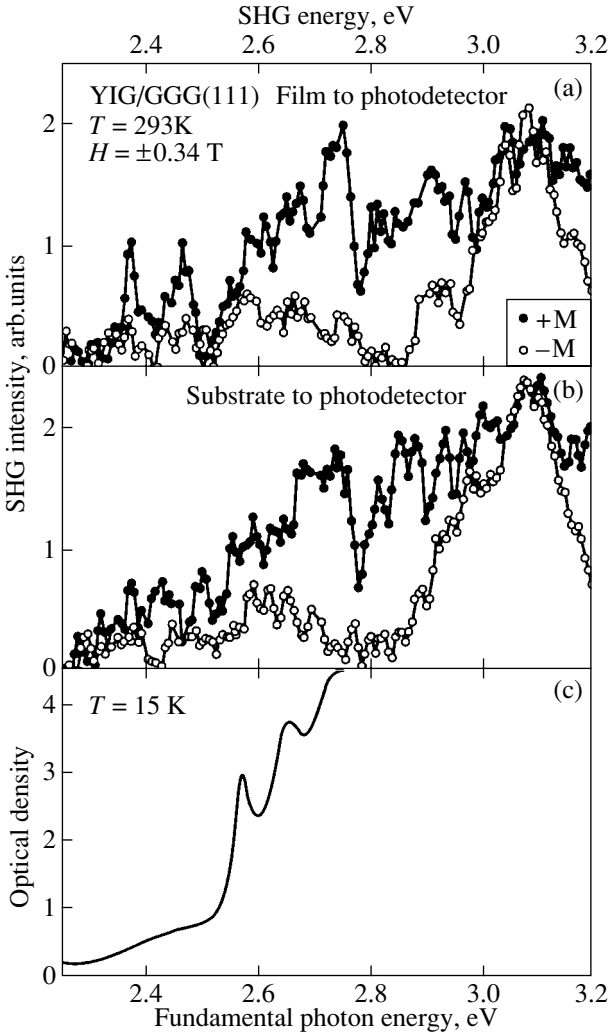

Fig. 3. SHG spectra in a YIG/GGG(111) film obtained for two opposite orientations of the magnetization **M** in transverse geometry: (a) SHG signal from the free film surface (film-to-photodetector case), (b) SHG signal from the film–substrate interface (substrate-to-photodetector), and (c) linear-absorption spectrum of the YIG/GGG(111) film.

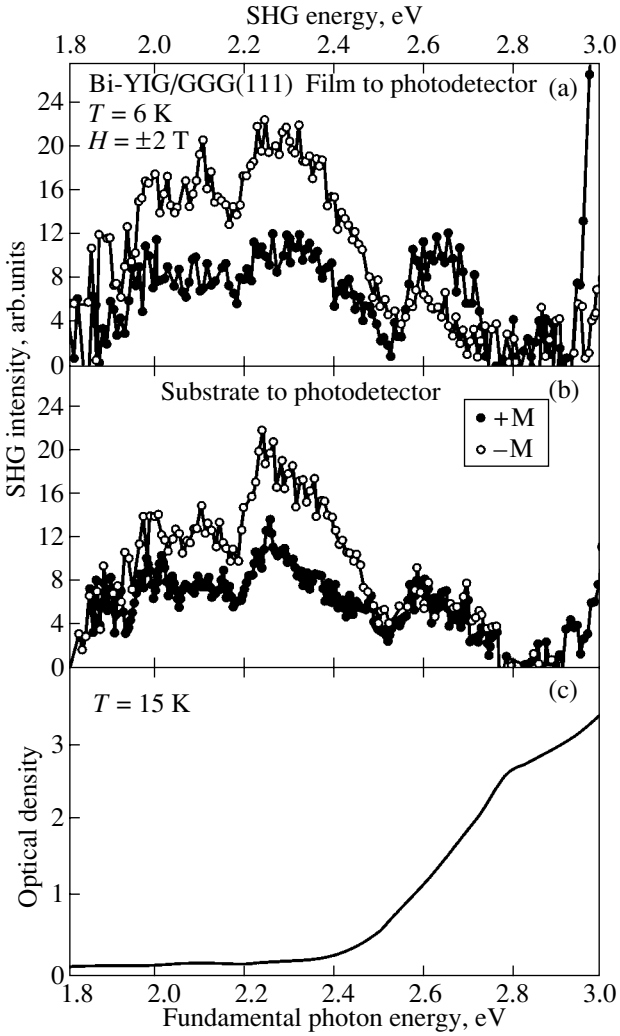

Fig. 4. Same as in Fig. 3 but for a Bi-YIG/GGG(111) film.

ferent. In particular, the splitting near 2.4 eV is clearly pronounced for the free film surface but poorly distinguishable for the more strained film surface interfacing with the substrate. Note that the magnetic contrast ρ^{SHG} varies from 0 to 100%. This implies that the crystallographic and magnetic contributions to SHG are comparable in magnitude. According to the electronic-level diagram shown in Fig. 1, some of the features in the SHG spectrum can be assigned to electron transitions in Fe^{3+} ions in the tetrahedral and octahedral crystal fields. The two features in the SHG spectrum near 2.57 and 2.66 eV can apparently be associated with the ${}^6A_1 \longrightarrow {}^4E, {}^4A_1$ electron transitions in the tetrahedral sublattice and ${}^6A_{1g} \longrightarrow {}^4E_g, {}^4A_g$ electron transitions in the octahedral sublattice. The oscillator strengths for the two absorption peaks reported to have been seen in the region of 2.9 and 3.2 eV are an order of magnitude larger than those for transitions near 2.6 eV. However, the spectral features observed in the SHG spectrum in the former region are of the same order of magnitude as those in the region of lower optical absorption.

Bismuth-substituted garnet films were shown to produce stronger SHG signals [20]. Figures 4a and 4b display SHG spectra obtained on a bismuth-substituted ferrite garnet film, Bi-YIG/GGG(111). Substitution of bismuth for yttrium brings about a substantial enhancement of SHG signals in the energy interval 2.0–2.4 eV. SHG spectra for a bismuth-substituted ferrite garnet film, Bi-YIG/SGGG(210), are presented in Figs. 5a and 5b. The SHG spectrum was measured in the range 1.7–3.1 eV at T = 6 K. The spectrum clearly reveals five bands with strong SHG signals and a high magnetic contrast. Note that the spectra obtained from the two sides of the film are different, as was the case with the YIG/GGG(111) and Bi-YIG/GGG(111) films. As in the case of (111)-type films, a substantial increase in

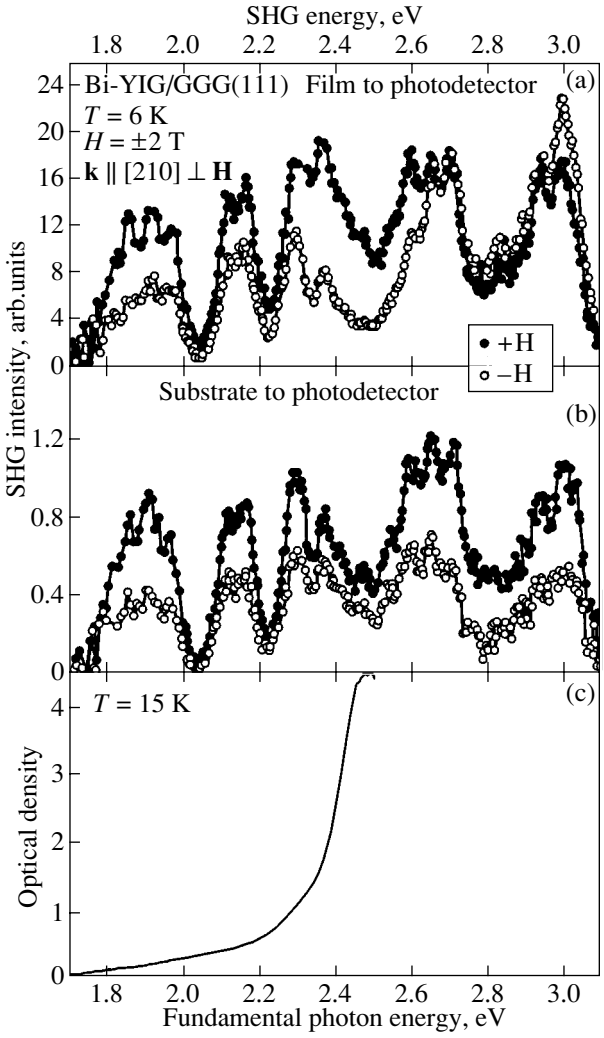

Fig. 5. Same as in Fig. 3 but for a Bi-YIG/SGGG(210) film.

the intensity of the linear-optical signal near the fundamental absorption edge does not entail a significant increase in the SHG intensity.

Figures 6a and 6b present characteristic rotational anisotropies of SHG signals observed in the Bi-YIG/GGG(111) and Bi-YIG/SGGG(210) films. The SHG signal intensity was measured in these experiments as a function of the rotation angle of the incoming and outgoing light polarization simultaneously in the 0°–360° range for the two opposite orientations of the magnetization M in transverse geometry. The relations thus obtained reflect the symmetry of the ferrite garnet films grown on (111)- and (210)-type substrates. A theoretical analysis of and experimental data on SHG signal anisotropy in films with different crystallographic orientations can be found in [20].

Figures 7a–7c show THG spectra obtained on three garnet films, YIG/GGG(111), Bi-YIG/GGG(111), and Bi-YIG/SGGG(210), respectively. Note that the observation of THG signals in electric-dipole approximation does not require violation of space inversion symmetry. Although the optical absorption and magnetooptical signals measured in the films studied differ substantially in magnitude, their THG spectra are similar. The ${}^6A_1 \longrightarrow {}^4T_2$ electron transition near 2.4 eV in the tetrahedral sublattice is well resolved in the THG spectrum and, particularly, in the weakly strained YIG/GGG(111) film. It should be pointed out that the strong increase in linear absorption seen to occur at energies above 3 eV is not accompanied by an enhancement of the SHG signals. Unlike in the SHG signals, no magnetic contrast was observed in the THG spectra to within experimental accuracy. This comes as a surprise, because phenomenological considerations allow a magnetic contribution to THG in both the longitudinal and transverse geometry.

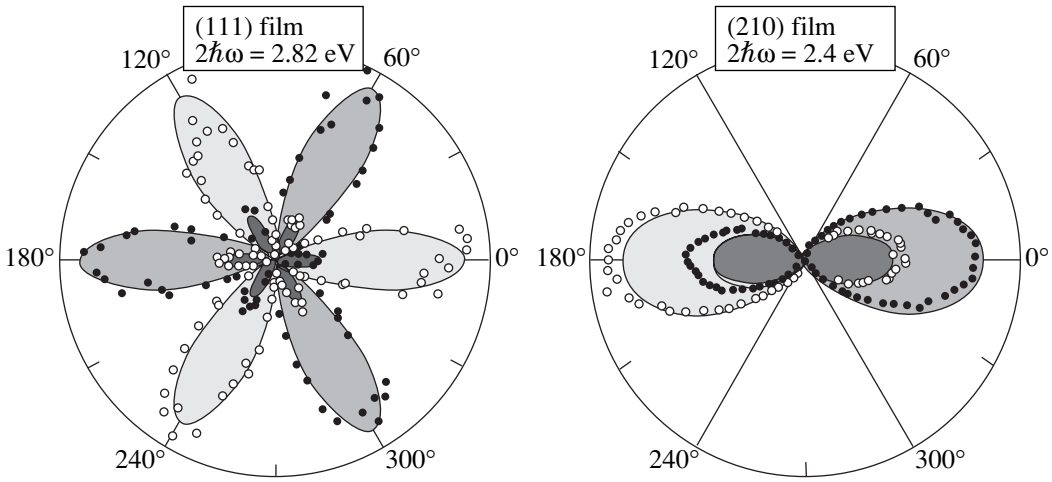

Fig. 6. Rotational anisotropies of SHG signals for Bi-YIG/GGG(111) and Bi-YIG/SGGG(210) films.

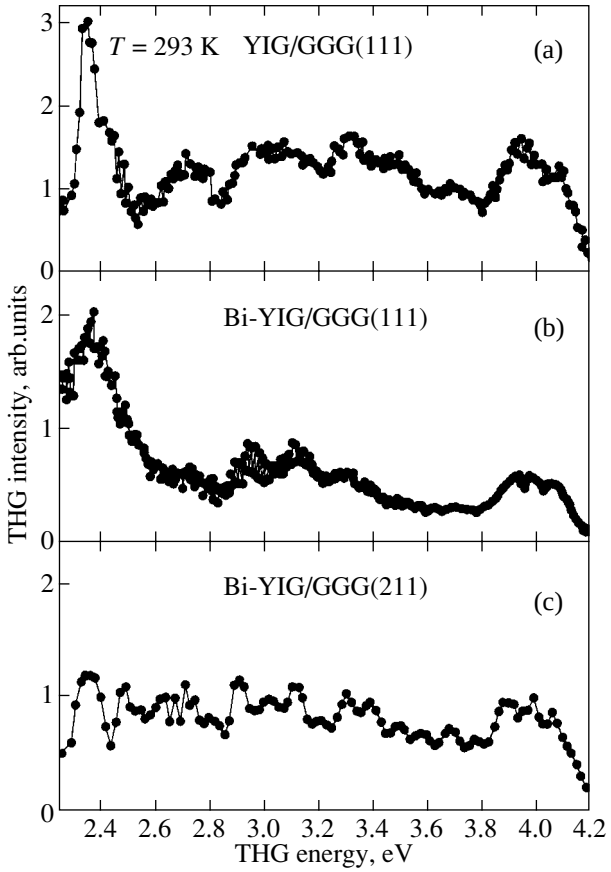

Fig. 7. THG spectra in (a) YIG/GGG(111), (b) Bi-YIG/GGG(111), and (c) Bi-YIG/SGGG(210) films.

6. CONCLUSIONS

To sum up, we have studied optical SHG spectra in anisotropic magnetic films of ferrite garnets on substrates with different crystallographic orientations within the photon energy range from 1.7 to 3.2 eV. The crystallographic and magnetic contributions to the total SHG signal intensity were revealed. The optical THG spectra were measured in the photon energy range 2.4–4.2 eV, below and above the fundamental absorption edge at ~3.2 eV. Whereas linear absorption increases for photon energies above 3 eV, SHG and THG signals do not exhibit any noticeable variation in intensity. These experimental data suggest that local *d–d* transitions provide a major contribution to nonlinear optical spectra. The contributions associated with charge-transfer and interband transitions are less significant and contribute little to the nonlinear optical susceptibilities. A very interesting and unusual result is the observation of a large magnetic contribution to SHG spectra with a magnetic contrast as high as 100%. At the same time, no magnetic contribution was observed in THG spectra. The data obtained on optical harmonic generation in ferrite garnet epitaxial films open up a new potential of nonlinear-optical methods and stimulate further experimental and theoretical research into higher order optical phenomena in magnetically ordered materials.

ACKNOWLEDGMENTS

The authors are indebted to H.-J. Weber for assistance in measuring the optical absorption spectra.

This study was supported by the Russian Foundation for Basic Research and by Deutsche Forschungsgemeinschaft. One of the authors (R.V.P.) wishes to acknowledge financial support from the Alexander von Humboldt Stiftung.

REFERENCES

1. J. Reif, J. C. Zink, C.-M. Schneider, and J. Kirschner, Phys. Rev. Lett. **67**, 2878 (1991).
2. J. Reif, C. Rau, and E. Matthias, Phys. Rev. Lett. **71**, 1931 (1993).
3. Th. Rasing, J. Magn. Magn. Mater. **175**, 35 (1997).
4. *Nonlinear Optics in Metals*, Ed. by K. H. Bennemenn (Clarendon Press, Oxford, 1998).
5. Special issue on Nonlinear Optics at Interfaces, Appl. Phys. B **68** (1999).
6. E. Hanamura, M. Fiebig, and Y. Tanabe, in *Magneto-Optics*, Ed. by S. Sugano and N. Kojima (Springer, Berlin, 2000).
7. A. Schülzgen, Y. Kawabe, E. Hanamura, *et al.*, Phys. Rev. Lett. **86**, 3164 (2001).
8. *Physics of Magnetic Garnets*, Ed. by A. Paoletti (North Holland, Amsterdam, 1978).
9. G. Winkler, *Magnetic Garnets* (Vieweg, Braunschweig, 1981).
10. *Magnetic Garnet Films*, Ed. by A. Paoletti, Thin Solid Films **114** (1984).
11. H. Landolt and R. Börnstein, *Numerical Data and Functional Relatioships in Science and Technology*, New Ser. Group III (Springer, Berlin, 1991), Vol. 27/e.
12. D. L. Wood and J. P. Remeika, J. Appl. Phys. **38**, 1038 (1967).
13. G. B. Scott and J. L. Page, Phys. Status Solidi B **79**, 203 (1977).
14. B. B. Krichevtsov, V. V. Pavlov, and R. V. Pisarev, Pis'ma Zh. Éksp. Teor. Fiz. **49**, 466 (1989) [JETP Lett. **49**, 535 (1989)]; Fiz. Tverd. Tela (Leningrad) **31** (7), 77 (1989) [Sov. Phys. Solid State **31**, 1142 (1989)].
15. O. A. Aktsipetrov, O. V. Braginskiĭ, and D. A. Esikov, Kvantovaya Élektron. (Moscow) **17**, 320 (1990).
16. G. Pertocelli, S. Martelucci, and M. Richetta, Appl. Phys. Lett. **63**, 3402 (1993).
17. R. V. Pisarev, B. B. Krichevtsov, V. N. Gridnev, *et al.*, J. Phys. C **5**, 8621 (1993).
18. V. V. Pavlov, R. V. Pisarev, A. Kirilyuk, and Th. Rasing, Phys. Rev. Lett. **78**, 2004 (1997).
19. V. V. Pavlov, R. V. Pisarev, A. Kirilyuk, and Th. Rasing, J. Appl. Phys. **81**, 4631 (1997).
20. V. N. Gridnev, V. V. Pavlov, R. V. Pisarev, *et al.*, Phys. Rev. B **63**, 184407 (2001).

21. F. J. Kahn, P. S. Pershan, and J. P. Remeika, Phys. Rev. **186**, 891 (1969).

22. J. P. van der Ziel, J. F. Dillon, Jr., and J. P. Remeika, AIP Conf. Proc. **5**, 254 (1971).

23. A. I. Galuza, V. V. Eremenko, and A. P. Kirichenko, Fiz. Tverd. Tela (Leningrad) **15**, 585 (1973) [Sov. Phys. Solid State **15**, 407 (1973)].

24. K. W. Blazey, J. Appl. Phys. **45**, 2273 (1974).

25. S. H. Wemple, S. L. Blank, J. A. Seman, and W. A. Biolsi, Phys. Rev. B **9**, 2134 (1974).

26. G. B. Scott, D. E. Lacklison, and J. L. Page, Phys. Rev. B **10**, 971 (1974).

27. B. B. Krichevtsov, O. Ochilov, and R. V. Pisarev, Fiz. Tverd. Tela (Leningrad) **25**, 2404 (1983) [Sov. Phys. Solid State **25**, 1380 (1983)].

28. T. K. Vien, J. L. Dormann, and H. Le Gall, Phys. Status Solidi **71**, 731 (1975).

29. A. S. Moskvin, A. V. Zenkov, E. I. Yuryeva, and V. A. Gubanov, Physica B (Amsterdam) **168**, 187 (1991).

30. V. V. Alekseev, V. V. Druzhinin, and R. V. Pisarev, Fiz. Tverd. Tela (Leningrad) **33**, 2669 (1991) [Sov. Phys. Solid State **33**, 1507 (1991)].

31. G. F. Dionne and G. A. Allen, J. Appl. Phys. **73**, 6127 (1993).

Translated by G. Skrebtsov

Physics of the Solid State, Vol. 45, No. 4, 2003, pp. 670–672. Translated from Fizika Tverdogo Tela, Vol. 45, No. 4, 2003, pp. 638–640.

MAGNETISM AND FERROELECTRICITY

Electronic Structure and the S *K* Absorption Spectra of Chromium-Containing Chalcogenide Spinels $Cd_{1-x}Cu_xCr_2S_4$

O. A. Leshcheva, N. Yu. Safontseva, and I. Ya. Nikiforov

Don State Technical University, Rostov-on-Don, 334010 Russia

e-mail: ngmarost@aaanet.ru

Received June 5, 2002

Abstract—The electronic structure and x-ray absorption spectra of sulfur in normal ferromagnetic spinels of the general formula $Cd_{1-x}Cu_xCr_2S_4$ (x = 0.05, 0.1, 0.15, 0.2) are calculated using the FEFF8 program. In these calculations, the self-consistent crystal potential is simulated in terms of the partially nonlocal model of exchange-correlation potential. The model is based on the Dirac–Fock approximation for core electrons and the Hedin–Lundquist approximation for valence electrons. The S *K* absorption edges are calculated in the approximation of full multiple scattering by a 27-atom cluster. In addition, one-, two-, and three-scattering paths within a 981-atom clusters are taken into account. The calculation demonstrates that the introduction of even insignificant amounts of copper atoms into a $CdCr_2S_4$ cluster leads to a shift in the main features of the S *K* adsorption edges toward the high-energy range. This can be associated with variations in the nearest environment of the absorbing atom and active participation of copper ions in the chemical bonding of chalcogenide spinels. © *2003 MAIK "Nauka/Interperiodica".*

1. INTRODUCTION

This work continues our investigations of the *K* absorption edge shape for *Me*(Mn, Mg, Ni, Zn)Fe_2O_4 ferrites with a spinel structure [1]. In the present work, solid solutions in the $CdCr_2S_4$–$CuCr_2S_4$ system with a normal spinel structure and ferromagnetic ordering of the magnetic moments with the Curie temperature of approximately 90 K are chosen as the object of investigation.

The chromium-containing spinels studied earlier have the general formula ACr_2X_4 (X = S, Se), which is usually valid for $A_{1-x}A'_xCr_2X_4$ solid solutions over the entire concentration range of the A' ion. However, for a series of solid solutions with A' = Cu, the limiting solubility is observed for A = Zn, Cd, and Mn. For example, $Cd_{1-x}Cu_xCr_2S_4$ homogeneous solid solutions are synthesized for copper concentrations $x \le 0.2$ and $x \ge 0.9$. These compounds are normal ferrimagnetic spinels with *p*-type conduction at $x \le 0.2$ and ferromagnetic spinels with *p*-type conduction for $x \ge 0.9$. As regards the $Cd_{1-x}Cu_xCr_2S_4$ solid solutions, where $CdCr_2S_4$ is a ferromagnet with *p*-type semiconductor properties and $CuCr_2S_4$ is a ferromagnet with *p*-type metal conduction, single-phase solid solutions can be prepared only for copper concentrations $x \le 0.2$. It should be noted that spinels in the $Cd_{1-x}Cu_xCr_2S_4$ system are characterized by ferrimagnetic ordering of magnetic moments localized at chromium ions and metamagnetic phase transitions.

To the best of our knowledge, reliable data on the x-ray emission and absorption spectra of atoms in $Cd_{1-x}Cu_xCr_2S_4$ solid solutions are not available. In order to verify the reliability of the results obtained, we performed calculations of the electronic structure in the spinel series from pure $CdCr_2S_4$ to pure $CuCr_2S_4$ with variations in the copper concentration in $Cd_{1-x}Cu_xCr_2S_4$ solid solutions. In our earlier work [2], we calculated the spectra of $CdCr_2S_4$ and $CuCr_2S_4$ compounds. A comparison showed that the main features revealed in the experimental and theoretical x-ray emission spectra and the S *K* absorption edges were in good agreement with the local partial densities of states.

2. CALCULATION PROCEDURE

The crystal structure of spinels with space group O_h^7–$F3dm$ represents a close face-centered cubic packing of anions with tetrahedral and octahedral holes partially occupied by the cations.

Solid solutions in the $Cd_{1-x}Cu_xCr_2S_4$ system belong to the structural type of normal spinels in which cadmium and copper cations occupy tetrahedral sites and chromium cations are located at octahedral sites. Thus, the ACr_2S_4 formula unit involves one *Me* (Cd, Cu) cation in the tetrahedral site and two chromium cations in the octahedral site [3]. The atomic positions in a spinel cluster were determined from the following formulas

for lengths of the tetrahedral l_t and octahedral l_o cation–anion bonds [4]:

$$l_t = \sqrt{3(1/8 + \delta)}a \quad \text{and} \quad l_o = (1/4 - \delta)a.$$

Here, a is the parameter of the spinel cubic unit cell consisting of 56 atoms, of which 32 are sulfur anions forming the face-centered lattice; $\delta \equiv u - 3/8$; and u is the anion parameter, which specifies the arrangement of the sulfur atoms and accounts for their displacements from ideal positions toward the [111] direction. In this work, we used the following parameters: $a = 10.242$ Å and $u = 0.39$ for $CdCr_2S_4$, and $a = 9.814$ Å and $u = 0.384$ for $CuCr_2S_4$ [4].

Spinels of the nonstoichiometric composition $Cd_{1-x}Cu_xCr_2S_4$ (where $x = 0.05$, 0.1, 0.15, and 0.2) have an ordered sublattice of sulfur atoms. In this sublattice, chromium cations occupy octahedral holes and a certain part of the cadmium cations are randomly replaced by copper cations in tetrahedral sites according to the atomic content of copper in the solid solution (5, 10, 15, and 20 at. %) [5].

In this work, the electronic structure and S *K* absorption edges were theoretically calculated using the FEFF8 program developed by Rehr, Albers, and Ankudinov [6]. This program is based on the approximation of high-order multiple scattering and includes the calculation of the x-ray photoabsorption cross section.

The shape of the S *K* absorption spectra of the spinels under investigation was calculated within a unified model proposed earlier in [1, 2]. However, in our case, the self-consistent crystal potential was simulated in the framework of the nonlocal exchange-correlation potential model. This model is based on the Dirac–Fock approximation for core electrons and the Hedin–Lundquist approximation for valence electrons. The self-consistent crystal potential was also calculated for a cluster containing up to 30 atoms, and the number of iterations was as large as ten.

3. RESULTS AND DISCUSSION

The figure shows the theoretical S *K* absorption edges for $CdCr_2S_4$ and $CuCr_2S_4$ compounds, as well as for $Cd_{1-x}Cu_xCr_2S_4$ solid solutions, where $x = 0.05$, 0.1, 0.15, and 0.2. The theoretical and experimental [7] S *K* absorption edges were superposed on the same energy scale, in which the energy position of the principal peak of the S *K* absorption edge was taken as the origin. A comparison of the x-ray absorption near-edge structure (XANES) calculations of the S *K* absorption edge and the local partial densities of states for $CdCr_2S_4$ demonstrated that the conduction band bottom in $CdCr_2S_4$ is formed by mixed free *p* states of sulfur and *s* and *p* states of cadmium and chromium. The *b* peak of the experimental S *K* absorption edge is associated with the hybridization of sulfur *p* states and cadmium *s* states. The features *c*' and *c*", which were not revealed in this

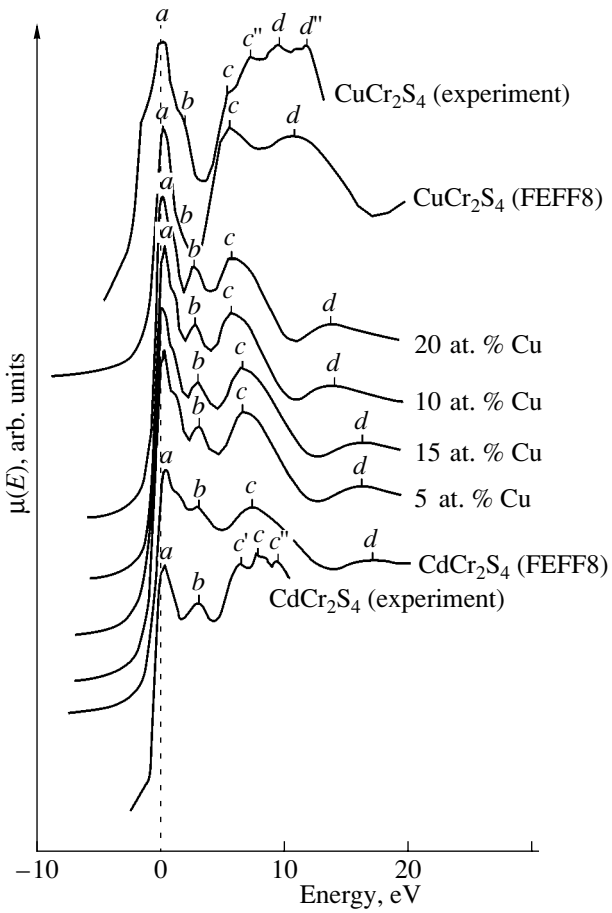

Theoretical S *K* absorption edges for $Cd_{1-x}Cu_xCr_2S_4$ solid solutions and experimental S *K* absorption edges for $CdCr_2S_4$ and $CuCr_2S_4$ [7].

calculation but were observed in the experimental S *K* absorption edge, degenerate into a single peak *c*. The *c* peak is also attributed to the hybridization of sulfur *p* states with chromium *p* and cadmium *p* states, as well as with chromium *s* states.

A similar comparison for $CuCr_2S_4$ showed that, in this case, the conduction band bottom is formed by strongly mixed free *p* states of sulfur, *s* and *p* states of copper, and *s* and *p* states of chromium. The shoulder *b* in the experimental S *K* absorption edge, which was also revealed in our calculation, can be interpreted as an admixture of copper *s* states and chromium *p* states to free sulfur *p* states. The *c*' and *c*" features observed in the experimental S *K* absorption edge degenerate into a single shoulder *c* in the theoretical absorption edge. This feature can be attributed to the hybridization of sulfur *p* states with *s* and *p* states of chromium and copper, which is confirmed by the corresponding peaks of the partial densities of states for copper and chromium. Similarly, the *d*' and *d*" features in the theoretical absorption edge degenerate into a single shoulder *d*, which is interpreted as an admixture of chromium *p* and copper *p* states to sulfur *p* states.

Energy location of the main features of the *SK* absorption edges for $Cd_{1-x}Cu_xCr_2S_4$ solid solutions

Crystal	*b*	*c*	*d*
$CdCr_2S_4$, experiment [7]	4.25	4.84	
$CdCr_2S_4$, FEFF8	4.25	4.77	5.98
$Cd_{0.95}Cu_{0.05}Cr_2S_4$	4.25	4.68	5.85
$Cd_{0.9}Cu_{0.1}Cr_2S_4$	4.24	4.68	5.84
$Cd_{0.85}Cu_{0.15}Cr_2S_4$	4.22	4.57	5.58
$Cd_{0.8}Cu_{0.2}Cr_2S_4$	4.21	4.56	5.54
$CuCr_2S_4$, FEFF8	4.08	4.57	5.17
$CuCr_2S_4$, experiment [7]	4.12	4.55	5.05

Note: The energy position of the principal absorption peak *a* (eV) is taken as the origin.

After introduction of the appropriate amount of copper atoms into a $CdCr_2S_4$ cluster, the *b*, *c*, and *d* features in the theoretical S *K* absorption edges shift to the low-energy range. Specifically, for the $Cd_{1-x}Cu_xCr_2S_4$ solid solution with $x = 0.05$, the *b* and *c* peaks are shifted by 0.01 and 0.09 eV, respectively (see table). As the copper content in the cluster increases, the specific features in the theoretical S *K* absorption edges shift to the lower energy range. It can be seen that, at a copper content of 20 at. %, the *b*, *c*, and *d* peaks are shifted by 0.4, 0.26, and 0.48 eV, respectively, with respect to their energy location for pure $CdCr_2S_4$. The tendency for the *b*, *c*, and *d* peaks to shift toward the low-energy range manifests itself over the entire range from 5 to 20 at. % Cu. Therefore, we can assume that a further increase in the number of copper atoms in the $CdCr_2S_4$ cluster should lead to a further shift. Upon the complete substitution of copper atoms for cadmium atoms, the aforementioned features will be shifted to the S *K* absorption edge for $CuCr_2S_4$. For this edge, the *b*, *c*, and *d* features are located lower in energy as compared to the corresponding features in the experimental S *K* absorption edge for $CdCr_2S_4$. The observed shift of the main features in the theoretical S *K* absorption edges to the low-energy range with an increase in the copper content in the $Cd_{1-x}Cu_xCr_2S_4$ solid solution can be explained by the lower location of the peaks in the density of states for copper as compared to that for cadmium. According to the Lotgering model [8], this difference is associated with the shift of the Fermi level in $CuCr_2S_4$ with respect to the Fermi level in $CdCr_2S_4$, which can also be responsible for different types of conduction in these compounds.

REFERENCES

1. N. Yu. Safontseva and I. Ya. Nikiforov, Fiz. Tverd. Tela (St. Petersburg) **43** (1), 61 (2001) [Phys. Solid State **43**, 61 (2001)].
2. N. Yu. Safontseva, I. Ya. Nikiforov, and O. A. Leshcheva, Khim. Fiz. Mezosk. **2** (2), 234 (2001).
3. E. V. Gorter, Usp. Fiz. Nauk **57** (2), 279 (1955).
4. V. M. Talanov, *Energetic Crystal Chemistry of Multisublattice Crystals* (Rostov Gos. Univ., Rostov-on-Don, 1986).
5. J. Krok-Kowalski, T. Gron, J. Warczewski, *et al.*, J. Magn. Magn. Mater. **168**, 129 (1997).
6. A. L. Ankudinov, B. Ravel, J. J. Rehr, and S. D. Conradson, Phys. Rev. B **58** (2), 7565 (1998).
7. Yu. V. Sukhetsky, A. V. Soldatov, and A. N. Gusatinskii, Physica B (Amsterdam) **176**, 219 (1992).
8. S. Methfessel and D. C. Mattis, *Magnetic Semiconductors* (Springer, Heidelberg, 1968; Mir, Moscow, 1972).

Translated by N. Korovin

Physics of the Solid State, Vol. 45, No. 4, 2003, pp. 673–674. Translated from Fizika Tverdogo Tela, Vol. 45, No. 4, 2003, pp. 641–642.

MAGNETISM AND FERROELECTRICITY

Dynamic Properties of Iron Borate Single Crystals in the High-Rate Range of Magnetization Reversal

O. S. Kolotov, A. V. Matyunin, and V. A. Pogozhev

Moscow State University, Vorob'evy gory, Moscow, 119899 Russia

Received June 18, 2002

Abstract—A third portion is found in the curve of pulsed magnetization reversal of iron borate single crystals with an extremely small switching coefficient $S_{w3} \approx (3–5) \times 10^{-3}$ Oe μs. This portion is attributed to switching off the possible channels of energy losses by magnetoelastic vibrations. © *2003 MAIK "Nauka/Interperiodica".*

1. INTRODUCTION

As is known, the problems concerning interactions between magnetic and elastic subsystems of crystals, energy losses due to these interactions, and their effect on the magnetization reversal rate are fundamental in the physics of transient processes in magnetic materials. The magnetoelastic interaction most clearly manifests itself in single crystals of iron borate ($FeBO_3$) [1–3]. A principal dynamic characteristic, namely, the curve of the pulsed magnetization reversal, represents the dependence of the rate of magnetization reversal τ^{-1} on the pulse amplitude of the magnetization reversal field H_s. At present, it has been established that this curve for $FeBO_3$ single crystals is completely governed by the specific features of the magnetoelastic interaction [3–6]. Specifically, the effect of freezing of the crystal lattice, which was observed earlier for the $FeBO_3$ magnet at frequencies ~10^{10} Hz [7, 8], becomes clearly pronounced in transient processes for magnetization reversal times $\tau = \tau_{cr1} = 15 \pm 2$ ns. For shorter times of magnetization reversal, there occurs a sharp decrease in the intensity of magnetoelastic vibrations that accompany transient processes and arise from shear strain waves propagating along the *C* axis. As a result, for the magnetization reversal time $\tau = \tau_{cr1}$, the energy loss due to excitation of magnetoelastic vibrations decreases, the rate of magnetization reversal increases drastically, and a kink appears in the curve $\tau^{-1}(H_s)$ at $H_s \sim 3–4$ Oe.

The frequency of the magnetoelastic mode studied is determined to be $F_c = 2V_c/d$ (where d is the thickness of the single crystal and V_c is the velocity of the transverse acoustic wave, which propagates along the *C* axis and depends on the external magnetic field) [2, 7–9]. For the field range considered here, the transverse acoustic wave velocity V_c is close to 4×10^5 cm/s. It is evident that this mode of magnetoelastic vibrations is not the sole possible one. We can expect that, with a further increase in the rate of magnetization reversal, the freezing of another magnetoelastic mode will manifest itself at $\tau^{-1} = \tau_{cr2}^{-1}$. It is assumed that this freezing will be accompanied by switching off the relevant channel of energy losses and changes in the dependence $\tau^{-1}(H_s)$. The aim of the present work was to reveal and analyze these variations.

2. EXPERIMENTAL TECHNIQUE

As in the aforementioned works, our experiments were performed on an induction setup. However, in order to increase the time resolution, the setup used in our measurements was modified significantly. In particular, the setup was equipped with a low-voltage spark peaker [10], which made it possible to decrease the width of the front of the magnetization reversal pulse to 0.3 ns. Moreover, the use of a compact magnetization reversal device and a removable coil of an additional resistor ($R = 500\ \Omega$) in the circuit provided a decrease in the voltage setting time in the recording channel to 0.25–0.3 ns. As a result, the time resolution of the setup was brought to 0.4–0.5 ns (instead of 1.4 ns in the initial variant).

We examined the 180° pulsed magnetization reversal. The initial state of technical saturation of the sample under investigation was achieved using the field H_0. The pulsed field H_p, which initiated the studied process, was in opposition to the field H_0. The resulting magnetization reversal fields $H_s = H_p - H_0$ are given below. Six samples from 24 to 100 μm thick were used in the experiments. For all these samples, the second kink expected by us was observed in the curve of the pulsed magnetization reversal.

3. RESULTS AND DISCUSSION

As an example, the curve $\tau^{-1}(H_s)$ obtained for a 34-μm-thick sample in the saturation field $H_{sat} = 1.8$ Oe with a mean period of shock magnetoelastic vibrations

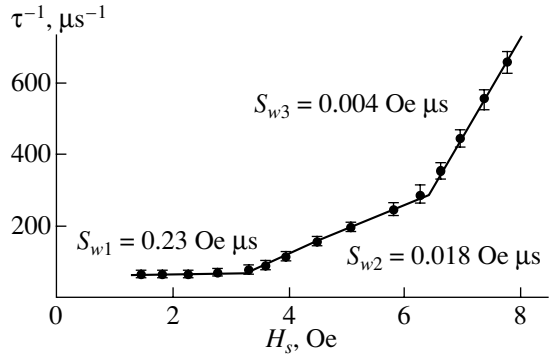

Fig. 1. Curve of the pulsed magnetization reversal.

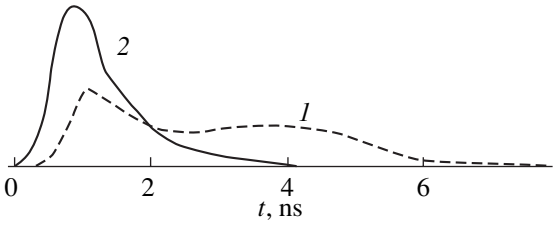

Fig. 2. Signals of magnetization reversal. H_s = (*1*) 4.8 and (*2*) 7.3 Oe.

$T_c = F_c^{-1}$ = 18 ns is shown in Fig. 1. It can be seen that another kink appears in the curve of the pulsed magnetization reversal in addition to the kink previously observed at the characteristic rate of magnetization reversal $\tau^{-1} = \tau_{cr1}^{-1}$ = 70 μs^{-1} in the field $H_s = H_{cr1}$ = 3.1 Oe. For this sample, the new kink is observed in the field $H_s = H_{cr2}$ = 6.3 Oe at the rate of magnetization reversal $\tau^{-1} = \tau_{cr2}^{-1}$ = 280 μs^{-1}. The next portion of the curve is approximated by a straight line with an extremely small switching coefficient $S_{w3} = \Delta H_s/\Delta\tau^{-1}$. For the sample under study, we obtained $S_{w3} = 4 \times 10^{-3}$ Oe μs. For the other samples, the S_{w3} values lie in the range $(3–5) \times 10^{-3}$ Oe μs. To the best of our knowledge, such small switching coefficients have never before been observed for the magnetic materials studied.

Figure 2 displays the signals recorded for the studied sample upon magnetization reversal in fields H_s = 4.8 (curve *1*) and 7.3 Oe (curve *2*). The former and latter fields correspond to approximately the midpoint of the second portion and the initial point of the third portion of the curve of the pulse magnetization reversal, respectively. It can be seen that, when changing over to the third portion of the curve, the signal noticeably changes in shape. Specifically, in the field range $H_s > H_{cr2}$, the principal change of the induction flux shifts to the onset of the process under discussion.

We have not yet been successful in revealing the magnetoelastic mode responsible for the magnetization behavior in fields $H_s > H_{cr2}$. Most probably, these vibrations are associated with longitudinal acoustic waves, for which the lag of the elastic subsystem of the crystal behind the magnetic subsystem should manifest itself at higher rates of magnetization reversal. The aforementioned waves can propagate not only along the *C* axis. In contrast to the mode studied earlier, whose fundamental harmonic frequency F_c is determined by the thickness of the single crystal, the magnetoelastic vibrations assumed in this work most likely exhibit a broader spectrum of frequencies. It is quite possible that the change in this spectrum is responsible for the variations in the signal shape and, on the whole, for the magnetization behavior in fields $H_s > H_{cr2}$.

REFERENCES

1. O. S. Kolotov, V. A. Pogozhev, G. V. Smirnov, and Yu. V. Shvyd'ko, Vopr. At. Nauki Tekh., Ser.: Obshch. Yad. Fiz., No. 29, 136 (1984).
2. O. S. Kolotov, V. A. Pogozhev, G. V. Smirnov, and Yu. V. Shvyd'ko, Fiz. Tverd. Tela (Leningrad) **29** (8), 2548 (1987) [Sov. Phys. Solid State **29**, 1471 (1987)].
3. O. S. Kolotov, Kim En Hen, A. P. Krasnozhon, and V. A. Pogozhev, Pis'ma Zh. Éksp. Teor. Fiz. **58** (1), 52 (1993) [JETP Lett. **58**, 53 (1993)].
4. O. S. Kolotov, Kim En Hen, A. P. Krasnozhon, and V. A. Pogozhev, Fiz. Tverd. Tela (St. Petersburg) **36** (1), 231 (1994) [Phys. Solid State **36**, 127 (1994)].
5. O. S. Kolotov, A. P. Krasnozhon, and V. A. Pogozhev, Fiz. Tverd. Tela (St. Petersburg) **40** (2), 305 (1998) [Phys. Solid State **40**, 277 (1998)].
6. A. V. Bukvin, O. S. Kolotov, and V. A. Pogozhev, Fiz. Tverd. Tela (St. Petersburg) **42** (8), 1437 (2000) [Phys. Solid State **42**, 1478 (2000)].
7. E. A. Turov and V. G. Shavrov, Usp. Fiz. Nauk **140** (3), 429 (1983) [Sov. Phys. Usp. **26**, 593 (1983)].
8. B. Diehl, W. Jantz, and B. I. Wettling, Curr. Top. Mater. Sci. **11** (1), 241 (1984).
9. M. N. Seavey, Solid State Commun. **10** (2), 219 (1973).
10. O. S. Kolotov, V. A. Pogozhev, and R. V. Telesnin, *Methods and Apparatus for Investigations into Impulse Properties of Thin Magnetic Films* (Mosk. Gos. Univ., Moscow, 1970).

Translated by N. Korovin

Physics of the Solid State, Vol. 45, No. 4, 2003, pp. 675–680. Translated from Fizika Tverdogo Tela, Vol. 45, No. 4, 2003, pp. 643–648.

MAGNETISM AND FERROELECTRICITY

The Influence of Interparticle Interaction on Magnetization Curves of Nano- and Microcrystal Ensembles

L. P. Ol'khovik*, M. M. Khvorov, N. M. Borisova*, Z. V. Golubenko*, Z. I. Sizova*, and E. V. Shurinova***

** Kharkov National University, pl. Svobody 4, Kharkov, 61077 Ukraine*

*** Institute of Chemical Thermophysics, National Academy of Sciences of Ukraine, Kiev, Ukraine*

Received July 2, 2003

Abstract—Reconstruction of magnetization curves for real close-packed systems of highly anisotropic ferrimagnetic $BaFe_{12}O_{19}$ single-domain nano- and microcrystals is carried out on the basis of the results of a study of interparticle magnetic interaction. These curves allowed us to distinguish general laws of magnetization of ensembles of randomly oriented single-domain particles predicted by the Stoner–Wohlfarth theory and to discuss special features found for microcrystals. *© 2003 MAIK "Nauka/Interperiodica".*

1. INTRODUCTION

Interparticle magnetic interaction, along with size and surface factors, plays an important role in the formation of magnetic properties of ensembles particles of small. The necessity of considering this problem appeared, in particular, when studying the magnetization processes in powder materials used for the production of media for high-density magnetic recording on the basis of substituted barium hexaferrite [1–5].

Interparticle magnetic interaction can be both positive and negative. Negative interaction stabilizes the demagnetized state of a sample and opposes the magnetization increase under the influence of an applied magnetic field. Positive interaction promotes the magnetization of a sample. Predominance of either positive or negative interaction between particles in a system depends on many factors, such as the packing density, texture, magnetic parameters (in particular, magnetic anisotropy), and external factors (magnetic field, temperature).

2. SAMPLE CHARACTERIZATION

In this work, magnetization processes in close-packed ensembles of single-domain nano- and micrometer-sized particles are considered in terms of interparticle interaction.

The object under investigation was a highly anisotropic ferromagnetic hexagonal barium ferrite with an unsubstituted magnetic matrix ($BaFe_{12}O_{19}$) with the following magnetic parameters at 300 K: uniaxial magnetocrystalline anisotropy constant $K_1 = 3.3 \times 10^6$ erg cm^{-3}, specific saturation magnetization σ_s = 68 G cm^3 g^{-1}, anisotropy field H_a = 17.8 kOe, and Curie temperature T_C = 733 K [6].

Nanocrystalline powders were produced with the use of cryochemical techniques, which provided high chemical homogeneity of the initial mixture and, consequently, a relatively low temperature of the reaction of ferrite formation [7, 8]. Both traditional [9] and modified [10] methods of precipitation from melt were used to produce microcrystalline powders. Mössbauer spectroscopy and x-ray diffraction investigations confirmed that the powders obtained were single-phase. The average diameter of particles in nanodispersed sample 1 is $\langle d \rangle$ = 55 nm; the average aspect ratio was $\langle d/h \rangle$ = 2.5 (h is the thickness of lamellar particles). Microdispersed samples have the following morphological characteristics: $\langle d \rangle$ = 0.5 μm and $\langle d \rangle/\langle h \rangle$ = 5 for sample 2 and $\langle d \rangle$ = 1.5 μm and $\langle d \rangle/\langle h \rangle$ = 4 for sample 3. The range of particle diameters in samples 1 and 2 completely cover the region of single-domain state existence (for barium hexaferrite, d_{cr} = 1.3 μm [11]). Sample 3 also contains multidomain particles.

Magnetization measurements were carried out on preliminarily thermally demagnetized powder samples (the packing factor was $p \sim 0.4$) in a field of up to 18 kOe at 300 K. At this temperature, as shown in [12], magnetization processes are not influenced by transitions of particles with close-to-critical volume to a superparamagnetic state.

3. INTERPARTICLE MAGNETIC INTERACTION

In order to investigate the interparticle interaction, we measured two main residual-magnetization curves: $m_r(H) = \sigma_r(H)/\sigma_r(\infty)$ and $m_d(H) = \sigma_d(H)/\sigma_d(\infty)$. The isothermal residual magnetization σ_r was determined by measuring minor and saturation hysteresis loops with a gradual increase in the amplitude of the measurement field; $\sigma_r(\infty)$ was obtained by extrapolating the σ_r =

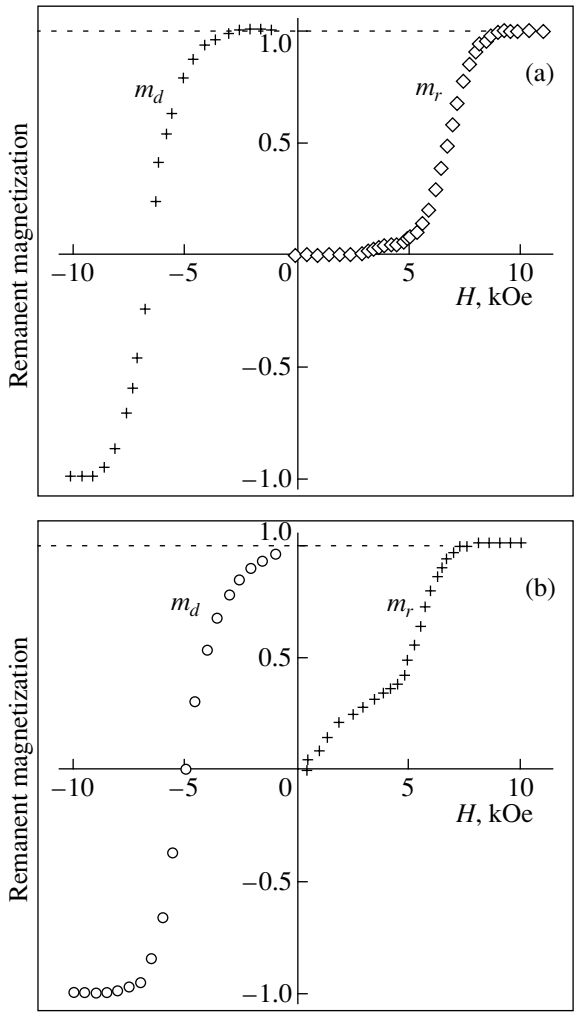

Fig. 1. Field dependences of residual magnetizations m_r and m_d: (a) nanodisperse sample 1 and (b) microdisperse sample 2.

$f(1/H)$ dependence to an infinitely large field. The residual magnetization σ_d was found by magnetizing a sample to saturation, then decreasing the field down to zero and reversing the field sign (direction), and then increasing the field up to a specified value and switching it off; like $\sigma_r(\infty)$, $\sigma_d(\infty)$ is a value extrapolated to an infinitely large field.

Experimental field dependences of m_r and m_d for the samples under investigation are presented in Fig. 1.

According to [13], the $m_r(H)$ and $m_d(H)$ dependences for a system of noninteracting single-domain uniaxial magnetic particles with random uniform distribution of their orientations are related through the ratio

$$m_d(H) = m_r(\infty) - 2m_r(H) = 1 - 2m_r(H). \quad (1)$$

In a theoretical model of noninteracting particles, the $m_d = f(m_r)$ dependence, known as the Henkel diagram [14], is linear, with m_d changing from 1 for $m_r = 0$ to –1 for $m_r = 1$ (curve *3* in Fig. 2). For a system of real particles, any deviation from linearity in the diagram indicates the presence of interaction between particles if the other parameters of the system correspond to the theoretical model. Concavity and convexity of the curve are indicative of negative and positive interactions, respectively. It was found that Henkel diagrams for powder samples 1 and 2, through differing in dispersity, have different shapes (Fig. 2). As follows from the curves, the resulting interaction is negative in the nanodispersed sample and is sign-variable in the microdispersed sample.

In order to analyze the magnetization curves and reveal the mechanisms determining their characteristics, we used a more informative modified method of

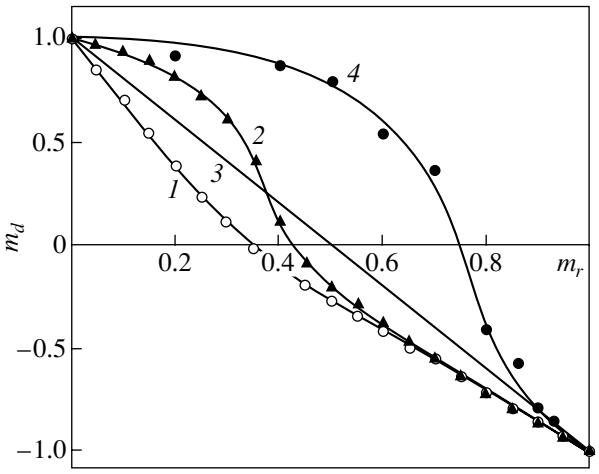

Fig. 2. Henkel diagram: (*1*) nanodisperse sample 1, (*2*) microdisperse sample 2, (*3*) theory [13], and (*4*) oriented magnetic film of substituted barium ferrite [1].

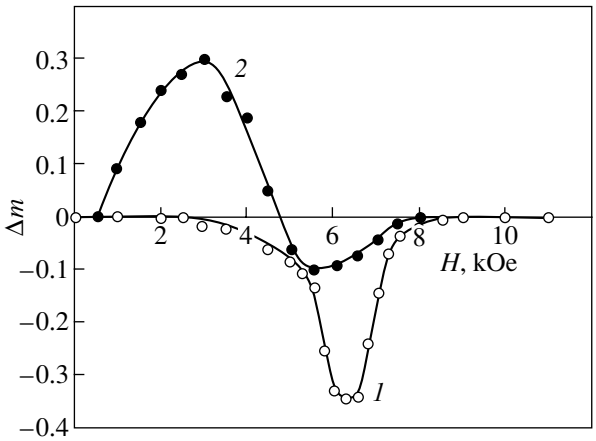

Fig. 3. Modified Henkel diagram (Kelly diagram): (*1*) nanodisperse sample 1 and (*2*) microdisperse sample 2.

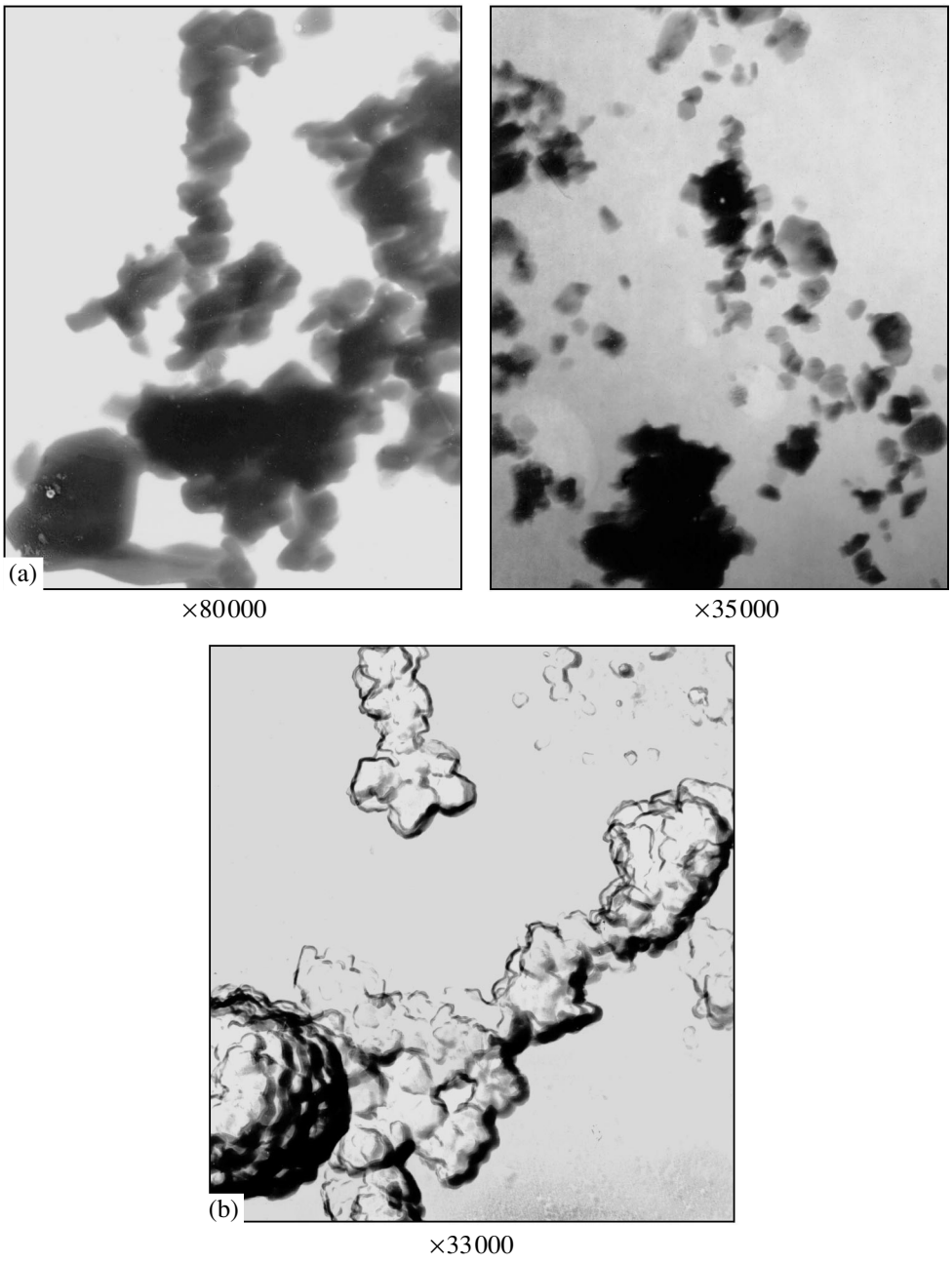

Fig. 4. Illustration of typical particle clusters in (a, b) nanocrystalline and (c, d, e) microcrystalline barium hexaferrite powders.

Kelly *et al*. [15]. The authors of [15] introduced the parameter

$$\Delta m(H) = m_d(H) - (1 - 2m_r(H)), \qquad (2)$$

which characterizes the deviation of an experimental m_d value from that calculated theoretically for an ensemble of noninteracting particles. This parameter determines the interaction sign and magnitude, depending on the applied field.

The $\Delta m(H)$ dependences in Fig. 3 show that the interaction between particles in the nanocrystalline powder sample is manifested over the field interval from 3.5 to 8 kOe. A study of the hysteresis loops revealed that this interval corresponds to magnetization irreversible processes [16]. The interaction is the strongest ($\Delta m = -0.34$) in a field of 6.5 kOe. The irreversibility range for the microcrystalline powder sample is much wider, from 0.5 to 8 kOe. However, negative interaction becomes noticeable only in fields from

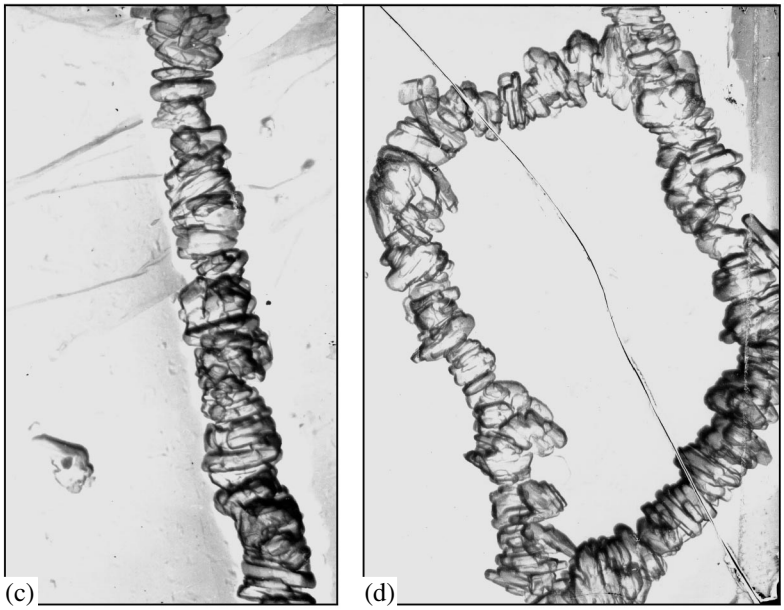

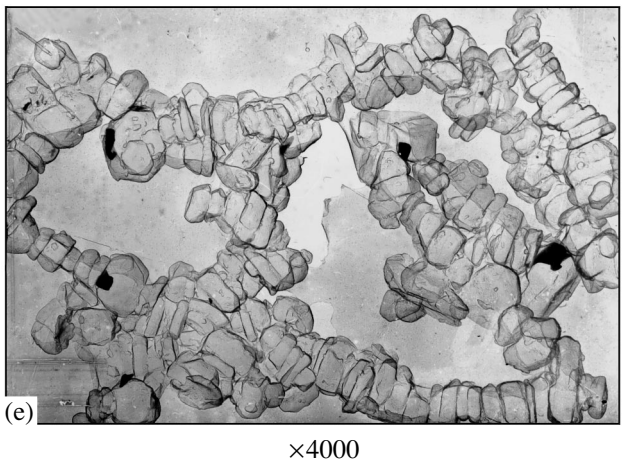

Fig. 4. (Contd.)

4.7 to 8 kOe and reaches its maximum magnitude ($\Delta m = -0.1$) in a field of 5.5 kOe. For fields from 0.5 to 4.7 kOe, the resulting interaction in the system of microparticles is positive, with the maximum $\Delta m = 0.3$ occurring at $H = 3$ kOe. Sufficiently large positive interaction in a disordered ensemble of particles seems, at first sight, to be unexpected, because the interaction of such a sign suggests the presence of texture. For example, as shown in [1], distinct positive interaction takes place in an oriented magnetic film on the base of substituted barium ferrite over the whole range of fields covered (curve *4* in Fig. 2).

Electron microscopy data were used to explain the different interparticle interactions observed in the samples under investigation.

4. ELECTRON MICROSCOPY

Electron-microscopical images of samples 1 and 2 particles obtained by means of an UMV-100L electron microscope from replicas prepared using different methods are presented in Fig. 4.

It turned out that a difference in particle aggregation exists even in nano- and microcrystalline powders that are not pressed. Stack clusters of particles are observed in micropowders (Fig. 4c). Such a structure is due to both morphological peculiarities in the particles (lamellar form) and strong uniaxial magnetocrystalline anisotropy (the easy direction coincides with crystal hexagonal axis **c**). Similar stacks are present in nanocrystalline powders to a significantly smaller extent (Fig. 4c), which can be explained by the fact that, though the morphology of nano- and microparticles is

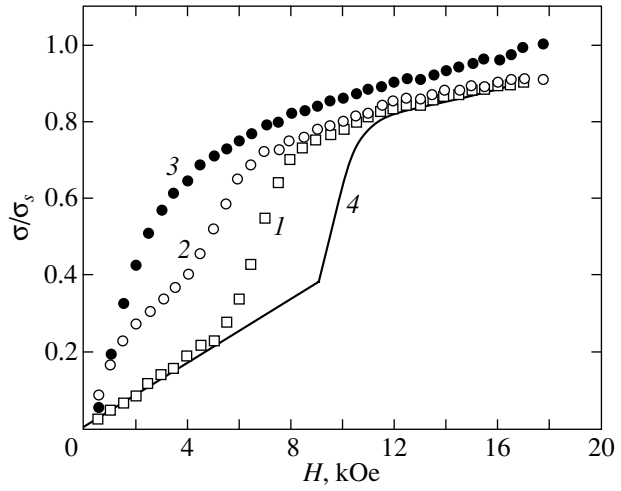

Fig. 5. Main magnetization curves of powder samples at 300 K compared to a theoretic Stoner–Wohlfarth curve: (*1*) sample 1, (*2*) sample 2, (*3*) sample 3, and (*4*) theory [20].

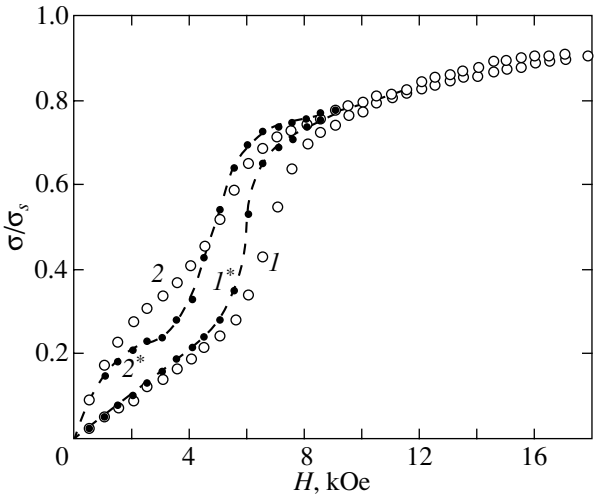

Fig. 6. Magnetization curves of close-packed ensembles of nano- and microparticles in the absence of interparticle interaction: (*1, 2*) initial curves (samples 1, 2) and (*1*, 2**) reconstructed curves.

the same, the role of magnetocrystalline anisotropy in nanoparticles is less important due to the considerable influence of surface anisotropy. As shown in [17, 18], the surface-anisotropy energy in nanocrystals, unlike that in microcrystals, becomes commensurate with the magnetocrystalline-anisotropy energy. Since these anisotropy constants are opposite in sign, their competition leads to the fact that a canted magnetic structure caused by a distorted geometry of exchange bonds is present throughout practically the entire volume of the nanocrystal [19]. The average angle of magnetic-moment deviation from hexagonal axis *c* can vary from particle to particle due to the spread in particle thickness. As can be seen from Fig. 4, the systems under investigation reveal a tendency to form closed structures (ring-shaped clusters of microcrystals and quasi-spherical clusters of nanocrystals), which is connected with demagnetization energy minimization. The possibility of having different particle arrangements and the fact that stack clusters of particles promote magnetization while ringlike agglomerates and quasi-spherical clusters prevent it were taken into account in making a comparative analysis of the magnetization curves in systems with different dispersivity.

5. MAGNETIZATION CURVES

Magnetization curves for real systems of single-domain particles of nano- and micrometric ranges (samples 1, 2) are presented in Fig. 5. For their analysis, we used an experimental curve for powder sample 3 containing multidomain particles and a numerically calculated Stoner–Wohlfarth theoretical curve [20] for a system of identical single-domain magnetic uniaxial noninteracting disordered particles under the assumption of coherent magnetization-vector rotation. To make the comparison convenient, the anisotropy field in the model system was taken to be equal to that for barium ferrite and magnetization was expressed in relative units. It can be seen from Fig. 5 that experimental curve *1* for nanodisperse sample 1 is similar in character to theoretical dependence (curve *4*). Curve *2* for microdispersed sample 2 has an unusual saddlelike character that is not described in the literature dealing with such objects, and lies between the curves for the nanodispersed sample and sample 3, which contains multidomain particles.

The magnetization curves obtained for single-domain particles were transformed with allowance for the specific interparticle interaction. The field dependences of magnetization were recalculated according to the formula $\sigma^*(H) = \sigma(H)[1 \pm \Delta m(H)]$, where σ is the experimental value of the specific magnetization and Δm is the correction for interaction [Eq. (2), Fig. 3]. The minus sign corresponds to the case of $\Delta m > 0$, and the plus sign, to the case of $\Delta m < 0$. Figure 6 shows the initial (*1, 2*) and reconstructed (*1*, 2**) magnetization curves. It is evident that the curve for the nanodispersed sample did not change in character. For the microdispersed sample, the reconstructed curve exhibits the distinct magnetization jump (which was veiled by interparticle interaction) predicted by Stoner–Wohlfarth theory to occur as a consequence of random orientation of easy axes of particles in the system. As mentioned above, the region of magnetization jump for both nano- and microdispersed samples corresponds to irreversible magnetization processes connected with the behavior of the ensemble of randomly oriented particles as a whole. In the initial range $H = 0.5$–3.5 kOe, corresponding to irreversible magnetization processes, curve *2** is basically different in character from that predicted by the theoretical model. The anomaly observed only in

the microcrystalline system is obviously connected with irreversible magnetization processes in individual particles. The magnetic structure of a microcrystal is more heterogeneous than that of a nanocrystal: the core of a particle has a magnetic structure analogous to that of a macrocrystal, while a near-surface region which makes up approximately 10% of the particle volume [18] has a characteristic canted magnetic structure. Therefore, the condition of coherent magnetization rotation assumed in the theoretical model is not satisfied in this case.

6. CONCLUSIONS

Thus, the main results of this work are the following.

It has been found that the sign, magnitude, and the field dependence of interparticle interaction in a close-packed system of highly anisotropic hexagonal-ferrite $BaFe_{12}O_{19}$ single-domain particles are affected by dispersivity: the resulting interaction between nanocrystals in the field interval covered is negative, while that between microcrystals is sign-variable. The different balance of interparticle interactions in the samples under investigation has been interpreted on the basis of electron-microscopy data.

This is the first time that the reconstruction of magnetization curves has been carried out taking into account interparticle interaction to reveal that the complex character of a microcrystal system magnetization curve has the features of magnetic behavior of a magnetic uniaxial Stoner–Wohlfarth particle ensemble with randomly oriented easy modernization axes. A magnetization curve anomaly that was observed in the low-field range is characteristic only of a microcrystalline system and is connected with irreversible magnetization of individual particles having spatially heterogeneous magnetic structure.

REFERENCES

1. P. R. Bissel and A. Lyberatos, J. Magn. Magn. Mater. **95**, 27 (1991).
2. G. W. Spratt, N. Kodama, H. Inoue, *et al.*, IEEE Trans. Magn. **27** (6), 4660 (1991).
3. P. Görnert, E. Sinn, H. Pfeiffer, *et al.*, J. Magn. Soc. Jpn. **15**, S2 (1991).
4. X. Batllee, M. Garcia del Muro, J. Tejada, *et al.*, IEEE Trans. Magn. **30** (2), 708 (1994).
5. M. El-Hilo, H. Pfeiffer, K. O'Grady, *et al.*, J. Magn. Magn. Mater. **129**, 339 (1994).
6. J. Smit and H. P. J. Wijn, *Ferrites* (Wiley, New York, 1959; Inostrannaya Literatura, Moscow, 1962).
7. T. G. Kuz'micheva, L. P. Ol'khovik, and V. P. Shabatin, Ukr. Patent No. 1,724,584, C 01 G 49/00/.
8. L. P. Ol'khovik, N. M. Borisova, T. G. Kuz'micheva, and V. P. Shabatin, J. Funct. Mater. **3** (1), 84 (1996).
9. L. P. Ol'khovik, Z. V. Golubenko, and V. M. Vintonyak, Ukr. Inventor's Certificate No. 1,832,603, B 22 F 9/16, H 01 F 1/11/.
10. I. I. Borisov, N. M. Borisova, L. P. Ol'khovik, M. M. Rudenko, and S. S. Tserevitinov, Ukr. Patent No. 2,022,716, D 22 F 9/16, H 01 F 1/11/.
11. K. Goto, M. Ito, and T. Sacurai, Jpn. J. Appl. Phys. **19** (7), 1339 (1980).
12. L. P. Ol'khovik, Z. I. Sizova, Z. V. Golubenko, and T. G. Kuz'micheva, J. Magn. Magn. Mater. **183**, 181 (1998).
13. E. P. Wohlfarth, J. Appl. Phys. **29**, 595 (1958).
14. O. Henkel, Phys. Status Solidi **7**, 919 (1964).
15. P. E. Kelly, K. O'Grady, P. I. Mayo, and R. W. Chantrell, IEEE Trans. Magn. **25**, 3881 (1989).
16. Z. V. Golubenko, T. G. Kuz'micheva, L. P. Ol'khovik, and Z. I. Sizova, Visn. Khar'k. Univ., Ser. Fiz. **5**, 77 (2001).
17. Z. V. Golubenko, A. S. Kamzin, L. P. Ol'khovik, *et al.*, Fiz. Tverd. Tela (St. Petersburg) **40** (10), 1894 (1998) [Phys. Solid State **40**, 1718 (1998)].
18. A. S. Kamzin, L. P. Ol'khovik, and Z. I. Sizova, Visn. Khar'k. Univ., Ser. Fiz. **3**, 115 (1999).
19. A. Kamzin, B. Stahl, R. Gellert, *et al.*, Fiz. Tverd. Tela (St. Petersburg) **42** (5), 873 (2000) [Phys. Solid State **42**, 897 (2000)].
20. E. C. Stoner and E. P. Wohlfarth, IEEE Trans. Magn. **27** (4), 3469 (1991).

Translated by A. Titov

Physics of the Solid State, Vol. 45, No. 4, 2003, pp. 681–684. Translated from Fizika Tverdogo Tela, Vol. 45, No. 4, 2003, pp. 649–652.

MAGNETISM AND FERROELECTRICITY

Structure and Magnetoresistance of $La_{0.67}Ca_{0.33}MnO_3$ Films Grown Coherently on (001)$NdGaO_3$

Yu. A. Boĭkov*, V. A. Danilov*, and A. Yu. Boĭkov**

**Ioffe Physicotechnical Institute, Russian Academy of Sciences, Politekhnicheskaya ul. 26, St. Petersburg, 194021 Russia*
e-mail: yu.boikov@mail.ioffe.ru
***Institute of Physics (Petrodvorets Branch), St. Petersburg State University,*
ul. Pervogo Maya 100, Petrodvorets, 198904 Russia

Received July 2, 2002

Abstract—40- to 120-nm-thick (001)$La_{0.67}Ca_{0.33}MnO_3$ films grown through laser evaporation on (001)$NdGaO_3$ were studied. The lattice parameters of the $La_{0.67}Ca_{0.33}MnO_3$ films measured in the substrate plane ($a_\parallel$ = 3.851 Å) and along the normal to its surface ($a_\perp$ = 3.850 Å) practically coincided with that of the pseudocubic neodymium gallate. The unit-cell volume of the $La_{0.67}Ca_{0.33}MnO_3$ film was slightly smaller than that of stoichiometric bulk samples. The position of the maximum in the temperature dependence of electrical resistivity did not depend on the thickness of the $La_{0.67}Ca_{0.33}MnO_3$ film. The negative magnetoresistance (MR ≈ –0.25, H = 0.4 T) of $La_{0.67}Ca_{0.33}MnO_3$ films reached a maximum at 239–244 K. © *2003 MAIK "Nauka/Interperiodica".*

1. INTRODUCTION

The anomalously strong magnetic-field and temperature dependence of the resistance R of the perovskite-like manganites $(La,Nd)_{1-x}Q_xMnO_3$ (Q = Ca, Sr, Ba, …), which becomes manifest as the spins in the manganese ion 3d shell undergo ferromagnetic ordering, accounts for the interest in their application in magnetic-disk-read heads and IR detectors [1, 2].

For $(La,Nd)_{1-x}Q_xMnO_3$ films to be of practical interest, they have to be thin enough for the ferromagnetic phase transition point T_c to be close to room temperature and for the magnetoresistance MR to be large enough in low magnetic fields. By now, it has been established [1] that both R and MR of $(La,Nd)_{1-x}Q_xMnO_3$ films depend strongly on their structure, the value of x in the chemical formula, and oxygen concentration. Biaxial mechanical stresses can bring about both a substantial growth and a decrease in T_c of manganite films [3, 4].

Using substrates with minimum lattice mismatch m [$m = (a_L - a_S)/a_S$, where a_S and a_L are the substrate and film lattice parameters, respectively] favors the obtainment of manganite films with reproducible values of MR without having to apply high-temperature annealing. The dependence of the electronic parameters of manganite films grown on substrates with a small m on thickness may permit estimation of the characteristic carrier localization length. Up to now, however, the literature has contained only fragmentary and quite frequently inconsistent experimental information on the structure and parameters of $(La,Nd)_{1-x}Q_xMnO_3$ films grown on substrates with a small m [5, 6].

The present communication reports on a study of the structure and electrophysical properties of $La_{0.67}Ca_{0.33}MnO_3$ (LCMO) films grown on substrates of neodymium gallate, whose pseudocubic unit-cell parameter practically coincides with that of the above manganite.

2. EXPERIMENT

The starting ceramic LCMO targets were evaporated in an oxygen environment (P_0 = 0.3 mbar) using the laser technique (KrF, λ = 248 nm, τ = 30 ns). The laser radiation density at the target surface was 2 J/cm^2. The substrates were (001)$NdGaO_3$ (NGO) single-crystal plates whose temperature was maintained equal to T_S = 760 K during the manganite film formation. The LCMO layer thickness on the substrate increased by 0.2 Å per pulse. The technology of LCMO film growth is described in detail in [5, 7].

Data on the phase composition of the LCMO films prepared, their orientation, and the film lattice parameters in the substrate plane and along its surface normal were obtained using x-ray diffraction techniques (Philips X'pert MRD, ω/2θ and φ scans, rocking curves). The free-surface morphology of the LCMO films was studied with an atomic-force microscopy (Nonoscope-IIIa, tapping mode).

The resistance R of the films was measured with an alternating current (f = 100 Hz) using an hp 4263A LCR meter in the van der Pauw geometry, both in a magnetic field H = 0.4 T and without it. Four silver contacts were deposited on an LCMO film in the corners of

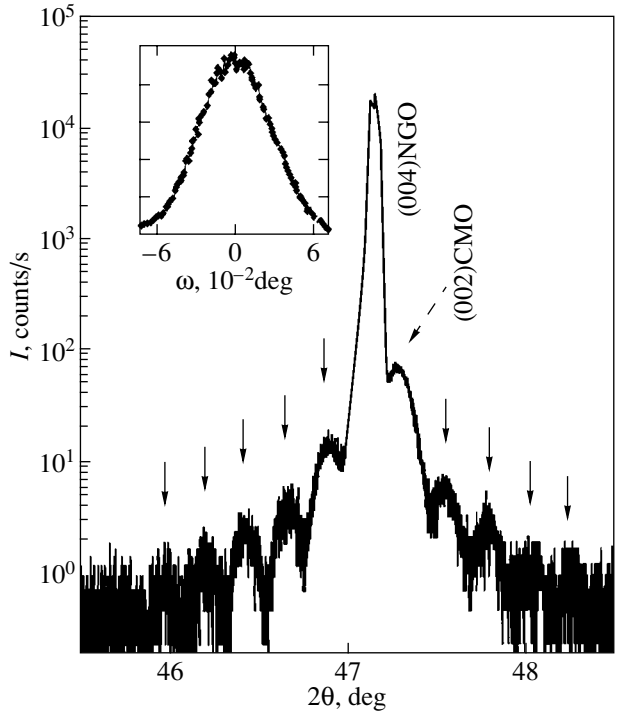

Fig. 1. X-ray diffraction pattern (Cu$K_{\alpha 1}$, ω/2θ) for a (40-nm) LCMO film grown on (001)NGO. Arrows identify the satellite peaks. Inset shows an ω–2θ rocking curve for the (101)LCMO reflection obtained on the same film.

a square by thermal evaporation from a tungsten boat. The electrical resistivity ρ of an LCMO film was calculated using the relation $\rho = (\pi d/\ln 2)R$ [8], where d = 40–120 nm is the LCMO film thickness.

3. EXPERIMENTAL RESULTS AND DISCUSSION

The mechanical stresses in a film depend on its thickness, growth conditions, and heat treatment, as well as on the parameters of the substrate material. Stress relaxation in LCMO films deposited on substrates with a large m can entail a strong change in the structure and electrophysical parameters of the films [9, 10].

In contrast to the available data on manganite films grown on substrates with a large lattice mismatch (m > 1%) [4], we did not find a systematic dependence of MR on the LCMO/NGO film thickness within an interval d = 40–120 nm.

When using single-crystal (001)NGO plates (the neodymium gallate orthorhombic unit-cell parameters are a = 5.502 Å, b = 5.426 Å, c = 7.706 Å; the parameter of the corresponding NGO pseudocubic cell is 3.851 Å [11]) as substrates for LCMO film growth, m is about 0.2%, which is several times smaller than that for the widely used strontium titanate and lanthanum aluminate single crystals. The temperature coefficients of linear expansion of NGO and LCMO have similar values in the interval from room temperature to T_S [12, 13].

3.1. Structure and Morphology of the LCMO Film Surface

The small difference between the lattice parameters provides favorable conditions for epitaxial growth of manganite films on the (001)NGO surface. The LCMO film cell parameter along the substrate normal $a_\perp$ = 3.850 ± 0.003 Å was calculated using the value of 2θ for the (004)LCMO reflection in measured x-ray diffractograms. Figure 1 shows a fragment of an x-ray diffraction pattern (ω/2θ, Cu$K_{\alpha 1}$) obtained in the case where the plane including the incident and reflected x-ray beams was oriented normal to the substrate plane. The widths of the satellite peaks, which are clearly pronounced near the (002) x-ray reflection from a manganite film, were used to monitor the thickness of the grown LCMO films. The effective lattice parameter in the substrate plane $a_\parallel$ = 3.851 ± 0.003 Å for the LCMO films was calculated from the relation $1/d_{(303)} = [(3/a_\perp)^2 + (3/a_\parallel)^2]^{1/2}$. The interplanar distance $d_{(303)}$ was derived from the value of 2θ for the (303) reflection in the x-ray diffraction pattern, which was measured with the substrate plane oriented at 45° to the plane including the incident and reflected x-ray beams. The parameter $a_\parallel$ did not depend on LCMO film thickness and coincided with the NGO pseudocubic lattice parameter. The effective lattice parameter $a_{\text{eff}} = (a_\parallel^2 a_\perp)^{1/3}$ = 3.851 Å for the grown films differs only slightly from the corresponding values (~3.858 Å [14]) obtained for stoichiometric bulk LCMO samples. The x-ray ϕ scan made on the (111)LCMO reflection had four equidistant peaks (spaced 90° apart). The exact coincidence of $a_\parallel$ with the neodymium gallate lattice parameter indicates that the manganite films with thicknesses of up to 120 nm were grown coherently on (001)NGO. In the case of (001)NGO substrates, coherent growth of relatively thick LCMO films is favored by the small elastic-stress energy, which is proportional to the product m^2d. When grown on substrates for which m > 1% ($LaAlO_3$), elastic-stress relaxation in an LCMO film starts already from thicknesses as small as 10–30 nm [4, 14].

The small difference between the $a_\parallel$ and $a_\perp$ parameters indicates that an LCMO film grown on an (001)NGO substrate is subjected to weak in-plane tensile mechanical stresses. The full width of the rocking curve measured at its half maximum (FWHM) for the (101) reflection from a manganite film 40 nm thick was 0.08°, which is approximately one third of the corresponding values obtained for epitaxial LCMO films grown on $LaAlO_3$ and $SrTiO_3$ [15]. As the LCMO/NGO film thickness increases in the interval 40–120 nm, the width of the rocking curve for the above x-ray reflection decreased by about 20–30%. The decrease in FWHM with increasing LCMO film thickness is appar-

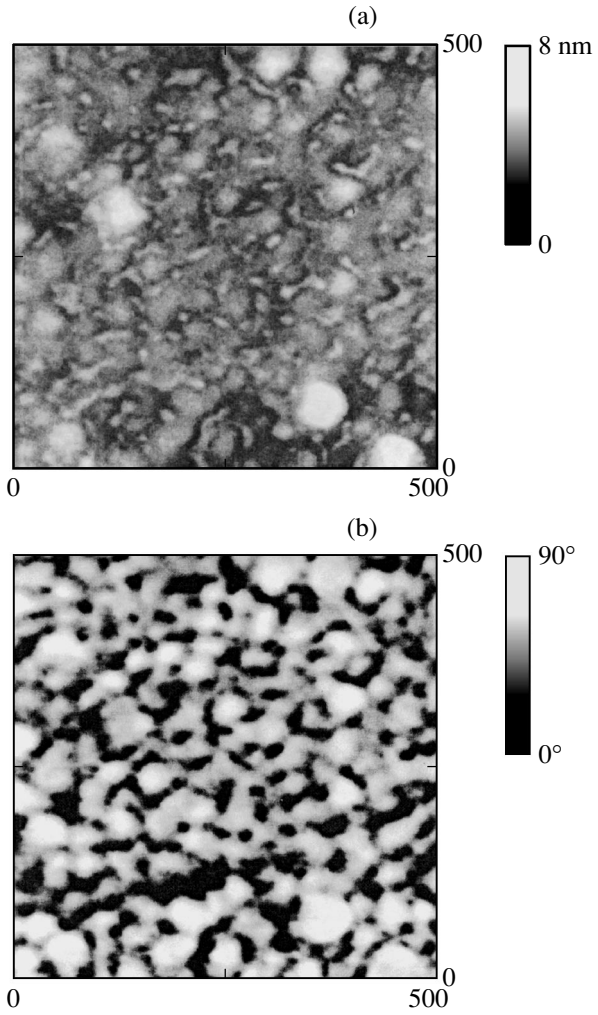

Fig. 2. Atomic-force microscope image of a free (40-nm) LCMO/NGO film surface obtained in (a) the height and (b) phase modes.

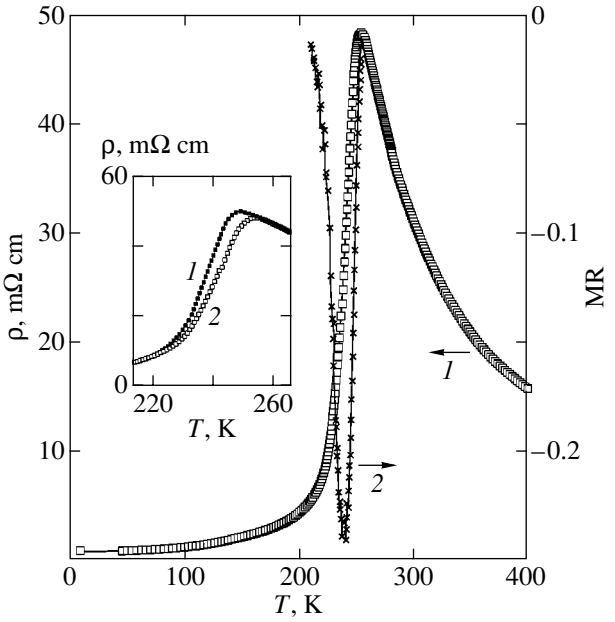

Fig. 3. Temperature dependences of (*1*) the electrical resistivity ρ and (*2*) magnetoresistance MR obtained for a (40-nm) LCMO/NGO film. Inset shows ρ(*T*) dependences measured on the same film at (*1*) $H = 0$ and (*2*) $H = 0.4$ T in the temperature interval near T_c. $f = 100$ Hz.

ently due to a decrease in the concentration of the film structural defects associated with mutual diffusion of the components between the LCMO and the substrate at temperatures close to T_S.

Free-surface images of a 40-nm-thick LCMO film obtained with an atomic-force microscope in the "height" and "phase" modes are presented in Fig. 2. The height-mode data indicate that the LCMO films consisted of grains whose size in the substrate plane was 20–30 nm (Fig. 2a). The grain boundaries are decorated by characteristic depressions. The manganite film also contains individual grains 60–90 nm in size. The density of such grains is of the order of 2×10^9 cm^{-2}. Figure 2b shows the signal phase variation occurring as the probe scans the LCMO film surface. The phase of a signal depends on the nanomechanical properties of the surface layer of the object under study. The similar signal phases obtained when scanning the surfaces of large and small grains (Fig. 2b) indicate the absence of significant compositional differences between them. The fine structure inside large grains could not be resolved.

The formation of grain boundaries in an LCMO film grown coherently on an NGO substrate can be due to a stoichiometry violation in the phase adsorbed on the substrate surface. The phase with distorted stoichiometry segregates at the boundaries of the growing stable LCMO islands, thus entailing the formation of thin interlayers near grain boundaries, whose composition differs from that in the grain bulk. The density of such boundaries can be reduced by recrystallizing the grown layer [5].

3.2. Electrophysical Parameters of LCMO Films

The temperature dependence of electrical resistivity of LCMO films measured at $H = 0$ exhibited a strong maximum at $T_R \approx 253$ K (Fig. 3), which is in good agreement with the corresponding data obtained on bulk stoichiometric LCMO samples and epitaxial LCMO films subjected to thermal treatment [16]. The rise in electrical resistivity of grown manganite films observed to occur with decreasing temperature in the interval 400 K $-T_R$ is caused, at least partially, by carrier localization resulting from Jahn–Teller distortion of the LCMO unit cell [1]. The LCMO lattice distortion increases with the temperature decreasing to T_c [17]. In the region 400–260 K the dependence of ρ on temperature for LCMO films could be well approximated by the relation $\rho(T) \sim \exp(-E_A/kT)$, where $E_A \approx 70$ meV is the

activation energy. The onset of ferromagnetic spin ordering in LCMO ($T \approx T_c$) is accompanied by a sharp increase in lattice symmetry [17]. The drop in the electrical resistivity of LCMO films with decreasing temperature ($T < T_R$) is favored both by the decrease in the relative spin disorder in the manganese 3*d* shell and by the decrease in lattice distortion.

A magnetic field, as well as a decrease in temperature, favors ferromagnetic ordering of the electron spins of the manganese ions. At $H = 0.4$ T, the electrical resistivity of a manganite film passed through a maximum at a temperature 3°–4° higher than that at $H = 0$ (see inset to Fig. 3). The negative magnetoresistance MR = $[\rho(H = 0.4\ \text{T}) - \rho(H = 0)]/\rho(H = 0)$ of grown LCMO/NGO films depended only weakly on their thickness (d = 40–120 nm) and reached a maximum value (≈–0.25) at temperatures T_{MR} = 239–244 K (Fig. 3). The absence of a low-temperature tail in the MR(T) dependence implies that grain boundaries do not affect charge transport noticeably in the grown LCMO/NGO films. In contrast to the extremely low magnetoresistance reported in [6] for manganite films grown on neodymium gallate substrates, the measured values of MR for the LCMO layers prepared in this study corroborate well with the data reported for LCMO/LAO and LCMO/LSATO in [13].

The highest values of the temperature coefficient of resistivity (β = 0.12–0.14 K^{-1}) for LCMO films were observed at temperatures close to T_{MR}. The maximum values of β measured on the LCMO/NGO films grown in this study are 20–30% less than the record-low values of the temperature coefficient of resistivity obtained for LCMO films annealed in an oxygen environment at a high temperature [2, 5].

4. CONCLUSIONS

Our results suggest that LCMO films 40–120 nm thick can be grown coherently on neodymium gallate substrates, with thicker manganite layers exhibiting a more perfect structure. LCMO/NGO films consist of grains with an average size of 30 nm. The maximum values of MR ≈ –0.25 obtained at $H = 0.4$ T on LCMO/NGO films with thicknesses ranging from 40 to 120 nm were measured at temperatures from 239 to 244 K.

ACKNOWLEDGMENTS

The study was partially supported by the Ministry of Science and Technology of the Russian Federation, project no. 4B19.

REFERENCES

1. Y. Tokura, in *Colossal Magnetoresistive Oxides*, Ed. by Y. Tokura (Gordon and Breach, Amsterdam, 2000), p. 2.
2. A. Goyal, M. Rajeswari, R. Shreekala, *et al.*, Appl. Phys. Lett. **71** (17), 2535 (1997).
3. E. S. Vlakhov, R. A. Chakalov, R. I. Chakalova, *et al.*, J. Appl. Phys. **83** (4), 2152 (1998).
4. R. A. Rao, D. Lavric, T. K. Nath, *et al.*, Appl. Phys. Lett. **73** (22), 3294 (1998).
5. Yu. A. Boĭkov, T. Klaeson, and A. Yu. Boĭkov, Zh. Tekh. Fiz. **71** (10), 54 (2001) [Tech. Phys. **46**, 1260 (2001)].
6. H. S. Wang, Q. Li, K. Liu, and C. L. Chien, Appl. Phys. Lett. **74** (15), 2212 (1999).
7. Yu. A. Boĭkov, D. Érts, and T. Klaeson, Fiz. Tverd. Tela (St. Petersburg) **42** (11), 2042 (2000) [Phys. Solid State **42**, 2103 (2000)].
8. T. I. Kamins, J. Appl. Phys. **42** (11), 4357 (1971).
9. B. Wiedenhorst, C. Hofener, Y. Lu, *et al.*, Appl. Phys. Lett. **74** (24), 3636 (1999).
10. O. I. Lebedev, G. van Tendeloo, S. Amelinckx, *et al.*, Phys. Rev. B **58** (12), 8065 (1998).
11. R. W. Wyckoff, *Crystal Structures*, 2nd ed. (Interscience, New York, 1960), Vol. 2, p. 393.
12. M. Sasaura, S. Miyazawa, and M. Mukaida, J. Appl. Phys. **68** (7), 3643 (1990).
13. E. O. Wollan and W. C. Koehler, Phys. Rev. **100** (2), 545 (1955).
14. C. J. Lu, Z. L. Wang, C. Kwon, and Q. X. Jia, J. Appl. Phys. **88** (7), 4032 (2000).
15. Yu. A. Boikov, D. Erts, and T. Claeson, Mater. Sci. Eng. B **79** (2), 133 (2001).
16. M. F. Hundley, M. Hawley, R. H. Heffner, *et al.*, Appl. Phys. Lett. **67** (6), 860 (1995).
17. P. G. Radaelli, M. Marezio, H. Y. Hwang, *et al.*, Phys. Rev. B **54** (13), 8992 (1996).

Translated by G. Skrebtsov

Physics of the Solid State, Vol. 45, No. 4, 2003, pp. 685–690. Translated from Fizika Tverdogo Tela, Vol. 45, No. 4, 2003, pp. 653–657.

MAGNETISM AND FERROELECTRICITY

NMR Excitation by an Electric Field as a Dynamic Manifestation of Magnetoelectric and Antiferroelectric Interactions

M. I. Kurkin, V. V. Leskovets, V. V. Nikolaev, E. A. Turov, and L. V. Turov

Institute of Metal Physics, Ural Division, Russian Academy of Sciences, ul. S. Kovalevskoĭ 18, Yekaterinburg, 620219 Russia

e-mail: kurkin@imp.uran.ru

Received July 5, 2002

Abstract—The possibility of excitation of NMR signals by an ac electric field in magnetically ordered crystals is discussed. Such signals can be recorded using the time-dependent component of the electric polarization vector. It is assumed that the electric and magnetic characteristics are coupled to each other through magnetoelectric and antiferroelectric interactions. Several types of magnetic structures are analyzed in which these interactions are not forbidden by symmetry. Such structures include two-sublattice single-position ferro- and antiferromagnetic phases in centrosymmetrical crystals, two-sublattice magnetic crystals without a center of symmetry (such as $KNiPO_4$), and four-sublattice antiferromagnetic crystals with three types of antiferromagnetism vectors (such as Cr_2O_3 and α-Fe_2O_3). © *2003 MAIK "Nauka/Interperiodica".*

1. MAGNETIC SPIN DYNAMICS ASSOCIATED WITH MAGNETOELECTRIC AND ANTIFERROELECTRIC INTERACTIONS

Magnetically ordered substances are mostly distinguished by their behavior in (static or high-frequency) magnetic fields [1]. The interest in their behavior in an electric field **E** was inspired by the discovery by Astrov of a magnetoelectric (ME) effect in Cr_2O_3 [2]. In [2], a sample of chromium oxide was magnetized by a static (more exactly, by quasi-static) electric field [the so-called $(ME)_E$ effect]. In [3], the electric polarization of this material was induced by a magnetic field **H** [$(ME)_H$ effect]. The magnetoelectric interaction responsible for this effect is described phenomenologically by invariants of the type

$$V_{\text{LMP}} = \varepsilon_{ijk} L_i M_j P_k \qquad (1)$$

in the thermodynamic potential Φ of a magnetic crystal. Here, M_j, L_i, and P_k are the components of ferromagnetism, antiferromagnetism, and electric-polarization vectors, respectively. In a two-sublattice model of a magnet with two different types of positions of magnetic atoms in a unit cell, characterized by magnetic moments $\mathbf{M}_1$ and $\mathbf{M}_2$, the vectors **M** and **L** are defined as

$$\mathbf{M} = \mathbf{M}_1 + \mathbf{M}_2, \quad \mathbf{L} = \mathbf{M}_1 - \mathbf{M}_2. \qquad (2)$$

Invariance of interaction (1) requires the fulfillment of certain conditions [4]. In particular, the invariance of expression (1) with respect to the inversion operation I requires the vector **L** to be centroantisymmetrical [5],

$$I\mathbf{L} = -\mathbf{L}, \qquad (3)$$

because vector **M** is always centrosymmetrical, while vector **P** is centroantisymmetrical. Expression (1) leaves room for two possibilities.

(i) $\mathbf{M} = \mathbf{M}_0 = \text{const}$; in this case, a change in **P** is related to a change in **L**.

(ii) $\mathbf{L} = \mathbf{L}_0 = \text{const}$; in this case, a change in **P** is accompanied by a change in **M**. The subscript 0 indicates that the basis vector corresponds to the ground (low-energy) state.

The first case corresponds to a collinear two-sublattice ferromagnet, and the second, to a collinear two-sublattice antiferromagnet. The ME effect discovered in [2] corresponds to the second possibility because $\mathbf{P} = \kappa\mathbf{E}$, where κ is the electric polarizability.

A large number of publications have been devoted to the study of the ME effect (see, e.g., the references in [5, Chapter 5]). However, many new effects of dynamic nature could be expected as a consequence of ME interaction described by invariant (1). The authors of the series of articles [6–10] seem to be the first to have drawn attention to the possibility of the excitation of purely antiferromagnetic magnons (at a constant vector **M**) using an ac electric field $\mathbf{E}(t)$. Such electrically active magnons were later named antimagnons [11]. The results obtained in [6–10] actually opened a new chapter in spin dynamics but, unfortunately, went unnoticed by most readers; the author of [11] had to rediscover them. However, the authors of [6–10] dealt only with antiferromagnets (with four sublatices, as a rule), whereas in [11], the analysis starts from the simple case of a two-sublattice ferromagnet with a single-position of multiple sites related by the center of inversion ($I \times 1 = 2$, $I \times 2 = 1$). Moreover, the concept of antimagnons covers a large number of possibilities. For example, antimagnons can be electrically active, magnetically

Table 1. Transformation coefficients corresponding to the symmetry elements of space group *Pmmm* for the vectors **L** and **M**

	I	2_x	2_y
M_x	+1	+1	–1
M_y	+1	–1	+1
M_z	+1	–1	–1
L_x	–1	+1	+1
L_y	–1	–1	–1
L_z	–1	–1	+1

active (in the presence of a static electric field **E**), and acoustically active.

The total number of magnetic sublattices is also very important. If a magnetic structure is characterized by several antiferromagnetism vectors **L**, there can exist the so-called antiferroelectric (AFE) interaction:

$$V_{\mathrm{LLP}} = \varepsilon_{ijk} L_{1i} L_{2j} P_k, \tag{4}$$

where one of the vectors $\mathbf{L}_{1,2}$ must be a centrosymmetric vector and the other, a centroantisymmetrical vector. It turns out that electrically active antimagnons can exist even in magnetic crystals which do not exhibit the linear static ME effect (for example, in hematite α-Fe_2O_3 and centrosymmetric orthoferrites).

An important feature of new magnons (antimagnons) is that they are associated with oscillations at exchange eigenfrequencies ω_{ex} which lay in the submillimeter region, since the total local magnetization vector $\mathbf{M}(\mathbf{r})$ does not take part in the oscillations. Exceptions to this can be provided by quasi-two-dimensional systems, specially prepared superstructures, etc. Quite naturally, the question arises as to whether there can exist any other low-frequency dynamic effects directly related to the ME and AFE interactions (this problem was not considered in [6–10]). This paper aims to answer this question by analyzing the magnetic structures of specific crystals.

We shall analyze natural oscillations of nuclear spins excited by an ac electric field $\mathbf{E}(t)$. (The effect of a static field on the NMR frequencies was studied previously in [12]). These oscillations are usually excited by the application of an ac magnetic field, and the effect is, therefore, called nuclear magnetic resonance (NMR) [13]. For magnetic substances, the corresponding frequencies lie in the radio-frequency region, 10^8–10^9 Hz [14], which is much lower than the exchange frequencies $\omega_{ex} = 10^{12}$ Hz. Thus, the resonance excitation of oscillations of nuclear magnetic moments by an electric field $\mathbf{E}(t)$ (nuclear magnetoelectric resonance, NMER) can be attributed to low-frequency effects of spin dynamics, in which we are interested.

Below, we calculate the hyperfine fields [caused by $\mathbf{E}(t)$] at nucleus sites for the following cases:

(i) ferromagnetic and antiferromagnetic phases of two-sublattice single-position magnetic crystals possessing a center of symmetry, (ii) two-sublattice antiferromagnetism in crystals without a center of symmetry (as in $KNiPO_4$), and (iii) four-sublattice antiferromagnetism in two phases (with a centrosymmetric basis vector **L** as in hematite α-Fe_2O_3, and with a centroantisymmetrical basis vector **L** as in Cr_2O_3).

The purpose of our calculations is to estimate the amplitude of the field $\mathbf{E}(t)$ required for the observation of NMER signals.

2. TWO-SUBLATTICE FERROMAGNETIC AND ANTIFERROMAGNETIC PHASES IN A CRYSTAL WITH A CENTER OF SYMMETRY

Consider a two-sublattice magnetic crystal belonging to space group $D_{2h}^1 = Pmmm$ with magnetic atoms in positions 2*i*. Table 1 presents the coefficients of the transformation of the components M_α and L_α ($\alpha = x, y, z$) by action of to the symmetry operation I, 2_x, and 2_y, taken as the generators of this group. These data allow one to write the magnetic terms of the thermodynamic potential that are invariant under the symmetry operations of the group *Pmmm*:

$$\begin{aligned}\Phi = \frac{1}{2}(\lambda_M M^2 + \lambda_L L^2 + K_x(M_x^2 + L_x^2) + K_y(M_y^2 + L_y^2)) \\ - \frac{1}{2M_0}(\varepsilon_1 L_x M_x P_x + \varepsilon_2 L_x M_y P_y + \varepsilon_3 L_x M_z P_z \\ + \varepsilon_4 L_y M_x P_y + \varepsilon_5 L_z M_x P_z + \varepsilon_6 L_y M_y P_x \\ + \varepsilon_7 L_z M_z P_x) + \frac{1}{2}\kappa^{-1} P^2 - \mathbf{PE} - \mathbf{MH},\end{aligned} \tag{5}$$

where λ_L and λ_M are the exchange parameters and K_α are the magnetic anisotropy constants. The equilibrium values of components M_α, L_α, and P_α are determined by minimizing Φ and depend on the type of equilibrium magnetic structure. Below, we analyze two types of such a structure: (a) the ferromagnetic structure with $\mathbf{M} \parallel \mathbf{z}$ and $L_z = 0$ and (b) the antiferromagnetic structure with $\mathbf{L} \parallel \mathbf{z}$ and $M_z = 0$. We restrict our consideration to the so-called "equal-in-moduli" approximation [4]:

$$L^2 + M^2 = 4M_0^2, \tag{6}$$

where M_0 is the sublattice magnetization. In addition, the NMR frequency is considered to be lower than the electron oscillation frequencies. In this case, the variations of **L** and **M** will follow, in a quasi-equilibrium manner, variations in the exciting field $\mathbf{E}(t)$ (due to ME and AFE interactions). This allows one to find **L** and **M** by minimizing the thermodynamic potential Φ.

2.1. Ferromagnetic phase with $\mathbf{M} \parallel \mathbf{z}$

This case corresponds to the conditions $\lambda_M < 0$ and $\lambda_L > 0$, under which the minimization of the potential in Eq. (5) yields only one magnetically active component of the field $E_z(t)$ related to the component of the antiferromagnetism vector:

$$L_x(t) = \frac{\kappa\varepsilon_3}{\lambda_L - \lambda_M + K_1} E_z(t). \quad (7)$$

Bearing in mind that only one component of the vector $\mathbf{M}$ is nonzero ($M_z = 2M_0$) and using Eqs. (2) and (7), we find the components of sublattice magnetizations $M_{1\alpha}$ and $M_{2\alpha}$:

$$\begin{aligned} M_{1x} = -M_{2x} &= \frac{1}{2}\kappa\varepsilon_3(\lambda_L - \lambda_M + K_x)^{-1} E_z(t), \\ M_{1y} &= M_{2y} = 0, \\ M_{1z} &= M_{2z} = M_0. \end{aligned} \quad (8)$$

To analyze the effect of oscillation of the vectors $\mathbf{M}_1$ and $\mathbf{M}_2$ on the behavior of nuclear spins, one should take into account the hyperfine interaction of the electronic $\mathbf{M}_j$ and nuclear $\mathbf{m}_j$ sublattice magnetizations ($j = 1, 2$) [14]:

$$\Phi_{hfi} = -\sum_{j=1}^{2} A_j \mathbf{M}_j \mathbf{m}_j,$$

where A is the hyperfine interaction parameter and the quantity

$$\mathbf{H}_{nj} = A\mathbf{M}_j \quad (9)$$

is the hyperfine field at the nucleus site on the jth sublattice.

The static part $H_n = AM_0$ determines the NMER frequency coinciding with the NMR frequency:

$$\omega_n = \gamma_n A M_0. \quad (10)$$

The time-dependent component

$$\delta H_{nj}(t) = AM_j(t) = H_n \frac{M_j(t)}{M_0} \quad (11)$$

is responsible for the excitation of oscillations of $\mathbf{m}_j$ by the field $\mathbf{E}(t)$. The ratio $M(t)/M_0$ can be estimated from the static $(\mathrm{ME})_E$ effect [15]. According to the data from [15] for Cr_2O_3, this ratio for $E = 10^5$ V/cm is

$$M_j(t)/M_0 \approx 10^{-4}. \quad (12)$$

Taking $H_n \approx 10^5$ Oe [12], the value of δH_n is estimated to be

$$\delta H_n \approx 10 \text{ Oe}. \quad (13)$$

The same value of δH_{nj} can be obtained in the case of ac magnetic fields $\mathbf{H}(t)$ with an amplitude of 0.1 Oe and a typical value of the enhancement factor $\eta = 10^2$ [14]. Smaller values of the amplitude of $\mathbf{E}(t)$ (10^4–10^3 V/cm) will possibly suffice to detect an NMER signal. It is worthwhile to notice that the variations of magnetization and polarization in the static $(\mathrm{ME})_E$ and $(\mathrm{ME})_H$ effects, respectively, depend on the magnitude of the ME susceptibility α. Its typical value for antiferromagnets is 10^{-3} [16], so that an external electric field $E = 10^4$ V/cm creates the magnetization $4\pi M \approx 0.03$ G and an external magnetic field $H = 10^4$ Oe produced the electric polarization $4\pi P = 3 \times 10^{-9}$ C/cm^2. Generally, the range of values of α is wide (10^{-6} to 10^{-2}); however, one should also take into account the temperature range in which the ME effect occurs. For example, the ME susceptibility of the antiferromagnet $TbPO_4$ is the highest ($\approx 10^{-2}$) at $T \approx 1.9$ K and that of Cr_2O_3, at $T \approx 290$ K.

2.2. Antiferromagnetic Phase with $\mathbf{L} \parallel \mathbf{z}$ ($\lambda_L < 0$, $\lambda_M > 0$)

As is the case with a ferromagnetic phase, the component $E_z(t)$ is magnetically active and is related to the component

$$M_x(t) = [\kappa\varepsilon_5 E_z(t) + H_x(t)]/(\lambda_M - \lambda_L + K_x). \quad (14)$$

There is only one nonzero component of the vector $\mathbf{L}$, namely, $L_z = 2M_0$; therefore, as in Subsection 2.1, one can find the components of the sublattice magnetizations:

$$\begin{aligned} M_{1x} = M_{2x} &= \frac{1}{2}[\kappa\varepsilon_3 E_z(t) + H_x]/(\lambda_M - \lambda_L + K_x), \\ M_{1y} &= M_{2y} = 0, \\ M_{1z} &= -M_{2z} = M_0. \end{aligned} \quad (15)$$

Neglecting the distinctions between ε_3 and ε_5 and between λ_L and λ_M, the hyperfine fields δH_{nj} at the nucleus sites can be estimated from Eqs. (11)–(13). However, there is a significant distinction between the cases considered in Subsections 2.1 and 2.2 due to the second term in Eq. (14). The matter is that the ME interaction described by Eq. (1) is weak; therefore, the field $\mathbf{E}(t)$ excites the electric subsystem more strongly than the magnetic subsystem. This presents difficulties in finding how to reach a high excitation level for magnetic subsystem without overheating the electric subsystem. The presence of the second term in Eq. (14) allows one to avoid this difficulty by exciting the magnetic subsystem using a magnetic field $H_x(t)$ and recording the electric signal related to $P_z(t)$. For brevity, this effect will be referred to as the combined NMER.

Table 2. Transformation coefficients corresponding to the symmetry elements of space group $Pna2_1$ for the vectors **L**, **M**, and **E**

	n_x	a_y	2_{1z}
E_y, M_x	+1	–1	–1
E_x, M_y	–1	+1	–1
M_z	–1	–1	+1
E_z, L_x	+1	+1	+1
L_y	–1	–1	+1
L_z	–1	+1	–1

3. TWO-SUBLATTICE ANTIFERROMAGNETISM IN CRYSTALS WITHOUT A CENTER OF SYMMETRY

This case is analyzed using compound $KNiPO_4$ as an example. The crystal symmetry of this compound is described by the space group $Pna2_1$. The symmetry elements n_x, a_y, and 2_{1z} (glide planes and screw axis) are taken as the generators of this group; the corresponding transformation coefficients for the vectors **M** and **L** are given in Table 2. As in the preceding section, by using the transformation coefficients, one can write the thermodynamic potential Φ that is invariant under the symmetry operations of this group. We draw attention to the fact that Φ now contains contributions from both ME and AFE interactions:

$$\begin{aligned}\Phi = \frac{1}{2}(\lambda_M M^2 + \lambda_L L^2 + K_z(M_z^2 + L_z^2) + K_y(M_y^2 + L_y^2)) \\ - \frac{1}{2M_0}(\varepsilon_1 L_x M_y P_x + \varepsilon_2 L_x M_x P_y + \varepsilon_3 L_y M_x P_x \\ + \varepsilon_4 L_z M_z P_y) - \frac{1}{2M_0}(\delta_1 L_x L_z P_x + \delta_2 L_z L_y P_y) \\ + \frac{1}{2}\kappa^{-1} P^2 - \mathbf{PE} - \mathbf{MH}.\end{aligned} \tag{16}$$

As shown experimentally in [17], the antiferromagnetic ordering in $KNiPO_4$ corresponds to the phase with $\mathbf{L} \parallel \mathbf{x}$. Within the equal-in-moduli approximation for the sublattices ($M_1^2 = M_2^2 = M_0^2$), the minimization of potential (16) yields the following expression for the components of the vectors **L** and **M** induced by the field $\mathbf{E}(t)$ [18]:

$$\begin{aligned}L_x = 2M_0, \quad L_z = \kappa\delta_1 E_x(t)/K_z, \\ M_y = [\kappa\varepsilon_1 E_x(t) + H_y(t)]/(\lambda_M - \lambda_L + K_z), \\ L_y = M_x = M_z = 0.\end{aligned} \tag{17}$$

From Eqs. (14) and (17), in view of condition (6), it follows that the component M_y in Eq. (17) is comparable in magnitude to M_x in Eq. (14) for the antiferromagnetic phase of a crystal with a center of symmetry, whereas the magnitude of L_z in Eq. (17) is much greater than L_x in Eq. (7):

$$\frac{L_z(t)}{L_x(t)} \approx \frac{\lambda_L}{K_z}. \tag{18}$$

For substances with the Néel temperature close to room temperatures ($T_N \approx 300$ K), we have

$$\frac{\lambda_L}{K_z} \approx 10^3. \tag{19}$$

This means that the time-dependent hyperfine field at the nucleus site with an amplitude $\delta H_n \approx 10$ Oe, as in Eq. (13), can be achieved in an ac electric field $\mathbf{E}(t)$ with an amplitude as low as 10^2 V/cm. On the other hand, the component M_y can be excited by an ac magnetic field $H_y(t)$, and the electrical signal can be recorded; i.e., one can use a combined NMER, which was discussed in the previous section (see Subsection 2.2)

4. FOUR-SUBLATTICE ANTIFERROMAGNETS Cr_2O_3 AND α-Fe_2O_3

Symmetry of these crystals is described by the space group D_{3d}^6 ($R\bar{3}c$). Magnetic ions occupy fourfold position 4*c* with local symmetry{3}.The exchange magnetic structures are characterized by three antiferromagnetic vectors $\mathbf{L}_a$, $\mathbf{L}_b$, and $\mathbf{L}_c$ and one ferromagnetic vector **M**:

$$\begin{aligned}\mathbf{L}_a &= \mathbf{M}_1 - \mathbf{M}_2 - \mathbf{M}_3 + \mathbf{M}_4, \\ \mathbf{L}_b &= \mathbf{M}_1 + \mathbf{M}_2 - \mathbf{M}_3 - \mathbf{M}_4, \\ \mathbf{L}_c &= \mathbf{M}_1 - \mathbf{M}_2 + \mathbf{M}_3 - \mathbf{M}_4, \\ \mathbf{M}_a &= \mathbf{M}_1 + \mathbf{M}_2 + \mathbf{M}_3 + \mathbf{M}_4.\end{aligned} \tag{20}$$

The expression for the thermodynamic potential is rather cumbersome, and we conveniently split it into several parts:

$$\Phi = \Phi_0 + \Phi_{hf} + \Phi_{ab} + \Phi_{ac}, \tag{21}$$

where

$$\begin{aligned}\Phi_0 = \frac{1}{2}(\lambda_a L_a^2 + \lambda_b L_b^2 + \lambda_c L_c^2 + \lambda_M M^2) \\ + \frac{1}{2}\kappa P^2 - \mathbf{PE} - \mathbf{MH},\end{aligned} \tag{22}$$

$$\begin{aligned}\Phi_{hf} = -\frac{1}{4M_0}[\varepsilon_{m1}(L_c^x M^x P^y + L_c^x M^y P^x + L_c^y M^x P_x \\ - L_c^y M^y P^y) + \varepsilon_{m2}(L_c^x M^x P^z + L_c^y M^y P^z) \\ + \varepsilon_{m3}(L_c^z M^x P^x + L_c^z M^y P^y) \\ + \varepsilon_{m4}(L_c^x M^z P^x + L_c^y M^z P^y) + \varepsilon_{m5} L_c^z M^z P^z],\end{aligned} \tag{23}$$

$$\Phi_{ab} = -\frac{1}{4M_0}[\varepsilon_{b1}(L_a^z L_b^x P^x + L_a^z P_b^y P^y) + \varepsilon_{b2}(L_a^x L_b^z P^x + L_a^y L_b^z P^y) + \varepsilon_{b3}(L_a^x L_b^x P^z + L_a^y L_b^y P^z) + \varepsilon_{b4} L_a^z L_b^z P^z], \quad (24)$$

$$\Phi_{ac} = -\frac{1}{4M_0}[\varepsilon_{c1}(-L_a^x L_c^x P^x + L_a^y L_c^y P^x + L_a^x L_c^y P^y + L_a^y L_c^x P^y) + \varepsilon_{c2}(L_a^x L_c^y P^z - L_a^y L_c^x P^z) + \varepsilon_{c3}(L_a^z L_c^y P^x - L_a^z L_c^x P^y) + \varepsilon_{c4}(L_a^x L_c^z P^y - L_a^y L_c^z P^y)]. \quad (25)$$

The inessential terms describing magnetic anisotropy are omitted.

The equilibrium values of the components of vectors $\mathbf{L}_j$ and $\mathbf{M}$ in the presence of a field $\mathbf{E}(t)$ were calculated for two types of antiferromagnetic structures inherent in a centrosymmetric crystal of α-Fe_2O_3 and a centroantisymmetrical crystal of Cr_2O_3.

4.1. NMER in Hematite (α-Fe_2O_3) ($\lambda_a < 0$, $\lambda_{b,c} > 0$)

The exchange magnetic structure of hematite is determined by the vector $\mathbf{L}_a$. For definiteness, we restrict ourselves to the magnetic state with $\mathbf{L}_a \parallel \mathbf{z}$, which is realized below the Morin point. Minimizing Φ of Eq. (21) yields the following components of $\mathbf{M}$ and $\mathbf{L}_j$:

$$M_x = M_y = M_z = 0, \quad L_a^x = L_a^y = 0, \quad L_a^z = 4M_0,$$
$$L_b^x = \kappa\varepsilon_{b1}E_x(t)/\lambda_b, \quad L_b^y = \kappa\varepsilon_{b1}E_y(t)/\lambda_b,$$
$$L_b^z = \kappa\varepsilon_{b4}E_z(t)/\lambda_b, \quad L_c^x = \kappa\varepsilon_{c3}E_y(t)/\lambda_c, \quad (26)$$
$$L_c^y = \kappa\varepsilon_{c3}E_x(t)/\lambda_c, \quad L_c^z = 0.$$

(In the equal-in-moduli model, $\lambda_{b,c} \longrightarrow \lambda_{b,c} - \lambda_a$.)

These components are close to $L_x(t)$ in Eq. (7) in order of magnitude; therefore, we can estimate the time-dependent component δH_{nj} of the hyperfine field using Eqs. (11)–(13). As follows from Eqs. (21)–(25), a combined NMER in hematite does not occur.

4.2. NMER in Cr_2O_3 ($\lambda_c < 0$, $\lambda_{a,b} > 0$)

The exchange magnetic structure of Cr_2O_3 is determined by the vector $\mathbf{L}_c \parallel \mathbf{z}$. Minimizing Φ in Eq. (21) yields the following components of $\mathbf{L}_j$ and $\mathbf{M}$:

$$L_b^x = L_b^y = L_b^z = 0, \quad L_c^x = L_c^y = 0, \quad L_c^z = 4M_0,$$
$$M_x = \kappa\varepsilon_{m3}E_x(t)/\lambda_b, \quad M_y = \kappa\varepsilon_{m3}E_y(t)/\lambda_b,$$
$$M_z = \kappa\varepsilon_{m5}E_z(t)/\lambda_b, \quad L_a^x = \kappa\varepsilon_{a4}E_y(t)/\lambda_a, \quad (27)$$
$$L_a^y = -\kappa\varepsilon_{a4}E_x(t)/\lambda_a, \quad L_c^z = 0.$$

(In equal-in-moduli model, $\lambda_{a,b} \longrightarrow \lambda_{a,b} - \lambda_c$.) The corresponding time-depending component δH_{nj} of the hyperfine field at the nucleus site can again be calculated using Eqs. (11)–(13); however, in contrast to hematite, the combined NMER can be used for Cr_2O_3.

CONCLUSIONS

Thus, the symmetry analysis of magnetic structures of several types shows that the most suitable objects for the observation of NMER signals are structures similar to $KNiPO_4$. The main feature of such a structure is that it does not possess a center of symmetry. This essentially extends the variety of invariants in the thermodynamic potential describing the magnetic and electrical properties of such crystals. The invariants of the type $L_\alpha L_\beta P_\gamma$, containing the components L_α and L_β belonging to the same vector $\mathbf{L}$, are of prime importance. Such invariants are responsible for rotation of the vector $\mathbf{L}$ due to the appearance of electric polarization $P_\gamma = \kappa E_\gamma$ induced by the field $\mathbf{E}$. It is important that such a rotation is not related to changes in the exchange structure and, hence, does not increase the exchange energy. This rotation increases only the magnetic anisotropy energy, but this increase is approximately 10^3 times smaller than the corresponding increase in the exchange energy; therefore, the angles of rotation of magnetic moments of the sublattices become larger to the some extent. Therefore, the application of alternating electric fields with quite a moderate amplitude (10^2 V/cm) makes it possible to obtain NMER signals with a signal-to-noise ratio typical of NMR. This is an essential advantage of the dynamic effect caused by the AFE interaction V_{LLP} of Eq. (4) over the static ME effect.

Another possibility to make use of the dynamic magnetoelectric properties is related to the effect which we referred to as the combined NMER. This type of NMER implies the excitation of nuclear spins by applying an ac magnetic field and the recording of the electric signal associated with the electric polarization vector. This possibility allows one to overcome the problem of overheating of a sample in an ac electric field of a large amplitude.

In closing, we should point out that, everything on the formulas obtained for NMER appears quite promising. As far as the experimental difficulties are concerned, they require discussion by experimenters.

ACKNOWLEDGMENTS

This study was supported by the Russian Foundation for Basic Research, project no 02-02-16440.

REFERENCES

1. S. V. Vonsovskiĭ, *Magnetism* (Nauka, Moscow, 1971; Wiley, New York, 1974).
2. D. N. Astrov, Zh. Éksp. Teor. Fiz. **38** (3), 984 (1960) [Sov. Phys. JETP **11**, 708 (1960)].
3. G. T. Rado and V. J. Folen, Phys. Rev. Lett. **7** (8), 310 (1961).
4. J. P. Rivera, Ferroelectrics **161** (1–4), 165 (1994).
5. E. A. Turov, A. V. Kolchanov, V. V. Men'shenin, I. F. Mirsaev, and V. V. Nikolaev, *Symmetry and Physical Properties of Antiferromagnet* (Fizmatlit, Moscow, 2001).
6. D. Ya. Yablonskiĭ and V. N. Krivoruchko, in *Problems of Physical Kinetics and Solid State Physics* (Naukova Dumka, Kiev, 1990), p. 444.
7. V. N. Krivoruchko and D. A. Yablonskiĭ, Fiz. Nizk. Temp. **14** (6), 656 (1988) [Sov. J. Low Temp. Phys. **14**, 363 (1988)].
8. D. A. Yablonskiĭ and V. N. Krivoruchko, Zh. Éksp. Teor. Fiz. **94** (9), 268 (1988) [Sov. Phys. JETP **67**, 1886 (1988)].
9. D. A. Yablonskiĭ and V. N. Krivoruchko, Fiz. Tverd. Tela (Leningrad) **30** (10), 3069 (1988) [Sov. Phys. Solid State **30**, 1765 (1988)].
10. V. V. Eremenko, V. N. Krivoruchko, N. M. Lavrinenko, and D. A. Yablonskiĭ, Fiz. Tverd. Tela (Leningrad) **30** (12), 3605 (1988) [Sov. Phys. Solid State **30**, 2070 (1988)].
11. E. A. Turov, Pis'ma Zh. Éksp. Teor. Fiz. **73** (2), 92 (2001) [JETP Lett. **73**, 87 (2001)]; Preprint No. 25/49(01), IFM UrO RAN, NISO UrO RAN (Inst. of Metal Physics, Ural Division, Russian Academy of Sciences, Yekaterinburg, 2001).
12. V. V. Leskovets and E. A. Turov, Fiz. Tverd. Tela (St. Petersburg) **42** (5), 110 (2000) [Phys. Solid State **42**, 903 (2000)].
13. A. Abragam, *The Principles of Nuclear Magnetism* (Clarendon, Oxford, 1961; Inostrannaya Literatura, Moscow, 1963).
14. E. A. Turov and M. P. Petrov, *Nuclear Magnetic Resonance in Ferro- and Antiferromagnets* (Nauka, Moscow, 1969; Wiley, New York, 1972).
15. T. H. O'Dell and E. A. D. White, Philos. Mag. **22**, 177 (1970); Philos. Mag. **22**, 649 (1970).
16. L. M. Holmes, Int. J. Magn. **7**, 111 (1974).
17. P. Fisher, M. Lujan, F. Kubel, and H. Schmid, Ferroelectrics **162** (1–4), 385 (1994).
18. V. V. Leskovets, M. I. Kurkin, V. V. Nikolaev, and E. A. Turov, Fiz. Tverd. Tela (St. Petersburg) **44** (7), 1272 (2002) [Phys. Solid State **44**, 1330 (2002)].

Translated by A. Zalesskiĭ

Physics of the Solid State, Vol. 45, No. 4, 2003, pp. 691–695. Translated from Fizika Tverdogo Tela, Vol. 45, No. 4, 2003, pp. 658–662.

MAGNETISM AND FERROELECTRICITY

Dynamic Stability of a Spiral Domain in an AC Magnetic Field

V. N. Mal'tsev, G. S. Kandaurova, and L. N. Kartagulov

Ural State University, pr. Lenina 51, Yekaterinburg, 620083 Russia

e-mail: vladimir.maltsev@usu.ru

Received March 13, 2002; in final form, July 15, 2002

Abstract—The dependence of the stability of a magnetic spiral domain in a film on the parameters of the film and its domain structure and on an external magnetic field is considered within a phenomenological model. The model allows one to explain a number of experimentally observed properties of dynamic spiral domains resulting from the process of self-organization of domains and domain walls in an iron-garnet film placed in an external ac magnetic field. *© 2003 MAIK "Nauka/Interperiodica".*

1. INTRODUCTION

When an iron-ferrite film with perpendicular anisotropy is placed in an ac magnetic field (of frequency $\omega \sim 10^2$–10^5 Hz) normal to the film plane, the domain structure of the film becomes highly excited [1–3]. In this state, self-organization of moving domain walls occurs, bringing about the formation of various stable dynamic domain structures (DDSs), such as spiral domains (SDs) and systems of concentric ring domains. Each type of DDS is characterized by its region of existence, i.e., the ranges of magnetic-field amplitudes and frequencies over which the structure is stable. Furthermore, it has been found that the formation of a DDS depends on the parameters of the domain structure and material [4]. Domain structures superficially similar to DDSs (spiral and ring DDSs) but existing in a dc magnetic field were experimentally investigated in detail in [5, 6]. In particular, it was reported in [5] that SDs can also exist in the absence of an external magnetic field.

Up to now, DDSs have not been adequately studied theoretically. A dynamic system of ring domains was theoretically investigated in [7, 8]. The properties of SDs have been investigated theoretically only in the static state [9, 10]. In [11], spiral structures (vortices) were treated as defects in magnetically ordered media. Within a micromagnetic approach, it was shown that in the static state, the vortices in two-dimensional ferromagnets are due to exchange interaction. In this paper, we investigate the dynamic behavior of SDs in a film and the effect of an ac magnetic field and of various parameters of the film and of the domain structure on the SD stability.

2. MODEL OF THE SPIRAL DOMAIN

We will not discuss the initial process of the SD formation, because our aim is to study the stability of the SD. It is probable that the SD is formed from a stripe domain having one freely moving end. When moving, the end is subjected to gyrotropic force and the domain is curved into a spiral. In this paper, we assume that an SD with given initial geometric parameters (such as the outer radius and the pitch of the spiral) has already formed and investigate the time dependence of the outer radius of the spiral for various parameters of the film and external magnetic field.

The geometry of the problem is shown in Fig. 1. The magnetization in the domains is normal to the plane of the film and is reversed in a jump in going through a domain wall of zero thickness (in Fig. 1, the white and grey domains have opposite magnetization directions). This approximation is valid for films of a high quality factor $Q = K/2\pi M^2$, where K is the uniaxial magnetic anisotropy constant and M is the saturation magnetization. Therefore, the magnetostatic energy of space charges is ignored and the uniaxial-anisotropy and exchange-interaction energies are included effectively in the surface energy density σ of the domain walls. Experimentally, SDs were observed to have the shape of an Archimedean spiral; deviations from this shape took place only at the periphery of an SD and were pro-

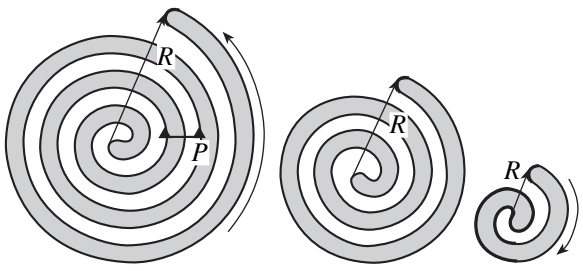

Fig. 1. Geometry of the problem. The radius R of the spiral increases in stripe-domain winding and decreases in its unwinding.

duced, perhaps, by the SD surroundings. In calculations, we assumed the spiral domain walls to be Archimedean spirals of pitch *P*.

Within these approximations, the SD energy [in units of $(2\pi M)^2h^3$] in an infinite film was found in [9] to be

$$E = E_H(m, r) + E_W(r, \beta) + E_M^l(m, r) + E_M^s(m, r, \beta), \quad (1)$$

where

$$E_H(m, r) = H(1-m)r^2 \quad (2)$$

is the Zeeman energy,

$$E_W(r, \beta) = \frac{l}{\pi}r^2\beta \times\left\{\sqrt{1+\frac{1}{(r\beta)^2}}+\frac{1}{(r\beta)^2}\ln[r\beta+\sqrt{1+(r\beta)^2}]\right\} \quad (3)$$

is the domain-wall energy,

$$E_M^l(m, r) = -\frac{(1-m^2)}{r}r^2+\frac{(1-m^2)}{4\pi}r^2 \times\left\{\frac{1}{r}-\frac{1}{64r^3}-2\left(\frac{1}{r}+\frac{1}{32r^3}\right)\ln(8r)\right\} \quad (4)$$

is the long-range part of the magnetostatic energy, and

$$E_M^s(m, r, \beta) = \frac{4r^2}{\pi^2\beta}\sum_{n=1}^{\infty}\sin^2\left(\frac{\pi n}{2}(1+m)\right) \times[1-(1-K(r))e^{-n\beta}-L(r, n\beta)] \quad (5)$$

is the short-range part of the magnetostatic energy. Here, we introduced the following notation:

$$K(r) = \frac{1}{8r^2}(1-2\ln[4r])+\frac{1}{128r^4},$$
$$L(r, n\beta) = \frac{1}{\pi r}E_1(n\beta)+\frac{1}{8r^2}E_2(n\beta)+\frac{1}{8\pi r^3}E_3(n\beta), \quad (6)$$

$$E_k(x) = \frac{(k-1)!}{x^k}, \quad (7)$$

h is the film thickness, $r = R/h$ is the reduced outer radius of the SD, $H = H_0/4\pi M^2$ is the reduced amplitude of the external magnetic field, $m = \bar{M}/M$ is the reduced average magnetization of the spiral, σ is the surface energy density of domain walls, $l = \sigma/4\pi M^2h$ is a characteristic length of the material (normalized to the film thickness), $p = P/h$ is the reduced pitch of the spiral, and $\beta = 2\pi h/P$ is the inverse pitch (wave vector) of the spiral.

Experiment shows [1–3] that application of an ac magnetic field $H_\sim = H_0\sin\omega t$ primarily affects the outer radius of the dynamic SD. We derived an equation describing the dynamics of this geometric parameter under the assumption that the SD is a stripe domain (of uniform width) curved into a spiral. In this case, the outer radius of the SD is determined only by the length L of the stripe domain. The SD length is varied as the outer end of the stripe domain moves along a trajectory described by the equation of an Archimedean spiral. This process is accompanied by a change in the SD energy due to energy dissipation in the domain walls of the outer end of the stripe domain:

$$\frac{dE}{dt} = \frac{\partial E}{\partial r}\frac{dr}{dt} = -kv^2, \quad (8)$$

where $v = dL/dt = (\partial L/\partial r)dr/dt$ is the velocity of the outer end of the stripe domain, $k = 2\pi ph/\mu$ is the coefficient of viscosity, and μ is the mobility of domain walls.

The final equation of motion of the outer radius of the SD was found to be

$$k^*\frac{dr}{dt} = -\left(\frac{\partial E_W(r, \beta)}{\partial r}+\frac{\partial E_H(m, r, H\cos(\omega t))}{\partial r} + \frac{\partial E_M^l(m, r)}{\partial r}+\frac{\partial E_M^s(m, r, \beta)}{\partial r}\right), \quad (9)$$

where $k^* = k(1+\beta^2r^2(t))$ is the effective coefficient of viscosity.

We solved Eq. (9) numerically using the fourth-order Runge–Kutta method for a given initial SD radius. The following parameters were varied: the reduced pitch p of the spiral, the characteristic length l, and the reduced amplitude H and frequency ω of the external field. Our main concern was to investigate the effect of these parameters on the behavior of the SD and its geometric parameters.

3. RESULTS AND DISCUSSION

First, we performed calculations for the static case (H = const); the results obtained are identical to those presented in [9]. In particular, we found the field $H^{(col)}$ at which the SD collapses and the field $H^{(\infty)}$ ($H^{(col)} > H^{(\infty)} > 0$) at which the SD radius tends to infinity (here and henceforth, the SD radius is taken to mean its maximum outer radius). At certain values of the pitch of the spiral and the characteristic length of the material of the film, the SD radius was found to be finite at $H = 0$. In [10], it was shown theoretically that the SD can exist in the absence of an external magnetic field, but with the energy minimum being less pronounced. Figure 2a shows the dependence of the SD energy on its outer radius for $p = 1.9$ and $l = 0.2$ in a zero external field. It can be seen that the SD energy is minimum at the SD radius $r_0 \approx 55$. A small change in the pitch of the spiral

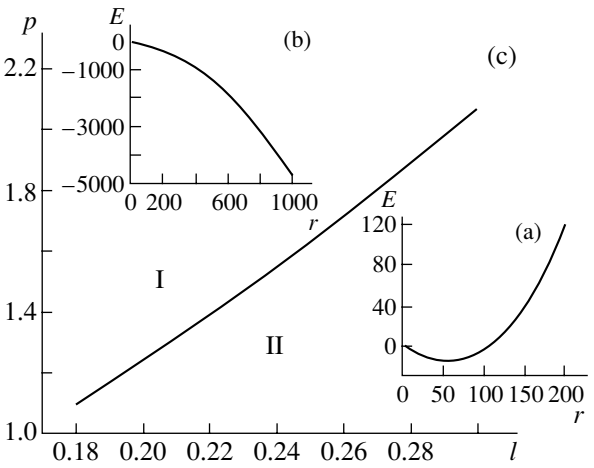

Fig. 2. Dependence of the SD energy E (in relative units) on the reduced radius r of the spiral with (a) $p = 1.9$ and (b) 2.0 in a film with $l = 0.2$; (c) regions of different SD stable states specified by reduced pitch p of the spiral and the characteristic length l of the material of the film.

causes the SD radius to tend to infinity in a zero magnetic field (Fig. 2b).

In the p–l plane, there are two regions where the dependence of the SD energy on outer SD radius is different at $H = 0$. The curve separating these regions is shown in Fig. 2c. The SD radius is infinite in region I and finite in region II. In terms of our model, the larger the SD radius, the higher the SD dynamic stability. Indeed, the SD radius can be decreased only through removal of the outer turn of the stripe domain from the spiral. For an SD of infinite radius, a decrease in radius will last for an infinite length of time; i.e., such an SD will be stable.

There is a relation between the dynamic behavior of the SD in an ac magnetic field and the dependence of the SD energy on its outer radius at $H = 0$. Indeed, the average value of an ac field over an oscillation period is zero; therefore, at small field amplitudes, the dynamic behavior of the SD is characterized by the minimum of the SD energy at $H = 0$. Figure 3 shows the behavior of the SD in an ac magnetic field in the cases where the initial SD radius is smaller (Fig. 3a) and larger (Fig. 3b) than the equilibrium radius r_0 in Fig. 2a for a film corresponding to region II in Fig. 2c. It can be seen that the SD radius averaged over an oscillation period relaxes to $r_0 \approx 55$. For films corresponding to region I in Fig. 2c, the SD radius tends to infinity (Fig. 3c).

The amplitude of oscillations of r increases with increasing amplitude of the external ac magnetic field. Therefore, for films corresponding to region II, the amplitude of SD radius oscillations will become equal to r_0 at a certain field amplitude and the SD will collapse. Thus, an increase in the field amplitude can be a destabilizing factor for dynamic SDs. In films corresponding to region II in Fig. 2c, SDs possess lower dynamic stability because of finiteness of their radius.

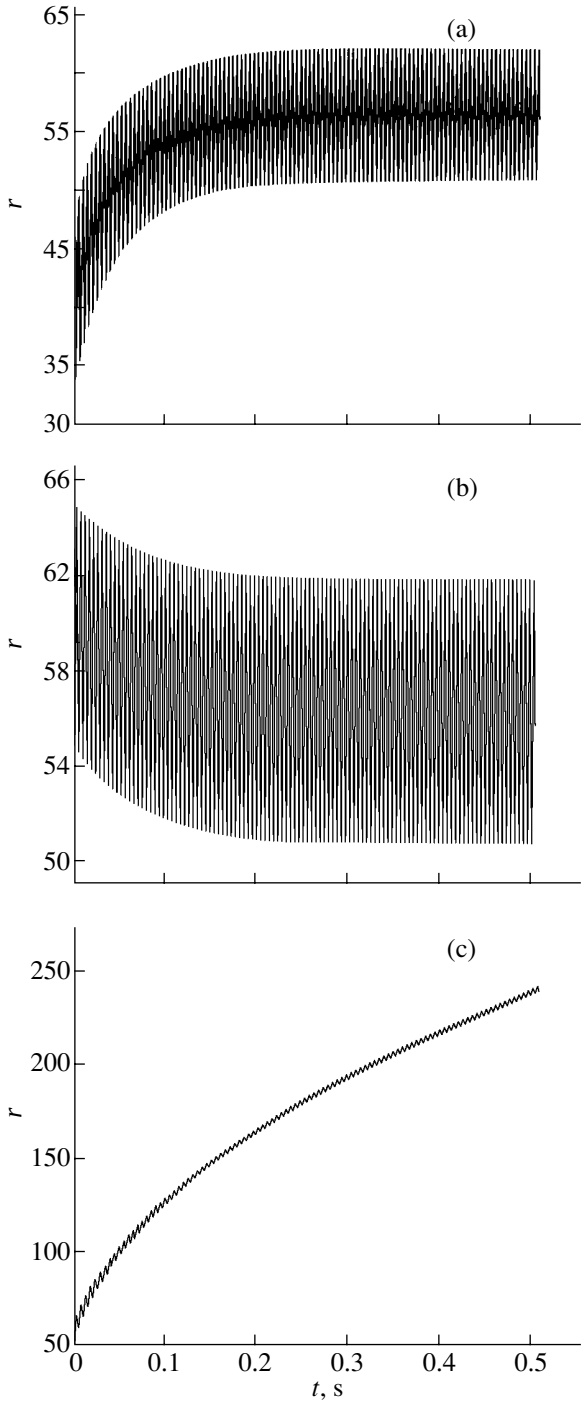

Fig. 3. Time dependence of the reduced radius r of the SD in an ac magnetic field of amplitude $H = 0.1$ and frequency $\omega = 300$ Hz for an SD state corresponding to region II in Fig. 2c ($l = 0.2$, $p = 1.9$) with the initial radius (a) smaller and (b) larger than the equilibrium radius r_0 at $H = 0$ in Fig. 2a and (c) for an SD state corresponding to region I in Fig. 2c ($l = 0.2$, $p = 2.0$).

On the other hand, calculations show that the amplitude of oscillations in r decreases with increasing fre-

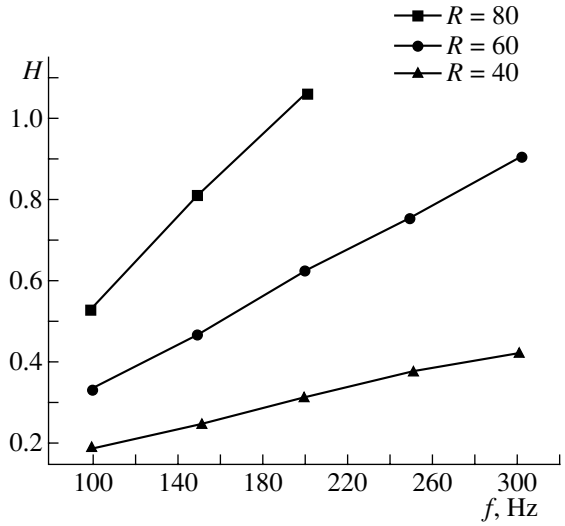

Fig. 4. Field-frequency dependence of the upper limit of the field-amplitude range within which the SD exists for various values of the initial SD radius; $l = 0.2$ and $p = 1.9$.

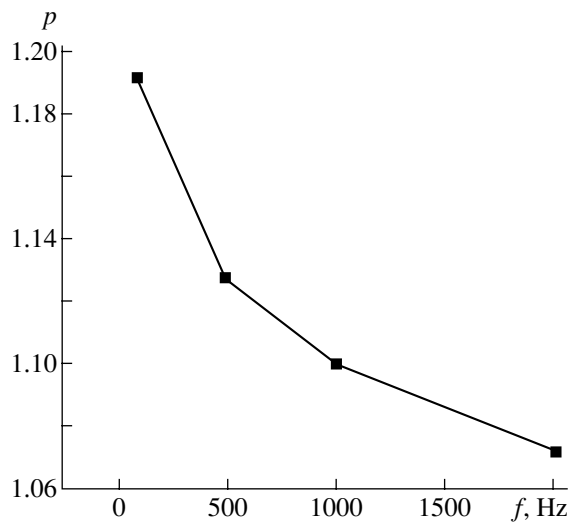

Fig. 5. Field-frequency dependence of the reduced pitch p of the SD for fixed field amplitude $H = 0.3$; $l = 0.2$ and $p = 1.9$.

quency of the ac magnetic field; therefore, an increase in the field frequency can be a stabilizing factor. Figure 4 shows the field-frequency dependences of the maximum field amplitudes at which the SD is still stable. It can be seen that as the field frequency is increased, the SD will be stable at progressively higher field amplitudes. A qualitatively similar frequency dependence of the upper limit of the field amplitude range within which the SD exists was observed experimentally in [2] at low frequencies. It is also seen from Fig. 4 that larger SDs are more stable, because they can exist in higher fields than can smaller SDs. This prediction is borne out by experiments. In [3], for example, large long-lived spirals were reported to be observed near the upper limit of the field amplitude range of existence of dynamic SDs. The dependences presented in Fig. 4 also suggest that, at a fixed field amplitude, the outer SD radius decreases with increasing frequency.

Calculations also revealed that the pitch of an SD depends on the field frequency. Figure 5 shows the frequency dependence of the maximum SD pitch above which the SD collapses. It can be seen that the domain structure changes as the field frequency is increased. This dependence agrees qualitatively with the experimental data presented in [2]. Our calculations presented in Figs. 4 and 5 were carried out for the same parameters of the material and domain structure as those of the samples studied in [2]. The calculated and experimentally measured quantities are of the same order of magnitude. However, the frequency dependence presented in Fig. 4 is steeper than the experimental one, which can be due to the fact that the SD has no surroundings in our model.

The influence of the magnetic-field frequency on the stability and pitch of an SD can be explained by the fact that, as the frequency increases, the amplitude of oscillations of r decreases and the minimum value of the oscillating SD radius increases; hence, the SD becomes more stable. On the other hand, the velocity of the outer SD end and, hence, the frictional force increase with increasing field frequency. Since the energy gained by the system in an oscillation period does not change, the outer SD end has to travel a shorter distance for this energy to be dissipated. Therefore, the domain structure is rearranged so that the outer SD end moves along an arc of a smaller radius (i.e., along a spiral with a smaller pitch), because in this case the length of a turn of the spiral decreases.

4. CONCLUSIONS

Thus, the results obtained within our phenomenological model are in qualitative agreement with the experimental data, which argues for the validity of the assumptions made. It has been found that the dynamic stability of the SD becomes higher with increasing frequency of the ac magnetic field but becomes lower with increasing field amplitude. This effect of the field parameters on the SD stability can be explained by the dependence of the oscillation amplitude of the outer SD radius on these parameters. It is worth noting that the dynamic stability of the SD is determined by its static stability in the absence of an external magnetic field and the static SD stability, in turn, depends on the parameters of the domain structure and the material of the film.

ACKNOWLEDGMENTS

This study was supported in part by the program "Fundamental Studies in the Field of Natural Sciences" (project no. E00-3.4-258) and the Civilian Research

and Development Foundation for the Independent States of the Former Soviet Union (grant no. REC-005).

REFERENCES

1. G. S. Kandaurova and A. É. Sviderskiĭ, Zh. Éksp. Teor. Fiz. **97** (4), 1218 (1990) [Sov. Phys. JETP **70**, 684 (1990)].
2. G. S. Kandaurova and Yu. V. Ivanov, Fiz. Met. Metalloved. **76** (1), 49 (1993).
3. G. S. Kandaurova, V. Kh. Osadchenko, A. A. Rusinov, and E. A. Rusinova, Pis'ma Zh. Éksp. Teor. Fiz. **63** (6), 453 (1996) [JETP Lett. **63**, 478 (1996)].
4. G. S. Kandaurova, A. É. Sviderskiĭ, V. P. Klin, and V. I. Chani, Pis'ma Zh. Tekh. Fiz. **20** (16), 40 (1994) [Tech. Phys. Lett. **20**, 663 (1994)].
5. K. V. Lamonova, Yu. A. Mamaluĭ, and Yu. A. Siryuk, Fiz. Tekh. Vys. Davleniĭ **6** (1), 33 (1996).
6. V. A. Zabolotskiĭ, Yu. A. Mamaluĭ, and E. N. Soĭka, Fiz. Tekh. Vys. Davleniĭ **7** (2), 74 (1997).
7. A. F. Gal'tsev and Yu. I. Yalyshev, Fiz. Met. Metalloved. **89** (3), 24 (2000).
8. V. N. Mal'tsev and N. M. Fakhrutdinov, Pis'ma Zh. Éksp. Teor. Fiz. **73** (1), 21 (2001) [JETP Lett. **73**, 17 (2001)].
9. A. B. Borisov and Yu. I. Yalyshev, Fiz. Met. Metalloved. **79** (5), 18 (1995).
10. K. V. Lamonova and Yu. A. Mamaluĭ, Fiz. Tekh. Vys. Davleniĭ **7** (2), 82 (1997).
11. A. B. Borisov, Pis'ma Zh. Éksp. Teor. Fiz. **73** (5), 279 (2001) [JETP Lett. **73**, 242 (2001)].

Translated by Yu. Epifanov

Physics of the Solid State, Vol. 45, No. 4, 2003, pp. 696–705. Translated from Fizika Tverdogo Tela, Vol. 45, No. 4, 2003, pp. 663–672.

MAGNETISM AND FERROELECTRICITY

Electromagnetic-Wave Reflectivity of the Surface of a Cubic-Ferrite Plate

V. D. Buchel'nikov, A. V. Babushkin, and I. V. Bychkov

Chelyabinsk State University, Chelyabinsk, 454021 Russia

e-mail: buche@csu.ru

Received April 15, 2002; in final form, July 16, 2002

Abstract—The electromagnetic-wave reflectivity of the surface of an insulating cubic-ferromagnet (ferrite) plate is calculated analytically and numerically with allowance for spin-wave damping. The frequency and magnetic-field dependences of the reflectivity are found at the orientational phase transition point and in the vicinity of this point for various values of the plate thickness. It is shown that the reflectivity exhibits anomalous behavior when the dynamic magnetic permeability becomes equal to the dielectric constant, as well as when dimensional resonances occur for electromagnetic or acoustic waves or ferromagnetic resonance takes place. At frequencies below the magnetoelastic gap in the quasi-spin-wave spectrum, the reflectivity may have anomalously low (down to zero) or anomalously high (up to unity) values. Such frequencies can lie in the microwave region. © *2003 MAIK "Nauka/Interperiodica".*

It was first shown theoretically in [1, 2] that the electromagnetic-wave (EMW) reflectivity of the surface of a semi-infinite insulating cubic ferromagnet (ferrite) can be controlled over a wide frequency range, up to a few gigacycles (microwave region), and its values can be varied from unity (total wave reflection) to zero (total absorption) by changing external parameters, such as temperature, magnetic field, and pressure. Such a behavior of the EMW reflectivity is associated with the anomalous change in the dynamic magnetic permeability near the orientational phase transition (OPT) point and various resonances. In [3], the EMW reflectivity of the surface of a semi-infinite insulating easy-plane antiferromagnet was investigated and it was shown that near the OPT point, the frequency range over which an anomalous decrease in reflectivity occurs becomes larger due to the exchange-induced increase in the magnetoelastic gap in the quasi-spin-wave spectrum. In [4], the reflectivity of EMWs incident on a semi-infinite conducting cubic ferromagnet or on the insulating easy-plane antiferromagnet–nonmagnetic- metal system was calculated theoretically in the gigahertz range and experimental data were presented on the EMW reflection from the surfaces of cobalt ferrite and antiferromagnetic $FeBO_3$ in the frequency range 8–12 GHz. It was shown that the reflectivity of a good ferrite conductor can be decreased by 50% near ferromagnetic resonance. The reflectivity of the insulating antiferromagnet–nonmagnetic-metal system also exhibits dips near quasi-ferromagnetic resonance. With properly adjusted demagnetizing factors and spin-wave damping coefficient, the calculations agree closely with the experimental data.

In this paper, we analytically and numerically calculate the EMW reflectivity of the surface of an insulating cubic-ferromagnet plate both far from and near the OPT point with allowance for spin-wave damping.

Let us consider a cubic-ferrite plate occupying the region $0 < z < d$. In the ground state, the magnetization of the plate is $\mathbf{M} \parallel \mathbf{z} \parallel \mathbf{H}_0$, where $\mathbf{H}_0$ is an external dc magnetic field. A linearly polarized monochromatic electromagnetic wave $\mathbf{h}$, e with $h_x = h_0\exp(ikz - i\omega t)$ and $e_y = -h_0\exp(ikz - i\omega t)$is incident normal from vacuum onto the $z = 0$ surface of the plate. In order to calculate the EMW reflectivity of the surface of the magnet, we should solve the set of coupled equations describing the propagation of interacting electromagnetic, elastic, and spin waves in the magnet. This set includes the elasticity equations, Maxwell's equations, and the Landau–Lifshitz equation for the magnetization [5, 6]:

$$\rho\ddot{U}_i = \frac{\partial\sigma_{ik}}{\partial x_k}, \quad \operatorname{curl}\mathbf{H} = \frac{\varepsilon}{c}\frac{\partial\mathbf{E}}{\partial t}, \quad \operatorname{curl}\mathbf{E} = -\frac{1}{c}\frac{\partial\mathbf{B}}{\partial t},$$
$$\operatorname{div}\mathbf{B} = 0, \quad \operatorname{div}\mathbf{E} = 0,$$
$$\dot{\mathbf{M}} = g[\mathbf{M}\times\mathbf{H}_{\text{eff}}] + \frac{1}{\tau_2}\mathbf{H}_{\text{eff}} - \frac{1}{\tau_1\mathbf{M}^2}[\mathbf{M}(\mathbf{M}\mathbf{H}_{\text{eff}})], \quad (1)$$
$$\mathbf{H}_{\text{eff}} = -\frac{\partial F}{\partial\mathbf{M}} + \frac{\partial}{\partial x_i}\frac{\partial F}{\partial(\partial\mathbf{M}/\partial x_i)},$$

where ρ is the density of the material; $\mathbf{U}$ is the displacement vector; $\sigma_{ik} = \partial F/\partial U_{ik}$ is the stress tensor; F is the free-energy density; U_{ik} is the strain tensor; $\mathbf{H}$ and $\mathbf{E}$ are the magnetic and electric fields, respectively; $\mathbf{B} = \mathbf{H} + 4\pi\mathbf{M}$ is the magnetic induction; c is the speed of light in vacuum; ε is the dielectric constant of the magnet; $\mathbf{M}$ is the magnetization; g is the gyromagnetic ratio; and τ_1

and τ_2 are the transverse and longitudinal relaxation times, respectively.

The free-energy density F of the magnet has the form [7]

$$\begin{aligned} F &= F_m + F_{me} + F_e - \frac{1}{2}\mathbf{H}_d\mathbf{M} - (\mathbf{H}_0 + \mathbf{h})\mathbf{M}, \\ F_m &= \frac{1}{2}\lambda(\mathbf{M}^2 - M_0^2) + \frac{\alpha}{2}\left(\frac{\partial \mathbf{M}}{\partial x_i}\right)^2 \\ &\quad + K_1(m_x^2 m_y^2 + m_y^2 m_z^2 + m_x^2 m_z^2), \\ F_{me} &= B_1(m_x^2 U_{xx} + m_y^2 U_{yy} + m_z^2 U_{zz}) \\ &\quad + 2B_2(m_x m_y U_{xy} + m_y m_z U_{yz} + m_x m_z U_{xz}), \\ F_e &= \frac{1}{2}C_{11}(U_{xx}^2 + U_{yy}^2 + U_{zz}^2) \\ &\quad + C_{12}(U_{xx}U_{yy} + U_{yy}U_{zz} + U_{xx}U_{zz}) \\ &\quad + 2C_{44}(U_{xz}^2 + U_{yz}^2 + U_{xy}^2), \end{aligned} \tag{2}$$

where F_m, F_{me}, and F_e are the magnetic, magnetoelastic, and elastic energy densities, respectively; $\mathbf{H}_d$ is the demagnetizing field; λ is the Lagrange multiplier, which is introduced to take into account the constancy of the magnitude of the magnetization vector $\mathbf{M}$; $\mathbf{m} = \mathbf{M}/M_0$; M_0 is the saturation magnetization; α is the exchange constant; K_1 is the first anisotropy constant; B_i are the magnetostriction constants; and C_{ik} are the elastic moduli.

We solve the set of equations (1) in the small-amplitude approximation by assuming that all parameters of the system vary as

$$\mathbf{A} = \mathbf{A}_0 + \boldsymbol{a}\exp(-i\omega t + ikz), \tag{3}$$

where $\mathbf{A}_0$ is the equilibrium value and $\boldsymbol{a}$ is a small deviation from this value.

Using representation (3) and linearizing Eqs. (1), we obtain a set of equations describing the propagation of small-amplitude waves in the ferromagnet:

$$\begin{aligned} &(c^2k^2/\varepsilon\omega^2 - \mu_\pm)h_\pm = 0, \quad e_\pm = \mp ickh_\pm/\varepsilon\omega, \\ &m_\pm = \chi_\pm h_\pm/M_0, \quad u_\pm = -ikB_2\chi_\pm h_\pm/\rho(\omega^2 - \omega_t^2), \end{aligned} \tag{4}$$

where $a_\pm = a_x \pm ia_y$ are the circular components, $\mu_\pm = 1 + 4\pi\chi_\pm$ is the dynamic magnetic permeability, and $\omega_t^2 = C_{44}k^2/\rho$ is the square of the frequency of a noninteracting elastic wave. The dynamic magnetic susceptibility has the form

$$\begin{aligned} \chi_\pm &= gM_0(\omega^2 - \omega_t^2)/[(\omega^2 - \omega_t^2) \\ &\times\left(\omega_{sk} \mp \frac{\omega}{1 \mp i\gamma}\right) + \omega_{me}\omega_t^2\Big], \end{aligned} \tag{5}$$

where $\omega_{sk} = \omega_0 + \omega_{me} + g\alpha M_0 k$, $\omega_0 = \omega_A + \omega_H = g(2K/M_0 + H)$ is the activation frequency of the spectrum of noninteracting spin waves, $H = H_0 - 4\pi M_0$ is the internal magnetic field, $K = K_1 + B_1^2/(C_{11} - C_{12}) - B_2^2/2C_{44}$ is the anisotropy constant renormalized due to magnetostriction [7], $\omega_{me} = gB_2^2/M_0C_{44}$ is the magnetoelastic frequency gap, $\gamma = 1/g\tau M_0$ is the dimensionless spin-wave damping constant, and $1/\tau = 1/\tau_1 + 1/\tau_2$.

The dispersion relation following from Eqs. (4) and relating the wave vectors of waves supported by the ferrite to their frequency has the form

$$\begin{aligned} &(k^2 - k_s^2)(k^2 - k_a^2)(k^2 - k_e^2) \\ &-\frac{\zeta_{sa}}{\alpha}k_a^2(k^2 - k_e^2) - \frac{\zeta_{es}}{\alpha}k_e^2(k^2 - k_a^2) = 0, \end{aligned} \tag{6}$$

where

$$\begin{aligned} k_s^2 &= [\pm\omega - \omega_0(1 \mp i\gamma)]/[g\alpha M_0(1 \mp i\gamma)], \\ k_a &= \omega/S_t, \quad k_e = \sqrt{\varepsilon}\omega/c, \quad S_t^2 = C_{44}/\rho, \end{aligned}$$

$\zeta_{sa} = B_2^2/\rho S_t^2 M_0^2$, and $\zeta_{es} = 4\pi$ are the wave vectors of noninteracting spin, elastic, and electromagnetic waves, the velocity of a transverse acoustic wave, and dimensionless magnetoelastic and electromagnetic-wave–spin interaction constants, respectively.

The six roots of dispersion equation (6) are wave numbers corresponding to six combined wave modes that can propagate in the ferrite. The amplitudes of these wave modes and their relation to the amplitude of the incident EMW can be found by solving the equations that follow from the boundary conditions and Eq. (6).

The set of boundary conditions for the ferrite plate includes the conditions of continuity of the normal components of the magnetic induction and the electric induction and of the tangential components of the electric- and magnetic-field strengths at the magnet boundaries, as well as the condition that the stress and the derivative of the magnetization be zero at these boundaries [5, 6]. Let $\mathbf{h}_R$, $\mathbf{e}_R$ be the reflected wave propagating in the region $z < 0$, and let $\mathbf{h}_d$, $\mathbf{e}_d$ be the transmitted wave propagating in the region $z > d$. We will denote the waves propagating along the inward normal to the $z = 0$ surface in the plate by $h_{i\pm}$ and the waves propagating in the opposite direction, by $h'_{i\pm}$. In this notation, the boundary conditions at the boundaries of the plate have the following form.

At $z = 0$,

$$\sum_{i=1}^{3}(h_{i\pm} + h'_{i\pm}\exp(ik_{i\pm}d)) = h_{0\pm} + h_{R\pm},$$

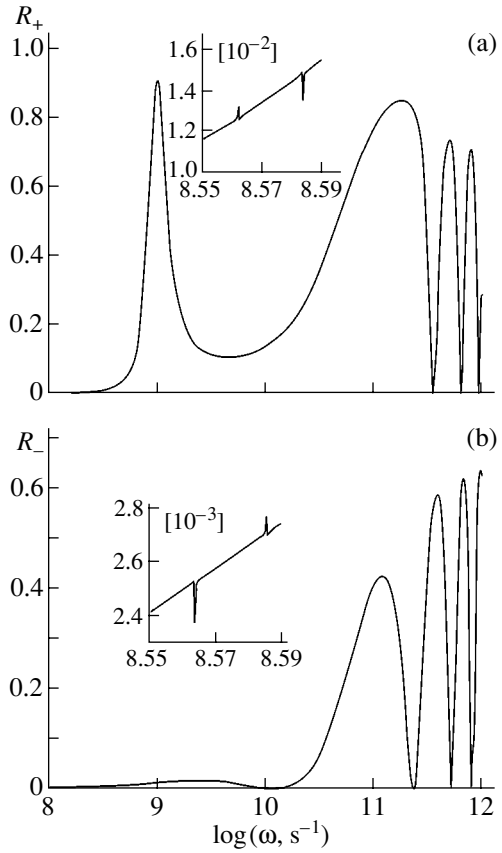

Fig. 1. Frequency dependence of the EMW reflectivity of the surface of a ferrite plate near the OPT point for H = 4050 Oe, $K = -1 \times 10^6$ erg/cm^3, $B_2 = 1 \times 10^7$ erg/cm^3, and $\gamma = 0.01$. The plate thickness $d = 0.1$ cm. Insets show the reflectivity anomalies due to dimensional resonances of acoustic waves.

$$\sum_{i=1}^{3} k_{i\pm}(h_{i\pm} - h'_{i\pm}\exp(ik_{i\pm}d)) = \sqrt{\varepsilon}k_e(h_{0\pm} - h_{R\pm}),$$

$$\sum_{i=1}^{3} \frac{k_{i\pm}^2 - k_2^2}{k_{i\pm}^2 - k_a^2}(h_{i\pm} + h'_{i\pm}\exp(ik_{i\pm}d)) = 0, \quad (7)$$

$$\sum_{i=1}^{3} k_{i\pm}(k_{i\pm}^2 - k_e^2)(h_{i\pm} - h'_{i\pm}\exp(ik_{i\pm}d)) = 0.$$

At $z = d$,

$$\sum_{i=1}^{3} (h_{i\pm}\exp(ik_{i\pm}d) + h'_{i\pm}) = h_{d\pm},$$

$$\sum_{i=1}^{3} k_{i\pm}(h_{i\pm}\exp(ik_{i\pm}d) - h'_{i\pm}) = \sqrt{\varepsilon}k_e h_{d\pm}, \quad (8)$$

$$\sum_{i=1}^{3} \frac{k_{i\pm}^2 - k_e^2}{k_{i\pm}^2 - k_a^2}(h_{i\pm}\exp(ik_{i\pm}d) + h'_{i\pm}) = 0,$$

$$\sum_{i=1}^{3} k_{i\pm}(k_{i\pm}^2 - k_e^2)(h_{i\pm}\exp(ik_{i\pm}d) - h'_{i\pm}) = 0.$$

In deriving Eqs. (7) and (8), we used Eqs. (4) to express the components of the magnetization, displacement vector, and electric-field strength in terms of the components of the magnetic field.

Using boundary conditions (7) and (8) and dispersion relation (6), one can find the EMW reflectivity of the surface of the ferrite plate:

$$R = \frac{1}{2}\left(\left|\frac{h_{R+}}{h_{0+}}\right|^2 + \left|\frac{h_{R-}}{h_{0-}}\right|^2\right) = (R_+ + R_-)/2, \quad (9)$$

where R_+ and R_- are the reflectivities of the ferrite plate for right- (RCP) and left-handed circularly polarized (LCP) incident waves, respectively.

In general, the expression for reflectivity (9) derived from Eqs. (6)–(8) is too cumbersome to be analyzed. For this reason, we found the EMW reflectivity of the surface of the ferrite plate by using numerical methods.

First, from dispersion relation (6), we numerically calculated the wave numbers $k_{i\pm}$ of the RCP and LCP wave modes supported by the magnet. Then, the wave numbers $k_{i\pm}$ are substituted into Eqs. (7) and (8) and from these equations the amplitudes of the RCP and LCP reflected waves are found. With these amplitudes, the EMW reflectivity is calculated from Eq. (9).

The numerical calculations are performed using the following parameter values typical of cubic ferrites:

$$g = 2 \times 10^7 \text{ s}^{-1}\text{ Oe}^{-1},\ \alpha = 10^{-12}\text{ cm}^2,\ M_0 = 500\text{ Oe},$$
$$\varepsilon = 10,\ \rho = 5\text{ g/cm}^3,\ S_t = 3 \times 10^5\text{ cm/s}. \quad (10)$$

The results for circularly polarized EMWs are presented in Figs. 1–7. The reflectivity of linearly polarized EMWs can be found using Eq. (9).

Before proceeding to a discussion of the results, we note that when EMWs propagate through the ferrite plate, standing waves arise in it. In addition to standing EMWs, standing elastic and spin waves can also arise in the plate due to the electromagnetic-wave–spin and magnetoelastic interactions. The conditions of existence of standing electromagnetic, elastic, and spin waves can be found using the results of the investigation performed in [8] (see [8, Fig. 1]). As is known, the minimum frequency of standing waves is determined by the condition

$$k_{i\pm}(\omega)d = \pi, \quad (11)$$

where $k_{i\pm}(\omega)$ are the roots of dispersion relation (6). When conditions (11) are met, the frequency dependence of the reflectivity can exhibit anomalies associated with dimensional resonances. By solving dispersion relation (6) graphically [8], we arrive at the following results.

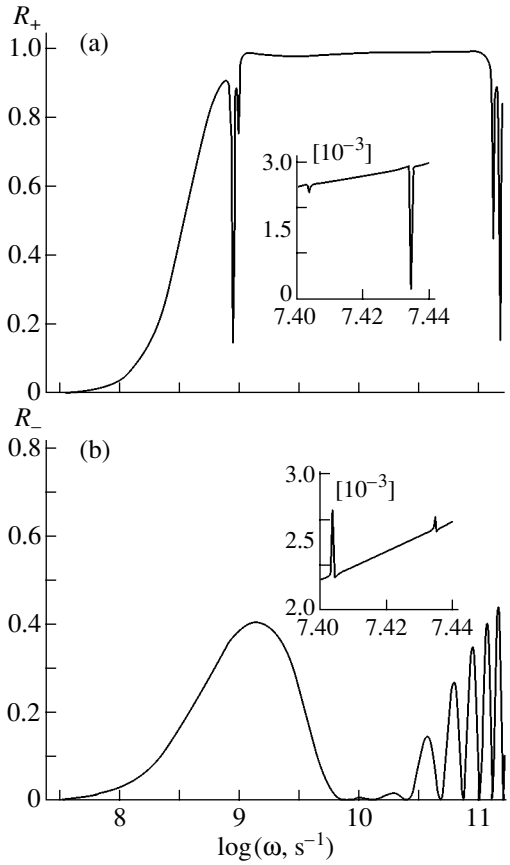

Fig. 2. Same as in Fig. 1, but for the plate thickness d = 1 cm.

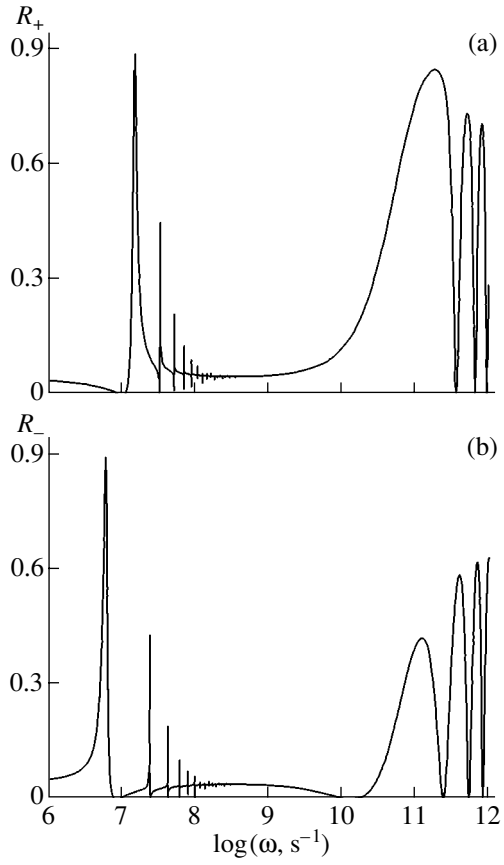

Fig. 3. Frequency dependence of the EMW reflectivity of the surface of a ferrite plate at the OPT point for H = 4000 Oe, $K = -1 \times 10^6$ erg/cm^3, $B_2 = 1 \times 10^7$ erg/cm^3, and $\gamma = 0.01$. The plate thickness d = 0.1 cm.

In the region $\omega \gg \omega_M + \omega_{s0}$ ($\omega_M = 4\pi g M_0$, $\omega_{s0} = \omega_{sk}(k = 0)$), the first resonances can occur at the frequencies

$$\omega \approx \pi c/[\varepsilon\mu_\pm(\omega)]^{1/2}d, \quad \omega \approx \pi S_\pm(\omega)/d, \quad \omega \approx g\alpha M_0\pi^2/d^2. \tag{12}$$

In this frequency range, we have $S_\pm(\omega) \approx S_t$ and $\mu_\pm(\omega) \approx 1$. In Eqs. (12), the first frequency corresponds to the appearance of standing RCP and LCP electromagnetic waves; the second frequency, to standing RCP and LCP elastic waves; and the third frequency, to standing spin waves.

In the region $\omega_M + \omega_{s0} \gg \omega \gg \omega_{s0}$, dimensional resonances occur at the frequencies

$$\omega \approx \pi c/[\varepsilon\mu_-(\omega)]^{1/2}d, \quad \omega \approx \pi S_\pm(\omega)/d, \quad \omega \approx g\alpha M_0\pi^2/d^2. \tag{13}$$

Here, we can also put $S_\pm(\omega) \approx S_t$. In this frequency range, RCP electromagnetic waves cannot propagate and the magnetic permeability $\mu_-(\omega)$ depends strongly on frequency [see below, Eq. (15)]. The permeability $\mu_-(\omega)$ can be estimated approximately as $\mu_-(\omega) \approx (\omega_M + 2\omega_{s0})/\omega$. In Eqs. (13), the first frequency corresponds to the appearance of standing LCP electromagnetic waves over the plate thickness; the second frequency, to standing RCP and LCP elastic waves; and the third frequency, to standing spin waves. Thus, in this frequency range, there are no dimensional resonances for RCP electromagnetic waves.

Finally, in the region $\omega \ll \omega_{s0}$, the first dimensional resonances occur at the frequencies

$$\omega \approx \pi c/[\varepsilon\mu_\pm(\omega)]^{1/2}d, \quad \omega \approx \pi S_\pm(\omega)/d. \tag{14}$$

In this frequency range, the permeability is virtually frequency independent and equal to $\mu_\pm(\omega) \approx (\omega_{s0} + \omega_M)/\omega_{s0}$, whereas the velocities $S_\pm(\omega)$ of RCP and LCP elastic waves, on the contrary, can depend strongly on frequency. Both near and far from the OPT point, we have $S_\pm(\omega) \approx S_t$. At the OPT point, the velocities of quasi-elastic waves can be approximated by the expressions [8] $S_+ \approx \sqrt{g\alpha M_0\omega}$ and $S_- \approx S_t\sqrt{\omega/\omega_{me}}$. In this case, Eqs. (14) can be rewritten as

$$\omega \approx g\alpha M_0\pi^2/d^2, \quad \omega \approx S_t^2\pi^2/\omega_{me}d^2. \tag{14a}$$

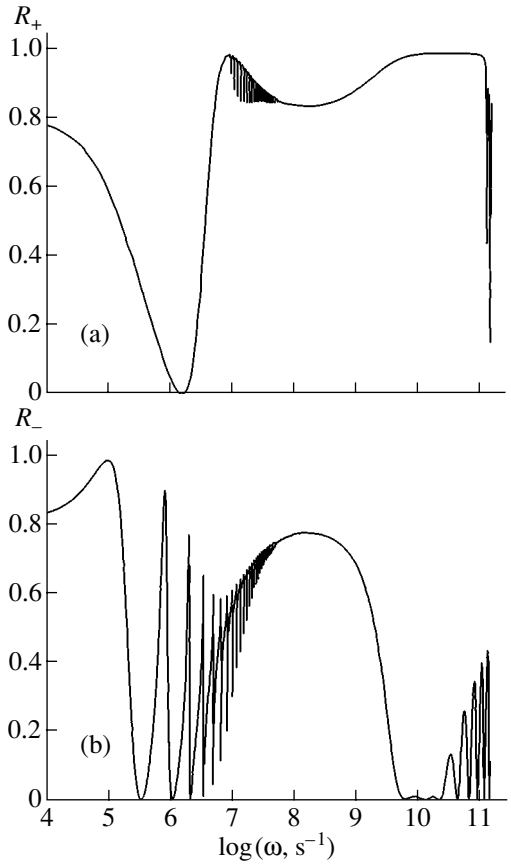

Fig. 4. Same as in Fig. 3, but for the plate thickness d = 1 cm.

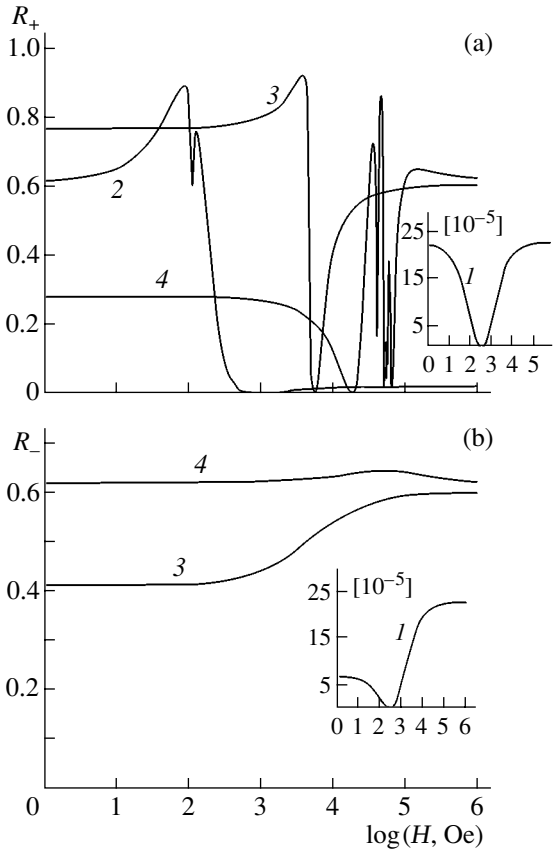

Fig. 5. Magnetic-field dependence of the EMW reflectivity of the surface of a ferrite plate for $K = 1 \times 10^5$ erg/cm^3, $B_2 = 1 \times 10^7$ erg/cm^3, and $\gamma = 0.01$. The plate thickness d = 0.1 cm. The EMW frequency ω is (*1*) 10^9, (*2*) 10^{10}, (*3*) 10^{11}, and (*4*) 10^{12} s^{-1}.

The first frequency in Eqs. (14) corresponds to the appearance of standing RCP and LCP electromagnetic waves in the plate, while the second frequency in Eqs. (14) and (14a) corresponds to standing RCP and LCP elastic waves, which become quasi-elastic at the OPT point [8]. For the parameter values in Eq. (10) typical of ferrite and for $K = -10^6$ erg/cm^3 and $H \approx$ 4050 Oe, we have $\mu_\pm(\omega) \approx 1.2 \times 10^2$, while for H = 4000 Oe [the OPT point, at which $\omega_0 = \omega_A + \omega_H = g(2K/M_0 + H) = 0$], we have $\mu_\pm(\omega) \approx 1.3 \times 10^4$.

At frequencies $\omega \approx \omega_M + \omega_{s0}$ and $\omega \approx \omega_{s0}$, the conditions of dimensional resonances become significantly more complicated, because the strong interaction between waves of different types heavily affects the dispersion relations of combined waves, especially in the case of RCP waves (see [8, Fig. 1]). At these frequencies, as well as at $\omega \approx 0$ (at the OPT point), the coupled electromagnetic and magnetoelastic wave modes cannot be separated into electromagnetic, elastic, and spin wave modes.

Numerical calculations show that at high frequencies ($\omega > 10^7$–10^9 s^{-1} for the parameter values in Eq. (10) typical of ferrite), the term $\omega_{me}\omega_t^2$ in the denominator in Eq. (5) for the magnetic susceptibility can be omitted and the spatial dispersion can be neglected in the expression for the frequency ω_{sk}. These approximations correspond to the case where the boundary conditions on the magnetization and elastic stresses are ignored. In this case, instead of the complicated problem of solving the set of coupled equations (1), it will suffice to solve the electrodynamic problem with the effective permeability $\mu_\pm$. According to Eq. (5), this permeability can be represented in the form

$$\mu_\pm = \mu'_\pm + i\mu''_\pm, \qquad (15)$$

where

$$\mu'_\pm = \frac{(1+\gamma^2)[\omega_{s0}(\omega_{s0}+\omega_M)(1+\gamma^2) \mp \omega(2\omega_{s0}+\omega_m)+\omega^2]}{[\omega_{s0}(1+\gamma^2) \mp \omega]^2 + \gamma^2\omega^2},$$

$$\mu_{\pm}'' = \frac{\gamma\omega\omega_M(1+\gamma^2)}{[\omega_{s0}(1+\gamma^2) \mp \omega]^2 + \gamma^2\omega^2}.$$

It follows that in the frequency range

$$\omega_1 < \omega < \omega_2, \tag{16}$$

where $\omega_{1,2} = [2\omega_{s0} + \omega_M \mp \sqrt{\omega_M^2 - 4\gamma^2\omega_{s0}(\omega_{s0}+\omega_M)}]/2$, the real part of the permeability for RCP electromagnetic waves is negative and such waves are not supported by the ferromagnet.

By solving the electrodynamic problem with the permeability given by Eq. (15), the ratios of the amplitudes of the reflected waves to the amplitudes of the incident waves can be found to be

$$\frac{h_{R\pm}}{h_{0\pm}} = \frac{(\varepsilon - \mu_{\pm})\sin(k_{\pm}d)}{(\varepsilon + \mu_{\pm})\sin(k_{\pm}d) - 2i\sqrt{\varepsilon\mu_{\pm}}\cos(k_{\pm}d)}, \tag{17}$$

where $k_{\pm} = \omega\sqrt{\varepsilon\mu_{\pm}}/c$. Using Eqs. (15) and (17), we find the EMW reflectivity defined by Eq. (9):

$$\begin{aligned} R_{\pm} = {} & [(\varepsilon - \mu_{\pm}')^2 + \mu_{\pm}''^2][4e^{-2k_{\pm}''d}\sin^2 k_{\pm}'d \\ & + (1 - e^{-2k_{\pm}''d})^2]/\{[(\sqrt{\varepsilon} + \sqrt{\mu_{\pm}})^2 + \mu_{2\pm}]^2 \\ & + [(\sqrt{\varepsilon} - \sqrt{\mu_{1\pm}})^2 + \mu_{2\pm}]^2 e^{-4k_{\pm}''d} \\ & - 2e^{-2k_{\pm}''d}\cos 2k_{\mp}'d[(\sqrt{\varepsilon} - \sqrt{\mu_{1\pm}})^2 \\ & - 6\varepsilon\mu_{2\pm} + \mu_{2\pm}(\mu_{2\pm} + 2\mu_{1\pm})] \\ & - 8\sqrt{\mu_{2\pm}}\varepsilon e^{-2k_{\pm}''d}\sin k_{\pm}'d(\varepsilon - \mu_{2\pm})\}, \end{aligned} \tag{18}$$

where $\mu_{1\pm} = (\sqrt{\mu_{\pm}'^2 + \mu_{\pm}''^2} + \mu_{\pm}')/2$, $\mu_{2\pm} = (\sqrt{\mu_{\pm}'^2 + \mu_{\pm}''^2} - \mu_{\pm}')/2$, $k_{\pm}' = \omega\sqrt{\varepsilon\mu_{1\pm}}/c$, and $k_{\pm}'' = \omega\sqrt{\varepsilon\mu_{2\pm}}/c$. This analytical expression was used to test the computer program for numerical calculations of the EMW reflectivity.

Figures 1–4 show the frequency dependences of the reflectivity for two values of the plate thickness. Figures 1 and 2 correspond to the case where the ferrite is near the OPT point, and Figs. 3 and 4 correspond to the ferrite at the OPT point.

It is seen from Figs. 1a and 2a that near the OPT point, there are three characteristic ranges in the frequency dependence of the reflectivity for RCP electromagnetic waves. At high frequencies ($\omega > 10^{11}$ s^{-1}), the reflectivity exhibits a series of alternating maxima and minima, which is typical of the case where dimensional EMW resonances take place in a plate. The frequency corresponding to the first dimensional resonance can be calculated from Eq. (12). For the parameter values in Eq. (10) and for $K = -10^6$ erg/cm^3 and $H = 4050$ Oe (corresponding to Figs. 1, 2), we have $\omega_M + \omega_{s0} \approx 1.2 \times 10^{11}$ s^{-1} and $\omega_{s0} \approx 1 \times 10^9$ s^{-1}. For a plate $d = 0.1$ cm thick, conditions (12) are met at $\omega \approx 3 \times 10^{11}$ s^{-1}, and for $d = 1$ cm, at $\omega \approx 3 \times 10^{10}$ s^{-1}. In the latter case, the frequency of the first resonance falls within the range [defined by Eq. (16)] where RCP electromagnetic waves cannot propagate; therefore, dimensional resonances will appear only above the upper limit of the frequency range in Eq. (16). These estimates correlate well with Figs. 1a and 2a. When the plate thickness is large, the dimensional resonances do not appear at high frequencies; thick plates can be considered semi-infinite for high-frequency EMWs. A more detailed analysis revealed that the reflectivity of thick plates also exhibits oscillations at high frequencies, but the amplitude of the oscillations is very small.

In the frequency range of Eq. (16) ($\omega \sim 10^9$–10^{11} s^{-1}), the reflectivity of a plate depends heavily on its thickness. At small plate thicknesses, we can expand the sine and exponential in the numerator of Eq. (18) into a power series and keep only the first terms. In this case, the reflectivity becomes proportional to the square of the plate thickness. The effect of the plate thickness on the reflectivity is clearly demonstrated in Figs. 1a and 2a. For RCP electromagnetic waves, the dimensional resonances do not occur in the frequency range of Eq. (16), as can be seen from Eq. (13). This conclusion is supported by numerical calculations (Fig. 2a). For low spin-wave damping and large plate thicknesses, the reflectivity of RCP electromagnetic waves is close to unity and virtually does not depend on frequency in the frequency range of Eq. (16) (Fig. 2a).

As the frequency range of Eq. (16) is approached both from below and from above, the reflectivity of RCP waves increases sharply. This increase can be explained as follows. Within the frequency range of Eq. (16), the real part of the permeability is negative for RCP waves. Below the lower limit of this range, the real and imaginary parts of the permeability for RCP waves are positive and increase sharply as the frequency $\omega_{s0} = \omega_0 + \omega_{me}$ is approached. In this case, according to Eq. (18), the reflectivity of RCP waves considerably increases, up to unity for low spin-wave damping. As the upper limit of the frequency range in Eq. (16) is approached from above, the real and imaginary parts of the permeability of RCP waves decrease sharply. However, as follows from Eq. (8), the reflectivity of RCP waves also increases in this case.

At still lower frequencies ($\omega < 10^9$ s^{-1}), the plate becomes transparent for EMWs, because the wavelength $\lambda \sim c/\omega$ at such frequencies is larger than the plate thickness (Figs. 1, 2). As the thickness of the plate increases, the transparency region shifts toward lower frequencies (cf. Figs. 1, 2).

For thick plates, the conditions of dimensional resonance for RCP electromagnetic waves can be met below the frequency range in Eq. (16). It follows from

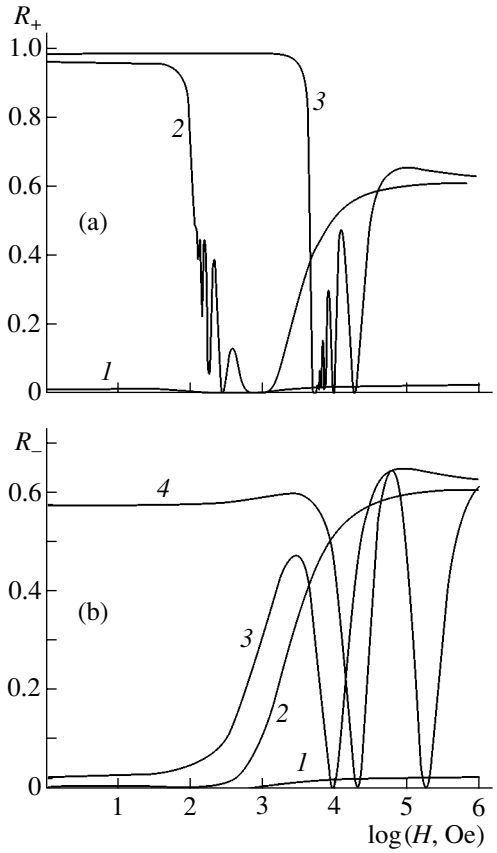

Fig. 6. Same as in Fig. 5, but for the plate thickness d = 1 cm.

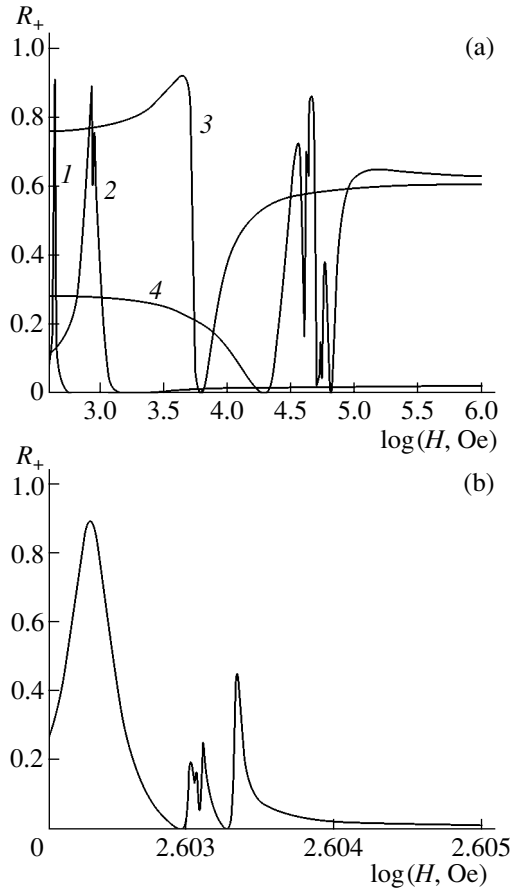

Fig. 7. Magnetic-field dependence of the EMW reflectivity R_+ of the surface of a ferrite plate for $K = -1 \times 10^5$ erg/cm^3, $B_2 = 1 \times 10^7$ erg/cm^3, and $\gamma = 0.01$. The plate thickness d = 0.1 cm. The EMW frequency ω is (a) (*1*) 10^9, (*2*) 10^{10}, (*3*) 10^{11}, and (*4*) 10^{12} s^{-1} and (b) 1.79×10^7 s^{-1}.

Eq. (14) that for the plate thickness d = 1 cm, the first dimensional resonance for RCP waves takes place at $\omega \approx 1 \times 10^9$ s^{-1}, which agrees with the numerical calculations presented in Fig. 2a.

From Eq. (15), it follows that the permeability for LCP electromagnetic waves is always positive and, near the OPT point, is much larger than unity. As the frequency is increased, the permeability decreases and becomes equal to the dielectric constant at a certain frequency, which causes the reflectivity of LCP waves in Eq. (18) to decrease at this frequency. This decrease corresponds to the first broad minimum (following the first maximum) in Figs. 1b and 2b. The subsequent minima in the frequency dependence of the reflectivity of LCP waves (Figs. 1b, 2b) correspond to dimensional resonances of EMWs. The frequency of the first resonance coincides with its estimate from Eq. (14): for the plate thickness d = 0.1 cm, this frequency is found from Eq. (14) to be $\omega \approx 3 \times 10^{11}$ s^{-1}, and for d = 1 cm, we have $\omega \approx 3 \times 10^{10}$ s^{-1}. As the plate thickness is increased, the dimensional resonances of LCP electromagnetic waves shift to progressively lower frequencies and disappear at high frequencies. The amplitude of the first maximum in the frequency dependence of the reflectivity of LCP waves increases with plate thickness (cf. Figs. 1b, 2b), while the width of the frequency range within which the plate is transparent for LCP electromagnetic waves decreases with increasing plate thickness.

In the frequency range of Eq. (16), the reflectivity of linearly polarized waves exhibits the anomalies of both reflectivities of RCP and LCP waves. Since the frequencies of dimensional resonances for RCP waves do not coincide with those for LCP waves, the amplitude of oscillations of the reflectivity of linearly polarized waves is significantly smaller than that of RCP and LCP waves.

As the magnetic field is increased above the OPT point, the spin-wave frequency ω_0 increases, with the consequence that the frequency range in Eq. (16) narrows and the anomalies in the frequency dependence of the reflectivity described above become smoother. With increasing spin-wave damping, the amplitudes of the peaks in the frequency dependence of the reflectivities of RCP, LCP, and linearly polarized waves decrease.

It can be seen from the insets to Figs. 1 and 2 that there are also a series of very narrow peaks at low frequencies. According to the estimates of the frequency of the first dimensional resonance from Eq. (14) presented above, these peaks are due to the effect of standing elastic waves on the magnetic permeability. Indeed, for the plate thicknesses $d = 0.1$ and 1 cm, the first dimensional resonances of elastic waves at low frequencies in the vicinity of the OPT point ($K = -10^6$ erg/cm^3, $H = 4050$ Oe) occur at $\omega \approx 9 \times 10^6$ and 9×10^5 s^{-1}, respectively. It follows from Figs. 1 and 2 that these peaks are, indeed, observed in the low-frequency range (near the intersection point of the dispersion curves of noninteracting waves) where the interaction between electromagnetic, elastic, and spin waves is the strongest [8]. Below and above this frequency range, the peaks of dimensional acoustic resonances sharply decrease in amplitude and virtually vanish far from this range. Since LCP electromagnetic and elastic waves interact with spin waves in the vicinity of the OPT point more weakly than do RCP electromagnetic and elastic waves, the acoustic-resonance anomalies in the reflectivity of LCP waves are smaller in magnitude than those of RCP waves. The magnitude of acoustic-resonance anomalies also depends strongly on spin-wave damping: the amplitude of the resonance peaks decreases with increasing spin-wave damping. Far from the OPT point, the dynamic magnetoelastic coupling is small and, therefore, there are virtually no dimensional resonances due to acoustic waves.

At the OPT point, the frequency dependence of the reflectivity is different (Figs. 3, 4). At high frequencies, there are virtually no changes in the behavior of the reflectivity, but at low frequencies, the changes are significant. First, the ferrite becomes opaque over a wide range of low frequencies ($\omega < 10^9$ s^{-1}) where it was transparent both near and far from the OPT point. This effect is due to the fact that the velocities (and, hence, wavelengths) of elastic and electromagnetic waves decrease significantly at the OPT point [8]. Second, in the low-frequency region, there are sharp peaks associated with dimensional acoustic resonances (Figs. 3, 4). The positions of these peaks depend on the thickness of the plate: the frequencies of the first resonances increase with decreasing plate thickness (cf. Figs. 3, 4). Estimations from Eqs. (13) and (14) give the following results for the frequencies of the first acoustic resonances. For the values of the ferrite parameters presented in Eq. (10) and for $K = -10^6$ erg/cm^3 and $H = 4000$ Oe, the acoustic dimensional resonances in the frequency range $\omega_M + \omega_{s0} \gg \omega \gg \omega_{s0}$ ($\omega_{s0} \approx 8.9 \times 10^6$ s^{-1} at the OPT point) appear starting from the frequency $\omega \approx 1 \times 10^7$ s^{-1}; in the frequency range $\omega \ll \omega_{s0}$, these resonances appear starting from 10 and 10^7 s^{-1} (for $d = 0.1$ cm) and from 10^{-1} and 10^5 s^{-1} (for $d = 1$ cm) for RCP and LCP acoustic waves, respectively. These estimates agree well with the numerical calculations presented in Figs. 3 and 4. The absence of acoustic resonances in the frequency dependence of the reflectivity of RCP waves at very low frequencies $\omega \ll \omega_{s0}$ can be due to the fact that these resonances occur at anomalously low frequencies and are not manifested in the scale used in Figs. 3 and 4. We also note that RCP acoustic waves are strongly attenuated at the OPT point, which can also be a reason for the absence of acoustic dimensional resonances at very low frequencies [9].

The frequency dependence of the reflectivity at the OPT point also exhibits dimensional resonances of RCP and LCP electromagnetic waves. At high frequencies, the frequencies of the first dimensional resonances of EMWs, as determined by Eqs. (12) and (13), are virtually coincident with those in the vicinity of the OPT point. For lower frequencies, calculations based on Eq. (14) show that in plates $d = 0.1$ and 1 cm thick, such resonances do not occur at the OPT point. This conclusion is supported by the numerical calculations presented in Figs. 3 and 4.

According to Eq. (5), the anomalies in the magnetic susceptibility for RCP and LCP waves take place at different frequencies. Therefore, the acoustic-resonance peaks in the frequency dependence of the reflectivity for these waves also differ in position (Fig. 3). The amplitude of the acoustic resonances is maximum for the first of them and decreases sharply with increasing frequency. The spacing between the resonance frequencies also decreases with increasing frequency. In the frequency ranges between acoustic resonances for RCP and LCP waves, the reflectivity of linearly polarized waves can have anomalously small values.

The curves in Figs. 3 and 4 exhibit a broad minimum which precedes the first dimensional-resonance peak in the reflectivity of RCP waves and follows the first peak in the reflectivity of LCP waves. The position of this minimum shifts toward lower frequencies with increasing plate thickness. This behavior of the reflectivity of RCP and LCP waves can be explained in terms of Eq. (5), from which it follows that at the OPT point, the magnetic susceptibility of the ferrite far exceeds unity at low frequencies. Therefore, due to the factor $(\omega^2 - \omega_t^2)$ in the numerator of Eq. (5), the dynamic permeability can decrease significantly (down to zero) at a certain frequency or become equal to the dielectric constant of the ferrite. In this case, the reflectivity is considerably decreased (down to zero). From Figs. 3 and 4, it follows that the minimum under discussion is near the dimensional resonances; therefore, the frequency of this minimum can be estimated as $\omega = \omega_t = S_t k \approx S_t \pi / d$. Using the parameter values in Eq. (10), we find that, for plate thicknesses $d = 0.1$ and 1 cm, the minimum of the reflectivity will be observed at frequencies $\omega \approx 10^7$ and 10^6 s^{-1}, respectively. These estimates correlate well with the positions of the first broad minima of the reflectivity of RCP and LCP waves in Figs. 3 and 4. The minimum of the RCP-wave reflectivity is so broad that

a few resonances take place within its width in the reflectivity of LCP waves (see, e.g., Fig. 4).

As the thickness of the plate is increased, the reflectivity at very low frequencies increases in magnitude and the ferrite becomes progressively less transparent. For large plate thicknesses, according to Eq. (14), dimensional resonances associated with quasi-elastic waves can also occur at very low frequencies. With increasing damping, the resonance peaks decrease in magnitude, but the reflectivity in the ranges between the peaks is affected only slightly.

The magnetic-field dependences of the EMW reflectivity are presented in Figs. 5–7. An analysis of these dependences revealed that the anomalies in them are also associated with the anomalous behavior of the dynamic magnetic susceptibility given by Eq. (5) and with dimensional resonances.

As indicated above, the reflectivity at high frequencies can be analyzed using Eqs. (15) and (18). It follows from Eq. (15) that the permeability for RCP electromagnetic waves exhibits a resonance peak at the magnetic-field strength

$$H_r = \frac{\omega - (1+\gamma^2)(\omega_A + \omega_{me})}{g(1+\gamma^2)}. \quad (19)$$

Therefore, the reflectivity of RCP electromagnetic waves will exhibit a resonance behavior only at the frequencies

$$\omega \geq \omega_3 = (1+\gamma^2)(\omega_A + \omega_{me}). \quad (20)$$

It also follows from Eq. (15) that in the range of magnetic fields

$$H_2 < H < H_1, \quad (21)$$

where

$$H_{1,2} = [2\omega - (2\omega_A + 2\omega_{me} + \omega_M)(1+\gamma^2) \pm \sqrt{\omega_M^2(1+\gamma^2)^2 - 4\omega^2\gamma^2}]/2g(1+\gamma^2),$$

the real part of the permeability for RCP electromagnetic waves is negative; therefore, RCP electromagnetic waves cannot propagate in this magnetic-field range.

The magnetic-field values at which dimensional resonances of EMWs occur are found from Eq. (11), which can be rewritten as

$$\mu_n(H) = \frac{\pi^2 c^2 n^2}{\omega^2 \varepsilon d^2}. \quad (22)$$

Equations (19)–(22) allow one to interpret the numerically calculated field dependences of the EMW reflectivity (Figs. 5–7).

Figures 5 and 6 show the magnetic-field dependences of the EMW reflectivity at various frequencies for $K = 1 \times 10^5$ erg/cm^3 and $B_2 = 1 \times 10^7$ erg/cm^3. For the parameter values given by Eq. (10), it follows from Eq. (20) that at low frequencies ($\omega < 1 \times 10^9$ s^{-1}), the permeability for RCP waves does not exhibit a resonance behavior for any magnetic-field strength. It also follows from Eqs. (15) and (21) that at low frequencies, the real part of the permeability for RCP waves is positive and varies monotonically. For LCP waves, the permeability is positive for any frequency and varies monotonically, without exhibiting a resonance behavior. At low frequencies, the values of the permeability $\mu_\pm$ can exceed the dielectric constant ε. Therefore, the field dependence of the reflectivity at low frequencies does not have to exhibit any sharp changes. The only minimum in the $R_\pm(H)$ dependences takes place at the point where $\varepsilon = \mu_\pm$; at this point, the reflectivity is virtually equal to zero and this minimum is the only one observed in Figs. 5 and 6 at low frequencies. Numerical calculations show that at frequencies $\omega < \omega_3 \approx 8 \times 10^9$ s^{-1}, the EMW reflectivity is anomalously small for any value of the magnetic field.

At high frequencies ($\omega > 1 \times 10^9$ s^{-1}), condition (20) is satisfied. The resonance peak in the permeability for RCP waves at $H = H_r$ given by Eq. (19) manifests itself in the field dependence of the reflectivity of RCP waves either as a shallow minimum (Fig. 5a for $\omega = 1 \times 10^{10}$ s^{-1}, $d = 0.1$ cm) or as a sharp decrease in the reflectivity (the other cases in Fig. 5a; Fig. 6a). The broad and deep minimum in the $R_+(H)$ curve corresponds to the condition $\varepsilon = \mu_+$. For LCP electromagnetic waves, the permeability is close to unity at high frequencies and, therefore, cannot be equal to the dielectric constant in this case. Condition (22) for dimensional resonances can be met at high frequencies; these resonances manifest themselves in the field dependence of the reflectivity of RCP waves as a few narrow minima (Figs. 5a, 7a) and in the LCP-wave reflectivity, as a few broad minima (Fig. 6b). The sharp increase in the reflectivity of RCP waves observed in Fig. 5a for $\omega = 1 \times 10^{10}$ and 1×10^{11} s^{-1} (curves *2*, *3*) in the range of low magnetic fields is due to the fact that the real part of the permeability in Eq. (22) is negative. At still higher frequencies ($\omega = 1 \times 10^{12}$ s^{-1}), the increase in the reflectivity in the field ranges beyond the resonances is due to an increase in the wavelength of the EMWs; the plate becomes less transparent to such waves.

If the anisotropy constant is negative, condition (20) can be satisfied even at low frequencies. In this case, the $R_+(H)$ curves near the OPT point exhibit sharp resonance peaks at low frequencies (Fig. 7b).

At low frequencies, the field dependences of the reflectivity can also exhibit specific features due to dimensional resonances in magnetic susceptibility (5) associated with acoustic waves. These resonances correspond to the peaks in the field dependence of the reflectivity in Fig. 7b.

Thus, our investigation of the reflection of electromagnetic waves from a plate of an insulating ferromagnet allows us to make the following conclusions.

It has been shown that if the magnetoelastic interaction is included, the frequency dependence of the EMW reflectivity exhibits anomalies associated with dimensional resonances of both electromagnetic and acoustic waves. The latter resonances are particularly pronounced at the OPT point.

The reflectivity for RCP electromagnetic waves can be anomalously large (up to unity) in the frequency range where the magnetic permeability for these waves is negative.

The EMW reflectivity becomes anomalously small (down to zero) when the dynamic permeability is equal to the dielectric constant.

At the OPT point, the EMW reflectivity can be anomalously large at low frequencies.

Analysis of the magnetic-field dependences of the EMW reflectivity revealed that at low frequencies (including the microwave region), the reflectivity can be anomalously small at any value of the magnetic field.

At higher frequencies, as the magnetic field is varied, the reflectivity of RCP electromagnetic waves becomes anomalously small when $\varepsilon = \mu_+$. This condition can be satisfied with the experimentally accessible magnetic fields.

Thus, by varying an external magnetic field, the EMW reflectivity of a plate of an insulating ferromagnet can be varied from unity to zero over a wide frequency range.

ACKNOWLEDGMENTS

This study was supported by the Russian Foundation for Basic Research, project no. 01-02-96445.

REFERENCES

1. V. D. Buchel'nikov, I. V. Bychkov, and V. G. Shavrov, Fiz. Tverd. Tela (St. Petersburg) **34** (11), 3408 (1992) [Sov. Phys. Solid State **34**, 1824 (1992)].
2. V. D. Buchel'nikov, I. V. Bychkov, and V. G. Shavrov, Akust. Zh. **40** (1), 158 (1994) [Acoust. Phys. **40**, 141 (1994)].
3. V. D. Buchel'nikov, I. V. Bychkov, V. S. Romanov, and V. G. Shavrov, Vestn. Chelyab. Univ., Ser. 6: Fiz., No. 1, 96 (1998).
4. V. D. Buchel'nikov, V. S. Romanov, G. A. Kraftmakher, and V. G. Shavrov, Radiotekhnika (Moscow), No. 8, 15 (2000).
5. A. I. Akhiezer, V. G. Bar'yakhtar, and S. V. Peletminskiĭ, *Spin Waves* (Nauka, Moscow, 1967; North-Holland, Amsterdam, 1968).
6. A. G. Gurevich and G. A. Melkov, *Magnetic Oscillations and Waves* (Nauka, Moscow, 1994).
7. V. D. Buchel'nikov, I. V. Bychkov, and V. G. Shavrov, Fiz. Met. Metalloved. **66** (2), 222 (1988).
8. V. D. Buchel'nikov, I. V. Bychkov, A. V. Babushkin, and V. G. Shavrov, Fiz. Met. Metalloved. **90** (4), 9 (2000).
9. V. D. Buchel'nikov and V. G. Shavrov, Fiz. Met. Metalloved. **68** (3), 421 (1989).

Translated by Yu. Epifanov

Physics of the Solid State, Vol. 45, No. 4, 2003, pp. 706–708. Translated from Fizika Tverdogo Tela, Vol. 45, No. 4, 2003, pp. 673–675.

MAGNETISM AND FERROELECTRICITY

Dynamic Shift in ^{57}Fe Nuclear Magnetoelastic Resonance Frequency in Iron Borate

I. V. Pleshakov

Ioffe Physicotechnical Institute, Russian Academy of Sciences, Politekhnicheskaya 26, St. Petersburg, 194021 Russia
e-mail: vp.shuv@pop.ioffe.rssi.ru

Received August 16, 2002

Abstract—The dynamic shift in NMR frequency associated with the magnetoelastic effect is studied in $FeBO_3$. It is shown that the shift is proportional to the *z* component of nuclear magnetization. The numerical values of parameters describing the nuclear magnetoelastic resonance are obtained, and these values agree well with the available data. © *2003 MAIK "Nauka/Interperiodica".*

Iron borate $FeBO_3$ attracts research attention as a material exhibiting a number of unusual and, possibly, practically useful properties. $FeBO_3$ is a noncollinear easy-plane antiferromagnet with a relatively high Néel temperature T_N = 348 K. This compound shows strong magnetoelastic properties, which specifically manifest themselves in the considerable renormalization of sound velocity in an external field [1]. The NMR line width in $FeBO_3$ is very narrow, which is not typical for most magnetically ordered substances. All these features allow one to observe a certain modification of nuclear magnetic resonance, namely, the nuclear magnetoelastic resonance (NMER) [2, 3]. It was shown in [3] that NMER is characterized by its own enhancement factor and a dynamic frequency shift (DFS, also called a "frequency-pulling effect") different from those associated with the ordered electron subsystem of magnetic materials [4]. DFS in NMER is a consequence of the repulsion of the magnetoelastic and nuclear dispersion branches in the vicinity of their intersection. In [3], the main features of NMER were studied; however, the most essential feature of the DFS characterizing its dynamic behavior, namely, the dependence of the magnitude of the shift on nuclear magnetization, remained unstudied. In this article, we present direct experimental evidence of this dependence.

According to [3], the dynamic shift associated with magnetoelastic oscillations is given by

$$\Delta\omega_{n\kappa} = -\frac{\omega_n}{2}\frac{\tilde{H}_{hf}(H-H_\kappa)}{(H-H_\kappa)^2+\Delta H_\kappa^2} = -\frac{\omega_n}{2}\frac{\tilde{H}^0_{hf}(H-H_\kappa)}{(H-H_\kappa)^2+\Delta H_\kappa^2}\frac{m_z}{m_0}, \quad (1)$$

where ω_n is the unshifted (unpulled) NMR frequency, H_{hf} is the hyperfine field exerted on the electron subsystem by the nuclear system ($H_{hf} = Am_z$, A is the hyperfine interaction constant, m_z is the z component of nuclear magnetization), H is the external magnetic field, H_κ is the field corresponding to the magnetoacoustic resonance in a sample at a given frequency, and ΔH_κ is the magnetoacoustic resonance width expressed in units of magnetic field strength. The tilde indicates exchange enhancement. In Eq. (1), we explicitly singled out the dependence of DFS on the relative nuclear magnetization through the hyperfine field, $H_{hf} = H^0_{hf}m_z/m_0$. Here, m_0 is the equilibrium nuclear magnetization and $H^0_{hf} = Am_0$ is the corresponding hyperfine field. From Eq. (1), it follows that NMER is most pronounced near the acoustic resonance of a sample. This resonance can be made to occur at a fixed frequency by using the dependence of the sound velocity on H [1].

Experimentally, this effect was studied by recording beat signals occurring due to the interference of the conventional NMR and the response of the nuclei inhomogeneously excited by a magnetoelastic wave (pure NMER). According to [4], the DFS caused by the electron subsystem in an antiferromagnet is described by

$$\Delta\omega_n = -\frac{\omega_n}{2}\frac{\tilde{H}_{hf}}{H+\tilde{H}'_a} = -\frac{\omega_n}{2}\frac{\tilde{H}^0_{hf}}{H+\tilde{H}'_a}\frac{m_z}{m_0}, \quad (2)$$

where $\tilde{H}'_a$ is the effective magnetic anisotropy field. Neglecting the small quantity ΔH_κ^2 [2, 5] and using Eqs. (1) and (2), one can easily find

$$\Delta\Omega = \Delta\omega_{n\kappa} - \Delta\omega_n \cong \frac{\omega_n}{2}\tilde{H}^0_{hf}\frac{H_\kappa+\tilde{H}'_a}{(H+\tilde{H}'_a)(H_\kappa-H)}\frac{m_z}{m_0}. \quad (3)$$

A single-crystal thin plate of iron borate enriched by ^{57}Fe isotope up to 80 at. % was used in the NMR experiments. The plate measured $2\times2\times0.2$ mm. ^{57}Fe NMR was observed at liquid-nitrogen temperature by record-

ing a free-induction signal excited by rf pulses 3 μs long with a carrier frequency of $\omega_n/2\pi = 75.4$ MHz. The rf field was directed along the easy-magnetization plane, which coincided with the sample plane. A static magnetic field was directed along the same plane perpendicular to the rf field and was varied within the range 0–250 Oe. The experimental setup was similar to that used in [3].

At $0 < H < 120$ Oe and $H > 230$ Oe, the induction signal exponentially decreased with the characteristic time $T_2^* \cong 60$ μs. In fields $H < 50$ Oe, NMR from the nuclei in domain walls was observed, and in stronger fields H, NMR from the nuclei in domains was observed [3, 5]. At two values of the external field ($H_{к1} = 170$ Oe, $H_{к2} = 192$ Oe), the rf pulses also excited short-lived signals of dimensional magnetoelastic resonances decaying with a characteristic time of 1.5–2 μs [6]. Within a sufficiently wide region of these resonances (as shown in the inset to Fig. 1), the form of the response signal qualitatively changed: the signal became nonmonotonic, and beat signals appeared.

The experiment was based on the fact that the z component of nuclear magnetization can be controlled by varying the repetition period T_{rep} of exciting pulses, i.e., by saturating the nuclear spin system. The dependence of the intensity of the induction signal obtained at the rf field amplitude corresponding to the maximum of the response signal (90° pulse) on the repetition period is shown in Fig. 1. The curve actually represents the dependence of m_z/m_0 on T_{rep}, since the recovery of the equilibrium nuclear magnetization after a 90° pulse obeys the law $m_z = m_0[1 - \exp(-t/T_1)]$ with the characteristic spin–lattice relaxation time T_1. The intensity was measured in the whole range of the existence of exponential induction decay. It was established that the intensity remains almost constant in magnitude for a signal coming from the nuclei in domains (inset to Fig. 1). Direct measurement of T_1 in the region of oscillations is impossible; however, as can be seen from Fig. 1, where the curves correspond to the fields at the edges of the oscillation range, the value $T_1 = 8$ ms, obtained in these fields, can be extrapolated to any field $H > 50$ Oe. Thus, each repetition period T_{rep} was related to a particular value of m_z/m_0.

In the range of oscillations, changes in the beat frequency $\Delta F = \Delta\Omega/2\pi$ with variation of repetition period T_{rep} were observed. The dependence of ΔF on m_z/m_0 obtained for two values of the external field close to $H_{к1}$ is shown in Fig. 2. The curves were calculated using Eq. (3) with parameters $\tilde{H}_a' \cong 60$ Oe [1, 3] and $H_{к1} = 170$ Oe (the effect of the second resonance at $H_{к2}$ was disregarded) and $\tilde{H}_{hf}^0$ as a fitting parameter. The adjusted value $\tilde{H}_{hf}^0 = 5 \times 10^{-3}$ differs only slightly from the previously obtained value 6.4×10^{-3} Oe [3]. Figure 2 also shows curves for a purely magnetoelastic DFS, i.e., for the hypothetical case of Eq. (1), where the contribution from the electron subsystem is disregarded. As one goes away from the resonance, the modulation depth of beats decreases [3]. This hampers the measurements, increases the error, and results in a noticeable spread of

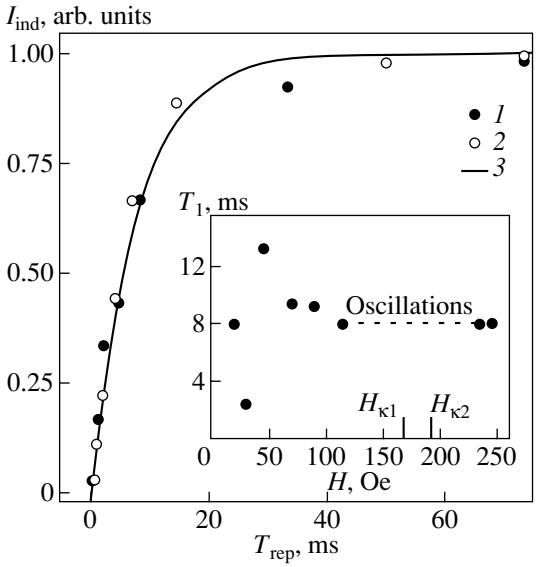

Fig. 1. Intensity of nuclear induction signal as a function of repetition period of rf pulses in fields (*1*) $H = 115$ and (*2*) 235 Oe, and (*3*) the saturation curve calculated for $T_1 = 8$ ms. The inset shows spin–lattice relaxation times within the range of field under study. The range of oscillations and the position of the resonance fields $H_{к1}$ and $H_{к2}$ are shown.

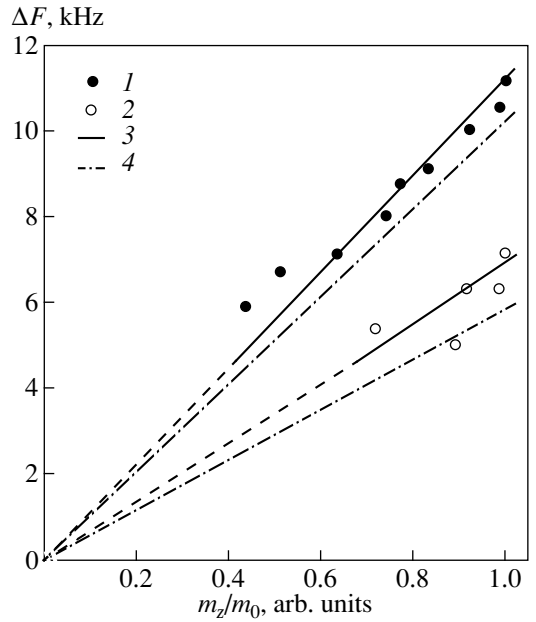

Fig. 2. Dependence of the dynamic frequency shift on the relative z component of nuclear magnetization: (*1, 2*) experimental data at $H = 150$ and 135 Oe, respectively; (*3*) calculation using Eq. (3) (with account of the electronic contribution); and (*4*) calculation using Eq. (1) (without regard for the electronic contribution).

the experimental points for $H = 135$ Oe. The decrease in repetition period reduces the signal and makes it impossible to obtain reliable results below $m_z/m_0 \approx 0.4$. Despite this, the graphs shown in Fig. 2 corroborate the linear dependence of DFS on the z component of nuclear magnetization and a considerable magnetoelastic contribution into this dependence in the range of magnetoacoustic resonance.

Thus, we experimentally verified the theoretically predicted behavior of DFS in the case of a strong nuclear–elastic coupling. These results give an additional support to the NMER model.

REFERENCES

1. M. H. Seavey, Solid State Commun. **10** (2), 219 (1972).
2. Kh. G. Bogdanova, R. A. Bagautdinov, V. A. Golenishchev-Kutuzov, *et al.*, Pis'ma Zh. Éksp. Teor. Fiz. **44** (5), 219 (1986) [JETP Lett. **44**, 279 (1986)].
3. M. P. Petrov, A. V. Ivanov, A. P. Paugurt, and I. V. Pleshakov, Fiz. Tverd. Tela (Leningrad) **29** (6), 1819 (1987) [Sov. Phys. Solid State **29**, 1044 (1987)].
4. E. A. Turov and M. P. Petrov, *Nuclear Magnetic Resonance in Ferro- and Antiferromagnets* (Nauka, Moscow, 1969; Wiley, New York, 1972).
5. N. M. Salanskiĭ, E. A. Glozman, and V. N. Seleznev, Zh. Éksp. Teor. Fiz. **68** (4), 1413 (1975) [Sov. Phys. JETP **41**, 704 (1975)].
6. A. P. Paugurt, I. V. Pleshakov, and A. V. Ivanov, Fiz. Tverd. Tela (Leningrad) **29** (10), 2959 (1987) [Sov. Phys. Solid State **29**, 1701 (1987)].

Translated by A. Zalesskiĭ

Physics of the Solid State, Vol. 45, No. 4, 2003, pp. 709–713. Translated from Fizika Tverdogo Tela, Vol. 45, No. 4, 2003, pp. 676–680.

MAGNETISM AND FERROELECTRICITY

Magnetic Anisotropy, First-Order Phase Transition, and Brown's Paradox in Rare-Earth Metals

Yu. P. Irkhin

Institute of Metal Physics, Ural Division, Russian Academy of Sciences, ul. S. Kovalevskoĭ 18, Yekaterinburg, 620219 Russia

e-mail: Irkhin@imp.uran.ru

Received April 5, 2002; in final form, August 20, 2002

Abstract—The anomalous behavior of magnetization curves (first-order magnetization process, FOMP) of highly anisotropic rare-earth metal compounds was studied. It is pointed out that FOMP assignment to a large contribution from higher magnetic anisotropy constants K_i comes into conflict with the point-ion approximation of crystal field theory. An alternative interpretation based on the multisublattice model is proposed; this model makes use only of first-order sublattice constants k_j derived from independent experimental NMR data. Direct calculations provide a satisfactory explanation of the FOMP in Tb_2Fe_{17}. A possible connection of the FOMP with Brown's paradox in the theory of domain structure and coercive force is proposed. © *2003 MAIK "Nauka/Interperiodica".*

1. INTRODUCTION

The magnetic properties of rare-earth metals (REMs), which exhibit an anomalous (jumplike) dependence of magnetization m on external field H, termed the first-order magnetization process (FOMP), have been dealt with in many studies. FOMP was first observed on cubic crystals by Bozorth as far back as 1936 [1]. Later, this effect was shown to exist in many highly anisotropic REM compounds, first in the RCo_5 system [2, 3] and subsequently in $R_2Fe_{14}B$ (see review [4]), R_2Fe_{17} [5–8], and some other systems [9, 10].

The FOMP problem is of interest in two respects. First, the mechanism of this phenomenon remains unclear. Second, a question immediately arises as to the extent to which the results of FOMP investigation are applicable to determination of the physical parameters introduced for its description. The magnetic-anisotropy (MA) model proposed in [11] and based on taking higher order MA constants into account is presently considered to be universally accepted. This approach permits one to describe the first-order phase transition for magnetization and determine the crystal field (CF) parameters A_n^m from $m(H)$ magnetization curves. Table 1 presents data for R = Pr and Tb in the $R_2Fe_{14}B$ compounds [12]. One readily sees that, for $n = 2$ and $n = 6$, the fitting parameters A_n^m are smaller and much larger, respectively, than the values A_{np}^m calculated in the point approximation of CF theory. A similar result was obtained in [5] for Tb_2Fe_{17}, where the fitting values of the MA constants K_2 and K_3 (Table 2) turned out to be an order of magnitude larger than K_1.

Thus, the FOMP cannot be explained by taking into account the first-order constant alone and the higher order constants K_i (necessary for adequate description of an experiment) need to be very large in many cases.

Table 1. Parameters A_{np}^m (in the CF point-ion approximation) and A_n^m (derived from the magnetic data taken from [12]) reduced to K for $R_2Fe_{14}B$

R	Parameter	n, m			
		2, 0	4, 0	6, 0	6, 4
Pr	A_n^m	82.6	−0.96	−0.15	−0.15
	A_{np}^m	550	−0.48	0.001	0.004
Tb	A_n^m	84	−0.98	−0.021	−0.114
	A_{np}^m	560	−0.49	0.001	0.005

1063-7834/03/4504-0709$24.00

Table 2. Fitting MA constants for Tb (in J/kg) in Tb_2Fe_{17} calculated in terms of the two-sublattice model [5] without inclusion (top line) and with inclusion (bottom line) of sublattice bending

K_1	K_2	K_3
–65	800	–660
–200	1300	–1045

In terms of the CF model in the point-ion approximation, one can readily show, using relations of CF theory [see Eqs. (4) and (5) below], that

$$\frac{K_n}{K_1} = \frac{\langle r_f^{2n}\rangle}{\langle r_f^2\rangle R^{2(n-1)}}\frac{\alpha_n}{\alpha_1}\frac{f_{2n}(J)}{f_2(J)}, \quad n = 1, 2, 3, \qquad (1)$$

and, therefore, $K_n/K_1 \ll 1$, because the product of the ratio of Stevens coefficients $\alpha_n/\alpha_1 \cong 10^{-2}$ ($n = 2$) multiplied by $\langle r_f^{2(n-1)}\rangle/R^{2(n-1)} \approx (0.5)^{2(n-1)}$ ($\langle r_f\rangle$ is the average f-shell radius, and R is the distance to the nearest neighbors) is found to be much smaller (for instance, for Tb) than $f_2(J)/f_{2n}(J)$, where $f(J)$ are the well-known polynomials of the REM ion angular momenta J. For instance, for Tb, the ratio in Eq. (1) is 10^{-2} for $n = 2$, which is at odds with the data in Table 2.

Thus, the excessively large values of K_2, K_3, and K_4, which are necessary to account for the FOMP, are in contradiction with CF theory. The hypothesis [13] according to which the major contribution to the CF is due not to nearest neighbor ions but to the 5*d* and 6*p* states of the rare-earth (RE) ion itself is not well developed and meets with criticism [13, 14]. Therefore, we put forward here an alternative magnetic-anisotropy model based on a real many-sublattice structure [15] and introduce sublattice MA coefficients without inclusion of higher order constants. This approach has a fundamental merit in that it allows experimental determination of the local sublattice constants from NMR and Mössbauer measurements, thus making it possible to carry out calculations practically without introducing any fitting parameters.

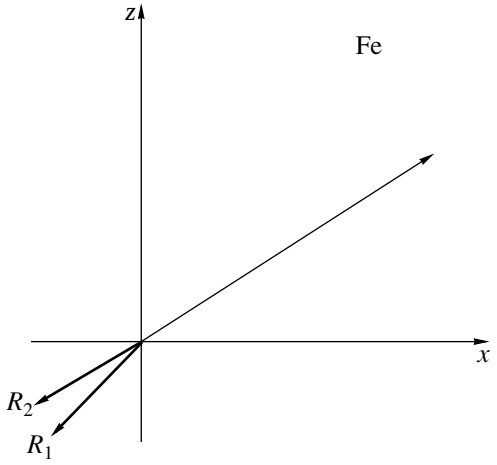

Fig. 1. Schematic magnetic structure of Tb_2Fe_{17} corresponding to antiferromagnetic exchange coupling between the Tb and Fe sublattices. All magnetic moments lie in the same plane, because the MA energy does not depend on azimuth φ if only the first MA constants are taken into account.

2. MAGNETIZATION AND MAGNETIC ANISOTROPY OF A THREE-SUBLATTICE MAGNET

The energy of a many-sublattice uniaxial magnet, including only the first MA constants k_i (i is the sublattice index), can be written as the sum of the exchange energy E_{ex}, the anisotropy energy E_A, and the interaction energy E_H with an external field H:

$$E = E_{ex} + E_A + E_H = -\sum_{i\neq j} I_{i,j}\cos\theta_{i,j} + \sum_i k_i \sin^2\theta_i - \sum_i m_i H\cos\theta_i, \qquad (2)$$

where $I_{i,j}$ is the exchange integral between sublattices, $\theta_{i,j} = \theta_i - \theta_j$, θ_i is the polar angle of the ith sublattice, and m_i is its magnetic moment.

We restrict ourselves subsequently to the case of three sublattices and consider the hexagonal structure of R_2T_{17}. We label by $i = 1$ the T sublattice, with $i = 2$ and 3 referring to the sublattices b and d of the RE ions. In accordance with experiment, we assume that $I_{12} = I_{13} = I$, and $I_{23} \ll I$, so that the latter term can be neglected by setting $I_{23} = 0$ in Eq. (2).

Note that, in our case, E_{ex} is independent of the difference between the sublattice azimuthal angles $\delta\varphi_i$ due to the requirement that the total energy be extremal in variables φ_i, which yields $\delta\varphi_i = 0$ if the MA energy is independent of φ.

The angles θ_i corresponding to the extremum of energy (2) can be found from the equations $\partial E/\partial\theta_i = 0$:

$$\begin{aligned} -If_1(x_1, x_2, x_3) + 2k_1x_1\sqrt{1-x_1^2} + m_1Hx_1 &= 0,\\ If_2(x_1, x_2) - 2k_2x_2\sqrt{1-x_2^2} + m_2Hx_2 &= 0,\\ If_3(x_1, x_3) - 2k_3x_3\sqrt{1-x_3^2} + m_3Hx_3 &= 0, \end{aligned} \qquad (3)$$

where $f_1 = f_2 + f_3$, $f_2 = x_1\sqrt{1-x_2^2} + x_2\sqrt{1-x_1^2}$, $f_3 = x_1\sqrt{1-x_3^2} + x_3\sqrt{1-x_1^2}$, and $x_i = \sin\theta_i$.

Here, the field **H** is aligned with the z axis; the square roots $\sqrt{1-x_i^2}$ are taken with the plus or minus sign, depending on the sign of $\cos\theta_i$; the angles θ_2 and θ_3 lie in the third quadrant (Fig. 1); and the angle θ_1 lies in the first quadrant.

Equations (3) are irrational, and the number of their roots depends on the coefficients in Eq. (3).

In our opinion, the most interesting of the R_2T_{17} compounds is Tb_2Fe_{17} (Fig. 1). First, the $m(H)$ dependence for this compound was studied on a single crystal sample within a broad range of fields up to 35 T, with a strong FOMP-type anomaly being observed in the range 3.2–4.9 T [5]. Second, as already mentioned, the calculations conducted in [5] with inclusion of higher order MA constants could be fitted to this anomaly only with very large values of K_2, K_3, and K_4 (Table 2). Finally, NMR studies of Tb_2Fe_{17} yielded data on the CF parameters which permit independent determination of the MA constants for the RE sublattices. For the Fe sublattice, these data can be extracted, as is usually done from the measurements made on Y_2Fe_{17}, which allows one to determine the coefficients in coupled equations (3).

The sublattice MA constants can be obtained from the relations (see, e.g., [15])

$$K = -3A_2^0\langle r_f^2\rangle\alpha_J(J-1/2)N_L, \quad (4)$$

$$A_2^0 = -\sum_R Q^*(R)\frac{3\cos^2\theta_R - 1}{2R^3}, \quad (5)$$

where A_2^0 is the CF parameter in units of K/a_0^2, a_0 is the Bohr radius, N_L is the number of formula units in 1 cm^3, and K is reduced to J through 1 K = 1.38×10^{-23} J. For Tb_2Fe_{17}, we have $N_L = 3.87\times10^{21}$ cm^{-3}.

The parameter A_2^0 for the positions b and d in Tb_2Fe_{17} was derived in [15] from NMR data [16]

$$A_2^0(b) = -253\ K/a_0^2, \quad A_2^0(d) = 80\ K/a_0^2. \quad (6)$$

Substituting the values from Eq. (6) into Eq. (4) and using the value of $K_1(Y_2Fe_{17})$ for k_{Fe}, we obtain finally the following set of MA constants (in units of J/cm^3):

$$k_{Tb}(2b) = -10.25, \quad k_{Tb}(2d) = 3.24, \quad k_{Fe} \cong -3. \quad (7)$$

To estimate the last parameter in our equations, namely, the exchange integral I, we have to take into account that it should be the largest; indeed, even in high fields (above FOMP), the Fe and $R = R(2b) + R(2d)$ sublattices retain a good collinearity, because the saturated magnetic moment for $H > 15$ T is 18.6 μ_B/f.u., which coincides with the sum of the Fe and R ion moments. In the region below the phase transition, the deviation from collinearity between the Fe and R sublattices is $\approx 2.5°$ [5]. The calculated noncollinearity between the RE sublattices ($\approx 20°$) is slightly larger because of the MA constants of these sublattices having opposite signs. No experimental data are available for the latter case.

The value chosen in [5] for the exchange parameter I_{RT} is 0.96×10^{-22} J, which corresponds to –10 J/cm^3. To meet the condition of small noncollinearity, we choose $I = -30$ J/cm^3 in our calculation. On adding this value to the quantities in Eq. (7), we can solve coupled equations (3) numerically.

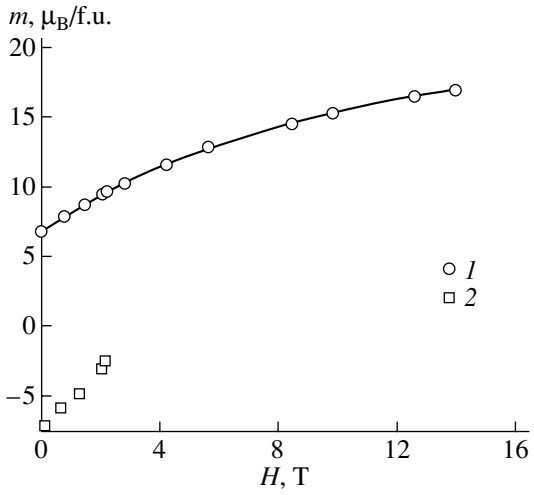

Fig. 2. Dependences of (*1*) m^+ and (*2*) m^- on magnetic field H in Tb_2Fe_{17}. m^- collapses at $H = 2.2$ T.

In the region of these values of the parameters, there are two branches of solutions $\{x_i\}$, which coincide in absolute value at $H = 0$ and approach each other as the sublattices rotate in an external field.

Knowing the solutions $\{x_i(H)\}$, we can calculate the magnetizations $m^{\pm}(H)$ for the branches with projections along and counter to the external field H from the equation (the roots are taken with the plus sign)

$$m^{\pm}(H) = \pm[m_1\sqrt{1-x_1^2} - m_2\sqrt{1-x_2^2} - m_3\sqrt{1-x_3^2}] \quad (8)$$

and then determine the energy $E^{\pm}(H)$ from Eq. (2). The values in Eq. (7) were varied slightly to obtain a magnetization as close as possible to the experimental curve. Figures 2 and 3 plot $m^{\pm}(H)$ and $m(H) = (m^+ + m^-)/2$ curves for the values $I = -30$, $k_1 = k_{Fe} = -3.7$, $k_2 = k_{Tb}(2b) = -10.3$, $k_3 = k_{Tb}(2d) = 7.8$ (all values in units of J/cm^3), $m_1 = 36.6$, and $m_2 = m_3 = 9$ μ_B/f.u.

As seen from Fig. 2, solutions (8) are substantially different in character; more specifically, whereas $m^+(H)$ is a smooth function and grows monotonically to reach saturation at high values of H, $m^-(H)$ decreases in absolute value when magnetized along the hard axis and ends in a cutoff at $H = H_{cr}$. Note that even at $H = 0$ the magnetizations $m^{\pm}$ are canted away from the easy plane by an angle θ_0; i.e., they lie on the easy-direction cones. As H increases, the m^+ cone contracts toward the z axis and m^- tends to fall onto the plane but does not reach it. The most important consequence is the collapse of the m^- branch at $H = H_{cr}^-$; this is what accounts for the jump in $m(H = H_{cr})$. The magnitude of the jump for the above parameters is $\Delta m^- \approx 11.6$ μ_B/f.u. and $\Delta m \approx 5.8$ μ_B/f.u. at $H_{cr} = 2.1$ T, a figure that agrees satisfactorily with experiment [5] (Figs. 2, 3). Note that the derivative

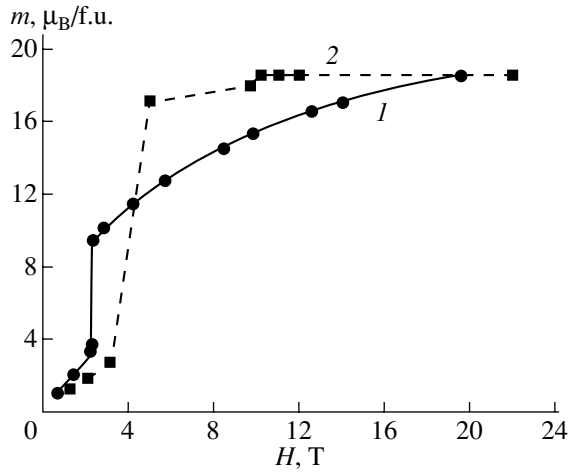

Fig. 3. (*1*) Calculated field dependence of $m = (m^+ + m^-)/2$ ($m^+ = m^-$ for $H > H_{cr}$) and (*2*) experimental curve [5]. The calculated FOMP field is $H = 2.2$ T.

$dm^-/dH \longrightarrow \infty$, which is a signature of the FOMP; however, m^+ continues to grow with increasing field above H_{cr} (FOMP II, according to the classification proposed in [11]).

3. ON THE RELATION OF THE FOMP TO THE DOMAIN STRUCTURE AND BROWN'S PARADOX

It is well known that, in highly anisotropic magnets, one should expect a large coercive force H_C, which in ideal cases should reach $2K/M_S$. In actual fact, however, the magnitude of H_C is substantially smaller (Brown's paradox). In the FOMP, the magnetization of R_2Fe_{17} drops in a jump to a low value for $H_{FOMP} = H_F$ (= 3.2 T for Tb_2Fe_{17}). It appears natural to assume that this effect, similar to Brown's paradox, is associated with the formation of a domain structure (DS) below H_F.

It should be noted that, unlike Brown's paradox observed under remagnetization along the easy axis, the FOMP occurs along the hard axis. In the latter case, DS formation under remagnetization becomes easier, because there is no potential barrier between the hard and easy directions associated with the anisotropy energy. Exchange energy can also contribute in these conditions. Unfortunately, no magnetization measurements have been made in easy directions on polished samples, although Tb_2Fe_{17} does exhibit a weak hysteresis (1–2 kOe) in the hard direction [5]. In actual fact, the jump is diffused in the 1.8-T interval and the onset of saturation spreads to 10 T (Fig. 3).

Reported attempts to explain Brown's paradox reduce to two possibilities: (i) the existence of regions (including the crystal surface) with low MA values, and (ii) the operation of a mechanism of inhomogeneous magnetization rotation involving nucleation of the reverse phase and subsequent DS formation.

The FOMP theory also makes use of the assumption of the existence of moving small-angle DSs, which give rise to a first-order phase transition [11]. The restriction to small angles draws from the necessity of expending energy in order to rotate magnetic moments against the external field under demagnetization. In inhomogeneous crystals, the restriction to the small-angle DSs, as well as energy limitations in Brown's paradox, can be lifted.

Thus, both the FOMP theory and Brown's paradox stumble onto similar difficulties. In the latter case, an expenditure of energy is required to surmount the potential barrier between the easy and hard axes, while in the FOMP, the loss of energy in a magnetic field should be compensated by a gain in MA energy in the transfer from the hard to the easy axis. Calculation of the FOMP energy for a complex sublattice structure (as in Tb_2Fe_{17}) is not an easy problem and, as shown by our computations, does not meet the necessary condition for an ideal lattice (as in Brown's paradox). The situation for a real crystal could be different; i.e., the condition $H_C < 2K/M_S$ will no longer have to be obeyed.

Thus, we come to the conclusion that an ideal crystal (in the absence of a mechanism of inhomogeneous rotation) should exhibit a normal hysteresis loop with $H_C = 2K/M_S$ and no FOMP. In our case, the Tb_2Fe_{17} crystal has strong concentration inhomogeneities [6], which may give rise to DS formation and the onset of the FOMP. The energy needed for domains to rotate against the field may also come from the system being nonequilibrium. Note that REM compounds reveal pronounced viscosity effects (see [17] and [4, p. 877]).

In our calculations (as mentioned in Section 2), the FOMP field is determined by collapse of the m^- branch for reverse phase domains. However, in order to take place, a reverse transition from m^+ to m^- requires extra energy which would compensate the difference between the interaction energy with the field E_H and the anisotropy energy E_A. Inhomogeneities in either the magnetic or crystalline state of the sample may serve as a source of this extra energy. In particular, the pinning and nucleation effects may play an important part in these phenomena [17]. Pinning is equivalent to domain wall quenching, and its inclusion may increase the magnitude of the jump near FOMP. Note also that domains of the reverse phase persist to fields of up to 10 T in orthoferrites and some other REM compounds [18].

Thus, the FOMP can be considered a manifestation of Brown's paradox.

An issue that still remains a subject of heated debate is spontaneous DS formation in an ideal crystal without involvement of external factors (defects, surface, etc.). Any evidence, either theoretical or experimental, supporting the operation of such a mechanism would be of interest. The principal effect here is inhomogeneous magnetization rotation under variation of an external magnetic field. According to [19], such a rotation can

be associated with nonlinear effects arising in differential equations for magnetization in the cases where one goes beyond linear theory. Note that the magnetization direction most favorable for the DS formation (see [19]) is along the hard axis, where instabilities arise at high enough fields $H > 0$. The existence of the FOMP in Tb_2Fe_{17} corresponds to this condition. One cannot exclude the possibility that the FOMP effect is also a part of this problem. This complex issue certainly deserves further study.

Thus, we have realized a new approach to the FOMP problem in the physics of highly anisotropic REM compounds and have shown the FOMP to be related to Brown's paradox in the DS theory. Joint analysis of experimental and theoretical developments reached in these areas of magnetism may prove important for clarifying unsolved problems, in particular, the mechanism of DS formation, the nature of the coercive force, and correct determination of the MA constants.

ACKNOWLEDGMENTS

The author is indebted to A.S. Ermolenko and V.V. Nikolaev for helpful discussions and to E.V. Rozenfel'd and V.Yu. Irkhin for valuable criticism.

This study was supported by the Russian Foundation for Basic Research, project no. 02-02-16440.

REFERENCES

1. R. M. Bozorth, Phys. Rev. **50**, 1076 (1936).
2. A. S. Ermolenko and A. F. Rozhda, IEEE Trans. Magn. **14** (5), 676 (1978).
3. G. Asti *et al.*, in *MASPES Technical Report* (Italy, 1979).
4. J. F. Herbst, Rev. Mod. Phys. **63** (4), 819 (1991).
5. R. Verhoef, P. H. Quang, R. J. Radwanski, *et al.*, J. Magn. Magn. Mater. **104–107**, 1473 (1992).
6. T. S. Zhao, T. W. Lee, K. S. Pang, and J. J. Lee, J. Magn. Magn. Mater. **140–144**, 1009 (1995).
7. X. C. Kou, F. R. de Boer, R. Grossinger, *et al.*, J. Magn. Magn. Mater. **177–181**, 1002 (1998).
8. J. Park, Y. Jo, J.-G. Park, *et al.*, J. Magn. Magn. Mater. **237**, 158 (2001).
9. S. A. Nikitin, I. S. Tereshina, Yu. V. Skurskiĭ, *et al.*, Fiz. Tverd. Tela (St. Petersburg) **43** (2), 279 (2001) [Phys. Solid State **43**, 290 (2001)].
10. N. K. Zaĭkov, A. N. Pirogov, N. V. Mushnikov, *et al.*, Pis'ma Zh. Éksp. Teor. Fiz. **72** (5), 623 (2000) [JETP Lett. **72**, 436 (2000)].
11. G. Asti and F. Bolzoni, J. Magn. Magn. Mater. **20** (1), 29 (1980).
12. M. Yamada, H. Kato, H. Yamamoto, and Y. Nakagawa, Phys. Rev. B **38** (1), 620 (1988).
13. R. Coehorn, J. Magn. Magn. Mater. **99** (1–3), 55 (1991).
14. B. Maloman, G. Venturini, R. Welter, *et al.*, J. Magn. Magn. Mater. **202** (3), 519 (1999).
15. Yu. P. Irkhin and V. Yu. Irkhin, Fiz. Tverd. Tela (St. Petersburg) **43** (2), 274 (2001) [Phys. Solid State **43**, 284 (2001)].
16. Y. Li, R. G. Grahem, D. St. P. Bunbury, *et al.*, J. Magn. Magn. Mater. **140–144**, 1007 (1995).
17. G. C. Hadjipanais and A. Kim, J. Appl. Phys. **63** (8), 3310 (1988).
18. Ya. S. Shur and V. I. Khrabrov, Zh. Éksp. Teor. Fiz. **57**, 1899 (1969) [Sov. Phys. JETP **30**, 1027 (1969)].
19. W. F. Brown, *Micromagnetics* (Interscience, New York, 1963; Nauka, Moscow, 1979).

Translated by G. Skrebtsov

Physics of the Solid State, Vol. 45, No. 4, 2003, pp. 714–717. Translated from Fizika Tverdogo Tela, Vol. 45, No. 4, 2003, pp. 681–684.

MAGNETISM AND FERROELECTRICITY

Magnetic and Orbital Structures of Manganites in the Electron Doping Region

S. M. Dunaevskiĭ and V. V. Deriglazov

St. Petersburg Nuclear Physics Institute, Russian Academy of Sciences, Leningradskaya oblast, Gatchina, 188350 Russia
e-mail: dunaevsk@mail.pnpi.spb.ru

Received August 26, 2002

Abstract—Total energies of various magnetic and orbital configurations of the $La_{1-y}Ca_yMnO_3$ manganites were calculated for the electron doping region $y > 0.5$ with inclusion of the manganese e_g level splitting. The state of the system was first established by total energy minimization in both the angle between the spins of neighboring Mn^{4+} ions and the two orbital-mixing angles defining the type of ordering in the system under study. The manganite phase diagrams constructed for $T = 0$ correctly reproduce the alternation of magnetic orbitally ordered structures, which is experimentally observed to occur with increasing electron concentration in the region of actual values of the Heisenberg interatomic exchange parameter, the Hund exchange parameter, and the hopping integral. © *2003 MAIK "Nauka/Interperiodica".*

1. INTRODUCTION

A specific feature in the physics of the $La_{1-y}Ca_yMnO_3$ manganites (y = 0–1) is the observed asymmetry of their phase diagrams with respect to the value $y = 0.5$ [1, 2], whose nature remains unclear. It was pointed out in [3] that one of the reasons for the asymmetry in the properties is the difference in the carrier spectra $E(\mathbf{k})$ of the antiferromagnetic (AFM) structures *A*, *G*, and *C*; this difference appears when orbital degeneracy of the e_g level is included in the double exchange model. It was shown in [4] that inclusion of orbital degeneracy not only causes the carrier spectrum $E(\mathbf{k})$ to change as one goes from one magnetic structure to another but also affects the conditions in which either collinear or canted (*A*, *G*, *C*, *F*) magnetic structures corresponding to the minimum of total energy form. To find the ground-state magnetic configuration of the system for a fixed value of $x = 1 - y$, the spectrum $E(\mathbf{k}, \theta)$ of carriers (electrons) in the canted *A*, *G*, *C*, and *F* magnetic structures, which depends on the angle θ between the spins of manganese ions located on different magnetic sublattices, had to be calculated. It should be noted that, in earlier publications [5–8], in calculating the energies of the AFM structures *A*, *G*, and *C*, the spectrum $E(\mathbf{k})$ derived for the ferromagnetic (FM) type of spin ordering ($\theta = 0$) was used with no total-energy minimization with respect to the angle θ made. Calculations in [4] yielded the experimentally observed phase alternation *G*–*C*–*A* with increasing carrier (electron) concentration in the region of actual values of the interatomic and intraatomic exchange. Correct qualitative description of the experimental data was attained only after taking into account the splitting of the manganese e_g level for the AFM structures *A* and *C* and assigning specific orbital ordering for each structure. In our present study, the type of orbital ordering (depending on distortions of the oxygen octahedron), rather than being specified, was found by minimizing the total energy with respect to the angle θ and two angles of orbital intraatomic mixing φ_i. In this way, the equilibrium magnetic and orbital configurations of the $La_{1-y}Ca_yMnO_3$ manganites were found for $T = 0$ and y = 0.5–1.

2. CALCULATION METHOD

This study deals with a calculation of the equilibrium magnetic and orbital manganite structures for T = 0 and y = 0.5–1; these conditions allow neglect of the intra- and interatomic Coulomb interactions in a first approximation.

We made use of an effective manganite Hamiltonian including double exchange, intraatomic Hund coupling of the e_g and t_{2g} electrons, the Heisenberg interaction between the local magnetic moments of t_{2g} electrons $\mathbf{S}_i$, and the Jahn–Teller splitting of the manganese e_g level:

$$H = \sum_{i\alpha\sigma} \varepsilon_{i\alpha\sigma} d^+_{i\alpha\sigma} d_{i\alpha\sigma} + \sum_{ij\alpha\beta\sigma'\sigma} t^{\sigma\sigma'}_{ij\alpha\beta} d^+_{i\alpha\sigma} d_{j\beta\sigma'} + \sum_{ij} J_{ij} \mathbf{S}_i \mathbf{S}_j + \sum_{i\alpha\beta\sigma} \Delta_i (d^+_{i\alpha\sigma} d^+_{i\beta\sigma}) \begin{pmatrix} \cos\varphi_i & \sin\varphi_i \\ \sin\varphi_i & -\cos\varphi_i \end{pmatrix} \begin{pmatrix} d_{i\alpha\sigma} \\ d_{i\beta\sigma} \end{pmatrix}. \quad (1)$$

The indices α and β label the e_g orbitals, *i* and *j* are indices numbering the atoms, $\varepsilon_{i\alpha\uparrow} = \varepsilon_{d\alpha} - J_H S$, $\varepsilon_{i\alpha\downarrow} = \varepsilon_{d\alpha} + J_H(S + 1)$, $\varepsilon_{d\alpha}$ is the energy of the unperturbed α-type e_g level of the Mn^{4+} ion, J_H is the intraatomic Hund integral (for Mn^{3+}, its calculated [3] value is 0.25 eV),

$d^{+}_{i\alpha\sigma}$ ($d_{i\alpha\sigma}$) are the creation (annihilation) operators of a α-type e_g electron at site i, σ is a spin index, $J_{ij} = J_{AFM}$ are the Heisenberg exchange integrals of localized t_{2g} electrons, and $t_{ij\alpha\beta}$ are the hopping integrals between the α and β orbitals of the ith and jth manganese ions. The explicit form of all hopping integrals for the atomic basis in which $|\alpha\rangle = |1\rangle = |z^2\rangle$ and $|\beta\rangle = |2\rangle = |x^2 - y^2\rangle$ can be found in [3]. In the double-exchange model, the hopping integral $t_{ij\alpha\beta}$ depends on the angle θ_{ij} between the local magnetic moments of the nearest neighbor manganese ions and the numerical value of t for manganites lies between 0.1 and 0.3 eV [3]. In the AFM structure G, $\theta_{ij} = \pi$ for the nearest neighbors. In the C structure, the Mn ion spins form FM chains perpendicular to the xy plane. In this plane, $\theta_{ij} = \theta_{xy} = \pi$, while in a chain, we have $\theta_{ij} = \theta_z = 0$. In the A structure, the adjacent FM planes, in which $\theta_{ij} = \theta_{xy} = 0$, are antiferromagnetically ordered with respect to one another, i.e., $\theta_{ij} = \theta_z = 0$, if the atoms labeled i and j belong to adjacent planes. In an FM structure, we always have $\theta_{ij} = 0$. In all the AFM structures considered here, the angle θ_{ij} can have only one nonzero value, because more complex AFM structures characterized by two different angles θ_{ij} have thus far not been observed experimentally in manganites. The parameter Δ_i describes the Jahn–Teller splitting of the originally degenerate e_g level. To take into account the effect of orbital ordering on the formation of a magnetic structure, we used an arbitrary atomic basis $|\alpha\rangle_i$ and $|\beta\rangle_i$ related to the original basis through the transformation

$$\begin{pmatrix} |\alpha\rangle_i \\ |\beta\rangle_i \end{pmatrix} = \begin{pmatrix} \cos\frac{\varphi_i}{2} & \sin\frac{\varphi_i}{2} \\ -\sin\frac{\varphi_i}{2} & \cos\frac{\varphi_i}{2} \end{pmatrix} \begin{pmatrix} |1\rangle_i \\ |2\rangle_i \end{pmatrix}, \qquad (2)$$

where φ_i is the intraatomic orbital-mixing angle. After such a transformation, the hopping integral $t_{ij\alpha\beta}$ becomes dependent on three angles: θ_{ij}, φ_i, and φ_j. Because this study deals with AFM structures consisting of only two magnetic sublattices, the possible orbital-ordering types coincide with the magnetic-configuration types (A, G, C, F). For instance, an orbital FM structure corresponds to only one mixing angle φ_i on all sites. In the AFM orbital structures A, G, and C, each sublattice is characterized by its orbital-mixing angle, φ_1 or φ_2, and the sublattices themselves are defined in the same way as are the magnetic configurations. Orbital structures are collinear for $\varphi_i = 0$ or π and canted for $\varphi_i \neq 0$.

Without the last term in the Hamiltonian (1), transformation (2) does not affect in any way the spectrum and total energy of the magnetic configurations. However, if the Jahn–Teller splitting of the e_g level is included, the electronic part of the total energy of the system becomes dependent on the type of orbital order (the values of φ_1 and φ_2). In $(La–Nd)_{1-y}Sr_yMnO_3$ (y = 0.52–0.62), experiments revealed the AFM structure A with a predominant occupation of $|2\rangle$-type orbitals. Furthermore, theory suggests [7, 10] that, in magnetic phase A, we have $2\Delta = \varepsilon_{d1} - \varepsilon_{d2} > 0$ (except in the case $y = 0$). The splitting for the magnetic phase C has the opposite sign [10]. The splitting 2Δ was accepted proportional to $x = 1 - y$ so as to obtain in the value $|\varepsilon_{d1} - \varepsilon_{d2}|$ = 0.3–0.5 eV [11] for the A phase of $LaMnO_3$ the limiting case of $y = 0$.

Numerical calculations were carried out for various electron concentrations $x = 1 - y$ and sets of the parameters J_H/t and J_{AFM}/t, where J_{AFM} = 1.5 meV (with no doping, T_N = 141 K for $CaMnO_3$). These results do not extend to a region in the immediate vicinity of the stoichiometric composition $x = 0.5$, because, in this study, we did not consider the magnetic CE structure related to charge ordering. The total energies of all configurations were minimized with respect to the corresponding angles θ and φ_i, thus yielding equilibrium magnetic and orbital structures for each value of the electron concentration.

The energy per manganese atom of phase G was calculated as

$$E_G(x, \theta, \varphi_1, \varphi_2) = -3J_{AFM}S^2\cos\theta + \int_{-\infty}^{\varepsilon_F} \varepsilon n_G(\varepsilon, \theta, \varphi_1, \varphi_2)d\varepsilon, \qquad (3)$$

where $S = 3/2$, ε_F is the Fermi level, and $n_G(\varepsilon, \theta, \varphi_1, \varphi_2)$ is the density of states in phase G. The density of states was found by summation of the $E(\mathbf{k}, \theta, \varphi_1, \varphi_2)$ spectrum over the corresponding Brillouin zone; this spectrum was calculated by diagonalizing the (8×8) Hamiltonian matrix [3] of the G structure modified by transformation (2). The total energies of all the other magnetic structures were calculated in a similar way [4].

3. RESULTS OF CALCULATIONS AND DISCUSSION

Figure 1 presents the band structures of the magnetic phases A and C. If the e_g level is not split (thick line), the band structure of both phases does not depend on the orbital-mixing angles. If the e_g level is split (Δ = 1), the electron bands undergo a change, depending on the actual type of orbital order. One readily sees that the $|x^2 - y^2\rangle$ FM orbital ordering for the A structure ($\varphi_{1,2} = \pi$, dotted line) is more favorable than the $|3z^2 - r^2\rangle$ ordering ($\varphi_{1,2} = 0$, thin solid line), while for the C structure, the reverse situation is true.

In the absence of free electrons, the magnetic phases can be arranged in order of increasing magnetic energy as G, C, A, and F. As x increases, competition between the kinetic and magnetic energies of the system realizes one of the magnetic states. Figure 2 displays phase diagrams of the $La_{1-y}Ca_yMnO_3$ system in the region x = 0–

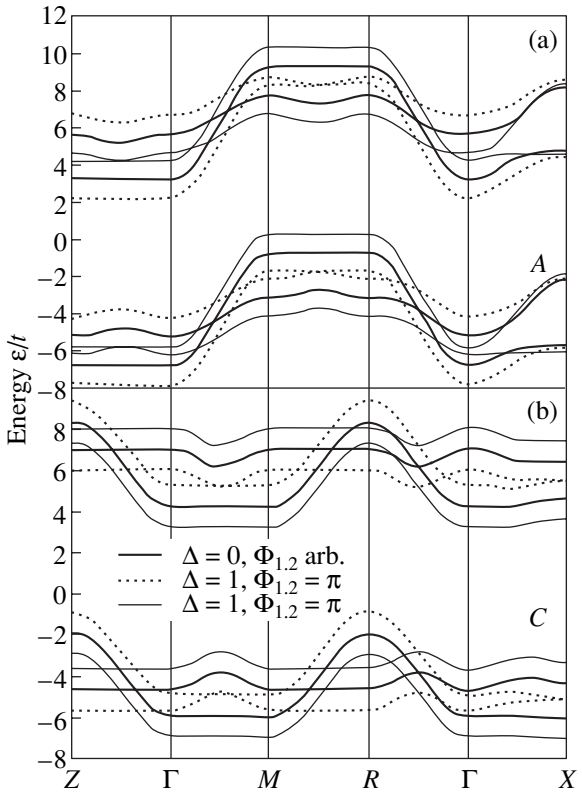

Fig. 1. Band structure of phases (a) *A* and (b) *C* for the cases of a degenerate e_g level (thick lines, $\Delta = 0$) and split e_g level ($\Delta = \pm t$) calculated for two types of ferromagnetic orbital order; $\varphi_{1,2} = 0$ (thin lines) and π (dots).

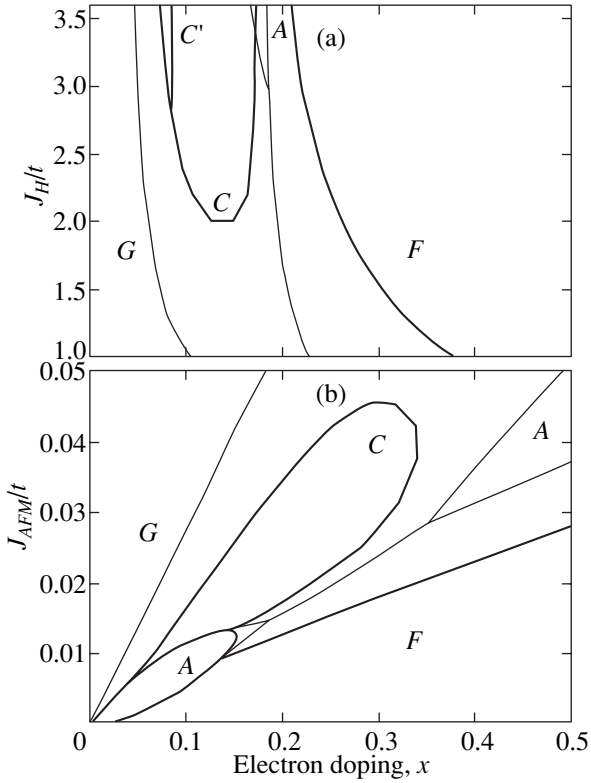

Fig. 2. Magnetic phase diagrams for the case of the degenerate e_g level ($\Delta = 0$) plotted in the (a) (J_H/t, x) and (b) (J_{AFM}/t, x) coordinates and calculated in the collinear approximation (thin lines) and with inclusion of canting (thick lines).

0.5 plotted for the unsplit e_g level in the (x, J_H/t) coordinates with the exchange parameter $J_{AFM} = 0.015t$ characteristic of $CaMnO_3$ at $t = 0.1$ eV and in the (x, J_{AFM}/t) coordinates for $J_H = 2.5t$. The thin lines identify phase boundaries in the collinear approximation, and the thick lines identify those with the possibility of spin canting. The FM phase is seen to be an equilibrium magnetic structure within a broad range of values of J_{AFM} and x. This is at odds with the experimental observation that for concentrations $x < 0.5$ the FM phase is encountered very rarely [9]. The magnetic phases usually observed in the electron doping region are *C* ($x \cong 0.1$–0.4) and *A* ($x \cong 0.4$–0.5) [12]. Calculations show that the "correct" phase alternation *G*–*C*–*A* with increasing x can occur in the collinear approximation only in the interval $0.033 < J_{AFM}/t < 0.043$, which corresponds to overly large values of J_{AFM}. Sublattice canting only aggravates the situation; indeed, the canted phase *G* displaces, to a large extent, the phases that are still collinear (with only one narrow region *C*' of canted phase *C* left at $x \cong 0.08$), with phase *A* completely disappearing in the intermediate doping region of $x > 0.4$. The corresponding canting angles for structure *G* are approximately proportional to x and reach 180° at the *G*–*F* boundary.

Figure 3 shows phase diagrams calculated with due account of the e_g level splitting, which is proportional to the electron concentration $2\Delta = 3tx$, and with optimization with respect to the spin angle θ and the orbital angles $\varphi_{1,2}$. Splitting changes the character of the phase diagrams dramatically. In the region $x \geq 0.4$, phase *A* again appears in the (x, J_H/t) diagram and the phase boundaries shift only slightly with increasing parameter J_H/t. As a result, the pattern of the (J_{AFM}/t, x) phase diagram becomes practically independent of J_H. In the canted *G* phase, FM orbital order of the type $|3z^2 - r^2\rangle$ ($\varphi_{1,2} = 0$) sets in. This ordering is threefold generate; indeed, the orbital orders $|3y^2 - r^2\rangle$ ($\varphi_{1,2} = 2\pi/3$) and $|3x^2 - r^2\rangle$ ($\varphi_{1,2} = 4\pi/3$) are equally probable. Phase *C* is collinear, with the exception of a small region *C*' with a $|3z^2 - r^2\rangle$ FM orbital order. The two collinear *A* phase regions featuring $|x^2 - y^2\rangle$ ($\varphi_{1,2} = \pi$) FM-type orbital order are connected by a narrow region *A*', where competition between orbital and spin ordering creates various combinations of the collinear or canted spin structure of type *A* with FM orbital order to which AFM orbital order may become admixed. The behavior of the canting angle ($\pi - \theta$) and of the orbital angles $\varphi_{1,2}$ along the dashed straight line passing through region *A*' is illustrated in the inset in the bottom panel of Fig. 3. The

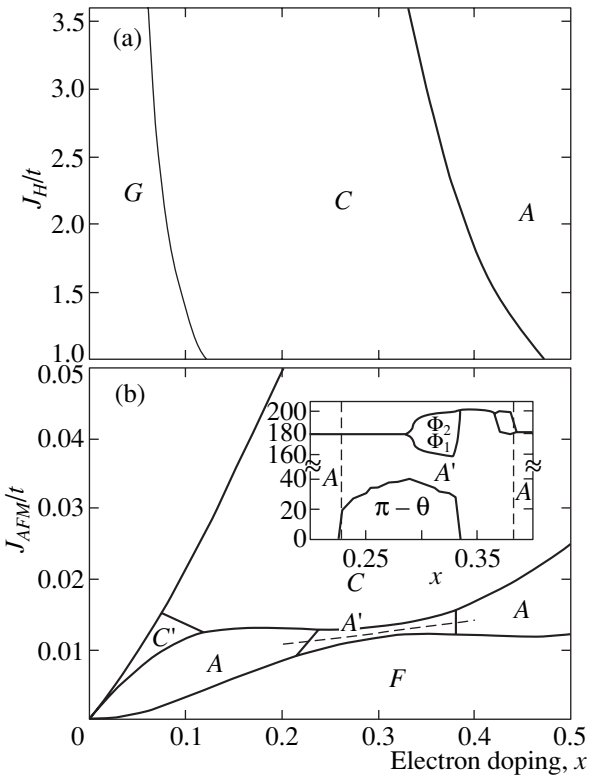

Fig. 3. Magnetic phase diagrams for the case of the degenerate e_g level ($\Delta \sim x$) plotted in the (a) (J_H/t, x) and (b) (J_{AFM}/t, x) coordinates; inset shows the doping dependence of the spin canting angle ($\pi - \theta$) and orbital mixing angles $\varphi_{1,2}$ along the dashed line passing through region A'.

FM orbital order of the FM phase F is similar to that of phase G.

The e_g level splitting stabilizes the magnetic and orbital orders, which are governed primarily by the magnitude of the splitting Δ and by its dependence on the degree of doping. In the region of actual values $0.013 < J_{AFM}/t < 0.02$, the alternation of the magnetic phases G–C–A and the position of phase boundaries agree well with experiment [9]. Numerical calculations also corroborate the experimentally observed collinearity of phases A and C, as follows, for instance, from data on neutron scattering in the A phase of $Nd_{1-y}Sr_yMnO_3$ ($y > 0.52$) [13] and in the C phase of $Sm_{1-y}Ca_yMnO_3$ ($y = 0.8$) [14].

4. CONCLUSIONS

Thus, we have presented results of numerical calculations of magnetic phase diagrams of manganites in the electron-doping range based on the dispersion relations $E(\mathbf{k})$ for the main types of antiferromagnetic ordering in manganites with due inclusion of the e_g level splitting, magnetic sublattice canting, and orbital ordering. The results obtained fit well enough to the available experimental data, namely, alternation of the magnetic structures with characteristic orbital order occurring with increasing x within the electron concentration range $x = 0$–0.5 for actual values of the intra- and interatomic exchange parameters.

ACKNOWLEDGMENTS

This study was supported by the Russian Foundation for Basic Research, (project no. 00-62-16729) and the Russia–Belarus Foundation, project no. 02-02-81012 Bel2002-a.

REFERENCES

1. S. Mori, C. H. Chen, and S. W. Cheong, Nature **392**, 473 (1998).
2. R. Maezono, S. Ishihara, and N. Nagaosa, Phys. Rev. B **57**, R13993 (1998).
3. S. M. Dunaevskiĭ, Fiz. Tverd. Tela (St. Petersburg) **43**, 2161 (2001) [Phys. Solid State **43**, 2257 (2001)].
4. S. M. Dunaevskiĭ and V. V. Deriglazov, Fiz. Tverd. Tela (St. Petersburg) **44** (12), 2169 (2002) [Phys. Solid State **44**, 2271 (2002)].
5. H. Shiba, R. Shina, and A. Takahashi, J. Phys. Soc. Jpn. **66**, 941 (1997).
6. J. van den Brink and D. Khomskii, Phys. Rev. Lett. **82**, 1016 (1999).
7. Liang-Jian Zou, Phys. Rev. B **63**, 155103 (2001).
8. G. Venketeswara Pai, Phys. Rev. B **63**, 064431 (2001).
9. T. Akimoto, Y. Maruyama, Y. Moritomo, *et al.*, Phys. Rev. B **57**, R5594 (1998).
10. R. Maezono, S. Ishihara, and N. Nagaosa, Phys. Rev. B **58**, 11583 (1998).
11. J. W. Liu, Z. Zeng, Q. Q. Zheng, and H. Q. Lin, Phys. Rev. B **60**, 12968 (1999).
12. R. Kajimoto, H. Yoshizawa, H. Kawano, *et al.*, Phys. Rev. B **60**, 9506 (1999).
13. H. Kawano, R. Kajimoto, H. Yoshizawa, *et al.*, Phys. Rev. Lett. **78**, 4253 (1997).
14. C. Autret, B. Raveau, M. Hervieu, *et al.*, J. Magn. Magn. Mater. (2002) (in press).

Translated by G. Skrebtsov

Physics of the Solid State, Vol. 45, No. 4, 2003, pp. 718–724. Translated from Fizika Tverdogo Tela, Vol. 45, No. 4, 2003, pp. 685–690.

LATTICE DYNAMICS AND PHASE TRANSITIONS

Resonance Fluorescence of Gamma Radiation under Conditions of Coherent Mixing of Mössbauer Sublevels

É. K. Sadykov, A. A. Yurichuk, and V. V. Arinin

Kazan State University, ul. Kremlevskaya 18, Kazan, 420008 Tatarstan, Russia

e-mail: esad@ksu.ru

Received June 18, 2002

Abstract—A method is proposed for calculating the resonance fluorescence spectrum of coherent gamma radiation with a finite linewidth under conditions when the sublevels of the ground nuclear state are coupled through a strong field. The spectrum line shape is substantially affected by both the coherent effects induced in the system by a strong field and the finite gamma-radiation width. The results obtained earlier and in this work give impetus to experimental investigations into the coherence of a quantum system and quantum interference of Mössbauer gamma transitions through the excitation of coherent magnetization dynamics or an optical subsystem in solids. © *2003 MAIK "Nauka/Interperiodica".*

1. INTRODUCTION

Mössbauer spectroscopy of materials in a coherently excited state is an important direction in solid-state physics [1, 2]. In recent years, considerable attention has been given to the study of the quantum interference phenomenon in the spectral region of Mössbauer transitions, which arises upon coherent excitation of the system and can be considered as a possible mechanism of inversionless amplification of gamma radiation [3–6]. In our previous work [7], we noted that coherence and quantum interference play a significant role in resonance fluorescence of gamma radiation. In particular, when the energy sublevels of an excited nuclear state are coupled by a strong radio-frequency or laser field, the intensity ratio of the spectral lines reemitted through these sublevels turns out to be very sensitive to the shape of the spectrum of pumping gamma radiation. The model described in [7] can be compared with the Σ or Λ model of a three-level system driven by two coherent fields (according to the classification accepted in optics [8, 9]). However, in the framework of our model, which includes two fields (for example, a gamma radiation field and a strong optical field) governed by different selection rules, this classification does not exhaust all possible experimental schemes. In this paper, we consider resonance fluorescence of gamma radiation in the case when the sublevels of the ground nuclear state are driven by a strong field (the *V* model). In [7], we ascertained that, for the Σ model, the measurements of the intensity ratio of lines in the scattering spectrum can provide more detailed data on the interference phenomena (coherence induced in the system) as compared to the analysis of the shape of the scattering spectrum. By contrast, in the case of the *V* model, it is this shape of the scattering spectrum that carries valuable information on the coherence in the system. The shape of the scattering spectrum, as in the model treated in [7], is determined, to a large extent, by the parameters of the pumping gamma radiation.

2. COMPUTATIONAL METHOD

Let us consider the *V* three-level model (Fig. 1). Levels *1* and *2* can be coupled through a radio-frequency or optical field, and levels *1* and *3* (*2* and *3*) are coupled by a gamma radiation field.

The density matrix for this system in the interaction representation satisfies the equation

$$\frac{d\hat{\rho}'}{dt} = -\frac{i}{\hbar}[\hat{H}'\hat{\rho}'] + \Lambda\hat{\rho}'. \quad (1)$$

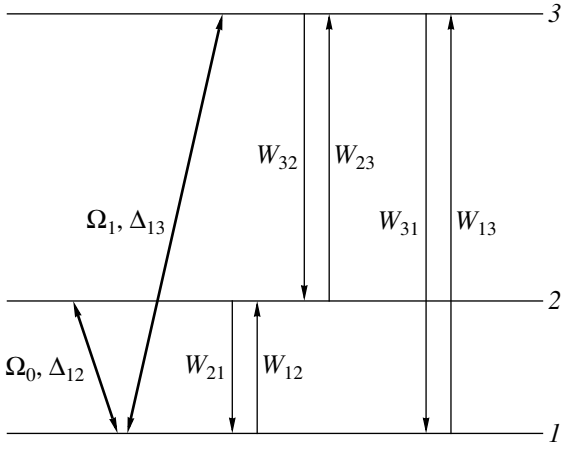

Fig. 1. Schematic representation of the *V* three-level model. Designations: W_{ij} are the parameters characterizing incoherent pumping radiation (W_{13}, W_{23}), spontaneous decay (W_{31}, W_{32}), and relaxation (W_{12}, W_{21}).

1063-7834/03/4504-0718$24.00 © 2003 MAIK "Nauka/Interperiodica"

Matrix **L** and vector **I** for the *V* three-level model

	1	2	3	4	5	6	7	8	**I**
1	$-\Gamma_{12}$	0	0	$-2i\Omega_0^*$	0	0	$-i\Omega_1^*$	$-i\Omega_0^*$	$i\Omega_1^*$
2	0	$-\Gamma_{13}$	0	$-i\Omega_1^*$	$-i\Omega_0^*$	0	0	$-2i\Omega_1^*$	$i\Omega_1^*$
3	0	0	$-\Gamma_{12}^*$	$2i\Omega_0$	$i\Omega_1$	0	0	$i\Omega_0$	$-i\Omega_0$
4	$-i\Omega_0$	0	$i\Omega_0^*$	$-(W_{12}+W_{21}+W_{23})$	0	0	0	$-(W_{12}-W_{32})$	W_{12}
5	0	$-i\Omega_0$	$i\Omega_1^*$	0	$-\Gamma_{23}$	0	0	0	0
6	0	0	0	$i\Omega_1$	0	$-\Gamma_{13}^*$	$i\Omega_0$	$2i\Omega_1$	$-i\Omega_1$
7	$-i\Omega_1$	0	0	0	0	$i\Omega_0^*$	$-\Gamma_{23}^*$	0	0
8	0	$-i\Omega_1$	0	$W_{23}-W_{13}$	0	$i\Omega_1^*$	0	$-(W_{31}+W_{32}+W_{13})$	W_{13}

Note: $\Gamma_{12} = (W_{12}+W_{13}+W_{21}+W_{23})/2 + i\Delta_{12}$, $\Gamma_3 = (W_{12}+W_{13}+W_{31}+W_{32})/2 + i\Delta_{13}$, and $\Delta_{23} = (W_{21}+W_{23}+W_{31}+W_{32})/2 + i(\Delta_{13}-\Delta_{12})$.

In this equation, the Hamiltonian $\hat{H}'$ is defined as

$$\hat{H}' = \exp(i\hat{H}_0 t/\hbar)(\hat{H}^d + \hat{H}^p)\exp(-i\hat{H}_0 t/\hbar), \quad (2)$$

where $\hat{H}_0$ is the zeroth-approximation Hamiltonian, $\hat{H}^d$ is the strong radio-frequency (or laser) field, and $\hat{H}^p$ is the pump field. According to [8, 9], we can write

$$\hat{H}_0 = \hbar\sum_{i=1}^{3}\varepsilon_i\hat{a}_i^+\hat{a}_i, \quad (3)$$

$$\hat{H}^d = \hbar\Omega_0\exp(-\omega_0 t)\hat{a}_2^+\hat{a}_1 + \hbar\Omega_0^*\exp(i\omega_0 t)\hat{a}_1^+\hat{a}_2, \quad (4)$$

$$\begin{aligned}\hat{H}^p = \hbar[&\Omega_1\exp(i\theta(t))\hat{a}_3^+\hat{a}_1\exp(-i\omega_1 t)\\ &+ \Omega_1^*\exp(-i\theta(t))\hat{a}_1^+\hat{a}_3\exp(i\omega_1 t)].\end{aligned} \quad (5)$$

Here, $\hat{a}_i$ and $\hat{a}_i^+$ are the Fermi operators and Ω_0 and Ω_1 are the amplitudes of the strong and pump fields, respectively, which are multiplied by the relevant matrix elements of the transitions.

In expression (5), the phase of the pump field is assumed to fluctuate and $\theta(t)$ is a random function governed by a Wiener–Levy process. The line shape of this field can be described by a Lorentzian function of width $2D$, which is determined from the relationship [10, 11]

$$\langle\dot{\theta}(t)\dot{\theta}(t')\rangle = 2D\delta(t-t'). \quad (6)$$

Preparatory to solving Eq. (1) with the interaction given by expression (5), we will first write out a solution to this equation in the case when expression (5) describes an interaction without fluctuations (see [8]); that is,

$$\frac{d}{dt}\mathbf{\Psi} = \mathbf{L}\mathbf{\Psi} + \mathbf{I}. \quad (7)$$

Here, **L** and **I** are a constant matrix and a constant vector, respectively (see table), which depend on Ω_0, Ω_1, and the parameters of irreversible processes [the second term in Eq. (1)]; and $\mathbf{\Psi}$ is a column vector with the following components:

$$\begin{aligned}\Psi_1 = \rho'_{12}\exp(-i\Delta_{12}t), \quad \Psi_2 = \rho'_{13}\exp(-i\Delta_{13}t),\\ \Psi_3 = \rho'_{21}\exp(i\Delta_{12}t), \quad \Psi_4 = \rho'_{22},\\ \Psi_5 = \rho'_{23}\exp(i(\Delta_{12}-\Delta_{13})t), \quad \Psi_6 = \rho'_{31}\exp(i\Delta_{13}t),\\ \Psi_7 = \rho'_{32}\exp(i(\Delta_{13}-\Delta_{12})t), \quad \Psi_8 = \rho'_{33}.\end{aligned} \quad (8)$$

In these relationships, $\Delta_{12} = \omega_0 - \varepsilon_2 + \varepsilon_1$ and $\Delta_{13} = \omega_1 - \varepsilon_3 + \varepsilon_1$ are the detunings of the frequencies ω_0 and ω_1 with respect to the corresponding resonance frequencies. Hereafter, all the frequencies will be given in units of W_{31} and the calculations will be performed under the condition $\varepsilon_2 - \varepsilon_2 = 30$ (Fig. 1).

As was shown by Narducci *et al.* [8], it is these solutions to Eq. (7) that make it possible to calculate the correlation functions for the polarization operators and, hence, the spectrum of spontaneous emission and the absorption spectrum of probe radiation.

The spectrum of spontaneous emission associated with a $j \longrightarrow i$ transition is given by the Fourier transform of the two-time correlation function:

$$\gamma(\tau_1, \tau_0) \propto \langle\hat{P}^{(-)}(\tau_1)\hat{P}^{(+)}(\tau_0)\rangle, \quad (9)$$

where $\hat{P}^{(+)} = \mu_{ij}\hat{a}_i^+\hat{a}_j$ is the positive part of the polarization operator.

The correlation function defined by Eq. (9) can be calculated using the quantum-regression theorem. For

this purpose, with the use of the solutions to Eq. (7), we first calculate the one-time average:

$$\langle \hat{P}^{(-)}(\tau_1)\rangle = \mathrm{Tr}[\mu_{ij}\hat{a}_j^+\hat{a}_i\hat{\rho}] = \mu_{13}\exp(i\omega_1\tau_1)\Psi_2(\tau_1) + \mu_{23}\exp(i\omega_1\tau_1 - i\omega_0\tau_1)\Psi_5(\tau_1). \quad (10)$$

When interaction (5) characterized by a pump field with a fluctuating phase is included in Eq. (1), the form of Eq. (7) is substantially changed; that is,

$$\frac{d}{dt}\mathbf{\Psi}' = [\mathbf{L} - i\theta(t)\mathbf{L}']\mathbf{\Psi}' + \mathbf{I}\exp(-i\dot{\theta}(t)). \quad (11)$$

The quantities $\Psi_2(\tau_1)$ and $\Psi_5(\tau_1)$, which are necessary for calculating the one-time average (10), are the components of the vector $\mathbf{\Psi}'$ (Ψ_1^-, Ψ_2, Ψ_3^-, Ψ_4^-, Ψ_5, Ψ_6^{--}, Ψ_7^{--}, Ψ_8^-). In turn, these components are determined by the components involved in expressions (8):

$$\Psi_i^- = \Psi_i\exp(-i\theta(t)), \quad \Psi_i^+ = \Psi_i\exp(i\theta(t)), \quad \Psi_i^{--} = \Psi_i\exp(-2i\theta(t)). \quad (12)$$

The matrix $\mathbf{L}$ and vector $\mathbf{I}$ in Eq. (11) are identical to those in Eq. (7). The diagonal matrix $\mathbf{L}'$ has the following nonzero components: $L'_{6,6} = L'_{7,7} = -2$, $L'_{1,1} = L'_{3,3} = L'_{4,4} = L'_{8,8} = -1$.

Equation (11) is a stochastic differential equation. After averaging over the stochastic variables, this equation takes the form [10, 11]

$$\frac{d}{dt}\langle\mathbf{\Psi}'\rangle = [\mathbf{L} - D(\mathbf{L}')^2]\langle\mathbf{\Psi}'\rangle + \mathbf{I}\langle\exp(-i\theta(t))\rangle = \mathbf{L}_1\langle\mathbf{\Psi}'\rangle + \mathbf{I}\langle\exp(-i\theta(t))\rangle. \quad (13)$$

A solution to this equation can be written in the following form (hereafter, we will drop the stochastic-average sign for the quantities $\mathbf{\Psi}'$):

$$\mathbf{\Psi}'(\tau_1) = \exp[\mathbf{L}_1(\tau_1 - \tau_0)]\mathbf{\Psi}'(\tau_0) + \int_{\tau_0}^{\tau_1} d\tau'\exp[\mathbf{L}_1(\tau_1 - \tau')]\mathbf{I}\langle\exp(-i\theta(\tau'))\rangle. \quad (14)$$

By making the substitution of the variables $\tau = \tau_1 - \tau_0$ and $\tau'' = \tau' - \tau_0$ and using the relationship $\langle\exp(-i\theta(\tau'))\rangle = \exp(-D(\tau' - \tau_0))\langle\exp(-i\theta(\tau_0))\rangle$, we obtain

$$\mathbf{\Psi}'(\tau) = \exp[\mathbf{L}_1\tau]\mathbf{\Psi}'(\tau_0) + \int_0^{\tau} d\tau''\exp[\mathbf{L}_1(\tau - \tau'')] \times \exp(-\mathbf{D}\tau'')\mathbf{I}\langle\exp(-i\theta(\tau_0))\rangle = \exp[\mathbf{L}_1\tau]\mathbf{\Psi}'(\tau_0) + \frac{\exp(\mathbf{L}_1\tau) - \exp(-\mathbf{D}\tau)}{\mathbf{L}_1 + \mathbf{D}} \times \mathbf{I}\langle\exp(-i\theta(\tau_0))\rangle. \quad (15)$$

Here, $\mathbf{D}$ is the number D multiplied by the unit matrix of the same order as that of the matrix $\mathbf{L}$.

The quantities $\Psi'_j(\tau_0)$ can be expressed in terms of the system operators at the instant of time $\tau = \tau_0$. For example, we have

$$\Psi'_2(\tau_0) = \langle\exp(-i\omega_1\tau_0)\rho_{13}(\tau_0)\rangle = \langle\exp(-i\omega_1\tau_0)\langle|3\rangle\langle 1|\rangle_{\tau_0}\rangle. \quad (16)$$

The two-time average $\langle\langle\hat{P}^{(-)}(\tau_1)\hat{P}^{(+)}(\tau_0)\rangle\rangle$ [see expression (9)], which is now also subjected to stochastic averaging, can be calculated from $\langle\langle\hat{P}^{(-)}(\tau_1)\rangle\rangle$ with the use of the quantum-regression theorem by substituting $\langle\langle|i\rangle\langle j|\hat{P}^{(+)}(\tau_0)\rangle_{\tau_0}\rangle$ and $\langle\exp(-i\theta(\tau_0))\hat{P}^{(+)}(\tau_0)\rangle$ for $\langle\langle|i\rangle\langle j|\rangle_{\tau_0}\rangle$ and $\langle\exp(-i\theta(\tau_0))\rangle$, respectively. This substitution leads to the appearance of variables that are not involved in the vector $\mathbf{\Psi}'$. In order to determine these variables, we introduce the vector $\mathbf{\Psi}''$ (Ψ_1, Ψ_2^+, Ψ_3, Ψ_4, Ψ_5^+, Ψ_6^-, Ψ_7^-, Ψ_8), which satisfies the matrix equation

$$\frac{d}{dt}\langle\mathbf{\Psi}''\rangle = [\mathbf{L} - D(\mathbf{L}'')^2]\langle\mathbf{\Psi}''\rangle + \mathbf{I} = \mathbf{L}_2\langle\mathbf{\Psi}''\rangle + \mathbf{I}. \quad (17)$$

Here, $\mathbf{L}''$ is a diagonal matrix with the following nonzero elements: $L''_{2,2} = L''_{5,5} = 1$, $L''_{6,6} = L''_{7,7} = -1$.

Since we consider the stationary case (the steady-state conditions), it is necessary to find an asymptotic solution to Eq. (17). For this purpose, we take the limit $\tau_0, \tau_1 \longrightarrow \infty$ in such a way that the difference $\tau = \tau_1 - \tau_0$ is finite.

Next, we take the Laplace transform of the sought correlation function in Eq. (9). The emission spectrum is proportional to the real part of the expression thus obtained; that is,

$$S(\omega) \propto S_1(\omega) + S_2(\omega), \quad (18)$$

where

$$S_1(\omega) = \mathrm{Re}\left[\sum_{j=1}^{2} M_{2j}(z_1)\Psi''_{j+6}(\infty) + \sum_{j=1}^{8} N_{2j}(z_1)I_j\Psi''_6(\infty)\right],$$

$$S_2(\omega) = \mathrm{Re}\left[\sum_{j=3}^{5} M_{5j}(z_2)\Psi''_{j+3}(\infty) + \sum_{j=1}^{8} N_{5j}(z_2)I_j\Psi''_7(\infty)\right].$$

Here, we introduced the following notation: $\mathbf{M}(z) = (\mathbf{z} - \mathbf{L}_1)^{-1}$, $\mathbf{\Psi}''(\infty) = \mathbf{L}_2^{-1}\mathbf{I}$, $\mathbf{N}(z) = (\mathbf{L}_1 + \mathbf{D})^{-1}[(\mathbf{z} - \mathbf{L}_1)^{-1} - (\mathbf{z} + \mathbf{D})^{-1}]$; $\mathbf{z}$ is equal to z multiplied by the unit matrix of the

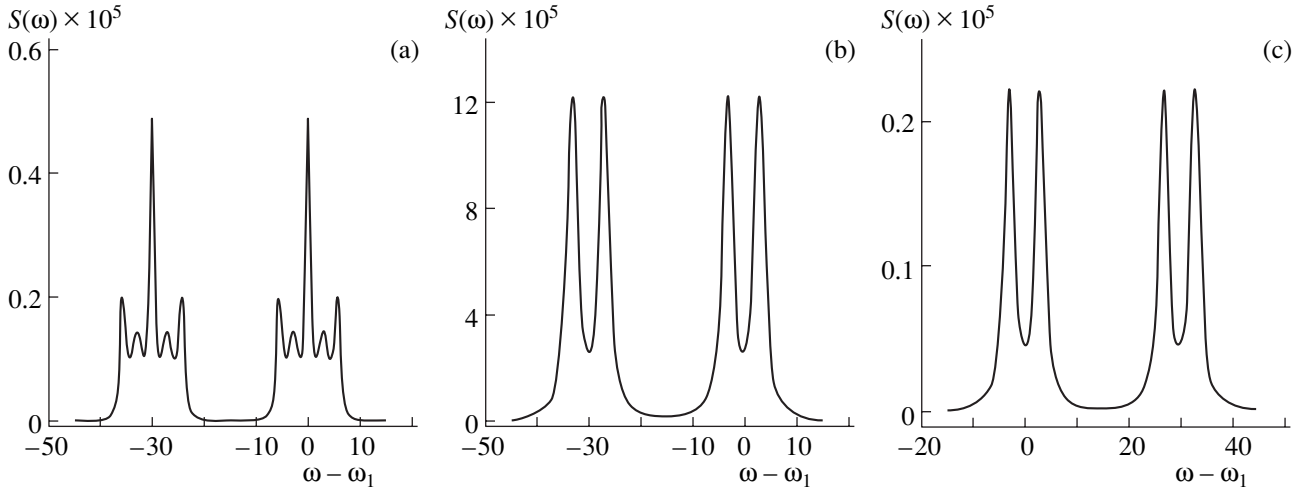

Fig. 2. Resonant scattering spectra $S = S_1 + S_2$: (a) $\Omega_1 = 0.01$, $\Omega_0 = 3$, $\Omega_1 = 0.01$, $\Omega_0 = 3$, $\Delta_{13} = \Delta_{12} = 0$, $W_{31} = W_{32} = 1$, $W_{21} = W_{12} = 0.1$, and $D = 0.5$; (b) $W_{13} = 0.01$, $\Omega_1 = 0$, $\Omega_0 = 3$, $\Delta_{13} = \Delta_{12} = 0$, $W_{31} = W_{32} = 1$, and $W_{21} = W_{12} = 0.1$; and (c) the same parameters as for panel (a) but at $D = 10$.

same order as that of the matrix **L**, $z_1 = i(\omega - \omega_1)$, and $z_2 = i(\omega - (\omega_1 - \omega_0))$.

It is known that, in the two-level approximation, the resonance fluorescence spectrum of coherent radiation can be represented as the sum of nonshifted and shifted scattering components [12] (with a delta-shape spectrum and a spectrum with a finite linewidth, respectively). A delta-shaped line in the scattering spectrum is also observed upon coherent pumping of the three-level system (for the *1–3* transition in Fig. 1). The algorithm proposed earlier in [8, 9] for numerical calculations disregards similar lines and describes only the spectrum of the shifted scattering component. Such an approach was justified for the problem solved by the authors in [8, 9], who analyzed the influence of quantum interference on the shape of spectral lines. It must also be remembered that the results of these calculations should be compared with experimental data after the contribution of the nonshifted scattering component is eliminated (see, for example, [13]). For pumping radiation with a finite linewidth, the scattering spectrum contains no delta-shaped component and corresponds to the experimentally observed spectrum. This is the principal feature of the technique developed in the present work (and in [7]). In the case of the formal substitution $D = 0$, this technique is reduced to the computational algorithm proposed in [8, 9].

3. RESULTS AND DISCUSSION

We are interested in elucidating the influence of the coherent mixing of states *1* and *2* (Fig. 1) on the resonant scattering gamma-ray spectrum associated with the *1–3* transition. The shape of the spectrum depends on the linewidth *D* of pumping radiation. Figure 2a displays the resonant scattering spectrum $S = S_1 + S_2$ that should be observed in the general case. In what follows, we will ignore the difference between the angular dependences of the intensities of the *3–1* (S_1) and *3–2* (S_2) transitions. The quintuplet structure of the spectra S_1 and S_2 is most likely attributed to both the coherence induced in the system by the coherent field Ω_0 and the coherence (partial) of the pump field. In order to justify this inference, we consider the spectra calculated under the assumption of incoherent pumping ($W_{13} \neq 0$, $\Omega_1 = 0$, Fig. 2b) and in the case when the linewidth *D* is relatively large ($W_{13} = 0$, $\Omega_1 \neq 0$, Fig. 2c). In both cases, the spectra consist of two doublets corresponding to the $3 \longrightarrow 1$ and $3 \longrightarrow 2$ transitions with Lorentzian lines of unit width (in the units used). These lines are shifted with respect to the centers of the doublets by the Rabi frequency ($\pm\Omega_0$). According to Zhu *et al.* [14], this result suggests the occurrence of coherence induced in the system by the coherent field Ω_0 rather than quantum interference due to gamma transitions. A comparison of the spectra shown in Figs. 2a–2c allows us to assume that the additional triplet structure observed in Fig. 2a most probably arises from coherence (and, hence, from monochromaticity) of probe radiation. In our opinion, the scattering spectrum displayed in Fig. 2a can be observed experimentally by using conventional Mössbauer spectroscopy in a strong field Ω_0 induced in the system [2, 4, 5] according to the method proposed by Artem'ev *et al.* [15]. It is these experimental conditions that correspond to the parameters used in our model for calculating the spectrum shown in Fig. 2a. Observations of the predicted spectra in Mössbauer experiments would mean that the Mössbauer radiation could play a particular role in the study of the coherence and quantum interference effects associated with Mössbauer gamma transitions, because there are no currently avail-

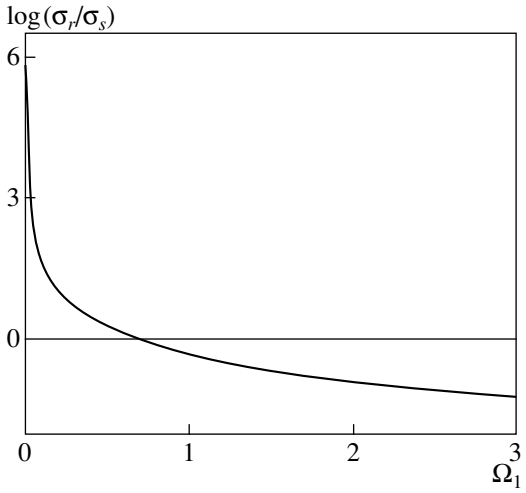

Fig. 3. Dependence of the ratio of the Rayleigh scattering intensity σ_r to the spontaneous scattering intensity σ_s on Ω_1 in the two-level approximation (calculations are performed according to the formulas taken from [17]).

able sources of coherent gamma radiation in this spectral region.

Deeper insight into the mechanism responsible for the specific features in the resonant scattering spectrum (Fig. 2a) can be gained by varying the parameters of the proposed model.

The conditions $W_{32} = 0$, $\Omega_0 = 0$, and $D = 0$ coincide with the conditions corresponding to the Mollow classical model [16]. Mollow was the first to treat a two-level system in a strong field and revealed a substantial change in the shape of the spectral lines. The basic result obtained in [16] lies in the fact that the scattering spectrum of coherent radiation with the amplitude Ω_1 (hereafter, we will assume that $D = 0$, unless otherwise specified) can be represented, according to the classification proposed in [17], as the sum of the Rayleigh (delta-shaped) and spontaneous scattering components (the nonshifted and shifted scattering components, respectively [12]). Note that the relative intensities of these components depend on the amplitude Ω_1. For small and large amplitudes Ω_1, the main contributions to scattering are predominantly made by the Rayleigh and spontaneous components, respectively (Fig. 3). It is believed that the spontaneous radiation, unlike its trivial manifestation in the Weisskopf–Wigner model, reflects the coherent dynamics of the quantum system in strong fields. In the limit of large amplitudes Ω_1, the spontaneous spectral component has a specific (triplet) shape. In the triplet, the separation between the lines is equal to $2\Omega_1$ and the width ratio of the central and satellite lines is 1 : 1.5 (Fig. 4a).

If the ground state of the two-level system is coupled to the third level (level *2* in Fig. 1) through a coherent field (i.e., at $\Omega_0 \neq 0$), we obtain the *V* model, which is well known in optics and was first studied by Narducci *et al.* [8]. The situation where $\Omega_1 > 1$ is most interesting from the optical standpoint. In this case, the spectrum also contains a triplet and is associated primarily with the spontaneous scattering. The separation between the triplet components is equal to twice the effective Rabi frequency $\Omega = \sqrt{\Omega_1^2 + \Omega_0^2}$. The surprising result obtained in [8] resides in an anomalous narrowing of the spectrum of spontaneous emission due to the *3–1* transition when the decay constant of state *2* is appreciably smaller than that of state *3* and $\Omega_0 \gg \Omega_1$. In [8], this phenomenon was explained by the suppression of the effect of vacuum fluctuations on the linewidth cor-

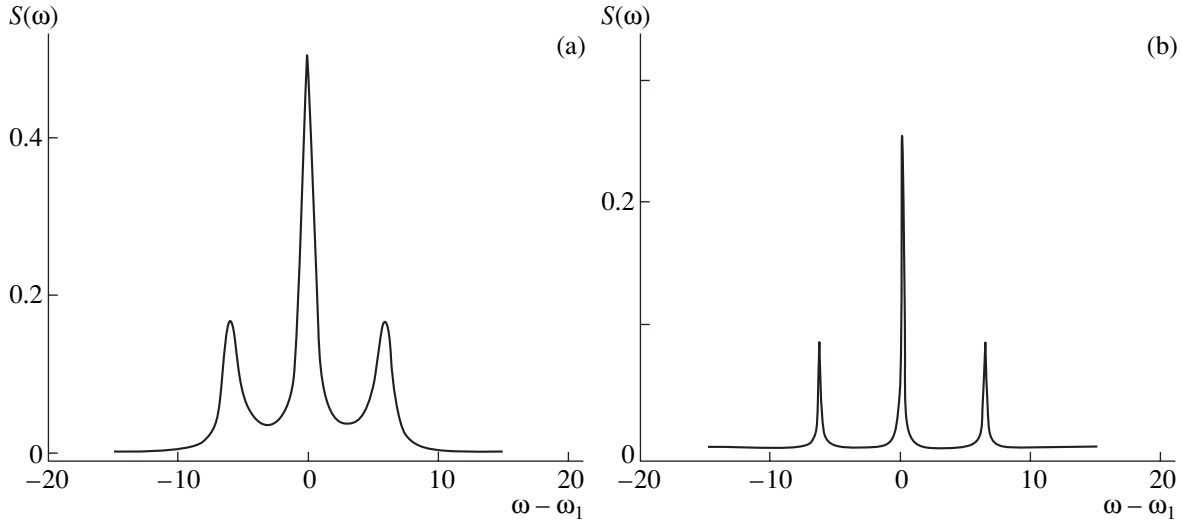

Fig. 4. Spontaneous scattering spectra (the *3–1* transition) calculated within (a) the two-level approximation ($\Omega_1 = 3$, $D = 0$, $W_{31} = 1$, $W_{32} = 0$, $W_{12} = 0$, $\Omega_0 = 0$) and (b) the *V* three-level model ($\Omega_1 = 1$, $\Omega_0 = 3$, $\Delta_{13} = \Delta_{12} = 0$, $W_{31} = 1$, $W_{32} = 0$, $W_{21} = 0.1$, $W_{12} = 0$, and $D = 0$).

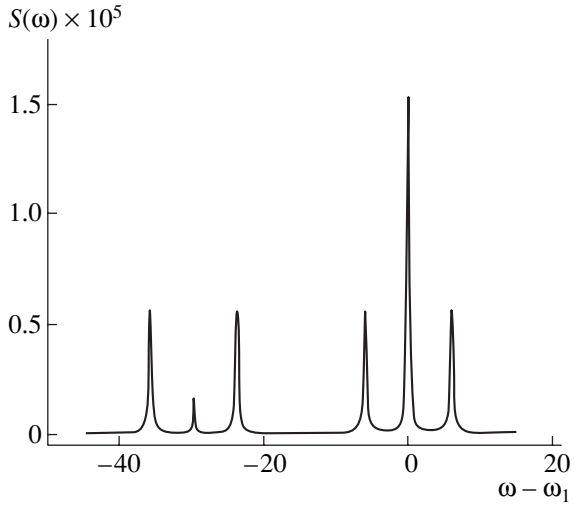

Fig. 5. Resonant scattering spectrum at a low intensity of the pump field. $\Omega_1 = 0.01$, $\Omega_0 = 3$, $\Delta_{13} = \Delta_{12} = 0$, $W_{31} = W_{32} = 1$, $W_{21} = 0.3$, $D = 0$, and $W_{12} = 0$.

responding to the *3–1* transition. Note that the width ratio of the triplet lines in this case is also equal to 1 : 1.5 at $W_{32} = 0$ (Fig. 4b) but becomes invalid at $W_{32} \neq 0$ [8]. The line narrowing revealed by the numerical method was interpreted in terms of the dressed-state model [8]. This interpretation is also applicable in the case where $\Omega_1 \ll 1$, provided the amplitude Ω is considerably larger than the decay constant $W_{31} = 1$. However, the case $\Omega_1 \ll 1$ is not particularly interesting because the dominant contribution to the scattering is made by the Rayleigh component (Fig. 3), whereas the triplet structure studied in [8] is caused by the spontaneous scattering component.

When analyzing the gamma-ray scattering, first and foremost, it is reasonable to consider the case of small amplitudes Ω_1 when the spontaneous scattering makes an insignificant contribution to the scattering associated with the *3–1* and *3–2* transitions. The spectra attributed to these transitions also have a triplet structure (Fig. 5), in which the separation between the components is equal to 2Ω and the width ratio is 1 : 1.5. The widths of these lines are determined by the values of W_{21} and can be noticeably less than W_{31}. However, this triplet does not arise from the narrowing of the spontaneous scattering spectrum (as in [8]) but is due to a broadening of the Rayleigh component. Unlike the Mollow model [16], the broadening of the delta-shaped spectrum stems from the uncertainty in the energy of state *2* (W_{21}) (the spontaneous Raman scattering *1–3–2*) and the finite width of level *1* (owing to the *1–2* resonant coupling). For $\Omega_0 = 0$, the spontaneous Raman scattering spectrum is also characterized by a finite linewidth (W_{21}).

At $D \neq 0$, there occurs an additional broadening of the triplet lines and the width ratio of these lines is not equal to 1 : 1.5. The nonzero value of D also implies a disturbance in the pumping coherence. As a consequence, the spectrum exhibits a doublet against the background of the triplet (as in Fig. 2a). The doublet is formed by Lorentzian lines of natural width according to the mechanism described for the spectrum shown in Fig. 2b.

4. CONCLUSIONS

Based on the data obtained in [7, 18, 19], we proposed a model of resonance fluorescence of gamma radiation with a finite linewidth in the case when the sublevels of the ground nuclear state are coupled through a strong field. Under these conditions, the shape of the scattering spectrum is associated with both the formation of dressed states in the system of nuclear sublevels and the finite linewidth of pumping radiation. The results obtained in this work and in [7] demonstrated that effects of a strong field in solids (including quantum interference effects in the gamma-ray spectral region) can be efficiently investigated using conventional Mössbauer spectroscopy.

ACKNOWLEDGMENTS

This work was supported by the Russian Foundation for Basic Research (project no. 01-02-17502), NIOKR RT (project no. 06-6.1-21/2001) (F), the American Civilian Research and Development Foundation for the Independent States of the Former Soviet Union (CRDF) (project no. REC 007), and UR (project no. 02.01.021).

REFERENCES

1. J. K. Srivastava, *Advances in Mössbauer Spectroscopy* (Elsevier, Amsterdam, 1983).
2. E. K. Sadykov, A. G. Isavnin, and A. I. Skvortsov, Hyperfine Interact. **107**, 257 (1997).
3. R. Coussement, M. van den Bergh, G. S'heeren, *et al.*, Phys. Rev. Lett. **71** (12), 1824 (1993).
4. O. A. Kocharovskaya, R. L. Kolesov, and Yu. V. Rostovtsev, Phys. Rev. Lett. **82** (23), 3593 (1999).
5. R. N. Shakhmuratov, A. Szabo, G. Kozyreff, *et al.*, Phys. Rev. A **62**, 043405 (2000).
6. E. K. Sadykov, L. L. Zakirov, and A. A. Yurichuk, Laser Phys. **11** (3), 409 (2001).
7. É. K. Sadykov, L. L. Zakirov, A. A. Yurichuk, and V. V. Arinin, Fiz. Tverd. Tela (St. Petersburg) **44** (8), 1439 (2002) [Phys. Solid State **44**, 1505 (2002)].
8. L. M. Narducci, M. O. Scully, G.-L. Oppo, *et al.*, Phys. Rev. A **42** (3), 1630 (1990).
9. A. S. Manka, H. M. Doss, L. M. Narducci, *et al.*, Phys. Rev. A **43** (7), 3748 (1991).
10. J. Gea-Banacloche and M. S. Zubairy, Phys. Rev. A **42** (3), 1742 (1990).
11. A. H. Toor, S.-Y. Zhu, and M. S. Zubairy, Phys. Rev. A **52** (6), 4803 (1995).

12. N. B. Delone and V. P. Kraĭnov, *Atom in a Strong Light Field* (Atomizdat, Moscow, 1978).
13. D. J. Gauthier, Y. Zhu, and T. W. Mossberg, Phys. Rev. Lett. **66** (19), 2460 (1991).
14. S.-Y. Zhu, L. M. Narducci, and M. O. Scully, Phys. Rev. A **52** (6), 4791 (1995).
15. A. M. Artem'ev, G. V. Smirnov, and E. P. Stepanov, Zh. Éksp. Teor. Fiz. **54** (3), 1028 (1968) [Sov. Phys. JETP **27**, 547 (1968)].
16. B. R. Mollow, Phys. Rev. **188** (5), 1969 (1969).
17. M. O. Scully and M. S. Zubairy, *Quantum Optics* (Cambridge Univ. Press, Cambridge, 1997).
18. Sh. Sh. Bashkirov, A. L. Beljanin, and E. K. Sadykov, Phys. Status Solidi B **93** (2), 437 (1979).
19. A. V. Mitin, Phys. Lett. A **84** (5), 283 (1981).

Translated by O. Borovik-Romanova

Physics of the Solid State, Vol. 45, No. 4, 2003, pp. 725–729. Translated from Fizika Tverdogo Tela, Vol. 45, No. 4, 2003, pp. 691–695.

LATTICE DYNAMICS AND PHASE TRANSITIONS

Effect of Phonon Decay Processes on the Formation of a Phonon Nonequilibrium Signal in Crystals with Two Two-Level Subsystems

E. I. Salamatov

Physicotechnical Institute, Ural Division, Russian Academy of Sciences, ul. Kirova 132, Izhevsk, 426000 Russia
e-mail: salam@otf.fti.udmurtia.su

Received July 10, 2002

Abstract—The effect of phonon decay on the characteristic propagation time and shape of a phonon nonequilibrium signal in disordered crystals, including crystals containing inelastic phonon scattering centers, is studied theoretically. Attention is focused on slow processes, which are typical of yttrium–aluminum garnet solid solutions and erbium-doped aluminates. It is shown that the temperature dependence of the arrival time of a phonon nonequilibrium signal in these systems can be governed, to a considerable extent, by phonon–phonon interactions. The results of the theoretical studies are compared with experimental data on the propagation of weakly nonequilibrium thermal phonons in solid solutions of rare-earth yttrium–aluminum garnets and aluminates. © *2003 MAIK "Nauka/Interperiodica".*

1. INTRODUCTION

Propagation of weakly nonequilibrium phonons injected by a warm generator ($S/T \ll 1$, where S is the amount by which the temperature of the generator exceeds that of the bath T) into a disordered crystal is determined, in general, by many factors depending on the actual experimental conditions, defect structure of the object under study, and the properties of its phonon subsystem [1–4]. The part played by phonon–phonon interaction in the propagation of phonons in disordered crystals has been dealt with in many theoretical and experimental publications [5–9]. It is presently well known that, in the case of strong anharmonicity, propagation of nonequilibrium phonons is not purely diffusive, i.e., is not characterized by a quadratic dependence of the arrival time of the maximum in the phonon nonequilibrium signal to the bolometer on sample length ($t_m \sim L^2$). It has been shown [5–7] that if phonon decay processes dominate in an anharmonic system, i.e., if the nonequilibrium-phonon occupation numbers $n(\omega) \ll 1$, then quasi-diffusion sets in, for which $t_m \sim L^{10/9}$ [5]. If, in addition to photon decay, phonon merging also plays a noticeable role [in the case of $n(\omega) \gg 1$], nonlocal phonon thermal conductivity may become realized, in which case $t_m \sim L^{8/5}$ [7].

These relations were derived under the assumption of defects in crystals acting as centers of elastic phonon scattering. This work was aimed at investigating systems which would also allow inelastic scattering associated with trapping centers of nonequilibrium phonons. Our earlier publication [10] proposed a theoretical model to describe the propagation of heat pulses in $Y_{3-x}Er_xAl_5O_{12}$ solid solutions, where paramagnetic erbium atoms act as phonon trapping centers. This model provided an explanation for the strong slowing down (by up to two orders of magnitude) of diffusive phonon propagation in these systems and permitted a description of the main anomalies in the temperature and concentration dependences of the time of signal arrival to the bolometer. While the phonon–phonon interaction effects were disregarded in [10], it was pointed out that the role of phonon–phonon interaction in slow heat-pulse propagation should be more significant than in the case of elastic phonon scattering only, because the heat pulse propagation time becomes comparable in magnitude to the characteristic lifetime of phonons governed by their anharmonicity. This study uses the model of [10] to investigate the effect of phonon–phonon interaction on the signal shape and the time of signal arrival to the bolometer as a function of sample length, temperature, and defect concentration in systems with nonequilibrium phonon trapping centers. The theoretical relations thus obtained are compared with the experimental data for solid solutions of yttrium–aluminum garnets and aluminates.

2. BASIC EQUATIONS

The rate equation describing the propagation of a phonon pulse with inclusion of phonon–phonon interaction cannot be solved in a general form, even under simplifying assumptions. To investigate this effect within the simple model of [10], we have to make two basic approximations. First, we consider only thermal-phonon decay processes. This restriction is validated by the condition $n(\omega) \ll 1$ [where $n(\omega)$ is the occupation number of injected phonons], which is always satisfied in the experiments to be discussed in this paper. Sec-

1063-7834/03/4504-0725$24.00 © 2003 MAIK "Nauka/Interperiodica"

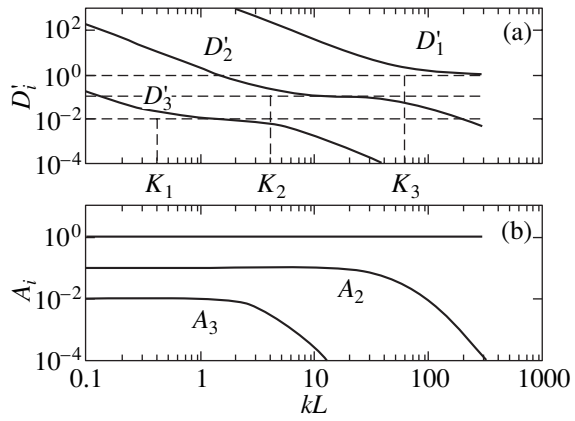

Fig. 1. Spatial dispersion curves of (a) effective diffusion coefficients and (b) weighting factors.

ond, we assume that the long-wavelength phonons forming in the course of thermal-phonon decay propagate ballistically and do not contribute to diffusion signal formation at the bolometer. While this approximation is certainly considerably more rough than the ones made in [5–7], it permits one to derive simple analytical expressions for the observed quantities and to analyze their dependence on the parameters of the problem. Furthermore, it will be shown below that these approximations also provide quantitative agreement with experimental data.

With these approximations, the coupled rate equations describing the heat pulse propagation take on the form

$$\begin{aligned}
&\partial n_q/\partial t + (\Gamma_a + \Gamma_{1,tq} + \Gamma_{2,tq} + \Gamma_L)n_q \\
&= \Gamma_L n_{q0} + \Gamma_a n_{q0} + \Gamma_{1,tq} n_{q0} + \Gamma_{2,tq} n_{q0}, \\
&\partial E_1/\partial t = (1/2\pi)^3 \int \omega_q \Gamma_{1,tq}(n_q - n_{1,t0}) d^3q, \\
&\partial E_2/\partial t = (1/2\pi)^3 \int \omega_q \Gamma_{2,tq}(n_q - n_{2,t0}) d^3q.
\end{aligned} \tag{1}$$

In contrast to [10], we consider here crystals with two independent two-level subsystems (TLSs), a situation characteristic of $Y_{3-x}Er_xAl_5O_{12}$ with intermediate erbium concentrations. In Eqs. (1), n_{q0} and $n_{i,t0}$ are the equilibrium phonon occupation numbers at the bath temperature and the effective temperature of the ith TLS, respectively; E_i is the TLS energy and $\Gamma_{i,tq}$ is the rate of phonon scattering from TLSs; and $\Gamma_L = -D_0\partial^2/\partial z^2$, D_0 is the phonon diffusion coefficient determined only by the elastic phonon scattering from defects, and Γ_a is the thermal-phonon decay rate. We assume that the long-wavelength phonons formed in the decay escape immediately to the helium bath; therefore, the corresponding term describes the thermal-phonon loss resulting from decay.

After linearization of Eqs. (1) and Laplace–Fourier transformation made as in [10], the coupled rate equations assume the form

$$\begin{aligned}
&(p + N_1\Gamma_1 + N_2\Gamma_2 + k^2D_0 + \Gamma_a)S_q(p,k) \\
&- N_1\Gamma_1 S_{1t}(p,k) - N_2\Gamma_2 S_{2t}(p,k) = S(0), \\
&p + (c_p/c_{1t}\Gamma_1)S_{1t}(p,k) - (c_p/c_{1t}\Gamma_1)S_q(p,k) = 0, \\
&p + (c_p/c_{2t}\Gamma_1)S_{2t}(p,k) - (c_p/c_{2t}\Gamma_2)S_q(p,k) = 0.
\end{aligned} \tag{2}$$

Here, S_i is the deviation of the temperatures of the subsystems ($i = q, 1t, 2t$) from the bath temperature; N_i is the ith-TLS concentration; Γ_i is the phonon scattering rate per ith-species defect; $c_p = 4\pi^4(T/T_D)^3/5$ and $c_{i,t} = (\Delta_i/T)^2\exp(-\Delta_i/T)/[1 + \exp(-\Delta_i/T)]^2$ are the specific-heats of the phonons and TLSs, respectively; Δ_i is a TLS parameter; and T_D is the Debye temperature. As in [10], in deriving Eqs. (2), we neglected the dependence of Γ_{tq} on q and restricted ourselves to an approximation linear in the defect concentration N_i.

We readily find the Fourier transform for the solution of Eqs. (2) to be

$$\begin{aligned}
S_q(t,k) = {} & A_1(k)e^{-D_2(k)k^2t} + A_2(k)e^{-D_2(k)k^2t} \\
& + A_3(k)e^{-D_3(k)k^2t}.
\end{aligned}$$

Figure 1 shows spatial-dispersion curves of the effective diffusion coefficients and weighting factors derived by numerically solving the characteristic equation of system (2). In general, the parameters $A_i(k)$ and the dimensionless diffusion coefficients $D_i' = D_i/D_0$ depend on five parameters similar to those introduced in [10]; $k_i^2L^2 = 2t_0\tau_i$, where τ_i is the phonon relaxation time for decay ($i = a$) and trapping by the two-level subsystems ($i = 1, 2$), and $C_i = c_p/(c_p + c_{it}N_i)$. The specific points identified in Fig. 1 are expressed through these parameters in the following way:

$$K_1 = k_aL, \quad K_2 = \sqrt{(k_aL)^2 + (k_2L)^2},$$

$$K_3 = \sqrt{(k_aL)^2 + (k_1L)^2 + (k_2L)^2},$$

$$C_m = C_1k_1^2/(k_a^2 + k_1^2 + k_2^2),$$

$$\begin{aligned}
C_0 &= c_p/(c_p + c_{1t}N_1 + c_{2t}N_2) \\
&= C_1C_2/(C_1 + C_2 - C_1C_2).
\end{aligned}$$

For definiteness, we assume subsequently that $C_1 > C_2$ and $k_1 > k_2$.

To analyze the results obtained using this model, we consider first the effect of phonon decay on heat pulse propagation in crystals which do not contain trapping centers.

3. SYSTEMS WITHOUT NONEQUILIBRIUM-PHONON TRAPPING CENTERS

In this case, we have $k_1 = k_2 = 0$. It follows from Eq. (2) that

$$D_1'(k) = (k^2 + k_a^2)/k^2, \quad A_1(k) = 1,$$

which yields

$$S_q(t) \simeq e^{-t/\tau_a} e^{-L^2/4D_0 t} \sqrt{\pi/4D_0 t}. \qquad (3)$$

This expression coincides formally with that derived in [10] and approximating the shape of the first peak in systems with nonequilibrium-phonon trapping systems, because both expressions describe the loss of phonons producing the phonon nonequilibrium signal. In the case of weak anharmonicity, the additional exponential cuts off the signal only at long times and, hence, increases the curvature of the signal trailing edge. Figure 2 presents signal trailing edges calculated under the assumption that the diffusion coefficient is dominated by Rayleigh scattering on point defects, i.e., $D_0 = v^2\tau_R/3 = v^2 3BT^4$, where v is the group velocity of long-wavelength phonons and the phonon decay rate can be expressed as $\Gamma_a = AT^5$ ($k_a^2 = ABL^2T^9/3v^2$). The parameters needed to calculate the curves in Fig. 2 were taken from [9, 11]: $B = 195\ \mathrm{s^{-1}\,K^{-4}}$, $A = 2.07 \times 10^{-4}\ \mathrm{s^{-1}\,K^{-5}}$, and $L = 0.5$ cm. In all calculations, we set $v = 7 \times 10^5\ \mathrm{s^{-1}}$ cm. For the parameters chosen in this way, the theoretical curves fit satisfactorily to experimental data (cf. [9, Fig. 1]).

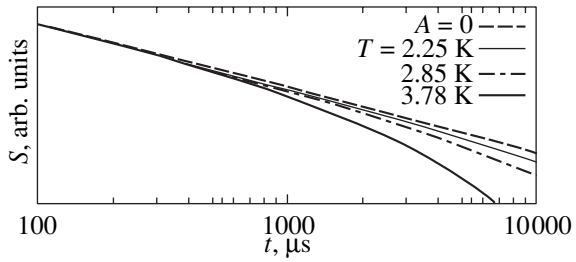

Fig. 2. Effect of a weak anharmonicity on the curvature of the trailing edge of the phonon nonequilibrium signal.

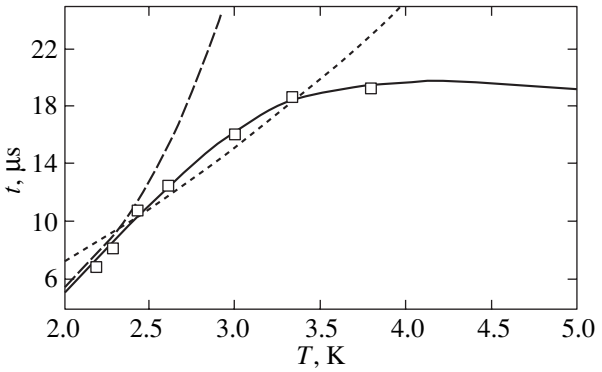

Fig. 3. Temperature dependence of the arrival time of signal maximum in the case of strong anharmonicity. (Squares are experimental points taken from [12]).

For large values of parameter k_a, where the condition $\tau_a \le t_0$ becomes valid, the shape of the phonon nonequilibrium signal varies strongly enough for the signal maximum arrival time to change:

$$t_{\max}(T) = \frac{\sqrt{1 + 4k_a^2(T)} - 1}{2k_a^2(T)} t_0(T). \qquad (4)$$

This relation is nonmonotonic; indeed, for low T, it scales as T^4, and for high temperatures, it falls off as $T^{-1/2}$. The maximum in the $t_{\max}(T)$ curve is reached at the temperature $T_{\max} = (20v^2/3BAL^2)^{1/9}$. Figure 3 shows a graphic comparison of this relation obtained for $B = 1200\ \mathrm{s^{-1}\,K^{-4}}$, $A = 800 \times 10^{-4}\ \mathrm{s^{-1}\,K^{-5}}$, and $L = 0.6$ cm with the function $t_0(T) \sim T^4$ and relation $t_{\max} \sim T^{1.8}$ used in [12] to process the experimental results (squares). These experimental data were obtained for the solid solution $Y_{1-x}Er_xAl_2O_3$ characterized by a strong anharmonicity. It appears that Eq. (4) fits to the experiment better; in our opinion, the too low position of the last experimental point is a manifestation of nonmonotonicity in the $t_{\max}(T)$ relation.

Thus, the results obtained permit the conclusion that the proposed model describes the available experimental data satisfactorily. To come to a final conclusion, one has to compare the theoretical curves with the results of a similar experiment performed on samples of different length, because, according to the above model, the signal maximum arrival time depends in a nontrivial way on sample length. At low temperatures, this dependence scales in a manner typical of diffusive phonon propagation, $t_{\max} \sim L^2$, but grows weaker with increasing temperature to become linear (in contrast to the result of the more rigorous approach used in [5], which yielded $t_{\max} \sim L^{10/9}$) for high T. Unfortunately, no studies of the effect of phonon decay in samples of various lengths (and concentrations) have thus far been carried out in these systems. Such measurements have been performed in $Y_{3-x}Er_xAl_5O_{12}$, in which one has to take into account phonon trapping centers.

4. CRYSTALS WITH NONEQUILIBRIUM-PHONON TRAPPING CENTERS

Consider a crystal with one two-level subsystem ($k_1 = 0$, $C_1 = 1$). This situation corresponds, in particular, to $Y_{3-x}Er_xAl_5O_{12}$solid solutions with high erbium concentrations. As pointed out in [10], in this case, the contribution of low-energy TLSs to C_0 is dominant in the temperature region under study and the high-energy TLSs may be neglected. Restricting ourselves to an analysis of slow processes only, we assume, in accor-

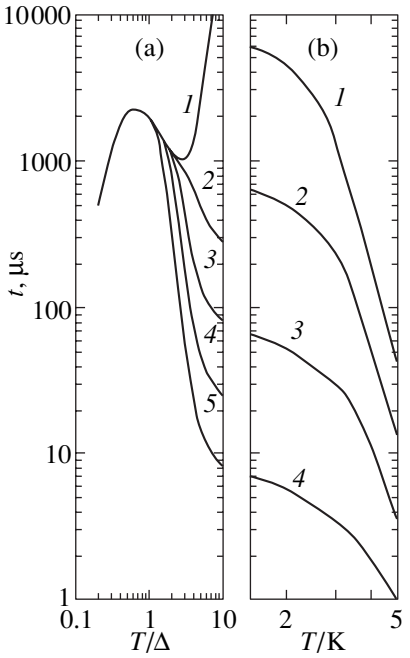

Fig. 4. Temperature dependence of the arrival time of signal maximum in systems with nonequilibrium-phonon trapping centers (a) for $L = 0.22$ cm and different values of parameter A (s^{-1} K^{-5}): (*1*) 0, (*2*) 10^{-4}, (*3*) 10^{-3}, (*4*) 10^{-2}, and (*5*) 10^{-1}; and (b) for $A = 10^{-1}$ s^{-1} K^{-5} and different values of parameter L (cm): (*1*) 0.22, (*2*) 0.11, (*3*) 0.055, and (*4*) 0.0275.

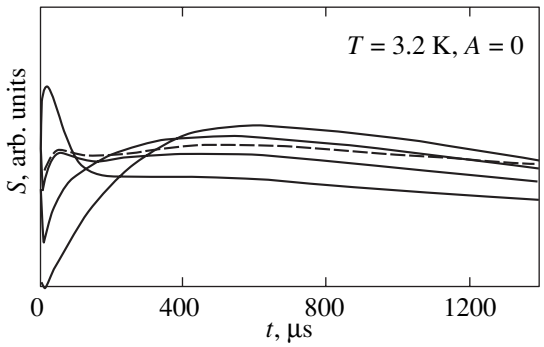

Fig. 5. Shape of the phonon nonequilibrium signal in $Y_{3-x}Er_xAl_5O_{12}$ crystals with two two-level subsystems calculated for different temperatures $T(K)$: (*1*) 3.0, (*2*) 3.2, (*3*) 3.4, and (*4*) 3.8.

dance with [10], that $k_2 \gg 1$ and $C_0 = C_2 \ll 1$. Then, we have

$$S_q(t) \sim \frac{1}{\sqrt{C_0 D_0 t}} \exp(-t/\tau_a) \exp(-L^2/4C_0 D_0 t),$$
$$t_{\max}(T) = \frac{\sqrt{1 + 4k_a^2(T)} - 1}{2k_a^2(T)} t_0(T)/C_0. \quad (5)$$

As shown in [10], the $t_{\max}(T)$ relation behaves for $A = 0$ in a nonmonotonic manner; namely, it first grows exponentially (for $T \le \Delta$), while at high temperatures, it decays in a scaled manner as $1/T$ ($\Delta \ll T_D$). Decay processes may give rise to a stronger power-law behavior of the high-temperature part of the $t_{\max}(T)$ curve, so that, for a large anharmonicity constant, $t_{\max}(T) \sim 1/T^{5.5}$. Figure 4 presents curves calculated for various values of parameter A (Fig. 4a) and sample length L (Fig. 4b). The curves in Fig. 4 were calculated with the following parameters: $\Delta = 1.8$ K, $T_D = 600$ K, and $B = 6500$ s^{-1} K^{-4}. The concentration of low-energy TLSs, which does not coincide with that of erbium impurity atoms [10], is $x = 0.5$ when reduced to $Y_{3-x}Er_xAl_5O_{12}$ formula units.

The curves presented in Fig. 4b fit well qualitatively to experimental data obtained on $Er_3Al_5O_{12}$ in [13] and reveal a transition from the quadratic $t_2(L)$ dependence to a linear one. Note that the possible reason for the strong temperature dependence of $t_{\max}(T)$ with a negative derivative, as discussed in [10], was different, namely, non-Rayleigh elastic scattering. Unfortunately, experiment does not make it possible to establish the actual character of elastic scattering.

For intermediate erbium concentrations ($x = 0.5$–1.5), the contributions of the low- and high-energy TLSs in $Y_{3-x}Er_xAl_5O_{12}$ solid solutions become significant and cause the appearance of two peaks corresponding to slow processes in the phonon nonequilibrium signal [13]. Spin–lattice relaxation experiments indicate that the TLS energy parameters are $\Delta_1 = 4.5$ K and $\Delta_2 = 28.8$ K [14]. Figure 5 illustrates the results obtained in a numerical solution of coupled equations (2) made taking into account the decay processes. The calculations were performed for $B = 1200$ s^{-1} K^{-4}, $A = 10^{-2}$ s^{-1} K^{-5}, $\Delta_1 = 4.5$ K, $x_1 = 0.06$, $\Delta_2 = 29$ K, $x_2 = 0.6$, $T_D = 630$ K, and $L = 0.5$ cm. As in [10], it was assumed that the rate of energy exchange between phonons and the TLSs depends exponentially on temperature [$\Gamma_i \sim \exp(-\Delta_i/T)$]. The theoretical relations thus obtained fit well to experimental data (compare with [13, Fig. 5]), which provides one more argument for the validity of the proposed model. For comparison, the dashed line shows an $S(t)$ relation calculated disregarding the decay processes ($A = 0$) for $T = 3.2$ K. As expected, anharmonicity most strongly affects the slowest processes, with a characteristic propagation time $t_m \sim t_0/C_0 \gg t_0$.

In general, no approximate analytical expressions for the temperature dependence of the arrival times of phonon nonequilibrium signal maxima to the bolometer can be obtained in the presence of two TLSs; therefore, we shall restrict ourselves to the limit of very fast energy exchange between phonons and TLSs. Under these conditions, k_1, $k_2 \longrightarrow \infty$, and an expression coinciding formally with Eq. (4) can readily be derived for the slowest process; in this expression, the parameter C_0 is now determined by both two-level subsystems and features a more complex temperature dependence. Figure 6 presents the corresponding curves calculated using Eq. (4) for different TLS concentration ratios. The curves in Fig. 6 were calculated with the same parameters as those

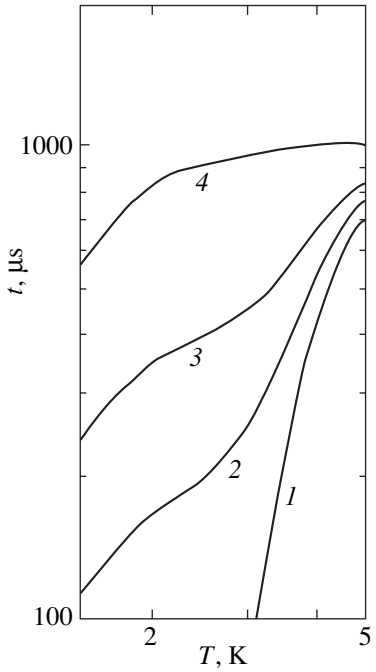

Fig. 6. Temperature dependence of the arrival time of signal maximum in systems with nonequilibrium-phonon trapping centers, calculated for different low-energy TLS concentrations x: (*1*) 0, (*2*) 0.03, (*3*) 0.06, and (*4*) 0.15.

in Fig. 5. One readily sees an infection point in the $t_m(T)$ dependence at a fairly high low-energy TLS concentration, which is in agreement with the unpublished experimental data obtained by S.N. Ivanov and coworkers on solid solutions $Y_{1-x}Er_xAl_2O_3$ at $x = 0.1$ and 0.15. As for the change in the temperature behavior of t_m with increasing concentration that is observed to occur in this system, it can be interpreted as a transition from one two-level system to the other.

5. CONCLUSIONS

Thus, taking into account decay processes within the model proposed earlier offered the possibility of describing a multiplicity of phenomena observed in experimental studies of heat pulse propagation in disordered systems with nonequilibrium-phonon trapping centers. The simplicity of the model and the versatility of its parameters gives one grounds to hope that this model will prove useful in describing transport processes in more complex systems, for instance, in cermets. Indeed, at the temperatures for which the experiments were conducted, the electron heat capacity of a small number of metallic inclusions in the dielectric matrix of such two-phase ceramics can be substantially higher than the lattice heat capacity of the matrix itself, thus resulting in small values of the parameter C, which, according to the proposed model, determines the heat pulse propagation time in the case of fast energy exchange between the subsystems. Due to the heat capacities of the electron and lattice subsystems having different temperature dependences, the contribution from the metallic phase to the formation of the phonon nonequilibrium signal can be observed experimentally.

ACKNOWLEDGMENTS

The author is indebted to S.N. Ivanov for helpful discussions and valuable criticisms and to E.N. Khazanov for providing unpublished experimental data.

This study was supported by the Russian Foundation for Basic Research, project nos. 00-02-17426 and 01-02-96463.

REFERENCES

1. R. J. Gutfeld and A. H. Nethercot, Jr., Phys. Rev. Lett. **12** (23), 641 (1964).
2. S. N. Ivanov, E. N. Khazanov, and A. V. Taranov, Pis'ma Zh. Éksp. Teor. Fiz. **40** (1), 20 (1984) [JETP Lett. **40**, 743 (1984)].
3. S. N. Ivanov and E. N. Khazanov, Zh. Éksp. Teor. Fiz. **88** (1), 294 (1985) [Sov. Phys. JETP **61**, 172 (1985)].
4. V. I. Kozub, Fiz. Tverd. Tela (St. Petersburg) **34** (5), 1429 (1992) [Sov. Phys. Solid State **34**, 759 (1992)].
5. D. V. Kazakovtsev and I. B. Levinson, Pis'ma Zh. Éksp. Teor. Fiz. **27** (3), 194 (1978) [JETP Lett. **27**, 181 (1978)].
6. D. V. Kazakovtsev and Y. B. Levinson, Phys. Status Solidi B **96** (1), 117 (1979).
7. I. B. Levinson, Zh. Éksp. Teor. Fiz. **79** (4), 1394 (1980) [Sov. Phys. JETP **52**, 704 (1980)].
8. S. N. Ivanov, E. N. Khazanov, and A. V. Taranov, Fiz. Tverd. Tela (Leningrad) **27** (9), 2791 (1985) [Sov. Phys. Solid State **27**, 1679 (1985)].
9. S. N. Ivanov, A. V. Taranov, and E. N. Khazanov, Zh. Éksp. Teor. Fiz. **99** (4), 1311 (1991) [Sov. Phys. JETP **72**, 731 (1991)].
10. E. I. Salamatov, Fiz. Tverd. Tela (St. Petersburg) **44** (5), 935 (2002) [Phys. Solid State **44**, 978 (2002)].
11. S. N. Ivanov, E. N. Khazanov, T. Paszkiewicz, *et al.*, Z. Phys. B **99** (4), 535 (1996).
12. B. A. Danil'chenko, S. N. Ivanov, D. V. Poplavskiĭ, *et al.*, Zh. Éksp. Teor. Fiz. **112** (1), 325 (1997) [JETP **85**, 179 (1997)].
13. S. N. Ivanov, A. G. Kozorezov, A. V. Taranov, and E. N. Khazanov, Zh. Éksp. Teor. Fiz. **100** (5), 1591 (1991) [Sov. Phys. JETP **73**, 880 (1991)].
14. S. N. Ivanov, A. V. Taranov, E. N. Khazanov, *et al.*, Zh. Éksp. Teor. Fiz. **94**, 274 (1988) [Sov. Phys. JETP **67**, 1021 (1988)].

Translated by G. Skrebtsov

Physics of the Solid State, Vol. 45, No. 4, 2003, pp. 730–735. Translated from Fizika Tverdogo Tela, Vol. 45, No. 4, 2003, pp. 696–700.

LOW-DIMENSIONAL SYSTEMS AND SURFACE PHYSICS

On the Structure of Strips Exhibiting the Integral Quantum Hall Effect in an Inhomogeneous 2D Electron System

V. Shikin

Institute of Solid-State Physics, Russian Academy of Sciences, Chernogolovka, Moscow oblast, 142432 Russia

Received March 28, 2002; in final form, June 3, 2002

Abstract—A formalism is developed to generalize the results obtained for "incompressible" strips exhibiting the integral quantum Hall effect in a spatially inhomogeneous 2D electron system to the cases of finite temperatures, significant electron density gradients, etc. Specifically, the concept of the "quality" of a given integer quantum Hall effect strip (channel) is introduced; the quality is proportional to the derivative $dn(x)/dx$ in the central part of the channel [$n(x)$ is the electron density distribution over the channel]. For a well-defined channel, this derivative tends to zero. If a noticeable gradient arises in the $n(x)$ distribution, the channel does not exhibit the quantum Hall effect and ceases to exist. The conditions are determined under which a channel exhibiting the integral quantum Hall effect breaks down. The results of calculations are used to interpret the available experimental data. © *2003 MAIK "Nauka/Interperiodica".*

1. It is well known that when a spatially inhomogeneous 2D electron system is placed in a magnetic field normal to the plane of the system, so-called incompressible strips (channels) exhibiting the integral quantum Hall effect (IQHE) can form in the sample; these channels determine the quantum Hall effect (QHE) observed in such samples. This hypothesis was put forward by several authors (see, e.g., [1–5]), but it was developed most fully into a theory in [4, 5], where analytical expressions were derived and the limits of applicability of the theory were indicated. In [4, 5], an ideal spinless electron gas was considered at a finite temperature (which allows one to neglect the electron correlations that give rise to fractional QHE) and spatial inhomogeneities of the electron density were treated within a semiclassical model. The latter approximation was assumed tacitly and implies that the theory developed in [4, 5] is valid if an inhomogeneous perturbation $e\varphi(x)$ of the electron motion can be included only in the semiclassical expression for the electron energy spectrum ϵ_l:

$$\epsilon_l = \hbar\omega_c(l + 1/2) + e\varphi(x_0), \tag{1}$$

where $\varphi(x)$ is the local value of the electric potential and x_0 is the position of the center of the electron orbit in p space.

In general, however, one should also take into account the shift x_0' in the position of the center of the electron orbit,

$$x_0' = x_0 - \frac{mc^2}{e^2H^2}e\varphi'(x_0), \tag{1a}$$

which arises in spatially inhomogeneous problems. Here, H is the magnetic field, m is the effective electron mass, and c is the speed of light.

The aim of this paper is to lift some restrictions in the theory developed in [4,5]. We assume the temperature to be finite as before, but include inhomogeneities of the electrochemical potential $\mu(x)$ in Eqs. (1) and (1a) and abandon the assumption of

$$dn_l(x)/dx \longrightarrow 0, \tag{2}$$

which was essentially employed in [4, 5] in constructing the electrostatics of an IQHE channel.

Our main interest is to determine the necessary conditions for an IQHE channel to exist. In terms of the theory proposed in [4, 5], a rough lower estimate of the width $2a_{\min}$ of an incompressible strip is

$$a_{\min} \geq l_H, \tag{3}$$

where l_H is the magnetic length. Indeed, each strip of width $2a_l$ is characterized by its local integral value of the magnetic filling factor ν_l. The concept of the filling factor ν_l is well defined over distances larger than the magnetic length. Therefore, for smaller distances, the semiphenomenological theory of incompressible channels developed in [4, 5] becomes unfounded.

In describing the properties of a channel, we will not use assumption (2); therefore, inequality (3) will not be a necessary condition. However, we propose an algorithm which enables one to estimate the derivative dn_l/dx at the center of a channel and verify the possible fulfillment of condition (2). If this condition is not met, the channel will not exhibit a clearly defined QHE.

2. Let us consider a two-dimensional Corbino disk with planar terminals in the quasi-one-dimensional approximation $(R_1 - R_2)/(R_1 + R_2) \ll 1$, where R_1 and R_2

1063-7834/03/4504-0730$24.00

are the outer and inner radii of the disk, respectively. By finding the piecewise smooth solution to the Dirichlet problem for the electric potential, we arrive at the following inhomogeneous addition $\delta n(x)$ to the electron density in the 2D region:

$$\delta n_0(x) = \frac{\kappa w W_{ab}}{\pi^2 e^2 (w^2 - x^2)}, \quad \int_{-w}^{+w} \frac{\delta n_0(s)}{(s-x)} ds = 0, \quad -w \le x \le +w. \tag{4}$$

Here, $2w = R_1 - R_2$ is the width of the 2D region between the metallic terminals, the x axis is taken to be along the radial direction, the origin is at the center of the 2D region, κ is the dielectric constant of the medium, and W_{ab} is the contact energy. In the limit of $a_B^* \ll w$, where a_B^* is the effective Bohr radius, Eq. (4) is a reasonable approximation at points far from $x = \pm w$; the integral in Eq. (4) is taken to be equal to its principal value.

In the presence of a magnetic field normal to the plane of the 2D system, there are points where the electron density satisfies the condition

$$\nu(x) = \pi l_H^2 [n_s + \delta n_0(x_l)] = l, \quad l = 1, 2, 3\ldots. \tag{5}$$

These points become centers at which incompressible IQHE strips arise. According to [4], these strips are independent of one another. We will take advantage of this fact below.

Within the lth strip, the equilibrium equation for the 2D gas of noninteracting electrons has the following form (the one-electron approximation was also used in [4, 5]):

$$\mu(x) = e\varphi(x) + \zeta(\nu_{var}(x), H) = \text{const}, \quad \zeta(\nu_{var}(x), H) = -T \ln S(\nu_{var}, H), \tag{6}$$

$$\nu_{var} = \nu(x) \quad \text{or} \quad \nu_*(x). \tag{7}$$

$$2S(H, T, \nu) = \left(\frac{1}{\nu} - 1\right) + \left[\left(\frac{1}{\nu} - 1\right)^2 + 4\epsilon\left(\frac{2}{\nu} - 1\right)\right]^{1/2}, \quad \epsilon = \exp(-\hbar\omega_c/T) \ll 1, \tag{8}$$

$$\nu(x) = \pi l_H^2 n(x), \quad l_H^2 - c\hbar/eH, \quad \nu < 2, \tag{9}$$

$$\nu_*(x) = \pi l_h^2 \left\{ n(x) - \frac{\langle \nu \rangle}{\hbar\omega_c} e\varphi''(x) \right\}, \tag{10}$$

$$\kappa e\varphi'(x) = 2e \int_{-w}^{+w} \frac{dn(s)}{(s-x)} ds. \tag{11}$$

Here, T is the temperature; integral equation (11), relating the electric potential $\varphi(x)$ and the electron density $\delta n(x)$, is valid if there are no additional screens near the disk. The two variants of $\nu(x)$ in Eq. (7) are defined by Eqs. (9) and (10) and correspond to the different approximations used to calculate $\mu(x)$: in the former case, inhomogeneities are included (as usual) only in ϵ_l in Eq. (1), while in the latter, perturbations of $\nu(x)$ are included self-consistently in Eqs. (1) and (1a).

The function $-T \ln S$, in combination with Eqs. (8) and (9), undergoes a jump as $\nu \longrightarrow 1$:

$$-T \ln S = \begin{cases} 0, & \nu \longrightarrow 1 - 0 \\ \hbar\omega_c, & \nu \longrightarrow 1 + 0 \end{cases} \tag{12}$$

with the jump being temperature-independent and with the transition region being of the order of T in size.

In the case of Eqs. (8) and (10), the jump is characterized by Eq. (12) in which

$$\nu_*(x) = 1 + \Delta(x), \tag{13}$$

$$\Delta(x) = \pi l_h^2 \left\{ \delta n(x) - \frac{\nu}{\hbar\omega_c} e\varphi''(x) \right\} \ll 1. \tag{14}$$

Equations (6), (8), and (10) were proposed in [6] to calculate $\mu(x)$ self-consistently when considering the magnetocapacitance of small 2D samples. We also note that the condition $\Delta(x) = 0$ was used in [7] as a additional relation [in combination with Eq. (11)] between the Hall voltage and the local electron density distribution over the cross section of an IQHE channel carrying a transport current. In this case, one has a closed set of equations for $\varphi(x)$ and $\delta n(x)$ not involving the quantity $\mu(x)$, which is not correct. In particular, instead of the (correct) Ohm law

$$j_i = \sigma_{ik} \partial\mu/\partial x_k,$$

its approximation in [7] [see formula (11) in that work],

$$j_i = \sigma_{ik} \partial\varphi/\partial x_k,$$

was used without explanation.

Returning to Eqs. (6), (8), (9), and (11), we note that they can be reduced to a single equation for $\delta n(x)$:

$$\frac{2e^2}{\kappa} \int_{-w}^{+w} ds \frac{[\delta n(s) - \delta n_0(s)]}{(s-x)} = \frac{T}{S(\nu)} \frac{\partial S}{\partial \nu} \frac{\partial \nu}{\partial x}. \tag{15}$$

In deriving Eq. (15), we used the fact that the integral in Eq. (4) is zero for the electron density $\delta n_0(x)$.

To solve Eq. (15), we employ an efficient approximate method which is conceptually identical to the one used in [4, 5]. First of all, we note that the quantity $\delta n(x)$ is significantly affected only over the range $\pm a$ centered at the point x_l of the channel of width $2a \ll 2w$. Therefore, the difference $\delta n(x) - \delta n_0(x)$ is significantly different from zero only over this range and the limits $\pm w$ can be replaced by $\pm a$ if $2a \ll 2w$. Furthermore, as in [4], we assume that the interaction between adjacent channels is weak. In what follows, we also assume that the filling factor of a channel is close to an integer;

therefore, the complicated function $S(\nu)$ in Eq. (8) can be replaced by its value for the integral value of the filling factor and Eq. (15) can be simplified to

$$\frac{4e^2\epsilon^{1/2}}{\kappa T}\int_{-a}^{+a} ds\frac{[\delta n(s)-\delta n_0(s)]}{(s-x)} = -\frac{d\nu}{dx}. \qquad (15a)$$

It follows from Eq. (15a) that the derivative $d\nu(x)/dx$ becomes exponentially small as $\epsilon \longrightarrow 0$.

In order to estimate $dn(x_l)/dx$, we use the approximation (as in [4])

$$\delta n(x)-\delta n_0(x) \simeq (n_l'-n_0')\delta x, \qquad (16)$$

where δx is reckoned from the center of the channel at hand. By evaluating the integral in Eq. (15a) in the vicinity of x_l, n_l' is found to be

$$n_l' = n_0'/(1+\gamma), \quad \gamma = \frac{\pi\kappa T l_H^2}{8ae^2\epsilon^{1/2}} \gg 1. \qquad (17)$$

The inequality $\gamma \gg 1$ can be satisfied primarily by making ϵ tend to zero; this inequality is a criterion for the validity of approximations (15a) and (16) and for the smallness of n_l' (i.e., the high quality of the channel).

The strip width $2a$ in Eq. (16) can be estimated using Eq. (15a). Rewriting this equation in the form

$$\frac{2\epsilon^{1/2}e}{T}\frac{d\varphi}{dx} = -\frac{d\nu}{dx} \qquad (18)$$

and substituting ν_l' from Eq. (17), we find

$$\frac{2\epsilon^{1/2}e}{T}\frac{d\varphi}{dx} = -\frac{d\nu_0/dx}{1+\gamma}. \qquad (19)$$

It follows from Eqs. (6) and (12) that the potential difference between the edges of the strip is $\hbar\omega_c$. Therefore, Eq. (19) can be written as

$$\frac{Td\nu_0/dx}{(1+\gamma)}a = \epsilon^{1/2}\hbar\omega_c, \qquad (19a)$$

from which, in the limit of $\gamma \gg 1$, we have

$$a^2 \simeq \kappa\hbar\omega_c/8e^2 n_0'(x_l). \qquad (20)$$

The estimate of the strip width $2a$ in Eq. (20) differs from the corresponding result obtained in [4] by a numerical factor of order unity, because the electrostatics of the channel in [4] is based on additional boundary conditions not used in deriving Eqs. (6) and (15). (In [4, 5], the electric field at the edges of the channel was assumed to vanish because of ill-founded condition (2), which was introduced to obtain a closed set of equations of electrostatics.)

Equation (17) gives a convenient criterion for the high quality of the strip. If

$$n_l' \ll n_0' \quad \text{i.e.,} \quad \gamma \gg 1, \qquad (21)$$

we have a well-defined IQHE channel. In the opposite extreme

$$n_l' \leq n_0' \qquad (21a)$$

the channel does not exhibit a pronounced IQHE.

It follows from Eq. (17) that the quality of a strip rapidly deteriorates with increasing temperature; numerical calculations in [8] also revealed this fact. It is also of interest that $\gamma \propto a^{-1}$; therefore, the quality of a channel becomes higher as its width decreases. This dependence can be interpreted as follows. The initial profile of the electron density $\delta n_0(x)$ in Eq. (4) does not depend on temperature; the channel width in Eq. (20) also does not depend on temperature (which is a particularly attractive feature of the theory developed in [4, 5], because this theory fails at $T = 0$). However, the slope n_l' in Eq. (17) is very sensitive to temperature. As the channel width is increased, condition (21) $n_l' \ll n_0'$ becomes progressively more difficult to be met, which manifests itself in the relation $\gamma \propto a^{-1}$.

However, such a dependence cannot persist with decreasing channel width down to $a \longrightarrow 0$, because in the long run the electrochemical potential in Eq. (6) becomes sensitive to the difference between ν and ν_*, which is defined by Eqs. (9) and (10), respectively. In our natural modification of the theory proposed in [4], the inclusion of inhomogeneities in Eq. (10) affects the electrochemical potential and, hence, the properties of narrow IQHE strips.

3. To modify the theory in [4], we conveniently start with Eq. (18), which, combined with Eq. (10), takes the form

$$2\epsilon^{1/2}T^{-1}e\varphi' = -\nu' + \frac{\pi l_H^2 e}{\hbar\omega_c}\varphi'''(x). \qquad (22)$$

It is seen from Eq. (22) that the formation of a channel is controlled by two competing parameters,

$$\epsilon^{1/2}T^{-1} \quad \text{and} \quad \pi l_H^2/a^2\hbar\omega_c. \qquad (22a)$$

If the former parameter is large in comparison with the latter, we have the situation described above. In the opposite extreme, which is highly probable in the case of small values of a, the parameters of the channel have to be recalculated from the beginning.

In general, we should first solve Eq. (22) for φ' with the boundary conditions

$$\varphi'(\pm a) = 0 \qquad (23)$$

(now, these conditions can be substantiated). The result is

$$\lambda e\varphi' = -h\omega_c\left[\int_{-a}^{x} n'(s)\sinh\lambda(x-s)ds - \frac{\sinh\lambda(x+a)}{\sinh 2\lambda a}\int_{-a}^{+a} n'(s)\sinh\lambda(a-s)ds\right], \quad (24)$$

$$\lambda^2 a^2 = \frac{2a^2\epsilon^{1/2}h\omega_c}{\pi l_H^2 T\nu_l}. \quad (25)$$

The parameter λa in Eq. (25) is a combination of the parameters in Eq. (22a) and controls the response of the electron density in the IQHE channel to thermodynamic jumps in the function $S(H, T, \nu_{var})$ in the vicinity of the singular points x_l defined by Eq. (2). If $\lambda a \gg 1$, we have the derivative n_l' corresponding to Eq. (9). In the opposite limit $\lambda a \ll 1$, we start with the simplified expression for $e\varphi'(0)$

$$e\varphi'(0) \simeq -h\omega_c n_l' a^2/2. \quad (26)$$

From the representation of electric potential (11) in the form of Eq. (15a), by using approximation (16) and the line of reasoning that led to Eq. (17), we obtain in this case

$$n_l' = n_0'(1+\delta), \quad \delta = a\kappa h\omega_c/8e^2. \quad (27)$$

In contrast to the parameter γ in Eq. (17), the parameter δ in Eq. (27) decreases with decreasing channel width a, as one might expect in the case where the derivatives of the electric potential are included in the theory. As in the case of Eq. (21a), we can find $a_{\min}$ from Eq. (27):

$$a > a_{\min}, \quad a_{\min} = 8e^2/\kappa h\omega_c = \frac{8l_H^2}{2\pi a_b^*}. \quad (28)$$

This inequality is a refinement of the rough estimate in Eq. (3).

We also present an expression for the channel width in the case where it is close to its minimum value:

$$-a^3 n_0'/(1+\delta) = 1/2\pi, \quad (29)$$

where δ is given by Eq. (27).

4. Let us discuss the experimental aspect of Eq. (28). One might expect that, under equilibrium conditions, for which Eq. (28) is derived, the array of incompressible strips of a 2D system (in the case where many channels arise in the system) would be separated from the edges of the 2D system by "normal" spacers, within which channels cannot form. This was indeed the case in the experiments in [9] on the linear electrooptic effect in a Corbino disk (see [9, Fig. 2]). The corresponding experimental data are presented in Fig. 1 (courtesy of W. Dietsche). Open circles represent the

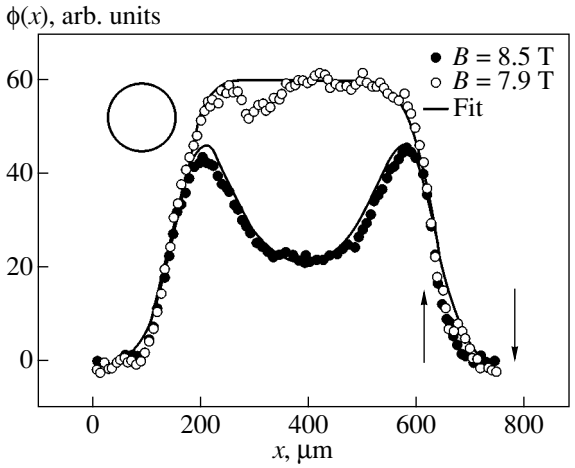

Fig. 1. Convolution $\phi(x)$ of the electric potential $\varphi(x)$ with a Gaussian for a Corbino disk. The 2D region is centered at the point x_0 = 390 μm. Solid curves are calculated from Eq. (30) for the normal state and Eqs. (31) and (32) for the anomalous state. Open (normal state) and solid circles (anomalous state) represent the data from [9]. The magnetic fields corresponding to these states are indicated at the top right of the figure. The circle at the top left gives an indication of the actual cross section of the laser beam. The arrows at the bottom right of the figure indicate the boundaries of the interval where the regions of the normal and anomalous behavior of $\phi(x)$ overlap. The finiteness of this interval is indicative of the existence of rings (near the edges of the disk) that exhibit normal electrical conduction and surround the anomalous region of the disk.

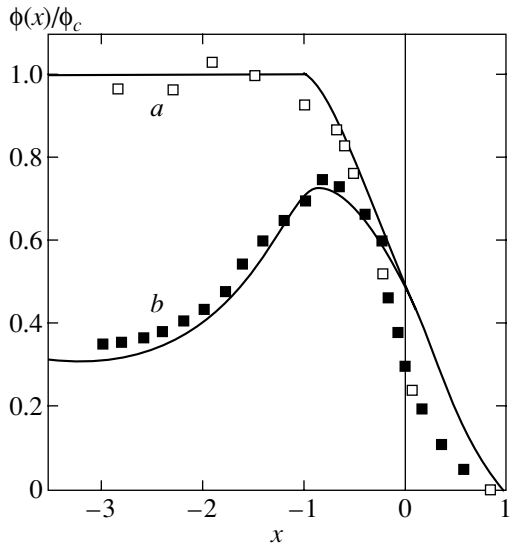

Fig. 2. Curve a is the normalized convolution $\varphi(x)/\phi_c$ calculated from Eq. (33) for the region of the normal state described by Eq. (30) near one of the edges of the Corbino disk. The coordinate x is measured in units of the radius of the laser beam; the origin is at the geometric edge of the 2D system. Open squares are the experimental data from [9]. Curve b is the convolution $\varphi(x)/\phi_c$ calculated from Eq. (33) for the anomalous state described by Eq. (31). Solid squares are the corresponding experimental data from [9].

electric potential for the 2D system in the normal state, where this system is a good conductor. Solid circles correspond to the 2D system in an anomalous state, where an array of IQHE channels arises in the central part of the Corbino disk (the question concerning the number of channels arising in experiments in [9] was discussed in [10]). It is noteworthy that the data on the electric potential for the normal and anomalous states overlap near the edges of the Corbino disk over a finite range of values of the coordinate x (the range is indicated by arrows). This range can exist only if there is a mechanism that prevents narrow IQHE channels forming in the regions of large electron density gradients.

We used the following parameters to describe the behavior of $\varphi(x)$ quantitatively. In the normal state,

$$\varphi(x) = \begin{cases} \varphi_0, & -w \le x \le +w \\ 0, & |x| \ge w. \end{cases} \tag{30}$$

The quantity φ_0, nominal width $2w$, and radius R are found by fitting Eqs. (30) and (32) to the experimental data from [9].

Using Eq. (4), the anomalous potential in the multichannel approximation [10] can be written in the form

$$\varphi(x) = \begin{cases} c_1/(w^2 - x^2), & -x_c \le x \le x_c \\ \varphi_0, & +x_c \le x \le +w \\ \varphi_0, & -w \le x \le -x_c. \end{cases} \tag{31}$$

The constant φ_0 is the same in Eqs. (30) and (31). The constants c_1 and x_c are chosen to fit the $\phi(x)$ distribution in Eqs. (30) and (31) most closely to the data from [9] in the QHE regime.

In practice, one should also allow for the finite cross section of the laser beam scanning the 2D samples in the experiments in [9]. For this purpose, we consider the convolution $\phi(x)$ of the electric potential with a Gaussian function characterized by an adjustable parameter R (laser-beam radius):

$$\phi(x) = \int_{-\infty}^{+\infty} \varphi(s) f(x-s) ds,$$
$$f(x) = \frac{1}{R\sqrt{\pi}} \exp(-x^2/R^2). \tag{32}$$

In Fig. 1, the convolutions calculated from Eq. (32) for the electric potentials in Eqs. (30) and (31) (solid curves) are compared with the data from [9] for the normal (open circles) and anomalous (solid circles) states. The fitted values of the parameters are $R \simeq 60$ μm, $x_0 = 390$ μm, $w = 240$ μm, and $x_c \simeq 180$ μm. Here, x_0 is the center position of the $\phi(x)$ distribution presented in the figure.

To make the picture complete, Fig. 2 presents the convolutions of the local electric potentials $\phi(x)$ given by Eqs. (30) and (31) with the rectangular profile of a scanning laser beam:

$$\phi(x) = \frac{1}{2R} \int_{x-R}^{x+R} \varphi(s) ds. \tag{33}$$

Clearly, a laser beam with a sharp profile is less suitable for investigating the details of the $\varphi(x)$ distribution near the edge of the disk.

Convolutions (32) of electric potentials (30) and (31) with a Gaussian agree well with the data from [9], which indicates that the Corbino disk in the QHE regime has a stripe structure. In the central region of the disk, there is an array of incompressible stripes whose internal structure remains unresolved because of the finiteness of the radius R. Rings exhibiting normal electrical conduction are observed near the edges of the 2D system; the width Δ of a ring is

$$\Delta = w - x_c \simeq 60 \text{ μm}. \tag{34}$$

Unfortunately, the data presented in [9] do not cover the range of magnetic fields from 7.9 to 8.5 T, which makes it impossible to investigate the influence of a magnetic field on the position and structure of IQHE strips. The absolute values of the observed electric fields are also lacking. Nevertheless, using Eq. (33), one can make an indirect estimate of the contact energy W.

Equation (28), in combination with Eq. (4), allows one to determine the critical interval $2x_c$ within which the strips in the Corbino disk can be considered to be incompressible and a method of average description can be used:

$$x_c = \xi_c w, \quad \xi_c \simeq 1 - \sqrt{\eta}, \quad \eta_0 \ll \eta \ll 1,$$
$$\eta = \frac{a_{\min}^2}{w^2} \frac{W}{\hbar\omega_c}, \quad \eta_0 = a_b^*/w. \tag{35}$$

Using Eqs. (28) and (35), it can be shown that the calculated and experimental values of x_c correlate well if $W \simeq 1$ eV.

In summary, we have shown that the width $2a$ of incompressible strips in a regular inhomogeneous 2D electron system cannot be made as small as one pleases. The ratio of the electron density gradient $dn(x_l)/dx$ at the center of a strip to its unperturbed value dn_0/dx was used to characterize the strip quality. This ratio changes from an exponentially small value to a value close to unity as the width $2a$ decreases. The critical strip width $2a_{\min}$ for this change is given by Eq. (28). Possible experimental manifestations of the existence of the critical width are discussed using the Corbino disk as an example.

ACKNOWLEDGMENTS

The author is grateful to W. Dietsche for helpful discussions and for providing an electronic version of the

data published in [9] and presented in Fig. 1 in this paper.

This study was supported in part by the Russian Foundation for Basic Research, project no. 02-02-17082.

REFERENCES

1. C. W. J. Beenakker, Phys. Rev. Lett. **64**, 216 (1990).
2. A. Cheng, Solid State Commun. **74**, 871 (1990).
3. A. Efros, Phys. Rev. B **45**, 11354 (1992).
4. D. Chklovskii, B. Shklovskii, and L. Glazman, Phys. Rev. B **46**, 4026 (1992).
5. D. B. Chklovskii, K. F. Matveev, and B. I. Shklovskii, Phys. Rev. B **47**, 12605 (1993).
6. V. Shikin and Yu. Shikina, Fiz. Tverd. Tela (St. Petersburg) **39**, 742 (1997) [Phys. Solid State **39**, 656 (1997)].
7. A. H. MacDonald, T. M. Rice, and W. F. Brinkman, Phys. Rev. B **28**, 3648 (1983).
8. K. Lier and R. Gerhardts, Phys. Rev. B **50**, 7757 (1994).
9. W. Dietsche, K. von Klitzing, and K. Ploog, Surf. Sci. **361**, 289 (1996).
10. V. Shikin, Pis'ma Zh. Éksp. Teor. Fiz. **71**, 95 (2000) [JETP Lett. **71**, 65 (2000)].

Translated by Yu. Epifanov

Physics of the Solid State, Vol. 45, No. 4, 2003, pp. 736–751. Translated from Fizika Tverdogo Tela, Vol. 45, No. 4, 2003, pp. 701–714.

LOW-DIMENSIONAL SYSTEMS AND SURFACE PHYSICS

Spontaneous Emission and Elastic Scattering of Light from Quantum-Well Excitons in a Fabry–Perot Microcavity

V. A. Kosobukin

Ioffe Physicotechnical Institute, Russian Academy of Sciences, Politekhnicheskaya ul. 26, St. Petersburg, 194021 Russia
e-mail: Vladimir.Kosobukin@mail.ioffe.ru

Received July 1, 2002

Abstract—A theory of spontaneous emission and elastic light scattering by quasi-two-dimensional excitons in a quantum well placed in a Fabry–Perot microcavity is developed. The problem is solved by means of electrodynamic Green's functions with inclusion of fluctuations of the quantum-well width and cavity wall shape treated as a perturbation. General expressions are found in a zero approximation of perturbation theory (plane interfaces) for the radiative decay rates of quasi-two-dimensional excitons and for their energy shifts in the cavity. The boundary conditions for the electromagnetic field are taken into account through the coefficients of inward light reflection from the cavity walls. Resonance contributions to the scattering cross sections, which differ in the polarizations (*p* or *s*) of the incident and scattered waves, are derived in the lowest (Born) approximation in quantum-well width fluctuations. The spectral and angular dependences of elastic light scattering are studied numerically for Gaussian and exponential correlation functions. It is shown that the contribution from quantum-well width fluctuations to light scattering exceeds that due to single interfaces (surfaces) of a heterostructure by two orders of magnitude. © *2003 MAIK "Nauka/Interperiodica".*

1. INTRODUCTION

An excited quantum state is quasi-stationary with respect to spontaneous photon emission if the state is confined in at least one dimension on a scale less than the wavelength of light. Like atomic excited states [1], the eigenenergies of localized collective excitations, such as excitons, plasmons, and polar optical phonons, undergo radiation shift and broadening. For instance, the broadening of a plasmon of frequency ω_p, which is spatially confined in d dimensions on a characteristic scale length $a \ll c/\omega_p$, is determined by the radiative decay rate $\Gamma_p \sim \omega_p(a\omega_p/c)^d$ [2].

Radiative decay of low-dimensional excitons [3, 4], which plays a major part in the optics of semiconductor quantum wells (wires, dots) near the fundamental absorption edge [3], has been attracting considerable interest recently. The radiation shift and broadening of exciton levels in a single quantum well [3–6] are manifest in reflection and transmission spectra of light [3]. Reemission of excitons in periodic structures with multiple quantum wells gives rise to the formation of coherent polariton states [3, 7], which become superradiant in Bragg structures [8]. The competition between the radiative and nonradiative exciton decay rates affects the character of light absorption dramatically, with the result that the absorption mechanism changes from the polariton to excitonic with increasing temperature, which governs the rate of nonradiative processes [9].

The specific features of spontaneous emission in quantum-well structures manifest themselves in inhomogeneous line broadening of optical spectra [10–12], light propagation [13], resonant elastic light scattering [14–18], and photoluminescence [19, 20]. Elastic light scattering, which includes absorption of a photon followed by coherent emission of a second photon, with the system transferring to the initial state [1], is a dominant exciton emission process at low optical-excitation densities [21]. An extremely important feature of the spontaneous emission of low-dimensional excitons, in addition to its being resonant, is its dependence on the direction of propagation and polarization [18]. Viewed from this standpoint, the existing theory of light scattering by quantum wells [16], which predominantly considers time-resolved spectra, has two major drawbacks. First, this theory treats, as a rule, quantum wells in a uniform dielectric, even though the spontaneous radiation and the associated effects may depend substantially on the dielectric environment of the quantum wells [12, 22]. Moreover, the polaritons forming in semiconductor microcavities [23] radically modify the radiative properties of a quantum well incorporated in the cavity, as well as the light-scattering spectrum in the region of the Rabi exciton–polariton splitting [24, 25]. Second, available publications usually ignore the fundamental issue of the absolute magnitude and angular dependence of the scattering intensity, even though it is these characteristics that contain most of the information on static structural disorder [18, 24, 26]. Also, the dynamics of light scattering may depend substantially on the actual disorder type, which manifests itself differently in different stages of the scattering process [27].

The goal of this study is to develop a general theory of spontaneous radiation and steady-state elastic light

scattering due to quantum-well low-dimensional excitons in a Fabry–Perot cavity. The problem is solved using the method of Green's functions, with exciton polarization fluctuations associated with a random modulation of the quantum-well width treated as a perturbation. The effect of the dielectric environment on the radiative decay of quasi-two-dimensional excitons in a quantum well of uniform width is studied in a zero approximation. The external medium is characterized by the coefficients of inward light reflection from the cavity walls. The probability of resonance elastic light scattering under steady-state conditions is calculated in the next (Born) approximation in fluctuations of the quantum-well width and cavity wall shape. The emphasis is placed on the analysis of the angular and polarization characteristics of light scattering associated with spatial fluctuations of exciton polarization in a quantum well.

This paper is organized as follows. The problem is formulated in Section 2. In Section 3, the radiation corrections to the eigenenergy of the quasi-two-dimensional exciton caused by radiation reflection from the cavity walls are calculated. External reflection of light from a cavity housing a quantum well is discussed in Section 4. A calculation of the resonant elastic light scattering by a quantum well in a cavity, performed in a general form, is presented in Section 5. Section 6 concerns a model of exciton polarization fluctuations originating from the quantum-well interfaces being statistically rough and calculation of the light-scattering cross sections for the case of a uniform background medium. The correlation functions of rough interfaces are discussed in Section 7. In Section 8, the results obtained are employed in a numerical calculation of the efficiency of elastic light scattering from a quantum well and rough walls of the cavity itself.

2. FORMULATION OF THE PROBLEM AND MAIN RELATIONS

Real quantum wells reside in a complex dielectric environment and exhibit a variety of structural imperfections. The most essential of them are spatial fluctuations of quantum-well width, which are caused by random roughness of its interfaces [28]. With this in mind, we will consider the model presented in Fig. 1. It includes a quantum well placed in a Fabry–Perot microcavity (subsequently referred to as the cavity), i.e., a layer of thickness D with a background dielectric constant ε_b. The effect of the external medium is included through the coefficients r_1 and r_2 of light reflection into the cavity from its boundaries $z = 0$ and $z = D$, respectively. It is assumed that a ground-state quasi-two-dimensional exciton with a Bohr radius comparable to the quantum well width is excited in the well. The exciton contribution to dielectric polarization of the quantum well under monochromatic excitation

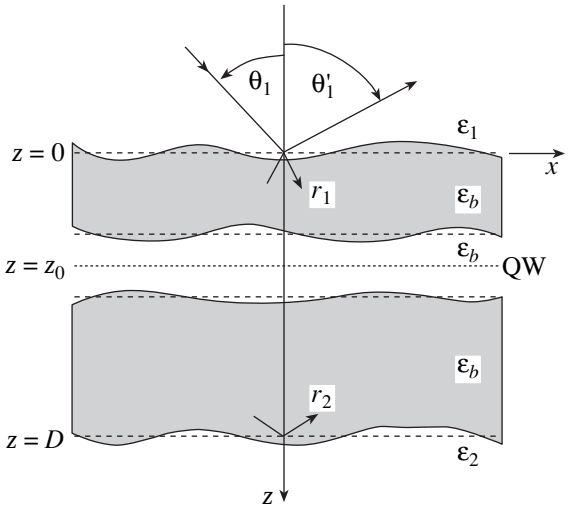

Fig. 1. Geometry of light scattering by a quantum well (QW) with midplane $z = z_0$ in a Fabry–Perot cavity ($0 < z < D$). Dashed lines specify the plane interfaces of an ideal structure, and solid lines present realizations of randomly rough interfaces. The direction in which angle θ_1' for the scattered light is reckoned is shown by an arrow.

with a frequency ω is described by a constitutive equation [6], which can be generalized to the form [17]

$$4\pi\mathbf{P}^{\mathrm{ex}}(z, \mathbf{R}; \omega) = \hat{\chi}^0(\omega, \mathbf{R})\Psi(z - z_0) \times \int dz'\Psi(z' - z_0)\mathbf{E}(z', \mathbf{R}; \omega). \quad (1)$$

Here, $\mathbf{E}$ is the total electric field and $\hat{\chi}^0(\omega, \mathbf{R})$ is a random exciton-susceptibility tensor, which depends on the lateral position vector $\mathbf{R} = (x, y)$. The envelope of the ground-state exciton wave function in Eq. (1) is assumed to be an even function, $\Psi(z) = \Psi(-z)$, which indicates neglect of the weak scattering caused by the quantum well being bent relative to the midplane $z = z_0$ [17, 18].

Taking the Fourier transform of Eq. (1),

$$\mathbf{E}(z; \mathbf{Q}, \omega) = \int d^2R \exp(-i\mathbf{Q}\cdot\mathbf{R})\mathbf{E}(z, \mathbf{R}; \omega) \quad (2)$$

we obtain

$$4\pi\mathbf{P}^{\mathrm{ex}}(z; \mathbf{Q}', \omega) = \int dz' \int \frac{d^2Q}{(2\pi)^2}\hat{\chi}^0(z, z'; \mathbf{Q}' - \mathbf{Q}, \omega)\mathbf{E}(z'; \mathbf{Q}, \omega), \quad (3)$$

where

$$\hat{\chi}^0(z, z'; \mathbf{Q}' - \mathbf{Q}, \omega) = [(2\pi)^2\delta(\mathbf{Q}' - \mathbf{Q})\hat{\bar{\chi}}^0(\omega) + \delta\hat{\chi}^0(\mathbf{Q}' - \mathbf{Q}, \omega)]\Psi(z - z_0)\Psi(z' - z_0). \quad (4)$$

This expression contains a diagonal tensor $\hat{\bar{\chi}}^0$ with components

$$\bar{\chi}^0_{\alpha\beta}(\omega) = \delta_{\alpha\beta}\cdot\bar{\chi}^0_{\alpha\alpha}(\omega) = \delta_{\alpha\beta}\frac{\bar{\Gamma}^0_\alpha}{\bar{\omega}^0_\alpha - \omega - i\gamma} = \delta_{\alpha\beta}\frac{\bar{\Gamma}^0_\alpha}{\bar{\Delta}^0_\alpha(\omega)}, \quad (5)$$

which do not depend on $\mathbf{R}$. In Eq. (5), $\delta_{\alpha\beta}$ is the Kronecker symbol and $\bar{\omega}^0_\alpha$ is the transition frequency of an exciton polarized along the Cartesian axis α and having nonradiative and radiative decay rates γ and $\bar{\Gamma}^0_\alpha$, respectively. The latter rate is proportional to the exciton oscillator strength, but its dependence on the quantum-well width [29] will be subsequently neglected. Approximation (5), which corresponds to an ideal quantum well with planar interfaces, is conventionally used when interpreting light reflection and transmission experiments [3].

The effects associated with lateral disorder in the quantum well will be described, in accordance with Eq. (4), with a tensor:

$$\delta\hat{\chi}^0(\mathbf{R},\omega) = \hat{\chi}^0(\mathbf{R},\omega) - \hat{\bar{\chi}}^0(\omega). \quad (6)$$

Considered from the viewpoint of statistical theory, the introduction of tensor $\hat{\bar{\chi}}^0$ in the form of Eq. (5) for real (i.e., disordered) quantum wells implies a certain averaging. In experiment, this averaging is effected by the propagating light wave; however, the character of this averaging cannot be analyzed in a strict enough manner.

The exciton contribution to the dielectric polarization of the quantum well can be represented in the form

$$\mathbf{P}^{\rm ex} = \mathbf{P}^0 + \delta\mathbf{P}^0. \quad (7)$$

In accordance with Eqs. (3)–(6), $\mathbf{P}^0$ is the regular and $\delta\mathbf{P}^0$ the fluctuation part of the quasi-two-dimensional exciton polarization in Eq. (3), which are expressed through $\hat{\bar{\chi}}^0$ from Eq. (5) and $\delta\hat{\chi}^0$ from Eq. (6), respectively. The fluctuation contribution $\delta\mathbf{P}^0$, as well as the tensor in Eq. (6), is considered a random perturbation in what follows, which is responsible for elastic (Rayleigh) light scattering.

In view of Eq. (7), we introduce the following sequence of equations for a layered medium with the background permittivity tensor $\varepsilon^0(z)\hat{I}$:

$$[\mathrm{curlcurl} - \varepsilon^0(z)k_0^2\cdot\hat{I}]\cdot\begin{pmatrix}\mathbf{E}^0(\mathbf{r})\\ \hat{G}^0(z,z';\mathbf{R}-\mathbf{R}')\\ \mathbf{E}^{\rm I}(\mathbf{r})\\ \mathbf{E}^{\rm II}(\mathbf{r})\end{pmatrix} = \begin{pmatrix}0 & (8)\\ \hat{I}\cdot\delta(\mathbf{r}-\mathbf{r}') & (9)\\ 4\pi k_0^2\mathbf{P}^0(\mathbf{r}) & (10)\\ 4\pi k_0^2\left\{\mathbf{P}^0(\mathbf{r}) + \sum_{m\ge 0}\delta\mathbf{P}^{(m)}(\mathbf{r})\right\} & (11)\end{pmatrix}.$$

Here, $\mathbf{r} = (\mathbf{R}, z)$, $k_0 = \omega/c$, and $\hat{I}$ is an identity tensor with components $I_{\alpha\beta} = \delta_{\alpha\beta}$. In solving Eqs. (8)–(11), one starts with the unperturbed operator $\hat{L}^0 = \mathrm{curlcurl} - \varepsilon^0(z)k_0^2\cdot\hat{I}$ in the left-hand part of these equations. Equations (8) and (9) define the electric field $\mathbf{E}^0$ and the tensor Green's function $\hat{G}^0$ for a multilayered medium without a quantum well. The solution $\mathbf{E}^{\rm I}$ to Eq. (10) describes the electromagnetic field in the same medium with plane interfaces but with inclusion of the quantum-well excitons. In stochastic equation (11), the perturbation for field $\mathbf{E}^{\rm II}$ is the exciton polarization fluctuation $\delta\mathbf{P}^{(0)} \equiv \delta\mathbf{P}^0$ of the quantum well ($m = 0$, $\delta\hat{\chi}^{(0)} \equiv \delta\hat{\chi}^0$) and the polarization contributions $\delta\mathbf{P}^{(m)}$ from the interfaces ($m \ge 1$) that do not belong to the quantum well.

We solve Eqs. (8)–(11) under the assumption that the incident wave (Fig. 1) has linear polarization *p* (TM wave) or *s* (TE wave) and a tangent wave vector component $\mathbf{Q} = Q\cdot\mathbf{e}_x$, where $\mathbf{e}_x$ is the unit vector of the *x* axis. Without the quantum well, the tangential components of the electric field excited in the cavity ($0 < z < D$) can be written in the form

$$E^0_{x,y}(\mathbf{r},t) = A_0^{p,s}\exp(-i\omega t + iQx)\times(e^{ikz} + r_2^{p,s}e^{ik(2D-z)}), \quad (12)$$

where $x(y)$ corresponds to $p(s)$ polarization and $E^0_z = (iQ/k^2)dE^0_x/dz$. In Eq. (12), $Q = \sqrt{\varepsilon_b}k_0\sin\theta$ (i.e., the angle θ) is a parameter of the problem, $k(Q) = \sqrt{\varepsilon_b k_0^2 - Q^2}$, and $r_2^{p,s}(Q)$ is the coefficient of internal reflection of light from the cavity wall at $z = D$ (Fig. 1).

We introduce operators $\hat{L}^{\rm I} = \hat{L}^0 - k_0^2\hat{\bar{\chi}}^0$ and $\hat{L}^{\rm II} = \hat{L}^{\rm I} - k_0^2\sum_{m\ge 0}\delta\hat{\chi}^{(m)}$, in which, according to Eq. (4), the

quantum-well tensors $\hat{\tilde{\chi}}^0$ and $\delta\hat{\chi}^{(0)} \equiv \delta\hat{\chi}^0$ ($m = 0$) are nonlocal in z and z'. Tensor $\delta\hat{\chi}^{(m)}$ ($m \geq 1$) in the operator $\hat{L}^{\mathrm{II}}$ is related to the dielectric polarization [30, 31]

$$\begin{aligned} &4\pi\delta\mathbf{P}^{(m)}(z, \mathbf{R}) \\ &= -(\varepsilon_m^+ - \varepsilon_m^-)\xi_m(\mathbf{R})\delta(z - z_m)\mathbf{E}(z, \mathbf{R}), \end{aligned} \tag{13}$$

caused by the roughness of the mth interface $z = z_m + \xi_m(\mathbf{R})$ between media with dielectric constants $\varepsilon_m^- = \varepsilon^0(z_m - 0)$ and $\varepsilon_m^+ = \varepsilon^0(z_m + 0)$, where $\varepsilon^0(z)$ is the dielectric function from Eqs. (8)–(11).

The corrections $\mathbf{E}^{\mathrm{I}} - \mathbf{E}^0$ and $\mathbf{E}^{\mathrm{II}} - \mathbf{E}^{\mathrm{I}}$ are calculated successively from differential equations (10) and (11), which can be expressed in terms of operators $\hat{L}^{(N)}$ with $N = \mathrm{I}$ and II as $\hat{L}^{(N)}\{\mathbf{E}^{(N)}, \hat{G}^{(N)}\} = \{0, \hat{I}\delta(\mathbf{r} - \mathbf{r}')\}$. These equations can be replaced by equivalent integral equations, which can be cast in a symbolic form [32, 33]:

$$F^{(N)} - F^{(N-1)} = \hat{G}^{(N-1)}(\hat{L}^{(N-1)} - \hat{L}^{(N)})F^{(N)}. \tag{14}$$

Here, $F^{(N)}$ stands for either vector $\mathbf{E}^{(N)}$ or tensor $\hat{G}^{(N)}$ of the Nth approximation and the multiplication sign denotes integration over argument z and summation over Cartesian indices that are common to two adjacent operators.

3. RADIATION CORRECTIONS FOR A QUASI-TWO-DIMENSIONAL EXCITON IN A CAVITY

Considering the solutions to Eqs. (8) and (9) to be known [30, 33], let us turn to Eq. (10), which describes the electrodynamics of an ideal quantum well in a cavity. Integral equations (14) for a quantum well with plane interfaces $z = z_0 \pm \bar{L}/2$ and susceptibility (5) in a multilayered medium are given by Eqs. (A.2) and (A.3) in the Appendix. In these expressions, the nonzero components $\chi_{\mu\nu}^{\mathrm{I}}$ of the exciton susceptibility tensor for an ideal quantum well placed in a cavity can be written as

$$\begin{aligned} \chi_{xx}^{\mathrm{I}}(Q, \omega) &= \frac{2\varepsilon_b}{k}\frac{\Gamma_x^0(Q)\Delta_z}{\Delta_+\Delta_-}, \\ \chi_{zz}^{\mathrm{I}}(Q, \omega) &= \frac{2\varepsilon_b k}{Q^2}\frac{\Delta_x\Gamma_z^0(Q)}{\Delta_+\Delta_-}, \\ \chi_{xz}^{\mathrm{I}}(Q, \omega) &= -\chi_{zx}^{\mathrm{I}}(Q, \omega) = i\frac{2\varepsilon_b}{Q}\frac{\Gamma_x^0(Q)\Gamma_z^0(Q)}{\Delta_+\Delta_-} \\ &\times\left(\frac{r_1^p e^{2ikz_0} - r_2^p e^{2ik(D-z_0)}}{1 - r_1^p r_2^p e^{2ikD}}\right), \end{aligned} \tag{15}$$

$$\chi_{yy}^{\mathrm{I}}(Q, \omega) = \frac{2k}{k_0^2}\frac{\Gamma_y^0(Q)}{\Delta_y} = \frac{\bar{\Gamma}_y^0 I_c^2(Q)}{\Omega_y^0 - \omega - i\gamma}. \tag{16}$$

Here, $r_1^\lambda(Q)$ and $r_2^\lambda(Q)$ are the coefficients of internal reflection of λ-polarized light from the cavity walls (Fig. 1):

$$\begin{aligned} \Delta_\alpha(Q, \omega) &= \Omega_\alpha^0(Q) - \omega - i\gamma, \\ \Delta_\pm(Q, \omega) &= \Omega_\pm^0(Q) - \omega - i\gamma, \end{aligned} \tag{17}$$

$$\begin{aligned} \Omega_\pm^0(Q) &= \frac{\Omega_x^0 + \Omega_z^0}{2} \\ &\pm \sqrt{\left(\frac{\Omega_x^0 - \Omega_z^0}{2}\right)^2 + \Gamma_x^0\Gamma_z^0\left(\frac{r_1^p e^{2ikz_0} - r_2^p e^{2ik(D-z_0)}}{1 - r_1^p r_2^p e^{2ikD}}\right)^2}, \end{aligned} \tag{18}$$

$$\begin{aligned} \Omega_x^0(Q) &= \omega_x^0 - i\Gamma_x^0 - i\Gamma_x^0 \\ &\times\left(\frac{r_1^p e^{2ikz_0} + r_2^p e^{2ik(D-z_0)} + 2r_1^p r_2^p e^{2ikD}}{1 - r_1^p r_2^p e^{2ikD}}\right), \end{aligned} \tag{19}$$

$$\begin{aligned} \Omega_z^0(Q) &= \omega_z^0 - i\Gamma_z^0 - i\Gamma_z^0 \\ &\times\left(\frac{-r_1^p e^{2ikz_0} - r_2^p e^{2ik(D-z_0)} + 2r_1^p r_2^p e^{2ikD}}{1 - r_1^p r_2^p e^{2ikD}}\right), \end{aligned} \tag{20}$$

$$\begin{aligned} \Omega_y^0(Q) &= \omega_y^0 - i\Gamma_y^0 - i\Gamma_y^0 \\ &\times\left(\frac{r_1^s e^{2ikz_0} + r_2^s e^{2ik(D-z_0)} + 2r_1^s r_2^s e^{2ikD}}{1 - r_1^s r_2^s e^{2ikD}}\right). \end{aligned} \tag{21}$$

In Eqs. (19)–(21), $\omega_\alpha^0 \equiv \omega_\alpha^0(Q)$ and $\Gamma_\alpha^0 \equiv \Gamma_\alpha^0(Q)$ are the frequency and radiative decay rate of exciton, respectively, in a quantum well located in a medium with a uniform background dielectric constant ε_b. These quantities have the form [3–6]

$$\begin{aligned} \omega_x^0(Q) &= \bar{\omega}_x^0 + \bar{\Gamma}_x^0\frac{k}{2\varepsilon_b}I_s, \\ \Gamma_x^0(Q) &= \bar{\Gamma}_x^0\frac{k}{2\varepsilon_b}I_c^2 = \tilde{\Gamma}_x^0\cos\theta, \end{aligned} \tag{22}$$

$$\begin{aligned} \omega_z^0(Q) &= \bar{\omega}_z^0 + \frac{\bar{\Gamma}_z^0}{\varepsilon_b}\left(I_0 + \frac{Q^2}{2k}I_s\right), \\ \Gamma_z^0(Q) &= \bar{\Gamma}_z^0\frac{1}{2\varepsilon_b}\frac{Q^2}{k}I_c^2 = \tilde{\Gamma}_z^0\frac{\sin^2\theta}{\cos\theta}, \end{aligned} \tag{23}$$

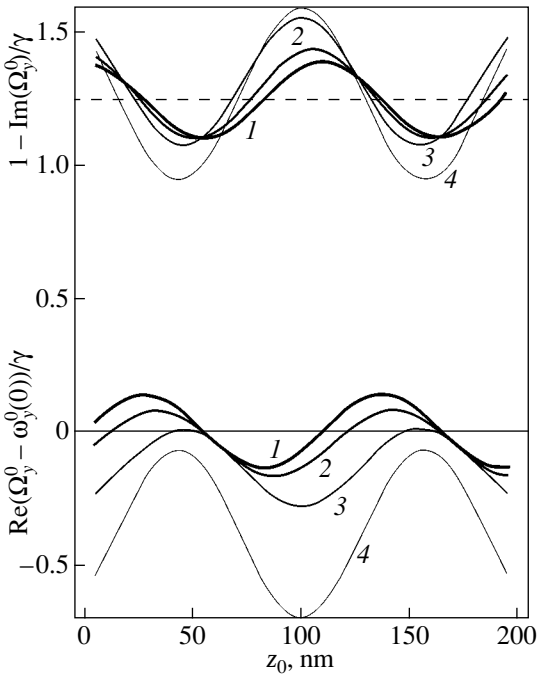

Fig. 2. Relative magnitudes of the radiative decay parameter $1 - \mathrm{Im}(\Omega_y^0)/\gamma$ (top series of curves) and of the frequency shift $(\mathrm{Re}\,\Omega_y^0 - \omega_y^0(0))/\gamma$ (bottom series) of excitons plotted as functions of quantum-well position z_0 in the cavity with D = 200 nm, ε_b = 12.5, and ε_1 = 1. The calculations were made using Eq. (21) for the 1*e*–1*lh* light-hole exciton with $\hbar\omega_y^0(0)$ = 1.6 eV, $\hbar\gamma$ = 1 meV, and $\hbar\tilde{\Gamma}_y^0$ = 0.25 meV located in a GaAs/AlGaAs quantum well of width $\bar{L}$ = 14 nm. Curves *1*–*3* relate to (*1*) ε_2 = 12.5, (*2*) 6, and (*3*) 1 for $\theta_1 = 0°$ (Q = 0), and curve *4*, to ε_2 = 1 for $\theta_1 = 75°$. Dashed line shows the relative total exciton decay rate $1 + \Gamma_y^0(0)/\gamma$ for the case of a uniform background medium ($\varepsilon_1 = \varepsilon_2 = \varepsilon_b$ = 12.5).

$$\omega_y^0(Q) = \bar{\omega}_y^0 + \bar{\Gamma}_y^0 \frac{k_0^2}{2k} I_s,$$
$$\Gamma_y^0(Q) = \bar{\Gamma}_y^0 \frac{k_0^2}{2k} I_c^2 = \tilde{\Gamma}_y^0 \frac{1}{\cos\theta}. \quad (24)$$

In Eqs. (22)–(24), the following notation was introduced:

$$I_c(Q) = \int dz \cos[k(Q)z]\Psi(z) = \int dz \exp[\pm ik(Q)z]\Psi(z),$$
$$I_s(Q) = \iint dz\,dz' \sin\{k(Q)|z - z'|\}\Psi(z)\Psi(z'), \quad (25)$$
$$I_0 = \int dz \Psi^2(z).$$

In practice, parameters (22)–(24) or $\tilde{\Gamma}_\alpha^0$ may be conveniently considered the starting parameters, with their values derived from experiment by fitting [3]. The constants $\tilde{\Gamma}_\alpha^0$ in the complex frequencies given by Eqs. (18)–(21) take into account exciton coupling with photons of the uniform medium, and the cavity-wall effect is characterized by coefficients r_1^λ and r_2^λ. The term $\hbar[\mathrm{Re}\,\Omega_\alpha^0(Q) - \bar{\omega}_\alpha^0]$ describes the radiation shift of the exciton energy level, and $-\hbar\,\mathrm{Im}\,\Omega_\alpha^0(Q)$ is its radiation width, which enters the total width $\hbar(\gamma - \mathrm{Im}\,\Omega_\alpha^0)$. According to Eq. (18), in general, the quantities $\Omega_\pm^0(Q)$ take into account electromagnetic interaction between excitons polarized along the x and z axes. Equations (22)–(24), derived from Eqs. (19)–(21) for $r_1^\lambda = r_2^\lambda = 0$, relate to a quantum well embedded in a uniform medium. In this case, $\chi_{xz}^{\mathrm{I}} = \chi_{zx}^{\mathrm{I}} = 0$ in Eq. (15); i.e., excitons with frequencies Ω_x^0 and Ω_z^0 defined by expressions (19) and (20) are no longer electromagnetically coupled. In general, in order for the condition $\chi_{xz}^{\mathrm{I}} = \chi_{zx}^{\mathrm{I}} = 0$ to be met, it is required that $r_1^p/r_2^p = e^{2ik(D-2z_0)}$. This can be used to determine the well position z_0 for which the x and z components of the exciton become independent (for instance, $z_0 = D/2$ for $r_1^p = r_2^p$).

The zeros of the resonance denominator in Eq. (16), which are determined by the condition $\Delta_y(Q, \omega) = 0$, yield the dispersion law for *s*-polarized exciton polaritons of an ideal quantum well in a cavity, and the roots of the equation $\Delta_\pm(Q, \omega) = 0$ define the dispersion law of *p*-polarized polaritons. The exciton frequency shift $\mathrm{Re}\,\Omega_\alpha^0 - \bar{\omega}_\alpha^0$ and the exciton decay rate $\gamma - \mathrm{Im}\,\Omega_\alpha^0$ oscillate depending on the quantum-well position z_0 in the cavity; this finding was apparently first pointed out in [22]. This effect is illustrated in Fig. 2, which displays the radiation corrections calculated from Eq. (21), primarily for the case of normal light incidence. We readily see that the radiation corrections to exciton frequency and decay exhibit oscillations, even if one of the coefficients, r_1^λ or r_2^λ, is zero. The reason for this is the interference of light associated with wave reflection both from the cavity walls and from the quantum well itself. These oscillations, whose amplitude is comparable to the exciton radiative-decay parameter, depend not only on z_0 but also on the cavity width D, the angle of incidence θ, and the frequency of light ω. While in the case of *p* polarization and for $\theta \neq 0$, the oscillations of the radiation corrections determined by the $\Delta_\pm(Q, \omega)$ functions for hybrid modes of excitons polarized along the x and z axes become more complex, their main features are retained.

4. LIGHT REFLECTION FROM A CAVITY WITH A QUANTUM WELL

The exciton radiation effects described in Section 3 depend substantially on the electric-field distribution over the cavity and determine, in turn, the resonance properties of this field. We shall assume that a light wave of polarization λ (i.e., *s* or *p*) propagates from the region $z = -\infty$, where $\varepsilon^0(z) = \varepsilon_1$ (Fig. 1), and calculate first the effect of the cavity on the optical properties of excitons in an ideal quantum well. The reflection coefficient $\rho_\lambda^{\mathrm{I}}(Q)$ enters the asymptotic solution ($z \longrightarrow -\infty$) to Eq. (A.2), which for a λ-polarized field takes on the form

$$E_{x,y}^{\mathrm{I}}(z;\, Q) \;=\; E_{x,y}^{\mathrm{inc}}[\exp(ik_1 z) + \rho_{p,s}^{\mathrm{I}}\exp(-ik_1 z)], \quad (26)$$

where $k_1(Q) = \sqrt{\varepsilon_1 k_0^2 - Q^2} = \sqrt{\varepsilon_1}k_0\cos\theta_1$ and $E_{x,y}^{\mathrm{inc}}$ are tangent projections of the incident wave amplitude. In Eq. (26),

$$\rho_p^{\mathrm{I}}(Q) \;=\; \rho_p^0 + \frac{ik}{2\varepsilon_b}\frac{\tau_+^p\tau_-^p}{(d_p^0)^2}\{\chi_{xx}^{\mathrm{I}}[F_+^p(z_0)]^2 - 2\chi_{xz}^{\mathrm{I}}Q/kF_+^p(z_0)F_-^p(z_0) - \chi_{zz}^{\mathrm{I}}Q^2/k^2[F_-^p(z_0)]^2\}, \quad (27)$$

$$\rho_s^{\mathrm{I}}(Q) \;=\; \rho_s^0 + \frac{ik_0^2}{2k}\frac{\tau_+^s\tau_-^s}{(d_s^0)^2}\chi_{yy}^{\mathrm{I}}[F_+^s(z_0)]^2 \quad (28)$$

for *p* and *s* polarized waves, respectively. In Eqs. (27) and (28),

$$d_\lambda^0(Q) \;=\; 1 - r_1^\lambda r_2^\lambda\exp(2ikD), \qquad \rho_\lambda^0(Q) \;=\; \frac{1}{d_\lambda^0}[r_2^\lambda\exp(2ikD) - r_1^\lambda], \quad (29)$$

with the last expression describing the reflection coefficient for a λ-polarized wave reflected from the cavity in the absence of the quantum well. The quantities $\chi_{\alpha\beta}^{\mathrm{I}}$ are given by Eqs. (15) and (16), where τ_+^λ and τ_-^λ denote the coefficients of electric-field transformation taking place as light crosses the interface $z = 0$ from medium 1 to the cavity and back and

$$F_\pm^\lambda(z;\, Q) \;=\; \exp(ikz) \pm r_2^\lambda\exp[ik(2D - z)]. \quad (30)$$

5. LIGHT-SCATTERING CROSS SECTIONS FROM A QUANTUM WELL IN A CAVITY

5.1. General Theory

Equations (11)–(14), treated in first order of perturbation theory [17, 18, 30, 31] in the quantities $\delta\hat{\chi}^{(m)}$, yield the following expression for the electric field of the scattered light:

$$E_\alpha^{\mathrm{II}}(\mathbf{r}) - E_\alpha^{\mathrm{I}}(\mathbf{r}) \;=\; k_0^2\int\frac{d^2Q'}{(2\pi)^2}e^{i\mathbf{Q}'\cdot\mathbf{R}} \times \sum_{m\geq 0}\sum_\mu \mathcal{G}_{\alpha\mu}^{\mathrm{I}}(z, z_m^-;\, \mathbf{Q}')\delta\chi_{\mu\mu}^{(m)}(\mathbf{Q}' - \mathbf{Q})E_\mu^{\mathrm{I}}(z_m^+;\, \mathbf{Q}). \quad (31)$$

Here, $z_m^\pm = z_m \pm 0$ for the *m*th plane interface ($m \geq 1$) and the notation $z_0^\pm$ for the quantum well ($m = 0$) indicates that integration in Eq. (A.4) with function $\Psi(z - z_0)$ has been performed. In Eq. (31), the field $\mathbf{E}^{\mathrm{I}}(z;\, \mathbf{Q})$ and the Green's function components

$$\mathcal{G}_{\alpha\beta}^{\mathrm{I}}(z, z';\, \mathbf{Q}') = \sum_{\mu,\nu}T_{\alpha\mu}(\varphi')G_{\mu\nu}^{\mathrm{I}}(z, z';\, |\mathbf{Q}'|)T_{\beta\nu}(\varphi') \quad (32)$$

correspond to the tangential components

$$\mathbf{Q} \;=\; \sqrt{\varepsilon_b}k_0\mathbf{e}_x\sin\theta, \qquad \mathbf{Q}' \;=\; \sqrt{\varepsilon_b}k_0[\mathbf{e}_x\cos\varphi' + \mathbf{e}_y\sin\varphi']\sin\theta' \quad (33)$$

of the incident and scattered wave vectors in the ideal quantum-well structure. In Eq. (32), the nonzero matrix elements that depend on the angle φ' between vectors $\mathbf{Q}' = (Q_x',\ Q_y')$ and $\mathbf{Q}$ can be written as $T_{xx} = T_{yy} = \cos\varphi' = Q_x'/Q'$, $-T_{xy} = T_{yx} = \sin\varphi' = Q_y'/Q'$, and $T_{zz} = 1$. At the $z = 0$ interface, components (33) of the incident and scattered wave vectors and the corresponding azimuthal angles are continuous and the polar angles θ and θ' transform, according to the refraction law $\sqrt{\varepsilon_b}\sin\theta = \sqrt{\varepsilon_1}\sin\theta_1$, to the angles θ_1 and θ_1' measured outside the cavity (Fig. 1).

Let us use Eq. (31) to calculate the electromagnetic energy flux scattered back into an element of solid angle $d\Omega_1' = \sin\theta_1' d\theta_1' d\varphi'$ ($z \longrightarrow -\infty$ in Fig. 1). Next, following [18, 30], we average this flux over the ensemble of realizations of tensors $\{\delta\hat{\chi}^{(m)}(\mathbf{R})\}$ (of their Fourier components $\{\delta\hat{\chi}^{(m)}(\mathbf{Q})\}$). The quantity $d\langle S\rangle/d\Omega_1'$ thus found, where $\langle S\rangle$ is the average value of the Poynting vector of scattered light, can be linearly expressed in the lowest (Born) approximation of perturbation theory through the correlation functions

$$\langle\delta\chi_{\mu\mu}^{(m)}(\mathbf{Q}' - \mathbf{Q})[\delta\chi_{\nu\nu}^{(m')}(\mathbf{Q}'' - \mathbf{Q})]^*\rangle \;=\; X_{\mu\nu}^{(m,m')}(\mathbf{Q}' - \mathbf{Q})(2\pi)^2\delta(\mathbf{Q}' - \mathbf{Q}''). \quad (34)$$

The presence of the delta function $\delta(\mathbf{Q}' - \mathbf{Q}'')$ in Eq. (34) indicates lateral translational invariance of the quantum well on the average.

In what follows, we assume the absence of correlation (statistical independence) between the responses of different rough interfaces, i.e., that $X_{\mu\nu}^{(m,m')} = \delta_{mm'}X_{\mu\nu}^{(m)}$

in Eq. (34). Then, the ratio of the energy $\cos\theta_1' d\langle S\rangle/d\Omega_1'$ scattered by a unit surface area to the energy $\cos\theta_1 c\sqrt{\varepsilon_1}|E_\lambda^{\rm inc}(Q)|^2/(8\pi)$ of the wave of amplitude $E_\lambda^{\rm inc}$ incident on this area determines the dimensionless total scattering cross section:

$$\frac{d\sigma(\lambda \longrightarrow \lambda')}{d\Omega_1'} = \frac{\varepsilon_1 k_0^6 \cos^2\theta_1'}{4\pi^2\cos\theta_1}\sum_m\sum_{\mu,\nu} M_{\mu\nu}^{\rm I}(z_m^-, \mathbf{Q}') \times X_{\mu\nu}^{(m)}(\mathbf{Q}'-\mathbf{Q})\frac{E_\mu^{\rm I}(z_m^+, \mathbf{Q})[E_\nu^{\rm I}(z_m^+, \mathbf{Q})]^*}{\left|E_\lambda^{\rm inc}(\mathbf{Q})\right|^2}. \quad (35)$$

Here, we introduced the notation $\lambda \longrightarrow \lambda'$ for the scattering channel $\lambda Q \longrightarrow \lambda'\mathbf{Q}'$ defined by polarization indices λ and λ' of the incident and scattered waves, respectively, either of which can be *p* or *s*. The elements of the Hermitian matrix ($M_{\mu\nu}^{\rm I} = (M_{\nu\mu}^{\rm I})^*$)

$$M_{\mu\nu}^{\rm I}(z_m^-; \mathbf{Q}') = \sum_\beta \mathcal{G}_{\beta\mu}^{\rm I}(z, z_m^-; \mathbf{Q}')[\mathcal{G}_{\beta\nu}^{\rm I}(z, z_m^-; \mathbf{Q}')]^* \quad (36)$$

are given by Eqs. (A.12) in the Appendix; in fact, for $z \longrightarrow -\infty$, they do not depend on *z*.

Because of the interfaces being uncorrelated, scattering cross section (35) reduces to the sum

$$\frac{d\sigma(\lambda \longrightarrow \lambda')}{d\Omega_1'} = \frac{d\sigma^{(0)}(\lambda \longrightarrow \lambda')}{d\Omega_1'} + \sum_{m=1}^{2}\frac{d\sigma^{(m)}(\lambda \longrightarrow \lambda')}{d\Omega_1'}, \quad (37)$$

in which the second term takes into account the contribution from the Fabry–Perot cavity walls to scattering.

5.2. Partial Contributions to the Light-Scattering Cross Section

Substituting Eq. (36) into Eq. (35), taking into account Eq. (32), and using the general properties of Green's functions of multilayered dielectric media [32, 33], we obtain the following expressions for the *m*th partial contribution to cross section (37) in different $\lambda \longrightarrow \lambda'$ scattering channels:

$$\frac{d\sigma^{(m)}(s \longrightarrow s)}{d\Omega_1'} = C_1\left|\tilde G_{yy}^{\rm I}\right|_{\mathbf{Q}'}^2 X_{yy}^{(m)}(\mathbf{Q}'-\mathbf{Q})\left|\frac{\tilde E_y^{\rm I}}{E_s^{\rm inc}}\right|_{\mathbf{Q}}^2 \cos^2\varphi', \quad (38)$$

$$\frac{d\sigma^{(m)}(s \longrightarrow p)}{d\Omega_1'} = C_1(\left|\tilde G_{xx}^{\rm I}\right|^2 + \left|\tilde G_{zx}^{\rm I}\right|^2)_{\mathbf{Q}'} \times X_{yy}^{(m)}(\mathbf{Q}'-\mathbf{Q})\left|\frac{\tilde E_y^{\rm I}}{E_s^{\rm inc}}\right|_{\mathbf{Q}}^2 \sin^2\varphi', \quad (39)$$

$$\frac{d\sigma^{(m)}(p \longrightarrow s)}{d\Omega_1'} = C_1\left|\tilde G_{yy}^{\rm I}\right|_{\mathbf{Q}'}^2 X_{xx}^{(m)}(\mathbf{Q}'-\mathbf{Q})\left|\frac{\tilde E_x^{\rm I}}{E_p^{\rm inc}}\right|_{\mathbf{Q}}^2 \sin^2\varphi', \quad (40)$$

$$\frac{d\sigma^{(m)}(p \longrightarrow p)}{d\Omega_1'} = C_1\Bigg\{(\left|\tilde G_{xx}^{\rm I}\right|^2 + \left|\tilde G_{zx}^{\rm I}\right|^2)_{\mathbf{Q}} \times X_{xx}^{(m)}(\mathbf{Q}'-\mathbf{Q})\left|\frac{\tilde E_x^{\rm I}}{E_p^{\rm inc}}\right|_{\mathbf{Q}}^2 \cos^2\varphi' + 2{\rm Re}\{[\tilde G_{xx}^{\rm I}(\tilde G_{xz}^{\rm I})^* + \tilde G_{zx}^{\rm I}(\tilde G_{zz}^{\rm I})^*]_{\mathbf{Q}'} \times X_{xz}^{(m)}(\mathbf{Q}'-\mathbf{Q})\left(\frac{\tilde E_x^{\rm I}(\tilde E_z^{\rm I})^*}{\left|E_p^{\rm inc}\right|^2}\right)_{\mathbf{Q}}\Bigg\}\cos\varphi' + (\left|\tilde G_{xz}^{\rm I}\right|^2 + \left|\tilde G_{zz}^{\rm I}\right|^2)_{\mathbf{Q}'} X_{zz}^{(m)}(\mathbf{Q}'-\mathbf{Q})\left|\frac{\tilde E_z^{\rm I}}{E_p^{\rm inc}}\right|_{\mathbf{Q}}^2\Bigg\}. \quad (41)$$

In Eqs. (38)–(41),

$$C_1(\theta_1', \theta_1) = \frac{\varepsilon_1 k_0^6}{4\pi^2}\frac{\cos^2\theta_1'}{\cos\theta_1}, \quad (42)$$

and $\tilde E_\alpha^{\rm I} \equiv E_\alpha^{\rm I}(z_m^+; Q)$ and $\tilde G_{\alpha\beta}^{\rm I} \equiv G_{\alpha\beta}^{\rm I}(z, z_m^-; Q')$ for $z \longrightarrow -\infty$; for a quantum well ($m = 0$), these quantities are expressed by relations (A.10) and (A.11), into which one should substitute Eqs. (A.5)–(A.9) with due account of Eq. (A.4).

6. MODEL OF EXCITON POLARIZATION FLUCTUATIONS IN A QUANTUM WELL

6.1. Model

Following [17], we introduce a model of lateral polarization fluctuations of quasi-two-dimensional excitons in a quantum well. Deviations of the quantum-well interfaces from a plane surface end up in the formation of islands, i.e., finite regions within which the quantum-well width can be considered nearly constant [28]. An essential factor for determination of the island size is that the quantum-well interfaces be statistically different; for instance, in GaAs-based quantum wells, the autocorrelation radius of the lower interface (GaAs on $Al_xGa_{1-x}As$) is substantially larger than that for the

upper one ($Al_xGa_{1-x}As$ on GaAs) [28]. In experiment, the cross section of a probing light beam covers an extremely large number of various islands, which act in this case as a statistical ensemble.

It is believed that the average distances between atomic steps on an interface can be as large as a few tens of nanometers [28]. One should, however, bear in mind that the atomic interface profile cannot be identified with an optical (dielectric) interface for the following reasons of a general nature. First, the most efficient part played in scattering is that by the spatial scatterer spectrum that corresponds to sizes comparable to the probing-light wavelength [26]. Second, as follows from atomic force micrographs, surface roughness of a semiconductor crystal can be characterized by two correlation lengths, namely, a small-scale one (a few tens of nanometers) and a large-scale one (a few hundreds of nanometers) [34]. The large-scale size becomes manifest in the angular dependence of elastic light scattering from the rough surface of a semiconductor in the region of its volume-excitonic resonances [34, 35]. Based on this reasoning, we assume that light scattering by quantum wells is substantially also contributed by large-scale exciton-polarization fluctuations, in which the extent of the exciton wave function within an island can considerably exceed the Bohr radius. Such excitons are delocalized and retain their individuality with respect to the quasi-two-dimensional exciton in an infinite quantum well of the same width.

Let the profile of the quantum-well interfaces at $z = z_0 - \bar{L}/2 + \zeta_1(\mathbf{R})$ and $z = z_0 + \bar{L}/2 + \zeta_2(\mathbf{R})$ be determined by random functions $\zeta_1(\mathbf{R})$ and $\zeta_2(\mathbf{R})$ of the vector $\mathbf{R} = (x, y)$. The random quantum-well width is given by

$$L(\mathbf{R}) = \bar{L} + \delta L(\mathbf{R}) = \bar{L} + \zeta_2(\mathbf{R}) - \zeta_1(\mathbf{R}), \quad (43)$$

where $\bar{L} = \langle L(\mathbf{R})\rangle$ is the average width of the quantum well, which is statistically uniform in its plane. Here and subsequently, the averaging over realization ensembles of the random functions $\{\zeta_1(\mathbf{R})\}$ and $\{\zeta_2(\mathbf{R})\}$ is denoted by $\langle\ldots\rangle$, with $\langle\zeta_n(\mathbf{R})\rangle = \langle\delta L(\mathbf{R})\rangle = 0$.

Because we are interested in the manifestations of large-scale fluctuations of the interface shape in optical spectra, we generalize Eq. (5) by accepting for the tensor in Eq. (1) the expression [17]

$$\chi^0_{\alpha\beta}(\mathbf{R}, \omega) = \delta_{\alpha\beta}\chi^0_{\alpha\alpha}(\mathbf{R}, \omega) = \delta_{\alpha\beta}\frac{\bar{\Gamma}^0_\alpha}{\omega^0_\alpha(\mathbf{R}) - \omega - i\gamma}, \quad (44)$$

where the exciton transition frequency $\omega^0_\alpha(\mathbf{R})$ is a random function of $\mathbf{R}$. Substituting Eq. (44) into Eq. (6), with due account of Eq. (5), yields the following expression for the fluctuation part of the susceptibility:

$$\delta\chi^0_{\alpha\beta}(\mathbf{R}, \omega) = \delta_{\alpha\beta}\bar{\chi}^0_{\alpha\alpha}(\omega)\frac{\bar{\omega}^0_\alpha - \omega^0_\alpha(\mathbf{R})}{\omega^0_\alpha(\mathbf{R}) - \omega - i\gamma}. \quad (45)$$

If the quantum-well width fluctuations are small ($\langle\langle(dL)^2\rangle^{1/2} \ll \bar{L}$), the frequency $\omega^0_\alpha(\mathbf{R})$ in Eq. (45) can be expanded in $\delta L = \zeta_2 - \zeta_1$ near $\bar{\omega}^0_\alpha \equiv \omega^0_\alpha(\bar{L})$. For $\langle(\delta\omega^0_\alpha)^2\rangle^{1/2} \ll \bar{\omega}^0_\alpha$, we obtain in a linear approximation in δL,

$$\delta\omega^0_\alpha(\mathbf{R}) = \omega^0_\alpha(\mathbf{R}) - \bar{\omega}^0_\alpha \approx \{\partial\omega^0_\alpha/\partial L\}_{L=\bar{L}}\delta L(\mathbf{R}) = -U_\alpha\delta L(\mathbf{R})/\bar{L}. \quad (46)$$

Within an island, the exciton transition energy as a function of quantum-well width is given by the relation $\hbar\omega^0_\alpha(L) = E_{gap} + E_{conf}(L) - E_{bind}(L)$. Here, E_{gap} is the band gap width of the corresponding bulk material, E_{conf} is the size-quantization energy of the unbound confined electron and hole, and E_{bind} is their Coulomb binding energy in the exciton. Because of $E_{bind} \ll E_{conf}$, which is a relation that always holds for usual quantum-well widths [36], the dependence of the exciton frequency shift in Eq. (46) on L is determined by the confinement energy of the unbound pair:

$$\hbar\omega^0_\alpha(L) - E_{gap} \approx E_{conf}(L) = \beta(\pi\hbar)^2/(2\mu L^2), \quad (47)$$

where μ is the reduced electron–hole mass. Using Eq. (47), we obtain the following estimate for the coefficient U_α in Eq. (46):

$$U_\alpha = 2\pi^2\beta\frac{R}{\hbar}\left(\frac{a_B}{\bar{L}}\right)^2, \quad (48)$$

which is the same for excitons of either polarization α provided that the effective masses of the carriers in them are the same. In Eq. (48), R is the Rydberg energy, a_B is the bulk exciton Bohr radius, and the constant $\beta \sim 1$ depends on the dimensionality of the quantum well modeling an island. In the model of a potential well with infinite walls, this constant can vary from $\beta = 1$ for a one-dimensional well (a laterally macroscopic island) to $\beta = 3$ (an island represented by a cubic quantum box with dimensions $\bar{L} \times \bar{L} \times \bar{L}$).

For $\langle(\delta\omega^0_\alpha)^2\rangle^{1/2} < \gamma$, taking Eqs. (5) and (46) into account in Eq. (45) yields

$$\delta\chi^0_{\alpha\alpha}(\mathbf{Q}' - \mathbf{Q}; \omega) = \bar{\chi}^0_{\alpha\alpha}(\omega)\frac{U_\alpha}{\bar{\Delta}^0_\alpha(\omega)}\frac{\delta L(\mathbf{Q}' - \mathbf{Q})}{\bar{L}} \quad (49)$$

in first order in $\delta L(\mathbf{R})$ or in the Fourier component $\delta L(\mathbf{Q})$. In meaning, expression (49) relates to quasi-free excitons whose energies are modulated in lateral directions in accordance with the quantum-well width varia-

tion in Eq. (43). Using approximation (49) for correlation function (34) of a quantum well ($m = 0$), we come to

$$X_{\mu\nu}^{(0)}(\mathbf{Q}' - \mathbf{Q}) = \frac{\bar{\chi}_{\mu\mu}^0(\omega)}{\bar{\Delta}_\mu^0(\omega)} \frac{U_\mu \langle |\delta L(\mathbf{Q}' - \mathbf{Q})|^2 \rangle U_\nu}{\bar{L}^2} \left[\frac{\bar{\chi}_{\nu\nu}^0(\omega)}{\bar{\Delta}_\nu^0(\omega)}\right]^*. \quad (50)$$

6.2. Light Scattering by a Quantum Well in a Uniform Medium

Let us derive now analytical expressions for the cross section of resonant elastic light scattering by a quantum well residing in a uniform dielectric background with $\varepsilon^0(z) \equiv \varepsilon_b$. In this case, the conditions $r_1^\lambda = r_2^\lambda = 0$, $\chi_{\alpha\beta}^I = 0$ ($\alpha \neq \beta$), $\theta_1 = \theta$, and $\theta_1' = \theta'$ are satisfied and the quantum-well contribution ($m = 0$) to cross section (37) for different scattering channels takes on the form

$$\frac{d\sigma^{(0)}(s \longrightarrow s)}{d\Omega'} = W(\mathbf{Q}' - \mathbf{Q})|S_y(\omega, \mathbf{Q}')|^2 \times |S_y(\omega, \mathbf{Q})|^2 \cos^2\varphi', \quad (51)$$

$$\frac{d\sigma^{(0)}(p \longrightarrow s)}{d\Omega'} = W(\mathbf{Q}' - \mathbf{Q})|S_y(\omega, \mathbf{Q}')|^2 \times C(\omega)|S_x(\omega, \mathbf{Q})|^2 \sin^2\varphi', \quad (52)$$

$$\frac{d\sigma^{(0)}(s \longrightarrow p)}{d\Omega'} = W(\mathbf{Q}' - \mathbf{Q})|S_x(\omega, \mathbf{Q}')|^2 \times C^{-1}(\omega)|S_y(\omega, \mathbf{Q})|^2 \sin^2\varphi', \quad (53)$$

$$\frac{d\sigma^{(0)}(p \longrightarrow p)}{d\Omega'} = W(\mathbf{Q}' - \mathbf{Q}) \times \{|S_x(\omega, \mathbf{Q}')|^2 |S_x(\omega, \mathbf{Q})|^2 \cos^2\varphi' - 2\mathrm{Re}[S_x(\omega, \mathbf{Q}')S_z^*(\omega, \mathbf{Q}')S_z^*(\omega, \mathbf{Q})S_x(\omega, \mathbf{Q})]\cos\varphi' + |S_z(\omega, \mathbf{Q}')|^2 |S_z(\omega, \mathbf{Q})|^2\}. \quad (54)$$

Here,

$$W(\mathbf{Q}' - \mathbf{Q}) = \frac{\varepsilon_b k_0^2 \cos\theta'}{4\pi^2} \frac{\langle |\delta L(\mathbf{Q}' - \mathbf{Q})|^2 \rangle}{\bar{L}^2}, \quad (55)$$

$$C(\omega) = \frac{U_x}{U_y} \left|\frac{\bar{\Delta}_y^0(\omega)}{\bar{\Delta}_x^0(\omega)}\right|^2 \frac{\bar{\Gamma}_x^0}{\bar{\Gamma}_y^0}. \quad (56)$$

The spectral function

$$S_\alpha(\omega, \mathbf{Q}) = \frac{\sqrt{U_\alpha \Gamma_\alpha^0(Q)}}{\omega_\alpha(Q) - \omega - i\Gamma_\alpha^0(Q) - i\gamma} \equiv \frac{\sqrt{U_\alpha \Gamma_\alpha^0(Q)}}{\Delta_\alpha(Q, \omega)} \quad (57)$$

describes the resonance properties of an α-polarized exciton. The parameters of function (57) for *p*-polarized radiation ($\alpha = x, z$) are determined by Eqs. (22) and (23), and for *s*-polarized radiation ($\alpha = y$), by Eqs. (24). Equations (51)–(57) are a generalization of the results reported in [18], which relate to the isotropic exciton susceptibility (to make a comparison with Eqs. (51)–(54) possible, one should enter the factor $\cos\theta'$ in [18, Eqs. (26), (30)]). As seen from Eqs. (52) and (53), in the Born approximation, the radiation scattered in the light-incidence plane ($\varphi' = 0$) is not depolarized.

7. STATISTICAL PROPERTIES OF ROUGH INTERFACES

For the interfaces (surfaces) $z = z_m + \xi_m(\mathbf{R})$ having random relief shape components $\xi_m(\mathbf{R})$, we introduce correlation functions:

$$\langle \xi_m(\mathbf{R})\xi_{m'}(\mathbf{R}')\rangle = h_m h_{m'} K_{mm'} g_{mm'}(|\mathbf{R} - \mathbf{R}'|). \quad (58)$$

Here, $h_m = \sqrt{\langle \xi_m^2(\mathbf{R})\rangle}$ is the rms roughness height of the *m*th surface; the dependence on the difference $|\mathbf{R} - \mathbf{R}'|$ in Eq. (58) indicates statistic uniformity of the system in a plane $z = \text{const}$. The functions $g_{mm'}(|\mathbf{R} - \mathbf{R}'|)$ and the coefficients $K_{mm'} = \langle \xi_m(\mathbf{R})\xi_{m'}(\mathbf{R}')\rangle/(h_m h_{m'})$ describe autocorrelation of the surface shape for $m = m'$ and cross-correlation for $m \neq m'$, with $-1 \leq K_{mm'} \leq 1 = K_{mm}$. The observed quantities, in particular, those given by Eqs. (51)–(54), are expressed through the Fourier transforms of functions (58); i.e.,

$$\langle \xi_m(\mathbf{Q})[\xi_{m'}(\mathbf{Q}')]^*\rangle = h_m h_{m'} K_{mm'} g_{mm'}(|\mathbf{Q}|)(2\pi)^2 \delta(\mathbf{Q} - \mathbf{Q}'), \quad (59)$$

where $\xi_m^*(\mathbf{Q}) = \xi_m(-\mathbf{Q})$ because of the function $\xi_m(\mathbf{R})$ being real. A set of two-point functions of the type of Eq. (58) is usually sufficient for interpretation of a light-scattering (diffraction) experiment [26].

Because the character of the interface correlation in real heterostructures is unknown, let us consider

$$g_{mm'}(|\mathbf{R}|) = \exp(-|\mathbf{R}|^2/\Lambda_{mm'}^2) \quad (60)$$

to be a Gaussian correlation function and

$$g_{mm'}(|\mathbf{R}|) = \exp(-|\mathbf{R}|/\Lambda_{mm'}) \quad (61)$$

to be an exponential correlation function, where $\Lambda_{mm'}$ is the transverse roughness correlation length. Elastic light scattering through bulk exciton states has shown [35] that Gaussian correlators (60) are appropriate for characterization of randomly rough semiconductor sur-

faces. On the other hand, some authors [20, 27] reported on the possibility of manifestation of an exponential correlation in quantum-well optics, which is characteristic of stepped surfaces [26]. We compare now the theoretical results on light scattering obtained using correlation functions of both types.

The statistical characteristics of rough quantum-well interfaces are determined by the correlators $\langle \delta L(\mathbf{R}) \delta L(\mathbf{R}') \rangle$ and the Fourier amplitudes of the type of Eq. (59), which enter the observable quantities (38)–(41) through Eq. (50). Let us substitute the function $\xi_0(\mathbf{Q}) \equiv \delta L = \zeta_2 - \zeta_1$ from Eq. (43) for ξ_m into Eq. (59) and the correlator $\langle |\delta L(\mathbf{Q})|^2 \rangle$ thus obtained into Eq. (55); this yields

$$W(\mathbf{Q}' - \mathbf{Q}) = \frac{\cos\theta'}{4\pi^2}\left(\frac{\sqrt{\varepsilon_b}k_0}{\bar{L}}\right)^2 \times \{\tilde{h}_1^2\tilde{g}_{11} + \tilde{h}_2^2\tilde{g}_{22} - \tilde{h}_1\tilde{h}_2 K[\tilde{g}_{12} + \tilde{g}_{21}]\}, \quad (62)$$

where $\tilde{h}_n = \sqrt{\langle \zeta_n^2(\mathbf{R}) \rangle}$ and $\tilde{g}_{nn'} \equiv \tilde{g}_{nn'}(|\mathbf{Q}' - \mathbf{Q}|) = \langle \zeta_n(\mathbf{Q}) \zeta_{n'}^*(\mathbf{Q}') \rangle$.

Inclusion of cross-correlation between statistically rough quantum-well interfaces does not bring about any specific effects, except an additional weak scattering caused by the quantum-well bending [17, 18]. Therefore, in what follows, we neglect the interface roughness cross-correlation; i.e., we set $\tilde{g}_{12} = \tilde{g}_{21} = 0$ in Eq. (62). We also assume, for the sake of simplicity, that both interfaces in a quantum well are statistically identical. Under these conditions in the case of Gaussian correlation (60), function (55) takes on the form

$$W_g(\mathbf{Q}' - \mathbf{Q}) = \frac{\cos\theta'}{2\pi}\left(\frac{\sqrt{\varepsilon_b}k_0 h_g \Lambda_g}{\bar{L}}\right)^2 \times \exp\left(-\frac{|\mathbf{Q}' - \mathbf{Q}|^2 \Lambda_g^2}{4}\right). \quad (63)$$

In the case of exponential correlation function (62), we obtain

$$W_e(\mathbf{Q}' - \mathbf{Q}) = \frac{\cos\theta'}{\pi}\left(\frac{\sqrt{\varepsilon_b}k_0 h_e \Lambda_e}{\bar{L}}\right)^2 \times \left(\frac{1}{1 + |\mathbf{Q}' - \mathbf{Q}|^2 \Lambda_e^2}\right)^{3/2}. \quad (64)$$

Each of the functions defined by Eqs. (63) and (64) assumes that both quantum-well interfaces have the same transverse autocorrelation length Λ and rms roughness height h, with the quantum-well width fluctuation being $\sqrt{(\delta L)^2} = \sqrt{2}h$.

Figure 3 compares dependences (63) and (64) on the correlation length Λ of the interface roughness of a GaAs/AlGaAs quantum well calculated for various values of the angle θ'. That these functions have maximum values $W_g \sim W_e \sim (h/\bar{L})^2$ is of fundamental importance; note that function (63) reaches its maximum at $\Lambda_g = 2/|\mathbf{Q}' - \mathbf{Q}|$, and function (64), at $\Lambda_e = \sqrt{2}/|\mathbf{Q}' - \mathbf{Q}|$. These estimates depend on the dimensionality of the roughness [24]. According to Eq. (33), $|\mathbf{Q}' - \mathbf{Q}| \sim \sqrt{\varepsilon_b}k_0$; therefore, the angular characteristic (indicatrix) of light scattering will have a clearly pronounced structure if the dielectric response of rough interfaces is correlated over the length $\Lambda_g \sim \Lambda_e \sim 1/\sqrt{\varepsilon_b}k_0$. This is in accord with the general conclusion [26] that wave scattering (diffraction) turns out to be most efficient in studies of static disorder whose spatial spectrum has components with correlation lengths on the order of the probing wavelength. By contrast, for $\Lambda|\mathbf{Q}' - \mathbf{Q}| \ll 1$, i.e., $\Lambda \ll 1/\sqrt{\varepsilon_b}k_0$, the angular response of the radiation in Eqs. (63) and (64) corresponds to quasi-isotropic scattering. For $\Lambda|\mathbf{Q}' - \mathbf{Q}| \gg 1$, i.e., for $\Lambda \gg 1/\sqrt{\varepsilon_b}k_0$, the scattered radiation is concentrated within a narrow solid angle about the direction of mirror reflection.

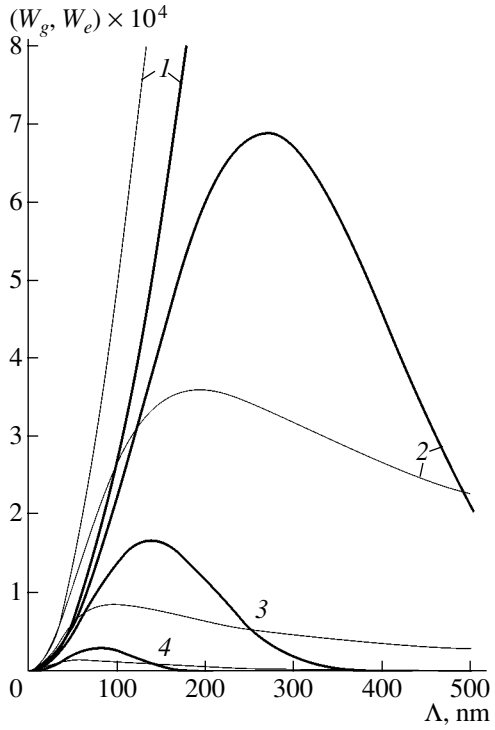

Fig. 3. Fourier components of the Gaussian W_g (thick lines) and exponential W_e (thin lines) shape autocorrelation functions of rough GaAs/AlGaAs quantum-well interfaces plotted vs. transverse correlation length Λ. Function W_g was calculated from Eq. (63), and function W_e, from Eq. (64), for $\hbar\omega_y^0(0) = 1.6$ eV, $\bar{L} = 14$ nm, $h = 0.2$ nm, $\varepsilon_b = 12.5$, $\theta = \varphi' = 0°$, and the following values of angle θ': (*1*) 5°, (*2*) 15°, (*3*) 30°, and (*4*) 60°.

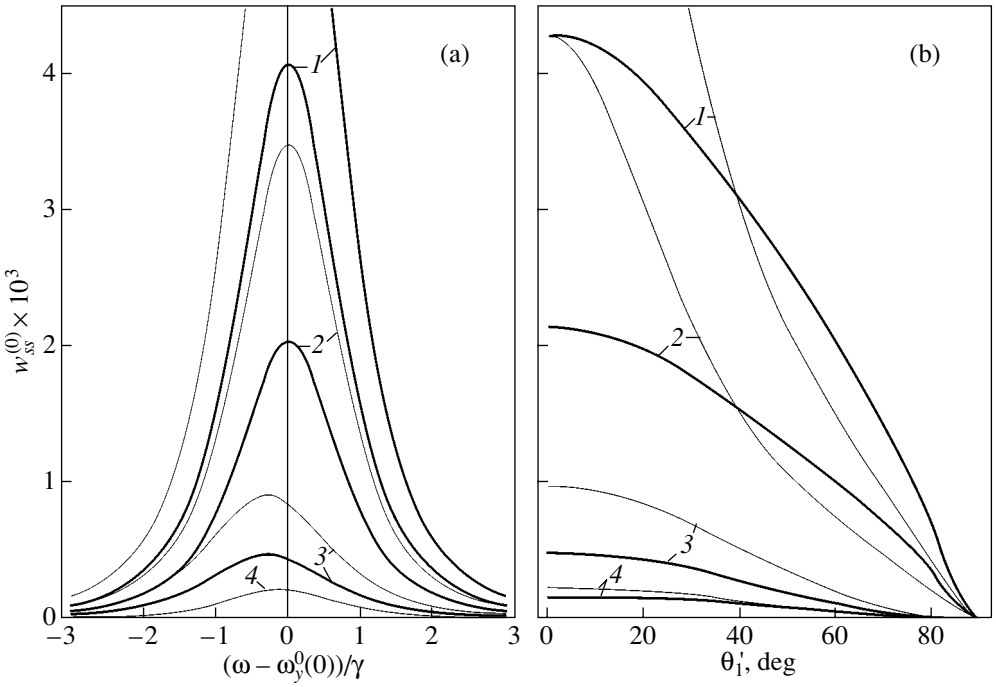

Fig. 4. Light scattering cross sections $w_{ss}^{(0)} \equiv d\sigma_{ss}^{(0)}(s \longrightarrow s)/d\Omega_1'$ plotted (a) vs. $(\omega - \omega_y^0(0))/\gamma$ for various angles θ_1' and (b) vs. angle θ_1' for $\omega = \omega_y^0(0)$ and $\hbar\omega_y^0(0) = 1.6$ eV ($\bar{L}$ = 14 nm). The parameters of the 1*e*–1*lh* exciton in the GaAs/AlGaAs quantum well are the same as in Fig. 2: $\hbar U_y = 50$ meV, $h = 0.2$ nm, $\Lambda = 50$ nm, $D = 200$ nm, and $z_0 = D/2$. The $w_{ss}^{(0)}$ spectra of panel (a) relate to $\theta_1 = 0$ and (*1*) $\varepsilon_1 = \varepsilon_2 = 12.5$, $\theta_1' = 15°$, $\varphi' = 0°$; (*2*) $\varepsilon_1 = \varepsilon_2 = 12.5$, $\theta_1' = 15°$, $\varphi' = 45°$; (*3*) $\varepsilon_1 = \varepsilon_2 = 1$, $\theta_1' = 20°$, $\varphi' = 0°$; and (*4*) $\varepsilon_1 = 1$, $\varepsilon_2 = 12.5$, $\theta_1' = 20°$, $\varphi' = 0°$. Thick lines relate to Gaussian (63), and thin lines, to exponential (64), correlation functions of rough interfaces.

8. NUMERICAL ANALYSIS

8.1. Light Scattering by a Quantum Well

The results of a numerical calculation of the quantum-well contributions $w_{\lambda\lambda}^{(0)} \equiv d\sigma^{(0)}(\lambda \longrightarrow \lambda)/d\Omega_1'$ to the scattering cross section in Eq. (37) are shown graphically in Figs. 4 and 5. The quantity $w_{ss}^{(0)}$ for the $s \longrightarrow s$ scattering channel was calculated from Eq. (38), and $w_{pp}^{(0)}$ for the $p \longrightarrow p$ channel was calculated using Eq. (41). The estimates were made for an anisotropic ground state (with $\tilde{\Gamma}_x^0 = \tilde{\Gamma}_y^0 = \tilde{\Gamma}_z^0/4$ [3, 17]) of the 1*e*–1*lh* light-hole quasi-two-dimensional exciton in a GaAs/AlGaAs quantum well. Equations (63) and (64) were used to take into account the Gaussian (thick lines in Fig. 4) or exponential (thin lines in Fig. 4) correlation between the quantum-well rough interfaces.

Let us compare the spectral and angular responses of the scattering intensity displayed in Figs. 4 and 5 for the $s \longrightarrow s$ and $p \longrightarrow p$ channels. We readily see that the scattering spectrum of the $p \longrightarrow p$ channel is more complex than that of the $s \longrightarrow s$ channel. This can be explained by the fact that both the incident and the scattered *p*-polarized wave can interact with two resonances having different frequencies, ω_x^0 from Eq. (22) and ω_z^0 from Eq. (23), whereas the $s \longrightarrow s$ scattering component reveals the only resonance with frequency ω_y^0 from Eq. (24). In the case of a uniform background, dielectric medium ($\varepsilon_1 = \varepsilon_2 = \varepsilon_b$ in Fig. 1), both dimensionless scattering cross sections (Figs. 4a, 5a) have the largest amplitude at resonance, which constitutes $w_{\lambda\lambda}^{(0)} \sim 10^{-2}$ for $\Lambda = 100$ nm. Figures 4a and 5a also show that the scattered intensity in vacuum ($\varepsilon_1 = 1$) is substantially weaker than that in a uniform semiconductor due to the light refraction and reflection from the cavity walls.

The difference between the scattering channels also manifests itself in the dependence of the quantities $w_{\lambda\lambda}^{(0)}$ on the angles θ_1 and θ_1', as well as on φ' (Figs. 4b, 5b). On the whole, the angular responses of scattering shown in the figures are intimately connected with the correlation properties of the interfaces discussed in Section 7. For a given roughness correlation length Λ,

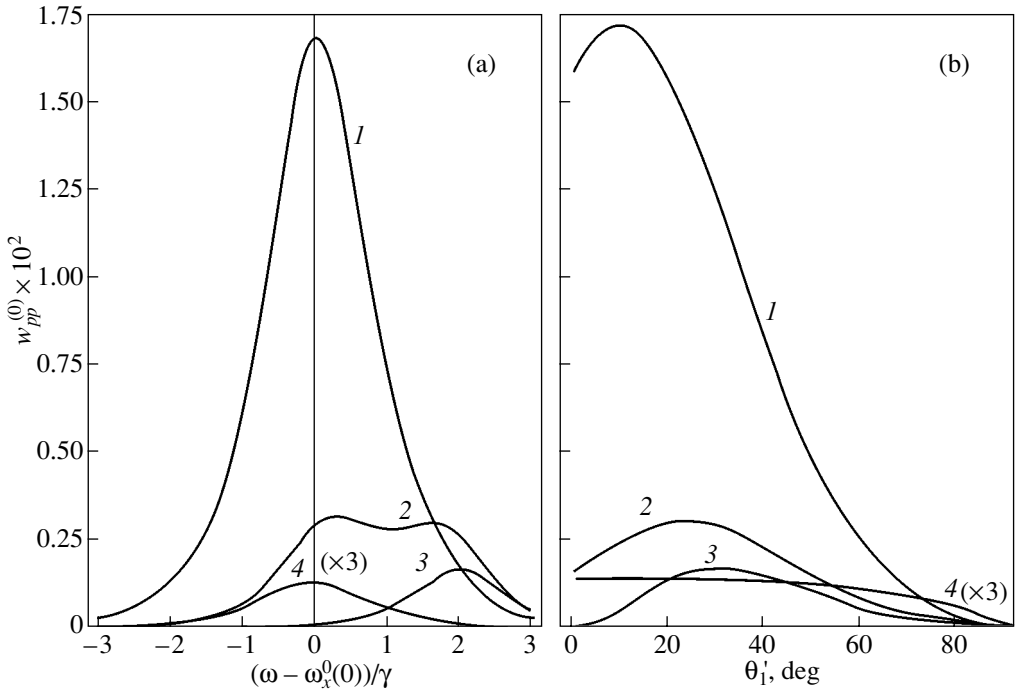

Fig. 5. (a) Spectral and (b) angular dependences of scattering cross sections $w_{pp}^{(0)} \equiv d\sigma^{(0)}(p \longrightarrow p)/d\Omega_1'$ for a GaAs/AlGaAs quantum well with $\hbar\omega_x^0(0) = 1.6$ eV, $\hbar\omega_z^0(0) = 1.602$ eV ($\bar{L} = 14$ nm), $\hbar\tilde{\Gamma}_x^0 = \hbar\tilde{\Gamma}_z^0/4 = 0.25$ meV, and $\hbar U_x = \hbar U_z = 50$ meV. The parameters used are $\varepsilon_2 = 12.5$, $D = 200$ nm, $z_0 = D/2$, $h = 0.2$ nm, and $\Lambda = 100$ nm. Spectra in panel (a) were calculated for $\theta_1' = 0°$ and (*1*) $\varepsilon_1 = 12.5$, $\theta_1 = 5°$, $\theta_1' = 10°$, $\varphi' = 0°$; (*2*) $\varepsilon_1 = 12.5$, $\theta_1 = 10°$, $\theta_1' = 30°$, $\varphi' = 60°$; (*3*) $\varepsilon_1 = 12.5$, $\theta_1 = 10°$, $\theta_1' = 30°$, $\varphi' = 90°$; and (*4*) $\varepsilon_1 = 1$, $\theta_1 = 18°$, $\theta_1' = 38°$, $\varphi' = 0°$. The angular dependences in panel (b) correspond to frequencies (*1*, *4*) $\omega_x^0(0)$, (*2*) $[\omega_x^0(0) + \omega_z^0(0)]/2$, and (*3*) $\omega_z^0(0)$.

the dependence of the scattered intensity on angles θ and θ' is determined by the quantity $|\mathbf{Q} - \mathbf{Q}'|$, with the condition $|\mathbf{Q} - \mathbf{Q}'|\Lambda \sim 1$ providing optimum estimation of correlation functions (63) and (64) from the standpoint of the amount of information that can be gained from an experiment. For $\Lambda \ll 1/k_0$, the light scattering from a quantum well in a cavity is practically isotropic in angle θ'. In these conditions, most of the radiation, for which $\theta' > \arcsin\sqrt{\varepsilon_1/\varepsilon_b} = \theta_{\max}'$, does not leave the cavity because of the strong dielectric contrast ($\varepsilon_1 \ll \varepsilon_b$) of the semiconductor/vacuum interface ($\theta_{\max}' \approx 16°$ for GaAs). By contrast, for $\Lambda \gg 1/k_0$, most of the radiation scattered by the quantum well escapes to vacuum within a small solid angle about the direction of mirror reflection from the plane (central) surface. These features also become manifest to a certain extent in the angular dependences of light scattering by a quantum well, which are plotted in Figs. 4b and 5b for the optimum conditions $|\mathbf{Q} - \mathbf{Q}'|\Lambda \sim 1$. On the whole, the differences in the angular dependence of light scattering that are due to the interfaces being differently correlated are insignificant; they can be, instead, considered quantitative. As a result, determination of the character of the interface shape correlation appears a more complex inverse scattering problem than calculation of the characteristic statistical parameters of the interface roughness.

The above estimates suggest that the cross sections of resonant light scattering by a quantum well exceed, by nearly two orders of magnitude, those measured [34, 35] in the range of bulk-exciton frequencies in the elastic scattering of light from a semiconductor surface with the same roughness scale. Indeed, the probability of light scattering by a quantum well within the total solid angle can be estimated as $W_{\mathrm{QW}} \sim [h\Lambda/(\lambda\bar{L})]^2$, where $\lambda = 2\pi/k_0$, Λ is the transverse correlation length, and h is the rms roughness height. Using Figs. 4 and 5, we find that $W_{\mathrm{QW}} \sim 10^{-3}$–$10^{-2}$ for GaAs-based quantum wells with roughness height $h \sim 10^{-1}$ nm. In the case of a rough semiconductor surface, the estimate of W_{QW} should be replaced by [35] $W_{\mathrm{RS}} \sim (h_s\Lambda_s/\lambda^2)^2$, where h_s and Λ_s are the surface roughness parameters entering the correlation function in Eq. (63). Hence, $W_{\mathrm{QW}}/W_{\mathrm{RS}} \sim$

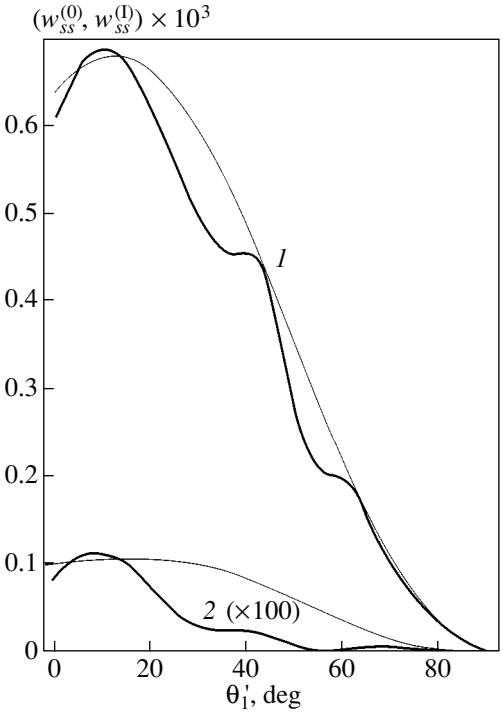

Fig. 6. Partial cross sections of light scattering by a quantum well (curves *1* for $w_{ss}^{(0)}$), and by two rough cavity walls (curves *2*, scaled by 1000 for $w_{ss}^{(I)} = w_{ss}^{(1)} + w_{ss}^{(2)}$), which enter the total scattering cross section of Eq. (37), plotted vs. incidence angle θ_1. Thin lines relate to $D\omega_y^0(0)/c = 2\pi$, and thick lines, to $D\omega_y^0(0)/c = 15\pi$. The calculations were made for the exciton resonance frequency $\omega = \omega_y^0(0)$, $\hbar\omega_y^0(0) =$ 1.6 eV, $\varepsilon_1 = 1$, $\varepsilon_2 = 6$, $z_0 = D/2$, $\theta_1 + \theta_1' = 18°$, $\varphi' = 0°$, and for the same parameters as in Fig. 4. Gaussian correlation functions with the same parameters, $h = 0.2$ and $\Lambda = 100$ nm, were used for all interfaces.

$(\lambda/\bar{L})^2$ if $h = h_s$ and $\Lambda = \Lambda_s \sim 1/k_0$; i.e., $W_{QW}/W_{RS} \sim 10^2$ for the same interface roughness height. A comparison of the estimates from Eqs. (51)–(55) with experiment [35] shows that light scattering effects from a single quantum well are readily observable for an interface roughness height $h \sim 10^{-1}$ nm. By increasing the $h/\bar{L}$ ratio, one can, in principle, obtain from Eqs. (38)–(41) somewhat larger intensities scattered from a quantum well; however, the condition $h < \gamma\bar{L}/U$ of the applicability of Eq. (49) must not be violated. Because this inequality assumes resonant interaction between exciton polarizations in different parts of the quantum well, its violation would indicate the need to invoke another model which would take into account exciton localization in islands whose dimensions along the interfaces are small.

8.2. Light Scattering from Cavity Walls

In real nanostructures, not only the quantum-well interfaces but also other boundaries can be statistically rough. The random roughness of the Fabry–Perot cavity walls accounts for the presence of the second term in the scattering cross section in Eq. (37). We compare this contribution from the cavity walls to light scattering with the above resonance contribution originating from quantum-well width fluctuations. To do this, we assume that the shape of the rough cavity walls (Fig. 1) can be approximated by random profile functions $z = \xi_1(\mathbf{R})$ and $z = D + \xi_2(\mathbf{R})$, respectively, which are not correlated. We take into account constitutive equations of the type of Eq. (13) with $z_1 = 0$ and $z_2 = D$ and calculate the independent contributions to the scattering cross section in Eq. (37) that are caused by random roughness of the cavity walls.

Figure 6 compares the contribution due to the rough Fabry–Perot cavity walls $w_{ss}^{(I)} = w_{ss}^{(1)} + w_{ss}^{(2)}$, with $w_{ss}^{(m)} \equiv d\sigma^{(m)}(s \longrightarrow s)/d\Omega_1'$ (curves *2*), under excitation by an *s*-polarized wave given by Eq. (12) with the contribution originating from quantum-well exciton resonance $w_{ss}^{(0)}$ (curves *1*) to the total scattering cross section $w_{ss} = w_{ss}^{(0)} + w_{ss}^{(I)}$. These quantities are plotted as functions of the angle of light incidence θ_1 for a fixed angle $\theta_1 + \theta_1' =$ const between the incident and the scattered fluxes; this condition is usually met in experiments [34]. We readily see that, for the same rms roughness height, light scattering from the Fabry–Perot cavity walls is two orders of magnitude smaller than that from a quantum well that is resonantly amplified by quasi-two-dimensional excitons. In the case of the Fabry–Perot cavity, the scattered intensity reveals an interference structure, which becomes evident for cavity widths sufficiently large as compared to the wavelength ($D \gg c/\omega$). Interference gives rise to scattered-intensity oscillations, but its inclusion does not affect, in any way, the above fundamental conclusion that the light scattering from cavity walls is relatively weak. In closing, we stress that, because the effect of cavity walls on the observable optical quantities has been taken into account by us through the light reflection coefficients, our theoretical results can be conveniently used in analyzing the emission and scattering of light by quantum wells located inside semiconductor microcavities of various nature.

9. CONCLUSIONS

The correlation theory of resonant elastic light scattering developed above suggests the following conclusions. Variation of the quantum-well width and the associated lateral fluctuations in quasi-two-dimensional exciton energy account for the elastic light scattering, which is resonantly amplified as compared to

the case of a single interface. As a consequence, the intensity of resonance scattering by a quantum well with atomically rough interfaces exceeds, by approximately two orders of magnitude, that due to single heterostructure interfaces with the same roughness. The magnitude of the radiation corrections to the energy and decay of a quasi-two-dimensional exciton confined to a quantum well residing in a Fabry–Perot cavity depends substantially on the actual position of the quantum well relative to the structure interfaces. These features of spontaneous radiation affect light scattering in real heterostructures and are essentially different for processes which differ in the linear polarization (*p* or *s*) of the incident and/or scattered waves. The spectral and angular dependences of the scattering probability derived with Gaussian and exponential correlation functions of interface roughness are qualitatively similar. This substantially complicates the solution of the inverse scattering problem bearing on determination of the type of statistics describing rough interfaces. At the same time, the scattering cross sections are expressed explicitly through interface shape correlation functions and, therefore, can be employed to derive the statistical parameters of interfaces from experimental data, as was done in [35].

APPENDIX

SOLUTION OF THE ELECTRODYNAMIC PROBLEM FOR A QUANTUM WELL IN A CAVITY

The solutions to Eqs. (8) and (9) for a multilayered medium with plane interfaces perpendicular to the *z* axis and with an isotropic dielectric permittivity tensor $\varepsilon^0(z)\hat{I}$ can be written as

$$\begin{aligned}&\{\mathbf{E}^0(z, \mathbf{R}), \hat{G}^0(z, z'; \mathbf{R})\}\\ &= \exp(iQx)\{\mathbf{E}^0(z, Q), \hat{G}^0(z, z'; Q)\}.\end{aligned} \tag{A.1}$$

In representation (A.1), the field components with Cartesian indices $\alpha = x, z$ (*p* polarization) and $\alpha = y$ (*s* polarization) are separated. The tensor $\hat{\bar{\chi}}^0$ of an ideal quantum well characterized by Eq. (5) is diagonal; therefore, representation (A.1) is valid for functions $\mathbf{E}^{\mathrm{I}}(z, \mathbf{R})$ and $\hat{G}^{\mathrm{I}}(z, z'; \mathbf{R})$ and integral equations (14) for their amplitudes take on the form

$$\begin{aligned}E^{\mathrm{I}}_\alpha(z) - E^0_\alpha(z) &= k_0^2\sum_\mu G^0_{\alpha\mu}(z, \bullet)\bar{\chi}^0_{\mu\mu}E^{\mathrm{I}}_\mu(\bullet)\\ &= k_0^2\sum_\mu G^0_{\alpha\mu}(z, \bullet)\frac{\chi^{\mathrm{I}}_{\mu\nu}}{I_c^2}E^0_\nu(\bullet),\end{aligned} \tag{A.2}$$

$$\begin{aligned}&G^{\mathrm{I}}_{\alpha\beta}(z, z') - G^0_{\alpha\beta}(z, z')\\ &= k_0^2\sum_\mu G^0_{\alpha\mu}(z, \bullet)\bar{\chi}^0_{\mu\mu}G^{\mathrm{I}}_{\mu\beta}(\bullet, z')\\ &= k_0^2\sum_\mu G^0_{\alpha\mu}(z, \bullet)\frac{\chi^{\mathrm{I}}_{\mu\nu}}{I_c^2}G^0_{\nu\beta}(\bullet, z')\end{aligned} \tag{A.3}$$

(the parameter *Q* is dropped). Here, we used the relation

$$f(\bullet) \equiv \int dz f(z)\Psi(z - z_0), \tag{A.4}$$

in which $f(z)$ is an arbitrary function, $\Psi(z - z_0)$ is the envelope of the wave function from Eq. (1), and I_c is given by Eq. (25). The second of the equalities in (A.2) and (A.3) results from a self-consistent solution of the equations corresponding to the first of the equalities in (A.2) and (A.3). The notation used in Eqs. (A.2) and (A.3) is

$$\chi^{\mathrm{I}}_{xx}(Q, \omega) = \frac{I_c^2}{\Delta(Q, \omega)}\left[\frac{1}{\bar{\chi}^0_{zz}(\omega)} - k_0^2 G^0_{zz}(\bullet, \bullet; Q, \omega)\right], \tag{A.5}$$

$$\chi^{\mathrm{I}}_{zz}(Q, \omega) = \frac{I_c^2}{\Delta(Q, \omega)}\left[\frac{1}{\bar{\chi}^0_{xx}(\omega)} - k_0^2 G^0_{xx}(\bullet, \bullet; Q, \omega)\right], \tag{A.6}$$

$$\begin{aligned}\chi^{\mathrm{I}}_{xz}(Q, \omega) &= -\chi^{\mathrm{I}}_{zx}(Q, \omega)\\ &= \frac{I_c^2}{\Delta(Q, \omega)}k_0^2 G^0_{xz}(\bullet, \bullet; Q, \omega),\end{aligned} \tag{A.7}$$

$$\begin{aligned}\Delta(Q, \omega) &= \left[\frac{1}{\bar{\chi}^0_{xx}(\omega)} - k_0^2 G^0_{xx}(\bullet, \bullet)\right]\\ &\times\left[\frac{1}{\bar{\chi}^0_{zz}(\omega)} - k_0^2 G^0_{zz}(\bullet, \bullet)\right] - k_0^4 G^0_{xz}(\bullet, \bullet)G^0_{zx}(\bullet, \bullet)\end{aligned} \tag{A.8}$$

for *p*-polarized light and

$$\chi^{\mathrm{I}}_{yy}(Q, \omega) = I_c^2\left[\frac{1}{\bar{\chi}^0_{yy}(\omega)} - k_0^2 G^0_{yy}(\bullet, \bullet; Q, \omega)\right]^{-1} \tag{A.9}$$

for *s*-polarized light.

As follows from Eqs. (A.2) and (A.3), in terms of susceptibilities (A.5)–(A.9), the Cartesian components of the exciting field can be expressed as

$$\begin{aligned}E^{\mathrm{I}}_\alpha(\bullet) &= \frac{1}{\bar{\chi}^0_{\alpha\alpha}I_c^2}[\chi^{\mathrm{I}}_{\alpha x}E^0_x(\bullet) + \chi^{\mathrm{I}}_{\alpha z}E^0_z(\bullet)],\\ E^{\mathrm{I}}_y(\bullet) &= \frac{\chi^{\mathrm{I}}_{yy}}{\bar{\chi}^0_{yy}I_c^2}E^0_y(\bullet),\end{aligned} \tag{A.10}$$

and the components of the tensor Green's function for the radiation problem ($z \longrightarrow -\infty$) can be expressed as

$$G^{\mathrm{I}}_{\alpha\beta}(z,\bullet) = [G^0_{\alpha x}(z,\bullet)\chi^{\mathrm{I}}_{x\beta} + G^0_{\alpha z}(z,\bullet)\chi^{\mathrm{I}}_{z\beta}]\frac{1}{\bar{\chi}^0_{\beta\beta}I_c^2},$$

$$G^{\mathrm{I}}_{yy}(z,\bullet) = G^0_{yy}(z,\bullet)\frac{\chi^{\mathrm{I}}_{yy}}{\bar{\chi}^0_{yy}I_c^2}, \tag{A.11}$$

with $E^0_\alpha(\bullet) = E^0_\alpha(z_0)I_c$ and $G^0_{\alpha\beta}(z,\bullet) = G^0_{\alpha\beta}(z,z_0)I_c$, where indices α and β denote x or z. The elements of matrix (34) assume the form (we drop the superscript 0 or I)

$$M_{xx} = (|G_{xx}|^2 + |G_{zx}|^2)\cos^2\varphi' + |G_{yy}|^2\sin^2\varphi',$$

$$M_{yy} = (|G_{xx}|^2 + |G_{zx}|^2)\sin^2\varphi' + |G_{yy}|^2\cos^2\varphi',$$

$$M_{zz} = |G_{xz}|^2 + |G_{zz}|^2,$$

$$M_{xy} = (|G_{xx}|^2 + |G_{zx}|^2 - |G_{yy}|^2)\cos\varphi'\sin\varphi' = M^*_{yx}, \tag{A.12}$$

$$M_{xz} = (G_{xx}G^*_{xz} + G_{zx}G^*_{zz})\cos\varphi' = M^*_{zx},$$

$$M_{yz} = (G_{xx}G^*_{xz} + G_{zx}G^*_{zz})\sin\varphi' = M^*_{zy}.$$

The preceding expressions in this appendix relate to an arbitrary layered medium. Functions $\hat{G}^0$ were obtained in an analytical form for structures whose function $\varepsilon^0(z)$ describes two, three [30], or four [33] macroscopically thick uniform dielectric layers. For the cavity model shown in Fig. 1, to which an unperturbed three-layer medium corresponds, the notation introduced in Eqs. (A.5)–(A.9) is as follows:

$$k_0^2 G^0_{xx}(\bullet,\bullet) = \frac{ik}{2\varepsilon_b}\left\{\frac{(1+r_1^p e^{2ikz_0})(1+r_2^p e^{2ik(D-z_0)})}{1-r_1^p r_2^p e^{2ikD}}I_c^2 + iI_s\right\}, \tag{A.13}$$

$$k_0^2 G^0_{zz}(\bullet,\bullet) = \frac{ik}{2\varepsilon_b}\left(\frac{Q}{k}\right)^2 \times\left\{\frac{(1-r_1^p e^{2ikz_0})(1-r_2^p e^{2ik(D-z_0)})}{1-r_1^p r_2^p e^{2ikD}}I_c^2 + iI_s\right\} - \frac{I_0}{\varepsilon_b}, \tag{A.14}$$

$$k_0^2 G^0_{xz}(\bullet,\bullet) = -k_0^2 G^0_{zx}(\bullet,\bullet) = \frac{iQ}{2\varepsilon_b}\frac{r_1^p e^{2ikz_0} - r_2^p e^{2ik(D-z_0)}}{1-r_1^p r_2^p e^{2ikD}}I_c^2, \tag{A.15}$$

$$k_0^2 G^0_{yy}(\bullet,\bullet) = \frac{ik_0^2}{2k} \times\left\{\frac{(1+r_1^s e^{2ikz_0})(1+r_2^s e^{2ik(D-z_0)})}{1-r_1^s r_2^s e^{2ikD}}I_c^2 + iI_s\right\}. \tag{A.16}$$

The integrals I_c, I_s, and I_0 are given by Eqs. (25).

ACKNOWLEDGMENTS

The author is indebted to A.V. Sel'kin for helpful discussions.

This study was supported by the Russian Foundation for Basic Research, project nos. 02-02-17601 and 00-02-17030.

REFERENCES

1. R. Loudon, *The Quantum Theory of Light* (Clarendon, Oxford, 1973; Mir, Moscow, 1976).
2. R. A. Ferrell, Phys. Rev. **111** (5), 1214 (1958); J. Crowell and R. H. Ritchie, Phys. Rev. **172** (2), 436 (1968); O. P. Burmistrova and V. A. Kosobukin, Phys. Status Solidi B **112** (2), 675 (1982).
3. E. L. Ivchenko and G. E. Pikus, *Superlattices and Other Heterostructures. Symmetry and Optical Phenomena*, 2nd ed. (Springer, Berlin, 1997).
4. D. Citrin, Phys. Rev. B **47** (7), 3832 (1993); Comments Condens. Matter Phys. **16** (5), 263 (1993).
5. L. C. Andreani and F. Bassani, Phys. Rev. B **41** (11), 7536 (1990).
6. E. L. Ivchenko, Fiz. Tverd. Tela (Leningrad) **33** (8), 2388 (1991) [Sov. Phys. Solid State **33**, 1344 (1991)].
7. V. A. Kosobukin, Fiz. Tverd. Tela (St. Petersburg) **34** (10), 3107 (1992) [Sov. Phys. Solid State **34**, 1662 (1992)].
8. E. L. Ivchenko, A. I. Nesvizhskiĭ, and S. Ĭorda, Fiz. Tverd. Tela (St. Petersburg) **36** (7), 2118 (1994) [Phys. Solid State **36**, 1156 (1994)]; E. L. Ivchenko, V. P. Kochereshko, A. V. Platonov, *et al.*, Fiz. Tverd. Tela (St. Petersburg) **39** (11), 2072 (1997) [Phys. Solid State **39**, 1852 (1997)].
9. V. A. Kosobukin, R. P. Seisyan, and S. A. Vaganov, Semicond. Sci. Technol. **8** (7), 1235 (1993); V. A. Kosobukin, Phys. Status Solidi B **208** (1), 271 (1998).
10. J. Hegarty, M. D. Sturge, C. Weisbuch, *et al.*, Phys. Rev. Lett. **49** (13), 930 (1982).
11. J. Humlicek, E. Schmidt, L. Bocanek, *et al.*, Phys. Rev. B **48** (8), 5241 (1993); S. Glutsch and F. Bechstedt, Phys. Rev. B **50** (11), 7733 (1994).
12. G. V. Astakhov, V. A. Kosobukin, V. P. Kochereshko, *et al.*, Eur. Phys. J. B **24** (1), 7 (2001).
13. T. Stroucken, A. Knorr, C. Anthony, *et al.*, Phys. Rev. Lett. **74** (12), 2391 (1995); G. Malpuech, A. Kavokin, W. Langbein, and J. M. Hvam, Phys. Rev. Lett. **85** (3), 650 (2000).
14. H. Stolz, D. Schwarze, W. Osten, and G. Weimann, Phys. Rev. B **47** (15), 9669 (1993).

15. B. Grote, C. Ell, S. W. Koch, *et al.*, Phys. Rev. B **64** (4), 045330 (2001).
16. R. Zimmermann, Nuovo Cimento D **17** (11–12), 1801 (1995); V. I. Belitsky, A. Cantarero, S. T. Pavlov, *et al.*, Phys. Rev. B **52** (23), 16665 (1995); D. S. Citrin, Phys. Rev. B **54** (20), 14572 (1996); R. Zimmermann, E. Runge, and F. Grosse, Pure Appl. Chem. **69**, 1179 (1997).
17. V. A. Kosobukin, Solid State Commun. **108** (2), 83 (1998).
18. V. A. Kosobukin, Fiz. Tverd. Tela (St. Petersburg) **41** (2), 330 (1999) [Phys. Solid State **41**, 296 (1999)].
19. M. Gurioli, F. Bogani, D. S. Wiersma, *et al.*, Phys. Rev. B **64** (16), 165309 (2001).
20. L. S. Braginsky, M. Yu. Zaharov, A. M. Gilinsky, *et al.*, Phys. Rev. B **63** (19), 195305 (2001).
21. S. Haacke, R. A. Taylor, R. Zimmermann, *et al.*, Phys. Rev. Lett. **78** (11), 2228 (1997); M. Gurioli, F. Bogani, S. Ceccherini, and M. Colocci, Phys. Rev. Lett. **78** (16), 3205 (1997); G. R. Hayes, S. Haacke, M. Kauer, *et al.*, Phys. Rev. B **58** (16), R10175 (1998).
22. Y. Merle d'Aubigne, A. Wasiela, H. Mariette, and T. Dietl, Phys. Rev. B **54** (19), 14003 (1996).
23. R. Houdre, R. P. Stanley, U. Oesterle, *et al.*, Phys. Rev. B **49** (23), 16761 (1994).
24. V. A. Kosobukin and A. V. Sel'kin, Fiz. Tverd. Tela (St. Petersburg) **42** (10), 1863 (2000) [Phys. Solid State **42**, 1914 (2000)]; Mod. Phys. Lett. B **15** (17–19), 782 (2001).
25. A. V. Shchegrov, J. Bloch, D. Birkedal, and J. Shah, Phys. Rev. Lett. **84** (15), 3478 (2000); D. M. Whittaker, Phys. Rev. B **61** (4), R2433 (2000).
26. J. M. Ziman, *Models of Disorder: The Theoretical Physics of Homogeneously Disordered Systems* (Cambridge Univ. Press, Cambridge, 1979; Mir, Moscow, 1982).
27. A. V. Shchegrov, D. Birkedal, and J. Shah, Phys. Rev. Lett. **83** (7), 1391 (1999).
28. J. Singh, K. K. Bajaj, and S. Chaudhuri, Appl. Phys. Lett. **44**, 805 (1984); F. Bechstedt and R. Enderlein, *Semiconductor Surfaces and Interfaces* (Akademie, Berlin, 1988), Ser.: Physical Research, Vol. 5.
29. E. L. Ivchenko, V. P. Kochereshko, P. S. Kop'ev, *et al.*, Solid State Commun. **70** (5), 529 (1989).
30. A. A. Maradudin and D. L. Mills, Phys. Rev. B **11** (4), 1392 (1975); Phys. Rev. B **12** (8), 2943 (1975).
31. D. L. Mills, Phys. Rev. B **12** (10), 4036 (1975).
32. A. A. Abrikosov, L. P. Gor'kov, and I. E. Dzyaloshinskiĭ, *Methods of Quantum Field Theory in Statistical Physics* (Nauka, Moscow, 1962; Prentice Hall, Englewood Cliffs, N.J., 1963).
33. V. A. Kosobukin, Preprint No. 1724, FTI (Ioffe Physicotechnical Inst., Russian Academy of Sciences, St. Petersburg, 1999).
34. A. V. Ankudinov, V. A. Kosobukin, S. O. Romanovskiĭ, *et al.*, in *Abstracts of 5th Russian Conference on Physics of Semiconductors* (Nizhni Novgorod, 2001), Vol. 1, p. 127.
35. V. A. Kosobukin and A. V. Selkin, Solid State Commun. **66** (3), 313 (1988); V. A. Kosobukin, M. I. Sazhin, and A. V. Selkin, Solid State Commun. **94** (11), 947 (1995).
36. G. Bastard, E. E. Mendez, L. L. Chang, and L. Esaki, Phys. Rev. B **26** (4), 1974 (1982); R. L. Greene, K. K. Bajaj, and D. E. Phelps, Phys. Rev. B **29** (4), 1807 (1984).

Translated by G. Skrebtsov

Physics of the Solid State, Vol. 45, No. 4, 2003, pp. 752–756. Translated from Fizika Tverdogo Tela, Vol. 45, No. 4, 2003, pp. 715–719.

LOW-DIMENSIONAL SYSTEMS AND SURFACE PHYSICS

Unoccupied Electron States in Low-Energy Electron Total-Current and Transmission Spectroscopy of Molybdenum Disulfide

O. F. Panchenko

Donetsk Physicotechnical Institute, National Academy of Sciences of Ukraine, Donetsk, 83114 Ukraine
e-mail: panch@mail.fti.ac.donetsk.ua

Received July 17, 2002

Abstract—A theoretical interpretation of the fine structure in the low-energy electron total-current spectra and low-energy electron transmission spectra measured along the normal to the (0001)MoS_2 single-crystal surface is proposed. The calculations took into account the energy dependence of band level broadening and the electronic structure of the high final unoccupied states (above the vacuum level E_{vac}), which become occupied by electrons entering a solid. A comparison with the available experimental and theoretical data is performed. The effects of the bulk band structure are shown to play a dominant role in the formation of the spectra (the extrema in the spectra identify the energy position of critical points, such as the band edges or the points of extremal curvature of the dispersion branches). The proposed method makes it possible to separate the bulk effects in spectra from surface effects, this approach can be used to advantage in monitoring the state of a surface in the course of its treatment. © *2003 MAIK "Nauka/Interperiodica".*

1. INTRODUCTION

The electron band structure $E(\mathbf{k})$ is a fundamental characteristic determining most of the physical properties of solids, for instance, the transport phenomena, optical, and photoemission (PE) properties. The band structure (more specifically, the electronic states near the Fermi level E_F) is also a major factor underlying the operation of solid-state electronic devices. Note that not only the energy positions of electronic states (which determine, for instance, the band gap width) but also the arrangement of these states in **k** space are important. Unoccupied high-lying states are traditionally studied using x-ray absorption spectroscopy (XAS) [1], bremsstrahlung isochromat spectroscopy (BIS) [1, 2], inner-shell characteristic electron energy loss spectroscopy (EELS) [1, 3], inverse photoelectron spectroscopy (IPES) [1, 4, 5], very low-energy electron diffraction (VLEED) [6, 7], low-energy secondary-electron emission spectroscopy (SEES) [8, 9], low-energy total-current (TC) spectroscopy (TCS) [5, 10–23] and its modification, and low-energy electron transmission spectroscopy (LEET) [24–28]. Having a high surface sensitivity and being nondestructive, the latter two methods are employed, in addition to analyzing elementary excitations and near-surface states, in monitoring surface cleanness in the course of surface treatments, determination of the work function, etc. Note also that the technical simplicity of these two methods permits their use in monitoring $E(\mathbf{k})$ parameters directly in the course of manufacture of semiconductor devices. Although high-lying states cannot be classed among states near E_F, the changes are interrelated.

Due to the specific features of their crystal and electronic structure [29], layered rare-metal dichalcogenides (RMDC) feature a number of unique properties; as a result, the related materials do not have analogs and cannot be replaced by an equivalent counterpart. Among these materials are layered binary compounds exhibiting strongly anisotropic atomic interactions. This factor accounts for the rich diversity of their anomalous properties, in particular, the structure of their energy levels, namely, their fine structure (FS), splitting, overlapping, and mutual position in **k** space. Indeed, single-crystal 2*H*-MoS_2 (a material prototype for optoelectronic and photovoltaic devices) possesses hexagonal crystal structure with trigonal-prismatic coordination (space group D_{6h}^4) and is a weakly ionic covalent compound (with $4d^5 5s$ outer-shell electron configuration of Mo). The relatively strong intra- and weak interlayer couplings (quasi-two-dimensionality) give rise to a strong modulation of the crystal field potential along the normal to the layer plane and, accordingly, to a strong scattering from this potential (intercalation of layered materials with alkali metals makes the former practically completely two-dimensional [30]). The RMDCs have a large unit cell and a hard nonlocal pseudopotential because of the existence of *d* bands. Numerous theoretical RMDC band structure calculations are fairly contradictory (particularly in what concerns the conduction band) and do not offer a detailed explanation of the nature of experimentally established features in optical and PE spectra. The band widths and their separations quoted

1063-7834/03/4504-0752$24.00

in various publications differ by several times. In this connection, investigation of TC and LEET spectra of RMDCs is of a certain interest, because data on the threshold characteristics of transition excitation in these compounds permit one to obtain valuable information on the properties of electrons in strongly hybridized *d*, *p*, and *s* states.

The present communication reports on a theoretical study and interpretation of the FS in the TC and LEET spectra of a 2*H*-MoS_2 (0001) surface based on bulk $E(\mathbf{k})$ and on the development of a technique of experimental-data treatment to extract the maximum possible information on the electron dispersion relation above E_{vac}.

2. THEORETICAL MODEL

A comprehensive analysis of the FS of experimental TC and LEET spectra turned out to be difficult because of the need to take into account the diverse physical processes occurring in the interaction of a flux of primary electrons I_p with the near-surface region of a crystal [31]. For instance, the positions of the maxima in the TC spectra $E_i = -d^2I/dE^2$ of single-crystal graphite obtained at various primary-electron incidence angles (wave vectors $\mathbf{k}$) have been studied and the final conduction-band states $E = E_i$ as a function of $E(\mathbf{k})$ have been constructed [11]. In this case, however, information on $E(\mathbf{k})$ can be distorted by the combined effect of the structure of various bands, which requires a more detailed theoretical consideration. There are several approaches to the interpretation of spectral features. In the first approach, the experimental TC [15–20] and LEET [24–26] spectra are compared with the calculated volume density of unoccupied electronic states $\rho(E)$; the level broadening is neglected, and only the positions of spectral lines rather than their shape and intensity are analyzed; the applicability of the limiting transition to one-dimensional (or three-dimensional [17]) $\rho(E)$ is not specified. Note that straightforward model calculations [28] demonstrated that this approach is not valid for interpretation of LEET spectra of graphite [variations of $\rho(E)$, except the band gaps are not reflected in these spectra]. The dynamic theory of low-energy electron diffraction (LEED) [20–23] (an alternative scattering-matrix formalism in dynamic LEED is presented in [32]) and the VLEED approach [6], where the vacuum wave function (superposition of the primary plane wave and of all diffracted beams) joins the wave function in the crystal (superposition of all Bloch waves), appear to be more adequate. Note that multiple-scattering methods [20–23, 32] are not applicable to an analysis of $E(\mathbf{k})$ and, furthermore, encounter difficulties with inclusion of the full crystal potential into the calculation.

The physical nature of the FS observed experimentally in TC and LEET spectra is determined by the mechanisms of low-energy electron interaction with the surface and is intimately connected with multiple scattering of the diffracted beam from the surface potential barrier. The experimentally measured spectra are actually derivatives (with respect to primary electron energy E_p) of the total (integrated) current in the sample circuit I as a function of E_p under the condition of complete secondary-electron collection and constant I_p. Note that $I = I_p - I_s$, where I_s is the current of the electrons escaping from the sample, both elastically and inelastically. Among the latter are the inelastically reflected primary electrons, the highly excited electrons of the solid, Auger electrons, and the true secondary electrons, whose emergence depends substantially on the magnitude of E_p. At low energies E_p (<10 eV), the elastic (quasi-elastic) reflection (in the interaction of electrons with the atoms and ions of the crystal lattice) dominates; this reflection further becomes comparable with the inelastic component (formation of electron–hole pairs) for $E_p \le 40$ eV. For energies below 100 eV, the fraction of elastic scattering is a few percent and electron–electron scattering involving interband transition excitation dominates. In addition to the excitation of interband transitions, the spectra can reveal threshold excitation of the solid under electron impact, more specifically, plasma oscillations, impurity and vacancy states, etc., which bring about broadening and a decrease in the amplitude of a spectral structure. The main spectral structure consists, however, of the features that reflect the fundamental properties of the material under study and are associated with the volume band structure $E(\mathbf{k})$ of the crystal.

We considered, as in [33–36], the scattering of electrons with a given momentum on a crystal within the approximation of the scattering probability being proportional to the number of final states at a given energy level E and a given direction of the quasi-momentum $\mathbf{\Omega}$. The current flowing through the sample can be written as

$$I(E, \Omega) = \frac{1}{V}\sum_{nk}[1 - f_F(E_{nk})]\left|\frac{1}{\hbar}\nabla_k E_{nk}\right| \times \delta(E - E_{nk})\delta(\mathbf{\Omega} - \mathbf{\Omega}_{nk}), \quad (1)$$

where E_{nk} is the electron dispersion relation $E(\mathbf{k})$; $\mathbf{\Omega}_{nk}$ is the unit vector along the $\nabla_k E_{nk}$ direction; $f_{\mathbf{F}}(E_{nk})$ is the equilibrium Fermi–Dirac occupation function, which is zero for $E > E_{vac}$; $E_{vac} = E_{\mathbf{F}} + e\varphi$, with $E_{\mathbf{F}} = 6$ eV [37] being the midgap energy and $e\varphi = 4.9$ eV [5] being the work function; and V is the crystal volume. Crossing over from summation over $\mathbf{k}$ to integration over the constant-energy surface $E_{nk} = E$, we obtain, neglecting diffraction from the crystal surface,

$$I(E, \mathbf{\Omega}) \propto \frac{1}{(2\pi\hbar)^3} \times \int \frac{dE'}{\pi} N(E', \mathbf{\Omega}) \frac{\hbar\Gamma(E')/2}{(E - E')^2 + \hbar^2\Gamma^2(E')/4}, \quad (2)$$

where $N(E, \mathbf{\Omega})$ is the number of energy bands along the $\mathbf{\Omega}$ direction for which the equality $E = E_{nk}$ holds. Here, we have taken into account the finite width $\hbar\Gamma(E) =$

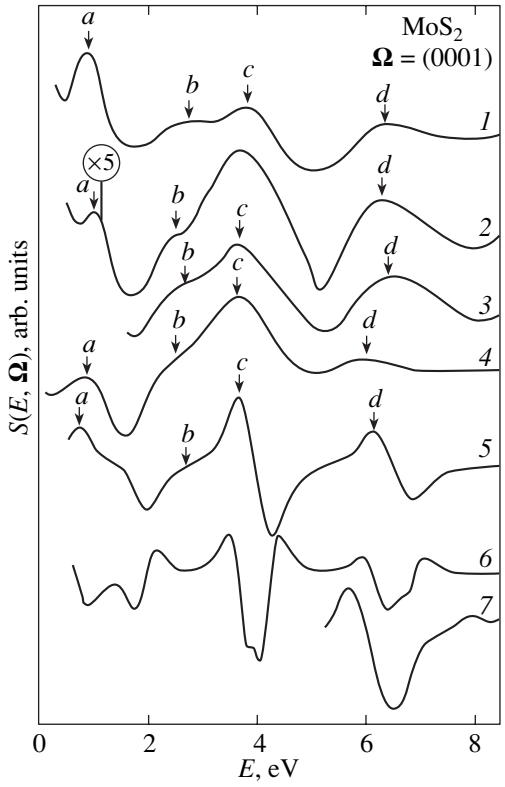

TC and LEET spectra measured along the normal to the (0001)2*H*-MoS_2 single-crystal surface: (*1*) TC experiment, $dI(E, \mathbf{\Omega})/dE$ [18]; (*2*) TC experiment, $dI(E, \mathbf{\Omega})/dE$ [15], $I_p \sim 10^{-8}$ A; (*3*) LEET experiment, $dI(E, \mathbf{\Omega})/dE$ [27], $I_p = 3 \times 10^{-11}$ A; (*4*) TC theory, $dI(E, \mathbf{\Omega})/dE$ [32]; (*5*) $dI(E, \mathbf{\Omega})/dE$ calculation; (*6*) $-d^2I(E, \mathbf{\Omega})/dE^2$ calculation; and (*7*) TC experiment, $-d^2I(E, \mathbf{\Omega})/dE^2$ [5]. Curves (*1–7*) are translated arbitrarily along the vertical axis. Energy E is reckoned from E_{vac}. Arrows identify the main features in the curves.

$\hbar/\tau(E)$ of the electronic levels by replacing the δ function in energy in Eq. (1) by the corresponding Lorentzian. The excited-state lifetime $\tau(E)$ (absorption potential V_i) against inelastic interactions was determined from the expression [38, 39]

$$\hbar/\tau(E) \sim \sqrt{E - E_0}(E - E_F)^2, \qquad (3)$$

where $E_0 = 0$ is the position of the valence band bottom.

Equation (2) is valid if the vector $\mathbf{\Omega}$ coincides in direction with the crystal symmetry axis (under normal electron beam incidence on the sample). The stepped $N(E, \mathbf{\Omega})$ function was constructed using the bulk band structure $E(\mathbf{k})$ of 2*H*-MoS_2, which was calculated by following layer-scattering method [37] developed in LEED studies. Note that the data obtained in [37] in calculations of the lowest unoccupied bands of 2*H*-MoS_2 ($E - E_F < 4$ eV) are in good agreement with the angular relations derived by IPES [5].

In taking into account the surface effects contributing to the formation of $N(E, \mathbf{\Omega})$, the following considerations should be included. The specific features in the electron spectrum of the RMDC surface originate from the fact that the electron spectrum characteristic of the bulk remains practically undistorted in the near-surface region; it is against this background that local surface states or surface resonances become manifest. This is corroborated by numerous PE studies (see, e.g., [40] for 2*H*-MoS_2). LEED studies [41] showed that the geometric structure of bulk 2*H*-MoS_2 is retained and has the same lattice parameters on the surface, the only difference being a compression of the interlayer distance by an amount of up to 5%. Note that the sensitivity of TC and LEET spectroscopy to the geometric structure of the surface turns out to be weaker [6] than that of conventional LEED [42] at higher energies. In [43], the 2*H*-MoS_2 surface obtained by cleavage in high vacuum (8×10^{-7} Pa) or by 3-keV Ar^+ ion bombardment was studied using Auger electron spectroscopy. The experimental data thus obtained revealed the formation of imperfections on the basal surface (defects and "edge" atoms), which was not accompanied by a substantial distortion of the volume structure.

3. RESULTS AND DISCUSSION

The figure displays experimental TC spectra $dI(E, \mathbf{\Omega})/dE$ (obtained in [18] and [15], curves *1* and *2*, respectively) and an LEET spectrum $dI(E, \mathbf{\Omega})/dE$ (curve *3*) [27] measured under normal incidence on the (0001) surface of a 2*H*-MoS_2 single crystal. The half-width ΔE of the primary-electron energy distribution was 0.5 eV [15, 18], and the electron energy was modulated with a frequency of 430 Hz [15] (400 Hz [18]) and an amplitude of 0.15 eV [15] (0.1 eV [18]). The intensity of the FS of the spectra is 1% of the primary-electron distribution maximum (not shown in the figure), which appears at the energy at which the electrons start to impinge on the sample. Also shown for comparison is a TC spectrum $dI(E, \mathbf{\Omega})/dE$ calculated in [32] using dynamic LEED theory (curve *4*) and a $dI(E, \mathbf{\Omega})/dE$ spectrum (curve *5*) calculated from Eq. (2) along the ΓA direction in the volume Brillouin zone, which is perpendicular to the layers and corresponds to normal-incidence TC and LEET spectra. The positions of the characteristic maxima in the curves are labeled *a*, *b*, *c*,… in order of increasing energy.

The differences in the position of the features in the experimental and theoretical curves can be attributed to the following factors.

(1) The rough character of band structure calculations for high-lying levels becomes manifest. There is a need for a self-consistent band theory which would take into account the strong RMDC lattice anisotropy, interband hybridization of states (*d–p* and *p–s* interaction), spin–orbit and interlayer coupling, the unusual features of the Mo *d* states, and the strong electron density variation combined with noticeable wave-function delocalization at high energies. According to [6], unoccupied high-lying electronic states may feature, contrary to the common viewpoint, considerable deviations from free-

electron dispersion and experience a pronounced influence from many-electron effects. The latter contribute to the broadening of the spectral structure (V_i) and to the decrease in its amplitude; this factor that should not be disregarded in the energy region where V_i and the band gap widths are of the same order of magnitude.

(2) Like any other spectroscopy, the TC and LEET methods have an intrinsic accuracy in the sense that the extrema in $dI(E, \mathbf{\Omega})/dE$ can be shifted slightly with respect to the energy band edges within 0.1–0.3 eV. It should also be pointed out that identification of the FS in TC (calculated curve *6* and experimental data [5] shown by curve *7*) and LEET spectra through the negative second derivative $-d^2I(E, \mathbf{\Omega})/dE^2$ is less efficient (see, e.g., [11]), because, in this case, the peaks shift markedly away from the band edges and a parasitic structure forms between them.

(3) There are experimental errors associated with the formation of a collimated low-energy electron beam, complete collection of the secondary electrons, deviation of the electron beam from the normal for the case of the faces being oriented with error, and with the high surface sensitivity of TC and LEET spectra, which is determined not only by the small depth of the region under study but also by a strong influence of the physicochemical surface processes [13, 14, 18, 24, 27]. For instance, the intensity of maximum *a* in the figure (curve *1*) decreases when oxygen is adsorbed [18]. Due to adsorption, maximum *b* shifts to lower energies by about 0.8 eV. Adsorbate or foreign atoms and impurities being present on the surface in comparatively high concentrations between the layers, as well as the easiness with which layer stacking faults form in the course of RMDC crystallization, gives rise to large-angle elastic scattering, thus opening new channels to electron penetration into the crystal. Additional structures associated with surface resonances may also appear in the spectra [42, 44]. Such resonances are formed by diffracted beams of energies slightly less than the threshold for escape to vacuum and exhibit small broadening compared to the features in bulk band structure $E(\mathbf{k})$. All these factors impose stringent requirements on the preparation and quality of the sample surface to be studied [27]. Cleavage and mechanical polishing of a sample in air performed before placing the sample in a high-vacuum chamber result in immediate contamination of the $2H$-MoS_2 surface, which is highly unstable. Surface contamination of layered materials can be eliminated by long-term, high-temperature (up to 600 K [27], 700 K [15], 1200 K [18]) heating in ultrahigh vacuum ($<5 \times 10^{-8}$ Pa [15], 10^{-7}–10^{-6} Pa [27]) directly before each measurement, with the surface cleanness (the absence of signals due to oxygen, carbon, and other impurities) thoroughly verified using Auger electron spectroscopy [18] or LEED [5, 27]. The criterion for surface cleanness should be the reproducibility of the spectral shape and of the magnitude of the surface potential as verified in a series of successive high-temperature treatments. At the same time, one should bear in mind that intense heat treatment may generally bring about undesirable changes in the state of the target, such as changes in its composition and crystal structure, phase transitions, and chemical reactions. Heat treatment is sometimes currently replaced with surface bombardment by ions of inert gases (complemented by LEED). This method results in the formation of radiation defects in the near-surface region of the crystal. Defect clusters may order to form superlattices. In addition to the amorphization of the surface layer, superstructures may form on the surface and in the course of crystal growth.

4. CONCLUSIONS

The demonstrated agreement between the main features of experimental and theoretical TC and LEET spectra demonstrates that a dominant part is played by volume band structure $E(\mathbf{k})$ in the formation of the spectral structure. The possibility appears of experimentally investigating the electron dispersion relation at energies substantially above E_{vac} and of using TC and LEET data in more consistent $E(\mathbf{k})$ calculations through identification of individual spectral features with the corresponding bands, which complements the traditionally employed optical and PE spectroscopy (PES). The extrema in the TC and LEET spectra (corresponding to jumps or thresholds of the $N(E, \mathbf{\Omega})$ function [33–36]) reflect the energy position of the critical points in $E(\mathbf{k})$, such as the band edges or extremal dispersion-branch curvature points. Investigation and interpretation of experimental TC and LEET spectra obtained at different primary-electron incidence angles may yield direct information on specific features of $E(\mathbf{k})$ throughout the Brillouin zone. This information can be used to advantage (in addition to VLEED spectroscopy) to analyze PES and inverse PES data. The dependence of the FS in TC and LEET spectra on the geometric structure and degree of order in the crystals under study was substantiated. The features associated with the volume band structure $E(\mathbf{k})$ can be accompanied in spectra by features originating from diffraction and surface states. The latter may contribute only monotonic variations and affect the shape of spectral features without changing the energy position of FS extrema. Separation of volume and surface properties in a study of TC and LEET spectra is possible when foreign particles are adsorbed. In this case, a change in the FS features will serve as a measure of defect content in the surface layer of the sample, which can be employed to advantage in monitoring surface quality during crystal treatment. The method developed in [45] allows one to separate volume from effects in spectra surface ones, as well as to describe the FS in the experimental behavior of the secondary electron emission coefficient $\sigma(E_p) = I_s/I_p$ without invoking the bulky formalism of dynamic LEED theory (as done, for instance, in [46, 47]).

ACKNOWLEDGMENTS

This study was supported by the State Foundation for Basic Research of Ukraine.

REFERENCES

1. *Unoccupied Electronic States: Fundamentals for XANES, EELS, IPS, and BIS*, Ed. by J. C. Fuggle and J. E. Inglesfield (Springer, Berlin, 1992).
2. A. Golgmann, W. Altmann, and V. Dose, Solid State Commun. **79** (6), 511 (1991).
3. A. Liebsch, *Electronic Excitation at Metal Surfaces* (Plenum, New York, 1997).
4. M. Sancrotti, L. Braicovich, C. Chemelli, and G. Trezzi, Solid State Commun. **66** (6), 593 (1988).
5. V. Langlais, H. Belkhir, J.-M. Themlin, *et al.*, Phys. Rev. B **52** (16), 12095 (1995).
6. V. N. Strocov, in *Electron Spectroscopies Applied to Low-Dimensional Materials*, Ed. by H. I. Starnberg and H. P. Hughes (Kluwer, Netherlands, 2000), p. 161.
7. I. Bartos, M. A. Van Hove, W. F. Chung, *et al.*, Surf. Sci. **402–404**, 697 (1998).
8. J. Devooght, J. C. Dehaes, A. Dubus, J. P. Ganachaud, and M. Cailler, *Theoretical Description of Secondary Electron Emission Induced by Electron or Ion Beam Impinging on Solids* (Springer, Berlin, 1998).
9. O. F. Panchenko, L. K. Panchenko, and J. A. Schaefer, Surf. Sci. **507–510**, 192 (2002).
10. S. Å. Lindgren, L. Walldén, J. Rundgren, and P. Westrin, Phys. Rev. B **29** (2), 576 (1984).
11. R. Claessen, H. Carstensen, and M. Skibowski, Phys. Rev. B **38** (17), 12582 (1988).
12. A. Otto and B. Reihl, Phys. Rev. B **41** (14), 9752 (1990).
13. M. Donath and K. Ertl, Surf. Sci. **262**, L49 (1992).
14. A. Dittmar-Wituski and P. J. Møller, Surf. Sci. **287/288**, 577 (1993).
15. P. J. Møller and M. H. Mohamed, Vacuum **35** (1), 29 (1985).
16. A. Dittmar-Wituski, M. Naparty, and J. Skonieczny, J. Phys. C: Solid State Phys. **18**, 2563 (1985).
17. R. Drube, J. Noffke, R. Schneider, *et al.*, Phys. Rev. B **45** (8), 4390 (1992).
18. S. A. Komolov, *Total Current Spectroscopy of Surface* (Gordon and Breach, Philadelphia, 1992).
19. P. J. Møller, S. A. Komolov, and E. F. Lazneva, J. Phys.: Condens. Matter **8**, 6569 (1996); J. Phys.: Condens. Matter **11**, 9581 (1999); J. Phys.: Condens. Matter **12**, 7705 (2000).
20. J.-V. Peetz, W. Schattke, H. Carstensen, *et al.*, Phys. Rev. B **46** (16), 10127 (1992).
21. R. C. Jaklevic and L. C. Davis, Phys. Rev. B **26** (10), 5391 (1982).
22. E. Tamura, R. Feder, J. Krewer, *et al.*, Solid State Commun. **55** (6), 543 (1985).
23. R. Schneider, K. Starke, K. Ertl, *et al.*, J. Phys.: Condens. Matter **4** (17), 4293 (1992).
24. L. Sanche, in *Excess Electrons in Dielectric Media*, Ed. by C. Ferradini and J.-P. Jay-Gerin (CRC Press, Boca Raton, FL, 1991), Chap. 1.
25. L. G. Caron, V. Cobut, G. Vachon, and S. Robillard, Phys. Rev. B **41**, 2693 (1990).
26. R. Naaman, A. Haran, A. Nitzan, *et al.*, J. Phys. Chem. **102**, 3658 (1998).
27. N. Ueno, K. Suzuki, M. Momoze, *et al.*, Jpn. J. Appl. Phys. **33** (1A), 319 (1994).
28. H. Yamane, H. Setoyama, S. Kera, *et al.*, Phys. Rev. B **64**, 113407 (2001).
29. W. Y. Liang, *Electronic Properties of Transition Metal Dichalcogenides and Their Intercalation Complexes*, Ed. by M. S. Dresselhaus (Plenum, New York, 1986), NATO Adv. Study Inst. Ser., Ser. B **148**.
30. H. I. Starnberg, H. E. Brauer, L. J. Holleboom, and H. P. Hughes, Phys. Rev. Lett. **70** (20), 3111 (1993).
31. W. S. M. Werner, Surf. Interface Anal. **31**, 141 (2001).
32. A. E. Smith and D. F. Lynch, Phys. Status Solidi B **124** (2), 649 (1984).
33. S. A. Komolov, O. F. Panchenko, and V. M. Shatalov, Fiz. Tverd. Tela (St. Petersburg) **34** (4), 1259 (1992) [Sov. Phys. Solid State **34**, 665 (1992)]; Fiz. Tverd. Tela **34** (11), 3489 (1992) [Sov. Phys. Solid State **34**, 1867 (1992)].
34. O. F. Panchenko and L. K. Panchenko, Phys. Lett. A **192** (2–4), 289 (1994).
35. S. A. Komolov, O. F. Panchenko, L. K. Panchenko, and V. M. Shatalov, Pis'ma Zh. Tekh. Fiz. **19** (3), 17 (1993) [Tech. Phys. Lett. **19**, 77 (1993)].
36. S. A. Komolov, O. F. Panchenko, and L. K. Panchenko, Fiz. Tverd. Tela (St. Petersburg) **38** (10), 3172 (1996) [Phys. Solid State **38**, 1733 (1996)]; Fiz. Tverd. Tela **41** (10), 1875 (1999) [Phys. Solid State **41**, 1722 (1999)].
37. K. Wood and J. B. Pendry, Phys. Rev. Lett. **31** (23), 1400 (1973).
38. V. M. Shatalov, O. F. Panchenko, O. M. Artamonov, *et al.*, Solid State Commun. **68** (8), 719 (1988).
39. O. F. Panchenko and L. K. Panchenko, Solid State Commun. **101** (7), 483 (1997).
40. K. Fives, I. T. McGovern, R. McGrath, *et al.*, J. Phys.: Condens. Matter **4** (25), 5639 (1992).
41. B. J. Mrstik, R. Kaplan, and T. Reinecke, Nuovo Cimento B **38** (2), 387 (1977).
42. R. O. Jones and P. J. Jennings, Surf. Sci. Rep. **9**, 165 (1988).
43. R. H. Williams, J. G. Higginbotham, and M. A. Whitaker, J. Phys. C: Solid State Phys. **5** (8), L191 (1972).
44. E. G. McRae, Rev. Mod. Phys. **51** (3), 541 (1979).
45. O. F. Panchenko, Surf. Sci. **482–485**, 723 (2001).
46. O. F. Panchenko and L. K. Panchenko, Fiz. Tverd. Tela (St. Petersburg) **35** (11), 3164 (1993) [Phys. Solid State **35**, 1560 (1993)].
47. O. F. Panchenko, Fiz. Tverd. Tela (St. Petersburg) **39** (10), 1727 (1997) [Phys. Solid State **39**, 1537 (1997)].

Translated by G. Skrebtsov

Physics of the Solid State, Vol. 45, No. 4, 2003, pp. 757–761. Translated from Fizika Tverdogo Tela, Vol. 45, No. 4, 2003, pp. 720–724.

LOW-DIMENSIONAL SYSTEMS AND SURFACE PHYSICS

Nonlinear Waveguide Modes Caused by Generation of Excitons and Biexcitons in Semiconductors in a Symmetrical Three-Layer Structure

O. V. Korovaĭ, P. I. Khadzhi, and S. I. Beril

Dniester State University, ul. Dvadtsat' Pyatogo Oktyabrya 128, Tiraspol, MD 3300 Moldova

e-mail: tdsu@tirastel.md

Received July 18, 2002

Abstract—A theory of nonlinear TE-polarized waveguide modes propagating inside a symmetrical planar three-layer structure with a linear core and nonlinear coatings is developed. The coatings are assumed to be nonlinear due to the optical exciton–biexciton conversion. The dispersion laws of the propagating waves are derived and investigated. © *2003 MAIK "Nauka/Interperiodica".*

1. INTRODUCTION

In view of the rapid development in integrated optics, investigation of the properties of waveguide (directed) modes in complex structures and nonlinear light guides has been of great interest in recent years [1, 2]. The spatial distributions of the fields of nonlinear waveguide modes have been studied in a number of papers using different model dielectric functions of nonlinear media [3–10]. The properties of nonlinear waveguide modes have usually been investigated using a dielectric function of the crystal whose dependence on the field of the propagating wave is represented by a quadratic (Kerr) correction with respect to the field. In a few papers, the properties of nonlinear waveguide modes were studied for non-Kerr media. The dielectric function of a medium should be determined self-consistently from constitutive equations of the Bloch type taking into account the specific mechanisms of the nonlinearity and the type of the quantum transitions. In this paper, we theoretically investigate the properties of nonlinear waveguide modes propagating inside a symmetrical three-layer structure.

2. STATEMENT OF THE PROBLEM AND BASIC EQUATIONS

Let us consider nonlinear TE-polarized waveguide modes propagating in a symmetrical three-layer structure consisting of a linear plate of thickness $2d$ ($-d \le z \le +d$) surrounded by semi-infinite nonlinear semiconductors on both sides. The plate is characterized by a dielectric constant ε_0, and the coatings are semiconductors. We assume that a light wave propagating in these semiconductors can generate excitons from the ground state of the crystal and simultaneously transform them into biexcitons due to the optical exciton–biexciton conversion. This effect can occur, e.g., in CdS and CdSe crystals type, in which the biexciton binding energy is vanishingly small. The giant oscillator strength of the optical exciton–biexciton conversion in these crystals makes it possible to consider nonlinear propagation of laser radiation at moderate excitation levels. To solve the problem, we use the dielectric function ε of the nonlinear medium, depending on the frequency ω and amplitude E of the electromagnetic field of the propagating wave that originates from the interaction between the light and excitons and biexcitons in the crystal:

$$\varepsilon = \varepsilon_\infty\left(1 - \frac{\omega_{LT}}{\Delta}\frac{E_s^4}{(E_s^2 - E^2)^2}\right). \quad (1)$$

This equation was obtained in [11] to investigate the properties of nonlinear surface waves. In Eq. (1), $E_s^2 = 2\Delta^2/\sigma^2$, $\Delta = \omega - \omega_0$ is the resonance detuning for the frequency ω of the propagating radiation from the frequency ω_0 of the exciton transition, $\omega_{LT} = 4\pi\hbar g^2/\varepsilon_\infty$ is the frequency of the longitudinal–transverse splitting of the excitonic state, ε_∞ is the background dielectric constant, g is the exciton–photon interaction constant, and σ is the optical exciton–biexciton conversion constant [12].

We use Eq. (1) to investigate the regularities of the steady-state propagation of the TE-polarized waveguide modes in the geometry shown in Fig. 1. Suppose that an electromagnetic wave propagates along the x axis and is characterized by wave vector k. The wave field contains a transverse electric E (parallel to the y axis) a magnetic H_z component, as well as the longitudinal component of the magnetic field H_x. The wave equations describing the spatial distribution of the electric field of the electromagnetic wave under steady-

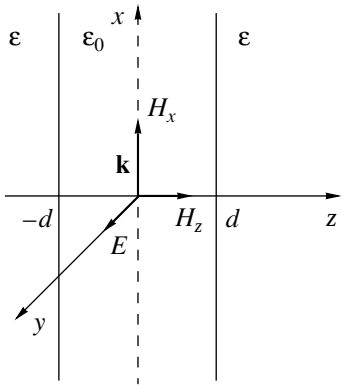

Fig. 1. Geometry of the light guide and the directions of the field components.

state conditions can be derived from the Maxwell equations to be

$$\frac{d^2E}{dz^2} = \frac{\omega^2}{c^2}\left[n^2 - \varepsilon_\infty\left(1 - \frac{\omega_{LT}}{\Delta}\frac{E_s^4}{(E_s^2 - E^2)^2}\right)\right]E, \quad |z| \geq d, \tag{2}$$

$$\frac{d^2E}{dz^2} = \frac{\omega^2}{c^2}(n^2 - \varepsilon_0)E, \quad |z| \leq d, \tag{3}$$

where $n = ck/\omega$ is the effective index of refraction of the medium and c is the speed of light in vacuum. We study spatially confined waveguide modes whose energy is localized in the region of the plate. For this reason, the amplitude of the field E and its derivative dE/dz corresponding to the solution to Eq. (2) should vanish at infinity. Introducing the new variable $x = \omega z/c$ and integrating Eq. (2) with the conditions at infinity yields the following equation for $|x| > D = \omega d/c$:

$$\left(\frac{dE}{dx}\right)^2 + W(E) = 0, \tag{4}$$

where

$$W(E) = -E^2\left(n^2 - \varepsilon_\infty + \varepsilon_\infty\frac{\omega_{LT}}{\Delta}\frac{E_s^2}{E_s^2 - E^2}\right). \tag{5}$$

Here, $W(E)$ is the potential energy of a nonlinear oscillator whose motion is described by the first integral (4).

It should be noted that for an optically linear medium, we have $W(E) = -E^2(n^2 - \varepsilon_0)$, where ε_0 is the dielectric constant of the plate. Extending this expression to the nonlinear case, one can represent $W(E)$ in the form $W(E) = -E^2(n^2 - \varepsilon^*)$, where, in accordance with Eq. (5), we have

$$\varepsilon^* = \varepsilon_\infty\left(1 - \frac{\omega_{LT}}{\Delta}\frac{E_s^2}{E_s^2 - E^2}\right). \tag{6}$$

Here, ε^* is referred to as the effective dielectric function of the medium. It follows from Eq. (4) that solutions to this equation in the form of waveguide modes exist only for amplitudes of the field $E(x)$ that satisfy the condition $W(E) \leq 0$. An analysis shows that, for $-\infty < \Delta < \infty$, solutions exist if $\varepsilon_{ex} = \varepsilon_\infty\left(1 - \frac{\omega_{LT}}{\Delta}\right)$ and $\varepsilon^* < n^2 < \varepsilon_0$. Only waves whose amplitude varies in the range

$$0 \leq E^2 \leq E_m^2 = \frac{n^2 - \varepsilon_{ex}}{n^2 - \varepsilon_\infty}E_s^2 \tag{7}$$

can exist. Here, ε_{ex} is the dielectric function of the linear medium in the region of the excitonic transition and E_m is the maximum amplitude of the wave field. As for the spatial distribution of the field $E(x)$ in this wave, it has a maximum in the region $|x| > D$. Integrating Eq. (4) yields the following solution for the spatial distribution of the field $E(x)$ outside the plate (for $|x| > D$):

$$\ln\frac{\sqrt{E_s^2 - E^2} + \sqrt{E_m^2 - E^2}}{\sqrt{E_s^2 - E_0^2} + \sqrt{E_m^2 - E_0^2}} + \frac{E_s}{E_m}\ln\left(\frac{E}{E_0}\frac{E_s\sqrt{E_m^2 - E_0^2} + E_m\sqrt{E_s^2 - E_0^2}}{E_s\sqrt{E_m^2 - E^2} + E_m\sqrt{E_s^2 - E^2}}\right) = q(x - D) \tag{8}$$

in the range $D \leq \bar{z} \leq \bar{z}_m$ and

$$\ln\frac{\sqrt{E_s^2 - E_m^2}}{\sqrt{E_s^2 - E^2} + \sqrt{E_m^2 - E^2}} + \frac{E_s}{E_m}\ln\left(\frac{E_s\sqrt{E_m^2 - E^2} + E_m\sqrt{E_s^2 - E^2}}{E\sqrt{E_s^2 - E_m^2}}\right) = q(x - x_m) \tag{9}$$

for $x \geq x_m$. Here, the position $x = x_m$ of the maximum of the field $E(x) = E_m$ is determined from the expression

$$q(x_m - D) = \ln\frac{\sqrt{E_s^2 - E_m^2}}{\sqrt{E_s^2 - E_0^2} + \sqrt{E_m^2 - E_0^2}} + \frac{E_s}{E_m}\ln\left(\frac{E_s\sqrt{E_m^2 - E_0^2} + E_m\sqrt{E_s^2 - E_0^2}}{E_0\sqrt{E_s^2 - E_m^2}}\right), \tag{10}$$

where $q = \sqrt{n^2 - \varepsilon_\infty}$ and E_0 is the field amplitude at the boundary of the light guide $x = D$. It follows from Eq. (9) that, for $x \gg x_m$, where $E \ll E_m$, the field decreases exponentially: $E \sim \exp(-\sqrt{n^2 - \varepsilon_{ex}}\,(x - x_m))$.

First, we consider the properties of the symmetrical (even) nonlinear waveguide modes. In the plate $|x| \le D$, the solution to Eq. (3) has the form

$$E = \frac{C}{p_0}\cos(p_0 x), \tag{11}$$

where $p_0 = \sqrt{\varepsilon_0 - n^2}$ and C is an integration constant which defines the field amplitude at the center of the plate in this case. Using the condition that the tangential components of the electric and magnetic fields should be continuous at the boundary $x = D$, we obtain from Eqs. (4) and (11)

$$p_0\tan(p_0 D) = \sqrt{n^2 - \varepsilon_\infty - \varepsilon_\infty\frac{\omega_{LT}}{\Delta}\frac{E_s^2}{E_s^2 - E_0^2}}. \tag{12}$$

This formula can be considered as a dispersion relation determining the $\omega(k)$ dependence or, in this case, the effective index of refraction n of the medium as a function of the resonance detuning Δ at fixed values of the layer thickness d and the parameter E_0, which is the amplitude of the wave field at the boundary between the media at the point $x = D$. It should be noted that the energy flux of the propagating wave can be experimentally controlled rather than the field amplitude. The total energy flux P through the cross-sectional area of the waveguide is the sum of the linear flux P_L in its core and the nonlinear flux P_{NL} in the coatings:

$$P_L = \frac{c^2 n}{4\pi\omega}\frac{E_0^2}{4p_0\cos^2(p_0 D)}(\sin(2p_0 D) + 2p_0 D), \tag{13}$$

$$P_{NL} = \frac{c^2 n}{8\pi\omega}\frac{1}{p_0}\left\{E_s E_m + \sqrt{(E_s^2 - E_0^2)(E_m^2 - E_0^2)} + (E_s^2 - E_m^2)\ln\frac{\sqrt{E_s^2 - E_0^2} + \sqrt{E_m^2 - E_0^2}}{E_s - E_m}\right\}. \tag{14}$$

Using Eq. (12) to eliminate E_0 from Eqs. (13) and (14), we find the $P(n, \Delta)$ dependence or, in other words, the dependence of the effective index of refraction n of the nonlinear light guide on the energy flux of the wave.

Now, we consider the antisymmetrical (odd) waveguide modes. For the internal region ($|x| \le D$), the solution is

$$E = \frac{C}{p_0}\sin(p_0 x). \tag{15}$$

As before, the solution for the external region is given by Eqs. (9)–(11). The energy flux in the plate is equal to

$$P_L = \frac{c^2 n}{4\pi\omega}\frac{E_0^2}{4p_0\sin^2(p_0 D)}(\sin(2p_0 D) - 2p_0 D), \tag{16}$$

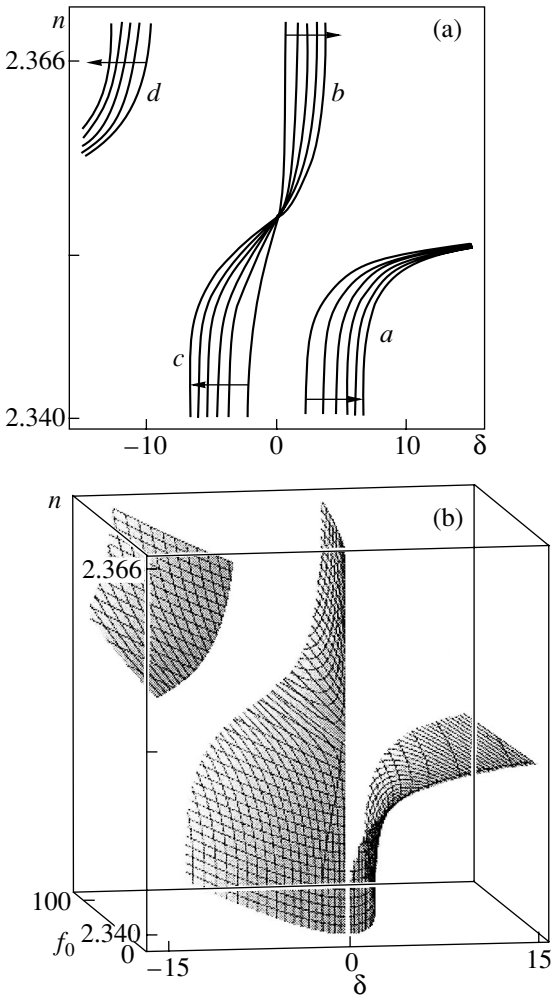

Fig. 2. Dependence of the effective index of refraction n of the system on the resonance detuning δ at different values of the field amplitude f_0 at the boundary between the media ($x = D$). $\varepsilon_0 = 5.6$, $\varepsilon_\infty = 5$, and $D = 4.72$. The arrows in panel (a) show the direction of the f_0 growth in different parts of the spectrum labeled by the letters *a*–*d*.

and the dispersion law is given by

$$p_0\cot(p_0 D) = -\sqrt{n^2 - \varepsilon_\infty - \varepsilon_\infty\frac{\omega_{LT}}{\Delta}\frac{E_s^2}{E_s^2 - E_0^2}}. \tag{17}$$

3. DISCUSSION

Let us normalize the resonance detuning Δ and the Rabi frequency σE_0 to the longitudinal–transverse splitting $\delta = \Delta/\omega_{LT}$ and $f_0 = \sigma E_0/\omega_{LT}$. First, we consider the dispersion law for symmetrical modes by using Eq. (12). For $f_0 > 0$, the dispersion law for each even waveguide mode exists in a spectral region consisting of three nonoverlapping parts: (1) $-\infty < \delta < -f_0/\sqrt{2}$, the long-wavelength branch; (2) $-f_0/\sqrt{2} < \delta < f_0/\sqrt{2}$, the

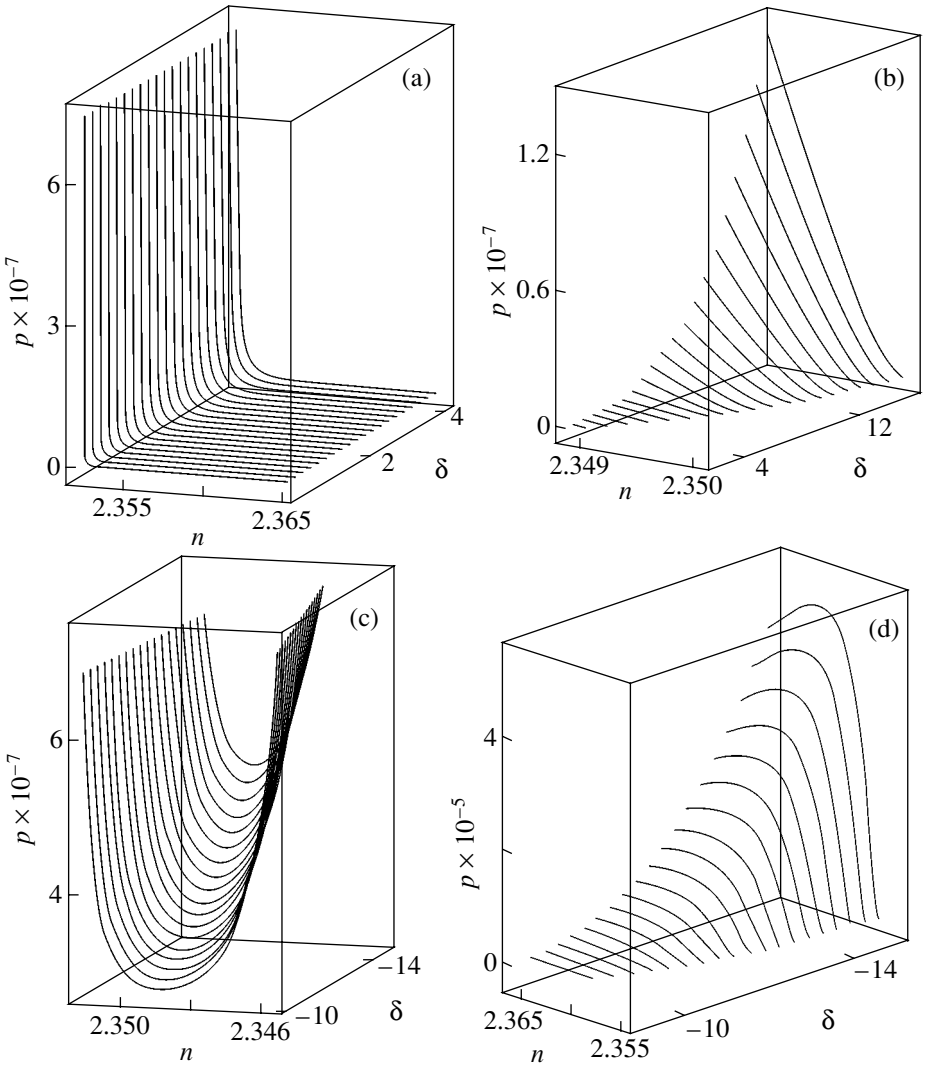

Fig. 3. The $n(p, \delta)$ dependence for parts *a–d* of the dispersion curves (Fig. 2). The values of the parameters ε_0, ε_∞, and D are the same as in Fig. 2.

intermediate branch; and (3) $f_0/\sqrt{2} < \delta < \infty$, the short-wavelength branch. In the geometry shown in Fig. 1, not only the zeroth mode but also higher modes depending on the thickness d of the linear layer and the values ε_0 and ε_∞ can exist. As the number of modes increases, the spectral regions of their existence do not overlap. For higher order modes, following the zeroth mode, the value of n decreases with increasing mode index. It should also be noted that such behavior of the modes is typical of the case $\varepsilon_0 > \varepsilon_\infty$. If $\varepsilon_0 \le \varepsilon_\infty$, the modes exist only in the short-wavelength region of the spectrum ($\delta > 0$).

We consider the dispersion law and the behavior of the $n(\delta, f_0)$ dispersion curves for the lowest even mode this mode using Eq. (12). In the linear approximation ($f_0 = 0$), the function $n(\delta)$ has two branches, short-wavelength and long-wavelength (with respect to $\delta = 0$). Figure 2 shows the dispersion law for the lowest even mode $n(\delta)$ at different values of f_0. If $f_0 \neq 0$, an intermediate branch appears in the vicinity of $\delta = 0$ (Fig. 2). It is seen that the short-wavelength branch of the dispersion law rises monotonically with increasing δ. At large values of δ, however, its rise becomes slower and the branch asymptotically approaches the limiting value of n determined by the thickness of the internal layer d and the ratio between ε_0 and ε_∞. As for the long-wavelength branch, it rises steeply up from a threshold value to $n = \sqrt{\varepsilon_0}$ with increasing δ and undergoes a short-wavelength shift as the value of f_0 increases. The region of existence of the intermediate branch expands with increasing f_0, and the branch itself consists of two parts, short-wavelength and long-wavelength.

The effective index of refraction n of the system increases sharply as δ increases and goes through the value $\delta = 0$. As the frequency f_0 grows, a long-wave-

length shift of the lower part and a short-wavelength shift of the upper part of this branch occur. Note that all three branches of the dispersion law indicated above exist in nonoverlapping spectral regions. Figure 2b shows the three-dimensional representation of the dispersion law $n(\delta, f_0)$ for the lowest even mode; the behavior of each branch with varying δ and f_0 is clearly seen in this figure.

Figure 3 shows the $n(p, \delta)$ dependence for the same values of the parameters as those in Fig. 2 ($p = P/P_0$, $P_0 = 4\pi\omega/c^2 n$). It is seen that there are four types of dependences for each spectral region shown in Fig. 2. The short-wavelength part of the dispersion law is shown in Fig. 3a. It is seen that n decreases monotonically with increasing energy flux. In the long-wavelength region ($\delta \geq 0$) of this part, the allowed values of the energy flux are vanishingly small. As the detuning δ grows, the range of allowed values of the energy flux expands. In the short-wavelength range of the intermediate branch of the dispersion law, the behavior of the energy flux as a function of n and δ is qualitatively the same (Fig. 3b). The longest wavelength part (Fig. 3c) is characterized by the minimum value of the energy flux depending on n. For this reason, an above-critical power is necessary to excite this mode in the given spectral region. An increase in δ leads to an increase in the minimum flux. Finally, the long-wavelength part of the intermediate branch of the dispersion law is shown in Fig. 3d. It is seen that the dependence of the energy flux on n has a maximum whose height increases with δ.

The spectral behavior of the dispersion laws of the antisymmetrical modes determined by Eq. (17) is qualitatively similar to that of the even modes. It should also be noted that, at a fixed f_0, the even and odd modes alternate depending on $n(\delta)$.

The results presented above show that, if the exciton–photon interaction and optical exciton–biexciton conversion are taken into account, the spectral (and intensity-dependent) behavior of the branches of the dispersion laws of a symmetrical waveguide with nonlinear coatings is significantly more complicated than that in the case of a Kerr nonlinearity [2–10, 13]. This is due to the complicated dependence of the dielectric function of the nonlinear medium on the frequency and amplitude of the field of the propagating wave. It is seen from Eq. (1) that the dielectric function exhibits resonance behavior not only in frequency but also in the amplitude of the field. A change in the amplitude of the field results in the appearance of new resonance frequencies, which are due to the renormalization of the semiconductor energy spectrum at strong excitation levels. In [14], it was shown that, in this case, the Autler–Towns effect occurs [14], which confirms that the eigenfrequencies of the nonlinear bulk polaritons change as the excitation level increases [15].

REFERENCES

1. *Surface Polaritons*, Ed. by V. M. Agranovich and D. L. Mills (North-Holland, Amsterdam, 1982; Nauka, Moscow, 1985).
2. N. L. Dmitruk, V. G. Litovchenko, and V. L. Strizhevskiĭ, *Surface Polaritons in Semiconductors* (Naukova Dumka, Kiev, 1989).
3. A. D. Boardman and T. Twardowski, J. Opt. Soc. Am. B **5**, 523 (1988).
4. K. M. Leung, J. Opt. Soc. Am. B **5**, 571 (1988).
5. L. Torner and J. P. Torres, IEEE J. Quantum Electron. **28**, 1571 (1992).
6. J. P. Torres and L. Torner, IEEE J. Quantum Electron. **29**, 917 (1993).
7. S. A. Vakulenko and I. A. Molotkov, Vestn. Leningr. Univ., Ser. 4: Fiz. Khim. **11**, 21 (1987).
8. Kh. S. Arutyunyan and K. A. Barsukov, Izv. Akad. Nauk Arm. SSR, Fiz. **20**, 125 (1985); Opt. Spektrosk. **58**, 1064 (1985) [Opt. Spectrosc. **58**, 650 (1985)].
9. S. J. Al-Bader and H. A. Jamid, IEEE J. Quantum Electron. **24**, 2052 (1988).
10. H. W. Schürmann, V. S. Serov, and Yu. V. Shestopalov, Phys. Rev. E **58**, 1040 (1998).
11. O. V. Korovaĭ and P. I. Khadzhi, Fiz. Tverd. Tela (St. Petersburg) **45** (2), 364 (2003) [Phys. Solid State **45**, 386 (2003)].
12. P. I. Khadzhi, *Nonlinear Optical Processes in Exciton and Biexciton Systems in Semiconductors* (Shtiintsa, Kishinev, 1985).
13. N. N. Akhmediev, K. O. Boltar', and V. M. Eleonskiĭ, Opt. Spektrosk. **53**, 906 (1982) [Opt. Spectrosc. **53**, 540 (1982)]; Opt. Spektrosk. **53**, 1097 (1982) [Opt. Spectrosc. **53**, 654 (1982)].
14. P. I. Khadzhi, A. V. Korovaĭ, and D. V. Tkachenko, Fiz. Tverd. Tela (St. Petersburg) **44**, 774 (2002) [Phys. Solid State **44**, 804 (2002)].
15. R. Shimano and M. Kuwata-Gonokami, Phys. Rev. Lett. **72**, 530 (1994).

Translated by A. Poushnov

Physics of the Solid State, Vol. 45, No. 4, 2003, pp. 762–767. Translated from Fizika Tverdogo Tela, Vol. 45, No. 4, 2003, pp. 725–729.

LOW-DIMENSIONAL SYSTEMS AND SURFACE PHYSICS

Quantum Hall Effect–Insulator Transition in the InAs/GaAs System with Quantum Dots

V. A. Kul'bachinskiĭ*, R. A. Lunin*, V. A. Rogozin*, A. V. Golikov*, V. G. Kytin*, B. N. Zvonkov*, S. M. Nekorkin*, D. O. Filatov*, and A. de Visser**

** Moscow State University, Vorob'evy gory, Moscow, 119899 Russia*

*** Van der Waals–Zeeman Institute, University of Amsterdam, 1018 XE Amsterdam, The Netherlands*

Received April 9, 2002; in final form, August 16, 2002

Abstract—The InAs/GaAs structures consisting of quantum-dot layers with electronic properties typical of two-dimensional systems are investigated. It is found that, at a low concentration of charge carriers, the variable-range-hopping conductivity is observed at low temperatures. The localization length corresponds to characteristic quantum-dot cluster sizes determined using atomic-force microscopy (AFM). The quantum Hall effect–insulator transition induced by a magnetic field occurs in InAs/GaAs quantum-dot layers with metallic conductivity. The resistivities at the transition point exceed the resistivities characteristic of electrons in heterostructures and quantum wells. This can be explained by the large-scale fluctuations of the potential and, hence, the electron density. © *2003 MAIK "Nauka/Interperiodica".*

1. INTRODUCTION

The quantum Hall effect–insulator transition is a fundamental phenomenon in the physics of two-dimensional systems [1–5]. At temperatures close to zero, two-dimensional electrons in a magnetic field perpendicular to the plane of a disordered two-dimensional gas can occur in three stable states: (i) an insulating state when the diagonal elements of the conductivity tensor σ_{xx} tends to zero and the diagonal elements of the resistivity tensor ρ_{xx} tends to infinity at $T \longrightarrow 0$; (ii) a Hall liquid state when $\sigma_{xx} \longrightarrow 0$, $\rho_{xx} \longrightarrow 0$, and the Hall component σ_{xy} of the conductivity tensor is quantized, i.e., $\sigma_{xy} = (e^2/h)s_{xy}$, where s_{xy} is an integer (the integer quantum Hall effect) or a rational fraction (the fractional quantum Hall effect); and (iii) a Hall insulating state when $\sigma_{xx} \longrightarrow 0$ and $\sigma_{xy} \longrightarrow 0$ at $T \longrightarrow 0$ but $\sigma_{xy} \propto (\sigma_{xx}^2)$, so that $\rho_{xy} \longrightarrow \rho_{xy}(0) \approx B/ne$, where n is the two-dimensional electron density, B is the magnetic field induction, and e is the elementary charge. In general, the state of a two-dimensional system is determined primarily by the magnetic field induction and the degree of disordering in the system [1]. According to the phase diagram proposed by Kivelson *et al.* [1] for a two-dimensional system, an increase in the magnetic field induction can lead to variations in the conducting properties, i.e., to metal–insulator transitions, in slightly disordered systems.

The metal–insulator transitions induced by magnetic fields have been studied to sufficient detail in two-dimensional systems with a high degree of ordering, for example, in heterojunctions and quantum wells [4–6]. However, the specific features of this phenomenon in two-dimensional systems with a high degree of disordering call for further investigation. In particular, it remains unclear how fluctuations of the potential and the electron density affect the quantum Hall–insulator transition in a two-dimensional system in the vicinity of the localization threshold.

A layer of quantum dots with a high surface density can be treated as a specific two-dimensional system. In such a structure, the wave functions of electrons can be delocalized through the overlap of the wave functions of electrons localized in adjacent quantum dots. The degree of disordering depends on the growth conditions of the structure. Actually, one way to decrease the spread in the positions and sizes of quantum dots is to grow these dots on vicinal surfaces of semiconductors [7, 8].

Structures with quantum-dot layers are new objects that are particularly suitable for investigation of strong and weak localizations of charge carriers, hoping conductivity, quantum Hall effect, and metal–insulator transitions in magnetic fields. Elucidation of the specific features of charge carrier transfer in InAs/GaAs quantum-dot layers is of considerable practical importance, because these systems are widely used in manufacturing semiconductor lasers [9], single-electron transistors, and memory elements [10] of the new generation.

In this work, we investigated the specific features of the transport properties and the quantum Hall effect–insulator transition in InAs quantum-dot layers in the GaAs matrix.

1063-7834/03/4504-0762$24.00 © 2003 MAIK "Nauka/Interperiodica"

2. SAMPLE PREPARATION AND EXPERIMENTAL TECHNIQUE

Samples containing InAs quantum-dot layers were grown through metalloorganic chemical vapor deposition under atmospheric pressure (the so-called MOC hydride epitaxy) at temperatures of 600–650°C. The growth was performed on a GaAs(001) semi-insulating substrate misoriented by 3° in the [110] direction with respect to the (001) plane. This substrate (referred to as the vicinal substrate) is characterized by the formation of steps whose height is equal to the thickness of one GaAs monolayer and width depends on the misorientation angle. The use of the vicinal surface for the dot growth makes it possible to obtain dots with a more uniform size distribution [7, 8]. In our experiments, we examined three samples. The structure of the studied samples consisted of 10 (samples *1, 3*) or 12 (sample *2*) stacks, each containing a 0.1-μm-thick GaAs layer and an InAs quantum-dot layer. This structure was capped with a GaAs cladding layer 0.1 μm thick. We measured the sheet conductivity. In *n*-type samples *1* and *3*, the electron concentrations per layer of quantum dots were equal to 4.0×10^{10} and 1.9×10^{11} cm^{-2} and the electron mobilities were 1000 and 5500 cm^2/Vs, respectively. In *p*-type sample *2*, we additionally prepared a δ-C doping layer, which was separated from the quantum-dot layer by a 5-nm-thick GaAs undoped spacer. In this sample, the hole concentration per layer of quantum dots was 2.7×10^{11} cm^{-2} and the hole mobility was approximately equal to 100 cm^2/Vs. The charge carrier concentrations were determined from the Hall effect at a temperature of 4.2 K. A schematic drawing of the structure of a *p*-type sample is given in Fig. 1.

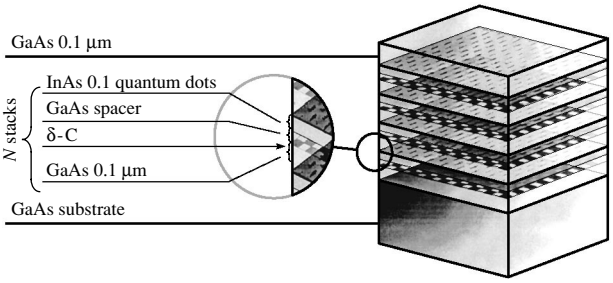

Fig. 1. Schematic drawing of the structure of the studied samples.

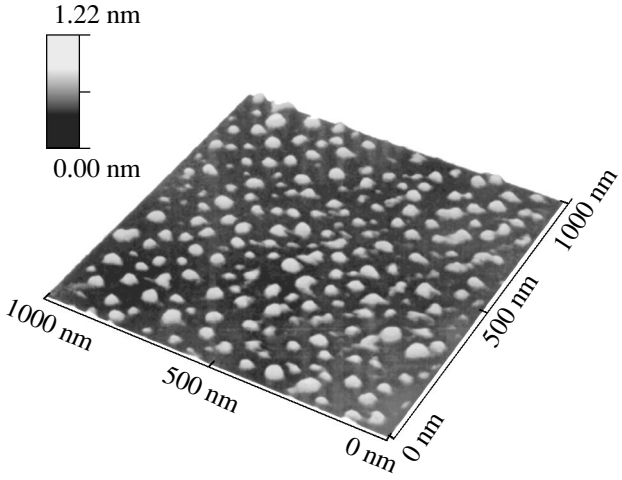

Fig. 2. AFM image of a quantum-dot layer after removal of a cladding layer by selective etching.

The morphology of the quantum-dot layer was investigated using a TopoMetrix® TMX-2100 Accurex™ atomic-force microscope (AFM) operating in a contact mode in air. In order to visualize the quantum dots, the cladding layer was subjected to selective etching in a mixture of a 0.8 *M* $K_3[Fe(CN)_6]$ solution in 0.3 *M* KOH with water and glycerol in the ratio 1 : 5 : 2. The technique of AFM observations was described in detail in [11]. Figure 2 displays the AFM image of the surface of a quantum-dot layer after etching. Quantum dots with lateral sizes of ~50 nm, a height of ~1.2 nm, and a surface density $N_S \approx 2 \times 10^{10}$ cm^{-2} are clearly distinguished in the AFM image. A histogram of the distribution of quantum dots over sizes *L* at the base is depicted in Fig. 3a. The probability density of the radial distribution $W(r)$ of quantum-dot clusters is presented in Fig. 3b. The probability $dP(r, \Delta r)$ of finding a cluster in the ring $(r, r + \Delta r)$ is defined by the equation $dP(r, \Delta r) = 2\pi r W(r)\Delta r$.

The magnetotransport measurements were performed using a standard method in the temperature range 1.35–4.2 K at a current of 1–2 μA along the quantum-dot layers. The Hall resistivity $\rho_{xy}(B)$ and the magnetoresistivity $\rho_{xx}(B)$ were measured in a magnetic field perpendicular to the quantum-dot layers, i.e., perpendicular to the current flow (hereafter, all the experimental resistivities will be given per layer of quantum dots). A magnetic field up to 10 T was induced by a superconducting solenoid. Stronger magnetic fields (up to 40 T) were generated at the University of Amsterdam with the use of the pulse method at a freely decaying current. This provided a means for the generation of quasi-stationary magnetic fields with a pulse duration of 1–2 s. The samples were placed in liquid helium in order to prevent their overheating. The temperature was varied through evacuation of helium vapors.

3. RESULTS AND DISCUSSION

3.1. Strong Localization of Charge Carriers

In the structures under investigation, the quantum dots are filled with charge carriers. At a sufficiently high concentration, the quantum dots can form two-dimensional electrons that exhibit the Shubnikov–de Haas and quantum Hall effects [12–15]. A decrease in the charge carrier concentration does not change the two-dimensional character of conductivity but can result in a crossover to hopping conductivity. Figure 4a shows the temperature dependences of the resistivity

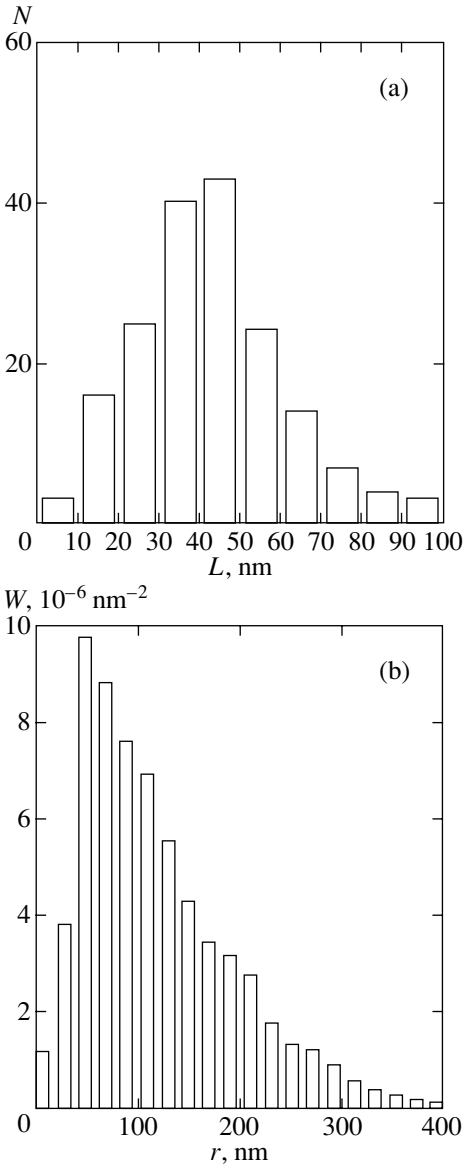

Fig. 3. (a) Distribution of the number of quantum dots N over sizes L at the base and (b) the probability density of the radial distribution $W(r)$ of quantum-dot clusters according to the AFM data.

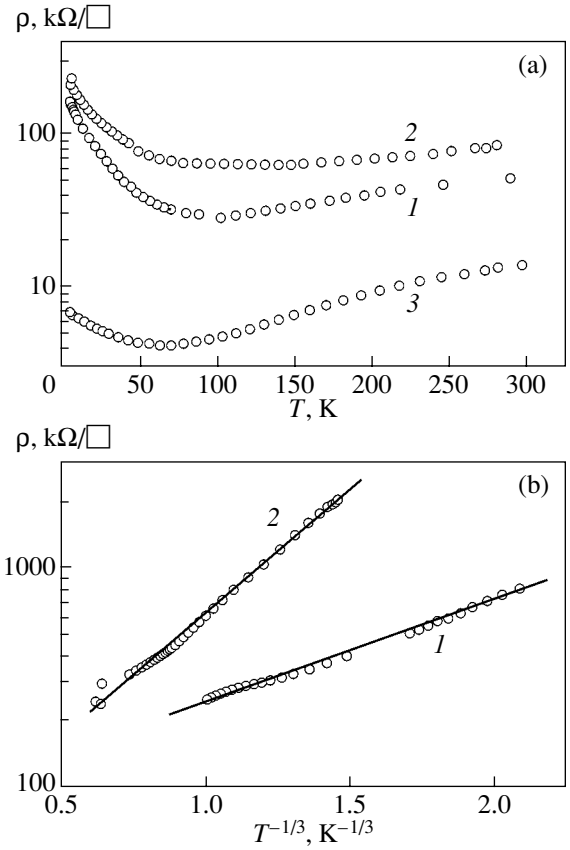

Fig. 4. (a) Temperature dependences of the resistivity (resistance per square) for (*1*) *n*-type sample *1*, (*2*) *n*-type sample *3*, and (*3*) *p*-type sample *2*. (b) Low-temperature portions of the temperature dependences of the resistivity for (*1*) sample *1* and (*2*) sample *2*.

for two *n*-type samples and one *p*-type sample. It can be seen from this figure that, in all cases, the resistivity passes through a minimum. This indicates that the resistivity of the studied samples at high temperatures increases with increasing temperature (as is the case in metals), whereas the localization effects become pronounced at the liquid-helium temperature. At low temperatures, samples *1* and *2* possess variable-range-hopping conductivity. In this temperature range, the resistivity of samples *1* and *2* obeys the Mott law for two-dimensional hopping conductivity and can be represented by the relationship $\rho = \rho_0 \exp\{(T_0/T)^{1/3}\}$ [16]. The low-temperature portions of the temperature dependences of the resistivity for these samples in the corresponding coordinates are depicted in Fig. 4b. The parameter T_0 is related to the density of states at the Fermi level N_{E_F} and the localization length a through the expression $T_0 = C(N_{E_F} a^2)^{-1}$, where $C = 13.8$ is the numerical coefficient [16]. For sample *2*, we have $T_0 \approx 17$ K; hence, it follows that, the localization length a calculated from the above expression is approximately equal to 80 nm. This value approximately corresponds to the probability density $W(r)$ of the radial distribution of quantum-dot clusters at the maximum (Fig. 3b). Consequently, as the temperature decreases, the charge carriers are localized not in single quantum dots but within an extended potential relief associated with quantum-dot clusters.

For sample *3* with a sufficiently high electron concentration, the temperature dependence of the resistivity in the low-temperature range is consistent with the quantum corrections to the two-dimensional conductivity [17]; i.e., it can be rectified in the R–ln$T$ coordinates. Moreover, the negative magnetoresistivity is observed

in weak magnetic fields. This also corresponds to a weak two-dimensional localization of electrons.

Figure 5 shows the dependences of the magnetoresistivity $\rho_{xx}(B)$ of the studied samples at different temperatures. It should be noted that the initial resistivities of samples *1* and *2* substantially exceed the value of $h/e^2 \approx 25.8$ kΩ per square (where h is the Planck constant and e is the elementary charge), which is treated as a conventional boundary between the metallic and dielectric states. As the magnetic field increases, the resistivity $\rho_{xx}(B)$ passes through a minimum. The nature of this minimum will be discussed below. The sign of the derivative $d\rho_{xx}/dT$ is considered to be the main criterion for metallic properties of a system ($\{d\rho_{xx}/dT\} > 0$ for a metal and $\{d\rho_{xx}/dT\} < 0$ for an insulator) [3]. For samples *1* and *2*, the negative derivative $d\rho_{xx}/dT < 0$ takes place over the entire range of magnetic fields. This result confirms the following inference drawn above from analyzing the temperature dependence of the resistivity without a magnetic field: samples *1* and *2* are characterized by a strong localization of charge carriers. The minima observed in the resistivity are associated with the change in both the localization length of the wave function of charge carriers and the density of states at the Fermi level under the effect of a magnetic field. In weak magnetic fields, the localization length of charge carriers increases, because the magnetic field suppresses interference of electron waves that experience different sequences of scattering events in the course of tunneling [18]. As was shown by Raikh [19], the density of states at the Fermi level also increases. These two factors are responsible for the negative magnetoresistivity. Strong magnetic fields generate an additional localizing potential, which leads to a decrease in the localization length of the wave function [16]. An increase in the magnetic field brings about a decrease in the density of states at the Fermi level at a filling factor of less than unity due to a shift in the maximum of the density of states toward the high-energy range. As a result, there arises positive magnetoresistivity in strong magnetic fields. The crossover from the negative to positive magnetoresistivity is observed in magnetic fields for which the filling factor is two [4]. For samples *1* and *2*, the magnetic fields corresponding to this crossover are approximately equal to 2 and 12 T, respectively.

Making allowance for the contraction of the electron wave function in the magnetic field, we obtain the following relationship between the resistivity ρ and the magnetic field B: $\rho = \rho_0 \exp(B^{1/2})$ [16]. The inclusion of the decrease in the density of states should lead to a stronger dependence. In our case, the magnetoresistivity in strong fields can be adequately described by the expression $\rho = \rho_0 \exp(B)$ (Fig. 5). Note also that the resistivities of samples *1* and *2* remain larger than h/e^2 over the entire range of magnetic fields.

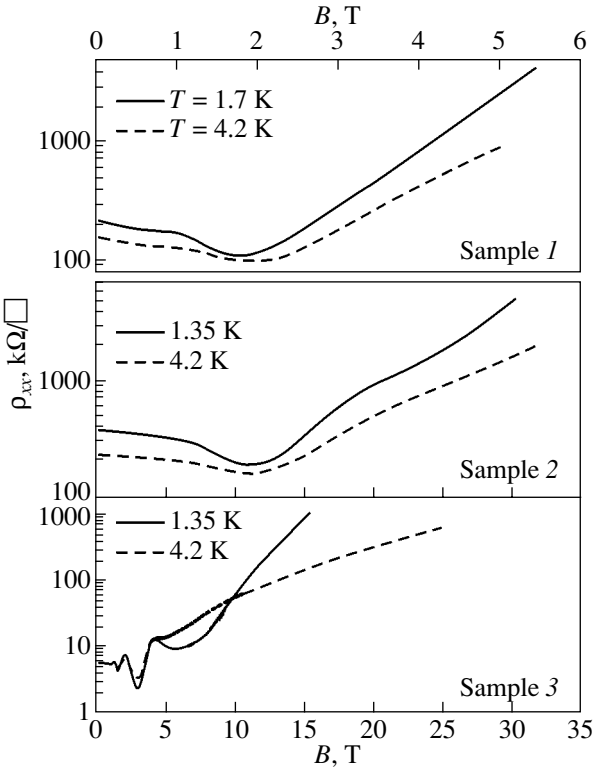

Fig. 5. Dependences of the magnetoresistivity ρ_{xx} (in kΩ per square) on the magnetic field for samples *1–3* at two temperatures.

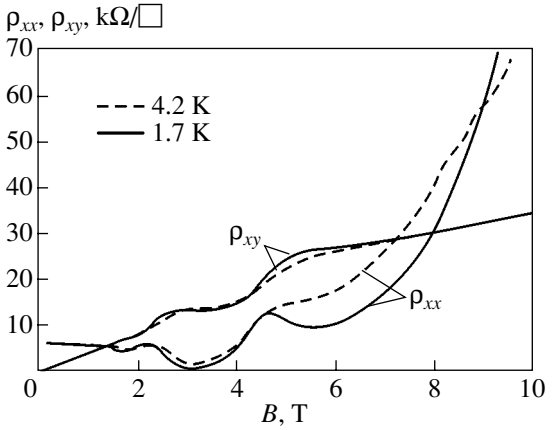

Fig. 6. Dependences of the magnetoresistivity ρ_{xx} and the Hall resistivity ρ_{xy} on the magnetic field for sample *3* at two temperatures.

3.2. The Quantum Hall Effect–Insulator Transition

Sample *3* with a relatively high electron concentration is characterized by the Shubnikov–de Haas effect, the quantum Hall effect, and the intersection of the field dependences of the magnetoresistivity measured at different temperatures (Fig. 6). At the intersection points, the derivative $d\rho_{xx}/dT$ changes sign and the quantum

Hall effect–insulator transition occurs. The positive derivative $d\rho_{xx}/dT > 0$ and a plateau in the dependences of the Hall resistivity ρ_{xy} on the magnetic field are observed in approximately the same fields. These plateaus correspond to filling factors of two and unity. Note that the quantum Hall plateau is retained after the intersection of the field dependences of the magnetoresistivity measured at two temperatures. On this basis, the phase formed upon transition was called the quantum Hall insulator [20]. The observed slope of the plateau in our case can be explained by relatively high temperatures of the measurements.

According to the existing theories of the quantum Hall effect–insulator transition [1, 5, 21], the resistivity ρ_{xx} at the transition point should be equal to h/e^2. However, the resistivity ρ_{xx} for sample *3* upon transition at $B \approx 9$ T from the quantum Hall state with a filling factor of unity to the insulating state with a zero filling factor is nearly twice as large as the value of h/e^2. This discrepancy can be explained in terms of the specific features of the two-dimensional system under consideration. In a quantum-dot layer, the overlap of the wave functions of electrons localized in different dots gives rise to two-dimensional electrons. In this case, the distances between quantum dots and their sizes are distributed in a random manner. As a result, the density of two-dimensional electrons in the layer fluctuates on a typical scale of variation in the size of quantum-dot clusters (Fig. 3b). Since the characteristic size of the electron wave function in a quantizing magnetic field is of the order of the magnetic length $l = (\hbar/eB)^{1/2} \approx 28$ nm (at the magnetic field induction $B = 1$ T), which is less than the cluster size, the energy at the Landau level also fluctuates in space. In the sample, the current predominantly flows through regions that have the highest concentrations of charge carriers and form a network of conducting channels. The effective length of the conducting channels can be considerably larger and their width can be appreciably smaller than those for a spatially homogeneous two-dimensional system. As a consequence, the resistivity of the structure in the quantum Hall regime can substantially exceed the maximum resistivity of a two-dimensional metal (h/e^2), even though the temperature dependence of the resistivity exhibits a metallic behavior.

4. CONCLUSIONS

Thus, it was demonstrated that, in InAs/GaAs structures with quantum-dot layers, the wave functions of charge carriers localized in adjacent quantum dots overlap at low temperatures. As a result, strongly localized two-dimensional charge carriers are generated and variable-range-hopping conductivity is observed at low temperatures. The localization length is approximately equal to 80 nm and agrees well with the characteristic quantum-dot cluster sizes determined from the AFM data.

At a high concentration of charge carriers, the temperature dependence of the resistivity and the negative magnetoresistivity in weak magnetic fields correspond to a weak two-dimensional localization regime. The Shubnikov–de Haas and quantum Hall effects are observed in stronger magnetic fields. The quantum Hall effect–insulator transition occurs in strong magnetic fields. It was found that the two-dimensional conductivity in the quantum Hall state at a filling factor of unity is less than the minimum metallic conductivity. In this case, the temperature dependence of the resistivity of the system exhibits metallic behavior. These findings can be explained by the strong spatial inhomogeneity of the system, in which the current passes through a network of channels formed by regions with the highest concentration of two-dimensional electrons.

ACKNOWLEDGMENTS

This work was supported by the Russian Foundation for Basic Research, project nos. 00-02-17493 and 01-02-16441. The AFM measurements were performed at the Research and Educational Center for Scanning Probe Microscopy (Nizhniĭ Novgorod State University) and were supported by the Russian– American Program "Basic Research and Higher Education" (BRHE) of the Ministry of Education of the Russian Federation and the American Civilian Research and Development Foundation for the Independent States of the Former Soviet Union (CRDF), project no. REC-001.

REFERENCES

1. S. Kivelson, D.-H. Lee, and S.-C. Zhang, Phys. Rev. B **46**, 2223 (1992).
2. E. Shimshoni, Phys. Rev. B **60**, 10691 (1999).
3. G. H. Kim, J. T. Nicholls, S. I. Khondaker, *et al.*, Phys. Rev. B **61**, 10910 (2000).
4. H. W. Jiang, C. E. Johnson, and K. L. Wang, Phys. Rev. B **46**, 12830 (1992).
5. D. Shahar, D. C. Tsui, and J. E. Cunninggham, Phys. Rev. B **52**, R14372 (1995).
6. T. Wang, K. P. Clark, G. F. Spencer, *et al.*, Phys. Rev. Lett. **72**, 709 (1994).
7. M. Kitamura, M. Nishioka, J. Oshino, and Y. Arakawa, Appl. Phys. Lett. **63**, 439 (1996).
8. V. G. Talalaev, B. V. Novikov, S. Yu. Verbin, *et al.*, Fiz. Tekh. Poluprovodn. (St. Petersburg) **34**, 467 (2000) [Semiconductors **34**, 453 (2000)].
9. F. Schafer, J. P. Reithmaier, and A. Forchel, Appl. Phys. Lett. **74**, 2915 (1999).
10. P. Recher, E. V. Sukhorukov, and D. Loss, Phys. Rev. Lett. **85**, 1962 (2000).
11. I. A. Karpovich, N. V. Baidus, B. N. Zvonkov, *et al.*, Phys. Low-Dimens. Semicond. Struct. **3/4**, 341 (2001).
12. V. A. Kulbachinskii, V. G. Kytin, R. A. Lunin, *et al.*, Microelectron. Eng. **43–44**, 107 (1998).

13. V. A. Kul'bachinskiĭ, V. G. Kytin, R. A. Lunin, *et al.*, Vestn. Mosk. Univ., Ser. 3: Fiz., Astron., No. 5, 53 (1998).
14. V. A. Kulbachinskii, V. G. Kytin, R. A. Lunin, *et al.*, Physica B (Amsterdam) **266**, 185 (1999).
15. V. A. Kul'bachinskiĭ, V. G. Kytin, R. A. Lunin, *et al.*, Fiz. Tekh. Poluprovodn. (St. Petersburg) **33**, 316 (1999) [Semiconductors **33**, 318 (1999)].
16. B. I. Shklovskiĭ and A. L. Éfros, *Electronic Properties of Doped Semiconductors* (Nauka, Moscow, 1979; Springer, New York, 1984).
17. T. A. Polyanskaya and Yu. V. Shmartsev, Fiz. Tekh. Poluprovodn. (Leningrad) **23** (1), 3 (1989) [Sov. Phys. Semicond. **23**, 1 (1989)].
18. V. N. Nguen, B. Z. Spivak, and B. I. Shklovskiĭ, Pis'ma Zh. Éksp. Teor. Fiz. **41** (1), 35 (1985) [JETP Lett. **41**, 42 (1985)].
19. M. E. Raikh, Solid State Commun. **75**, 935 (1990).
20. M. Hilke, D. Shahar, S. H. Song, *et al.*, Nature **395**, 675 (1998).
21. H. L. Zhao, B. Z. Spivak, M. P. Gelfand, and S. Feng, Phys. Rev. B **44**, 10760 (1991).

Translated by O. Borovik-Romanova

Physics of the Solid State, Vol. 45, No. 4, 2003, pp. 768–781. From Fizika Tverdogo Tela, Vol. 45, No. 4, 2003, pp. 730–741.

LOW-DIMENSIONAL SYSTEMS AND SURFACE PHYSICS

Electrodynamical Treatment of the Electron–Hole Long-Range Exchange Interaction in Semiconductor Nanocrystals[1]

S. V. Goupalov*,, P. Lavallard***, G. Lamouche****, and D. S. Citrin***

** School of Electrical and Computer Engineering, Georgia Institute of Technology, Atlanta, Georgia, 30332-0250 USA*

*** Ioffe Physicotechnical Institute, Russian Academy of Sciences, St. Petersburg, 194021 Russia*

**** Groupe de Physique des Solides, CNRS, UMR 7588, Université Denis Diderot and Université Pierre et Marie Curie, 75251 Paris, Cedex 05, France*

***** Institut des Matériaux Industriels, CNRC, Boucherville, Quebec, J4B-6Y4 Canada*

e-mail: goupalov@ece.gatech.edu

Received September 12, 2002

Abstract—We show that the contribution to the fine structure of the ground exciton level in a semiconductor nanocrystal due to the long-range part of the electron–hole exchange interaction can be equivalently described as arising from the mechanical exciton interaction with the exciton-induced macroscopic longitudinal electric field. Particular cases of nanocrystals with cubic and wurtzite crystal lattice in the strong confinement regime are studied taking into account the complex structure of the valence band. A simplified model accounting for the exciton ground-level splitting and exploiting an effective local scalar susceptibility is established. © *2003 MAIK "Nauka/Interperiodica".*

1. INTRODUCTION

The electron–hole exchange interaction in excitons confined in semiconductor nanocrystals (NCs) of radius R less than the bulk exciton Bohr radius a_B has attracted much attention in recent years. Such interest stems from the fact that, due to the strong size quantization of the electron and the hole, the exchange-induced exciton-level splittings become very large compared with those in bulk semiconductors. These splittings were observed in CdSe NCs embedded in glassy matrices and polymer films and have been intensively studied by a number of experimental groups [1–6].

The electron–hole exchange interaction is usually divided into long-range (nonanalytical) and short-range (analytical) parts [7–9] and can be accounted for in different ways. According to Agranovich and Ginzburg [10] (see also [11]), the term "mechanical exciton" stands for the case where only the direct Coulomb interaction between the electron and the hole is taken into account. The "Coulomb exciton" is obtained by the further inclusion of the short-range exchange interaction plus either the long-range electron–hole exchange interaction or, equivalently, the mechanical exciton interaction with the exciton-induced macroscopic longitudinal electric field. In bulk direct-gap semiconductors, the short-range exchange leads to the splitting of the ground-state exciton level into several sublevels. The number of these sublevels corresponds to the number of irreducible representations contained in the direct product $\Gamma_c \times \Gamma_v$, where Γ_c and Γ_v are the irreducible representations according to which the electron states at the bottom of the conduction band and at the top of the valence band transform under symmetry operations. The long-range electron–hole exchange interaction, or, alternatively, the mechanical-exciton interaction with the exciton-induced macroscopic longitudinal electric field, leads to a further splitting of the optically active exciton states to the longitudinal and transverse components with respect to the direction of the exciton wave vector. This is the case of the Coulomb exciton that will be studied in the present paper. Speaking more generally, the linear part of the light–matter interaction in semiconductors for the near-absorption-edge spectral region can be accounted for either by the interaction of the Coulomb exciton with the transverse part of the electromagnetic field (scheme *A* in terms of [12], which we adopt here) or by the interaction of the mechanical exciton (split by the short-range exchange) with the full Maxwell field (scheme *B*). The detailed analysis of the relation between these two schemes was recently performed by Cho [12].

The theoretical study of the electron–hole exchange interaction for both bulk materials and NCs was mainly performed following scheme *A*. In the framework of the effective mass approximation, the theory of electron–hole exchange interaction for excitons in bulk semiconductors was constructed by Pikus and Bir [7, 8] and by Denisov and Makarov [9]. For the case of NCs of spherical shape, it was generalized by one of the present authors and Ivchenko [13, 14], who for the first time outlined the crucial role of the long-range exchange interaction in the fine structure of excitonic levels in quantum dots (see also [15]). A reasonable agreement

[1] This article was submitted by the authors in English.

with experimental data was obtained for the case of CdSe NCs [14]. Franceschetti *et al.* performed calculations of the electron–hole exchange interaction in CdSe NCs based on atomistic pseudopotential wave functions [16]. By expanding the Coulomb potential between two points located in the vicinities of different atomic sites in powers of the reciprocal separation between the sites, they obtained the multipole decomposition of the long-range exchange interaction in a NC and showed numerically that the monopole–monopole term of this expansion is predominant. It is worth noting, however, that the scale of the long-range exchange interaction with the NC size reported in [16] contradicts that obtained in the framework of the effective mass approximation [13, 14]. Another treatment alternative to the effective mass approximation is the method of expansion via Wannier functions (see [17, 18] and references therein). For the case of quantum dots this method was adopted by Takagahara [19]. He showed that, for excitons confined in NCs of spherical shape, the matrix elements of the long-range exchange Hamiltonian in this method vanish identically in the case of a simple (twofold degenerate at the Γ point) valence band. The work of Takagahara served as the basis for [1–3], which entirely neglected the long-range exchange interaction in its interpretation of the experimental data even for the case of the complex structure of the valence band.

Very recently one of the present authors and Ivchenko considered the long-range exchange interaction in a bulk semiconductor in the framework of the orthogonal empirical tight-binding model [20]. They analytically formulated the problem in terms of the inter- and intra-atomic matrix elements of the velocity operator and showed that these give nonequivalent contributions to the long-range exchange. Expanding the Coulomb potential between two points located in the vicinities of different atomic sites in powers of the reciprocal separation between the sites up to the dipole approximation, they found that the contribution of the monopole–monopole term of this expansion to the long-range exchange is due to interatomic transitions. If the latter are ignored, only the contribution of the dipole–dipole term governed by intra-atomic transitions survives in the long-range exchange Hamiltonian. In the general case, there is also a contribution from the monopole–dipole term which is due to both inter- and intra-atomic transitions [21]. It was also shown that the effective mass approximation corresponds to neglecting the intra-atomic transitions while the method of the expansion via Wannier functions applied in [17–19] ignores the interatomic ones. The theory was naturally generalized for the case of NCs of spherical shape. The contribution of the monopole–monopole term to the matrix element of the long-range exchange interaction on the size-quantized functions was represented both in a form similar to that of [16] and via the effective-mass envelope functions. Although the effective-mass method ignores both contributions of the monopole–dipole and dipole–dipole terms, it was found to be a good approximation in the case of CdSe NCs, since according to [16] the contribution of the monopole–monopole term dominates over all other contributions. The importance of the monopole–monopole contribution was also recently confirmed by Lee *et al.* [22], who performed numerical calculations of the electron–hole exchange interaction in CdSe NCs in the framework of the empirical tight-binding model formulated in terms of Coulomb and exchange integrals on atomic orbitals. The method of expansion via Wannier functions, however, seems to be a good approach for the specific case of CuCl NCs where the bulk exciton Bohr radius is very small, so that the weak confinement regime ($R \gg a_B$) is always realized [23].

The scheme *B* was successfully applied in [24, 25] to the case of CuCl NCs where $R \gg a_B$, the bulk longitudinal-transverse splitting is very large, and the lowest energy exciton state is formed by the hole from the simple (twofold degenerate at the Γ point) valence band.

In the first part of the present paper we will show that, in the case of excitons formed by the hole from the complex (fourfold degenerate at the Γ point) valence band in semiconductor NCs of a radius less than the bulk exciton Bohr radius ($R \ll a_B$), the exchange-induced splittings of the ground-state exciton level can be also obtained following scheme *B*. We will derive the expression for the polarized-light-induced linear macroscopic polarization of the semiconductor NC in terms of the effective-mass approximation. Once the polarization is written, only the Maxwell equations will be used to obtain the frequency renormalization of the exciton resonance. Note that to solve the same problem following scheme *A*, one has to deal with a 8×8 Hamiltonian [13, 14]. The difficulty of this problem is reflected in scheme *B* in the fact that the linear nonlocal susceptibility has a tensor character. Therefore, the question arises as to whether the nonlocal tensor susceptibility can be replaced by some effective local scalar one, thus in practice greatly simplifying the problem. In the second part of this paper we will present an effective susceptibility that leads to the same frequency renormalization of the exciton resonance as the rigorous treatment presented in the first part and discuss a simple physical picture associated with this model.

We conclude our article by showing how the formalism developed in the first two parts can be applied to the case of NCs with a wurtzite crystal lattice. In all previous works addressing this case [13, 14, 26], the long-range-exchange-induced corrections were first found for the cubic structure NCs and then the crystal-field-induced corrections due to the wurtzite structure of the material were added. We show that within scheme *B* the wurtzite structure of the NC can be introduced from the very beginning. To that end we consider two close-lying resonances simultaneously excited by monochromatic light. We show how the results previously obtained within scheme *A* can be derived in the framework of scheme *B*.

2. EXCITON SIZE QUANTIZATION

In this section we will specify the model describing the electron and the hole states in a quantum dot to be used throughout the present paper.

Let us consider a spherical NC of a cubic semiconductor whose valence band may be described by the spherical Luttinger Hamiltonian; i.e., it is assumed that the Luttinger parameters $\gamma_2 = \gamma_3 \equiv \gamma$. In the strong confinement limit ($R \ll a_B$) the wave function of the electron–hole pair is determined primarily by the reflections of the electron and the hole from the quantum-dot walls, while the Coulomb interaction between them is merely a weak perturbation. Then, to a zeroth-order approximation in the Coulomb interaction, the mechanical-exciton (or rather electron–hole pair) two-particle wave function can be written as the product of the electron and the hole single-particle wave functions. We will accept here the model of the spherical quantum dot with infinitely high barriers. A simple boundary condition of the electron and the hole envelope functions vanishing at the NC-matrix interface will be applied.

The electronic states in a spherical quantum dot are characterized by the electron orbital angular momentum l_e. The lowest energy electron state corresponds to $l_e = 0$. For an infinitely high barrier, the electron wave function has the form

$$\psi_m^{(e)}(\mathbf{r}_e) \equiv \phi(r_e)|m\rangle = \frac{1}{\sqrt{2\pi R}}\frac{\sin(\pi r_e/R)}{r_e}|m\rangle, \quad (1)$$

where the spin index m assumes the values $\pm 1/2$.

The state of a confined hole from the fourfold spin-degenerate band of Γ_8 symmetry (the hole spin $J_h = 3/2$; its projection $n = \pm 3/2, \pm 1/2$) cannot be characterized by any definite value of the hole orbital angular momentum L. In the spherical approximation for the Luttinger Hamiltonian ($\gamma_2 = \gamma_3 \equiv \gamma$), this is the total hole angular momentum $\mathbf{F}_h = \mathbf{J}_h + \mathbf{L}$, which serves as a good quantum number [27]. The hole state is, therefore, $(2F_n + 1)$-fold degenerate due to the projection F_z of the angular momentum $\mathbf{F}_h$ along an arbitrary axis z.

For the ground state we have $F_h = 3/2$, $F_z = \pm 3/2, \pm 1/2$. The wave function of the hole in this state can be written as [3, 14]

$$\psi_{F_z}^{(h)}(\mathbf{r}_h) = \sum_n \mathcal{R}_{n, F_z}(\mathbf{r}_h)|n\rangle, \quad (2)$$

where the components of the matrix $\hat{\mathcal{R}}(\mathbf{r})$ can be expressed through Wigner $3jm$ symbols,

$$\mathcal{R}_{n, F_z}(\mathbf{r}) = R^{-3/2}\sum_{L=0,2} f_L\left(\frac{r}{R}\right)(-1)^{3/2 - L/2 + F_z} \times 2\sum_M \begin{pmatrix} 3/2 & L & 3/2 \\ n & M & -F_z \end{pmatrix} Y_{LM}\left(\frac{\mathbf{r}}{r}\right), \quad (3)$$

Y_{LM} are the normalized spherical harmonics defined as in [28],

$$f_L(x) = \mathcal{C}\left[j_L(\phi^{(h)}x) + (-1)^{L/2}\frac{j_2(\phi^{(h)})}{j_2(\sqrt{\beta}\phi^{(h)})} \times j_L(\sqrt{\beta}\phi^{(h)}x)\right], \quad (4)$$

j_L are the spherical Bessel functions, $\beta = (\gamma_1 - 2\gamma)/(\gamma_1 + 2\gamma)$ is the light-to-heavy hole mass ratio, γ_1 and γ are the Luttinger parameters in the spherical approximation, $\phi^{(h)}$ is the first root of the equation

$$j_0(x)j_2(\sqrt{\beta}x) + j_2(x)j_0(\sqrt{\beta}x) = 0, \quad (5)$$

and $\mathcal{C}$ is determined by the normalization condition

$$\int_0^1 [f_0^2(x) + f_2^2(x)]x^2 dx = 1.$$

Note that the definition of the functions $f_L(x)$ should be consistent with those of spherical harmonics. To keep the definition of [14] for $f_L(x)$ we introduced a factor of $(-1)^{L/2}$ in Eq. (3).

The wave function of the mechanical exciton with the total exciton angular momentum $\mathcal{F}_{exc} = 1$ and its projection $\mathcal{F}_z = F_z + m$ can be composed of the electron (1) and the hole (2) wave functions using the summation rule for angular momenta:

$$|\text{exc}, 1\mathcal{F}_z\rangle = (-1)^{1+\mathcal{F}_z}\sqrt{3}\sum_m \begin{pmatrix} 3/2 & 1/2 & 1 \\ \mathcal{F}_z - m & m & -\mathcal{F}_z \end{pmatrix} \times \psi_m^{(e)}(\mathbf{r}_e)\psi_{\mathcal{F}_z - m}^{(h)}(\mathbf{r}_h). \quad (6)$$

Substituting Eqs. (1) and (2) we obtain

$$|\text{exc}, 1\mathcal{F}_z\rangle = (-1)^{1+\mathcal{F}_z}\sqrt{3}\sum_{m,n} \begin{pmatrix} 3/2 & 1/2 & 1 \\ \mathcal{F}_z - m & m & -\mathcal{F}_z \end{pmatrix} \times \phi(r_e)\mathcal{R}_{n, \mathcal{F}_z - m}(\mathbf{r}_h)|mn\rangle. \quad (7)$$

Using Eq. (7) we can derive an expression for the complex conjugated covariant spherical σ component ($\sigma = \pm 1, 0$) of the NC ground state–exciton transition dipole moment density matrix element in the form

$$\langle 0|\hat{d}_\sigma^*(\mathbf{r})|\text{exc}, 1\mathcal{F}_z\rangle = -\sum_{m,n}\frac{ie\hbar}{m_0 E_g}\langle\bar{n}|p_\sigma^*|m\rangle\Phi_{mn}^{1\mathcal{F}_z}(\mathbf{r}), \quad (8)$$

where e is the electron charge, m_0 is the free-electron mass, E_g is the band gap energy, $\langle\bar{n}|p_\sigma^*|m\rangle$ is the matrix element of the complex conjugated covariant spherical σ component of the momentum operator calculated between the electron Bloch function $|m, \mathbf{k} = 0\rangle$ and $|\bar{n}$,

$\mathbf{k} = 0\rangle$ (the hole state n, $\mathbf{k}$ and the electron state $\bar{n}$, $-\mathbf{k}$ are related through a time-reversal operation), and

$$\Phi_{mn}^{1\mathcal{F}_z}(\mathbf{r}) = (-1)^{1+\mathcal{F}_z}\sqrt{3}\phi(r)\begin{pmatrix} 3/2 & 1/2 & 1 \\ \mathcal{F}_z - m & m & -\mathcal{F}_z \end{pmatrix} \times \mathcal{R}_{n,\mathcal{F}_z - m}(\mathbf{r}). \quad (9)$$

In what follows it will be convenient to recast Eq. (9) in the form

$$\Phi_{mn}^{1\mathcal{F}_z}(\mathbf{r}) = 2\sqrt{3}\phi(r)R^{-3/2}\sum_{L=0,2} D_{L,m,n}^{\mathcal{F}_z} f_L(r/R) \times Y_{L,\mathcal{F}_z - m - n}(\mathbf{r}/r), \quad (10)$$

where we used Eq. (3) and introduced the coefficients

$$D_{L,m,n}^{\mathcal{F}_z} = (-1)^{1/2-m-L/2}\begin{pmatrix} 3/2 & 1/2 & 1 \\ \mathcal{F}_z - m & m & -\mathcal{F}_z \end{pmatrix} \times \begin{pmatrix} 3/2 & L & 3/2 \\ n & \mathcal{F}_z - m - n & m - \mathcal{F}_z \end{pmatrix}. \quad (11)$$

3. MACROSCOPIC LINEAR POLARIZATION

In this section we will derive an expression for the resonant exciton contribution to the macroscopic linear polarization density. A similar derivation for the exciton resonance in a quantum well was carried out in [29].

Suppose that circularly or linearly polarized light excites from the NC ground state an exciton with the total angular momentum $\mathcal{F} = 1$ and its projection in an arbitrary direction $\mathcal{F}_z$. In the first order of the perturbation theory we can write for the time-dependent wave function of the NC

$$|t\rangle = |0\rangle + \mathcal{C}_{\mathcal{F}_z}(t)|\text{exc}, 1\mathcal{F}_z\rangle e^{-i\omega_0 t}, \quad (12)$$

where $|0\rangle$ is the wave function of the NC ground state and ω_0 is the frequency of the resonance corresponding to the mechanical exciton (with the short-range part of the exchange interaction taken into account). The resonant exciton contribution to the macroscopic linear polarization density is given by the matrix element of the dipole moment operator density on functions (12). For its covariant spherical σ component we have

$$P_{\text{exc},\sigma}(\mathbf{r}, t) = \langle t|\hat{d}_\sigma(\mathbf{r})|t\rangle = \mathcal{C}_{\mathcal{F}_z}(t)e^{-i\omega_0 t}\langle 0|\hat{d}_\sigma(\mathbf{r})|\text{exc}, 1\mathcal{F}_z\rangle + \mathcal{C}^*_{\mathcal{F}_z}(t)e^{i\omega_0 t}\langle \text{exc}, 1\mathcal{F}_z|\hat{d}_\sigma(\mathbf{r})|0\rangle. \quad (13)$$

Here we omit the superscript in $\mathbf{P}_{\text{exc}}^{(\mathcal{F}_z)}(\mathbf{r}, t) \equiv \mathbf{P}_{\text{exc}}(\mathbf{r}, t)$, although it is understood. Substituting Eq. (12) into the Schrödinger equation

$$i\hbar\frac{\partial}{\partial t}|t\rangle = (\hat{H}_0 + \hat{V})|t\rangle, \quad (14)$$

where $\hat{H}_0$ is the Hamiltonian of the unperturbed electronic system and $\hat{V}$ describes the mechanical-exciton interaction with the Maxwell electric field, we obtain

$$i\hbar\frac{d\mathcal{C}_{\mathcal{F}_z}(t)}{dt} = \langle \text{exc}, 1\mathcal{F}_z|\hat{V}|0\rangle e^{i\omega_0 t} = -e^{i\omega_0 t}\int d\mathbf{r}\sum_\mu \langle \text{exc}, 1\mathcal{F}_z|\hat{d}_\mu(\mathbf{r})|0\rangle \times (E^\mu(\mathbf{r})e^{-i\omega t} + E^{\mu *}(\mathbf{r})e^{i\omega t}). \quad (15)$$

Here $E^\mu(\mathbf{r})$ is the contravariant μ component of the amplitude of the Maxwell electric field. The solution of Eq. (15) is given by

$$\mathcal{C}_{\mathcal{F}_z}(t) = i\hbar^{-1}\int_{-\infty}^{t} dt'\int d\mathbf{r}\sum_\mu \langle \text{exc}, 1\mathcal{F}_z|\hat{d}_\mu(\mathbf{r})|0\rangle \times (E^\mu(\mathbf{r})e^{i(\omega_0 - \omega)t'} + E^{\mu *}(\mathbf{r})e^{i(\omega_0 + \omega)t'}). \quad (16)$$

Taking into account that the resonant frequency ω_0 has a negative imaginary part (adiabatic switching), performing integration, and omitting the nonresonant term, we obtain

$$\mathcal{C}_{\mathcal{F}_z}(t) = \hbar^{-1}\frac{e^{i(\omega_0 - \omega)t}}{\omega_0 - \omega}\Lambda, \quad (17)$$

where

$$\Lambda = \int d\mathbf{r}\sum_\mu \langle \text{exc}, 1\mathcal{F}_z|\hat{d}_\mu(\mathbf{r})|0\rangle E^\mu(\mathbf{r}).$$

Substituting Eq. (17) into Eq. (13) we finally obtain

$$P_{\text{exc}}^\sigma(\mathbf{r}, t) = P^*_{\text{exc},\sigma}(\mathbf{r}, t) = \hbar^{-1}\frac{\exp(-i\omega t)}{\omega_0 - \omega}\langle 0|\hat{d}^*_\sigma(\mathbf{r})|\text{exc}, 1\mathcal{F}_z\rangle\Lambda + \hbar^{-1}\frac{\exp(i\omega t)}{\omega_0 - \omega}\langle \text{exc}, 1\mathcal{F}_z|\hat{d}^*_\sigma(\mathbf{r})|0\rangle\Lambda^*. \quad (18)$$

Equation (18) gives an expression for the resonant-exciton contribution to the macroscopic linear polarization density. Note that, since we accepted the model of the spherical quantum well with infinitely high barriers, the macroscopic polarization density (18) satisfies the boundary condition $\mathbf{P}_{\text{exc}}(r = R, t) = 0$.

4. PRINCIPAL EQUATIONS

In this section we will show how the exciton-induced macroscopic longitudinal electric field affects the energy of the optically active excitonic states. Since the NC radius is much less than the wavelength of light, we can neglect the effect of retardation within the NC. In the nonretarded limit the Maxwell electric field does not include the field reemitted by the polarization and, therefore, its transverse part is represented by the electric field of incident light $\mathbf{E}^{(0)}(\mathbf{r}, t)$ ($\nabla \cdot \mathbf{E}^{(0)}(\mathbf{r}, t) \equiv 0$). The longitudinal part of the Maxwell electric field may be expressed through the gradient of a scalar potential, $\varphi(\mathbf{r}, t)$. For this potential from the Maxwell equation $\nabla \cdot \mathbf{D} = 0$, we have

$$\varepsilon_b(r)\Delta\varphi(\mathbf{r}, t) = \sum_\mu \nabla_\mu 4\pi P^\mu_{\text{exc}}(\mathbf{r}, t)$$

$$= \frac{4\pi\Lambda \exp(-i\omega t)}{\hbar(\omega_0 - \omega)}\sum_\mu \nabla_\mu \langle 0|\hat{d}^*_\mu(\mathbf{r})|\text{exc}, 1\mathcal{F}_z\rangle \quad (19)$$

$$+ \frac{4\pi\Lambda^* \exp(i\omega t)}{\hbar(\omega_0 - \omega)}\sum_\mu \nabla_\mu \langle \text{exc}, 1\mathcal{F}_z|\hat{d}^*_\mu(\mathbf{r})|0\rangle,$$

where $\varepsilon_b(r) = \varepsilon_b^{(1)}\theta(R - r) + \varepsilon_b^{(2)}\theta(r - R)$; $\varepsilon_b^{(1)}$ and $\varepsilon_b^{(2)}$ are, respectively, the NC and the host medium background permittivities; and $\theta(x)$ is the Heaviside step function. In order to avoid the second term in the right-hand side of Eq. (19), let us make a rotating-wave approximation about ω; i.e., we multiply both sides of Eq. (19) be $\exp(i\omega t)$ and average over time. Then we obtain

$$\varepsilon_b(r)\Delta\varphi(\mathbf{r}) = \sum_\mu \nabla_\mu 4\pi P^\mu_{\text{exc}}(\mathbf{r})$$

$$= \frac{4\pi\Lambda}{\hbar(\omega_0 - \omega)}\sum_\mu \nabla_\mu \langle 0|\hat{d}^*_\mu(\mathbf{r})|\text{exc}, 1\mathcal{F}_z\rangle, \quad (20)$$

where $P^\mu_{\text{exc}}(\mathbf{r})$ is the contravariant μ component of the time-averaged linear polarization density. We can write the latter as

$$P^\mu_{\text{exc}}(\mathbf{r}) = \sum_\sigma \int d\mathbf{r}' \chi^\mu_\sigma(\mathbf{r}, \mathbf{r}')E^\sigma(\mathbf{r}'), \quad (21)$$

where

$$\chi^\mu_\sigma(\mathbf{r}, \mathbf{r}') = \frac{\langle 0|\hat{d}^*_\mu(\mathbf{r})|\text{exc}, 1\mathcal{F}_z\rangle\langle \text{exc}, 1\mathcal{F}_z|\hat{d}_\sigma(\mathbf{r}')|0\rangle}{\hbar(\omega_0 - \omega)} \quad (22)$$

is the time-averaged linear susceptibility of scheme *B* relating the Maxwell electric field to the macroscopic linear polarization density. Here we omit the superscript at $\hat{\chi}^{(\mathcal{F}_z)}(\mathbf{r}, \mathbf{r}') \equiv \hat{\chi}(\mathbf{r}, \mathbf{r}')$ to simplify the notation.

Introducing the Green function $G(\mathbf{r}, \mathbf{r}')$ of Eq. (20) for the scalar potential as

$$\varepsilon_b(r)\Delta G(\mathbf{r}, \mathbf{r}') = -\delta(\mathbf{r} - \mathbf{r}') \quad (23)$$

and integrating by parts [30], we can rearrange it in the form

$$\varphi(\mathbf{r}) = \varphi_0(\mathbf{r}) + \frac{4\pi\Lambda}{\hbar(\omega_0 - \omega)}$$

$$\times \sum_\mu \int d\mathbf{r}' \langle 0|\hat{d}^*_\mu(\mathbf{r}')|\text{exc}, 1\mathcal{F}_z\rangle \nabla'_\mu G(\mathbf{r}, \mathbf{r}'), \quad (24)$$

where $\varphi_0(\mathbf{r})$ is an arbitrary solution of the homogeneous Laplace equation satisfying boundary conditions. Thus, for the contravariant component of the total Maxwell electric field we obtain

$$E^\sigma(\mathbf{r}) = E^{\sigma(0)}(\mathbf{r}) - \frac{4\pi\Lambda}{\hbar(\omega_0 - \omega)}(-1)^\sigma$$

$$\times \int d\mathbf{r}' \sum_\mu G_{-\sigma\mu}(\mathbf{r}, \mathbf{r}')\langle 0|\hat{d}^*_\mu(\mathbf{r}')|\text{exc}, 1\mathcal{F}_z\rangle, \quad (25)$$

where

$$E^{\sigma(0)}(\mathbf{r}) = E^{\mathcal{F}_z(0)}(\mathbf{r})\delta_{\sigma, \mathcal{F}_z} \approx E^{\mathcal{F}_z(0)}\delta_{\sigma, \mathcal{F}_z}$$

stands for the amplitude of the incident light and

$$G_{-\sigma\mu}(\mathbf{r}, \mathbf{r}') = \nabla_{-\sigma}\nabla'_\mu G(\mathbf{r}, \mathbf{r}'). \quad (26)$$

Comparing Eqs. (24) and (25) we note that in the long wavelength limit one can formally consider the full Maxwell field to be longitudinal by letting $\varphi_0(\mathbf{r}) = -(\mathbf{r} \cdot \mathbf{E}^{(0)})$. Multiplying both sides of Eq. (25) by $\langle \text{exc}, 1\mathcal{F}_z|\hat{d}_\sigma(\mathbf{r})|0\rangle$, integrating over $\mathbf{r}$, and summing over σ, we obtain

$$\Lambda = \Lambda^{(0)} - \frac{\Lambda\delta\omega^{(1\mathcal{F}_z)}}{\omega_0 - \omega} \quad (27)$$

or

$$\Lambda = \frac{\Lambda^{(0)}(\omega_0 - \omega)}{\omega_0 + \delta\omega^{(1\mathcal{F}_z)} - \omega}, \quad (28)$$

where

$$\Lambda^{(0)} = \int d\mathbf{r} E^{\mathcal{F}_z(0)}(\mathbf{r})\langle \text{exc}, 1\mathcal{F}_z|\hat{d}_{\mathcal{F}_z}(\mathbf{r})|0\rangle,$$

$$\delta\omega^{(1\mathcal{F}_z)} = 4\pi/\hbar \int d\mathbf{r} \int d\mathbf{r}' \sum_{\sigma, \mu}(-1)^\sigma G_{-\sigma\mu}(\mathbf{r}, \mathbf{r}') \quad (29)$$

$$\times \langle \text{exc}, 1\mathcal{F}_z|\hat{d}_\sigma(\mathbf{r})|0\rangle\langle 0|\hat{d}^*_\mu(\mathbf{r}')|\text{exc}, 1\mathcal{F}_z\rangle.$$

Substituting Eq. (28) into Eq. (18) we see that the exciton-induced linear polarization, which is responsible for all the exciton-related linear optical properties of the system, has the pole at $\omega = \omega_0 + \delta\omega^{(1\mathcal{F}_z)}$. The expression for the Maxwell electric field (25) naturally contains this pole as well. Thus, $\delta\omega^{(1\mathcal{F}_z)}$ is the renormalization of the exciton resonant frequency due to the long-range exchange interaction. The latter can be also expressed via the averaged linear susceptibility (22):

$$\delta\omega^{(1\mathcal{F}_z)} = 4\pi(\omega_0 - \omega) \times \int d\mathbf{r} \int d\mathbf{r}' \sum_{\sigma,\mu} (-1)^{\sigma} G_{-\sigma\mu}(\mathbf{r}, \mathbf{r}') \chi^{\mu}_{\sigma}(\mathbf{r}', \mathbf{r}). \quad (30)$$

Equations (29) and (30) give the difference in energy (divided by $\hbar$) between the optically active states of the Coulomb and the mechanical (with the short-range exchange interaction taken into account) excitons confined in a semiconductor NC.

To conclude this section let us write the contravariant μ component of the time-averaged linear polarization density in the form

$$P^{\mu}_{\text{exc}}(\mathbf{r}) = \int d\mathbf{r}' \alpha^{\mu}_{\mathcal{F}_z}(\mathbf{r}, \mathbf{r}') E^{\mathcal{F}_z(0)}(\mathbf{r}'). \quad (31)$$

Here,

$$\alpha^{\mu}_{\mathcal{F}_z}(\mathbf{r}, \mathbf{r}') = \frac{\langle 0|\hat{d}^*_{\mu}(\mathbf{r})|\text{exc}, 1\mathcal{F}_z\rangle\langle \text{exc}, 1\mathcal{F}_z|\hat{d}_{\mathcal{F}_z}(\mathbf{r}')|0\rangle}{\hbar(\omega_0 + \delta\omega^{(1\mathcal{F}_z)} - \omega)} \quad (32)$$

is the linear susceptibility of scheme *A* relating the incident electric field to the time-averaged linear polarization density. It is the susceptibility most directly related to optical spectroscopy and, as one can see, contains the renormalized resonant pole.

5. GREEN FUNCTION

The Green function for the scalar potential defined by Eq. (23), for both $\mathbf{r}$ and $\mathbf{r}'$ within the sphere ($r < R$, $r' < R$), consists of two terms:

$$G(\mathbf{r}, \mathbf{r}') = G^0(\mathbf{r}, \mathbf{r}') + G^1(\mathbf{r}, \mathbf{r}'). \quad (33)$$

The first term

$$G^0(\mathbf{r}, \mathbf{r}') = \frac{1}{4\pi\varepsilon_b^{(1)}|\mathbf{r} - \mathbf{r}'|} \quad (34)$$

represents the Green function for the case $\varepsilon_b^{(1)} = \varepsilon_b^{(2)}$, and the second term

$$G^1(\mathbf{r}, \mathbf{r}') = \frac{\varepsilon_b^{(1)} - \varepsilon_b^{(2)}}{\varepsilon_b^{(1)}} \sum_{l=0}^{\infty} \frac{1}{2l+1} \frac{l+1}{\varepsilon_b^{(1)} l + \varepsilon_b^{(2)}(l+1)} \frac{r^l r'^l}{R^{2l+1}} \times \sum_{l_z=-l}^{l} Y_{ll_z}(\mathbf{r}/r) Y^*_{ll_z}(\mathbf{r}'/r') \quad (35)$$

allows for a difference in the NC and the host medium background permittivities.

6. RESONANT FREQUENCY RENORMALIZATION DUE TO ELECTRON–HOLE LONG-RANGE EXCHANGE INTERACTION

In this section we will consider the resonant frequency renormalization arising due to the first term in Eq. (33).

Substituting Eqs. (26), (33), and (34) into Eq. (29) and integrating by parts [30] we can rewrite the latter in the form

$$\hbar\delta\omega_0^{(1\mathcal{F}_z)} = \int d\mathbf{r} \int d\mathbf{r}' \frac{\rho(\mathbf{r})\rho^*(\mathbf{r}')}{\varepsilon_b^{(1)}|\mathbf{r} - \mathbf{r}'|}, \quad (36)$$

where $\rho(\mathbf{r}) = -(\nabla \cdot \langle \text{exc}, 1\mathcal{F}_z|\hat{\mathbf{d}}(\mathbf{r})|0\rangle)$ may be interpreted as an effective charge density induced by the optical transition. In [12, 23, 25, 26] Eq. (36) was interpreted as the Coulomb energy of this effective induced charge density. This interpretation is misleading. In fact, if we have a given charge density and intend to calculate its Coulomb energy, we should exclude domains where $\mathbf{r} = \mathbf{r}'$ while evaluating the integrals in Eq. (36), unless they make infinitesimal contributions to the integrals. This means that, if it turns out that the integrand of Eq. (36) contains contributions proportional to $\delta(\mathbf{r} - \mathbf{r}')$, then the latter must be excluded from further consideration. Comparing Eq. (36) with Eqs. (26), (29), and (34) one can see that the integrand of Eq. (36) does in fact contain a term proportional to the Dirac δ function, since it always arises when one takes the second derivative of the Coulomb potential. This term makes the main contribution to the resonant frequency renormalization [14]. In Section 9 we will show that the same δ function appears during a formal solution of electrostatic boundary problems. However, in practice it is convenient to compute the exciton resonant frequency renormalization due to the first term in Eq. (33) by transformation into the $\mathbf{k}$ space [14].

Below we will apply the general equations derived in Sections 4 and 5 to the concrete model introduced in

Sections 2 and 3. Substituting Eq. (34) into Eq. (29) we get

$$\delta\omega_0^{(1\mathcal{F}_z)} = \frac{1}{2\pi^2\hbar\varepsilon_b^{(1)}}\int d\mathbf{k}\sum_{\sigma,\mu}\frac{k^\sigma k_\mu}{k^2} \times\langle \text{exc}, 1\mathcal{F}_z|\hat{d}_\sigma(\mathbf{k})|0\rangle\langle 0|\hat{d}_\mu^*(\mathbf{k})|\text{exc}, 1\mathcal{F}_z\rangle, \tag{37}$$

where

$$\langle 0|\hat{d}_\sigma^*(\mathbf{k})|\text{exc}, 1\mathcal{F}_z\rangle = \int d\mathbf{r}e^{-i\mathbf{k}\cdot\mathbf{r}}\langle 0|\hat{d}_\sigma^*(\mathbf{r})|\text{exc}, 1\mathcal{F}_z\rangle \tag{38}$$

is the Fourier transform of the dipole moment density operator matrix element. By using Eq. (8) and the exponent expansion via spherical harmonics, Eq. (38) may be further recast in the form

$$\langle 0|\hat{d}_\sigma^*(\mathbf{k})|\text{exc}, 1\mathcal{F}_z\rangle = -2\sqrt{3}\frac{ie\hbar}{m_0E_g} \times\sum_{L=0,2}\sum_{m,n}D_{L,m,n}^{\mathcal{F}_z}\langle\bar{n}|p_\sigma^*|m\rangle I_L(kR)Y_{L,\mathcal{F}_z-m-n}(\mathbf{k}/k), \tag{39}$$

where the function

$$I_L(y) = 2\sqrt{2\pi}(-1)^{L/2}\int_0^1 dx x f_L(x)\sin(\pi x)j_L(xy)$$

was introduced in [14] and the coefficients $D_{L,m,n}^{\mathcal{F}_z}$ are defined by Eq. (11). Substituting Eq. (39) into Eq. (37) we obtain

$$\delta\omega_0^{(1\mathcal{F}_z)} = \frac{6e^2\hbar}{\pi^2\varepsilon_b^{(1)}m_0^2E_g^2}\sum_{\substack{L=0,2\\L'=0,2}}\sum_{\substack{m,n\\m',n'}}D_{L,m,n}^{\mathcal{F}_z}D_{L',m',n'}^{\mathcal{F}_z}A_{\substack{m,n\\m',n'}}^{\mathcal{F}_zLL'} \times\int_0^\infty dk k^2 I_L(kR)I_{L'}(kR), \tag{40}$$

where

$$A_{\substack{m,n\\m',n'}}^{\mathcal{F}_zLL'} = \sum_{\sigma,\mu}\langle m'|p_\sigma|\bar{n}'\rangle\langle\bar{n}|p_\mu^*|m\rangle\int d\Omega_{\mathbf{k}}Y_{L',\mathcal{F}_z-m'-n'}^*(\Omega_{\mathbf{k}}) \times Y_{L,\mathcal{F}_z-m-n}(\Omega_{\mathbf{k}})\frac{k^\sigma k_\mu}{k^2}. \tag{41}$$

Using the technique developed in the quantum theory of angular momentum [28], we can perform the angular integration in Eq. (41) and obtain

$$A_{\substack{m,n\\m',n'}}^{\mathcal{F}_zLL'} = \sum_{\sigma,\mu}\sum_{l,M}(2l+1)\sqrt{(2L+1)(2L'+1)} \times\begin{pmatrix}1 & L' & l\\ 0 & 0 & 0\end{pmatrix}\begin{pmatrix}1 & L & l\\ 0 & 0 & 0\end{pmatrix}\begin{pmatrix}1 & L' & l\\ \sigma & \mathcal{F}_z-m'-n' & -M\end{pmatrix} \times\begin{pmatrix}1 & L & l\\ \mu & \mathcal{F}_z-m-n & -M\end{pmatrix}\langle m'|p_\sigma|\bar{n}'\rangle\langle\bar{n}|p_\mu^*|m\rangle. \tag{42}$$

Using Eq. (42) we can further recast Eq. (40) in the form

$$\delta\omega_0^{(1\mathcal{F}_z)} = \frac{6e^2\hbar}{\pi^2\varepsilon_b^{(1)}m_0^2E_g^2} \times\sum_{\substack{L=0,2\\L'=0,2}}\sum_{l,M}(2l+1)\sqrt{(2L+1)(2L'+1)}B_{L,l,M}^{\mathcal{F}_z}B_{L',l',M'}^{\mathcal{F}_z} \times\begin{pmatrix}1 & L' & l\\ 0 & 0 & 0\end{pmatrix}\begin{pmatrix}1 & L & l\\ 0 & 0 & 0\end{pmatrix}\int_0^\infty dk k^2 I_L(kR)I_{L'}(kR), \tag{43}$$

where

$$B_{L,l,M}^{\mathcal{F}_z} = \sum_{m,n,\mu}D_{L,m,n}^{\mathcal{F}_z}\langle\bar{n}|p_\mu^*|m\rangle\begin{pmatrix}1 & L & l\\ \mu & \mathcal{F}_z-m-n & -M\end{pmatrix}. \tag{44}$$

Recalling that, for the canonical basis of the Bloch functions $|m\rangle$, $|n\rangle$ [31],

$$\langle m|p_\mu|\bar{n}\rangle = \langle\bar{n}|p_\mu^*|m\rangle = 2p_{cv}(-1)^{1-\mu}\begin{pmatrix}1/2 & 3/2 & 1\\ m & n & -\mu\end{pmatrix}, \tag{45}$$

where $p_{cv} = i\langle S|\hat{p}_x|X\rangle$ is the interband matrix element of the momentum operator, we can perform summation in Eq. (44) and express $B_{L,l,M}^{\mathcal{F}_z}$ through a Wigner 6*j* symbol as (see, e.g., [28])

$$B_{L,l,M}^{\mathcal{F}_z} = (-1)^{L/2+1-\mathcal{F}_z}2p_{cv}/3 \times\begin{Bmatrix}1/2 & 3/2 & 1\\ L & 1 & 3/2\end{Bmatrix}\delta_{l1}\delta_{M\mathcal{F}_z}. \tag{46}$$

Introducing the longitudinal-transverse splitting for a bulk exciton by

$$\hbar\omega_{\mathrm{LT}} = \frac{4}{\varepsilon_b^{(1)} a_{\mathrm{B}}^3}\left(\frac{e\hbar p_{cv}}{m_0 E_g}\right)^2 \tag{47}$$

and substituting Eq. (46) into Eq. (43) we obtain

$$\delta\omega_0^{(1\mathcal{F}_z)} = \frac{2\omega_{\mathrm{LT}}}{\pi^2}\left(\frac{a_{\mathrm{B}}}{R}\right)^3 \times \sum_{\substack{L=0,2\\ L'=0,2}} (-1)^{(L+L')/2}\sqrt{(2L+1)(2L'+1)} \times \begin{Bmatrix} 1/2 & 3/2 & 1 \\ L & 1 & 3/2 \end{Bmatrix}\begin{Bmatrix} 1/2 & 3/2 & 1 \\ L' & 1 & 3/2 \end{Bmatrix} \times \begin{pmatrix} 1 & L' & 1 \\ 0 & 0 & 0 \end{pmatrix}\begin{pmatrix} 1 & L & 1 \\ 0 & 0 & 0 \end{pmatrix}\int_0^\infty dy y^2 I_L(y) I_{L'}(y). \tag{48}$$

Substituting explicit values of the 3*jm* and 6*j* Wigner symbols [28], we finally obtain the renormalization of the exciton resonant frequency:

$$\delta\omega_0^{(1\mathcal{F}_z)} = \frac{4\pi}{9}\zeta(\beta)\omega_{\mathrm{LT}}\left(\frac{a_{\mathrm{B}}}{R}\right)^3, \tag{49}$$

where the function

$$\zeta(\beta) = \frac{1}{(2\pi)^3}\int_0^\infty dy y^2 [I_0(y) + I_2(y)]^2 \tag{50}$$

was introduced in [14]. The exchange splitting given by Eq. (49) coincides with that extracted from the corresponding exchange spin Hamiltonian

$$-\frac{\pi}{9}\zeta(\beta)\hbar\omega_{\mathrm{LT}}\left(\frac{a_{\mathrm{B}}}{R}\right)^3(\boldsymbol{\sigma}\cdot\mathbf{J}), \tag{51}$$

obtained in [13, 14]. Here σ_x, σ_y, σ_z and J_x, J_y, J_z are, respectively, the Pauli matrices and the matrices of the projections of the angular momentum $J = 3/2$, which refers to the total angular momentum of the quantized hole. Note that, once we know the resonant frequency renormalization (49), we can readily reconstruct the exchange spin Hamiltonian. One can see from Eq. (49) that the exciton resonant frequency renormalization does not depend on the value of $\mathcal{F}_z$. That is what one would expect, since the exchange interaction (51) splits the exciton ground state into sublevels characterized by different values of the total exciton angular momentum and degenerate with respect to its projections.

7. INCLUSION OF DIFFERENCE IN THE BACKGROUND PERMITTIVITIES OF THE NANOCRYSTAL AND THE HOST

In this section we will study the effect of difference in the background permittivities of the NC and the host on the frequency renormalization of the excitonic resonance. Substituting Eq. (35) into Eq. (26) we obtain

$$G^1_{-\sigma\mu}(\mathbf{r},\mathbf{r}') = \frac{\varepsilon_b^{(1)} - \varepsilon_b^{(2)}}{\varepsilon_b^{(1)}}\sum_{l=0}^\infty \frac{R^{-(2l+1)}}{2l+1}\frac{l+1}{\varepsilon_b^{(1)} l + \varepsilon_b^{(2)}(l+1)} \times \sum_{l_z=-l}^{l} \nabla_{-\sigma}[r^l Y_{ll_z}(\mathbf{r}/r)]\nabla'_\mu[r'^l Y^*_{ll_z}(\mathbf{r}'/r')]. \tag{52}$$

Further substituting Eq. (52) into Eq. (29) we have

$$\delta\omega_1^{(1\mathcal{F}_z)} = \frac{4\pi}{\hbar}\frac{\varepsilon_b^{(1)} - \varepsilon_b^{(2)}}{\varepsilon_b^{(1)}}\sum_{l=0}^\infty \frac{R^{-(2l+1)}}{2l+1}\frac{l+1}{\varepsilon_b^{(1)} l + \varepsilon_b^{(2)}(l+1)} \times \sum_{l_z=-l}^{l} W^*_{\mathcal{F}_z l l_z} W_{\mathcal{F}_z l l_z}, \tag{53}$$

where

$$W_{\mathcal{F}_z l l_z} = \int d\mathbf{r}\sum_\sigma (-1)^\sigma \langle \mathrm{exc}, 1\mathcal{F}_z|\hat{d}_\sigma(\mathbf{r})|0\rangle \times \nabla_{-\sigma}[r^l Y_{ll_z}(\mathbf{r}/r)]. \tag{54}$$

Using Eqs. (8) and (9), we obtain

$$W_{\mathcal{F}_z l l_z} = (-1)^{1+\mathcal{F}_z}\frac{ie\hbar}{m_0 E_g} \times \sqrt{3}\sum_m \begin{pmatrix} 3/2 & 1/2 & 1 \\ \mathcal{F}_z - m & m & -\mathcal{F}_z \end{pmatrix} I^{(l,l_z)}_{m,\mathcal{F}_z - m}, \tag{55}$$

where the coefficients

$$I^{(l,l_z)}_{m,\mathcal{F}_z - m} = \sum_n \int d\mathbf{r}\phi(r)\mathcal{R}_{\mathcal{F}_z - m, n}(\mathbf{r})(\mathbf{p}_{m\bar{n}})[r^l Y_{ll_z}(\mathbf{r}/r)] \tag{56}$$

were introduced in [14] and $\mathbf{p}_{m\bar{n}} \equiv \langle m|\mathbf{p}|\bar{n}\rangle$. Using Eqs. (3) and (45) and applying the technique described

in [28], we can perform the angular integration in Eq. (56) to obtain

$$I^{(l,l_z)}_{m,\mathcal{F}_z-m} = (-1)^{l+\frac{l+1}{2}+l_z}\sqrt{l(2l+1)4}p_{cv} \times \begin{pmatrix} 3/2 & 1/2 & l \\ \mathcal{F}_z-m & m & -l_z \end{pmatrix} \begin{Bmatrix} 1/2 & l & 3/2 \\ l-1 & 3/2 & 1 \end{Bmatrix} \times R^{-3/2}\int_0^R f_{l-1}(r/R)\phi(r)r^{l+1}dr, \quad (57)$$

where l can assume the values 1 or 3. Noting that for $l = 3$ the Wigner 3jm symbol in Eq. (57) vanishes identically and substituting the explicit expression for $\phi(r)$ from Eq. (1), we obtain [14]

$$I^{(l,l_z)}_{m,\mathcal{F}_z-m} = \frac{(-1)^{l_z+1}\sqrt{6}p_{cv}\delta_{l1}}{\sqrt{\pi}} \begin{pmatrix} 3/2 & 1/2 & 1 \\ \mathcal{F}_z-m & m & -l_z \end{pmatrix} \times \int_0^1 f_0(x)\sin(\pi x)xdx. \quad (58)$$

Substituting Eq. (58) into Eq. (55) we get

$$W_{\mathcal{F}_z l l_z} = \frac{ie\hbar}{m_0 E_g}\frac{\sqrt{2}p_{cv}\delta_{l_z\mathcal{F}_z}}{\sqrt{\pi}} \times \int_0^1 f_0(x)\sin(\pi x)xdx. \quad (59)$$

Combining Eqs. (47), (53), and (59) we finally obtain

$$\delta\omega_1^{(1\mathcal{F}_z)} = \frac{4}{3}\omega_{LT}\left(\frac{a_B}{R}\right)^3\frac{\varepsilon_b^{(1)}-\varepsilon_b^{(2)}}{\varepsilon_b^{(1)}+2\varepsilon_b^{(2)}} \times \left[\int_0^1 f_0(x)\sin(\pi x)xdx\right]^2. \quad (60)$$

This result can be alternatively derived from the corresponding part of the exchange spin Hamiltonian obtained in [14].

8. EFFECTIVE LOCAL SCALAR SUSCEPTIBILITY

In this section we will construct an effective local scalar susceptibility describing an excitonic resonance in a spherical semiconductor nanocrystal. We will show that even in such a simple model it is possible to account for the fine structure of excitonic levels due to the long-range electron–hole exchange interaction.

The first attempts to derive the long-range exchange induced splitting using the local scalar susceptibility were made by one of the present authors led by his physical intuition [32]. Below we show how this can be carried out correctly.

Consider a sphere of volume $V_{NC} = 4\pi R^3/3$ and background dielectric permittivity $\varepsilon_b^{(1)}$ surrounded by a medium with background dielectric permittivity $\varepsilon_b^{(2)}$. Suppose that inside the sphere there is a concentric core sphere of volume V_{core} whose dielectric constant $\varepsilon_{core}(\omega)$ contains a resonant contribution,

$$\varepsilon_{core}(\omega) = \varepsilon_b^{(1)} + \frac{\varepsilon_b^{(1)}\omega_{NC}}{\omega_0-\omega}, \quad (61)$$

where ω_0 is the frequency of the optically active mechanical exciton (with the short-range part of the exchange interaction taken into account) in the spherical NC of radius R and ω_{NC} characterizes the oscillator strength of the exciton transition. V_{core} and ω_{NC} are the effective parameters of this model. To obtain the frequency renormalization of the excitonic resonance due to the mechanical exciton interaction with the exciton-induced macroscopic longitudinal electric field we can proceed as in Section 4. To that end we will suppose that the electric field inside the core sphere is homogeneous; i.e., in Eq. (21) $E^\sigma(\mathbf{r}') \equiv E^\sigma$. Then we obtain that the time-averaged linear susceptibility

$$\tilde{\chi}^\mu_\sigma(\mathbf{r},\mathbf{r}') \equiv \tilde{\chi}^\mu_\sigma = \frac{\varepsilon_b^{(1)}\omega_{NC}}{4\pi(\omega_0-\omega)V_{core}}\delta_{\mu\sigma}\delta_{\mu\mathcal{F}_z} \quad (62)$$

for $\mathbf{r}$ and $\mathbf{r}'$ inside the core sphere and zero outside. Strictly speaking, to use the equations in Section 4, the function $\tilde{\chi}^\mu_\sigma(\mathbf{r},\mathbf{r}')$ should be continuous at the points $r = R_{core}$, $r' = R_{core}$, where R_{core} is the radius of the core sphere. To satisfy this condition we can assume that, when $r \longrightarrow R_{core}$, $r' \longrightarrow R_{core}$, $\tilde{\chi}^\mu_\sigma(\mathbf{r},\mathbf{r}')$ continuously approaches zero within very small vicinities of the points $r = R_{core}$, $r' = R_{core}$. Substituting Eq. (62) into Eq. (30) we have

$$\delta\omega^{(1\mathcal{F}_z)} = \frac{\varepsilon_b^{(1)}\omega_{NC}}{V_{core}}\int d\mathbf{r}\int d\mathbf{r}'(-1)^{\mathcal{F}_z}G_{-\mathcal{F}_z\mathcal{F}_z}(\mathbf{r},\mathbf{r}'), \quad (63)$$

where the integration is performed within the core sphere ($r, r' < R_{core}$). Taking into account that [14]

$$(-1)^{\mathcal{F}_z}G^0_{-\mathcal{F}_z\mathcal{F}_z}(\mathbf{r},\mathbf{r}') = \frac{1}{3\varepsilon_b^{(1)}}\delta(\mathbf{r}-\mathbf{r}'), \quad (64)$$

$$(-1)^{\mathcal{F}_z} G^1_{-\mathcal{F}_z \mathcal{F}_z}(\mathbf{r}, \mathbf{r}') = \frac{\varepsilon_b^{(1)} - \varepsilon_b^{(2)}}{\varepsilon_b^{(1)}}$$

$$\times \sum_{l=0}^{\infty} \frac{l(l+1)(2l+1)}{\sqrt{2l-1}} \frac{1}{\varepsilon_b^{(1)} l + \varepsilon_b^{(2)}(l+1)} \frac{r^{l-1} r'^{l-1}}{R^{2l+1}} \quad (65)$$

$$\times \sum_{l_z, M, M'} (-1)^M \begin{pmatrix} 1 & l-1 & l \\ \mathcal{F}_z & M' & l_z \end{pmatrix} \begin{pmatrix} 1 & l-1 & l \\ -\mathcal{F}_z & M & -l_z \end{pmatrix}$$

$$\times Y_{l-1, M}(\mathbf{r}/r) Y_{l-1, M'}(\mathbf{r}'/r'),$$

and

$$\int Y_{l-1, M}(\mathbf{r}/r) d\Omega_{\mathbf{r}} = (4\pi)^{-1/2} \delta_{l1} \delta_{M0},$$

we immediately obtain

$$\delta\omega^{(1\mathcal{F}_z)} = \frac{\omega_{\mathrm{NC}}}{3} \left(1 + 2 \frac{\varepsilon_b^{(1)} - \varepsilon_b^{(2)}}{\varepsilon_b^{(1)} + 2\varepsilon_b^{(2)}} \frac{V_{\mathrm{core}}}{V_{\mathrm{NC}}} \right). \quad (66)$$

The δ function entering into Eq. (64) and hidden in Eqs. (29) and (30) was mentioned at the beginning of Section 6. It also appears while proceeding following scheme *A*, where it enters the matrix element of the long-range exchange interaction Hamiltonian [14, 20]. In [20] it was highlighted that this δ function has a macroscopic meaning unlike the short-range exchange interaction associated with characteristic distances of the order of the crystal lattice constant. This statement is further supported by the present consideration in the framework of scheme *B*, where the above-mentioned δ function appears during formal solution of a macroscopic electrostatic problem. Below we also present an alternative and more traditional derivation of Eq. (66) that does not apply any singular functions.

Comparing Eq. (66) with Eqs. (49) and (60), we can determine the parameters of the model developed in this section:

$$\omega_{\mathrm{NC}} = \frac{4\pi}{3} \zeta(\beta) \omega_{\mathrm{LT}} \left(\frac{a_{\mathrm{B}}}{R} \right)^3, \quad (67)$$

$$V_{\mathrm{core}} = V_{\mathrm{NC}} \frac{3 \left[\int_0^1 f_0(x) \sin(\pi x) x dx \right]^2}{2\pi\zeta(\beta)} = R^3 \frac{2 \left[\int_0^1 f_0(x) \sin(\pi x) x dx \right]^2}{\zeta(\beta)}. \quad (68)$$

The ratio $V_{\mathrm{core}}/V_{\mathrm{NC}}$ is plotted in the figure as a function of the light-to-heavy hole effective-mass ratio β. One can see that $V_{\mathrm{core}} < V_{\mathrm{NC}}$ for any value of β. We can further combine Eqs. (67) and (68) to obtain

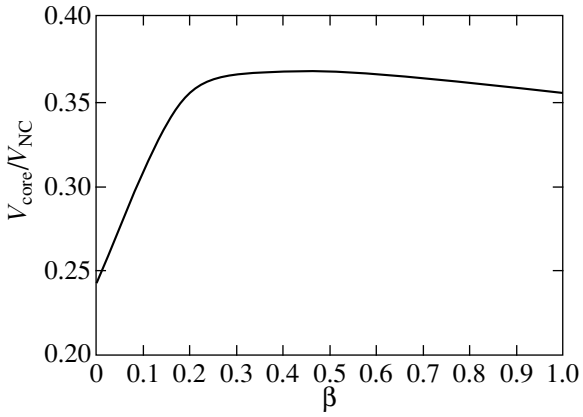

The ratio of the effective core sphere volume V_{core} to the NC volume V_{NC} as a function of the light-to-heavy hole effective-mass ratio β.

$$\omega_{\mathrm{NC}} = \frac{8\pi\omega_{\mathrm{LT}} a_{\mathrm{B}}^3}{3V_{\mathrm{core}}} \left[\int_0^1 f_0(x) \sin(\pi x) x dx \right]^2 = \frac{4\pi}{\hbar \varepsilon_b^{(1)} V_{\mathrm{core}}} \left| \int \langle \mathrm{exc}, 1\mathcal{F}_z | \hat{d}_{\mathcal{F}_z}(\mathbf{r}) | 0 \rangle d\mathbf{r} \right|^2. \quad (69)$$

Note that the parameter ω_{NC} characterizing the oscillator strength of the NC ground state-exciton transition within the present model is equal to the analogous bulk-exciton parameter ω_{LT} multiplied by the square of the electron and hole envelope functions overlap integral and by the ratio of the bulk-exciton volume $4\pi a_{\mathrm{B}}^3/3$ to the core sphere volume V_{core}. Substituting Eq. (69) into Eq. (62) we have

$$\tilde{\chi}_\sigma^\mu = \frac{\left| \int \langle \mathrm{exc}, 1\mathcal{F}_z | \hat{d}_{\mathcal{F}_z}(\mathbf{r}) | 0 \rangle d\mathbf{r} \right|^2}{V_{\mathrm{core}}^2 \hbar(\omega_0 - \omega)} \delta_{\mu\sigma} \delta_{\mu\mathcal{F}_z}. \quad (70)$$

Comparing this expression with Eq. (22) we see that

$$\tilde{\chi}_\sigma^\mu = V_{\mathrm{core}}^{-2} \delta_{\mu\sigma} \delta_{\mu\mathcal{F}_z} \int d\mathbf{r} \int d\mathbf{r}' \chi_{\mathcal{F}_z}^{\mathcal{F}_z}(\mathbf{r}, \mathbf{r}'). \quad (71)$$

Equation (71) establishes the relation between the rigorous treatment developed in the first part of the present paper and the simplified model of this section. It shows that we can suppose that the only component of the electric field different from zero is that in the direction of the polarization of the incident light; thus, we can use the space-averaged linear susceptibility. At the same time we must assume that the exciton is confined within an effective volume given by Eq. (68) which is less than the real NC volume.

We will conclude this section by noting that, along with the rather formal derivation of Eq. (66) given above, another very simple derivation may be presented. The latter is based on the fact that, as was already mentioned in Section 4, in the long-wavelength limit the full Maxwell field may be treated as longitudinal. Then we can write the electrostatic potential as [33, 34]

$$\varphi(r) = \begin{cases} -(\mathbf{r}\mathbf{E}^{(0)})(1 - A/r^3), & \text{when } r > R \\ -C(\mathbf{r}\mathbf{E}^{(0)})(1 - D/r^3), & \text{when } R_{\text{core}} < r < R \\ -B(\mathbf{r}\mathbf{E}^{(0)}), & \text{when } r < R_{\text{core}}, \end{cases} \tag{72}$$

where A, B, C, and D are constants to be determined from the boundary conditions. Requiring that φ and $\varepsilon\partial\varphi/\partial r$ be continuous at the interfaces, we obtain [34]

$$B = \frac{9V_{\text{NC}}\varepsilon_b^{(1)}\varepsilon_b^{(2)}}{V_{\text{NC}}(\varepsilon_{\text{core}}(\omega) + 2\varepsilon_b^{(1)})(\varepsilon_b^{(1)} + 2\varepsilon_b^{(2)}) + 2V_{\text{core}}(\varepsilon_{\text{core}}(\omega) - \varepsilon_b^{(1)})(\varepsilon_b^{(1)} - \varepsilon_b^{(2)})}. \tag{73}$$

Substituting Eq. (61) into Eq. (73) we find that B, and, therefore, the electric field inside the core sphere, contains a pole whose frequency is different from ω_0 by the value of $\delta\omega^{(1\mathcal{F}_z)}$ given by Eq. (66).

9. APPLICATION TO WURTZITE STRUCTURE NANOCRYSTALS

In this section we will show how the formalism developed above may be applied to NCs of semiconductors with wurtzite crystal lattice. This case is quite important since the most widely used CdSe NCs for experimental studies [1–6] possess wurtzite crystal structure.

To describe the states near the top of the valence band in bulk hexagonal crystals with wurtzite structure, one can add a perturbative term responsible for the crystal-field splitting [35] to the spherical Luttinger Hamiltonian:

$$\hat{\mathcal{H}}_{\text{cr}} = -\frac{\Delta_{\text{cr}}}{2}(J_z^2 - 5/4),$$

where Δ_{cr} is the energy of the crystal-field induced splitting in a bulk semiconductor and J_z now refers to the hole spin. As a result, the valence band splits into two bands characterized by the absolute values of the hole spin projections in the C_6 axis.

Hence, the ground level of the mechanical exciton confined in a spherical wurtzite structure NC is split into two fourfold degenerate sublevels. The upper level state is a superposition of two states with $\mathcal{F}_z = 0$ and two states with $\mathcal{F}_z = \pm 1$, where $\mathcal{F}_z$ stands for the mechanical exciton total angular momentum projection in the C_6 axis. We will denote the latter two states as $\pm 1^{\tilde{U}}$. The lower level state is a superposition of states with $\mathcal{F}_z = \pm 2$ and those with $\mathcal{F}_z = \pm 1$, which will be denoted as $\pm 1^{\tilde{L}}$. The energy difference between the upper and the lower sublevels of the mechanical exciton will be denoted as Δ. Since Δ is quite small compared with the unperturbed resonant exciton energy, the circularly polarized light propagating along the C_6 axis would excite states with $\mathcal{F}_z = \pm 1$ from both the upper and the lower sublevels. Below we will show how to account for this case.

The wave function of either the $+1^{\tilde{U}}$ or the $+1^{\tilde{L}}$ state is given by

$$\begin{aligned} |\text{exc}, +1^{\tilde{U},\tilde{L}}\rangle &= \tilde{C}_{1/2}^{\tilde{U},\tilde{L}}\psi_{1/2}^{(e)}(\mathbf{r}_e)\psi_{1/2}^{(h)}(\mathbf{r}_h) \\ &+ \tilde{C}_{-1/2}^{\tilde{U},\tilde{L}}\psi_{-1/2}^{(e)}(\mathbf{r}_e)\psi_{3/2}^{(h)}(\mathbf{r}_h) \\ &\equiv \sum_m \tilde{C}_m^{\tilde{U},\tilde{L}}\psi_m^{(e)}(\mathbf{r}_e)\psi_{1-m}^{(h)}(\mathbf{r}_h), \end{aligned} \tag{74}$$

where $-\tilde{C}_{1/2}^{\tilde{U}} = \tilde{C}_{-1/2}^{\tilde{L}} = 1$, $\tilde{C}_{-1/2}^{\tilde{U}} = \tilde{C}_{1/2}^{\tilde{L}} = 0$. In what follows we will not first take into account the short-range part of the exchange interaction. However, it is worth noting that in the present formalism this would only affect the values of the constants $\tilde{C}_m^{\tilde{U},\tilde{L}}$ and the initial energy difference between the $\pm 1^{\tilde{U}}$ and $\pm 1^{\tilde{L}}$ states.

Comparing Eqs. (74) and (6) and using Eqs. (8), (10), and (11) we obtain

$$\begin{aligned} &\langle 0|\hat{d}_\sigma^*(\mathbf{r})|\text{exc}, +1^{\tilde{U},\tilde{L}}\rangle \\ &= -\sum_{m,n}\frac{ie\hbar}{m_0E_g}\langle\bar{n}|p_\sigma^*|m\rangle\tilde{\Phi}_{mn}^{\tilde{U},\tilde{L}}(\mathbf{r}), \end{aligned} \tag{75}$$

where

$$\begin{aligned} \tilde{\Phi}_{mn}^{\tilde{U},\tilde{L}}(\mathbf{r}) &= 2\sqrt{3}\phi(r)R^{-3/2} \\ &\times \sum_{L=0,2} D_{L,m,n}^{\tilde{U},\tilde{L}} f_L(r/R)Y_{L,1-m-n}(\mathbf{r}/r), \end{aligned} \tag{76}$$

$$D^{\tilde{U},\tilde{L}}_{L,m,n} = \frac{1}{\sqrt{3}}(-1)^{1/2-m-L/2}\tilde{C}^{\tilde{U},\tilde{L}}_{m} \times \begin{pmatrix} 3/2 & L & 3/2 \\ n & 1-m-n & m-1 \end{pmatrix}. \quad (77)$$

Suppose that the circularly polarized light propagating along the C_6 axis excites from the NC ground state an exciton with projection in this axis $\mathcal{F}_z = +1$. Then, instead of Eq. (12), for the time-dependent wave function of the NC we will have

$$|t\rangle = |0\rangle + C^{\tilde{L}}(t)|\text{exc}, +1^{\tilde{L}}\rangle e^{-i\omega_{\tilde{L}}t} + C^{\tilde{U}}(t)|\text{exc}, +1^{\tilde{U}}\rangle e^{-i\omega_{\tilde{U}}t}, \quad (78)$$

where $\omega_{\tilde{L}}$ and $\omega_{\tilde{U}}$ are the frequencies of the lower and the upper levels of the mechanical exciton ground state, respectively. Repeating the derivation of Section 3 we will find

$$C^{\tilde{U},\tilde{L}}(t) = \hbar^{-1}\frac{e^{i(\omega_{\tilde{U},\tilde{L}}-\omega)t}}{\omega_{\tilde{U},\tilde{L}}-\omega}\Lambda^{\tilde{U},\tilde{L}}, \quad (79)$$

where

$$\Lambda^{\tilde{U},\tilde{L}} = \int d\mathbf{r}\sum_{\mu}\langle\text{exc}, +1^{\tilde{U},\tilde{L}}|\hat{d}_{\mu}(\mathbf{r})|0\rangle E^{\mu}(\mathbf{r}).$$

Then, instead of Eq. (20) we will have

$$\varepsilon_b(r)\Delta\varphi(\mathbf{r}) = \frac{4\pi\Lambda^{\tilde{L}}}{\hbar(\omega_{\tilde{L}}-\omega)}\sum_{\mu}\nabla_{\mu}\langle 0|\hat{d}^{*}_{\mu}(\mathbf{r})|\text{exc}, +1^{\tilde{L}}\rangle + \frac{4\pi\Lambda^{\tilde{U}}}{\hbar(\omega_{\tilde{U}}-\omega)}\sum_{\mu}\nabla_{\mu}\langle 0|\hat{d}^{*}_{\mu}(\mathbf{r})|\text{exc}, +1^{\tilde{U}}\rangle. \quad (80)$$

In deriving Eq. (80) and averaging over time, we assumed $\omega_{\tilde{U}} \approx \omega_{\tilde{L}} \approx \omega_0$. If we further proceed as in Section 4, then instead of Eq. (27) we will find a system of two coupled equations:

$$\begin{cases} \Lambda^{\tilde{L}} = \Lambda^{\tilde{L}(0)} - \dfrac{\Lambda^{\tilde{L}}\Xi^{\tilde{L}\tilde{L}}}{\omega_{\tilde{L}}-\omega} - \dfrac{\Lambda^{\tilde{U}}\Xi^{\tilde{L}\tilde{U}}}{\omega_{\tilde{U}}-\omega} \\ \Lambda^{\tilde{U}} = \Lambda^{\tilde{U}(0)} - \dfrac{\Lambda^{\tilde{L}}\Xi^{\tilde{U}\tilde{L}}}{\omega_{\tilde{L}}-\omega} - \dfrac{\Lambda^{\tilde{U}}\Xi^{\tilde{U}\tilde{U}}}{\omega_{\tilde{U}}-\omega}. \end{cases} \quad (81)$$

Here

$$\Xi^{\tilde{\alpha}\tilde{\beta}} = 4\pi\int d\mathbf{r}\int d\mathbf{r}'\sum_{\sigma,\mu}(-1)^{\sigma}G_{-\sigma\mu}(\mathbf{r},\mathbf{r}') \times\langle\text{exc}, +1^{\tilde{\alpha}}|\hat{d}_{\sigma}(\mathbf{r})|0\rangle\langle 0|\hat{d}^{*}_{\mu}(\mathbf{r}')|\text{exc}, +1^{\tilde{\beta}}\rangle \quad (82)$$

and $\tilde{\alpha}, \tilde{\beta} = \tilde{U}, \tilde{L}$. From Eq. (81) for, e.g., $\Lambda^{\tilde{L}}$ we find

$$\Lambda^{\tilde{L}}[(\omega_{\tilde{U}}-\omega+\Xi^{\tilde{U}\tilde{U}})(\omega_{\tilde{L}}-\omega+\Xi^{\tilde{L}\tilde{L}})-\Xi^{\tilde{L}\tilde{U}}\Xi^{\tilde{U}\tilde{L}}] = \Lambda^{\tilde{L}(0)}(\omega_{\tilde{U}}-\omega+\Xi^{\tilde{U}\tilde{U}})(\omega_{\tilde{L}}-\omega)-\Xi^{\tilde{L}\tilde{U}}\Lambda^{\tilde{U}(0)}(\omega_{\tilde{L}}-\omega). \quad (83)$$

The zeros of the expression in the square brackets in the left-hand side of Eq. (83) give the new renormalized frequencies of the exciton states:

$$\omega_{1,2} = \frac{\omega_{\tilde{U}}+\omega_{\tilde{L}}+\Xi^{\tilde{U}\tilde{U}}+\Xi^{\tilde{L}\tilde{L}}}{2} \pm 1/2\sqrt{(\omega_{\tilde{U}}+\omega_{\tilde{L}}+\Xi^{\tilde{U}\tilde{U}}+\Xi^{\tilde{L}\tilde{L}})^2-4(\omega_{\tilde{U}}\omega_{\tilde{L}}+\Xi^{\tilde{U}\tilde{U}}\omega_{\tilde{L}}+\Xi^{\tilde{L}\tilde{L}}\omega_{\tilde{U}}+\Xi^{\tilde{L}\tilde{L}}\Xi^{\tilde{U}\tilde{U}}-\Xi^{\tilde{L}\tilde{U}}\Xi^{\tilde{U}\tilde{L}})}. \quad (84)$$

If we neglect, for the sake of brevity, the difference in the NC and the host matrix background permittivities, then for $\Xi^{\tilde{\alpha}\tilde{\beta}}$ we will have (the derivation is similar to that of Eq. (49) in Section 6)

$$\Xi^{\tilde{\alpha}\tilde{\beta}} = \sum_{m,m'}\tilde{C}^{\tilde{\alpha}}_{m}\tilde{C}^{\tilde{\beta}}_{m'}\begin{pmatrix} 3/2 & 1/2 & 1 \\ m-1 & -m & 1 \end{pmatrix} \times\begin{pmatrix} 3/2 & 1/2 & 1 \\ m'-1 & -m' & 1 \end{pmatrix}\frac{4\pi}{3}\zeta(\beta)\omega_{\text{LT}}\left(\frac{a_{\text{B}}}{R}\right)^3. \quad (85)$$

Substituting the explicit values of the Wigner 3*jm* symbols and $-\tilde{C}^{\tilde{U}}_{1/2} = \tilde{C}^{\tilde{L}}_{-1/2} = 1$, $\tilde{C}^{\tilde{U}}_{-1/2} = \tilde{C}^{\tilde{L}}_{1/2} = 0$ we obtain

$$\Xi^{\tilde{U}\tilde{U}} = \frac{\pi}{9}\zeta(\beta)\omega_{\text{LT}}\left(\frac{a_{\text{B}}}{R}\right)^3 \equiv \tilde{\eta}, \quad \Xi^{\tilde{L}\tilde{L}} = 3\tilde{\eta}, \quad \Xi^{\tilde{L}\tilde{U}} = \Xi^{\tilde{U}\tilde{L}} = \sqrt{3}\tilde{\eta}. \quad (86)$$

Choosing the zero of energy in the middle of the upper and the lower sublevels so that $\omega_{\tilde{U}} = \Delta/2$, $\omega_{\tilde{L}} = -\Delta/2$ and substituting Eq. (86) into Eq. (84) we find

$$\omega_{1,2} = 2\tilde{\eta} \pm \sqrt{4\tilde{\eta}^2+\Delta^2/4-\tilde{\eta}\Delta}. \quad (87)$$

The symmetry of the problem dictates that the short-range and the long-range parts of the exchange interac-

tion lead to additive contributions to the resonant frequencies renormalization. This means that the short-range part can be taken into account if we simply substitute the value of $\tilde{\eta}$ by the magnitude of $\bar{\eta}$, which was introduced in [13, 14] and takes into account both parts of the exchange interaction. However, it is possible to introduce the short-range induced splitting initially. If we denote the parameter responsible for the short-range exchange interaction in a NC by $\eta \equiv \bar{\eta} - \tilde{\eta}$, then we will have

$$\omega^{\tilde{U},\tilde{L}} = 2\eta \pm \sqrt{4\eta^2 + \Delta^2/4 - \eta\Delta}$$

and

$$\tilde{C}_{1/2}^{\tilde{U},\tilde{L}} = \mp\sqrt{\frac{\sqrt{f^2+d} \pm f}{2\sqrt{f^2+d}}},$$

$$\tilde{C}_{-1/2}^{\tilde{U},\tilde{L}} = \sqrt{\frac{\sqrt{f^2+d} \mp f}{2\sqrt{f^2+d}}},$$

where $f = -\eta + \Delta/2$, $d = 3\eta^2$. One can check that Eqs. (84) and (85) lead in this case to Eq. (87), where $\tilde{\eta}$ should be substituted by $\bar{\eta}$, i.e.,

$$\omega_{1,2} = 2\bar{\eta} \pm \sqrt{4\bar{\eta}^2 + \Delta^2/4 - \bar{\eta}\Delta}. \quad (88)$$

This result coincides with that obtained in scheme *A* [13, 14].

Light linearly polarized along the C_6 axis would excite one of the states with $\mathcal{F}_z = 0$. The other one possessing lower energy due to the short-range exchange interaction is optically inactive [1–3, 13, 14]. Thus, this case is quite similar to that of cubic structure NCs and needs no special consideration.

The energy-level diagrams for excitons confined in wurtzite structure NCs, as well as a comparison of calculated splittings with available experimental data, can be found in [14].

Generalization of the treatment developed in Section 8 for the case of wurtzite structure NCs becomes straightforward by using Eq. (71).

10. CONCLUSIONS

We have provided an explicit demonstration that the contribution to the fine structure of the ground exciton level in a semiconductor NC due to the long-range part of the electron–hole exchange interaction can be equivalently described as arising from the mechanical exciton interaction with the exciton-induced longitudinal electric field. Proceeding in this manner we reproduced all the results initially obtained as long-range exchange induced splittings [13, 14] in the framework of the effective-mass approximation. However, the present treatment is more instructive, since it enables one to understand better the limits of validity of the calculation (such as those imposed by the necessity of taking into account the retardation effect) and some peculiarities of the Coulomb interaction (such as those leading to the term in the long-range exchange Hamiltonian proportional to the Dirac δ function). We also established a simplified model that allows the use of a scalar linear susceptibility averaged over space in order to account for the effect under consideration. The price of this simplification is the supposition that the exciton is confined within some effective core volume which is less than the real NC volume. This effective volume constitutes a new parameter. However, once the parameter is found and the model itself is proved for a particular case of a cubic structure NC, it can be used, e.g., in order to account for the case of a wurtzite structure NC [36]. Nevertheless, we gave a rigorous treatment of the latter case, since it cost us little space and allowed us to demonstrate the power of the developed formalism.

ACKNOWLEDGMENTS

We would like to thank E.L. Ivchenko for his encouragement in writing the present paper and his critical reading of the manuscript.

The work of S.V.G. and D.S.C. was funded by the Office of Naval Research and the National Science Foundation through ECS-0072986 and DMR-0073364 and also by the State of Georgia through the Yamacraw program. P.L. and S.V.G. benefited from financial support provided by INTAS (code 99-O-0858).

REFERENCES

1. M. Nirmal, D. J. Norris, M. Kuno, *et al.*, Phys. Rev. Lett. **75**, 3728 (1995).
2. D. J. Norris, Al. L. Efros, M. Rosen, and M. G. Bawendi, Phys. Rev. B **53**, 16347 (1996).
3. Al. L. Efros, M. Rosen, M. Kuno, *et al.*, Phys. Rev. B **54**, 4843 (1996).
4. M. Chamarro, C. Gourdon, P. Lavallard, *et al.*, Phys. Rev. B **53**, 1336 (1996).
5. M. Chamarro, M. Dib, C. Gourdon, *et al.*, in *Proceedings of Mater. Res. Soc. Symposium* (Boston, 1996), p. 396.
6. U. Woggon, F. Gindele, O. Wind, and C. Klingshirn, Phys. Rev. B **54**, 1506 (1996).
7. G. E. Pikus and G. L. Bir, Zh. Éksp. Teor. Fiz. **60**, 195 (1971) [Sov. Phys. JETP **33**, 108 (1971)]; Zh. Éksp. Teor. Fiz. **62**, 324 (1972) [Sov. Phys. JETP **35**, 174 (1972)].
8. G. L. Bir and G. E. Pikus, *Symmetry and Strain-induced Effects in Semiconductors* (Nauka, Moscow, 1972; Wiley, New York, 1974), Chap. 4.
9. M. M. Denisov and V. P. Makarov, Phys. Status Solidi B **56**, 9 (1973).
10. V. M. Agranovich and V. L. Ginzburg, *Crystal Optics with Spatial Dispersion and Excitons* (Nauka, Moscow, 1979; Springer, Berlin, 1984).
11. S. V. Goupalov, E. L. Ivchenko, and A. V. Kavokin, Zh. Éksp. Teor. Fiz. **113**, 703 (1998) [JETP **86**, 388 (1998)].

12. K. Cho, J. Phys. Soc. Jpn. **68**, 683 (1999).
13. S. V. Goupalov and E. L. Ivchenko, J. Cryst. Growth **184/185**, 393 (1998); Acta Phys. Pol. A **94**, 341 (1998).
14. S. V. Goupalov and E. L. Ivchenko, Fiz. Tverd. Tela (St. Petersburg) **42**, 1976 (2000) [Phys. Solid State **42**, 2030 (2000)].
15. S. V. Goupalov, E. L. Ivchenko, and A. V. Kavokin, Superlattices Microstruct. **23**, 1209 (1998).
16. A. Franceschetti, L. W. Wang, H. Fu, and A. Zunger, Phys. Rev. B **58**, 13367 (1998).
17. F. Bassani and G. Pastori Parravicini, *Electronic States and Optical Transitions in Solids* (Pergamon, Oxford, 1975; Nauka, Moscow, 1982).
18. K. Cho, Phys. Rev. B **14**, 4463 (1976).
19. T. Takagahara, Phys. Rev. B **47**, 4569 (1993).
20. S. V. Goupalov and E. L. Ivchenko, Fiz. Tverd. Tela (St. Petersburg) **43**, 1791 (2001) [Phys. Solid State **43**, 1867 (2001)].
21. Note that the term "dipole–dipole," as well as "monopole–monopole", etc., refers here to the coefficients of the expansion of the Coulomb potential in the series near the atomic sites and not to the character of the spatial dependence of the corresponding matrix elements of the long-range exchange Hamiltonian on the band states. The spatial dependence of the matrix element of the long-range exchange Hamiltonian corresponding to the monopole–monopole term consists of a term proportional to the δ function and the remaining part. The spatial dependence of this remaining part coincides with that of the matrix element of the long-range exchange Hamiltonian corresponding to the dipole–dipole term as soon as intra-atomic matrix elements of the velocity operator are substituted by interatomic ones.
22. S. Lee, L. Jönsson, J. W. Wilkins, *et al.*, Phys. Rev. B **63**, 195318 (2001).
23. H. Ajiki and K. Cho, Phys. Rev. B **62**, 7402 (2000).
24. A. I. Ekimov, A. A. Onushchenko, M. E. Raikh, and Al. L. Efros, Zh. Éksp. Teor. Fiz. **90**, 1795 (1986) [Sov. Phys. JETP **63**, 1054 (1986)].
25. K. Cho, H. Ajiki, and T. Tsuji, Phys. Status Solidi B **224**, 735 (2001).
26. H. Ajiki and K. Cho, in *Proceedings of International Conference EXCON2000*, Ed. by K. Cho and A. Matsui (World Sci., Singapore, 2001), p. 177.
27. D. Schechter, J. Phys. Chem. Solids **23**, 237 (1962).
28. D. A. Varshalovich, A. N. Moskalev, and V. K. Khersonskiĭ, *Quantum Theory of Angular Momentum* (Nauka, Leningrad, 1975; World Sci., Singapore, 1988).
29. Y. Fu, M. Willander, E. L. Ivchenko, and A. A. Kiselev, Phys. Rev. B **55**, 9872 (1997).
30. The validity of the formula for integration by parts for integrands containing the Coulomb potential can be proven by transformation into the **k**-space.
31. E. L. Ivchenko and G. E. Pikus, *Superlattices and Other Heterostructures. Symmetry and Optical Phenomena*, 2nd ed. (Springer, Berlin, 1997).
32. P. Lavallard, J. Cryst. Growth **184/185**, 352 (1998).
33. L. D. Landau and E. M. Lifshitz, *Electrodynamics of Continuous Media* (Fizmatgiz, Moscow, 1959; Pergamon Press, Oxford, 1960).
34. P. Lavallard, M. Rosenbauer, and T. Gacoin, Phys. Rev. A **54**, 5450 (1996).
35. Al. L. Efros, Phys. Rev. B **46**, 7448 (1992).
36. P. Lavallard, G. Lamouche, and S. V. Goupalov (in press).

Physics of the Solid State, Vol. 45, No. 4, 2003, pp. 782–787. Translated from Fizika Tverdogo Tela, Vol. 45, No. 4, 2003, pp. 742–747.

LOW-DIMENSIONAL SYSTEMS AND SURFACE PHYSICS

Carbon Segregation on a Tungsten Surface

N. D. Potekhina, N. R. Gall', E. V. Rut'kov, and A. Ya. Tontegode

Ioffe Physicotechnical Institute, Russian Academy of Sciences, Politekhnicheskaya ul. 26, St. Petersburg, 194021 Russia

Received May 29, 2002; in final form, August 19, 2002

Abstract—New measurements are performed and a comprehensive analysis of experimental data is made on the dependence of equilibrium carbon coverage θ on a tungsten surface on its temperature and the degree of carbon loading. It is shown that if the volume is free of carbon, the variation of θ for $T \geq 1400$ K can be approximately described by the balance between the carbon flows through the boundary with the activation energy for transition into the bulk $E_1 = 4.6$ eV and the segregation energy $\Delta E = 1.7$ eV. For tungsten loaded preliminarily with carbon to a content of $\approx 10^{-2}$ at. %, the $\theta(T)$ relation cannot be described in terms of the equilibrium conditions with constant E_1 and ΔE, because these quantities depend on the degree of carbon loading; E_1 grows from 4.6 to 6.8 eV and ΔE grows from 1.7 to 2.3 eV with an increase in carbon content from 0 to 10^{-2} at. %. These variations are attributed to the bonds becoming stronger in carbon-loaded tungsten with increasing carbon content. © *2003 MAIK "Nauka/Interperiodica".*

1. INTRODUCTION

The formation and properties of surface tungsten carbide were studied in [1, 2] as functions of the total amount of absorbed carbon. It was shown that high-temperature adsorption of carbon produces first a specific state on the surface, the surface carbide (SC), with its atomic concentration $N_S = N_{ML} = 1 \times 10^{15}$ cm^{-2} (a carbon monolayer) coinciding with that of the (100) surface tungsten atoms. The extra carbon falling on the surface penetrates into the bulk of the metal through the surface carbide layer thus formed. The SC breaks up because of carbon penetrating into the bulk at temperatures $T \geq T^*$, with the breakup temperature T^* being the higher, the higher the carbon content in the sample. In other words, dissolved carbon makes the SC stronger. We also obtained annealing curves, i.e., the relations connecting the surface coverage by carbon $\theta(T) = N_S(T)/N_{ML}$ under SC breakup with the tungsten ribbon temperature [1, 2]. It turned out that the $\theta(T)$ relations differ strongly depending on the actual amount of dissolved carbon. The $\theta(T)$ curves yielded estimates for some activation energies of carbon transport from the surface into the bulk and back. The present communication reports on a continuation of these studies, including a series of measurements and a more comprehensive analysis of all the available experimental data. This analysis was aimed at estimating the kinetic parameters of the carbon interaction with tungsten as a function of the metal bulk loading by carbon and at developing a model description of this interaction.

2. MEASUREMENT RESULTS

Experiments were conducted in an ultrahigh-vacuum, high-resolution Auger spectrometer providing direct Auger spectral studies of a high-temperature sample, which is a point of fundamental importance [3]. The measurement technique described in [1–4] permitted determination of the absolute surface concentration of carbon on W(100) in the course of the surface carbide breakup. We used thin tungsten ribbons measuring $50 \times 1 \times 0.02$ mm. The textured W samples, cleaned by high-temperature annealing at 2700 K, were predominantly W(100) oriented. Carbon was deposited on both sides of a ribbon $L = 2 \times 10^{-3}$ cm thick; therefore, we shall consider the results of measurements made on one half of a symmetric plate. Each half has $m = L/2d$ layers of symmetry (100), where d is the interlayer distance. For a bcc crystal, $d = a_0/2$, where $a_0 = 3.16$ Å is the tungsten lattice constant. For $L = 0.02$ mm, we have $m = 6.33 \times 10^4$.

Tungsten loading by carbon was effected either using a source of atomic carbon [5] or through exposure to benzene vapor, which automatically provided double-sided carbon deposition on the ribbon. A more detailed description of this technique can be found in [2]. As already mentioned, carbon deposited on clean tungsten at temperatures from 1200 to 1400 K builds up in an adlayer to a concentration $N_S = N_{ML} = 1 \times 10^{15}$ cm^{-2} (surface carbide). Figure 1 (curve *1*) shows an annealing curve $\theta(T)$ obtained immediately after the SC formation (with the substrate volume being still practically free of carbon). This curve was found to be irreversible; indeed, the slow cooling of the ribbon following its heating to 2000 K did not bring about SC formation through the release of carbon from the tungsten bulk even though the total amount of carbon did not change, because the loss of carbon by desorption from tungsten occurs at higher temperatures, $T \geq$ (2300–2400) K.

If after the SC formation the tungsten bulk is saturated with carbon (to about eight monolayers per half of the ribbon volume), the annealing curves $\theta(T)$ become reversible (curve *2* in Fig. 1). Each point corresponds to 20 s of annealing. Note that curve *2* was reproduced

well under both increasing and decreasing temperature and did not depend on the exposure time at each point. This indicates the absence of a concentration gradient in the volume; i.e., carbon was distributed uniformly over the ribbon thickness. This also indicates the onset of equilibrium between carbon atoms in the volume and on the surface. Let us consider the mathematical formalism for these two cases (curves *1*, *2* in Fig. 1).

2.1. Carbon Monolayer Annealing on a Carbon-Free Tungsten Sample

2.1.1. Without inclusion of the solubility limit. We introduce the filling of the *i*th layer in the volume by carbon, $\phi_i = N_i/N_{ML}$, where N_i is the carbon concentration in the *i*th near-surface sample layer. We denote by $k_1(T)$ and $k_2(T)$ the rate constants of adatom transport from the surface into the volume and in the reverse direction, respectively. The variation of surface coverage by adatoms $\theta(t)$ in the initial stage of their diffusion into the bulk, analyzed in terms of the equilibrium fluxes at the interface (the quasi-stationary boundary condition),

$$k_1\theta = k_2\phi(T, t) \tag{1}$$

is given by the following equation, which was derived in [5]:

$$\theta(t) \approx \theta_0\left[1 - \frac{2k_1(T)\sqrt{Dt}}{\sqrt{\pi}k_2(T)d} + \ldots\right], \tag{2}$$

where θ_0 is the coverage at $t = 0$ and $D(T) = D_0 \times \exp(-E_D/kT)$ is the diffusion coefficient of carbon atoms. Taking the diffusion parameters from [6] as $D_0 = 9 \times 10^3$ cm^2 s^{-1} and $E_D = 1.75$ eV, we come to the conclusion that, in the anneal time $t = 20$ s, the diffusion length $\lambda = \sqrt{Dt}$ for carbon atoms in tungsten reaches one half the ribbon thickness $L/2 = 10^{-3}$ cm only for $T \geq 1700$ K (Table 1) and that, in the initial stage of monolayer breakup ($T \leq 1500$ K), there is a concentration gradient in the volume with the surface coverage varying with time according to Eq. (2). By equating the change $\Delta\theta(T)$ (which can be derived from curve *1* in Fig. 1) to the difference $[\theta_0 - \theta(t)]$ from Eq. (2), we find the ratio $k_1/k_2(T)$ expressed through $\Delta\theta(t)$ and $\sqrt{Dt}$ for different $T \leq 1500$ K:

$$\frac{k_1T}{k_2(T)} \simeq \frac{\sqrt{\pi}}{2}\frac{d\Delta\theta(T, t)}{\sqrt{Dt}\theta_0}. \tag{3}$$

The Arrhenius rule permits one to present this ratio in the form of an exponential,

$$k_1(T)/k_2(T) = k_1^0/k_2^0\exp(-DE/kT), \tag{4}$$

where $\Delta E = E_1 - E_2$ is the difference between the activation energies for adatom transport from the adlayer into the volume (E_1) and back to the adlayer (E_2) and k_1^0 and k_2^0 are the prefactors in the rate constants. Assuming that $k_1^0 = k_2^0$, we obtain $\Delta E(T) = kT\ln[k_2(T)/k_1(T)]$ from Eq. (4) and find the difference $\Delta E(T) = 1.7$ eV for $1400 \leq T \leq 1500$ K. On the other hand, if we assume carbon diffusion to be very fast, such that the metal volume is filled by carbon uniformly at each instant of time, i.e.,

$$\phi = [\theta_0 - \theta(t)]/m, \tag{5}$$

then the monolayer breakup with time, without having to invoke quasi-steady state equation (2) at the boundary, can be described by

$$d\theta/dt \simeq -k_1\theta + k_2(\theta_0 - \theta)/m. \tag{6}$$

The solution to Eq. (6) has the form

$$\theta(t) = \theta_0/(1 + \alpha)[1 + \alpha\exp(-k_1t(\alpha + 1)/\alpha)], \tag{7}$$

where

$$\alpha(T) = mk_1(T)/k_2(T) = \alpha_0\exp(-\Delta E/kT), \quad \alpha_0 = mk_1^0/k_2^0. \tag{8}$$

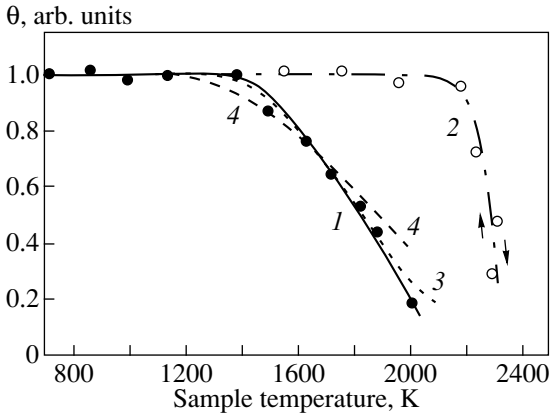

Fig. 1. Carbon coverage θ on the W(100) surface vs. the substrate temperature plot obtained under annealing of a carbon monolayer ($N_S = N_{ML} = 1 \times 10^{15}$ cm^{-2}): (*1*) the bulk of tungsten is free of carbon ($T \leq 1400$ K); (*2*) carbon-loaded sample (20 monolayers of carbon in the ribbon bulk); and (*3*, *4*) calculations made using (*3*) Eq. (23) for $\Delta E = E_1 - E_2 = 1.72$ eV and (*4*) Eq. (22) for $\Delta E = 1.90$ eV.

Table 1. The relative diffusion length traversed in time $t = 20$ s, the equilibrium onset time t_e, and the loading ϕ_λ in $m\lambda$ near-surface layers ($m_\lambda = \lambda/d$)

T, K	1400	1500	1600	1700
$2\lambda/L$	0.3	0.49	0.74	1.1
t_e, s	133	25	5.4	1.3
$\phi_\lambda \times 10^{-6}$	1.1	2.9	4.3	4.7

For $t \longrightarrow \infty$, we obtain the equilibrium coverage:

$$\theta_e(T) = \theta(t \longrightarrow \infty) = \theta_0/[1 + \alpha(T)]. \quad (9)$$

For $t \longrightarrow 0$, we have

$$\Delta\theta = \theta_0 - \theta(t) = \alpha\theta_0/(1 + \alpha) \times [1 - \exp(-k_1 t(1 + \alpha)/\alpha)] \longrightarrow k_1 t\theta_0. \quad (10)$$

To estimate $k_1(T)$, we assume that the initial stage in the adlayer breakup, when the flux into the volume becomes larger than that going in the opposite direction, is described by Eq. (10): $\Delta\theta(T) = k_1^0 t\theta_0 \exp(-E_1/kT)$. Substituting $\Delta\theta(T)$ from curve *1* in Fig. 1 for $T = 1400$, 1450, and 1500 K and $t = 20$ s (the time the sample is kept at each anneal point), we come to the estimate $E_1 = 4.6$ eV for $k_1^0 = k_2^0 = 10^{13}$ s^{-1}.

We conventionally define the time at which equilibrium coverage is reached as

$$t_e(T) = \frac{\alpha(T)}{k_1[1 + \alpha(T)]} = \frac{m}{k_2(T) + mk_1(T)}, \quad (11)$$

when the term depending on time in Eq. (10) decreases e times. The values of $t_e(T)$ calculated with the use of the above estimates, $\Delta E = 1.7$ eV and $E_1 = 4.6$ eV, are listed in Table 1. We readily see that equilibrium in a carbon monolayer annealed for 20 s can set in only for $T > 1500$ K, when the anneal time becomes longer than t_e. By assuming that, for $T > 1500$ K, the volume equilibrium is reached in the time of annealing, we can once more determine $\alpha_e(T)$ from Eq. (9), but this time we will use the experimental values of $\theta(T) = \theta_e(T)$ taken from Fig. 1 for $T > 1500$ K:

$$\alpha_e(T) = \frac{\theta_0}{\theta_e(T)} - 1. \quad (12)$$

It was found that the values of $\alpha_e(T)$ thus obtained are fitted well by an exponential,

$$\bar{\alpha}(T) = m\exp(-\Delta E_e/kT), \quad (13)$$

in which $\Delta E_e = 1.72 \pm 0.02$ eV, which agrees well with the value $\Delta E = 1.7$ eV derived from Eq. (3) with inclusion of the concentration gradient for $T < 1500$ K. Thus, we obtained the same estimate for the difference $E_1 - E_2$ using different approximations to describe the $\theta(T)$ relation, namely, for $T < 1500$ K, where carbon is nonuniformly distributed over the ribbon volume, and for $T > 1500$ K, where the impurity is distributed uniformly over the ribbon volume. It turned out that Eq. (9) for the equilibrium value of $\theta(T)$, if the $\alpha(T)$ relation from Eq. (13) is substituted into it with $\Delta E = 1.72$ eV, satisfactorily approximates the whole $\theta(T)$ curve in Fig. 1 (curve *3*), which indicates that the deviation from steady state and the nonuniformity of carbon distribution in the volume for $T < 1500$ K affect the behavior of $\theta(T)$ during the annealing insignificantly.

2.1.2. Effect of the solubility limit. Let us compare the real filling of the ribbon volume by carbon atoms, $\phi_{\lim}(T)$, with the limiting carbon solubility in tungsten. The solubility limit, which determines the maximum percentage of carbon atoms per substrate atom, is given by an empirical formula [7],

$$\log n_{\lim}(\text{at. \%}) = 2.03 - 6510/T \quad (\text{for } 1700\text{–}2600 \text{ K}). \quad (14)$$

This means that there are $100n_{\lim}$ (at. %) carbon atoms per tungsten atom. Because one unit cell of the (100) atomic layer contains one W atom, the same quantity actually represents the limiting degree of filling of one unit cell in the atomic W layer by carbon atoms:

$$\phi_{\lim}(T) = n_{\lim}(\text{at. \%}) \times 100. \quad (15)$$

Extrapolating Eq. (14) to temperatures $T < 1700$ K yields $\phi_{\lim}(1400 \text{ K}) \simeq 2.4 \times 10^{-5}$. If the fraction $\Delta\theta$ of the carbon that diffused into the volume is uniformly distributed, we obtain $\phi = \Delta\theta/m$; therefore, for $\Delta\theta(1400) \simeq 0.02$ and $m = 6.33 \times 10^4$, we have $\phi(1400) \sim 3 \times 10^{-7}$. However, as shown above, at $T = 1400$ K, there is a concentration gradient in the volume and carbon is distributed over a layer of thickness $\sim\lambda$ near the surface, which is 3.3 times smaller than $L/2$ for $T = 1400$ K (Table 1). Therefore, the average filling in this layer $\phi_\lambda = \Delta\theta/m_\lambda(1400 \text{ K}) \simeq 1 \times 10^{-6}$, while being 3.3 times $\phi(1400 \text{ K})$ for uniform distribution over the volume, is still 20 times smaller than the limiting value $\phi_{\lim}(1400 \text{ K})$ (Table 2). This means that the breakup of a monolayer with time can be described by Eqs. (6)–(10) without taking into account $\phi_{\lim}$ and that the persistence of SC up to $T^* = 1400$ K is due to the high activation energy $E_1 = 4.6$ eV rather than to the low solubility limit for $T \leq 1400$ K. Thus, annealing of a carbon monolayer on pure tungsten is described well enough by a model that assumes uniform carbon distribution over the volume in accordance with Eq. (9) and with the parameters $\Delta E = E_1 - E_2 \simeq 1.7$ eV and $E_1 \simeq 4.6$ eV ($E_2 = 2.9$ eV). According to this model, equilibrium between the surface coverage $\theta(T)$ and volume filling $\phi(T)$ is determined by the ratio of the constants $k_1(T)$ and $k_2(T)$ involved in boundary condition (1):

$$\theta(T)/\phi(T) = k_2(T)/k_1(T). \quad (16)$$

At equilibrium, the $\theta(T)$ relation should be reversible, so that under ribbon cooling, we should have obtained the same $\theta(T)$ dependence. In actual fact, however, at low carbon coverages $\theta_0 \leq 1$, this is not the case and a fraction of carbon atoms remains in the bulk of the metal without returning to the surface under cooling, as expected from Eq. (16); carbon atoms are possibly captured by traps or at grain boundaries. The concentration of such traps can be estimated. Indeed, dissolution of one carbon monolayer in m substrate layers produces an average volume concentration $n_C = (mv_0)^{-1}$, where v_0 is the crystal unit-cell volume. For $m = 6.33 \times 10^4$ and $v_0 = 3.15 \times 10^{-23}$ cm^{-3}, we obtain $n_C \simeq 5 \times 10^{17}$ cm^{-3}. Cooling

Table 2. Parameters characterizing the diffusion processes in the W–C system

Ψ_0	ϕ_1	T_m	T^*	$\phi_{lim}(T^*)$	$\phi_1/\phi_{lim}(T^*)$	$E_1(T^*)$, eV
1	1.1×10^{-6}*	1000	1400	2.4×10^{-5}	0.05	4.55
4	4.7×10^{-5}	1500	1950	4.9×10^{-4}	0.1	6.3
8.5	1.2×10^{-4}	1650	2100	8.5×10^{-4}	0.14	6.8
10	1.4×10^{-4}	1700	2100	1.0×10^{-3}	0.14	6.8

Note: Ψ_0 is the number of carbon monolayers diffused into one half of the ribbon; $\phi_1 = (\Psi_0 - 1)/m$ is the loading of bulk layers by carbon; T_m is the lowest temperature at which the bulk can be loaded to $\phi_1 = \phi_{lim}(T_m)$; T^* is the temperature at which a monolayer starts to dissolve; ϕ_{lim} is the maximum loading of the bulk with carbon; and E_1 is the activation energy for carbon transport from the monolayer into the bulk.

*Refers to $\phi_\lambda(T^*)$.

drives less than one half of the monolayer onto the surface. This means that the trap concentration in the volume of the ribbon can reach $\sim 3 \times 10^{17}$ cm^{-3}.

It was shown in [8] that if the surface coverage does not reach a geometric monolayer in segregation during the cooling, this implies the existence of lateral repulsion in the adlayer. Taking into account next-to-nearest neighbors, surface saturation can decrease to $\theta = 0.25$. Although the calculations in [8] were conducted for the case of volume loading to $\phi_c = 10^{-4}$, the results obtained do not depend on the impurity concentration. In our case, however, with a large amount of carbon absorbed, the surface coverage of tungsten by C atoms returns under cooling to the monolayer state and the $\theta(T)$ dependences are reversible (Fig. 2). This behavior allows only one interpretation, namely, that all traps were filled during the preliminary loading and that there is no lateral repulsion in the C/W adlayer.

2.2. Carbon Monolayer Annealing on Carbon-Loaded Tungsten Ribbons

As already noted, in the case where the tungsten volume is saturated by carbon, carbon monolayer breakup caused by the C atoms entering the bulk of the metal occurs at a higher temperature T^* than in the case of pure tungsten and the breakup onset temperature T^* is higher, the larger the saturation. Table 2 lists the values of T^* for various numbers $\Psi_0 = N_0/N_{ML}$ of carbon monolayers loaded in one half of the ribbon (N_0 is the total amount of carbon per 1 cm^2 of one half of the ribbon, i.e., per volume $(L/2) \times 1 \times 1$ cm).

Let us check whether the onset of the monolayer breakup is connected with the carbon solubility limit in this case. Let us determine the lowest temperature T_m needed for loading of a given amount of carbon into the ribbon. Obviously, the preliminary carbon loading ϕ_1 should not exceed the limiting amount $\phi_{lim}(T_m)$, i.e., it should satisfy the condition

$$\phi_1 = (\Psi_0 - 1)/m \le \phi_{lim}(T_m). \quad (17)$$

The values of T_m derived from a comparison of $\phi_1(\Psi_0)$ with the solubility from Eq. (15) are listed in Table 2. We readily see that the monolayer breakup onset temperature is 400–450 K higher than the minimum temperature T_m at which a given amount of carbon can be incorporated into the volume. In other words, even at a volume carbon concentration that is significantly lower than the limit, $\phi_1 < \phi_{lim}$, monolayer breakup does not start until the temperature rises even further, reducing the ratio $\phi_1/\phi_{lim}(T)$ to the values presented in Table 2. It looks as if monolayer dissolution under preliminary loading is impeded not by the solubility limit but rather by the high activation energy E_1 for carbon dissolution, which is higher, the larger the amount of preliminarily loaded carbon. To estimate $E_1(\Psi_0)$ for $\Psi_0 \gg 1$, we again invoke Eq. (10). At the very beginning of monolayer breakup, at $T \ge T^*$, when $\Delta\theta(T)$ is very small and is determined by the accuracy of measurement, we have $\Delta\theta = k_1\theta_0 t$. For $\Delta\theta(T) \simeq (1\text{–}2) \times 10^{-2}$, $t = 20$ s, and $k_1^0 = 10^{13}$ s^{-1}, we use the relation $E_1 = kT \ln[k_1^0 T/\Delta\theta(T)]$ to

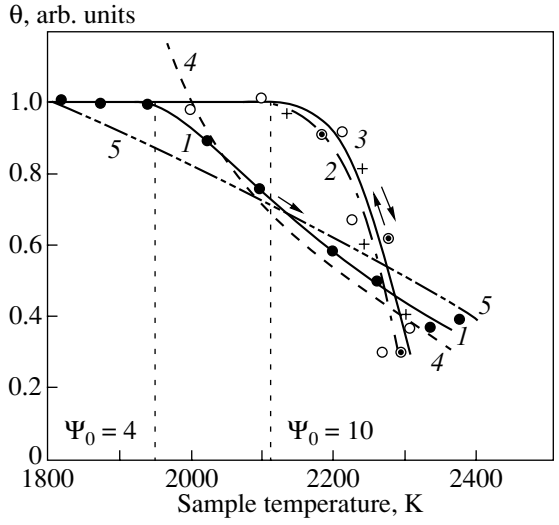

Fig. 2. Equilibrium carbon coverage plotted vs. temperature for the case of Ψ_0 carbon monolayers dissolved in one half of the ribbon bulk. Experiments were made for Ψ_0 equal to (*1*) 4, (*2*) 8.5, and (*3*) 10. Calculations were performed for $\Psi_0 = 4$: (*4*) from Eq. (23), $\Delta E = 1.74$ eV; (*5*) from Eq. (22), $\Delta E = 1.92$ eV.

obtain the values of $E_1(\Psi_0)$ given in Table 2 for $\Psi_0 = 4$, 8.5, and 10. As seen from Table 2, E_1 increases considerably (up to 6.8 eV) with increasing number of dissolved carbon monolayers in the tungsten volume. In the estimates, we assumed that the prefactor k_1^0 does not depend on the degree of volume saturation by carbon. As mentioned above, the reversibility of the $\theta(T)$ curves implies equilibrium in the W–C system and uniform carbon distribution over the ribbon thickness at each value of $T > T^*$. Since the carbon concentration in the volume at a large loading may become comparable to the solubility limit, the equation of equilibrium should be written in a more complete form:

$$k_1\theta(1-\phi/\phi_{\lim}) = k_2\phi(1-\theta), \quad \phi = (\Psi_0 - 1)/m. \quad (18)$$

Whence we obtain the relation

$$\alpha(T) = m\frac{k_1(T)}{k_2(T)} = \frac{\Psi_0 - \theta}{\theta}\left(\frac{1-\theta}{1-\phi/\phi_{\lim}}\right), \quad (19)$$

which connects the rate constants on the left with the measurable quantities on the right. We denote the quantity $\alpha(T)$ thus found by $\alpha^{ex}(T)$. Representing it in the form of exponential (8), we find $\Delta E^{ex}(T)$ for each temperature

$$\Delta E^{ex}(T) = E_1 - E_2 = kT\ln\left[m\frac{k_1^0}{k_2^0\alpha^{ex}(T)}\right] \quad (20)$$

under the assumption of $k_1^0 = k_2^0$. Next, we determine the average value $\overline{\Delta E}$ for the whole temperature interval considered and calculate the function

$$\bar{\alpha}(T) = m\exp(-\overline{\Delta E}/kT). \quad (21)$$

For known $\bar{\alpha}(T)$, Eq. (19) yields an equation for $\bar{\theta}(T) \le 1$,

$$\bar{\theta}^2\left(1 - \frac{\bar{\alpha}}{m\phi_{\lim}}\right) - \bar{\theta}\left[\bar{\alpha} + 1 + \Psi_0\left(1 - \frac{\bar{\alpha}}{m\phi_{\lim}}\right)\right] + \Psi_0 = 0. \quad (22)$$

Neglecting the factors $(1 - \theta)$ and $(1 - \phi/\phi_{\lim})$ in Eqs. (18) and (19), we obtain the solution

$$\bar{\theta}(T) \simeq \frac{\Psi_0}{1 + \bar{\alpha}(T)}, \quad (23)$$

which coincides with Eq. (9) for the carbon-free tungsten, i.e., for $\Psi_0 = \theta_0$. The bar refers here to the quantities calculated with the use of $\bar{\alpha}(T)$ given by Eq. (21), with the averaged value $\overline{\Delta E}$. Let us analyze the equilibrium curves in Fig. 2 for the case of $\Psi_0 \gg 1$. For $\Psi_0 = 4$, from Eq. (19) without the second factor on the right, we find $\alpha_1^{ex}(T)$, and with inclusion of this factor, $\alpha_3^{ex}(T)$. Presenting these data in the form of exponential (21), we obtain $\overline{\Delta E}_1 = (1.74 \pm 0.04)$ eV and $\overline{\Delta E}_3 = (1.92 \pm 0.12)$ eV. Note that both values are close to the corresponding figures for the case $\Psi_0 = 1$ ($\overline{\Delta E}_1 = 1.72$ eV, $\overline{\Delta E}_3 = 1.90$ eV), for which the $\bar{\theta}_{1,3}(T)$ relations calculated from Eqs. (23) and (22), respectively (curves *3*, *4* in Fig. 1), approximate the course of experimental curve *1* in Fig. 1. In the case of preliminarily loaded tungsten, however, the situation is radically different. Figure 2 presents experimental curves plotted for $\Psi_0 = 4$, 8.5, and 10 and calculated $\theta(T)$ relations for the case $\Psi_0 = 4$. Calculations made using Eqs. (22) and (19) with inclusion of $(1 - \theta)$ and $\phi_{\lim}$ yield curve *5*, which describes a slower decay than the one observed experimentally and a breakup onset for $T \ll T^*$, while Eq. (23) for $\bar{\theta}_1(T)$ does not show saturation for $T < T^*$ and describes a temperature dependence for which the curvature has a sign opposite to that observed experimentally. As the deposited carbon dose Ψ_0 increases, the semiempirical $\theta_1(T)$ and $\theta_3(T)$ relations deviate more and more widely from experiment. The reason for this deviation lies apparently in that the properties of the substrate, i.e., the activation energies E_1 and E_2 and the ratio of the rate coefficients $k_1(T)$ and $k_2(T)$, depend on the degree of volume loading with carbon, which decreases with increasing T, $\phi(T) = [\Psi_0 - \theta(T)]/m$. Indeed, parameter $\alpha^{ex}(T)$ derived from the experimental data cannot be presented in the form of an exponential with $\Delta E = \text{const}$. The quantity $\Delta E_3(T)$ in Eq. (19) for $\Psi_0 = 8.5$ decreases in the temperature interval 2100–2300 K from 2.3 to 1.6 eV and cannot be replaced by the constant $\overline{\Delta E}_3 = 1.9$ eV obtained by averaging. It appears reasonable to assume that the amount of loaded carbon affects the energy difference ΔE, which governs the kinetics of equilibrium diffusion processes in the W–C system. As the temperature T increases, the relative saturation $\phi(T)/\phi_{\lim}(T)$ of the volume by carbon for a given Ψ_0 decreases; hence the activation energy E_1 for carbon transfer from the monolayer into the carbon-loaded metal volume should also decrease, with the result that ΔE_1 should decrease with increasing T. The same relation can be seen in Table 2; namely, when a carbon monolayer on pure tungsten ($\Psi_0 = 1$) dissolves, the ratio $\phi_1/\phi_{\lim}(T)$ near the surface is smaller by a factor two to three than that for $\Psi_0 \ge 4$, where annealing occurs at higher T. Therefore, $E_1(T^*)$ for the carbon-loaded tungsten is larger by a factor of approximately 1.5 than that for pure tungsten. In these conditions, Eqs. (18) and (19), which describe the equilibrium between opposite carbon flows crossing the tungsten surface, may serve only for a rough estimate of the parameters $\alpha(T)$ and ΔE for different carbon loadings and Eqs. (20)–(22) for $\theta(T)$ become no longer valid,

because they disregard the $\alpha(\Psi_0)$ dependence. Thus, the activation energies E_1 and E_2 and their difference ΔE are functions of the relative saturation $\phi_1/\phi_{lim}(T)$ of the sample with carbon. Because the difference ΔE, while decreasing with increasing T, remains nevertheless of the order of 2 eV for any value of Ψ_0, the increase in E_1 entails an increase in the activation energy E_2 of carbon escaping onto the surface of carbon-loaded tungsten. It may be conjectured that the presence of a large amount of carbon in the tungsten bulk confers rigidity to the lattice, which enhances the energies E_1 and E_2 and changes the $k_1(T)/k_2(T)$ ratio, with variation of Ψ_0, θ, and ϕ_{lim}.

3. DISCUSSION OF RESULTS AND CONCLUSIONS

A study of equilibrium segregation of carbon on W(100) with the temperature decreasing from 2073 to 1400 K was also made in [9]. An analysis of those results made on the basis of the equilibrium equation $k_1\theta = k_2\phi(1 - \theta)$, where $\phi = (1 - \theta)/m$, yielded $\Delta E = 2.43 \pm 0.10$ eV [9]. This analysis was conducted under the assumption that, at $T = 1400$ K, the metal volume was free of carbon and that the carbon on the surface had a density $N_S = 6.1 \times 10^{14}$ cm^{-2}. The segregation kinetics yielded the activation energy of volume diffusion for carbon, $E_D = 2.56 \pm 0.35$ eV [9]. Equating $E_D = E_2$ results in $E_1 = 4.99$ eV; this figure exceeds the value found in our study for the dissolution of a carbon monolayer in pure tungsten by ~0.5 eV. The figure $E_D = 2.56$ eV obtained in [9] is, however, substantially larger than the carbon diffusion energy in tungsten known from the literature, $E_D \simeq 1.75$ eV [7]. Our experiments on the onset of carbon dissolution into the bulk of tungsten through a carbide surface layer at $T \sim 750$–800 K yield convincingly for E_D a value close to or less than 2 eV.

In [9], dissolution of a carbon layer with $\theta_0 \leq 1$ was studied in a carbon-free W single crystal; these are conditions under which the equality of C fluxes at the boundary roughly describes the temperature dependence of coverage. This is possibly the reason why the authors of [9] did not come up against the impossibility of describing the dissolution of a monolayer in a carbon-loaded tungsten in the same manner.

To sum up, we have carried out an analysis of equilibrium annealing curves $\theta(T)$ obtained experimentally for tungsten ribbons with different degrees of carbon loading. A simple model describing equilibrium between the adsorbed and dissolved carbon was used to estimate the difference $\Delta E = E_1 - E_2$ between the activation energies E_1 for transfer from the monolayer into the bulk and E_2 for escape onto the surface. This difference is usually referred to as the segregation energy [9].

It has been shown that carbon segregation and monolayer recovery under sample cooling occur at carbon concentrations that are greatly lower than the carbon solubility limit. This implies that the segregation is driven not by the carbon concentration reaching the solubility limit but rather by the ratio of the transfer rates from the surface into the bulk and back onto the surface. Based on this model, we came to the conclusion that both the energies E_1 and E_2 and their difference ΔE depend on the degree of tungsten loading by carbon. Note that the higher the carbon loading, the higher the dissolution activation energy E_1, which varies from 4.6 eV for dissolution of a carbon monolayer on pure tungsten ($\Psi_0 = 1$) to 6.8 eV for carbon-loaded samples ($\Psi_0 = 10$). These changes may be interpreted as the bonding in carbon-loaded tungsten becoming stronger with increasing amount of incorporated carbon. This entails an increase in both activation energies, E_1 (4.6 $\longrightarrow$ 6.8 eV) and E_2 (2.6 $\longrightarrow$ 4.5 eV), such that the quantity ΔE is not a constant and varies within an interval 1.6–2.3 eV. In this case, the equilibrium concentrations of an impurity on the surface and in the bulk are determined by the ratio of the impurity transport rates into the bulk and in the opposite direction.

ACKNOWLEDGMENTS

This study was supported by the Ministry of Science and Technologies of the Russian Federation, program "Surface Atomic Structures" (project no. 4.6.99).

REFERENCES

1. N. R. Gall', E. V. Rut'kov, and A. Ya. Tontegode, Izv. Akad. Nauk SSSR, Ser. Fiz. **63**, 1980 (1988).
2. V. N. Ageev, E. Yu. Afanas'eva, N. R. Gall', *et al.*, Pis'ma Zh. Tekh. Fiz. **12**, 565 (1986) [Sov. Tech. Phys. Lett. **12**, 231 (1986)].
3. N. R. Gall, E. V. Rut'kov, A. Ya. Tontegode, and M. M. Usufov, Appl. Surf. Sci. **191**, 185 (1985).
4. N. R. Gall, E. V. Rut'kov, A. Ya. Tontegode, *et al.*, J. Chem. Vap. Deposition **6**, 72 (1997).
5. N. D. Potekhina, Fiz. Tverd. Tela (St. Petersburg) **41**, 1772 (1999) [Phys. Solid State **41**, 1569 (1999)].
6. G. V. Samsonov and I. M. Vinitskiĭ, *Handbook of Refractory Compounds* (Metallurgiya, Moscow, 1976; Plenum, New York, 1980).
7. E. Fromm and E. Gebhardt, *Gase und Kohlenstoffin Metallen* (Springer, Berlin, 1976; Metallurgiya, Moscow, 1980).
8. J. Jäger, Surf. Sci. **310**, 292 (1994); Surf. Sci. **315**, 143 (1994).
9. K. J. Rowlings, S. D. Foulias, and B. J. Hopkins, Surf. Sci. **109**, 513 (1987).

Translated by G. Skrebtsov

Physics of the Solid State, Vol. 45, No. 4, 2003, pp. 788–792. Translated from Fizika Tverdogo Tela, Vol. 45, No. 4, 2003, pp. 748–752.

POLYMERS AND LIQUID CRYSTALS

Size Effect of Nanostructured Formations on Scattering of Optical Phonons in Poly(ethylene terephthalate)

V. I. Vettegren*, V. A. Marikhin*, V. B. Kulik*, and L. S. Titenkov**

** Ioffe Physicotechnical Institute, Russian Academy of Sciences, Politekhnicheskaya ul. 26, St. Petersburg, 194021 Russia*

*** Moscow State Textile University, Malaya Kaluzhskaya ul. 1, Moscow, 119991 Russia*

e-mail: Victor.Vettegren@pop.ioffe.rssi.ru

Received July 9, 2002

Abstract—The temperature dependence of the half-width of the infrared (IR) absorption band at a frequency of 971.5 cm^{-1} in the spectra of poly(ethylene terephthalate) (PET) is investigated for crystallized and amorphous PET samples in which the lengths of *trans* sequences are approximately equal to 4–7 and 2–3 nm, respectively. The observed increase in the half-width with increasing temperature is explained by inelastic scattering of phonons of stretching vibrations of the macromolecular skeleton by other phonons. The half-width of the band at 971.5 cm^{-1} in the IR spectra of the amorphous polymer is approximately 1.5 times larger than that in the spectra of the crystallized polymer. This is associated with the violation of the wave-vector selection rules due to a small length of the *trans* sequences in the amorphous sample. © *2003 MAIK "Nauka/Interperiodica".*

1. INTRODUCTION

The first investigations into the nature of the broadening of the regularity bands in the infrared (IR) and Raman spectra of polymers were carried out in [1–5]. These bands correspond to vibrations of macromolecular segments with a regular structure (an analog of quasi-one-dimensional crystals) [6, 7]. The broadening of the regularity bands in the spectra of polymers, as in the spectra of crystals, is interpreted in terms of finite lifetimes of optical phonons due to inelastic collisions with other phonons [8, 9]. Consequently, the regularity bands should have a symmetric dispersion shape and the half-width of these bands should be inversely proportional to the lifetime of optical phonons. However, the regularity bands, in some cases, have an asymmetric shape. According to Zbinden [10], this phenomenon can be associated with the fact that the wave-vector selection rules are violated, and, hence, phonons with a nonzero wave vector contribute to the spectrum.

The aim of this work was to separate the contribution of the finite lifetime of optical phonons from the contribution of the violation of the wave-vector selection rules to the broadening of the IR absorption band at a frequency of 971.5 cm^{-1} in the spectra of poly(ethylene terephthalate) (PET). For this purpose, we analyzed the spectra of crystallized and amorphous PET samples in which the lengths of regular sequences were equal to 4–7 and 2–3 nm, respectively.

2. SAMPLE PREPARATION AND EXPERIMENTAL TECHNIQUE

Amorphous PET films 20–200 μm thick with the molecular mass $M = 2 \times 10^4$ were prepared through pressing from a melt followed by rapid cooling in water at room temperature. Crystallization was accomplished by annealing the amorphous films at a temperature of 430 K for 6 h. The IR spectra were measured on DS-403G and Specord-75IR spectrophotometers at different temperatures with the use of cells similar to those described in [11] but without optical windows. Correction for distortions caused by radiation of the heated sample and cell walls was made using a procedure developed earlier in [11]. The bandwidth of the spectral slit in the range 900–1000 cm^{-1} was equal to 2 cm^{-1} and did not exceed 0.15 of the half-width (~13 cm^{-1}) of the band at a frequency of 971.5 cm^{-1} for the crystallized sample at 90 K. With the aim of minimizing dynamic distortions, the scanning velocity was no higher than 1 cm^{-1}/min.

3. CHANGES IN THE HALF-WIDTH OF THE BAND ASSOCIATED WITH STRETCHING VIBRATIONS OF THE SKELETON OF PET MOLECULES UPON HEATING

The absorption band at a frequency of 971.5 cm^{-1} in the IR spectra of the crystallized and amorphous PET samples (Fig. 1) is assigned to the stretching vibrations of interatomic bonds in the skeleton of the *trans* sequences of PET macromolecules [6, 7]. At a temperature of 20°C, the frequency at the maximum of the band in the IR absorption spectrum of the amorphous polymer is equal to 974.6 cm^{-1} and the half-width of this band is 21 cm^{-1}. In the spectrum of the crystallized sample, the maximum of the band under investigation is located at a frequency 3.5 cm^{-1} lower, i.e., at 971.5 cm^{-1}, and the half-width is 15 cm^{-1}.

1063-7834/03/4504-0788$24.00 © 2003 MAIK "Nauka/Interperiodica"

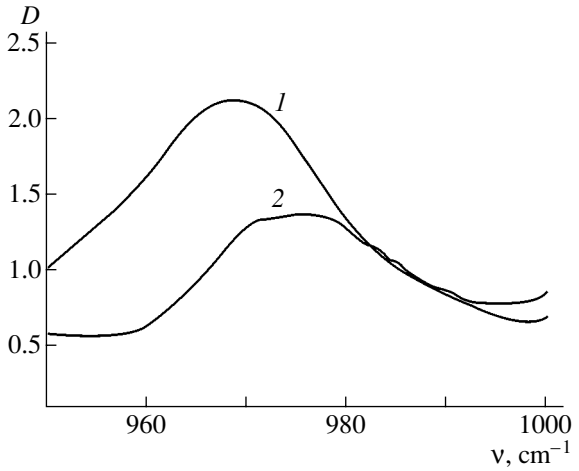

Fig. 1. IR absorption bands at 971.5 cm^{-1} in the spectra of (*1*) crystallized and (*2*) amorphous PET samples at a temperature of 300 K.

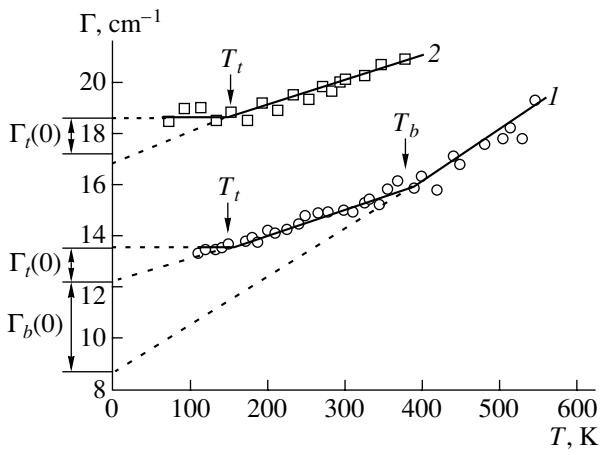

Fig. 2. Temperature dependences of the half-width of the band at 971.5 cm^{-1} in the IR spectra of (*1*) crystallized and (*2*) amorphous PET samples.

The temperature dependence of the half-width of the band in the IR spectra was analyzed in the temperature range from 90 to 540 K for the crystallized sample and from 90 to 380 K for the amorphous sample. (At higher temperatures, the amorphous sample underwent crystallization, which led to an additional shift in the frequency at the maximum of the band and a decrease in the half-width.) It can be seen from Fig. 2 that an increase in the temperature is accompanied by an increase in the half-width of the band. This effect is reversible in the above temperature ranges: the half-width of the band upon cooling decreases and follows a dependence similar to that observed upon heating. The shape of the bands for the amorphous and crystallized samples remains unchanged at all temperatures.

Three portions can be distinguished in the temperature dependence of the half-width of the band in the IR spectra of the crystallized sample (Fig. 2, curve *1*). In the first portion (90–180 K), the slope of the dependence $\Gamma(T)$ tends to zero with a decrease in the temperature. This made it possible to estimate the half-width $\Gamma(0)$ at $T \longrightarrow 0$ as follows: $\Gamma(0) \sim 13$ cm^{-1}. In the second portion (180–380 K), the half-width of the band increases almost proportionally to the temperature. The proportionality coefficient is determined to be $(\partial\Gamma/\partial T) = 0.011$ cm^{-1}/K. In the third portion (390–500 K), the proportionality coefficient $\partial\Gamma/\partial T$ increases to 0.019 cm^{-1}/K.

As was shown earlier by Schmidt [12], the integral absorption coefficient of the band at 971.5 cm^{-1} for unoriented PET samples increases proportionally to the crystallinity. In the spectra of our samples, the integral absorption coefficient of this band for the crystallized sample is approximately 15 times larger than that for the amorphous sample. Consequently, in the crystallized PET sample, the *trans* sequences are predominantly located in crystallites.

The crystallinity of unoriented PET samples crystallized at temperatures no higher than 470 K is usually equal to 40–50% [13–15]. According to electron microscopy, crystallization of PET at a constant pressure from solutions [16], melts [17, 18], and vitreous phases [19] brings about the formation of lamellas composed of folded macromolecules. The lamella thickness depends on the crystallization temperature but does not exceed 10–20 nm. Upon crystallization from the vitreous state under conditions similar to those used in the present work (crystallization temperature, 430 K; time, 6 h), the typical large spacings (lamella thicknesses), according to small-angle x-ray diffraction, were determined to be ≈11 nm [13]. Taking into account the crystallinity, we can draw the inference that the sizes of crystallites along the molecular chain are equal to 4–5 nm.

At temperatures above 430 K, the lamella sizes in PET increase [20]. For example, upon heating to 500 K, the lamella thickness reaches 15 nm and the crystallite size increases to 7 nm [14]. At the maximum temperature of heating of the crystallized sample in our work (540 K), the crystallite size along the chain (the length of the *trans* sequence) does not exceed 6–7 nm.

The maximum wavelength of vibrations of the *trans* sequence is twice as large as its length; i.e., it is approximately equal to 12–14 nm. This is one order of magnitude larger than the monomer unit length (1.075 nm [21]). Therefore, the mechanism of broadening of the absorption bands in the IR spectra can be analyzed in terms of the vibration theory developed for infinitely long molecules with a regular structure in the anharmonic approximation [1, 2]. According to this theory, the broadening of the bands in the IR and Raman spectra is caused by the anharmonicity of vibrations [6, 7]. In turn, the anharmonicity leads to breaking of the dynamic independence of the vibrations and their relaxation with the characteristic time τ_r. The character-

istic time corresponds to an uncertainty in the vibrational frequency (energy), for which the measure is the natural half-width of bands $\Gamma = 1/2\pi c\tau_r$, where c is the velocity of light.

Kosobukin [1, 2] theoretically investigated the natural broadening of the regularity bands in the spectra of polymers within the third-order anharmonic approximation. It was demonstrated that relaxation of optical phonons is governed by two processes in which the phonon energy is expended in forming four new phonons. The temperature dependence of the half-width $\Gamma(T)$ has the form

$$\Gamma(t) \approx \Gamma_t(0)(n_{t1} + n_{t2} + 1) + \Gamma_b(0)(n_{b1} + n_{b2} + 1), \quad (1)$$

where the subscripts t and b refer to the first and second processes, respectively; $\Gamma_t(0)$ and $\Gamma_b(0)$ are the contributions of the first and second processes to the half-width at $T = 0$ K, respectively; and $n_{t1,2}$ and $n_{b1,2}$ are the mean phonon occupation numbers. The occupation numbers are related to the temperature T and the frequency ν through the Bose expression [7]

$$n = \left(\exp\frac{h\nu}{k_B T} - 1\right)^{-1}, \quad (2)$$

where h and k_B are the Planck and Boltzmann constants, respectively.

As a rule, the frequencies of phonons with subscripts $t2$ and $b2$ are higher than those with subscripts $t1$ and $b1$ [3]. Therefore, it can be assumed that the relationship $n_{t2} \approx n_{b2} \approx 0$ holds over the entire temperature range covered. Hence, relationship (1) can be rewritten in the following form:

$$\Gamma(T) \approx \Gamma_t(0)(n_{t1} + 1) + \Gamma_b(0)(n_{b1} + 1). \quad (3)$$

The characteristic temperature can be defined as

$$T_C \equiv \frac{h\nu_{max}}{3k}, \quad (4)$$

where ν_{max} is the maximum vibrational frequency. Above the temperature T_C, the mean phonon occupation numbers vary in proportion to the temperature ($n \sim k_B T/h\nu = T/3T_C$). Below the temperature T_C, we have $n \approx 0$. Consequently, at low temperatures ($T < T_{t1}$), the occupation numbers are small in magnitude ($n_{t1} = n_{b1} \approx 0$) and the half-width can be determined as $\Gamma(T) \sim \Gamma(T) \approx \Gamma_t(0) + \Gamma_b(0) = \Gamma(0)$.

At $T \geq T_t$, the occupation numbers n_t increase approximately in proportion to the temperature, whereas the occupation numbers n_b are close to zero. As a result, the slope of the temperature dependence of the half-width [see expression (3)] can be represented by the relationship

$$\frac{d\Gamma}{dT} \approx \frac{3\Gamma_t(0)k_B}{h\nu_t} = \frac{\Gamma_t(0)}{T_t}. \quad (5)$$

At $T \geq h\nu_b/k_B = T_b$, the occupation numbers n_b also increase almost proportionally to the temperature and the slope of the dependence $\Gamma(T)$ should increase as follows:

$$\frac{d\Gamma}{dT} = \frac{\Gamma_t(0)}{T_t} + \frac{\Gamma_b(0)}{T_b}. \quad (6)$$

The experimental temperature dependence of the half-width of the absorption band under investigation (Fig. 2) is in good qualitative agreement with the aforementioned theoretical predictions. In actual fact, the half-width is temperature independent at low temperatures ($T < T_t = 170$ K) and increases almost proportionally to the temperature at $T > 180$ K and the slope of the quasi-linear dependence $\Gamma(T)$ increases at $T \geq T_b = 380$ K. By extrapolating the quasi-linear portions of the temperature dependence of the half-width in the temperature ranges $T < 170$ K and $180 < T < 380$ K to zero temperature ($T = 0$ K), we obtain the contribution $\Gamma_t(0)$ to the half-width at $T = 0$ K: $\Gamma_t(0) \approx 1.4$ cm^{-1}. Then, we extrapolate the quasi-linear portion of the dependence $\Gamma(T)$ at temperatures above 390 K to $T = 0$ K and find the contribution $\Gamma_b(0) \approx 3.5$ cm^{-1}. The sum of these contributions is the half-width of the band at $T = 0$ K: $\Gamma(0) = \Gamma_t(0) + \Gamma_b(0) \approx 4.9$ cm^{-1}.

Let us now compare the experimental and theoretical [calculated from relationships (5) and (6)] slopes of the dependence $\Gamma(T)$. The calculated and experimental values of $d\Gamma/dT$ are equal to 0.008 [relationship (5)] and 0.011 cm^{-1}/K in the temperature range $180 < T < 380$ K and 0.016 [relationship (6)] and 0.019 cm^{-1}/K at $T > 380$ K, respectively. It can be seen that the experimental slopes of the temperature dependence of the half-width of the band at 971.5 cm^{-1} are close to the calculated values. With the use of the characteristic temperatures, the frequencies of the phonons involved in inelastic collisions [see expression (3)] were estimated as $\nu_t \approx 380$ cm^{-1} and $\nu_b \approx 780$ cm^{-1}.

The temperature dependence of the half-width of the absorption band in the spectra of the amorphous PET sample (Fig. 2, curve *2*) is approximately parallel to that of the crystallized sample. Therefore, the increase in the half-width of the band in the spectra of the amorphous PET sample can also be explained in terms of inelastic scattering of optical phonons. However, the half-width of the band in the spectra of the amorphous sample is larger in magnitude than that in the spectra of the crystallized sample over the entire range of temperatures.

4. BROADENING OF THE REGULARITY BANDS DUE TO VIOLATION OF THE SELECTION RULE

As is known [20, 22], macromolecules of polymers in the amorphous state adopt a statistical ball conformation. According to the large-angle x-ray diffraction data [23], this ball is characterized by a short-range order extending over regions ~ 2–3 nm in size. Actually, polymer molecules in the studied samples involve *trans* sequences whose lengths fall in the ranges 4–7 nm

(crystallized samples) and 2–3 nm (amorphous samples). The sequence length is comparable to the mean free path of optical phonons (as a rule, it is approximately equal to ten monomer units, i.e., ~ 10 nm) in the former case and is considerably less than this path in the latter case. For short sequences, the selection rules ($\mathbf{q} = 0$, where $\mathbf{q}$ is the phonon wave vector) are violated and phonons with a nonzero wave vector contribute to the IR spectrum. This leads to asymmetric broadening of the band. Now, we consider this situation in greater detail.

The wave function of a phonon with a wave vector $\mathbf{q}_0$ in a crystal whose linear size L is comparable to the mean free path of phonons can be written in the form [24, 25]

$$\Psi(\mathbf{q}_0, \mathbf{r}) = \Phi(\mathbf{q}_0, \mathbf{r})\exp(-2r^2/L^2) = \Psi'(\mathbf{q}_0, \mathbf{r})u(\mathbf{q}_0, \mathbf{r}),$$

where $\exp(-2r^2/L^2)$ is the weighting function, which accounts for the decrease in the vibration amplitude $u(\mathbf{q}_0, \mathbf{r})$ at the end of the sequence.

The shape of the spectral band can be described by the expression [25]

$$D(\omega) \cong \int \frac{|C(0, q)|^2 d^3q}{(\omega - \omega(q))^2 + (\Gamma_0/2)^2},$$

where Γ_0 is the natural broadening of the band, $\omega(q)$ is the dispersion, and $C(q_0, q)$ is the Fourier coefficient of the wave function $\Psi'(\mathbf{q}_0, \mathbf{r})$. The Fourier coefficient is defined by the equation

$$C(q_0, q) = 1/(2\pi)^3 \int \Psi'(\mathbf{q}_0, \mathbf{r})\exp(-i\mathbf{q}_0\mathbf{r})d^3r.$$

The *trans* sequence can be represented as a thin rod whose diameter is substantially less than the length. In this case, the Fourier coefficient can be given by the formula [25]

$$|C(0, q)|^2 \cong \exp\left(-\frac{q^2L^2}{16\pi^2}\right)\left|1 - \mathrm{erf}\left(\frac{eqL}{\sqrt{32}\pi}\right)\right|^2$$

and the expression for the shape of the spectral band takes the form

$$D(\omega) = \int_0^{2\pi/a} \frac{\exp\left(-\frac{q^2L^2}{16\pi^2}\right)\left|1 - \mathrm{erf}\left(\frac{iqL}{\sqrt{32}\pi}\right)\right|^2}{(\omega - \omega(q))^2 + (\Gamma_0/2)^2} dq, \quad (7)$$

where $a = 1.075$ nm is the length of the monomer unit of the PET molecule.

By substituting $\Gamma_0 = 10$ cm^{-1} into expression (7) and choosing the dispersion relation in the form $\omega(q) = \omega_0 - (0.6q)^2$ (where ω_0 is the frequency of the band at the maximum at a specified temperature), we calculate the dependences of the frequency at the maximum and the half-width of the band on the length of the *trans* sequence. It can be seen from Fig. 3 that the frequency at the maximum and the broadening of the band are virtually independent of the size of the *trans* sequence at $L \geq 7$ nm and increase drastically with a decrease in the length of the *trans* sequence at $L < 5$ nm. For example, at $L = 2$ nm, the frequency at the maximum is shifted toward the high-frequency range by 2.5 cm^{-1} and the half-width increases from 10 to 15 cm^{-1}.

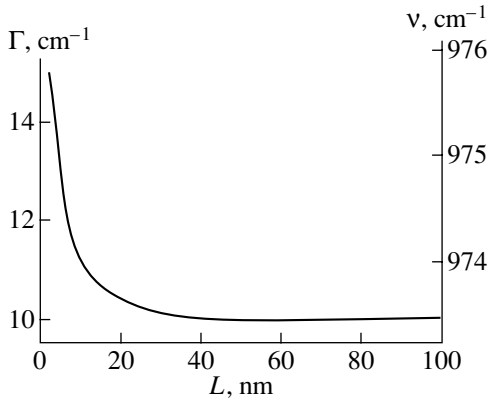

Fig. 3. Calculated dependences of the frequency at the maximum and the half-width of the band at 971.5 cm^{-1} on the length of the *trans* sequence in the PET molecule.

5. DISCUSSION

The length of the *trans* sequences in the crystal regions of PET is approximately equal to 4–5 nm at temperatures up to 450 K. It is seen from Fig. 3 that the broadening of the band due to the violation of the selection rule can be estimated at ≈3.5 cm^{-1}. As the temperature increases from 450 to 540 K, the length of the *trans* sequence increases to ≈7 nm, whereas the broadening decreases to 2 cm^{-1}. Taking into account these changes and the dependence depicted in Fig. 3, we calculated the temperature dependence of the half-width of the band at 971.5 cm^{-1} for the crystallized sample. The results of our calculations are presented in Fig. 4 (curve *1*). The extensions of the calculated dependence in the temperature ranges 90–180, 180–380, and 390–540 K, as well as its extrapolation to $T = 0$ K, are also shown in Fig. 4 (indicated by dashed lines). The first and second extrapolated curves intersect the ordinate axis at the points corresponding to 10 and 8.5 cm^{-1}, respectively. The third extrapolated curve passes through the origin of the coordinates. As a result, the contribution $\Gamma_t(0)$ is approximately equal to 1.5 cm^{-1}; i.e., it coincides with the value calculated without considering the violation of the selection rules. At the same time, the contribution $\Gamma_b(0)$ turns out to be approximately equal to 8.5 cm^{-1}, which is 2.4 times larger than that obtained without regard for the violation of the selection rule $\mathbf{q} = 0$. The difference between the values of $\Gamma_b(0)$ stems from the fact that an increase in the temperature above 450 K leads to an increase in the size of

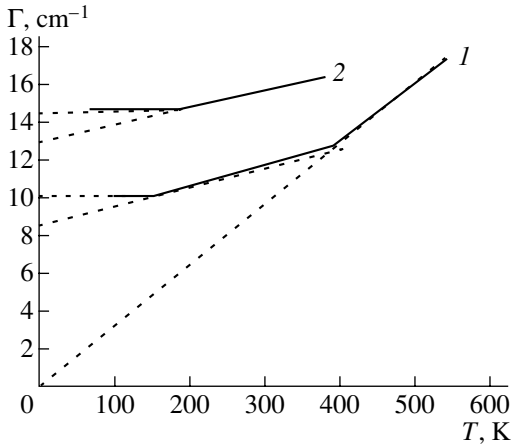

Fig. 4. Calculated temperature dependences of the half-width of the band at 971.5 cm^{-1} in the IR spectra of (*1*) crystallized and (*2*) amorphous PET samples. Calculations are performed with due regard for the violation of the selection rules.

the *trans* sequences and, hence, in the slope of the dependence $\Gamma(T)$ at $T > 390$ K.

In the amorphous polymer sample, the length of the *trans* sequences falls in the range 2–3 nm. As is seen from Fig. 3, the additional broadening due to the violation of the wave-vector selection rule can be estimated at ≈ 5 cm^{-1}. After subtraction of this value from the experimental half-width at 100 K (19.5 cm^{-1}), the half-width thus obtained is approximately 4.5 cm^{-1} larger than the value calculated for the crystallized polymer sample with allowance made for the violation of the selection rule. The difference between the half-widths is associated with the fact that the amorphous polymer contains *trans* sequences of different lengths. Consequently, the band observed in the IR spectrum can be considered a superposition of bands attributed to *trans* sequences of different lengths.

The temperature dependence of the half-width calculated with due regard to the violation of the selection rules for the amorphous polymer (Fig. 4, curve *2*) is aligned parallel to that for the crystallized sample. This implies that the inclusion of the violation of the selection rules does not affect the value of $\Gamma_t(0)$. Unfortunately, the crystallization of the sample at temperatures above 390 K makes it impossible to determine the value of $\Gamma_b(0)$.

6. CONCLUSION

Thus, the broadening of the regularity band at 971.5 cm^{-1} in the IR spectra of the PET samples is due to both inelastic scattering of phonons of stretching vibrations of the macromolecular skeleton by other phonons and the violation of the selection rules owing to the small length of the *trans* sequences in PET molecules.

ACKNOWLEDGMENTS

This work was supported by the Russian Foundation for Basic Research, project no. 01-03-32773.

REFERENCES

1. V. A. Kosobukin, Mekh. Polim., No. 4, 579 (1971).
2. V. A. Kosobukin, Mekh. Polim., No. 1, 3 (1971).
3. V. I. Vettegren and V. A. Kosobukin, Opt. Spektrosk. **35**, 589 (1971).
4. A. I. Gubanov and V. A. Kosobukin, Mekh. Polim., No. 1, 33 (1975).
5. V. I. Vettegren, L. S. Titenkov, and S. V. Bronnikov, J. Therm. Anal. **38** (5), 1031 (1992).
6. P. C. Painter, M. Coleman, and J. L. Koenig, *The Theory of Vibrational Spectroscopy and Its Application to the Polymeric Materials* (Wiley, New York, 1986).
7. J. Dechant, R. Danz, W. Kimmer, and R. Schmolke, *Ultrarotspectroscopische Untersuchungen an Polymeren* (Akademie-Verlag, Berlin, 1972).
8. A. A. Maradudin, *Theoretical and Experimental Aspects of the Effects of Point Defects and Disorder on the Vibration of Crystals* (North-Holland, Amsterdam, 1965).
9. O. Madelung, *Festköpertheorie* (Springer-Verlag, Berlin, 1972), Vols. 1, 2.
10. R. Zbinden, *Infrared Spectroscopy of Polymers* (Academic, New York, 1964).
11. V. I. Vettegren, L. S. Titenkov, and R. R. Abdul'manov, Zh. Prikl. Spektrosk. **16** (2), 251 (1984).
12. P. J. Schmidt, J. Polymer Sci. A **1** (8), 1271 (1963).
13. G. Groeninckx, H. Reynaers, H. Berghmans, and G. Smets, J. Polym. Sci., Polym. Phys. Ed. **18** (4), 1311 (1980).
14. H. G. Zachmann and H. A. Stuart, Macromol. Chem. **41** (1), 131 (1960).
15. E. H. Muller, Colloid Polym. Sci. **252** (3), 696 (1974).
16. Y. Yamashita, J. Polym. Sci., Part A: Gen. Pap. **3** (1), 81 (1965).
17. N. C. Watkius and D. Hansen, Text. Res. J. **38** (2), 338 (1968).
18. A. Miyagy and B. Wunderlich, J. Polym. Sci., Part A: Gen. Pap. **10** (10), 2073 (1972).
19. G. S. Y. Yeh and P. H. Geil, J. Macromol. Sci., Phys. B **1** (2), 235 (1967).
20. V. A. Marikhin and L. P. Myasnikova, *Supramolecular Structure of Polymers* (Khimiya, Leningrad, 1977).
21. Ph. Geil, *Polymer Single Crystals* (Wiley, New York, 1963).
22. P. J. Flory, Faraday Discuss. Chem. Soc. **68** (1), 14 (1979).
23. B. K. Vainshtein, *Diffraction of X-ray by Chain Molecules* (Akad. Nauk SSSR, Moscow, 1963; Elsevier, Amsterdam, 1966).
24. H. Richter, Z. P. Wang, and L. Ley, Solid State Commun. **39**, 625 (1981).
25. I. H. Campbell and P. M. Fauchet, Solid State Commun. **58**, 739 (1986).

Translated by O. Borovik-Romanova

Physics of the Solid State, Vol. 45, No. 4, 2003, pp. 793–796. Translated from Fizika Tverdogo Tela, Vol. 45, No. 4, 2003, pp. 753–755.

POLYMERS AND LIQUID CRYSTALS

Anomalies in the Magnetic Behavior of a Rapidly Cooled Chromium Mesogen

N. E. Domracheva*, I. V. Ovchinnikov*, A. Turanov*, and G. Lattermann**

** Zavoiskiĭ Physicotechnical Institute, Kazan Scientific Center, Russian Academy of Sciences, Sibirskiĭ trakt 10/7, Kazan 29, 420029 Tatarstan, Russia*

*** Universität Bayreuth, Bayreuth, D-95440 Germany*

e-mail: domracheva@mail.knc.ru

Received July 1, 2002

Abstract—This paper reports on the results of investigations into the magnetic behavior of a chromium mesogen containing the liquid-crystal columnar phase $L\mathrm{CrCl_3}$, where L is an azacyclononane ligand. It is found that the magnetic susceptibility of $L\mathrm{CrCl_3}$ remains constant in the temperature range from 4.2 to 10 K. This effect manifests itself upon rapid cooling of an $L\mathrm{CrCl_3}$ sample in the mesophase and exhibits relaxation behavior. The relaxation magnetoelectric effect is explained in terms of the multiwell potential of the system and a thermally nonequilibrium orientational distribution of electric dipole moments of the Cr–Cl bonds involved. © *2003 MAIK "Nauka/Interperiodica".*

1. INTRODUCTION

Recent syntheses and studies of metallomesogens, i.e., compounds that contain transition metals and are capable of forming a liquid-crystal phase, have given a better insight into the physics of liquid crystals and their optical, electrical, and magnetic properties [1, 2]. It is known that, upon cooling, the liquid-crystal phase of many metallomesogens undergoes a glass transition. In this case, the supramolecular structure formed in the mesophase is retained, which makes it possible to create ordered low-dimensional molecular structures and to investigate their properties at low temperatures. In our earlier work [3], the specific features observed in magnetic and electrical properties of columnar phases of the chromium mesogen $L\mathrm{CrCl_3}$ (Fig. 1) were analyzed using electron paramagnetic resonance and dielectric spectroscopy. These features manifest themselves at $T = 328$ K in a columnar (Col_{xd}) phase and, as a rule, are associated with the condensation of the soft mode. It is assumed that the specific features revealed in the properties of the chromium mesogen can indicate a possible transition from the paraelectric state to the dipole-ordered state. Local dipole ordering in a column composed of $L\mathrm{CrCl_3}$ molecules can be due to correlated distortions of the Cr–Cl bonds along the molecular column and displacements of Cr^{3+} ions from the centrosymmetric sites. As a consequence, the electric dipole moment of a Cr–Cl bond exhibits several discrete orientations and for each orientation there is a potential well.

Since the chromium mesogen characterized by a multiwell potential exhibits both magnetic (paramagnetic) and electric dipolar properties simultaneously, this compound can be treated as a material possessing magnetoelectric properties similar to those examined in [4–9]. In these works, an external action on the samples under investigation was produced by a nonstationary electric field. Another way to create an unsteady (thermally nonequilibrium) state in the dipole system is to cool the studied compound rapidly. In the present work, we investigated the magnetic properties of the chromium mesogen under these conditions.

2. EXPERIMENTAL TECHNIQUE AND RESULTS

The magnetic resonance investigations were performed on a Thomson EPR spectrometer operating at a frequency of 9 GHz. The magnetic measurements were carried out on an SQUID magnetometer. The temperature was stabilized with an accuracy of better than 0.1 K. In both cases, the magnetic experiments were performed with an $L\mathrm{CrCl_3}$ chromium mesogen prepared from the same batch as was used earlier in [3]. However, the chromium mesogen sample studied in the present work was obtained in a vitrified liquid-crystal state through rapid (for ~1 min) cooling of the $L\mathrm{CrCl_3}$ compound in a Col_{xd} dipole-ordered mesophase. It was revealed that the observed magnetic behavior of the chromium mesogen substantially depends on the pre-

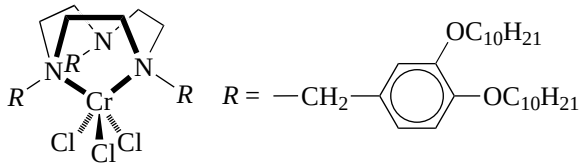

Fig. 1. Structural formula of an $L\mathrm{CrCl_3}$ metallomesogen.

1063-7834/03/4504-0793$24.00 © 2003 MAIK "Nauka/Interperiodica"

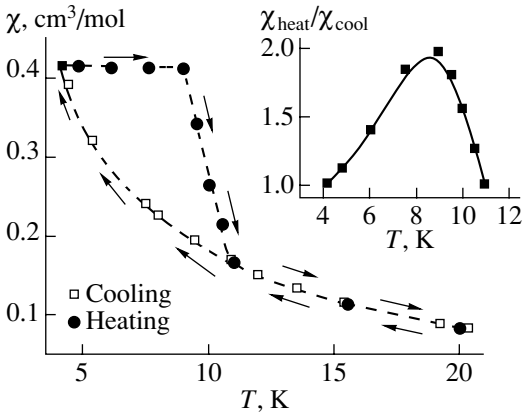

Fig. 2. Temperature dependences of the magnetic susceptibility in the course of heating and cooling of the LCrCl$_3$ complex.

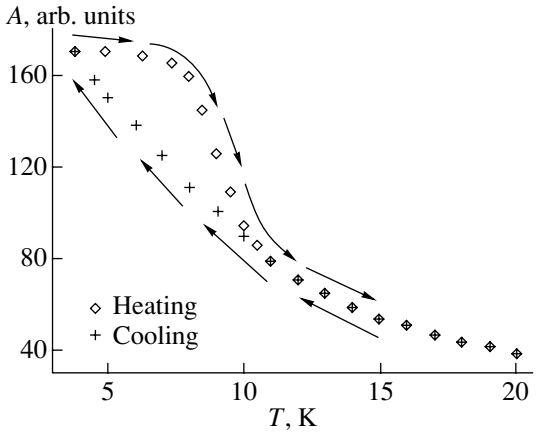

Fig. 3. Temperature dependences of the integrated intensity A of the Cr^{3+} EPR line in the course of heating and cooling of the LCrCl$_3$ sample.

history of the sample, i.e., on the conditions used for preparing the low-temperature phase. During heating of the sample under investigation, all the measurements were conducted in the temperature range from 4.2 to 300 K. Then, similar measurements were carried out in the course of cooling. Figure 2 shows the temperature dependences of the magnetic susceptibility in the course of heating and cooling of an LCrCl$_3$ liquid-crystal sample vitrified from the dipole-ordered phase. It can be seen from Fig. 2 that, during heating of the sample preliminarily subjected to rapid cooling in the mesophase, the magnetic susceptibility remains unchanged in the temperature range 4.2–10 K and then decreases drastically. In the course of subsequent cooling, the magnetic susceptibility of the sample increases monotonically with decreasing temperature in accordance with the Curie–Weiss law $\chi_{CW} = C/(T - \Theta) + \chi_{dia}$, where C is a constant corresponding to the spin $S = 3/2$ and $\Theta = 0.65$ K is the Curie–Weiss temperature [3]. It should be noted that the temperature dependences of the magnetic susceptibility measured during heating and cooling of the LCrCl$_3$ sample do not coincide at temperatures below $T = 11$ K. At these temperatures, the magnetic susceptibility of the chromium mesogen exhibits a hysteresis with a memory effect; i.e., during cooling, the temperature dependence of the magnetic susceptibility passes through the same point at which the magnetic susceptibility began to change in the course of heating.

After two heating–cooling cycles, the sample was transformed into the initial Col$_{xd}$ dipole-ordered mesophase and was then vitrified. Under these conditions, all the anomalies observed earlier in the behavior of the magnetic susceptibility again manifested themselves.

Moreover, we examined the relaxation behavior of the observed effect. For this purpose, the sample subjected to rapid cooling was heated and allowed to stand at $T = 7$ and 7.6 K. It was found that, in these cases, the equilibrium magnetic susceptibility χ_{CW} was attained for 7 and 3.5 min, respectively.

The EPR measurements revealed a similar behavior in the temperature dependence of the integrated intensity $A = I\Delta H^2$ (where I is the peak height of the first derivative and ΔH is the linewidth between the peaks) of the Cr^{3+} EPR line, which is proportional to the magnetic susceptibility. Figure 3 depicts the experimental temperature dependences of the integrated intensity of the Cr^{3+} EPR line in the course of heating and cooling of the LCrCl$_3$ sample. The EPR spectrum of the sample vitrified from the Col$_{xd}$ mesophase exhibits a single weakly asymmetric line, which is characterized by a linewidth $\Delta H \sim 500$ G and remains virtually unchanged in the temperature range covered. As can be seen from Figs. 2 and 3, the anomalies revealed in the magnetic behavior of the studied sample with the use of the EPR method are considerably less pronounced than those observed in the measurements with the SQUID magnetometer. This discrepancy can be explained by the fact that the recording of the observed effect calls for a fast-response instrument for measuring the intensities of the EPR lines, whereas, in our case, the EPR signals were measured using a conventional recorder.

3. DISCUSSION

As was noted above, the magnetic susceptibility χ of the sample remains nearly constant in the temperature range 4.2–10 K and decreases drastically (by a factor of approximately 2.7) in the vicinity of the Curie temperature $T_C \approx 9$ K (see the heating curve in Fig. 2). This behavior of the magnetic susceptibility formally corresponds to a phase transition from a ferromagnetic state to an ordered state with the ferromagnetic Curie temperature $T_C \approx 9$ K. A similar behavior of the magnetic susceptibility is observed in quasi-two-dimensional Heisenberg layered ferromagnets (see, for example, [10]). In this case, the exchange constant (J/k) can be

estimated by two methods, namely, in disordered ($T/T_C > 1$) [3] and magnetically ordered ($T/T_C < 1$) [10] states of the material. As follows from these estimates, the exchange constants $(J/k)_1 = 0.13$ K above T_C and $(J/k)_2 = 19$ K below T_C differ significantly. Such a disagreement and obvious relaxation behavior of the observed effect permit us to discard this variant. Below, we will discuss the possible manifestation of the relaxation magnetoelectric effect in the vitrified sample.

In paramagnetic materials, the relaxation magnetoelectric effect manifests itself in a noticeable increase in the magnetization of the paramagnetic sample (spin polarization) upon switching on (switching off) a dc or ac electric field. To the best of our knowledge, this effect was revealed in two single-crystal materials, namely, SrO doped with Co^{2+} ions [4, 5] and pleochroic quartz containing Al^{3+}–O^- centers formed upon the $Al^{3+} \longrightarrow Si^{4+}$ isomorphous substitution in SiO_4 tetrahedra [6–9]. The relaxation magnetoelectric effect was observed in dielectric materials involving paramagnetic centers associated not only with the magnetic moment but also with the electric dipole moments characterized by several discrete orientations. In the former case (Co^{2+} ions), a noncentrosymmetric impurity ion is capable of tunneling between single potential wells. In the latter case (Al^{3+}–O^- centers), an electron hole (at an O^- ion) can also tunnel between the two nearest neighbor oxygen ions. In both cases, the above tunneling corresponds to a reorientation of the electric dipole.

After switching on (switching off) the electric field, the system of reorienting electric dipoles occurs in a nonequilibrium state. In the system where there is a coupling between electric and magnetic dipoles, subsequent sufficiently slow switching off (switching on) the electric field E can bring about short-time deviations of the magnetization (spikes of the EPR signal) from its equilibrium values due to an increase in the spin polarization of the paramagnetic ions involved. The possible models allowing for the observed increase in the spin polarization were proposed in [4–9].

In the aforementioned works, the change in the external electric field led to variations in the Stark gaps (in other words, the spacings between minima of single potential wells), the rate of tunneling of particles between lattice sites, and the coupling between the systems of electric and magnetic dipoles.

The fundamental difference between our experiments and earlier investigations (see above) lies in the fact that, in our case, no external electric field was applied and a molecular sample vitrified from the liquid-crystal phase was used instead of a single-crystal sample.

In the case when one of the coupled subsystems (i.e., either the electric dipole subsystem or the spin subsystem) is disturbed from an equilibrium, the other subsystem should also come out of equilibrium owing to the interaction between them. In the $L\mathrm{CrCl}_3$ compound, the electric dipole subsystem can be disturbed from an equilibrium through a rapid cooling in the dipole-ordered phase. Relaxation of this subsystem toward an equilibrium state can be accompanied by both the redistribution of Zeeman sublevel populations [6–9] and displacements of the potential wells [4, 5] due to variations in the internal electric field (i.e., due to Stark splittings). In any case, the switching on or switching off the external electric field in [4–9] brought about an increase in the spin polarization.

The temperature behavior of the effect observed in our experiments is similar in appearance to the temperature dependence of the increase in the relative magnetization in an ac electric field [6, 11]. Compared to the equilibrium magnetic susceptibility, which is described by the Curie–Weiss law, the nonequilibrium magnetic susceptibility increases by a factor of approximately two (χ_{heat}/χ_{cool}) (see the inset in Fig. 2).

We also tested an alternative qualitative spin-glass interpretation of the observed effect.

It is known that spin-glass systems [12] undergo long-term relaxation due to nonergodicity of the vitreous phase. This manifests itself in the fact that the magnetic susceptibility χ_{FC} of a spin-glass system cooled in an external magnetic field remains unchanged in the range below the temperature T_g, which corresponds to freezing of orientational states of the magnetic moments. The results presented in Fig. 2 also suggest the presence of an external magnetic field. If the magnetic behavior of the studied mesogen were to be governed by the spin-glass mechanism, the magnetic susceptibility χ_{ZFC} of the sample cooled in a zero external magnetic field would decrease drastically below T_g. However, the results of our measurements demonstrated that, upon cooling of the chromium mesogen in a zero magnetic field, the magnetic susceptibility χ_{ZFC} remains constant in the temperature range 4.2–6.5 K and then sharply decreases to an equilibrium value χ_{CW}.

4. CONCLUSIONS

The relaxation magnetoelectric effect observed in the vitrified liquid-crystal phase is of considerable interest in respect to the search for new low-dimensional materials with magnetoelectric properties. We believe that the molecular system found makes it possible to observe the relaxation magnetoelectric effect in external electric fields. In particular, there is great interest in analyzing the quasi-stationary increase in the magnetization of a paramagnetic material in an ac electric field [6, 7, 9] and in inducing the maser effect [5].

ACKNOWLEDGMENTS

We would like to thank N.N. Garif'yanov for his assistance in measurements using the SQUID magnetometer.

This work was supported by the Russian Foundation for Basic Research, project no. 02-03-32179.

REFERENCES

1. *Metallomesogens: Synthesis, Properties, and Applications*, Ed. by J. L. Serrano (VCH, Weinheim, 1996).
2. I. V. Ovchinnikov and Yu. G. Galyametdinov, Ros. Khim. Zh. **45** (3), 74 (2001).
3. N. E. Domracheva, I. V. Ovchinnikov, A. Turanov, *et al.*, Fiz. Tverd. Tela (St. Petersburg) **43** (6), 1145 (2001) [Phys. Solid State **43**, 1188 (2001)].
4. V. S. Vikhnin, L. S. Sochava, V. A. Krylov, and Yu. N. Tolparov, Pis'ma Zh. Éksp. Teor. Fiz. **40** (10), 426 (1984) [JETP Lett. **40**, 1248 (1984)].
5. V. É. Bursian, V. S. Vikhnin, and L. S. Sochava, Izv. Akad. Nauk SSSR, Ser. Fiz. **52** (3), 477 (1988).
6. I. V. Matyash, A. B. Brik, A. P. Zayats, and V. V. Mazykin, *Radiospectroscopy of Quartz* (Naukova Dumka, Kiev, 1987).
7. A. B. Brik, in *Radiospectroscopy of Solids*, Ed. by A. B. Roĭtsin and V. M. Maevskiĭ (Naukova Dumka, Kiev, 1992).
8. A. B. Brik, I. V. Matyash, and S. S. Ishchenko, Zh. Éksp. Teor. Fiz. **79** (5), 1902 (1980) [Sov. Phys. JETP **52**, 960 (1980)].
9. A. B. Brik, Fiz. Tverd. Tela (Leningrad) **24** (2), 500 (1982) [Sov. Phys. Solid State **24**, 282 (1982)].
10. W. E. Estes, D. B. Losee, and W. E. Hatfield, J. Chem. Phys. **72** (1), 630 (1980).
11. A. B. Brik, Fiz. Tverd. Tela (Leningrad) **27** (12), 3687 (1985) [Sov. Phys. Solid State **27**, 2222 (1985)].
12. S. L. Ginzburg, *Irreversible Processes in Spin Glasses* (Nauka, Moscow, 1989).

Translated by O. Borovik-Romanova

Physics of the Solid State, Vol. 45, No. 4, 2003, pp. 797–801. Translated from Fizika Tverdogo Tela, Vol. 45, No. 4, 2003, pp. 756–760.

POLYMERS AND LIQUID CRYSTALS

Dielectric and Optical Properties of a 5-Propyl-2-(*p*-Cyanophenyl)-Pyridine Liquid Crystal

B. A. Belyaev, N. A Drokin, and V. F. Shabanov

Kirensky Institute of Physics, Siberian Division, Russian Academy of Sciences, Akademgorodok, Krasnoyarsk, 660036 Russia

e-mail: belyaev@iph.krasn.ru

Received July 17, 2002

Abstract—The temperature dependences of the dielectric and optical parameters for a 5-propyl-2-(*p*-cyanophenyl)-pyridine (3CP) liquid crystal are investigated in the vicinity of the nematic–isotropic phase transition. The dielectric spectra of the 3CP compound in the crystalline, nematic, and isotropic phases are measured in the frequency range 1–1000 MHz, and the Debye approximations of the measured spectra are obtained. Analysis of the dependence of the static permittivity on the director orientation with respect to the direction of the electric pump field demonstrates that the angle between the dipole moment and the long axis of the molecule is approximately equal to 15°. © *2003 MAIK "Nauka/Interperiodica".*

1. INTRODUCTION

As is known, the frequency dispersion of the permittivity is one of the basic properties of liquid crystals. Elucidation of the nature of the dispersion, and, especially, the influence of different factors on this property, is an important problem in both theoretical and applied physics. At present, the region of dispersion associated with the relaxation of liquid-crystal molecules, which, as a rule, corresponds to frequencies of the meter wavelength range, has been adequately studied for many liquid-crystal systems. However, there exist a number of liquid crystals whose high-frequency dielectric properties are as yet poorly understood. This can be explained by the fact that the relaxation frequencies for this group of liquid crystals fall in the decimeter wavelength range in which precision dielectric measurements involve considerable difficulties. Among these materials is a 5-propyl-2-(*p*-cyanophenyl)-pyridine (3CP) nematic liquid crystal. The structural formula of the 5-propyl-2-(*p*-cyanophenyl)-pyridine liquid-crystal compound is presented in Fig. 1. Investigation into the optical and dielectric properties of the 3CP nematic liquid crystal is of particular interest, because this compound is similar in molecular structure to the well-known and thoroughly studied liquid crystals of the alkylcyanobiphenyl group *n*CB (n = 5–9) [1–5]. The only difference between them lies in the fact that, in the rigid core of the 3CP molecule, one carbon atom in either of the two benzene rings is replaced by a nitrogen atom. Moreover, the number of methylene fragments (n = 3) in the alkyl tail of the 3CP molecule is rather small for liquid crystals. The 3CP compound undergoes a phase transition from the solid crystalline state to the nematic liquid-crystal state at T_0 = 43.5°C and a transition from the nematic state to the disordered isotropic liquid state at T_c = 47.4°C.

In this work, we experimentally investigated the temperature and frequency dependences of the permittivity, determined the refractive indices, and numerically approximated the dielectric spectra measured for the 5-propyl-2-(*p*-cyanophenyl)-pyridine compound in different phase states over a wide frequency range (f = 1–1000 MHz).

2. EXPERIMENTAL TECHNIQUE

The permittivities in the frequency range 1–30 MHz were measured on a Tesla BM560 standard *Q*-meter with the use of a measuring cell in the form of a parallel-plate capacitor. In the meter and decimeter wavelength ranges, the dielectric measurements were performed with specially devised high-sensitive sensors based on microstrip resonators of a ring type [6]. The small-step tuning of the sensors was carried out using calibrated inductors and electrically controlled capacitors (varactors), which were connected in series with the strip conductor in the antinodal region of a microwave magnetic field for the first oscillation mode of the microstrip resonator [7]. A capacitive measuring cell fabricated in the form of an interdigitation with a gap of 150 μm was placed at the antinode of a microwave electric field of the resonator. A liquid-crystal sample 200 μm thick was positioned on the interdigitation bounded by a glass border. The sample was shielded from contamination by a fluoroplastic film. The sensor

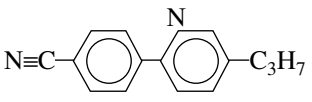

Fig. 1. Structural formula of the 5-propyl-2-(*p*-cyanophenyl)-pyridine liquid-crystal compound.

1063-7834/03/4504-0797$24.00 © 2003 MAIK "Nauka/Interperiodica"

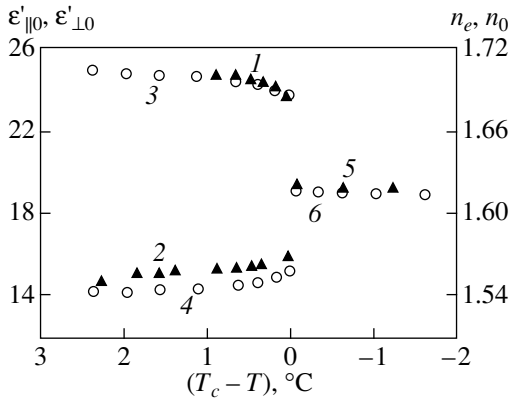

Fig. 2. Temperature dependences of the optical (closed symbols) and dielectric (open symbols) parameters for the 3CP liquid crystal in the temperature range of the transition from the nematic phase to the isotropic liquid phase.

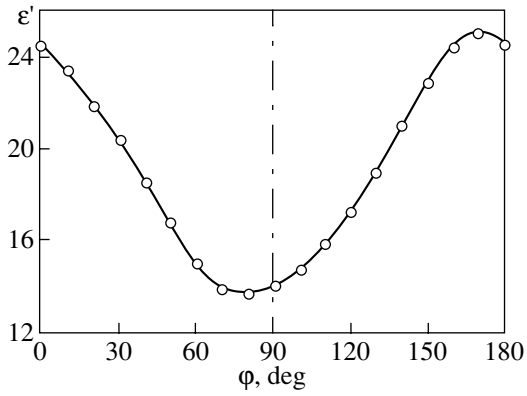

Fig. 3. Dependence of the permittivity of the 3CP liquid crystal on the angle between the director of molecules and the direction of the microwave pump field.

design made it possible to measure the dielectric spectra with a high accuracy despite the relatively small volume of the studied sample.

The real permittivities ε' were determined according to a standard technique, i.e., by measuring the difference in the resonance frequencies of the sensors with and without the sample. The imaginary permittivities ε'' were calculated from the change in the loaded Q-factor of the resonator after the liquid-crystal sample was placed in it. The amplitude–frequency characteristics of the microstrip sensors were recorded on an R4-37 automated meter intended for measuring complex transmission gain factors. The absolute errors in determining the dielectric characteristics were no larger than $\delta\varepsilon' \sim 0.05$ and $\delta\varepsilon'' \sim 0.1$. The required angle φ between the long axes of molecules in the 3CP sample and the direction of the microwave electric field in the measuring cell was specified by the appropriate direction of the static magnetic field $H = 2500$ Oe. The measurements were performed in a thermostat in the temperature range 0–50°C. The temperature was maintained accurate to ±0.1 K.

The temperature dependences of the ordinary (n_0) and extraordinary (n_e) refractive indices were measured at the wavelength $\lambda = 0.589$ μm with the use of an IRF-454B refractometer with a homeotropic orientation of the director in the measuring cell.

3. RESULTS AND DISCUSSION

The experimental temperature dependences of the ordinary n_0 (closed symbols *1*) and extraordinary n_e (closed symbols *2*) refractive indices are depicted in Fig. 2. This figure also shows the temperature dependences of the real parts of the longitudinal $\varepsilon'_\parallel$ (open symbols *3*) and transverse $\varepsilon'_\perp$ (open symbols *4*) permittivities, which were measured in parallel and perpendicular orientations of the liquid-crystal director with respect to the electric pump field. The heating rate of the studied sample was approximately equal to 4 K/h. The permittivities were measured at the pump frequency $f = 1$ MHz, at which the frequency dispersion does not manifest itself. In actual fact, the permittivities thus obtained are close to the static permittivities $\varepsilon'_{\parallel 0}$ and $\varepsilon'_{\perp 0}$. As could be expected, the optical and dielectric parameters exhibit a jump at the nematic–isotropic transition temperature ($T_c - T = 0$) of the liquid crystal. It is worth noting that the measured parameters only slightly depend on the temperature in both the nematic (curves *1–4*) and isotropic (curves *5*, *6*) phases.

Figure 3 shows the dependence of the real permittivity of the studied sample in the nematic phase on the angle between the direction of the static magnetic field **H** orienting the liquid-crystal molecules and the direction of the microwave electric field. This dependence was also measured at the pump frequency $f = 1$ MHz, which lies outside the frequency dispersion region of the sample. As is clearly seen, the dependence depicted in Fig. 3 is asymmetric about the vertical line passing through the point $\varphi = 90°$. At this angle, the long axes of the 3CP molecules are perpendicular to the pump field. Most likely, the observed asymmetry of the dependence $\varepsilon'(\varphi)$ indicates that the dipole moment μ of the molecule deviates from the long molecular axis. The deviation angle can be easily calculated from the shift in the minimum of the curve $\varepsilon'(\varphi)$ with respect to 90°. This angle is determined to be $\beta \approx 15°$.

Judging from the sufficiently high values of the static permittivities ($\varepsilon'_{\parallel 0} \approx 25$ and $\varepsilon'_{\perp 0} \approx 14.4$) and the dielectric anisotropy ($\Delta\varepsilon' = \varepsilon'_{\parallel 0} - \varepsilon'_{\perp 0} = 11.4$) of the studied sample, the 3CP molecules possess a relatively large dipole moment. It is well known [1–4] that, for all homologs ($n = 5$–9) of the liquid crystals belonging to the alkylcyanobiphenyl group *n*CB, in which the dipole moment ($\mu = 4.3$ D) is associated with the –C≡N cyano group, the dielectric parameters, as a rule, do not

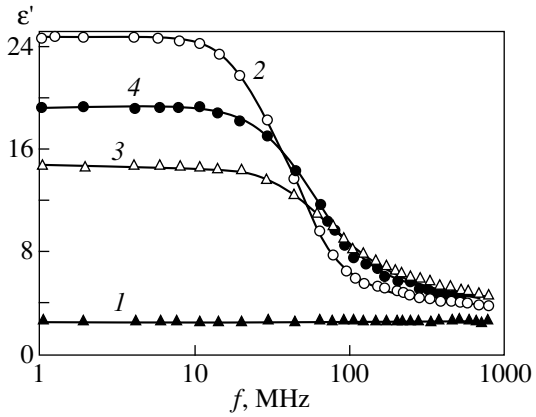

Fig. 4. Frequency dependences of the permittivity of the 3CP liquid crystal measured at different temperatures. T = (*1*) 0, (*2*, *3*) 45, and (*4*) 49°C.

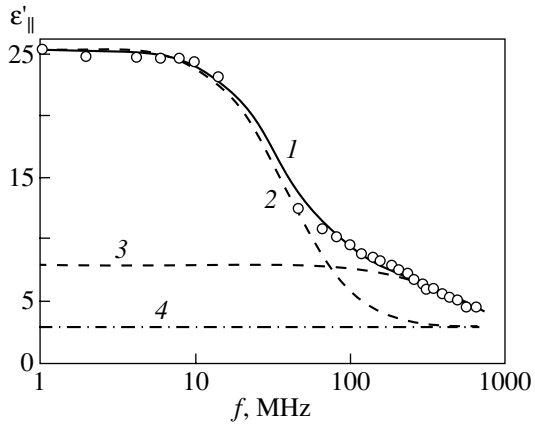

Fig. 5. Numerical approximation of the frequency dependence of the longitudinal permittivity by the sum of two Debye processes with different relaxation times.

exceed $\varepsilon'_{\|0}$ = 15–17, $\varepsilon'_{\perp 0}$ = 6–8, and $\Delta\varepsilon'$ = 8–9 in the temperature range $+1 < (T_c - T) < +5$°C. From the aforesaid it follows that, owing to the presence of the pyridine ring in molecules of the 3CP liquid crystal, the dipole moment of the 3CP molecule is 40–50% larger than that of the molecules of the alkylcyanobiphenyl liquid crystals.

The frequency dependences of the real permittivity for the 3CP sample in different states of the mesophase are shown in Fig. 4. Curve *1* was measured at T = 0°C, when the sample was in the solid crystalline state. Curves *2* and *3* represent the frequency dependences of the permittivities $\varepsilon'_{\|}$ and $\varepsilon'_{\perp}$, respectively, which were measured for the sample at T = 45°C in the nematic liquid-crystal state. Curve *4* was recorded at T = 49°C, when the sample was in the isotropic state. It can be seen that, in the solid phase, the dispersion is virtually absent and the permittivity is estimated as $\varepsilon'_s = 2.63 \pm 0.02$. It is interesting to note that this permittivity coincides very closely with the square of the refractive index $n_{is}^2 = 2.624$ for the high-temperature isotropic liquid phase of the 3CP liquid crystal. This indicates that, in the solid crystalline phase, the orientational contribution from the rotation of the dipole moment to the permittivity is absent and the observed value of ε'_s can be associated with the quick-response processes of displacement of intramolecular electric charges.

In order to describe the frequency dispersion of the longitudinal (parallel) $\varepsilon'_{\|}(f)$ and transverse (perpendicular) $\varepsilon'_{\perp}(f)$ permittivities of the 3CP sample in the nematic phase, we used different approaches. The longitudinal permittivity was approximated with due regard for the fact that the dipole moment of the molecule deviates from the long molecular axis through the angle β. According to the universally accepted concepts regarding the possible mechanisms of dielectric polarization in liquid crystals [1–4, 8], the dispersion can be approximated by the sum of two Debye processes with different relaxation times [9]; that is,

$$\varepsilon'_{\|}(f) - n_e^2 = \frac{(\varepsilon'_{\|0} - n_e^2)g_1}{1 + \omega^2\tau_{\|1}^2} + \frac{(\varepsilon'_{\|0} - n_e^2)g_2}{1 + \omega^2\tau_{\|2}^2}, \qquad (1)$$

where n_e is the extraordinary refractive index, $\varepsilon'_{\|0}$ is the static permittivity, $\omega = 2\pi f$, $\tau_{\|1}$ and $\tau_{\|2}$ are the relaxation times of two processes, and g_1 and g_2 are the weighting factors corresponding to these processes ($g_1 + g_2 = 1$).

The occurrence of two relaxation processes in the liquid crystal under investigation can be explained, in particular, by the misalignment of the dipole moment μ and the long axis of the liquid-crystal molecule. As a result, the longitudinal permittivity contains a contribution from the transverse component of the dipole moment μ and vice versa. Curve *1* in Fig. 5 represents the results of the numerical approximation performed for the experimental spectrum $\varepsilon'_{\|}(f)$ according to relationship (1). This curve is plotted for the following parameters of the liquid crystal: $\varepsilon'_{\|0}$ = 25.2, $\tau_{\|1} = 5 \times 10^{-9}$ s, $\tau_{\|2} = 3.8 \times 10^{-10}$ s, n_e = 1.7, g_1 = 0.78, and g_2 = 0.22.

As can be seen from Fig. 5, the frequency dependence of the longitudinal permittivity calculated within the proposed approximation is in good agreement with the experimental data over the entire frequency range covered. Dashed line *2* in Fig. 5 corresponds to the dispersion calculated at weighting factors g_1 = 1 and g_2 = 0 and fits the experimental data well only in the low-frequency dispersion region. Dashed line *3* represents the frequency dependence obtained at g_1 = 0.78 and g_2 = 0.22, which, by contrast, agrees reasonably with the experimental data only in the high-frequency dispersion region. Dot-dashed line *4* indicates the n_e^2 value to

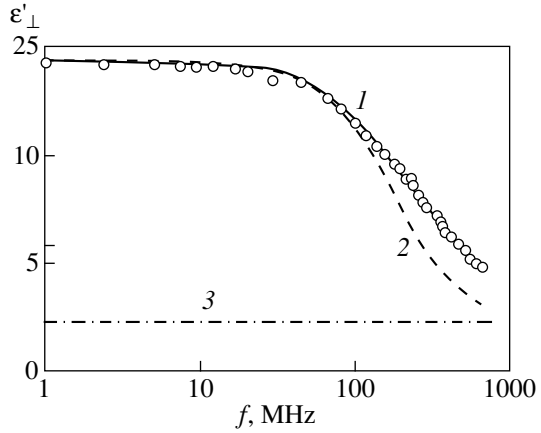

Fig. 6. Approximation of the frequency dependence of the transverse permittivity in terms of the Debye relaxation process with a continuous distribution of relaxation times.

which the longitudinal permittivity of the 3CP liquid crystal tends when $f \longrightarrow \infty$.

It should be noted that the relaxation times $\tau_{\parallel 1}$ and $\tau_{\parallel 2}$ characterize the dipole relaxation upon rotation of the molecule about the short and long axes. The ratio of the weighting factors g_2/g_1 is equal to the tangent of the angle β between the dipole moment and the long axis of the molecule. In our case, we have $\beta = 15.7°$. As can be seen, this value agrees closely with the angle $\beta \approx 15°$, which was determined from the experimental angular dependences of the permittivity (Fig. 3).

Let us now consider the transverse permittivity of liquid crystals whose relaxation frequency upon perpendicular pumping is higher than that upon parallel pumping. Under these conditions, the approximation of the transverse permittivity by one Debye relaxation process or even the sum of two Debye processes, as a rule, offers poor agreement with the experimental data. It can be seen from Fig. 6 that an increase in the frequency leads to an increase in the discrepancy between the experimental spectrum $\varepsilon'_\perp(f)$ (points in Fig. 6) and the Debye dependence with one relaxation time (dashed line *2*). This allows us to assume that small-scale vibrations of mobile alkyl groups in liquid-crystal molecules manifest themselves at high frequencies. In this situation, the dielectric relaxation times can be conveniently represented in the form of a continuous distribution in a specified time range. On this basis, the dielectric spectrum can be described by the expression [9]

$$\varepsilon'_\perp(f) - n_0^2 = (\varepsilon'_{\perp 0} - n_0^2)\int_0^\infty \frac{G(\tau)}{1 + (2\pi f\tau)^2} d\tau, \qquad (2)$$

where n_0 is the ordinary refractive index and $G(\tau)$ is the distribution function of relaxation times. In our case, the frequency dependence $\varepsilon'_\perp(f)$ was approximated by the Fröhlich distribution function [10], which is conveniently used in practical calculations; that is,

$$G(\tau) = \frac{kT}{u_0}\frac{1}{\tau}, \quad \tau_0 \le \tau \le \tau_1 = \tau_0 \exp(u_0/kT),$$
$$G(\tau) = 0, \quad \tau_1 \le \tau \le \tau_0, \qquad (3)$$

where u_0 is the boundary energy, which determines the range of uniform height distribution of the potential barriers of dipoles: $0 \le \delta u \le u_0$. The specific feature of the distribution function (3) is that it depends on the temperature. Since the relative width $(\tau_1 - \tau_0)/\tau_0$ of the relaxation time distribution decreases with an increase in the temperature, this dependence can be represented in the form

$$\frac{\tau_1 - \tau_0}{\tau_0} = \exp(u_0/kT) - 1. \qquad (4)$$

Next, we take the integral in expression (2) from τ_0 to τ_1 with due regard for the distribution function (3). As a result, the frequency dependence of the real part of the transverse permittivity has the form

$$\varepsilon'_\perp(f) - n_0^2 = (\varepsilon'_{\perp 0} - n_0^2)$$
$$\times \left[1 - \frac{kT}{2u_0}\ln\left(\frac{1 + \omega^2\tau_0^2\exp(2u_0/kT)}{1 + \omega^2\tau_0^2}\right)\right]. \qquad (5)$$

The results of the numerical approximation carried out according to formula (5) are shown by curve *1* in Fig. 6. This curve almost coincides with the experimental points. Dot-dashed line *3* in Fig. 6 indicates the n_0^2 level to which the transverse permittivity of the liquid crystal tends when $f \longrightarrow \infty$. Curve *1* is constructed for the following parameters: $\varepsilon'_{\perp 0} = 14.4$, $T = 318$ K, $u_0 = 1.52 \times 10^{-14}$ erg, $n_0 = 1.55$, $\tau_0 = 1.85 \times 10^{-10}$ s, and $\tau_1 = 2.39 \times 10^{-9}$ s. Note that, in this case, the relative width of the continuous distribution of relaxation times appears to be comparatively small: $(\tau_1 - \tau_0)/\tau_0 \approx 10$. However, the results obtained should be treated as tentative because, in the present work, the dielectric measurements were performed in an insufficiently wide range of frequencies. In order to refine the parameters of the approximation, it is necessary to use the experimental data obtained over the entire dispersion region. Moreover, as follows from the experimental results, the dielectric spectra of liquid crystals in the high-frequency dispersion region can exhibit resonance features [11], which should also be taken into account when approximating the spectra $\varepsilon'(f)$ [12]. It should be noted that curve *2* in Fig. 6 is plotted according to the Debye equation with one relaxation time $\tau_D = 9 \times 10^{-10}$ s, which approximately corresponds to the midpoint of the range $(\tau_1 - \tau_0)$.

The frequency dependence of the permittivity for the 3CP liquid crystal in the disordered isotropic phase

was also approximated on the basis of relationships (2) and (3), because it is quite reasonable that the isotropic phase is characterized by a continuous distribution of relaxation times. The excellent agreement between the calculated and experimental data was achieved with the following parameters for the liquid crystal in the isotropic phase: $\varepsilon'_{0is} = 19.3$, $T = 322$ K, $u_0 = 2.28 \times 10^{-13}$ erg, $n_i = 1.6$, $\tau_0 = 2.1 \times 10^{-10}$ s, and $\tau_1 = 6.12 \times 10^{-9}$ s. A comparison of these parameters with those for the 3CP liquid-crystal compound in the nematic phase shows that the energy u_0 increases by one order of magnitude and that the upper limit of the relaxation time range changes significantly. As a result, the relative width $(\tau_1 - \tau_0)/\tau_0$ increases by a factor of more than two.

4. CONCLUSIONS

Thus, the permittivities of the 5-propyl-2-(*p*-cyanophenyl)-pyridine liquid-crystal compound in different phase states were measured over wide ranges of frequencies and temperatures. It was found that the dipole moment of the 3CP molecule significantly deviates from the long molecular axis. The deviation angle was determined to be $\beta \approx 15°$. It was demonstrated that the frequency dependence of the longitudinal permittivity $\varepsilon'_{\parallel}(f)$ for the 3CP liquid crystal in the nematic phase is adequately described by the sum of two Debye processes with different relaxation times. However, when approximating the transverse permittivity $\varepsilon'_{\perp}(f)$ in the nematic phase and the permittivity $\varepsilon'_{is}(f)$ in the isotropic phase of the 3CP compound, the Debye formulas should account for the continuous distribution of relaxation times in a specified time range. It was revealed that the temperature dependences of the static permittivities are similar to those of the refractive indices in the temperature range of the phase transition from the nematic liquid crystal to the isotropic liquid.

ACKNOWLEDGMENTS

This work was supported by the Russian Foundation for Basic Research, project no. 00-03-32206.

REFERENCES

1. D. A. Dunmur, M. R. Manterfield, W. H. Miller, and J. K. Dunleavy, Mol. Cryst. Liq. Cryst. **45**, 127 (1978).
2. P. G. Gummins, D. A. Dunmur, and D. A. Laidler, Mol. Cryst. Liq. Cryst. **30**, 109 (1975).
3. B. R. Ratna and R. Shashidar, Mol. Cryst. Liq. Cryst. **42**, 185 (1977).
4. J. M. Wacrenier, C. Druon, and D. Lippens, Mol. Phys. **43**, 97 (1981).
5. B. A. Belyaev, N. A. Drokin, V. F. Shabanov, and V. N. Shepov, Fiz. Tverd. Tela (St. Petersburg) **42** (5), 956 (2000) [Phys. Solid State **42**, 987 (2000)].
6. B. A. Belyaev, N. A. Drokin, and V. N. Shepov, Zh. Tekh. Fiz. **65** (2), 189 (1995) [Tech. Phys. **40**, 216 (1995)].
7. B. A. Belyaev, N. A. Drokin, V. F. Shabanov, and V. N. Shepov, Zh. Tekh. Fiz. **72** (4), 99 (2002) [Tech. Phys. **47**, 470 (2002)].
8. L. M. Blinov, *Electro-Optical and Magneto-Optical Properties of Liquid Crystals* (Nauka, Moscow, 1978; Wiley, New York, 1983).
9. A. A. Potapov and M. S. Mitsek, *Dielectric Polarization* (Irkutsk. Gos. Univ., Irkutsk, 1986).
10. H. Frölich, *Theory of Dielectrics*, (Oxford Univ. Press, Oxford, 1958; Inostrannaya Literatura, Moscow, 1960).
11. B. A. Belyaev, N. A. Drokin, V. F. Shabanov, and V. N. Shepov, Pis'ma Zh. Éksp. Teor. Fiz. **66** (4), 251 (1997) [JETP Lett. **66**, 271 (1997)].
12. B. A. Belyaev, N. A. Drokin, V. F. Shabanov, and V. N. Shepov, Fiz. Tverd. Tela (St. Petersburg) **42** (3), 564 (2000) [Phys. Solid State **42**, 577 (2000)].

Translated by O. Borovik-Romanova

Physics of the Solid State, Vol. 45, No. 4, 2003, pp. 802–808. Translated from Fizika Tverdogo Tela, Vol. 45, No. 4, 2003, pp. 761–766.

FULLERENES AND ATOMIC CLUSTERS

Thermodynamic and Dilatometric Properties of the Dimerized Phase of a C_{60} Fullerene

A. V. Markin*, N. N. Smirnova*, B. V. Lebedev†*, A. G. Lyapin, M. V. Kondrin**, and V. V. Brazhkin****

** Research Institute of Chemistry, Nizhniĭ Novgorod State University, pr. Gagarina 23/5, Nizhniĭ Novgorod, 603950 Russia*

*** Vereshchagin Institute of High-Pressure Physics, Russian Academy of Sciences, Troitsk, Moscow oblast, 142190 Russia*

e-mail: alyapin@hppi.troitsk.ru

Received July 4, 2002

Abstract—This paper reports on the results of complex investigations into the structural, thermodynamic, and dilatometric properties of the C_{60} dimerized phase prepared under compression of a C_{60} fullerite at a pressure up to 8 GPa and a temperature of 290 K. It is demonstrated that the dimerized phase has a face-centered cubic structure with a lattice parameter $a = 14.02 \pm 0.05$ Å. The dimeric structure of the studied sample is confirmed by x-ray diffraction analysis. According to the dilatometric data, the volume jump observed in the vicinity of the orientational transition for the dimerized phase is estimated to be approximately 30 times less than that for the C_{60} fullerite. The temperature dependence of the heat capacity of the $(C_{60})_2$ crystalline dimer is examined using precision adiabatic vacuum calorimetry under normal pressure in the temperature range from $T \longrightarrow 0$ K to 340 K. The results obtained are used in the calculations of thermodynamic functions, namely, the heat capacity $C_p^0(T)$, the enthalpy $H^0(T) - H^0(0)$, the entropy $S^0(T)$, and the Gibbs function $G^0(T) - H^0(0)$. The fractal dimension D is determined as a function of the heat capacity. The standard entropy of the formation of the $(C_{60})_2$ crystalline dimer from a simple compound (graphite) at $T = 298.15$ K and normal pressure is calculated. © *2003 MAIK "Nauka/Interperiodica".*

1. INTRODUCTION

It is known that appropriate treatment of C_{60} fullerite crystals at high pressures and temperatures brings about the formation of stable (graphite or diamond) and numerous metastable carbon states [1–9]. For example, in the stability region of a C_{60} molecular cluster, crystalline polymerized phases of C_{60} can be formed as a result of the [2 + 2] cycloaddition reaction between two parallel C=C double bonds of the neighboring carbon atoms on the surface of two C_{60} molecules [10]. Among the most important crystalline polymerized phases are linear (one-dimensional) C_{60} polyfullerenes, planar (two-dimensional) C_{60} polyfullerenes of two types, crystals of nearly continuous three-dimensional C_{60} polymers, and weakly polymerized phases formed by $(C_{60})_2$ dimer molecules. An increase in the pressure and temperature during treatment of C_{60} fullerite crystals leads to distortion and decay of the C_{60} molecules with the formation of amorphous disordered phases in which carbon atoms reside in the sp^2 and sp^3 hybridized states [5, 8, 9].

In order to gain a better insight into the nature of C_{60} metastable phases, it is necessary to use a combination of spectral, x-ray diffraction, and high-precision calorimetric methods [11–14]. The influence of physical conditions (pressure p and temperature T) of preparing the C_{60} crystalline polymerized phases on their thermodynamic properties was noted for the first time in [15]. The first results of the study of the orientational phase transition in C_{60} partially dimerized phases were reported in [16]. However, the fundamental understanding of the mechanism of phase transformations in C_{60} calls for detailed structural investigation and physicochemical interpretation of the orientational transition in the aforementioned phases.

The aim of the present work was to investigate the structural, thermodynamic, and dilatometric properties of the C_{60} dimerized phase, which was synthesized under compression of a C_{60} fullerite at a pressure up to 8 GPa and a temperature of 290 K. For this purpose, we measured the temperature dependence of the heat capacity of the $(C_{60})_2$ crystalline phase at temperatures ranging from 6 to 340 K, examined the physical transformations during heating and cooling of the dimerized phase, and evaluated the thermodynamic characteristics of these transformations. The results obtained were used to calculate thermodynamic functions, namely, the heat capacity $C_p^0(T)$, the enthalpy $H^0(T) - H^0(0)$, the entropy $S^0(T)$, and the Gibbs function $G^0(T) - H^0(0)$ in the temperature range from $T \longrightarrow 0$ to 340 K and the standard entropy of formation of the $(C_{60})_2$ crystalline dimer from a simple compound (graphite) at 298.15 K and normal pressure. Moreover, we determined the fractal dimension D as a function of the heat capacity.

† Deceased.

2. SAMPLE PREPARATION AND EXPERIMENTAL TECHNIQUE

2.1. Synthesis and Structure of the Samples under Investigation

The samples to be studied were synthesized using a C_{60} fullerite prepared at the Institute of Organometallic Chemistry, Russian Academy of Sciences (Nizhniĭ Novgorod). According to high-performance liquid chromatography, the impurity content in the C_{60} fullerite did not exceed 0.2 wt %. The C_{60} fullerite was treated at a pressure of 8 GPa and a temperature of 290 K for ~1 min in a toroid-type high-pressure chamber [17] with the use of a copper container. The high-pressure chamber was calibrated against the phase transitions in Bi. Since the effective volume of the chamber was limited, several compression cycles under identical conditions were carried in order to synthesize the required amount of the sample. The structure of the studied samples was determined by x-ray diffraction (CuK_α radiation) on a diffractometer and with the use of x-ray powder diffraction photographs. In the latter case, a finely dispersed powder of NaCl was added for precise calibration. Hereafter, the prepared sample of the C_{60} dimerized phase will be designated as DS.

2.2. Dilatometric Measurements

The thermal expansion was measured using a capacitance dilatometer with a design similar to that described in [18]. The elongation per unit length of the sample was calculated from the temperature dependence of the measuring capacitance $C(T)$ according to the formula

$$\frac{\Delta d}{d} = \frac{\pi\varepsilon_0 r^2(1+\alpha_{Cu}(T))^2}{d} \times\left(\frac{1}{C(T)} - \frac{1}{C(T_0 = 273\ \mathrm{K})} + d\alpha_{Cu}(T)\right). \quad (1)$$

Here, $\alpha_{Cu}(T)$ is the thermal expansion coefficient of the material of the measuring cell (in our case, copper), d is the length of the sample, Δd is the elongation of the sample, and r is the radius of the measuring capacitor plates. The setup was calibrated against the aluminum (99.999%) sample. The discrepancy between the obtained results and the data available in the literature [19] did not exceed 5%. The temperature variation was accomplished by cooling the measuring cell in liquid-nitrogen vapors, followed by controlled heating at a rate of 0.007 K/s.

2.3. Instruments and Techniques for Heat Capacity Measurements

The heat capacity of the DS sample was measured on a BKT-3 automated adiabatic vacuum calorimeter. The design of the calorimeter and the technique of measuring the heat capacity C_p^0 were described in [20, 21]. The results of calibration and tests of the calorimeter demonstrated that the error in measuring the heat capacity of the materials is ± 2% at the liquid-helium temperature, decreases to ± 0.5% at 40 K, and is approximately equal to ± 0.2% in the temperature range 40–340 K.

The heat capacity C_p^0 of the DS sample was examined in the temperature range 6–340 K. A weighed portion (0.5723×10^{-3} kg) of the material was placed in a calorimetric cell. In three series of measurements, we obtained 209 experimental values of C_p^0. In all cases, the heat capacity of the studied sample constituted from 25 to 50% of the total heat capacity of the calorimetric cell with the material. The experimental values of C_p^0 were averaged on a computer with the use of power and semilogarithmic polynomials. The averaging was performed in such a way that the root-mean-square deviation of the experimental points from the averaged curve $C_p^0 = f(T)$ did not exceed the error in measuring the heat capacity.

3. RESULTS AND DISCUSSION

3.1. Structural Investigation

The x-ray diffraction data (CuK_α radiation) obtained for the DS sample are in reasonable agreement with those for the C_{60} initial fullerite (see, for example, [3, 4]). The positions of the diffraction reflections observed are well described under the assumption of a face-centered cubic structure composed of C_{60} molecules. Note that the lattice parameter of the DS sample $a = 14.02 \pm 0.05$ Å is somewhat smaller than that of the C_{60} initial fullerite ($a_0 = 14.17$ Å). Owing to the decrease in the lattice parameter, the weak reflection (200) is seen in the diffraction curves of the DS sample. This reflection is absent in the diffraction curves of the C_{60} initial sample due to the extinction caused by the effect of C_{60} molecules.

With the use of the lattice parameter a, it is possible to estimate the fraction of pairs of the nearest neighbor C_{60} molecules, which are covalently bonded through the [2 + 2] cycloaddition reaction [10]. According to the model of partially polymerized face-centered cubic phases of C_{60} [7, 22], a pair of nearest neighbor molecules (bonded through covalent or van der Waals interactions) can occur in two different states. Within this model, by analogy with the Vegard law for solid solutions, the lattice parameter a for a polymerized face-centered cubic phase can be described, to a first approximation, by a linear function of the fraction of polymerized molecular pairs n_p; that is,

$$a = a_0 + (a_p - a_0)n_p. \quad (2)$$

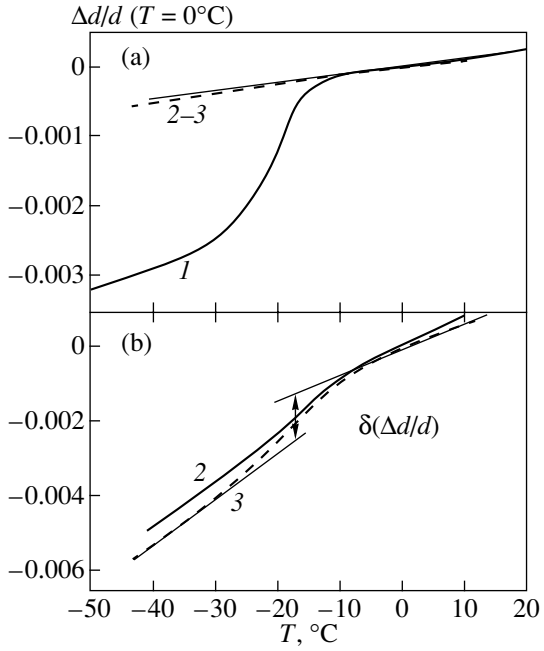

Fig. 1. (a) Temperature dependences of the linear size of (*1*) the pressed C_{60} fullerene sample and (*2*, *3*) two DS samples. (b) The same dependences on an enlarged scale. Arrows illustrate the procedure of determining the volume jump associated with the contribution of the orientational transition occurring in the C_{60} fullerite impurity.

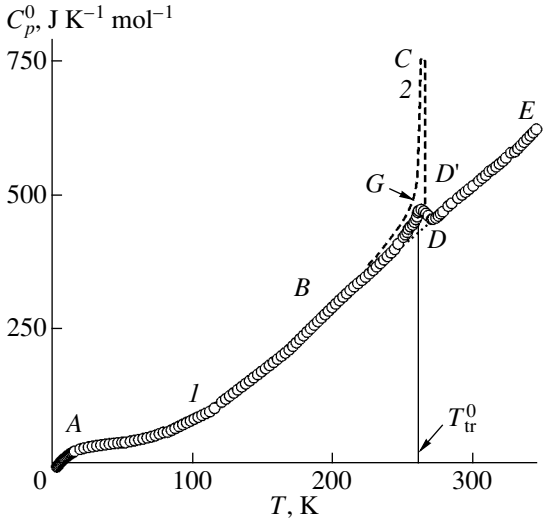

Fig. 2. Temperature dependences of the heat capacity of (*1*) the DS sample and (*2*) the C_{60} initial fullerite [24].

In this case, the extreme structures are the face-centered cubic lattice of the initial fullerite (a_0 = 14.17 Å) and the completely three-dimensionally polymerized phase with the lattice parameter a_p. In [7, 22], the lattice parameter for the completely polymerized phase was estimated as $a_p \sim$ 12.2–12.3 Å. Hence, we obtain $n_p \simeq$ 0.076–0.080 for the DS sample. With due regard for the number of nearest neighbors Z = 12 in the face-centered cubic lattice, it is easy to calculate that the probability of forming a covalent bond between two molecules is approximately equal to 0.91–0.96. From analyzing the structural data, we can make the inference that the DS sample consists predominantly of the $(C_{60})_2$ dimerized phase with a low content of C_{60} (approximately 4–9%). Note that this estimate of the fraction of the C_{60} initial fullerite in the DS sample is relatively rough, because, first, formula (2) is not exact and, second, the dimerized phase can contain linear molecules with a higher degree of polymerization, for example, $(C_{60})_3$.

3.2. Dilatometric Investigation

The experimental temperature dependences of the linear size of the DS sample are depicted in Fig. 1. It can be seen that, at temperatures close to 260 K, the C_{60} initial fullerite is characterized by a volume jump due to a phase transition from the orientationally ordered simple cubic phase to the orientationally disordered face-centered cubic phase [23]. However, the analogous anomaly for the DS sample is substantially less pronounced. It is clear that the observed decrease in the volume jump in the phase transition range is associated with the dimerization of the C_{60} fullerite.

Since the linear expansion coefficients were different at temperatures below and above the volume anomaly (Fig. 1b), the volume jump ΔV upon the orientational phase transition in the DS sample was determined from the midpoint of the phase transition range. As a result, we obtained ΔV (DS)/ΔV (C_{60}) ~ Δd (DS)/Δd (C_{60}) ~ 0.03.

Under the assumption that, for the studied sample, the residual volume anomaly observed in the vicinity of 260 K is determined by the contribution of the C_{60} fullerite impurity, the fraction of C_{60} in the DS sample can be estimated at ~3–4%. However, the actual structural transition in the DS sample can be more intricate in character. In particular, the orientational effects associated with $(C_{60})_2$ dimers can play a significant role, on the one hand, and the interaction of C_{60} molecules with surrounding dimers can affect the volume jump, on the other.

3.3. Thermodynamic Characteristics

All the experimental data on the heat capacity C_p^0 and the dependence $C_p^0 = f(T)$ (curve *1*) are presented in Fig. 2. For comparison, Fig. 2 also shows the temperature dependence of the heat capacity of the C_{60} initial fullerite (curve *2*) according to the data taken from [24]. It can be seen from Fig. 2 that, in the range 185–280 K, the physical transformation manifests itself in the temperature dependences $C_p^0 = f(T)$ for both the DS sample and the C_{60} fullerite. However, judging from the ratio

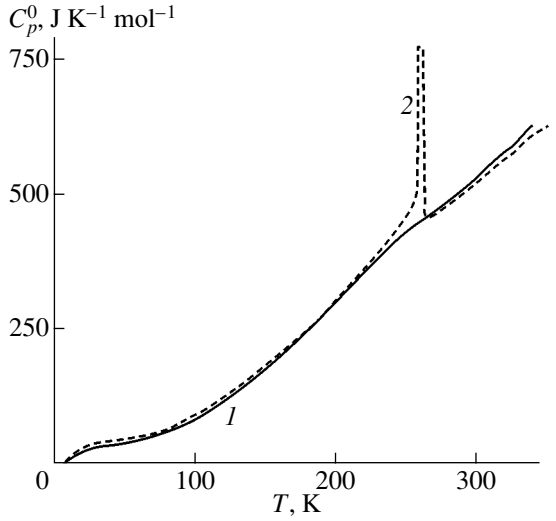

Fig. 3. Temperature dependences of (*1*) the calculated heat capacity of the $(C_{60})_2$ crystalline dimer and (*2*) the heat capacity of the C_{60} initial fullerite [24].

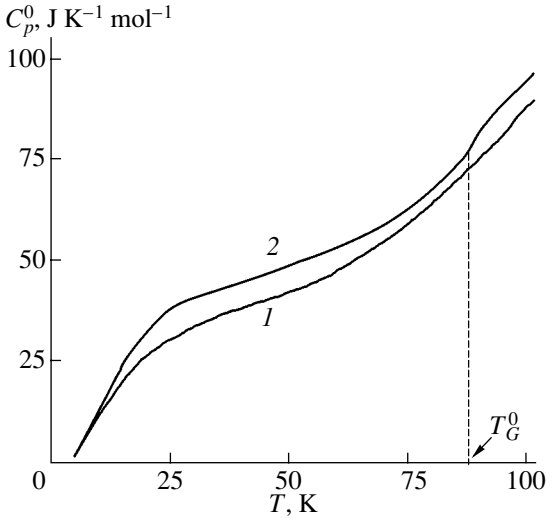

Fig. 4. Temperature dependences of the heat capacity of (*1*) the $(C_{60})_2$ crystalline dimer and (*2*) the C_{60} initial fullerite [24] in the low-temperature range.

between the areas under the corresponding portions of the heat capacity curves (*BGDB* and *BCD'B* in Fig. 2) in the transition range, the enthalpy of transition in the DS sample is several times less than that in the C_{60} fullerite. According to [23–25], the transformation in the C_{60} fullerite upon heating is associated with the phase transition from the orientationally ordered simple cubic phase to the orientationally disordered face-centered cubic phase in which the C_{60} molecules execute almost free rotations. This transformation is the reversible phase transition. The transition temperature T_{tr}^0 for the DS sample is equal to 261.2 K when it is taken as the temperature of the maximum apparent heat capacity of the sample in the transition range 185–280 K ($C_{p,\max}^0$ = 474.2 J K^{-1} mol^{-1}). The enthalpy of the transition $\Delta H_{tr}^0 = 0.77 \pm 0.03$ kJ mol^{-1} was graphically determined as the area bounded by the curve *BGDB* (Fig. 2). The characteristics of the transition in the C_{60} fullerite are as follows [24]: the transition range, 185–275 K; T_{tr}^0 = 260.7 K ($C_{p,\max}^0$ = 34747 J K^{-1} mol^{-1}); and $\Delta H_{tr}^0 = 7.46 \pm 0.15$ kJ mol^{-1}. It is reasonable to assume that the transition in the DS sample under consideration is due to the presence of the C_{60} initial fullerite, which does not transform into $(C_{60})_2$ in the course of treatment under a pressure p and temperature T. On this basis, the content of the C_{60} fullerite in the DS sample can be easily estimated from the relationship

$$n\ (\mathrm{C_{60}}, \text{mol \%}) = [\Delta H_{tr}^0(\mathrm{DS})/\Delta H_{tr}^0(\mathrm{C_{60}})] \times 100\% \quad (3)$$

by substituting the corresponding numerical values.

The C_{60} content thus calculated for the DS sample is equal to 10 mol %, which agrees well with the C_{60} fraction determined from the x-ray diffraction data. In further calculations, we will assume that the studied sample contains 10 mol % C_{60} and 90 mol % $(C_{60})_2$.

The normal heat capacity of the DS sample [the mixture of C_{60} and $(C_{60})_2$] in the transition range were obtained by interpolating the curve $C_p^0 = f(T)$ from the point *B* to the point *D* (the dotted line *BD* in Fig. 2). By using the heat capacities of the mixture (the DS sample) and the C_{60} fullerite [24] and knowing the quantitative composition of the mixture, the heat capacity of the $(C_{60})_2$ dimer per mole of C_{60} can be calculated from the formula

$$0.9C_p^0\{(\mathrm{C_{60}})_2\} + 0.1C_p^0(\mathrm{C_{60}}) = C_p^0(\mathrm{DS}), \quad (4)$$

where $C_p^0\{(C_{60})_2\}$, $C_p^0(C_{60})$, and $C_p^0(DS)$ are the molar heat capacities of the dimer, fullerite, and DS sample at the corresponding temperatures. Now, we express $C_p^0\{(C_{60})_2\}$ from formula (4), substitute the numerical values of C_p^0 at the corresponding temperatures, and calculate the heat capacities of the $(C_{60})_2$ dimer per mole of C_{60}.

The results obtained were used to construct the temperature dependence of the calculated heat capacity C_p^0 of the $(C_{60})_2$ crystalline dimer (Figs. 3, 4). For comparison, the dependence $C_p^0(T)$ for the C_{60} initial fullerite [24] is also plotted in Figs. 3 and 4. A comparison of these dependences shows that, in the temperature range from $T \longrightarrow 0$ K to T = 120 K, the heat capacity C_p^0 of $(C_{60})_2$ is less than the heat capacity of C_{60}; the maximum difference (32%) is observed at 25 K. In the tem-

Thermodynamic functions of the $(C_{60})_2$ crystalline dimer per mole of C_{60} (M = 720.66 g mol^{-1}) at p = 101.325 kPa

T, K	$C_p^0(T)$, J K^{-1} mol^{-1}	$H^0(T) - H^0(0)$, kJ mol^{-1}	$S^0(T)$, J K^{-1} mol^{-1}	$-[G^0(T) - H^0(0)]$, kJ mol^{-1}
5	3.11	0.00410	1.10	0.00139
10	11.9	0.0420	5.99	0.0179
15	19.24	0.1197	12.20	0.06330
20	25.10	0.2315	18.59	0.1404
25	29.83	0.3710	24.80	0.2490
30	33.36	0.5294	30.56	0.3875
40	38.14	0.8890	40.88	0.7461
50	42.24	1.291	49.83	1.201
100	87.40	4.342	90.34	4.692
150	180.6	10.85	141.8	10.43
200	302.9	22.87	210.1	19.16
250	433.1	41.40	292.3	31.68
298.15	528.3	64.49	376.5	47.77
300	532.8	65.47	379.8	48.47
340	628.5	88.62	452.1	65.10

perature range from 120 to 250 K, the heat capacity C_p^0 of the dimer exceeds the heat capacity of the C_{60} fullerite by no more than 2%. At $T > 250$ K, the heat capacities C_p^0 of both compounds almost coincide (the difference is within the limits of experimental error in the given temperature range). No indications of any physical transformation are observed in the dependence $C_p^0(T)$ for $(C_{60})_2$.

Apart from the large numerical differences between the heat capacities C_p^0 of the studied dimer and the C_{60} fullerite, these compounds differ in the behavior of the temperature dependence of the heat capacity. Evidently, this is associated with the difference in the heterodynamics of their structures. According to the Tarasov theory of heat capacity of solids [26, 27], which, like the Debye theory of heat capacity [28, 29], is a special case of multifractal generalization of the heat capacity theory, the heat capacity C_p^0 of solids with chain, layered, and three-dimensional structures at low temperatures is proportional to T^1, T^2, and T^3, respectively. In the fractal theory of heat capacity [28, 29], the exponent of T in the heat capacity function is referred to as the fractal dimension and is denoted by D. It is of interest to evaluate the fractal dimension of the $(C_{60})_2$ crystalline dimer and to compare it with the corresponding dimension of the C_{60} fullerite. Yakubov [28] demonstrated that the fractal dimension D can be estimated from the slope of the straight-line portions in the experimental dependence of the heat capacity $\ln C_v$ on $\ln T$. This particularly follows from the relationship

$$C_v = 3D(D+1)kN\gamma(D+1)\xi(D+1)(T/\Theta_{\max})^D, \quad (5)$$

where N is the number of particles in the molecule, k is the Boltzmann constant, $\gamma(D+1)$ is the gamma function, $\zeta(D+1)$ is the Riemann ζ function, and $\Theta_{\max}$ is the characteristic temperature. According to Iztotov *et al.* [29], the fractal dimension D can vary from 1 to 4.

Without loss in accuracy, we can assume that $C_p^0 = C_v$ at $T < 50$–60 K. From the dependence of $\ln C_p^0$ on $\ln T$ for the $(C_{60})_2$ dimer with the use of relationship (5), we find that $D = 1$ and $\Theta_{\max} = 120.4$ K in the temperature range 20–50 K. In this temperature range, relationship (5) with the above parameters D and $\Theta_{\max}$ reproduces the experimental heat capacities C_p^0 to within an error of 1%. At lower temperatures, the heat capacity of any material irrespective of its heterodynamic structure (chain, layered, chain–layered, and other structures) obeys the Debye law ($C \sim T^3$).

At $T < 12$ K, the heat capacity C_p^0 of the dimer can be adequately described by the Debye law:

$$C_p^0 = nD_0(\Theta_{D_0}/T), \quad (6)$$

where D_0 is the Debye heat capacity function and n and Θ_{D_0} are the fitting parameters. At $n = 3$ and $\Theta_{D_0} = 41.60$ K, relationship (6) reproduces the experimental heat capacities C_p^0 in the temperature range 7–12 K to within an error of approximately 0.6%.

At $T < 50$ K, the C_{60} fullerite has the fractal dimension $D = 3$, which is consistent with its three-dimensional structure. For a C_{60} dimer characterized by the normal intermolecular interaction at temperatures from 20 to 50 K, we obtain $D = 1$. Most likely, this dimension

is retained at $T > 50$ K. Consequently, the $(C_{60})_2$ crystalline dimer has a chain structure.

The data obtained from the dependence $C_p^0(T)$ for the $(C_{60})_2$ crystalline dimer were used for calculating its thermodynamic functions in the range from $T \longrightarrow 0$ K to 340 K (see table). The enthalpy $H^0(T) - H^0(0)$ and the entropy $S^0(T)$ were determined by numerical integration of the curves $C_p^0 = f(T)$ and $C_p^0 = f(\ln T)$ over the temperature. The Gibbs function $G^0(T) - H^0(0)$ was calculated from the values of $H^0(T) - H^0(0)$ and $S^0(T)$ at the corresponding temperatures. The procedure of calculating the functions was described, for example, in [30].

The entropy $\Delta_r S^0$ of the dimerization reaction at 298.15 K,

$$2C_{60}(cr) \longrightarrow (C_{60})_2(cr), \quad (7)$$

was calculated from the entropy of the dimer (see table) and the entropy of the C_{60} initial fullerite [24]. In relationship (7), the physical (crystalline) state of the reactants is given in parentheses. According to relationship (7), we have $\Delta_r S^0 = -100$ J K^{-1} mol^{-1}. As could be expected, the entropy in reaction (7) decreases, as is the case in any association reaction. When calculating the entropy $\Delta_r S^0$ of the dimer, we assumed that $S^0(0) = 0$.

The standard entropy $\Delta_f S^0$ of the formation of the crystalline dimer from a simple compound (graphite),

$$120C(gr) \longrightarrow (C_{60})_2(cr) \quad (8)$$

was calculated from the absolute entropies of the graphite (gr) [31] and the dimer (see table). At 298.15 K, this entropy of formation was determined to be $\Delta_f S^0 = 64.2$ J K^{-1} mol^{-1}. The relatively small change in the entropy in the process under investigation can be explained by the fact that both the initial carbon (graphite) and the final product (the C_{60} fullerene dimer) are highly ordered systems with covalent bonds.

4. CONCLUSIONS

Thus, the DS sample synthesized under compression of a C_{60} fullerite at a pressure of 8 GPa and a temperature of 290 K was thoroughly studied using structural, thermodynamic, and dilatometric methods. The results obtained in these investigations are in good agreement. It was demonstrated that the dimerized phase consists predominantly of the $(C_{60})_2$ dimer with an insignificant amount of the C_{60} initial fullerite. According to different techniques, the content of the C_{60} initial fullerite in the studied phase was estimated at ~3–10%.

ACKNOWLEDGMENTS

This work was supported by the International Association of Assistance for the promotion of cooperation with scientists from the New Independent States of the former Soviet Union (project no. 00-807), the Russian Foundation for Basic Research (project nos. 02-03-06510, 01-03-32061, 00-03-40136, and 01-02-17543), and the Ministry of Science and Technologies of the Russian Federation (project no. 15.01.1996).

REFERENCES

1. Y. Ywasa, T. Arima, R. M. Fleming, *et al.*, Science **264**, 1570 (1994).
2. I. O. Bashkin, V. I. Rashchupkin, A. F. Gurov, *et al.*, J. Phys.: Condens. Matter **6**, 7491 (1994).
3. M. Nunnez-Requeiro, L. Marques, J.-L. Hodeau, *et al.*, Phys. Rev. Lett. **74**, 278 (1995).
4. V. V. Brazhkin, A. G. Lyapin, Yu. V. Antonov, *et al.*, Pis'ma Zh. Éksp. Teor. Fiz. **62**, 328 (1995) [JETP Lett. **62**, 350 (1995)].
5. V. D. Blank, S. G. Buga, G. A. Dubitsky, *et al.*, Phys. Lett. A **220**, 149 (1996).
6. V. V. Brazhkin and A. G. Lyapin, Usp. Fiz. Nauk **166**, 893 (1996) [Phys.–Usp. **39**, 837 (1996)].
7. V. V. Brazhkin, A. G. Lyapin, S. V. Popova, *et al.*, Phys. Rev. B **56**, 11465 (1997).
8. V. V. Brazhkin, A. G. Lyapin, R. N. Voloshin, *et al.*, Pis'ma Zh. Éksp. Teor. Fiz. **69**, 822 (1999) [JETP Lett. **69**, 869 (1999)].
9. V. A. Davydov, L. S. Kashevarova, A. V. Rakhmanina, *et al.*, Phys. Rev. B **61**, 11936 (2000).
10. A. M. Rao, P. Zhou, K. A. Wang, *et al.*, Science **259**, 955 (1993).
11. B. Sundqvist, A. Fransson, A. Inaba, *et al.*, Annu. Rep. Microcalorim. Res. Center Fac. Sci. Osaka Univ. **6**, 705 (1998).
12. A. Inaba, T. Matsuo, A. Fransson, and B. Sundqvist, J. Chem. Phys. **110**, 12226 (1999).
13. B. V. Lebedev, K. B. Zhogova, N. N. Smirnova, *et al.*, Thermochim. Acta **364**, 23 (2000).
14. B. V. Lebedev, K. B. Zhogova, V. D. Blank, and R. Kh. Bagramov, Izv. Akad. Nauk, Ser. Khim., No. 2, 277 (2000).
15. B. V. Lebedev and A. V. Markin, Fiz. Tverd. Tela (St. Petersburg) **44**, 419 (2002) [Phys. Solid State **44**, 434 (2002)].
16. M. N. Kondrin, A. G. Lyapin, V. V. Brazhkin, and S. V. Popova, Fiz. Tverd. Tela (St. Petersburg) **44**, 431 (2002) [Phys. Solid State **44**, 447 (2002)].
17. L. G. Khvostantsev, L. F. Vereshchagin, and A. P. Novikov, High Temp.–High Press. **9**, 637 (1977).
18. R. Pott and R. Schefzyk, J. Phys. E **16**, 444 (1983).
19. F. R. Kroeger and C. A. Swenson, J. Appl. Phys. **43**, 853 (1977).
20. V. M. Malyshev, G. A. Mil'ner, E. L. Sorkin, and V. F. Shibakin, Prib. Tekh. Éksp., No. 6, 195 (1985).
21. R. M. Varushchenko, A. I. Druzhinina, and E. L. Sorkin, J. Chem. Thermodyn. **29**, 623 (1997).
22. V. V. Brazhkin, A. G. Lyapin, and S. V. Popova, Pis'ma Zh. Éksp. Teor. Fiz. **64**, 755 (1996) [JETP Lett. **64**, 802 (1996)].

23. P. A. Heiney, J. E. Fisher, A. R. McChie, *et al.*, Phys. Rev. Lett. **66**, 2911 (1991).
24. B. V. Lebedev, K. B. Zhogova, T. A. Bykova, *et al.*, Izv. Akad. Nauk, Ser. Khim., No. 9, 2229 (1996).
25. A. Dvorkin, H. H. Szwarc, and H. Allouchi, C. R. Acad. Sci., Ser. II **312**, 979 (1991).
26. V. V. Tarasov, Zh. Fiz. Khim. **24**, 111 (1950).
27. V. V. Tarasov and G. A. Yunitskiĭ, Zh. Fiz. Khim. **39**, 2077 (1965).
28. T. S. Yakubov, Dokl. Akad. Nauk SSSR **310**, 145 (1990).
29. A. D. Iztotov, O. V. Shebershneva, and K. S. Gavrichev, in *Proceedings of the All-Russian Conference on Thermal Analysis and Calorimetry* (Kazan, 1996), p. 200.
30. B. V. Lebedev, Thermochim. Acta **297**, 143 (1997).
31. *Thermodynamic Constants of Materials: A Handbook*, Ed. by V. P. Glushko (VINITI, Moscow, 1965), No. 1, Part 1.

Translated by O. Borovik-Romanova